Capricorn
DISTAL FOOTPRINTS

MRIWA M436: Distal Footprints of Giant Ore Systems, Capricorn WA – Case Study

MRIWA Report Number 436

Compilation Editor: T. Munday

20 May 2019

CSIRO Technical Report Number: EP192958

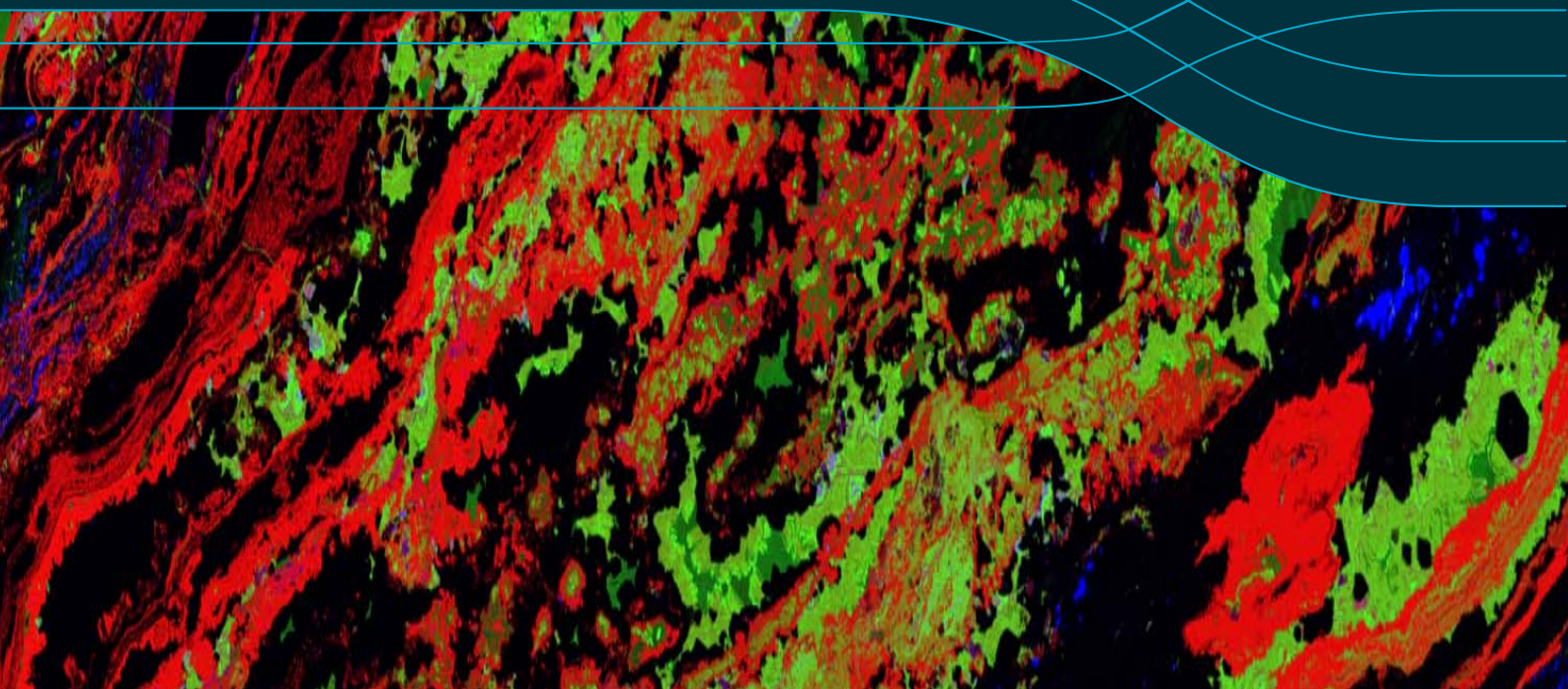

NRSP NATIONAL RESOURCE SCIENCES PRECINCT
CSIRO
Curtin University
THE UNIVERSITY OF WESTERN AUSTRALIA
Geological Survey of Western Australia
SCIENCE AND INDUSTRY ENDOWMENT FUND
mriwa Minerals Research Institute of Western Australia

Citation

Munday, T.J. (Editor), 2019, MRIWA M436: Distal Footprints of Giant Ore Systems, Capricorn WA – Case Study, CSIRO, Australia.

Technical Report Number EP192958, 288p.

Cover Photo
Maia Mapper Data from a piece of drill core for the 'Black Zone' at Abra. The colour scheme for all the images is Fe (red), Mn (green) and Zn (blue). The core shows magnetite banding (bright red) interlayered with zoned dolomite (bright green), colloform sulphides and more quartz rich layers (black). The Zn occurs as sphalerite (ZnS) which is bright blue and also in the dolomite as a purple layer within the more Fe-rich (ankeritic) carbonate. This image potentially records the timing of Zn ingress into the rocks with respect to carbonate growth (Source: M. Pearce, CSIRO).

Industry Sponsors

Table of Contents

Table of Figures

Tables

Appendices

Project Description

To define distal footprints of ore systems under cover and how to detect them in complex weathered terrains, a research study of the Capricorn region, in the central-west of Western Australia, was proposed. This is an area of known mineral potential that had received relatively little research attention even though it lies between the Pilbara and Yilgarn Cratons, two of the most significant mineral economic regions in the world. In this vast area, there are some large deposits (Plutonic, Degrussa, Paulsens, Abra), and known ore systems for a range of commodities including Fe, Au, Cu, Zn, U and Pb. The region is characterized by a complex geological evolution spanning over 3 billion years, paucity of outcrop and a complex regolith cover, and presents a daunting exploration challenge. Overall, this project sought to extend our understanding of the evolution of the Capricorn mineral system within the context of a tectonically complex geological history and establish how the footprints of the evolving mineral system can be identified both laterally and through the thick expanse of regolith and cover that mask the area. It also aimed to develop exploration approaches and appropriate toolkits that significantly improve exploration success in the region. The approach taken was to integrate regional- and lithospheric-scale datasets with prospect-scale focused studies to determine and develop scale-dependent criteria for the recognition of distal footprints. The proposed research provided a detailed examination of the extensive cover sequences that both hinder our ability to detect ore deposits but also present an opportunity to host them (e.g. CID, channel U, supergene Au). The project outcomes were not only to be directly applicable to the Capricorn region but were also intended to have application to exploration in covered terrains elsewhere.

The three year project represented a new and exciting collaboration between internationally recognized, multi-disciplinary researchers in a team comprising over 12 full time scientists from the CET at UWA, Applied Geology at Curtin University and the Discovery Program of CSIRO.

The MRIWA component of the project built on an existing investment of $4M federal Science and Industry Endowment Fund (SIEF), industry and WA research institutions and specifically supported programs in hydrogeochemistry and geochemical mapping of the lithosphere. There was also a major component of training of new geoscientists. It was envisioned that the MRIWA-funded Themes 4-6 would have 3 Research Fellows, and at least 2 PhDs and 1 Masters, with supervision from multiple core parties as appropriate. These new staff were also given the chance to interact and collaborate with the Research Fellows and students from Themes 1-3.

This report summarizes progress made to-date against the deliverables for the MRIWA supported Themes detailed below:

Theme 4: Hydrogeochemistry for Deep Geological Sensing

Deliverables – Theme 4:

- Hydrogeochemical indicators of deep geology across the region;
- Direct concentrations of ore related elements in groundwater in this greenfields region;
- Lithogeochemical mapping using lithological indices from soil and groundwater chemistry;
- Integration of surficial and groundwater chemistry with AEM, and comparison with other geophysical results;
- Utility of groundwater isotopes and other chemistry for structural interpretation;
- Sulphur isotopes in fluid and mineralization interpretation.

Theme 5: Geochemical Mapping for Lithospheric Evolution, Metal Reservoirs & Predictive Targeting

Deliverables – Theme 5:

- Regional distribution of zircon ages and crystallization temperatures from Capricorn igneous rocks;
- Source region analysis of zircons in Capricorn basins over time;
- Regional pattern of juvenile vs crustal sources for zircon in basement and basins;
- Map of crustal interaction during magma emplacement recorded by oxygen isotopes in zircon;
- Integration of the above datasets to form a 4D model of mantle and crustal interaction, and the driving tectonic processes, through the Capricorn region over time;
- New high precision combined multiple sulphur isotope and trace element data from a wide range of sulphide-bearing sedimentary and igneous rocks;
- New interpretative products to understand the complex interaction between spatially variable sulphur isotopic signature and setting of mineral systems;
- Training of a new generation of geoscientists who understand isotopic geochemistry in a spatial context;
- Integration of spatially referenced stable and radiogenic isotopic datasets at multiple scales;
- Summary of evolution of the Capricorn Orogen based on isotope systematics of sedimentary and igneous rocks;
- Quantification of the degree of crustal assimilation in the igneous suites in order to establish their potential fertility;
- Multiple sulphur isotope and sulphide mineral chemistry maps across the Capricorn Orogen.

Theme 6: 3D Digital Model Using Virtual Environments for Data Integration and Visualization

Deliverables – Theme 6:

- Integrated geochemical and geophysical datasets;
- A twiki with live data upload to ensure rapid internal and external communication of research results;
- A GIS product (updated bi-annually and kept live) capturing all relevant datasets;
- 3D digital data-set.

Executive Summary

Theme 4: Hydrogeochemistry for Deep Geological Sensing

The Capricorn hydrogeochemistry study builds on previous work in the Yilgarn Craton, creating a seamless dataset that covers much of Western Australia. This study has developed a provisional review of the mineral prospectivity of the region using groundwater geochemistry, defining areas of interest requiring further investigation.

In the Capricorn, groundwater samples were collected from 1035 wells and bores, in most cases the water table was within 20 m of the surface. Samples were also taken from known mineral deposits to provide examples of the geochemical signature associated with mineralisation in the region. Field measurements included pH, Eh, EC and temperature. Separate field prepared sub-samples were collected for cation, anion, alkalinity, and Au/PGE analysis. Robust statistical methods were applied to combine bailed and flowing samples using a derived contamination factor that is tailored to the individual measured parameters. Rescaling normal or log-normal data and the creation of indices for lithology discrimination, Au, U and sulfide mineralisation improved the utility of hydrogeochemical data. All samples were analysed for $\delta^{18}O$, $\delta^{2}H$ and selected samples were analysed for $\delta^{34}S$ and associated $\delta^{18}O$ from SO_4^{2}.

A number of different parameters can be used to indicate rock types from hydrogeochemical data even when there is deep weathering or transported cover. Higher dissolved concentrations of elements can indicate mafic (Cr, V) or granitic (U, F) rocks and ratios between elements (e.g. K excess, relative to Rb) and can differentiate between granitic and sedimentary terrains. These determinations are improved by multi-element indices.

The work tests the utility of previously derived mineral exploration indices, and has resulted in the creation of new indices designed for the geology of the Capricorn Orogen. Hydrogeochemical exploration for Au using Au, Ag, As and combined element indices such as AuMin was able to delineate areas of known mineralisation and target new areas of interest. The FeS index developed in the north Yilgarn Craton did not prove to be very effective in the Capricorn, but the AcidS index has anomalism linked to most of the known deposits and provides new areas of interest. There are several areas in the Capricorn that have U concentrations greater than those in close proximity to known deposits in the north Yilgarn. Spatially, the carnotite saturation index predicts most of the known U prospects and provides new targets in the Capricorn.

The utility of groundwater as a sample medium able to 'see through' cover was tested in two case study regions. In the Bryah Basin, groundwater possesses the chemical signature of mafic rocks but due to the thickness of transported cover soil sample chemistry does not reflect the underlying lithologies. At the polymetallic Abra deposit groundwater possesses anomalous Pb and W concentrations related to the buried deposit, whilst soil samples are proven to be ineffective at targeting mineralisation.

Oxygen and hydrogen isotopes highlight groundwater samples that have a composition suggestive of a water source other than meteoric water. This water source has mixed with meteoric water and may be linked to faults, mineralisation or hydrothermal alteration. Light $\delta^{34}S$ values and associated light $\delta^{18}O$ successfully identified mineralisation at Paulsens Au deposit and have the potential to target new areas of mineralisation.

This research further demonstrates the value of groundwater chemistry for defining lithology, hydrothermal alteration and mineralisation in areas with and without cover. Stable isotopes have been used systematically across the region to assist in delineating new areas of interest.

Theme 5: Geochemical Mapping for Lithospheric Evolution, Metal Reservoirs & Predictive Targeting

Theme 5A: To See an Orogen in a Grain of Zircon: Crustal Evolution and Source to Sink Sediment Routing in the Capricorn Orogen, a Synthesis of Zircon Geochronology and Geochemistry

The Capricorn Orogen comprises the metamorphosed margins of the Pilbara and Yilgarn Cratons bounding various metasediments and granitoids that developed across over a billion years (~2.2-1.0 Ga) during the assembly of the West Australian Craton and later intracratonic reworking. As a result of its relatively protracted and complex geological history and development of cover sequences, details of the Capricorn Orogens crustal evolution remain poorly constrained. Here, integrated geochronology and geochemical analyses of magmatic and detrital zircons from across the Capricorn Orogen, are used to inform understanding of the Capricorn Orogens overall tectonic evolution, critical episodes of juvenile additions to the crust, unit relationships, and subsequent regional denudation and basin formation history. Over 4000 split-stream U/Pb and trace-element analyses and ~850 Hf- and O-isotope analyses were conducted on magmatic zircons from 91 samples focused on the northern margin of the Yilgarn Craton, Archean Inliers on the southern and northern margins of the Capricorn Orogen, as well as the major intrusive units of the Gascoyne Complex. A comprehensive database of detrital zircon geochronology has been compiled from across the Capricorn Orogen (totalling 5610 analyses) and integrated with a further 6046 new, split-stream integrated geochronological and trace-element geochemical analyses of detrital zircons from outcrop and core samples across the Paleoproterozoic Yerrida, Bryah and Padbury Basins and through the Mesoproterozoic Edmund and Collier Basins.

Geochronological and isotopic data (more evolved Hf and increasing $\delta^{18}O$ over time) demonstrate that limited juvenile mantle input was associated with orogenic magmatism in the Gascoyne Province, with significant crustal reworking and local isotopic distinction characterising Capricorn Orogen granites. Paleoarchean (~3.3 Ga) ages in the Marymia Inlier and similarities in O- and Hf-isotopic character suggest correlation of the western Marymia Inlier to the Narryer Terrane. Similarly, overlap in the O- and Hf-isotope space of Halfway Gneiss zircons suggests that the Glenburgh Terrane is compatible from the Yilgarn Craton and may reflect a rifted and recombined crustal block. Overall, rejuvenation of the crust is recognised in the south along the Yilgarn Craton margin from 3000-2100 Ma, and in the north during 2100-1750 Ma. Although mineralisation is typically associated with structural trends across the Gascoyne Province, there are some indications that juvenile input in the region of the Marymia Inlier may be relevant to mineralisation.

Provenance analysis of detrital zircons show a southern-derived dominance of detritus from the Yilgarn Craton through Paleoproterozoic basins on the southern margin of the Capricorn Orogen. Geochronology and trace- element geochemistry in the Yerrida and Bryah Basin highlight local mafic magmatism associated with rifting of the northern Yilgarn Craton margin at ~2.1 Ga. Increasing amounts of Gascoyne Province detritus are reflected in the progressively younger southern Capricorn Orogen basins, reflecting the approaching volcanic arc and eventual collision of the Gascoyne and Yilgarn crustal blocks. Similarly, basins on the northern margin of the Capricorn Orogen reflect increasing Gascoyne Province detritus up sequence as a consequence of Glenburgh-Pilbara collision. Complexities in the detrital zircon signatures of the Edmund and Collier Basins can be correlated with larger depositional sequences previously recognised, and in turn regional tectonic-driven changes in catchments. New maximum depositional ages are defined for the Ullawarra Formation (~1.4 Ga; Edmund Basin) and Ilgarari Formation (~1.05 Ga; Collier Basin).

Theme 5B: Tracing Sulfur Pathways Through the Lithosphere

It is widely accepted that the anomalous sulfur isotopic signature Δ33S ≠ 0‰ that occurs in a restricted range of rock types throughout the geological record formed by mass independent fractionation of sulfur (MIF-S) prior to the ~2.4 Ga Great Oxygenation Event. This signal was created in the atmosphere, transported to the water column and preserved as sulfate and sulfide in the Archean sedimentary rock record. As sulfur is the primary complexing ligand for gold transport in aqueous fluids, recent work has demonstrated that the MIF-S signal can be recycled to the hydrothermal record. Here, we harness this knowledge and develop a methodology to use of Δ33S (and MIF-S) as an isotopic tracer of sulfur pathways through the lithosphere and subsequently to mineral systems. First, we develop reference materials to analyse multiple sulfur isotopes in a variety of sulfides typical of ore deposits. Next, we compile 5500 measurements from literature of δ34S and Δ33S from sediments through time in order to better define the threshold of a recycled MIF-S signature in Δ33S space. This background work enables us to investigate major sulfide occurrences across the Yilgarn Craton including orogenic gold, Ni-komatiite and volcanogenic hosted massive sulfide deposits. The observation of this signal in many of these environments demonstrates that Archean sediments form an important source reservoir of sulfur for these mineral systems. From this, we are able to infer tectonic processes controlling sulfur mobility at the craton-to district- to deposit-scale. Finally, we move to the Proterozoic time period, when MIF-S could no longer be created, and investigate how this Archean signal is recycled through the lithosphere to the margin of the Yilgarn Craton: the Capricorn Orogen. We observe that near the margins of the Capricorn Orogen, Proterozoic granitoids recycle the MIF-S signal, indicating that subduction processes controlled the transfer of sulfur from the metal-endowed Yilgarn Craton to newly formed magmatic rocks. At the smaller scale, we investigate how sulfur isotopes can aid in exploration and vectoring to basin-hosted deposits. The outcomes from this study have enhanced the application of MIF-S (Δ33S) as a powerful and indelible tracer to understand the source and emplacement pathways of sulfur-bearing fluids through the lithosphere across the Archean-Proterozoic transition.

Theme 6: 3D Digital Model Using Virtual Environments for Data Integration and Visualization

Theme 6A: Data Integration and Visual Analytics

The Data Integration Theme enabled building the original SIEF project to a Program from crust to surface, with critical data integration. The data sets collected in Themes 1 to 5 are large and multi-scale. It was critical to enable integration and visualisation of these data sets and to develop tools for virtual interrogation of the data and production of 3D models that can be used in exploration targeting.

Theme 6 developed a dedicated data management process and runs alongside the project to capture the data and enable data integration between software packages. The system includes a data upload and cataloguing tool for data managers that simplifies the elimination of ambiguities in the data received from varying sources. The tool also features integration with the International GeoSample Number (IGSN) system that plays an important role in the curation of samples. IGSN provides a mechanism for the identification of new and legacy samples, as well as derived sub-samples. It ensures transparency and reproducibility in geochemical sampling campaigns that involve a diversity of sampling methods. Hence, diverse geochemical and isotopic results are linked back to the parent sample, particularly where multiple children of that sample have also been analysed. This study has demonstrated the effectiveness of the proposed approach while maintaining the flexibility to adapt to various media types, which is critical in the context of a multi-disciplinary project. The unambiguous identification of samples ultimately adds to the goal of enabling synoptic integration of heterogeneous geochemical datasets for regional-scale exploration.

The field sampling practices have been reviewed and methods and tools developed to improve the accuracy of data acquisition as well as the efficiency of the sampling process. This resulted in developing new modules for the discipline-agnostic platform – the Field Acquired Information Management System (FAIMS). The FAIMS framework can be adapted to a diverse range of scenarios, different kinds of samples, each with its own peculiarities, integration with GPS, and the ability to associate photographs taken with the device embedded camera with captured data. The system supports reliable mechanisms for data replication as an added level of redundancy. It was successfully trialed on several field sampling campaigns and proved to be an efficient replacement of a paper-based sampling protocol. The use of a common platform allowed us to adopt the framework within multiple disciplines, improve data acquisition times, and reduce human-introduced errors.

In collaboration with the geophysics theme (Theme 2, Program 2.1 – Regional Cover Characterisation using Airborne Electromagnetic Data) the Data Integration Theme explored high-performance data-intensive processing and visualisation of Airborne Electromagnetic (AEM) survey data. This provided insights into how the industry can benefit from new generation processing power and data integration for planning and targeting in exploration campaigns, model development and simulation of mineral system processes as well as to output the data through a common platform. The system prototype was developed with the modular architecture in mind allowing the platform to be adapted for new scientific disciplines and data processing and visualisation techniques.

Theme 6B: Imaging 3D Structure of the Paleoproterozoic Yerrida Basin with Integrated Structural Interpretation and Modelling

The Distal Footprints of Giant Ore Systems Project was conducted in the Capricorn Orogen, Western Australia and amalgamated earth science disciplines to provide a toolbox for mineral exploration. There are six themes, each dealing with a unique aspect of mineralising systems: architecture, tectonics and geodynamics; cover; distal footprints; hydrogeochemistry; geochemistry and 3D technologies. These contributions draw from two themes: architecture and tectonics and; 3D technologies to determine the architecture of the Paleoproterozoic Yerrida Basin. A range of geological and geophysical techniques were integrated to produce a structural interpretation and forward model that illuminated basin structure. These results were then used to construct a 3D model which was tested against the geophysical data to support the proposed architecture. Of particular interest was a significant high-amplitude gravity anomaly that appeared bound by the extents of the basin, and hinted at extensive, high-density rocks that are not evident from the mapped geology. Modelling of the gravity data suggested the extent and magnitude of the observed anomaly require a significant amount of high density material, and considerably more than currently thought to be present in the Basin. These high density rocks are proposed to be a combination of mafic intrusions related to both the argillaceous Juderina and basaltic Killara formations, confirmed by geochemistry. The mafic content of the Juderina Formation may indicate a tectonic environment for VMS-style mineralisation, which is considered in the context of a 3D model.

Acknowledgements

The work described in this report would not have been possible without the support of MRIWA, SIEF and our industry partners. Their contributions are acknowledged with thanks.

This report was compiled with the unflinching efforts of Cheryl Harris, and the project team gratefully acknowledges and appreciates her efforts.

Theme 4:

Hydrogeochemistry for Deep Geological Sensing

Robert L. Thorne, Nathan Reid, David J. Gray, Brian Ballsun-Stanton, Nicole Bardwell, Jens Klump, Aaron Davis, Shawn Ross, Adela Sobotkova

1 Theme 4: Hydrogeochemistry for Deep Geological Sensing

Robert L. Thorne, Nathan Reid, David J. Gray, Brian Ballsun-Stanton, Nicole Bardwell, Jens Klump, Aaron Davis, Shawn Ross, Adela Sobotkova

1.1 Introduction

The Capricorn Orogen region is a ~1000 km X ~500 km wide, variably deformed, region of Western Australia located between the Pilbara and Yilgarn Cratons (Figure 1.1). The region has been shown to record seven major orogenic events between ~2215 Ma and ~ 1000 Ma (Johnson et al. 2013). The Capricorn Orogen contains complex regolith, with continuous weathering from at least the beginning of the Mesozoic (Pillans, 2005), as well as large regions of exposed saprock and areas with thin, dominantly transported, cover.

The Capricorn region represents a large, relatively underexplored region, where few large mineral deposits have been found. The Proterozoic and Mesoproterozoic basins which form a significant part of the region (Figure 1.1) are particularly challenging for exploration. The area is significantly untenemented and has high potential prospectivity related to its position between the Yilgarn and Pilbara Cratons.

The lack of known major deposits within the region and the difficulties inherent in exploring within the sedimentary basins make hydrogeochemical exploration methods suited to the area. Hydrogeochemistry provides a low impact and environmentally sensitive method for quickly gaining chemical information about lithology at depth. Groundwater geochemistry can show broader signatures (e.g., alteration haloes) than other sample media (drill core), as the chemistry is influenced by immediate contact with rocks as well as other materials which have previously influenced the groundwater (Gray et al. 2016).

A reconnaissance hydrogeochemical map of critical areas of the Capricorn Orogen and surrounds has been created in order to obtain under cover lithological and structural information, highlight areas of interest to mineral exploration and understand baseline chemistry for environmental management. In conjunction, particularly with regolith studies, this database will also have the capability to test the effectiveness of surface-based sampling technologies such as soil-sampling, radiometrics and ASTER mapping. Previous developments, primarily within the adjacent north Yilgarn Craton, have included advanced techniques for obtaining mineral saturation data, normalised indices and other valuable exploration geochemical data (Gray et al. 2009, 2014, 2016a).

This project has tested and refined previously developed exploration indices, and tested the utility of various isotope analyses to improve understanding and exploration using groundwater. Potential benefits from this project include:

- An understanding of the hydrogeochemistry of the Capricorn Orogen. This enables better anomaly contrast and development of indices for exploration and support further exploration;
- Specific prospectivity analyses of parts of the Capricorn, a hitherto poorly explored area;
- Demonstration of the use of chalcophile (As, Sb, Mo, W) haloes for exploration;
- Providing lithological information in covered terranes;
- Hydrogeochemistry as part of effective exploration in craton margins and basins;

- Indication of alteration signatures,
    - Uranium – primary and secondary styles
    - Lode Au – Au, Ag, As, Mo, Sb
    - Base metals (VHMS and NiS) targeting – W, As, Co, PGEs, SO_4 anomalism, NO_3
- Using various isotope analyses to add value to standard hydrogeochemistry.

1.2 Background

1.2.1 Regional geological settings

The Capricorn Orogen encompasses the deformed margins of the Yilgarn and Pilbara Cratons (Johnson et al., 2013) (Figure 1.1). The Capricorn Orogen includes a number of distinct sedimentary basins formed subsequent to the formation of the West Australia Craton when the area was subject to episodic intracontinental reworking, including sedimentation. The Paleoproterozoic Ashburton, Blair and Bresnahan Basins are found along the northern margin of the orogen. The Ashburton and Bresnahan Basins unconformably overlie rocks of the Hamersley Basin which forms the southern part of the Pilbara Craton (Cawood and Tyler, 2004). The centre of the orogen is composed of the Mesoproterozoic Edmund and Collier groups (Bangemall Supergroup) which are the youngest rocks in the region and consist of 4-10 km of siliciclastic and carbonate metasedimentary rocks. The stratigraphy of the Edmund and Collier groups is divided broadly by Martin and Thorne (2004) into 6 Depositional Packages. This terrane is herein referred to as the Edmund-Collier Basin. The Edmund-Collier Basin sediments were deposited during a period of intracratonic extensional reactivation of the orogen structures, and the lithologies and depositional environments are described in detail by Cutten et al. (2016). Two periods of dolerite sill intrusion into the Edmund-Collier Basin are evident; the Edmund basin was intruded by the 1465 Ma Narimbunna Dolerite (Wingate, 2002), and the Collier Basin (and to a lesser extent Edmund Basin) was intruded in a second event by the Kulkatharra Dolerite 1070 Ma. The Paleoproterozoic Padbury, Bryah, Yerrida and Eraheedy Basins are situated along the southern margin of the orogen. The 3 km thick Yerrida and 5 km thick Earaheedy basins unconformably overlie the northeastern margin of the Yilgarn Craton (Pirajno et al., 2004). Mafic igneous rocks occur within both the Yerrida and Bryah basins. These basins have been subjected to low-medium grade metamorphism and varying degrees of deformation

The Gascoyne Province in the south west of the orogen (Figure 1.1) is divided into several tectonometamorphic zones predominantly comprised of felsic batholiths and the Glenburgh Terrane in the south, which represents a continental crustal fragment exotic to both the Pilbara and Yilgarn Cratons (Johnson et al., 2013). The Gascoyne Province is separated from the Yilgarn Craton by the Errabiddy Shear Zone in the south, and passes with decreasing metamorphic grade into the sediments of the Ashburton Basin to the north (Thorne, 1990).

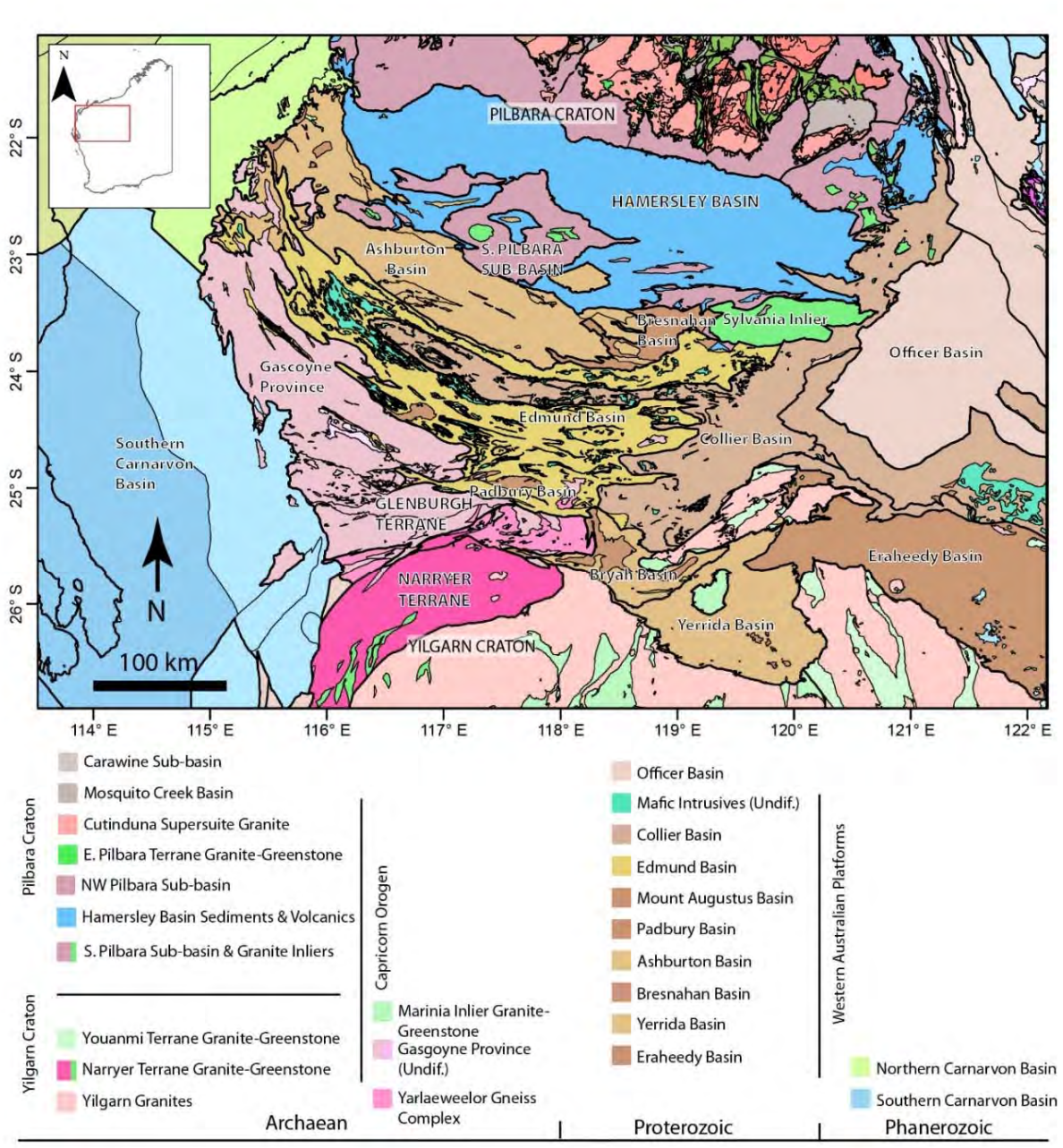

Figure 1.1. The geology of the Capricorn Orogen. Map data extracted from the Geological Survey of Western Australia *1: 2.5M Tectonic Unit 2017* dataset, (GSWA 2017).

1.2.2 Physical features

The topography of the Capricorn Orogen generally increases in height from the west to the east. The maximum elevation is found at Mt. Augustus at 1105 m above sea level (asl). The eastern Edmund-Collier Basin possesses the greatest relief in the area, with plains 400 m above sea level and hills commonly above 800 m, overall elevation reduces towards the west but local relief remains high. The Ashburton Basin region possesses relatively low relief compared to the central Edmund-Collier Basin area, strike hills can run for 10's to 100's of km in a north west, south east orientation, with most no more than 350 m asl. There is a general decrease in topography of the surrounding plains from 200 - 350 m in the south east to 75 – 100 m in the NW. South eastern portions of the Capricorn Orogen have a low relief and are dominated by colluvial-alluvial plains, and hills in the region are no more than 200 m above the surrounding plains.

Both regionally and locally the topography of the region is influenced by the underlying lithology and structures. Increasing relief in the central and eastern portions is controlled by the uplift, deformation and differential erosion of the Edmund-Collier Basin sediments following the 1321–1171 Ma Mutherbukin Tectonic Event (Johnson et al., 2011; Korhonen et al., 2015). The SE of the study area around the Bryah Basin has a high proportion of mafic rocks and is defined by flat to undulating terrain contrasting with rounded hills composed of iron formations further to the north. Hill belts generally follow a north-west/south-east orientation aligned with the strike of the exposed sedimentary packages. Felsic volcanic rocks of the western Gascoyne Province are generally less recessive and form low boulder covered hills and tors and undulating terrain, more rarely breakaways can be found on granitic rocks.

Broad plains in the region follow major drainages, including the Gascoyne River in the south of the region, East and West Lyons River and the Ashburton River in the north of the area. These drainages broadly run from the east to the west.

1.2.3 Climate

The region has a moderate arid tropical climate, characterised by high daytime temperatures in summer and low winter minima. Mean average rainfall is approx. 250 mm (http://www.bom.gov.au/) with high inter annual variation associated with irregular tropical cyclones.

1.2.4 Vegetation

The vegetation profile across the Capricorn varies from Mulga scrub to the south becoming more grassland dominated towards the north (Gardner et al 1959). *Acacia aneura* (mulga) is common across much of the Capricorn Orogen and is found in most landscape settings. *Trodia* species (spinifex grass) dominates sand plains and dunes whilst ephemeral grasses are seasonally present across colluvial and alluvial plains. Larger Eucalypts follow major drainages.

1.2.5 Regolith

The interaction of mechanical, chemical and biological processes combined with variations in bedrock will produce a specific landscape and regolith. Both transported and in-situ regolith is present in the Capricorn region, bedrock is exposed over large areas, or it may be covered by a thin layer of soil and regolith. Transects undertaken across the central and southern portions of the Capricorn by Thorne et al. (2018a) have identified four major regolith-landform provinces, each with its own unique regolith, landscape and geochemical expression (Figure 1.2):

1. Exposed crystalline basement
2. Deeply weathered
3. Upland Basin
4. Lowland Basin

The west is comprised of the Exposed crystalline Basement Province, thin lithosols dominate and granitic tors are common in a dissected landscape and soil composition reflects the underlying substrate. The south west Deeply Weathered Province is defined by thick saprolite developed over both sediments and volcanics. Ferruginous nodules and pisoliths are present at surface and weathering profiles capped by duricrust are common. Thick (up to 100 m) paleochannel sequences are found throughout the area, these are represented by mottled clays and sands. The lithologies in the north and central regions are dominated by Mesoproterozoic basin sediments and can be split into two geomorphic provinces. The Upland Basin Province is highly dissected and possesses several generations of ferruginous pisoliths and nodules, ferricrete, silcrete

and calcrete developed in colluvium and alluvium. Palaeochannel sediments are commonly located on the flanks of hills and as low mounds and hills formed after topographic inversion. The Lowland Basin Province is dominated by hardpan, calcrete and colluvial/alluvial plains below low hills on which basin sediments are exposed.

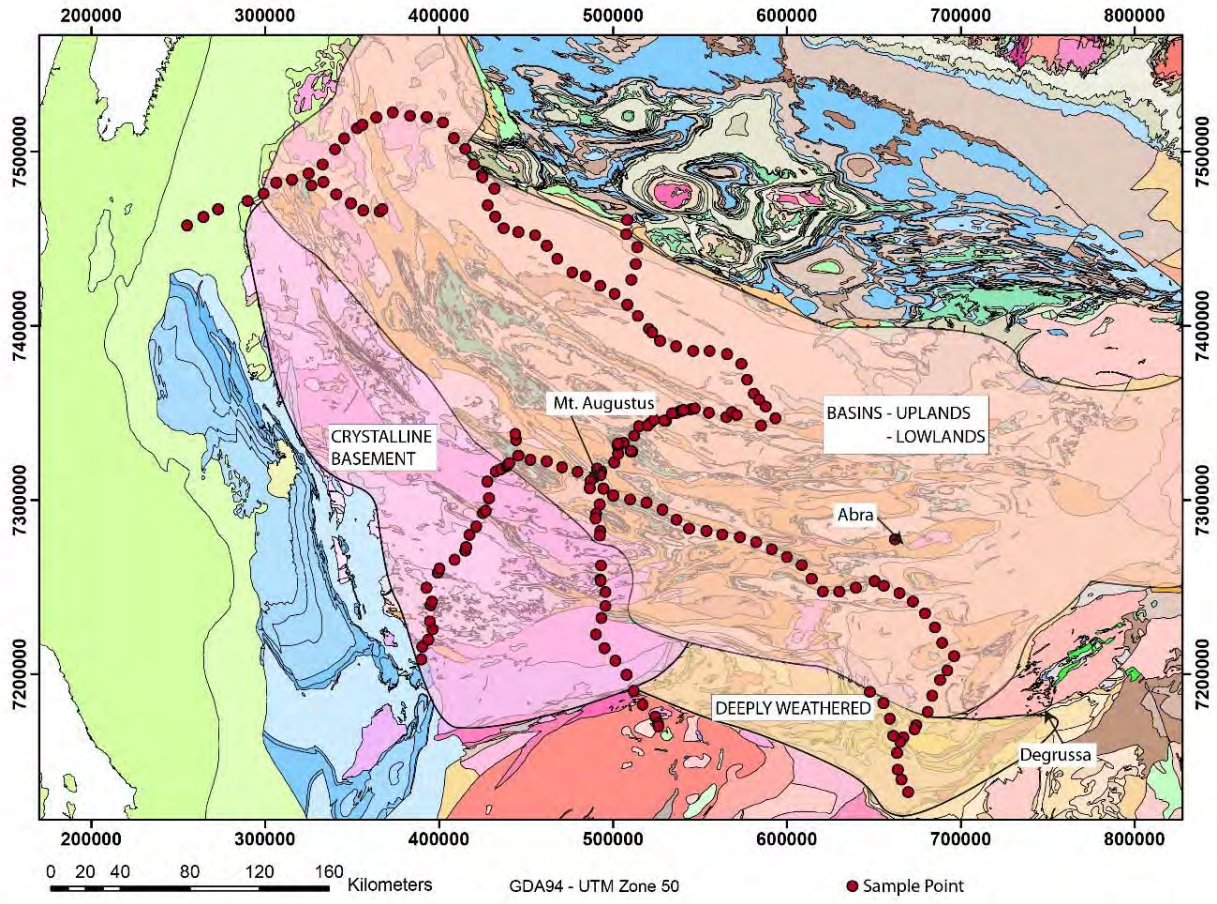

Figure 1.2. The four geomorphic provinces of the Capricorn Orogen. Red dots represent sample points along the regolith transects (Thorne et al. 2018a).

1.2.6 Mineral deposits

The Capricorn Orogen has relatively few major resource projects (Figure 1.3): base metal deposits are the most common, and include DeGrussa (Cu, Au) Abra (Pb, Cu, Zn), Ilgarari (Cu), Prairie Downs (Zn, Pb, Ag) and Horseshoe Lights (Cu, Au, Ag). Other deposits in the region include the Au (Ag) Plutonic, Peak Hill, Fortnum, Paulsens, and Glenburgh deposits. Manganese bearing sediments are found within the Edmund Basin and surface supergene Mn mineralisation occurs along strike. Where these sediments have undergone supergene enrichment by weathering processes they can form large Mn deposits e.g. Butcherbird in the east. Many minor mineral occurrences have been documented across the region (Figure 1.3). Uranium and REE occurrences are present through the Gascoyne Province and eastern Ashburton Basin, whilst Au and base metal anomalies can be found within the central and western Ashburton Basin sediments. Gold occurrences are most common within the south east in the Padbury and Bryah Basins and associated with the Marymia Inlier. Even including all known mineral occurrences there is still a distinct lack of known mineralisation within the major sedimentary basins in the region.

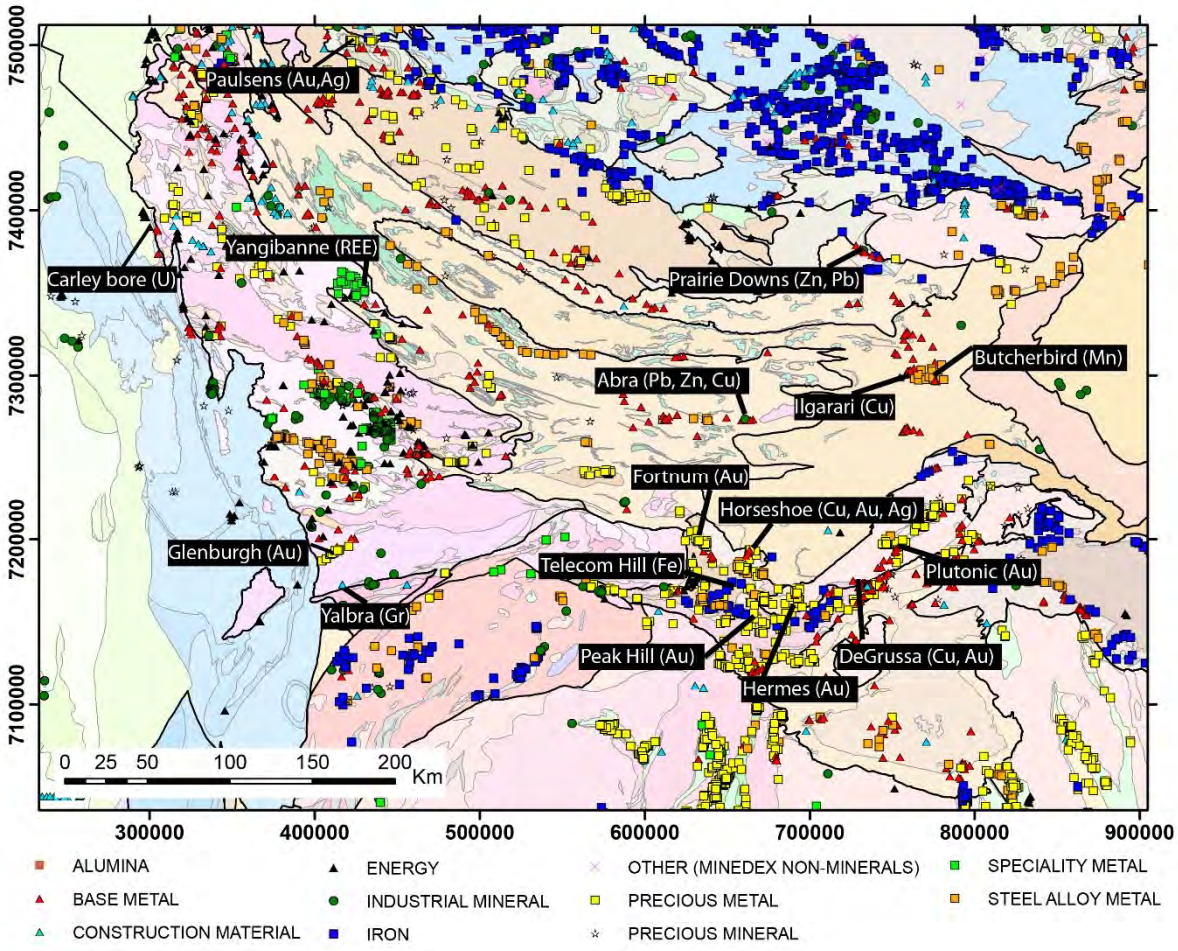

Figure 1.3. Mineral occurrences in the Capricorn Orogen, major deposits in the region are labelled. Map data extracted from the Geological Survey of Western Australia, Mines and mineral deposits dataset, (GSWA 2018a).

1.3 Sampling and Analysis

1.3.1 Sample collection

The standard methods used are described in detail in Gray et al. (2016), with an abridged description here. In the Capricorn Orogen, groundwater samples were collected from 1035 sites (Figure 1.4), including wells and bores used for livestock and human consumption, the majority of samples were derived from groundwater with the water table within 20 m of the surface. Samples were also taken from known mineral deposits (Figure 1.4), to provide examples of the geochemical signature associated with mineralisation in the region. Gaps in the sampling are due to physical access problems, and station access limitations as well as a large gap in the centre of the Capricorn where further sampling is possible but beyond the scope of this project. Suitable sites for sampling were determined by using topographic maps with bore locations marked, combined with GPS/Arc GIS on a field laptop and printed maps. The most effective collection method (711 samples, Figure 1.5) was direct sampling from actively pumping farm (windmill, solar) bores, as close to the pumping stem as possible, to avoid any possible in-train contamination or precipitation. Another 324 samples were collected using a flow-through bailer (Figure 1.6) fitted with one-way valves, due to abandonment or access difficulties. Where possible, bailed samples were collected 5 m below the surface, but 1 m was often the limit in abandoned wells.

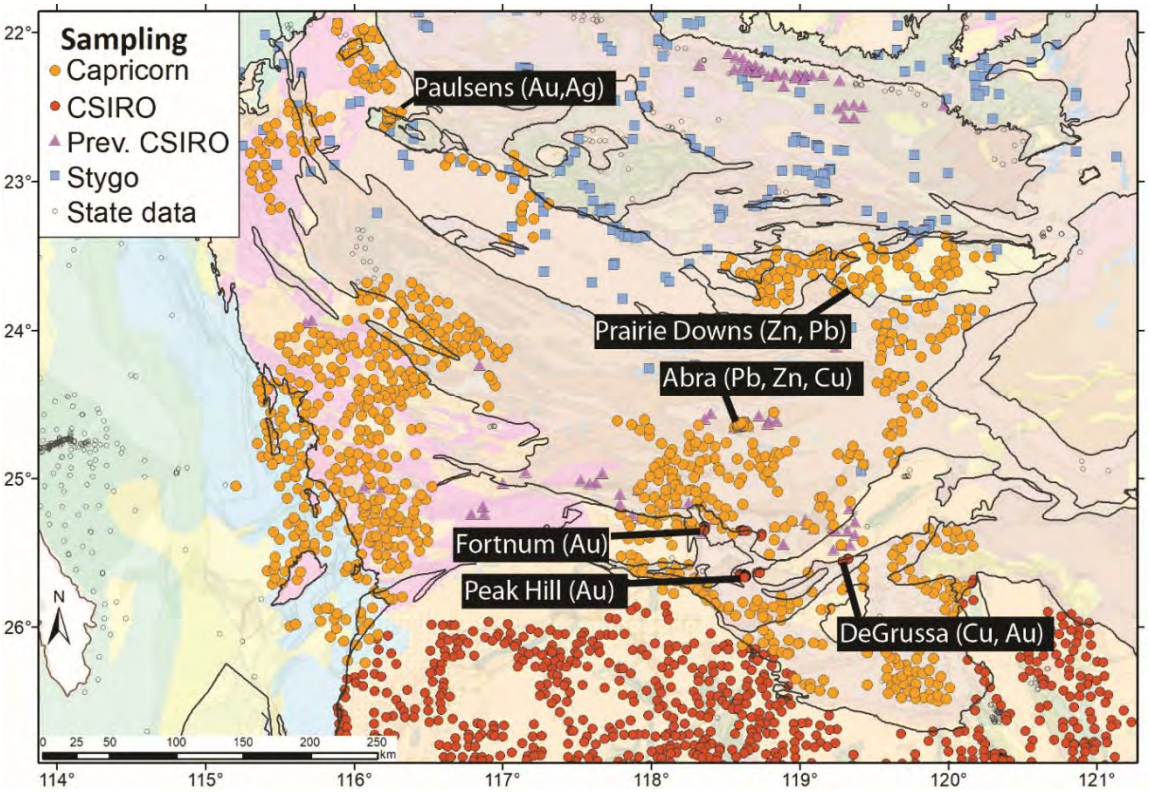

Figure 1.4. Sampling points within the Capricorn and adjacent terrains. Samples taken specifically for this project are shown in orange. Previous CSIRO sampling initiatives are shown in red and purple, whilst blue squares represent Stygofauna sampling of the Pilbara region, Western Australia (WA) by Halse et al., (2014). State date is represented by white circles. Deposits sampled as case studies are labelled.

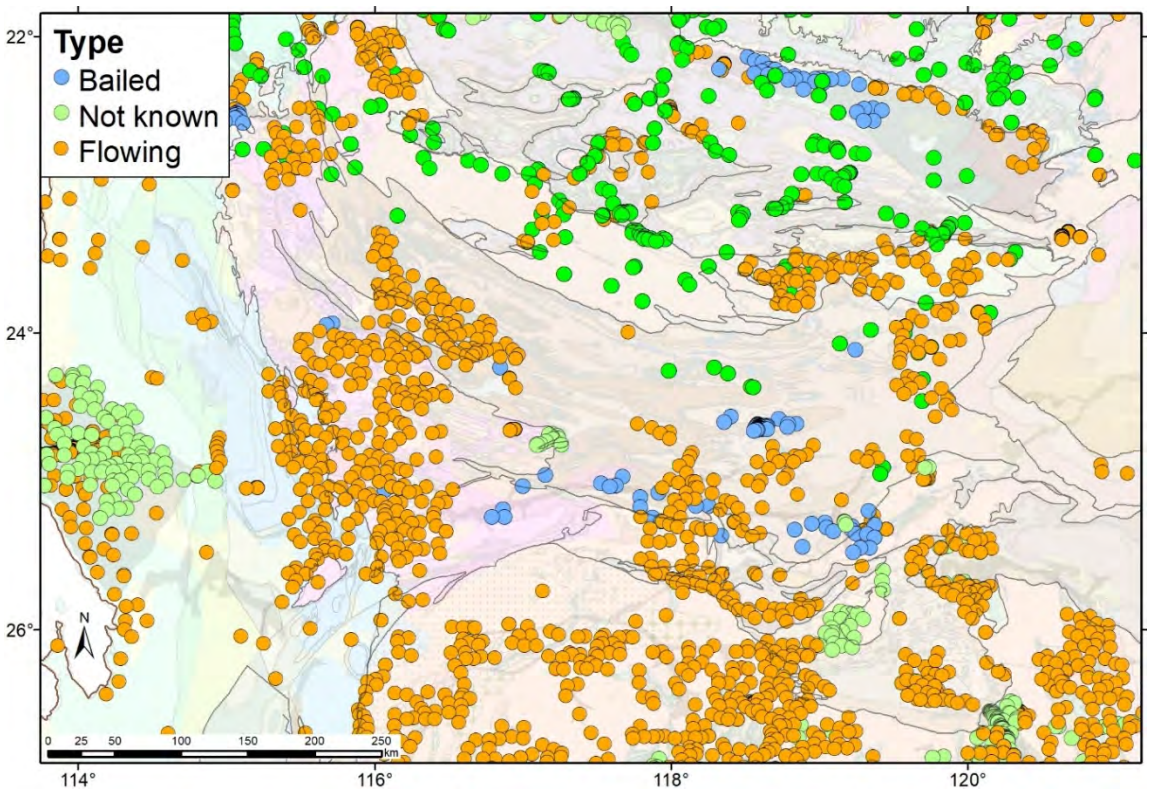

Figure 1.5. Groundwater sample points within the Capricorn Orogen, showing method of collection.

Figure 1.6. Example of bailers (with polychain cable on reel) and a dip probe for water table depth (red reel with metal probe and measuring tape).

The depth of the water table was recorded with a dip meter. Waters were analysed for pH, temperature, conductivity (EC) and oxidation potential (Eh) at the time of sampling. Electrode calibrations were performed twice-weekly for conductivity and Eh, in case conditions changed or irregular measurements occurred. The pH electrode required 3 buffered solutions (pH 4, 7 and 10) and was calibrated daily. The Eh electrode used a Ag/AgCl reference electrode and ZoBell's check solution (ZoBell, 1946) was used to standardise against the theoretical hydrogen electrode. The conductivity meter used a 58 mS/cm standard solution for calibration. Saturated KCl (3.5 M) was used to store the electrodes. Estimated maximum measurement errors are: pH ±0.02; temperature ±0.5°C; conductivity ±2 % and Eh ±20 mV. An unfiltered sample was collected, with overfilling to remove all air, for later HCO_3^- analysis by alkalinity titration in the laboratory. High density polyethylene bottles were used (Figure 1.7), with filtering to 0.45 µm pore size using nitrocellulose filter papers. Previous investigations (Noble and Gray, 2010) demonstrated highly correlated results for 0.1 vs 0.45 µm for most elements, with the exception of Fe and Al. At each site the filtration equipment (Figure 8) was thoroughly rinsed with deionised water and a new filter paper inserted. Approximately 100 mL water was filtered and collected (with rinsing) for anion analysis. Subsequently, an additional 100 mL was filtered and then collected (with double rinsing) for Inductively Coupled Plasma Optical Emission Spectroscopy (ICP-OES) and Inductively Coupled Plasma Mass Spectrometry (ICP-MS) analysis. Concentrated nitric acid (69 %) of high purity analytical grade was added to these samples in the laboratory to 0.2 % v/v.

Figure 1.7. Water sample bottles.

Figure 1.8. Filtration equipment for water sampling, showing (L to R) hand pump, syringe and small filter, Nalgene® filter unit, filter papers, deionised water and another filter unit.

Carbon sachets (comprised of 1 g of activated carbon in a nylon mesh) were placed in a 1000 mL bottle with 10 g NaCl to provide an approximate ionic balance between samples irrespective of initial water sample salinity. The solutions were agitated on a bottle roller for at least 1 week, at which point the carbon was extracted for low level (ng/L) detection of Au, Ag, Pt and Pd.

1.3.2 Laboratory analyses

A set volume (20 mL) of the sealed, unfiltered sample was titrated for HCO_3^- with a known concentration of acid (e.g. 0.01 M HCl) to an endpoint of pH = 4.3 at CSIRO Laboratories in Kensington, WA. Major anions (Cl, SO_4, Br, F and NO_3) were analysed using the filtered sample by Ion Chromatography (IC) at CSIRO Laboratories Waite, SA. The IC system was a Dionex ICS-2500 system with 2mm AS19 anion separation column and potassium hydroxide eluent generated on line, followed by conductivity detection after chemical suppression. With a flow rate of 0.25 mL per minute the anions F^-, Cl^-, Br^-, NO_3^- and SO_4^- are eluted between 3.5 and 25 minutes. Each ion concentration is calculated from peak areas using a 25 µL injection and compared to calibration graphs generated from a set of mixed standards with a known range of concentrations. A sample split was sent to CSIRO Waite Laboratory, SA for analysis of Total N, Dissolved Organic Carbon (DOC) and PO_4.

Major and trace elements were analysed using the acidified and filtered samples by ICP-OES and ICP-MS. Elements Al, B, Ca, Cr, Cu, Fe, K, Li, Mg, Mn, Na, P, S, Si, Sr and Zn were analysed by ICP-OES at CSIRO Waite Laboratory, SA. Trace elements (Ag, As, Ba, Cd, Ce, Co, Cr, Cu, Dy, Er, Eu, Ga, Hf, Ho, La, Lu, Mo, Nb, Nd, Ni, Pb, Pr, Rb, Sb, Sc, Sm, Sn, Sr, Ta, Th, U, V, W, Y, Yb, Zn and Zr) were analysed by ICP-MS at CSIRO Waite Laboratory, SA. Detection limits for ICP analyses are affected by salinity, with more saline samples having higher detection limits due to increased dilution requirements.

Dissolved Au, Ag (occasionally), Pt and Pd were below detection in the majority of groundwater samples, hence the use of an activated carbon sachet to pre-concentrate these critical pathfinders and target elements. The carbon analysis was performed by Bureau Veritas Minerals in Canningvale, WA, with the carbon ashed and then dissolved in aqua-regia. The solution was analysed by ICP-MS.

Filtered water samples were sent to James Cook University (Cairns, Australia) for analysis of $\delta^{18}O$ and $\delta^{2}H$ by Cavity Ring-Down Spectrometry (CRDS). Water vapour was separated from non-volatile dissolved and particulate contaminants, minimising spectral interferences. Comparison of isotopic data for a range of water samples analysed by Diffusion Sampling-CRDS (DS-CRDS) and Isotope Ratio Mass Spectrometry shows significant linear correlations between the two methods allowing for accurate standardisation of DS-CRDS data. The isotopic effects of variable air temperature, water vapour concentration, water pumping rate and dissolved organic content were found to be either negligible or correctable by analysis of water standards.

Sulfur and oxygen isotopes from sulfate were analysed by adding excess $BaCl_2$ to the sample to form a stable $BaSO_4$ precipitate, which was subsequently separated by filtration in the laboratory, rinsed and dried. The $BaSO_4$ precipitate was sent to the Isotope Science Laboratory, Department of Physics and Astronomy, University of Calgary (Canada), for $\delta^{34}S$ and $\delta^{18}O\_SO^4$ isotope analysis on a Carlo Erba NA 1500 elemental analyser interfaced with a VG_ Prism II mass spectrometer. High temperature reaction of the $BaSO_4$ with V_2O_5 and SiO_2 generated SO_2 for $\delta^{34}S$. Sulfur isotope compositions are reported using the conventional $\delta\ ^{34}S$ scale in parts per thousand (‰).

Sr isotopes were analysed by weighing an aliquot of each water sample is into a clean savillex beaker which is then evaporated to dry at 70^o C. The dry residue is dissolved in 3 M HNO_3 and loaded onto an ion exchange column, via prepFast (Elemental Scientific, Inc, Omaha, Neb, USA), containing 100 µL of Sr-Spec resin for chromatography. Matrix elements are eluted with 3 M HCl and Sr is collected by elution with 0.05 M HCl.

The purified Sr solution is dried and dissolved in 2 % HNO_3 for measurement. Samples are accompanied by appropriate reference materials and procedure blanks.

Sr isotope ratios are measured using Neptune MC-ICP-MS. Isotopes measured are ^{84}Sr, ^{86}Sr, ^{87}Sr and ^{88}Sr. Also, ^{85}Rb is monitored to ensure complete removal and ^{83}Kr is monitored as it is a contaminant in the plasma gas (Ar). Instrument operation is confirmed be repeat measurements of NIST 987 Sr carbonate. Measurement consists of 70, 4 second integrations. $^{87}Sr/^{86}Sr$ ratios are measured and corrected for mass bias using $^{86}Sr/^{88}Sr = 0.1194$.

- **Solution Modelling**

Equilibrium activity diagrams were derived using The Geochemist's Workbench® version 10. Solution chemical speciation and degree of mineral saturation were computed from the solution compositions using the program PHREEQE (Parkhurst *et al*., 1980). Saturation indices (SI) for each water sample were calculated for various minerals. If the SI for a mineral is within the zero range (determined for every mineral based on stoichiometry, thermodynamic accuracy and analytical issues; generally ranging from -0.2 to 0.2 for major element minerals to -1 to 1 for minor element minerals), the water is in equilibrium with that mineral, under the conditions specified. Where the SI is below the zero range, the solution is under-saturated with respect to that mineral, so that, if present, the phase may dissolve. If the SI is greater than zero the solution is over-saturated with respect to this mineral, which can potentially precipitate from solution.

Note that SI determinations only specify possible reactions, as kinetic constraints may rule out reactions that are thermodynamically allowed. For example, waters are commonly in equilibrium with calcite, but may become dolomite over-saturated, due to the slow rate of precipitation of this mineral (Drever, 1982). However, this method provides some understanding of solution processes at a site and adds value in determining whether the spatial distribution of an element is correlated with geological phenomena such as lithology or mineralisation, or whether they are related to weathering or environmental effects. For example, if Ca distribution is controlled by equilibrium with gypsum in all samples, then the spatial distribution of dissolved Ca will reflect SO_4 concentration alone and have no direct exploration significance.

1.4 Quality Control

Summary statistics for each element for the Capricorn dataset are listed in Table 1.1. Similar statistics for previous sampling are given in the relevant reports (Gray et al., 2009; 2012, 2016a). Laboratory standards (TM26.4 and HAMIL 20.2, Environment Canada), blanks and duplicate samples were used at a ratio of 1 every 20 for internal and external analyses for quality control, as shown in Table 1.2.

Using duplicates, blanks and standards the errors for each element were calculated as half absolute relative difference errors in % and 95% confidence errors on the batch. The errors are defined as:

Half absolute relative difference = ((assay1 - assay2) / (assay1 + assay2)) x 100

$$95\%\ \text{confidence} = 1.96\left(\frac{\sigma}{\sqrt{n}}\right)$$

Where 1.96 is the 95th percentile of a normal distribution with a mean value of 1, σ is the standard deviation of all assay1-assay2 values, and *n* is the number of duplicates. The 95% confidence error was applied to the differences, the % differences and the half relative difference; the confidence of the differences was used to determine new detection limits to filter out erroneous noise and the last two could give a percent error that could be applied to all values. Elements with errors less than 10% were acceptable, whereas those greater than 10% and with greater than 2 times detection limit were investigated in more detail and often culled.

Table 1.1. Summary statistics for Capricorn groundwaters. Results are in mg/L or *µg/L or **ng/L (activated C).

Element	n	Min	Max	Median	Stdev	5th	10th	25th	50th	75th	90th	95th	99th
WT	665	1	60	9	7.6	2.9	3.8	5.6	9.0	14	20	25	39
Temp	965	7.1	37.7	24.9	3.3	18.6	20.2	22.3	24.9	26.7	27.8	28.8	31.3
pH	1007	5.81	9.12	7.48	0.42	6.94	7.06	7.25	7.48	7.81	8.13	8.27	8.66
Eh_mV	1019	-280	465	197	139	27	84	134	197	361	389	401	446
TDS	1024	61	18832	1186	1877	339	422	670	1186	2305	3935	5436	9770
Ag**	901	1	1462	20	64	1	1	6	20	46	74	95	200
Al	819	0.025	0.46	0.025	0.022	0.025	0.025	0.025	0.025	0.025	0.025	0.025	0.045
As*	1008	0.05	135	1	7.1	0.05	0.05	0.4	1	2.1	4.9	8.5	27
Au**	1024	2	3070	2	134	2	2	2	2	2	2.59	4	20.4
B	1017	0.018	18.4	0.72	1.08	0.21	0.27	0.43	0.72	1.21	1.96	2.72	5.21
Ba*	1022	0.8	1250	60	87.3	6.72	12.8	35.2	60	97.9	160	209	410
Br	1008	0.05	33	1.96	3.26	0.40	0.58	0.97	1.96	3.90	6.85	8.75	16.8
Ca	1022	1.83	1080	77.3	89.0	24	33.3	51.3	77.3	115	186	257	445
Cd*	1003	0.04	4.5	0.1	0.23	0.09	0.1	0.1	0.1	0.1	0.1	0.1	0.70
Ce*	965	0.05	4.2	0.1	0.14	0.1	0.1	0.1	0.1	0.1	0.1	0.1	0.19
Cl	1023	5	7669	405	881	65	98	181	405	855	1702	2391	4452
Co*	1012	0.05	406	0.2	16.3	0.076	0.1	0.2	0.2	0.2	0.49	1.00	26.5
Cr*	1002	0.1	46.7	0.2	5.53	0.2	0.2	0.2	0.2	1.4	4	9.6	34.3
Cs*	547	0.1	14.9	0.25	1.04	0.2	0.2	0.25	0.25	0.25	0.8	1.46	4.98
Cu*	1022	0.3	572	5.6	39	0.8	1	1.77	5.6	15.6	36.9	62.1	206
DOC	991	0.052	119	1.13	5.74	0.37	0.48	0.69	1.13	1.74	3.23	5.18	21.4
F	785	0.05	8.16	1.02	0.93	0.36	0.47	0.69	1.02	1.61	2.47	3.09	4.67
Fe	956	0.0006	49.7	0.025	1.95	0.002	0.002	0.006	0.025	0.025	0.052	0.15	1.04
Ga*	987	0.02	1.5	0.02	0.048	0.02	0.02	0.02	0.02	0.02	0.02	0.02	0.02
Ge*	934	0.05	9.4	0.2	0.32	0.08	0.1	0.16	0.2	0.2	0.2	0.25	0.78
HCO3	1017	25.1	1832	320	174	113	162	232	320	435	532	650	941
K	1022	0.25	421	12.4	26.0	2.09	3.6	6.74	12.4	24.8	42.3	61.2	139
La*	980	0.1	2	0.1	0.064	0.1	0.1	0.1	0.1	0.1	0.1	0.1	0.10
Li*	1022	0.04	345	12.3	40	0.1	0.4	2.47	12.3	33.1	66.5	96.5	214
Mg	1022	1.49	809	69.3	80.5	20.2	27.2	40.8	69.3	113	189	245	408
Mn*	1022	0.1	29740	3.2	985	0.1	0.6	1.2	3.2	12.6	138	382	1302
Mo*	1014	0.1	178	2.3	13.3	0.2	0.4	0.9	2.3	7	16.4	29.7	62.9
Na	1022	2.76	4630	248	516	43.6	64.7	126	248	531	1010	1397	2387
Nb*	927	0.1	2.1	0.1	0.089	0.1	0.1	0.1	0.1	0.1	0.1	0.1	0.4
Ni*	1003	0.1	111	2	5.47	0.7	1	2	2	2	2	4.34	20.9
NO3	1017	0.04	707	46.1	60.9	1.39	6	19.1	46.1	75.0	115	161	303
Pb*	987	0.04	20.7	0.11	0.84	0.07	0.1	0.1	0.11	0.26	0.5	0.8	2.7
Pd**	910	0.5	94	0.5	4.12	0.5	0.5	0.5	0.5	0.5	1.53	3.37	4.67
PO4	992	0.003	6.83	0.070	0.54	0.02	0.02	0.03	0.07	0.13	0.27	0.85	2.69
Pt**	908	0.5	1460	0.5	53.8	0.5	0.5	0.5	0.5	1	1.56	2.43	14
Rb	1019	0.0002	0.28	0.009	0.022	0.001	0.002	0.003	0.0087	0.019	0.039	0.056	0.10
Sb*	927	0.1	4.3	0.1	0.22	0.1	0.1	0.1	0.1	0.1	0.1	0.2	1.27
Sc*	934	0.1	1.1	0.1	0.21	0.1	0.1	0.1	0.1	0.4	0.6	0.7	0.9
Se*	999	0.07	212	3.1	8.06	0.2	0.6	1.6	3.1	5.4	8.9	11.5	24
Si	1020	0.58	65	30.2	13.3	7.15	11.1	21.1	30.2	37.8	47.5	53.5	59.7
Sn*	775	0.2	19	0.2	0.74	0.2	0.2	0.2	0.2	0.2	0.2	0.2	0.7
SO4	1023	1.2	3924	164	322	20	40	76	164	353	593	824	1472
Sr	1016	0.025	10.2	0.56	1.01	0.16	0.21	0.32	0.56	1.08	1.92	2.74	5.44
Ta*	980	0.03	0.4	0.03	0.016	0.03	0.03	0.03	0.03	0.03	0.03	0.03	0.1
Te*	944	0.1	3.8	0.1	0.18	0.1	0.1	0.1	0.1	0.1	0.1	0.475	0.9
Tl*	997	0.08	7.6	0.1	0.24	0.1	0.1	0.1	0.1	0.1	0.1	0.1	0.25
TN	988	0.013	351	11.2	20.5	0.75	1.95	5.12	11.2	17.8	27.8	40.0	103
U*	1022	0.03	721	4.89	55.9	0.2	0.43	1.54	4.89	21.2	61.8	111	273
V*	1022	0.09	370	18.6	38.2	0.73	1.72	5.9	18.6	37.0	66.3	98.8	208
W*	1002	0.1	23.3	0.1	0.92	0.1	0.1	0.1	0.1	0.1	0.27	0.7	2.99
Y*	1002	0.05	0.8	0.1	0.037	0.07	0.1	0.1	0.1	0.1	0.1	0.1	0.24
Zn*	1022	1.1	880	24.6	62.4	9	11.6	16	24.6	36.0	67.6	104	380
Zr*	980	0.05	2.2	0.1	0.088	0.1	0.1	0.1	0.1	0.1	0.1	0.1	0.319
$\delta^{18}O_{SO4}$	145	3.03	29.5	13.3	2.81	8.63	10.3	12.0	13.3	14.2	15.0	16.2	25.9
$\delta^{34}S$	145	5.25	15.8	8.55	1.90	6.53	6.99	7.57	8.55	9.90	11.6	12.8	15.5
δ18O	997	-11.6	5.44	-5.43128	1.56	-6.96	-6.64	-6.09	-5.43	-4.69	-3.49	-2.57	1.16
δ2H	997	-85.2	13.5	-40.5	8.44	-50.7	-48.3	-44.7	-40.5	-36.9	-31.5	-26.0	-10.2

Table 1.2. Duplicate, standard and blank errors for elements/compounds used in the project. Note: many of the REE were regularly below detection. Orange coloured errors were considered moderately high (>10 % error) and red coloured errors were very high and often were due to detection limit issues. Results are in mg/L, *µg/L or **ng/L (activated C).

	Duplicates difference		Duplicates %diff		Duplicates HRD		HAMIL 20.2			TM 26.4			Blanks		Max error	Max error
Element	stdev	95% confidence	stdev	95% confidence	stdev	95% confidence	stdev	% confiden	%error	stdev	% confiden	%error	stdev	% confiden	ppb/ppm	%
Ag_MS*	0.105	0.032	20.753	6.276	18.456	5.582	nd	nd	nd	0.269	0.110	1.781	nd	nd	0.110	6.276
Ag_Carb**	16.004	4.840	59.070	17.865	70.672	21.373							11.622	6.576	6.576	11.573
Al	0.024	0.007	14.396	4.354	11.388	3.444	nd	nd	nd	0.045	0.018	22.773	nd	nd	0.018	22.773
As*	0.176	0.053	14.654	4.432	9.430	2.852	0.187	0.077	8.351	0.592	0.242	2.745	nd	nd	0.242	8.351
Au**	26.619	8.050	25.290	7.648	19.842	6.001							0.285	0.161	8.050	7.648
B	0.202	0.061	9.478	2.866	6.151	1.860	0.098	0.040	38.176	nd	nd	nd	0.100	0.056	0.061	38.176
Ba*	10.466	3.165	8.741	2.644	5.232	1.582	1.435	0.587	1.992	1.457	0.596	2.278	1.011	0.572	3.165	2.644
Bi*	0.043	0.013	18.051	5.459	13.387	4.049	nd	nd	nd	0.186	0.076	2.690	nd	nd	0.076	5.459
Br	0.830	0.251	38.140	11.535	45.451	13.746							nd	nd	0.251	13.746
Ca	5.987	1.811	6.534	1.976	4.164	1.259	2.582	1.055	2.108	1.587	0.649	2.944	0.256	0.145	1.811	2.944
Cd*	0.055	0.017	27.667	8.367	47.392	14.333	nd	nd	nd	0.398	0.162	1.902	nd	nd	0.162	14.333
Ce*	0.040	0.012	35.496	10.735	169.615	51.296	nd	nd	nd	nd	nd	nd	nd	nd	0.012	51.296
Cl	202.100	61.121	25.592	7.740	25.720	7.778							3.367	1.905	61.121	7.778
Co*	0.061	0.018	20.187	6.105	15.055	4.553	0.135	0.055	76.221	0.280	0.114	1.399	nd	nd	0.114	76.221
Cr*	0.147	0.045	10.726	3.244	7.320	2.214	nd	nd	nd	0.509	0.208	1.682	nd	nd	0.208	3.244
Cs*	0.070	0.021	16.665	5.040	13.874	4.196	0.062	0.025	5.744	nd	nd	nd	nd	nd	0.025	5.744
Cu*	3.294	0.996	19.960	6.036	17.169	5.192	0.217	0.089	5.924	0.561	0.229	1.501	0.353	0.199	0.996	6.036
Dy*	0.020	0.006	16.487	4.986	12.945	3.915	nd	nd	nd	nd	nd	nd	nd	nd	0.006	4.986
Er*	0.020	0.006	16.487	4.986	12.945	3.915	nd	nd	nd	nd	nd	nd	nd	nd	0.006	4.986
Eu*	0.020	0.006	16.487	4.986	12.945	3.915	nd	nd	nd	nd	nd	nd	nd	nd	0.006	4.986
Fe_OES	0.047	0.014	21.523	6.509	16.591	5.018	nd	nd	nd	nd	nd	nd	nd	nd	0.014	6.509
Fe_MS*	34.638	10.476	23.334	7.057	20.622	6.237	nd	nd	nd	0.941	0.385	1.819	2.964	1.677	10.476	7.057
F	0.874	0.264	28.828	8.718	27.264	8.245							0.167	0.094	0.264	8.718
Ga*	0.032	0.010	15.470	4.679	11.903	3.600	nd	nd	nd	0.335	0.137	3.172	nd	nd	0.137	4.679
Gd*	0.020	0.006	16.487	4.986	12.945	3.915	nd	nd	nd	nd	nd	nd	nd	nd	0.006	4.986
Ge*	0.019	0.006	14.070	4.255	9.275	2.805	nd	nd	nd	nd	nd	nd	nd	nd	0.006	4.255
HCO3	10.845	3.280	2.246	0.679	1.176	0.356							12.230	6.920	6.920	0.679
Hf*	0.032	0.010	16.101	4.869	12.340	3.732	nd	nd	nd	nd	nd	nd	nd	nd	0.010	4.869
Ho*	0.020	0.006	16.487	4.986	12.945	3.915	nd	nd	nd	nd	nd	nd	nd	nd	0.006	4.986
In*	0.032	0.010	16.101	4.869	12.340	3.732	nd	nd	nd	nd	nd	nd	nd	nd	0.010	4.869
K	4.207	1.272	9.780	2.958	6.413	1.940	0.346	0.142	3.454	0.235	0.096	12.639	0.074	0.042	1.272	12.639
La*	0.046	0.014	34.975	10.577	169.704	51.323	0.137	0.056	81.251	nd	nd	nd	nd	nd	0.056	81.251
Li*	2.001	0.605	6.364	1.925	3.719	1.125	0.241	0.098	1.552	0.329	0.134	2.775	0.070	0.040	0.605	2.775
Lu*	0.020	0.006	16.487	4.986	12.945	3.915	nd	nd	nd	nd	nd	nd	nd	nd	0.006	4.986
Mg	14.073	4.256	8.352	2.526	5.260	1.591	1.221	0.499	3.486	0.951	0.388	6.530	0.478	0.270	4.256	6.530
Mn*	59.214	17.908	28.699	8.680	25.123	7.598	nd	nd	nd	0.620	0.253	2.438	0.486	0.275	17.908	8.680
Mo*	0.664	0.201	12.196	3.688	9.856	2.981	0.222	0.091	2.728	0.316	0.129	1.705	0.099	0.056	0.201	3.688
Na	84.640	25.598	6.646	2.010	4.185	1.266	3.934	1.608	3.865	3.151	1.288	14.854	1.057	0.598	25.598	14.854
Nb*	0.065	0.020	16.101	4.869	12.340	3.732	nd	nd	nd	nd	nd	nd	nd	nd	0.020	4.869
Nd*	0.021	0.006	18.749	5.670	14.473	4.377	nd	nd	nd	nd	nd	nd	nd	nd	0.006	5.670
Ni*	0.186	0.056	15.776	4.771	10.770	3.257	0.177	0.072	4.854	0.463	0.189	1.664	nd	nd	0.189	4.854
NO3	15.083	4.562	31.904	9.649	32.447	9.813							0.871	0.493	4.562	9.813
NPOC	0.679	0.205	24.844	7.514	22.770	6.886							1.124	0.636	0.636	7.514
P	0.337	0.102	18.102	5.474	15.728	4.756	nd	nd	nd	nd	nd	nd	nd	nd	0.102	5.474
Pb*	1.093	0.331	23.213	7.020	17.195	5.200	0.138	0.056	12.570	0.319	0.130	1.390	0.045	0.025	0.331	12.570
Pd**	0.466	0.141	23.024	6.963	17.430	5.271							0.784	0.443	0.443	6.963
PO_4-P	0.027	0.008	25.296	7.650	23.479	7.101							0.009	0.005	0.008	7.650
Pr*	0.020	0.006	16.487	4.986	12.945	3.915	nd	nd	nd	nd	nd	nd	nd	nd	0.006	4.986
Pt**	0.969	0.293	22.148	6.698	16.580	5.014							0.483	0.273	0.293	6.698
Rb*	2.141	0.647	13.503	4.084	11.828	3.577	0.339	0.139	2.311	0.490	0.200	2.004	nd	nd	0.647	4.084
S	9.080	2.746	6.412	1.939	4.058	1.227	0.933	0.381	2.397	0.622	0.254	4.281	0.152	0.086	2.746	4.281
Sb*	0.023	0.007	11.462	3.466	7.641	2.311	0.129	0.053	16.129	0.199	0.081	2.655	nd	nd	0.081	16.129
Sc*	0.079	0.024	17.898	5.413	13.076	3.954	nd	nd	nd	nd	nd	nd	nd	nd	0.024	5.413
Se*	0.333	0.101	8.965	2.711	5.689	1.720	0.126	0.051	19.087	0.370	0.151	2.279	nd	nd	0.151	19.087
Si	4.967	1.502	10.425	3.153	6.975	2.109	0.246	0.101	24.191	0.200	0.082	23.601	nd	nd	1.502	24.191
Sm*	0.020	0.006	16.487	4.986	12.945	3.915	nd	nd	nd	nd	nd	nd	nd	nd	0.006	4.986
Sn*	0.198	0.060	30.017	9.078	96.077	29.056	nd	nd	nd	0.393	0.160	2.824	nd	nd	0.160	29.056
Sr	0.201	0.061	7.612	2.302	4.719	1.427	0.028	0.011	2.866	0.015	0.006	5.637	nd	nd	0.061	5.637
SO4	56.941	17.221	25.843	7.816	25.777	7.796							2.045	1.157	17.221	7.816
Ta*	0.032	0.010	16.101	4.869	12.340	3.732	nd	nd	nd	nd	nd	nd	nd	nd	0.010	4.869
Tb*	0.020	0.006	16.487	4.986	12.945	3.915	nd	nd	nd	nd	nd	nd	nd	nd	0.006	4.986
Te*	0.144	0.044	33.769	10.213	7.118	2.153	nd	nd	nd	nd	nd	nd	nd	nd	0.044	10.213
Th*	0.063	0.019	16.101	4.869	12.340	3.732	nd	nd	nd	nd	nd	nd	nd	nd	0.019	4.869
Tl*	0.033	0.010	18.232	5.514	13.761	4.162	nd	nd	nd	0.100	0.041	0.832	nd	nd	0.041	5.514
Tm*	0.020	0.006	16.487	4.986	12.945	3.915	nd	nd	nd	nd	nd	nd	nd	nd	0.006	4.986
TN	4.475	1.353	21.219	6.417	21.297	6.441							0.085	0.048	1.353	6.441
U*	1.247	0.377	7.744	2.342	5.115	1.547	0.063	0.026	4.983	0.263	0.107	1.456	0.136	0.077	0.377	4.983
V*	1.169	0.354	9.127	2.760	6.475	1.958	0.052	0.021	3.787	0.490	0.200	1.568	0.153	0.087	0.354	3.787
W*	0.034	0.010	14.396	4.354	11.388	3.444	0.039	0.016	7.286	0.164	0.067	1.051	nd	nd	0.067	7.286
Y*	0.021	0.006	15.972	4.831	12.536	3.791	nd	nd	nd	nd	nd	nd	nd	nd	0.006	4.831
Yb*	0.020	0.006	16.487	4.986	12.945	3.915	nd	nd	nd	nd	nd	nd	nd	nd	0.006	4.986
Zn*	5.064	1.531	18.456	5.582	13.485	4.078	0.650	0.266	4.435	2.862	1.170	2.310	8.753	4.952	4.952	5.582
Zr*	0.035	0.011	15.475	4.680	11.896	3.598	nd	nd	nd	nd	nd	nd	nd	nd	0.011	4.680
$\delta^{18}O_{SO4}$	0.103	0.031	1.844	0.558	0.957	0.289									0.031	0.558
$\delta^{34}S$	0.176	0.053	4.309	1.303	2.260	0.684									0.053	1.303
δ18O	0.057	0.017	1.172	0.354	0.715	0.216							0.836	0.473	0.473	0.354
δ2H	0.257	0.078	0.829	0.251	0.500	0.151							4.471	2.530	2.530	0.251

1.4.1 Determination of Contamination Factor

Minimising sample contamination is critical in any geochemical survey, methods for determining this are discussed in detail in Gray et al. (2016), and the derived protocol described here. For this hydrogeochemical sampling project the greatest concerns were additions from the decomposition of organic matter in the water and/or from metals from the pipe/bore materials. To determine which samples were contaminated and to what degree, samples were separated based upon whether they were free flowing or bailed and a Contamination Value (CV) calculated, according to:

$$CV = Mean\left(\log_{10}\frac{P}{0.277} , \log_{10}\frac{OC}{6.94} , \log_{10}\frac{Fe}{0.234} , \log_{10}\frac{Mn}{0.059} , \log_{10}\frac{Zn}{546} \right)$$

(Zn in µg/L, all other elements in mg/L).

These variables were chosen for this terrain as they are significantly increased in contaminated samples (from organic contamination or dissolving metal pipes). Other variables such as Eh and HCO_3 also show effects but these are very intermittent, and still have range overlaps between uncontaminated and highly contaminated samples. The denominators used for each of the variables are the 98th percentile for each variable in the flowing bore dataset.

The calculated CV was used to calculate a contamination factor (CF), splitting the samples into 6 CF classes:

CF 1: Flowing bores (all other CF groups are bailed samples)

CF 2: CV < -0.8 (bailed, uncontaminated)

CF 3: -0.8 < CV < -0.417 (bailed, very slightly contaminated)

CF4: -0.417 < CV < -0.1 (bailed, slightly contaminated)

CF5: -0.1 < CV < 0.3 (bailed, contaminated)

CF6: 0.3 > CV (bailed, highly contaminated)

All elements were plotted to determine contamination effects, and for what contamination class elemental analytical data needs to be removed. Probability plots were coloured by contamination class (Figure 1.9 – Figure 1.12). Data for each element that was different from the class 1 (uncontaminated) were culled (Table 1.3). Such differentiation is possible as this data is an unbiased set (not just focused sampling over ore deposits). This contamination factor methodology can be used in future hydrogeochemical surveys.

One note of caution with this method is that using this contamination factor around weathering sulfides, can lead to a false positive for contamination. This did not come up as an issue in the previous north Yilgarn mapping but within the Capricorn this was noted as an issue around the Prairie Downs and Abra sampling. Several of these samples had very anomalous Fe, Mn and Zn which was not contamination from metal pipes but was a direct result of the weathering of pyrite and other sulfides. In this case half of the 'CF6' samples were actually drill holes into sulfides. This highlights the need for validation of the most 'contaminated' samples against the field data and components of organic contaminants (Eh, DOC, PO_4).

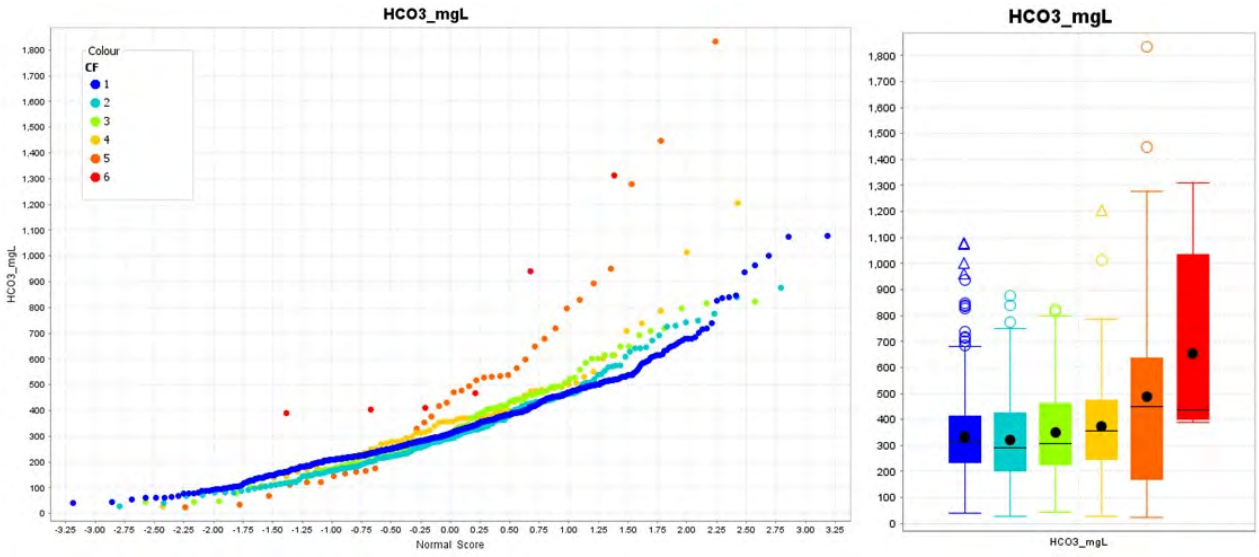

Figure 1.9. Contamination factor probability plot split of HCO_3 concentrations. CF Groups 1 (flowing), 2, 3 and 4 have similar probability populations indicating they are the only groups unaffected by contamination. Separation of the lines indicates differences in the sample groups, and Groups 5 and 6 are culled from the data set for HCO3 concentrations. Data is also represented as boxplots: median (black line), mean (black dot), quartiles (1st and 4th whiskers), outliers (circles) and extreme outliers (triangles).

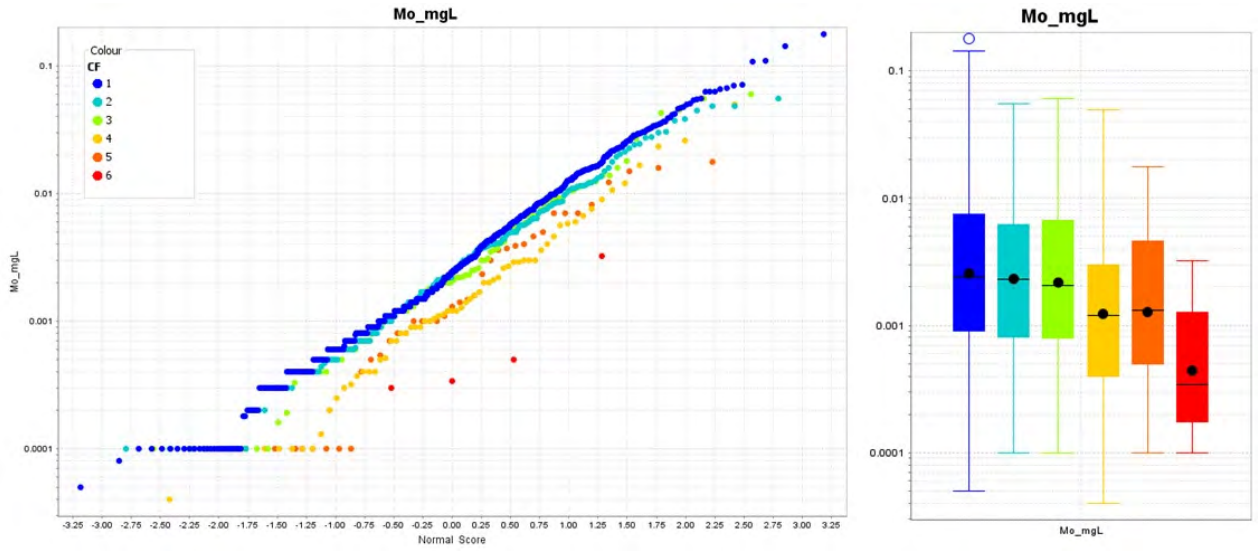

Figure 1.10. Contamination factor probability plot split of Mo concentrations. CF Groups 1 (flowing), 2 and 3 have similar probability populations indicating they are the only groups unaffected by contamination, whereas groups 4, 5 and 6 are culled from the data set for Mo concentrations.

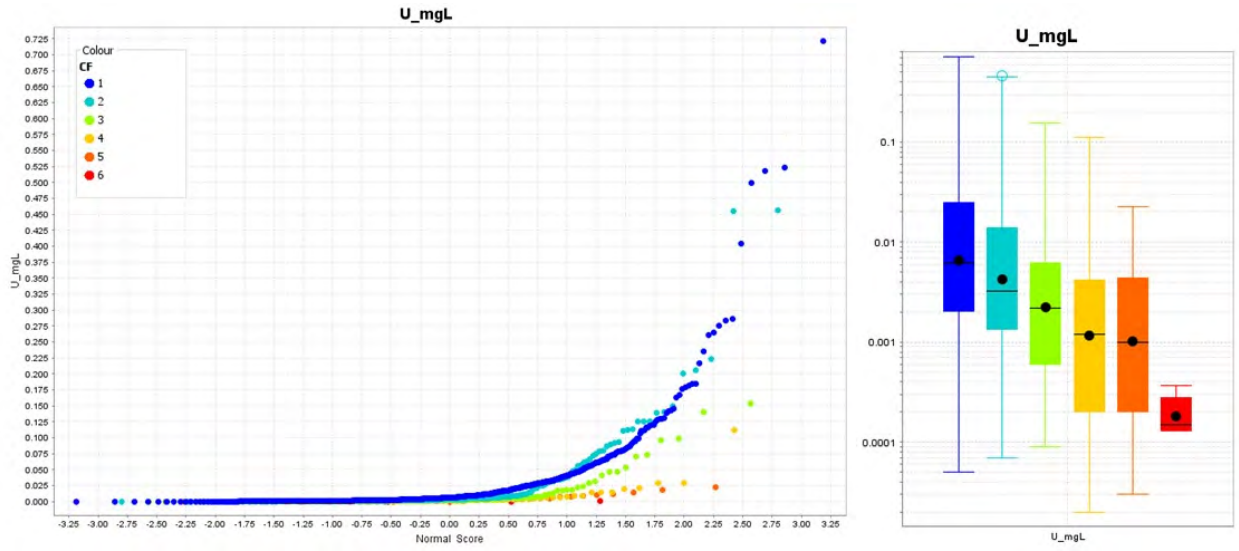

Figure 1.11. Contamination factor probability plot split of groundwater U concentrations. Class 1, 2, and 3 have similar probability populations and therefore unaffected by contamination, whereas groups 4, 5 and 6 are culled from the U data set.

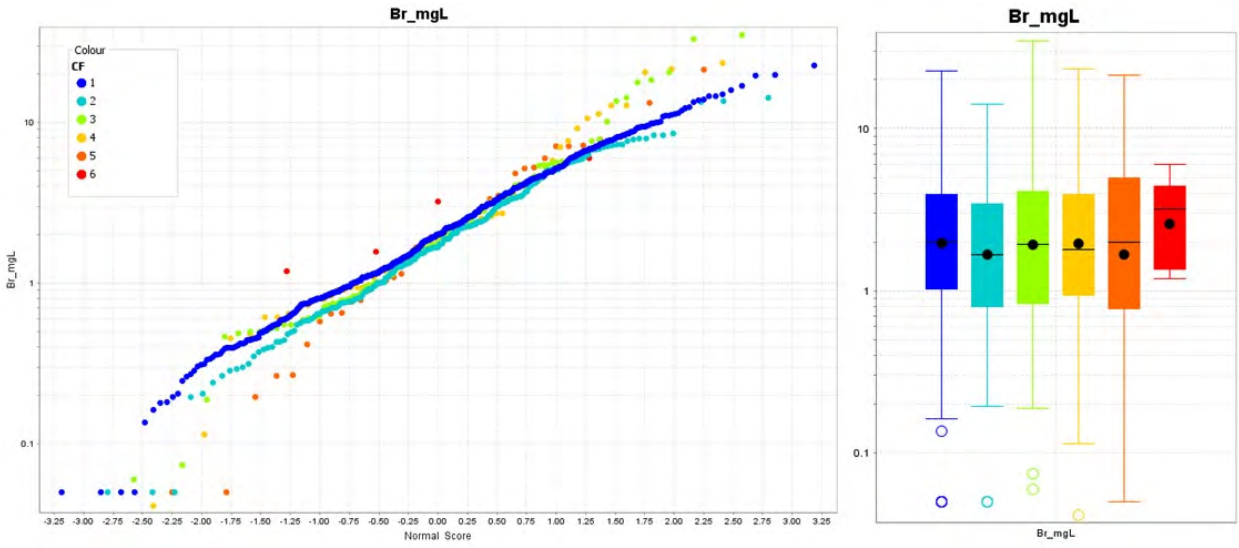

Figure 1.12. Contamination factor probability plot split of groundwater Br concentrations. The various CF Groups were not statistically distinguished.

Table 1.3. Influence of contamination on each measured component, i.e., those with only CF 1 kept are the most influenced by contamination, whereas CF 6 kept indicates the whole data set was used.

Element	CF kept	Element	CF kept	Element	CF kept
DOC	1	Si	2	F	5
Al	2	SO_4	2	K	5
B	2	V	2	Mg	5
Ba	2	Zn	2	Na	5
Co	2	Fe	3	Pd	5
Cr	2	pH	3	Rb	5
Cu	2	U	3	Sr	5
Eh	2	Mo	4	TDS	5
HCO_3	2	REE	4	W	5
Mn	2	Sn	4	Ag	6
Ni	2	Au	5	As	6
NO_3	2	Br	5	Li	6
Pb	2	Ca	5	Pt	6
PO_4	2	Cd	5		
Sb	2	Cl	5		

1.4.2 Elemental indices

Each element concentration was scaled from 0 to 1 based on the 0.1th and 99.9th percentile of the data (if normal distribution) or of the logged data (if log normal distribution) (e.g., Figure 1.13). There are some detection issues with this process as some elements have many samples below detection which were set as the zero value and hence skew the normal (or log normal) distribution at the low end.

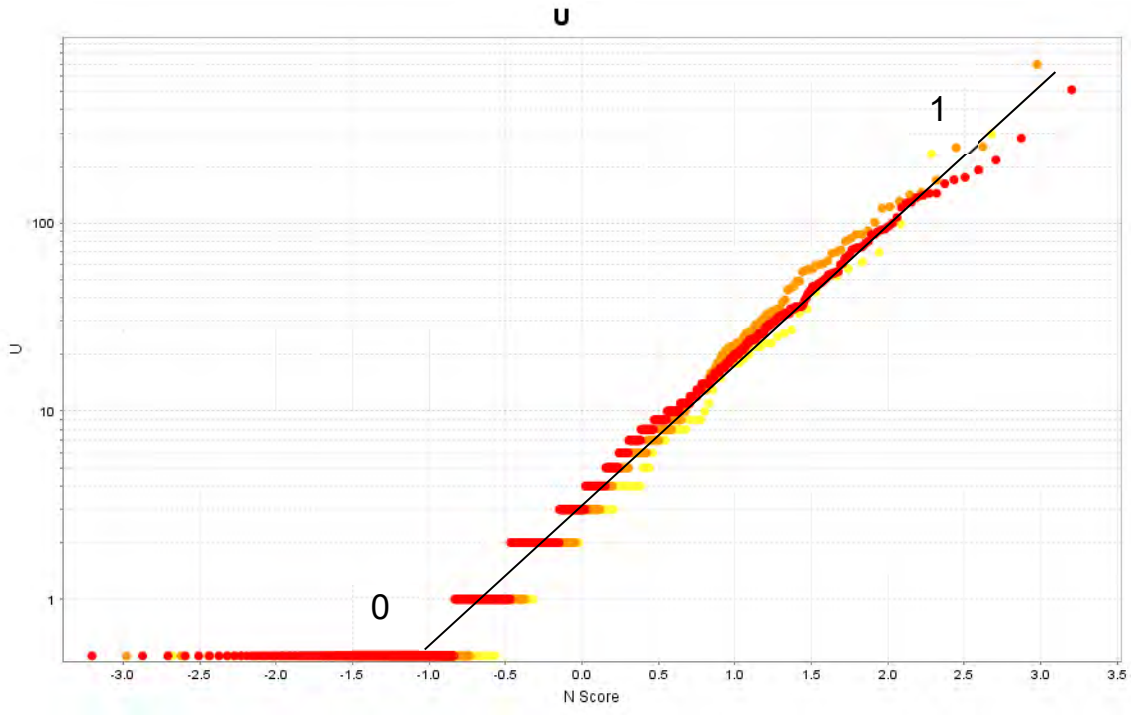

Figure 1.13. Uranium example of elemental index generation. The base10 logarithm of uncontaminated classes 1 – 2.2 (Figure 1.11) was taken and then scaled between 0 and 1.

1.4.3 Multielement indices

Elemental indices were added (or subtracted) together to create exploration detection tools. Previously (Gray and Noble 2006), multi-element indices were used to show the presence of weathering sulfides, Fe-rich sulfides and Ni-rich sulfides (Table 1.4). Other new multielement indices are used for lithology discrimination and to improve recognition of Au and base metal anomalism (Table 1.4). The Capricorn is not known to possess Ni systems analogous to those within the north Yilgarn (komatiite related) and therefore the index used to identify this mineralisation was used in the Capricorn to identify other sulfide systems.

Table 1.4. Multi-element indices used the Capricorn hydrogeochemical interpretation.

Label	Type/target	Formula
FeS	Weathering of barren sulfides	pH+Eh+Fe+Mn
AcidS	Attack on wall-rocks from acid produced from sulfides	Mo+Ba+Li+Al
Ni Min	Mineralised sulfides	Ni+Co+W+Pt
Au Min	Regional Au targets	Au+Ag+As
Au MinC	Capricorn Au	2*Au+Ag+Sb+As
Litho1	Lithology mapping/Mafics	V+Cr-2*U
SEND1	Sulfate enrichment/nitrate depletion	$2*SO_4$CLDSW-NO_3

1.4.4 Element excess and depletion

Using element ratios (compared to Cl or Na), some samples were observed to be in excess or deficit relative to the ion ratio observed for sea water. The distance away from the sea water dilution/evaporation line was determined, and provided a numerical measurement of the excess or depletion. For example, this was done for SO_4 with respect to Cl, for K and Rb with respect to Na, and for Ca with respect to Sr. At close scales, sulfate excess is particularly important for evaluating changes related to weathering sulfide ore bodies in shallow groundwater. At broader sampling (> km spacing), sulfate excess is lower and related to faults and other geological structures (Gray et al. 2016a).

The other major element indices are strongly controlled by lithology and hydrothermal alteration. For example, Sr relative to Ca (Figure 1.14) is useful in distinguishing between basic and acid lithologies. The derived formulas are listed below (all in mg/L except Rb in µg/L).

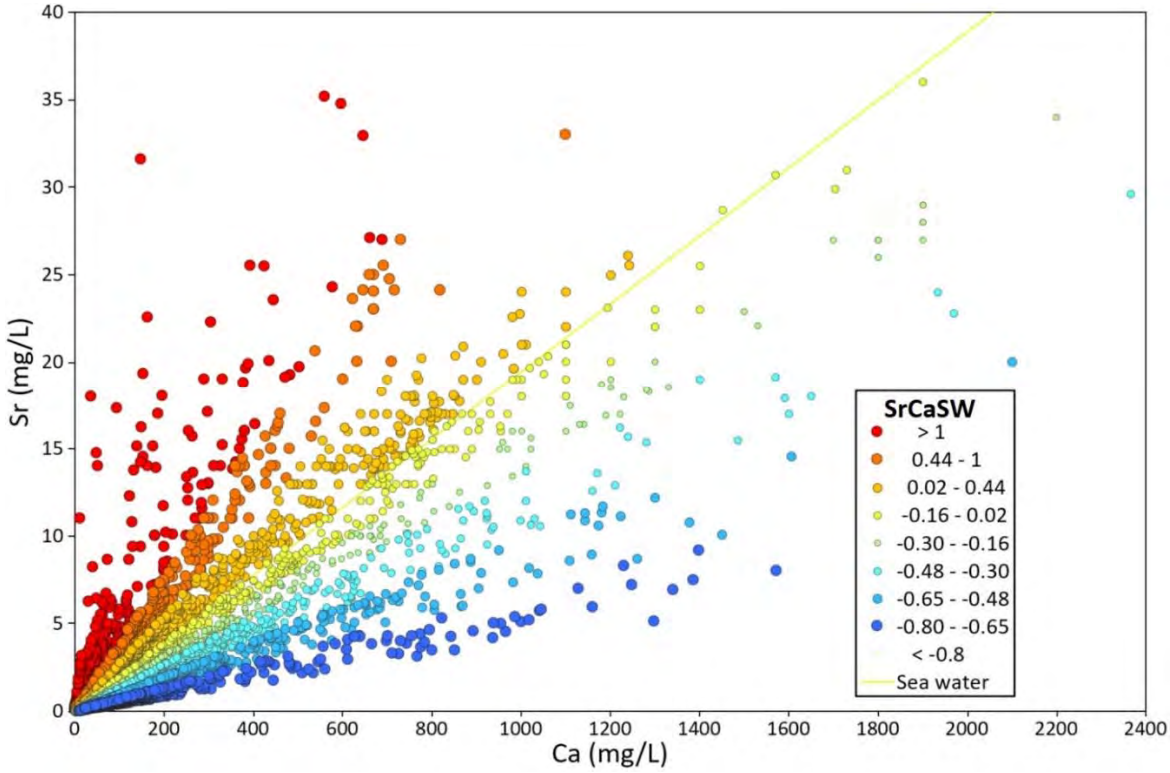

Figure 1.14. Example of calculation of Ca:Sr excess (relative to a general upper limit for "normal" Ca:Sr). These values are normalised to Sr content.

KNaSW = [2 x (K - 0.0363 x Na)]/[0.0363 x (Na + 500)] ... Na < 500 mg/L
= [K - 0.0363 x Na]/[0.0363 x Na] ... Na ≥ 500 mg/L

MgNaSW = [2 x (Mg - 0.1194 x Na)]/[0.1194 x (Na + 500)] ... Na < 500 mg/L
= [Mg - 0.1194 x Na]/[0.1194 x Na] ... Na ≥ 500 mg/L

CaNaSW = [Ca - 2 x (0.0381 x Na)]/[0.0381 x (Na + 500)] ... Na < 500 mg/L
= [Ca - 0.0381 x Na]/[0.0381 x Na] ... Na ≥ 500 mg/L

MgCaSW = [2 x (Mg – 3.14 x Ca)]/[3.14 x (Ca + 20)] ... Ca < 20 mg/L
= [Mg – 3.14 x Ca]/[3.14 x Ca] ... Ca ≥ 20 mg/L

SrCaSW = [2 x (Sr - 0.0195 x Ca)]/[0.0195 x (Ca + 20)] ... Ca < 20 mg/L
= [Sr - 0.0195 x Ca]/[0.0195 x Ca] ... Ca ≥ 20 mg/L

RbKSW = [2 x (Rb - 0.306 x K)]/[0.306 x (K + 20)] ... K < 20 mg/L
= [Rb - 0.306 x K]/[0.306 x K] ... K ≥ 20 mg/L

SO_4ClSW = [2 x (SO_4 - 0.1396 x Cl)]/[0.1396 x (Cl + 500)] ... Cl < 500 mg/L
= [SO_4 - 0.1396 x Cl]/[0.1396 x Cl] ... Cl ≥ 500 mg/L

BrClSW = [2 x (Br - 0.00345 x Cl)]/[0.00345 x (Cl + 500)] ... Cl < 500 mg/L
= [Br - 0.00345 x Cl]/[0.00345 x Cl] ... Cl ≥ 500 mg/L

The different calculation methods for lower ion concentrations minimise skewing data due to analytical errors close to detection limits. At higher concentrations these become a ratio difference:

e.g. for Na > 500 mg/L
- KNaSW = 2 means the K/Na sample ratio is 3 x sea water
- KNaSW = 1 means the K/Na sample ratio is 2 x sea water
- KNaSW = 0 means the K/Na sample ratio is equal to that of sea water
- KNaSW = -0.5 means the K/Na sample ratio is half that of sea water
- KNaSW = -0.75 means the K/Na sample ratio is one quarter that of sea water
- KNaSW = -0.95 means the K/Na sample ratio is one twentieth that of sea water

1.5 FAIMS Sampling Application Development

As part of the Capricorn Distal Footprints project, Drs Nathan Reid and Jens Klump worked on the generation of a field sampling application with in-built integration with the International Geo Sample Number (IGSN) project run by Dr Klump. Recording data electronically in the field naturally holds a number of advantages over pen and paper. Consistency between sampling teams is maintained, transcription errors are negated and the time taken at each individual sample location is significantly reduced. Due to the relatively straightforward procedure developed for groundwater sampling and field parameter analysis, the Capricorn Hydrogeochemistry project was identified as the ideal test case for the development of a field sampling application.

The hydrogeochemistry field data book developed by Reid et al. (2012) formed the basis for the sampling procedure. This book was turned into the original 'alpha' test for the mobile application, which was trialled at the initial Prairie Downs field sampling campaign with moderate success. This, in turn, led to a more streamlined hydrogeochemical sampling protocol as well as to the development of sampling protocols for other material types (e.g., vegetation, soils, rocks). This process has evolved (Reid et al., 2015; Golodoniuc et al., 2015; Klump et al., 2015) and has now reached the phase where fast and reliable collection of scientific data in remote areas is possible. The approach is backed by a unified platform – the Field Acquired Information Management System (FAIMS).

The app was developed together with the FAIMS at Macquarie University and is based on the open source FAIMS mobile platform. The FAIMS mobile platform has proved valuable due to the ability to customise data collection methodologies for any field research. FAIMS is an open source framework for mobile field data acquisition, developed for archaeological field data collection. The FAIMS framework can easily be adapted to a diverse range of scenarios, different kinds of samples, each with its own peculiarities, integration with GPS, and the ability to associate photographs taken with the device embedded camera with captured data.

Various customisations were trialled in the field throughout the course of the project and the feedback contributed to further improvement of the mobile application. The background for the sampling protocols for each sample type has come from CSIRO background IP. All customisations feature automatic date and position recording and reproduce the established CSIRO data recording workflows. The geochemical sampling customisation features an interactive GIS component, allowing the user to enter field observations as annotations to a map (Figure 1.15). The open communication protocols and file formats used by FAIMS modules allow easy integration with existing spatial data infrastructures and third-party applications, such as ArcGIS. It has basic mapping functionality showing the sampled points overlying maps (as GeoTIFF) that can be pre-loaded, it shows your current location, and allows for drawing of points and simple polygons to be later exported as shape files. This is complete with a tracking tool that you can use to gain distance and direction to a sample point in the field.

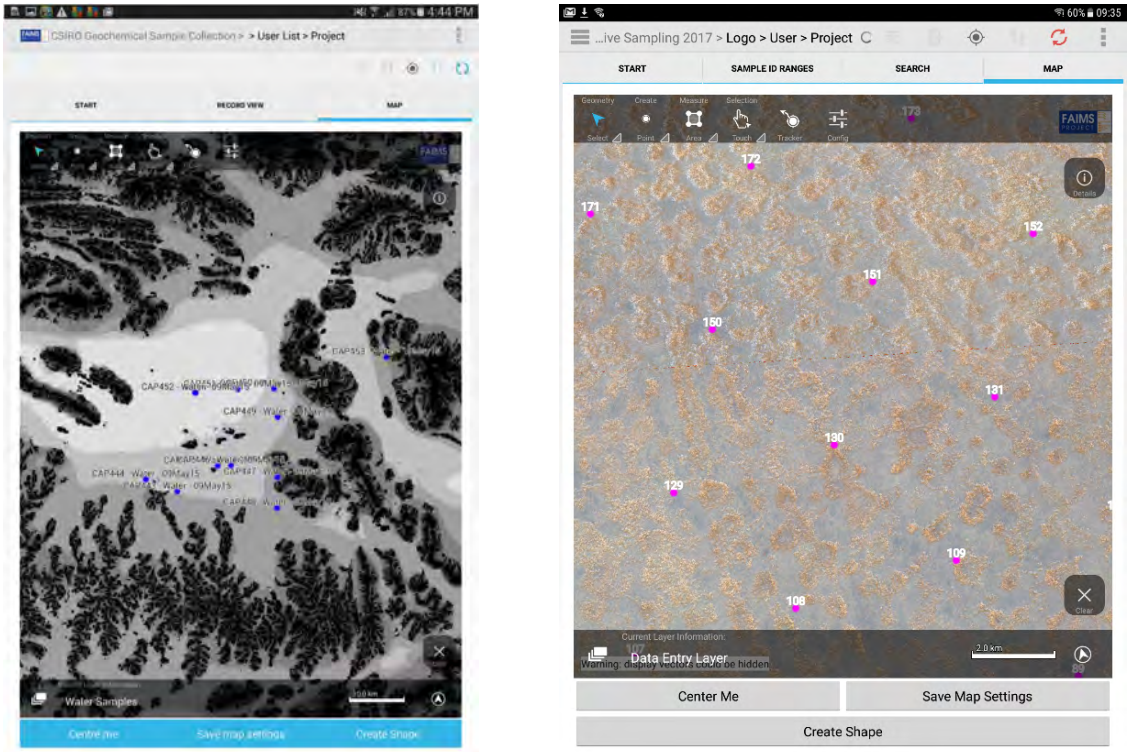

Figure 1.15. Mapping: water samples overlying the MrVBF imagery (left). Soil samples overlying satellite imagery (right).

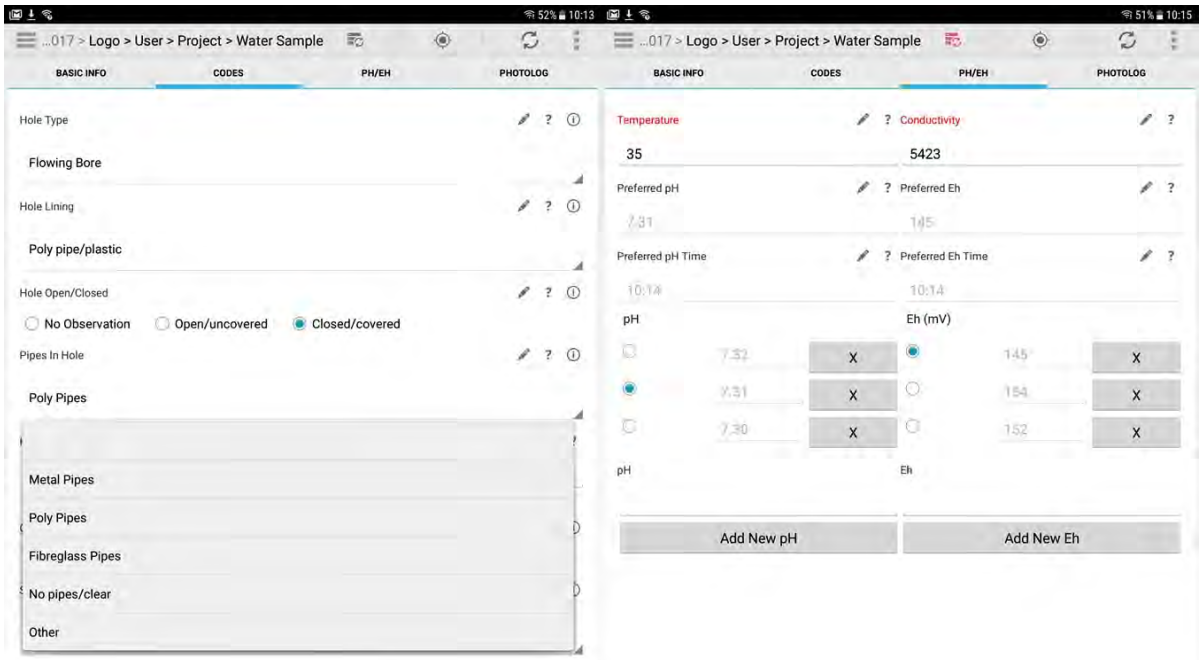

Figure 1.16. Water sample site information with dropdown options (left) and field chemical parameters (right).

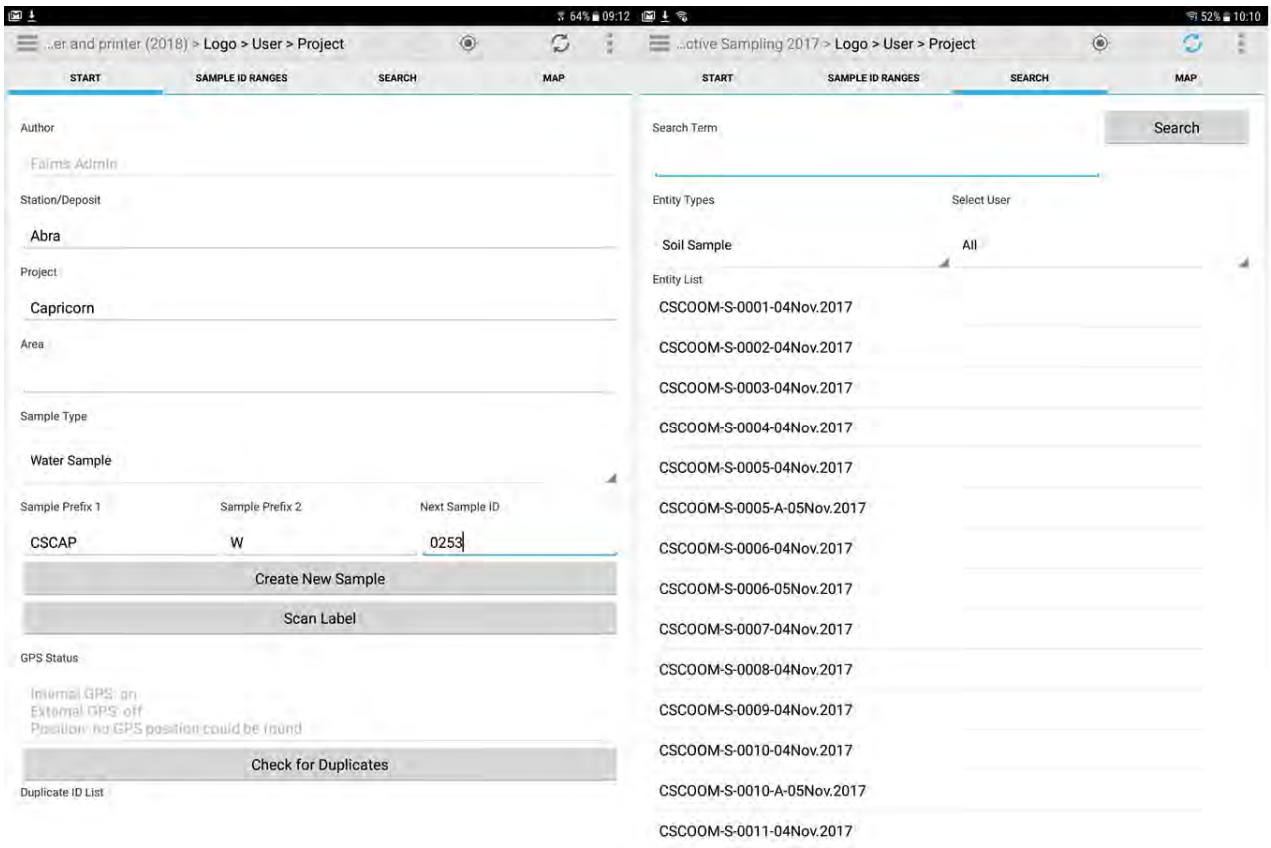

Figure 1.17. Sample generation and project details screen (left). Database querying and sample editing (right).

The FAIMS customisation allows for using inbuilt or external GPS to locate sample points, and incorporates standard and incremental sampling names which can be easily converted into an IGSN. Sampling can be documented not only in metadata, but also accompanied by photographic documentation and sketches. Our customisation is augmented with dropdown menu fields specific to each sample type and user defined tags (Figure 1.16). The customisation also provides users with an overview of all records from a field campaign in a records viewer (Figure 1.17).

A particular challenge is the remoteness of the sampling locations, hundreds of km away from network access. The first trial raised the issue of backup without access to the internet, so in collaboration with the FAIMS team and Solutions First, we commissioned a vehicle mounted portable server (Figure 1.18). This server box is constantly syncing with the tablets in the field via portable Wi-Fi access point (up to 100 m). It has a UPS that can run for up to 45 minutes when the vehicle is turned off, and a 1TB hard drive for storage of all data and photographs. The server can be logged into via any of the field tablets or laptop to download all the data collected to date or to just view it on the server. The data is provided as a database of ingestion, and csv for field processing and also as shape files for GIS mapping.

Figure 1.18. Field app and server being used in the field.

This application has led to significant time savings in the field with the added benefit of no further data entry required in the evenings or at the end of trip. The framework runs on compatible Android devices (e.g., tablets, smart phones) with the network infrastructure supported by a FAIMS Server. The server component is installed in a field vehicle to provide data synchronisation between multiple mobile devices, backup and data transfer. The data entry process was streamlined and followed the workflow that field crews were accustomed to with added data validation capabilities.

The use of a common platform allowed us to adopt the framework within multiple disciplines, improve data acquisition times, and reduce human-introduced errors.

The FAIMS framework along with custom-made data logging customisations is released under open-source licence and is readily available for industry uptake. Commercial organisations (eg. Solutions First) also manufacture FAIMS Server autonomous boxes. The successful trials of this application in the Capricorn Distal Footprints project has meant that all hydrogeochemical sampling by CSIRO is now performed using the app.

1.6 Results

The results section is separated based on groundwater lithological and regional trends, then sulfide (Ni and VHMS), Au and U commodities followed by isotopes and case studies. The appendices contain all data and calculated indices. Most distribution plots use natural breaks in the data.

To gain a more comprehensive understanding of groundwater chemistry across the region, results from the analysis of the samples from this study were combined with data from the northern portion of the hydrogeochemical mapping of the north Yilgarn (Gray et al. 2016a) and hydrogeochemical data from a stygofauna study (Halse et al., 2014) as well as previous CSIRO and state data (Figure 1.4). The Stygo Pilbara groundwater dataset and previous CSIRO data was subjected to a thorough QA/QC assessment (Gray et al. 2016b). Data that did not pass the assessment was rejected. Erroneous data (from well contamination and/or analytical or transcribing errors) was minimised, with seamless geochemical mapping across datasets. Data are plotted on the geology base map. Major terrains are delineated and labelled in Figure 1.1.

1.6.1 Major geochemical parameters

The majority of groundwater samples are relatively shallow (<20 m; Figure 1.19), neutral to alkaline (Figure 1.20) and oxidised (Figure 1.21). There is no pronounced variation in pH or Eh with lithology. Although acidic groundwaters can be an indicator of weathering sulfides this is generally difficult to observe on a regional scale. In general, groundwater interacting with granitic rocks will be weakly acidic to neutral, whereas waters above ultramafic rocks will be neutral to alkaline due to the alkaline minerals within these rocks. There is no observable difference between the granitic and sedimentary basin lithologies of the Capricorn. There are some acidic groundwaters in the Collier Basin and one sample associated with the Abra deposit that may be indicative of weathering sulfides. Reduced groundwaters have been related to local sources such as paleochannel sediments, sulfides or deep sources moving along fault systems (Gray et al., 2016a).

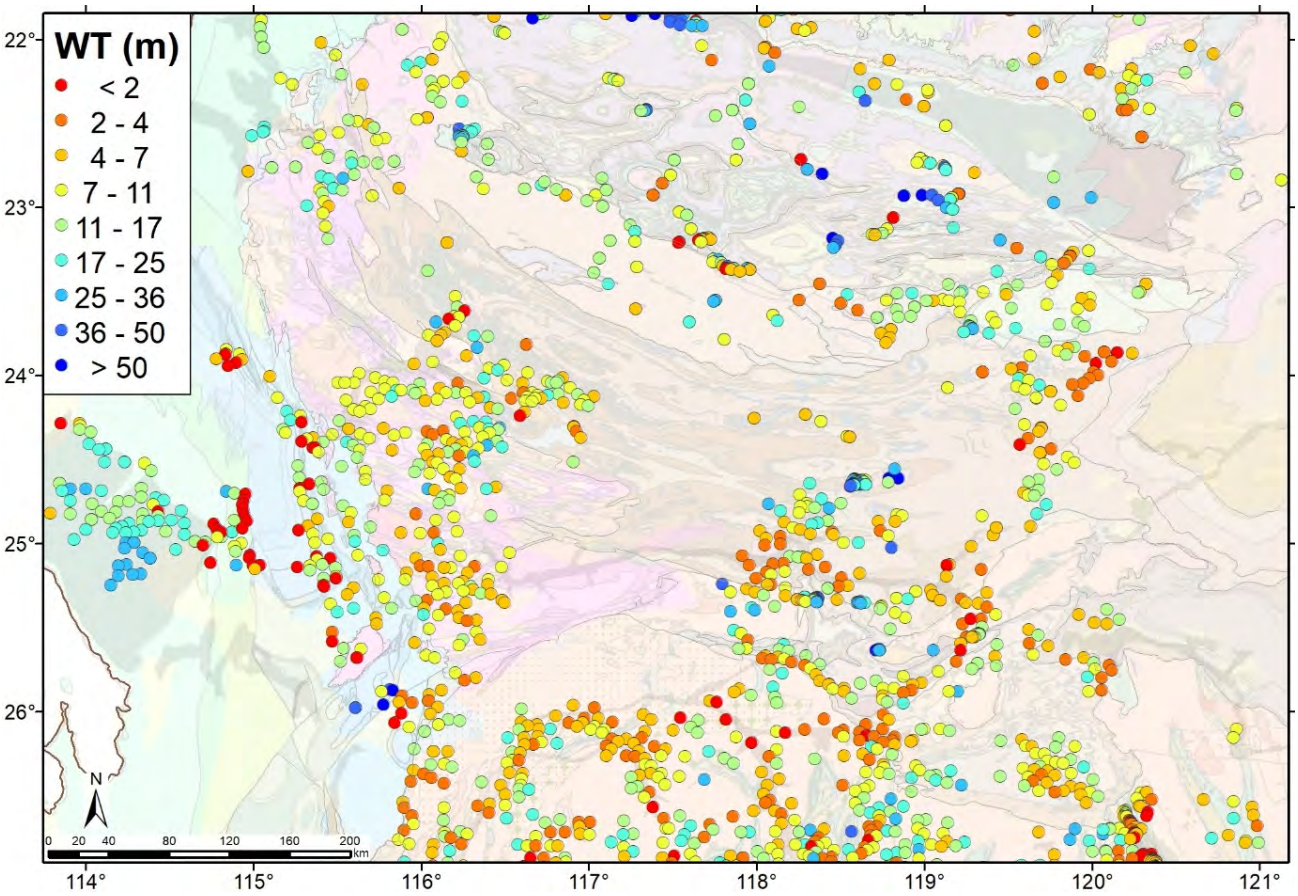

Figure 1.19: Water table depth across the Capricorn Orogen.

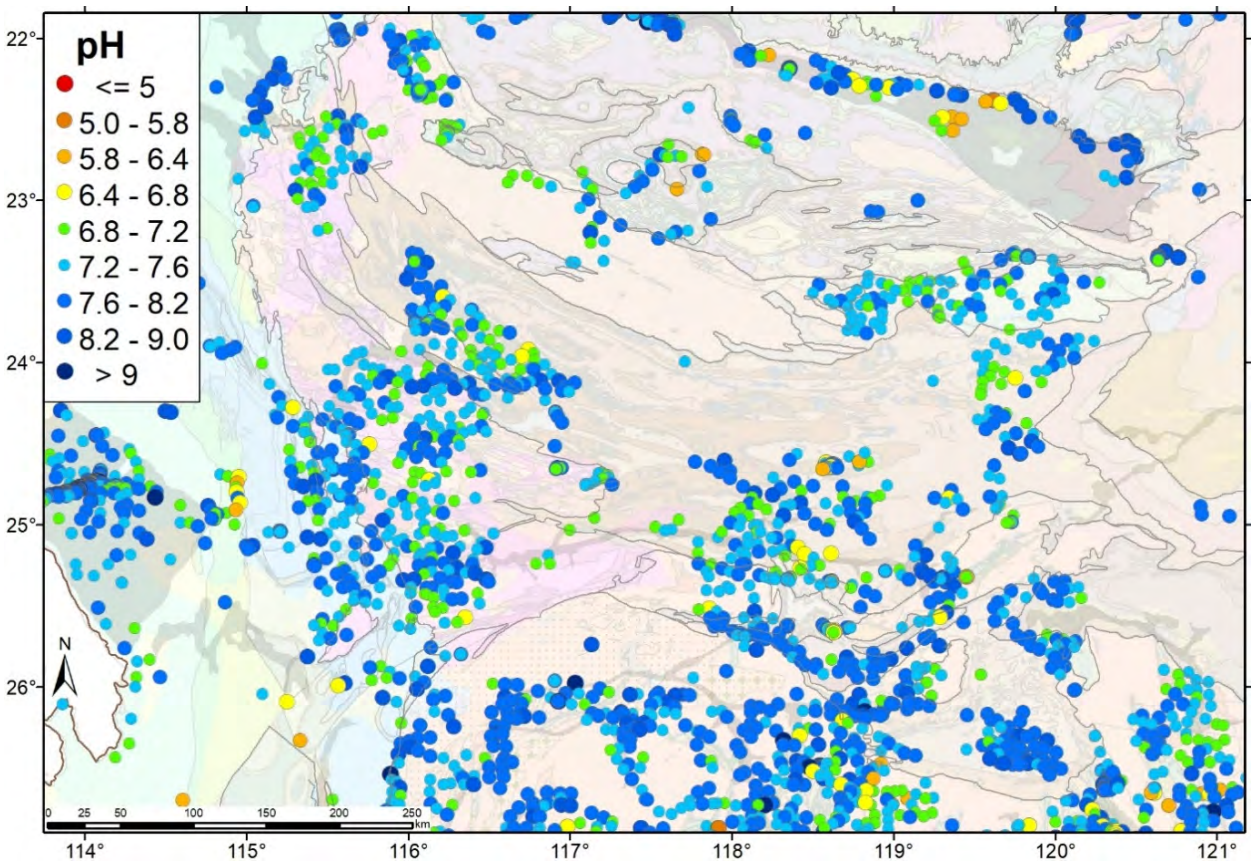

Figure 1.20. Groundwater pH conditions for the Capricorn Orogen.

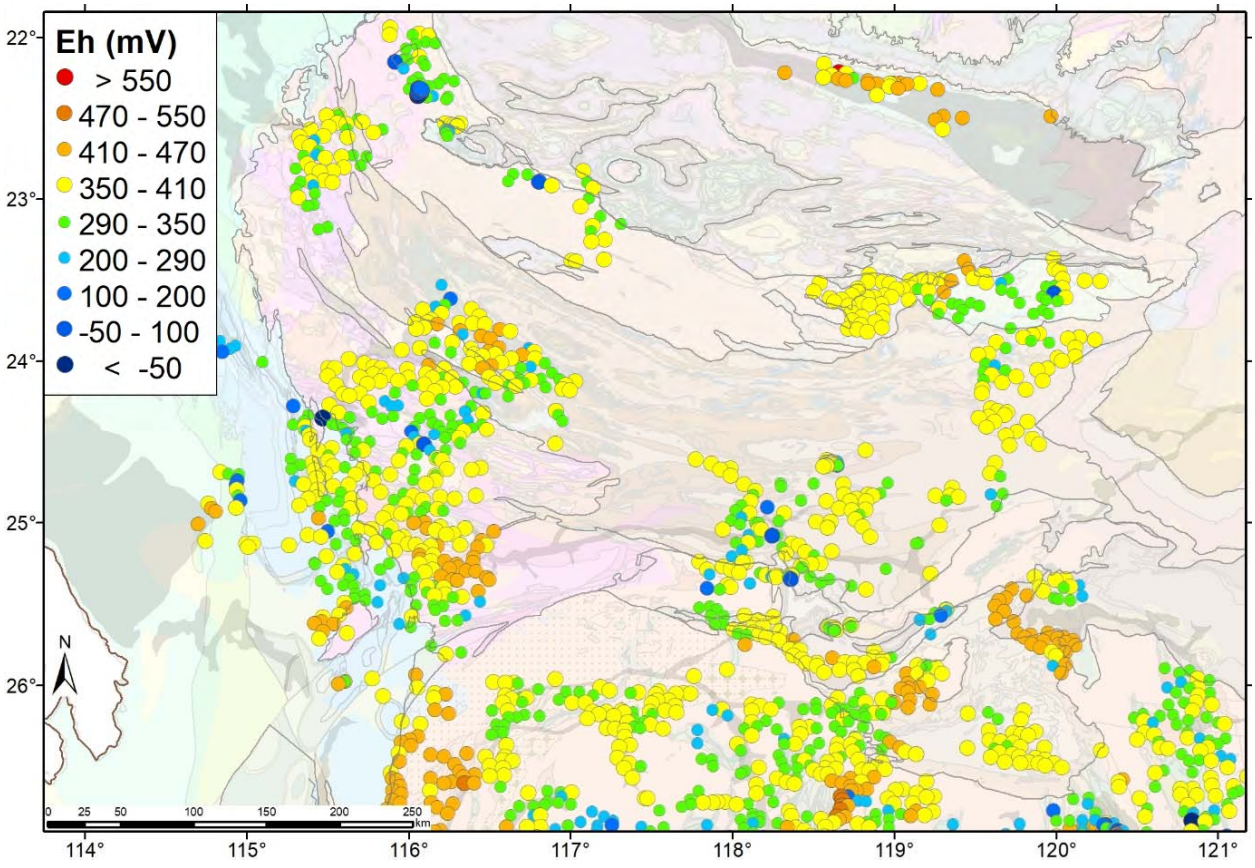

Figure 1.21. Groundwater Eh conditions for the Capricorn Orogen.

Groundwater in the Capricorn Orogen is generally fresh to slightly brackish (<3000 ppm TDS) but broad variations related to lithology are evident (Figure 1.22). The granitic Gascoyne province and Sylvania inlier are both generally more saline (TDS >3200 mg/L) than the Capricorn Orogen sedimentary basins. The most saline samples in the region (TDS >30000 mg/L) are found within the Phanerozoic Southern Carnarvon Basin. The most saline water in the central Edmund-Collier basin are within the Gascoyne drainage/paleodrainage system (Figure 1.22). This trend reflects a general pattern for water to become more saline as it approaches paleo-drainage channels and/or valley floors (Gray et al. 2016a).

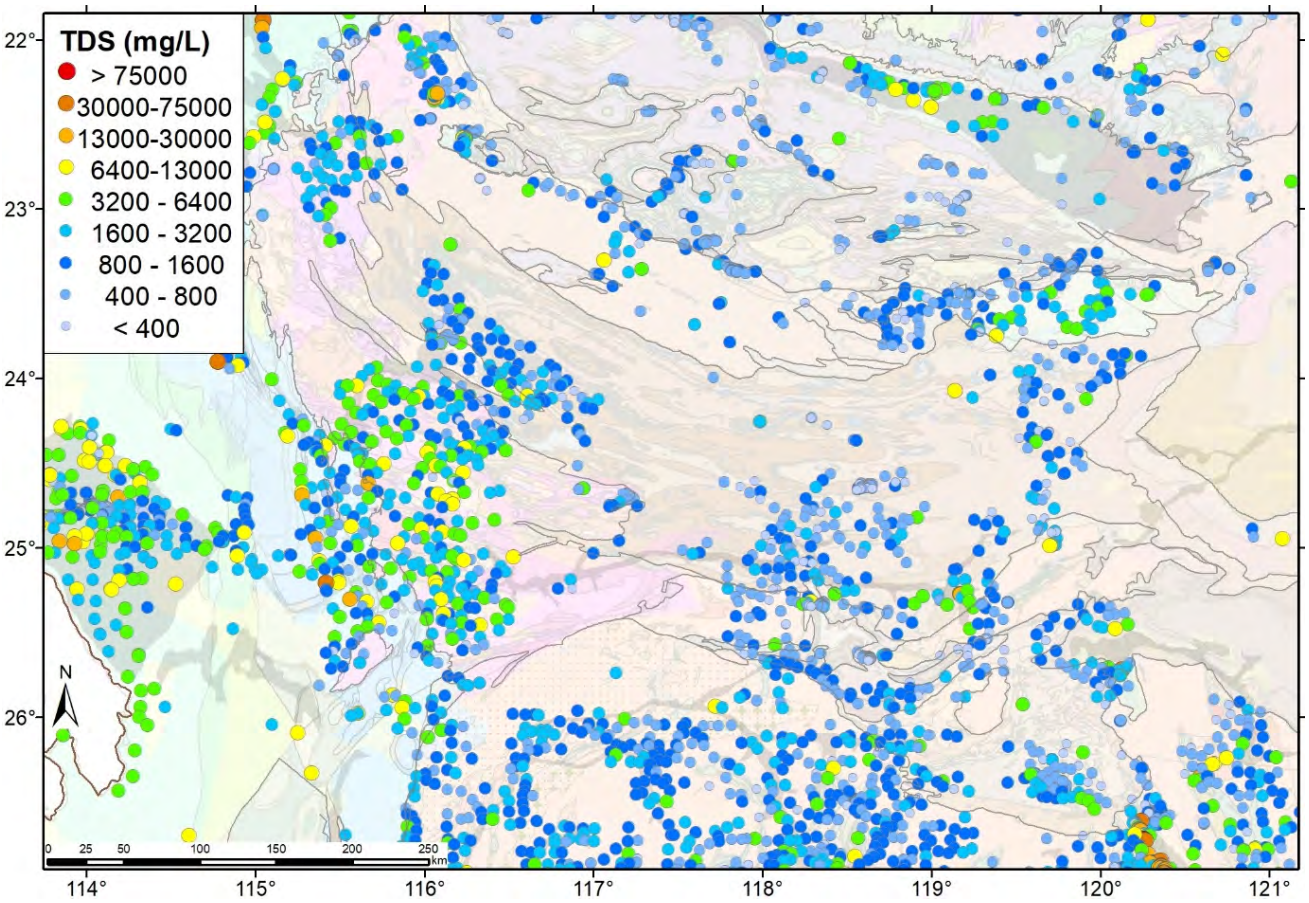

Figure 1.22. Groundwater salinities (TDS) for the Capricorn Orogen.

1.6.2 Lithological indicators and background values

The simplest lithological differences that can be distinguished within groundwater chemistry is between granitic/felsic rocks and mafic/ultramafic rocks. Dissolved Cr in groundwater has proven to be a reliable indicator of mafic and ultramafic rocks (Gray et al. 2016a). The south of the Bryah Basin is comprised of the metabasites of the Narracoota Formation and this is highlighted by the highly elevated Cr concentrations, with the majority of samples in the area containing more than 11 µg/L Cr (Figure 1.23).

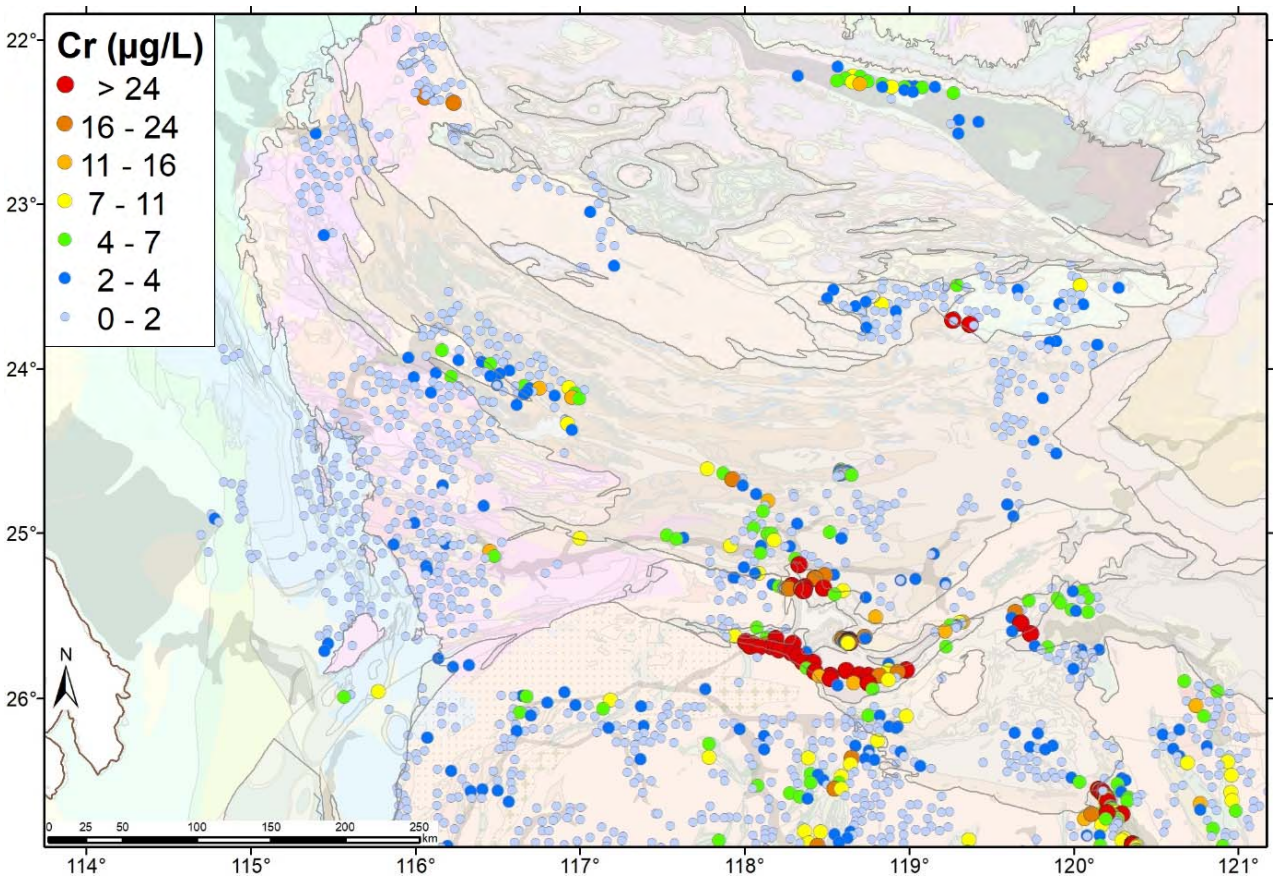

Figure 1.23. Groundwater Cr distribution for the Capricorn Orogen.

Dissolved V may also reflect large scale lithology, with mafic units having greater V concentrations than granites (Gray et al. 2014) (Figure 1.24). In the Capricorn this relationship does not always hold true as seen with the Gascoyne Province where mapped granites have higher concentrations of V than expected. This may represent V-rich granitoids or smaller (than mapping scale) mafic units within the granitic terrain. Lithium is more weakly correlated with mafic lithologies (Figure 1.25), but dissolved Li distribution shows higher concentrations (40-70 µg/L) over the Sylvania Inlier and Gascoyne province. The western edge of the study areas possesses very high Li concentrations (> 330 µg/L) over the Phanerozoic rocks, the source of which has yet to be determined.

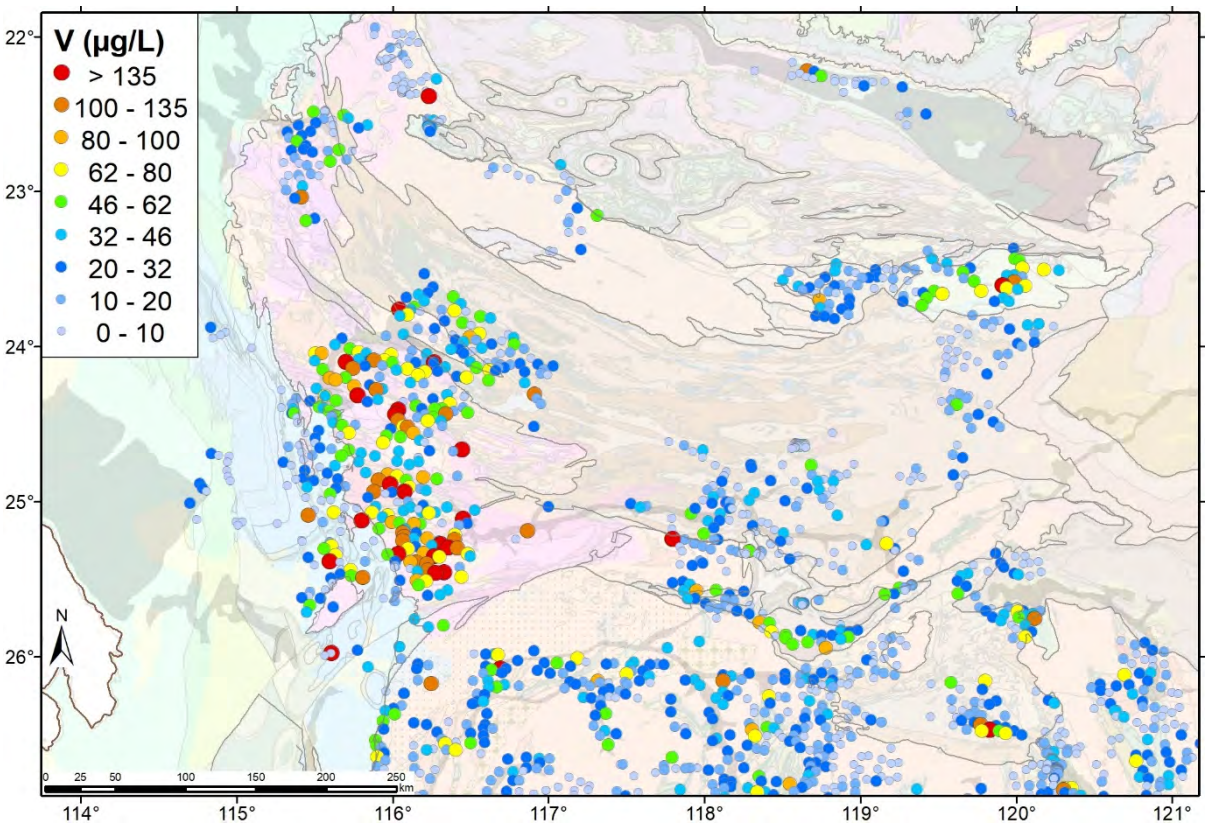

Figure 1.24. Dissolved V distribution for the Capricorn Orogen.

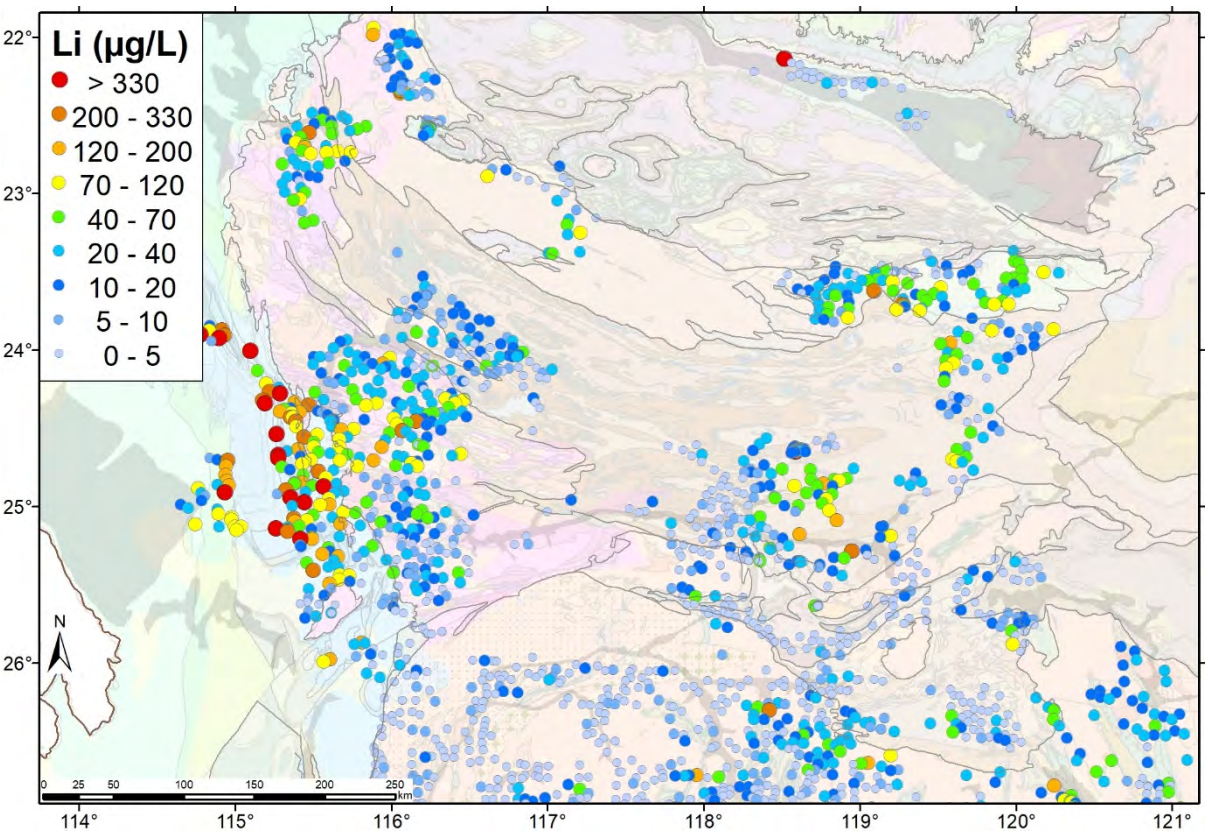

Figure 1.25. Dissolved Li distribution for the Capricorn Orogen.

Given that the major lithologies in the region are defined by either granitic rocks or basin sedimentary units it is not surprising that elements such as U (Figure 1.26) prove to be an element capable of discriminating lithological variations. Elevated dissolved U concentrations are mainly confined to the granitic dominated regions of the Gascoyne Province and Sylvania Inlier, with the majority of groundwaters having U concentrations above 16 µg/L.

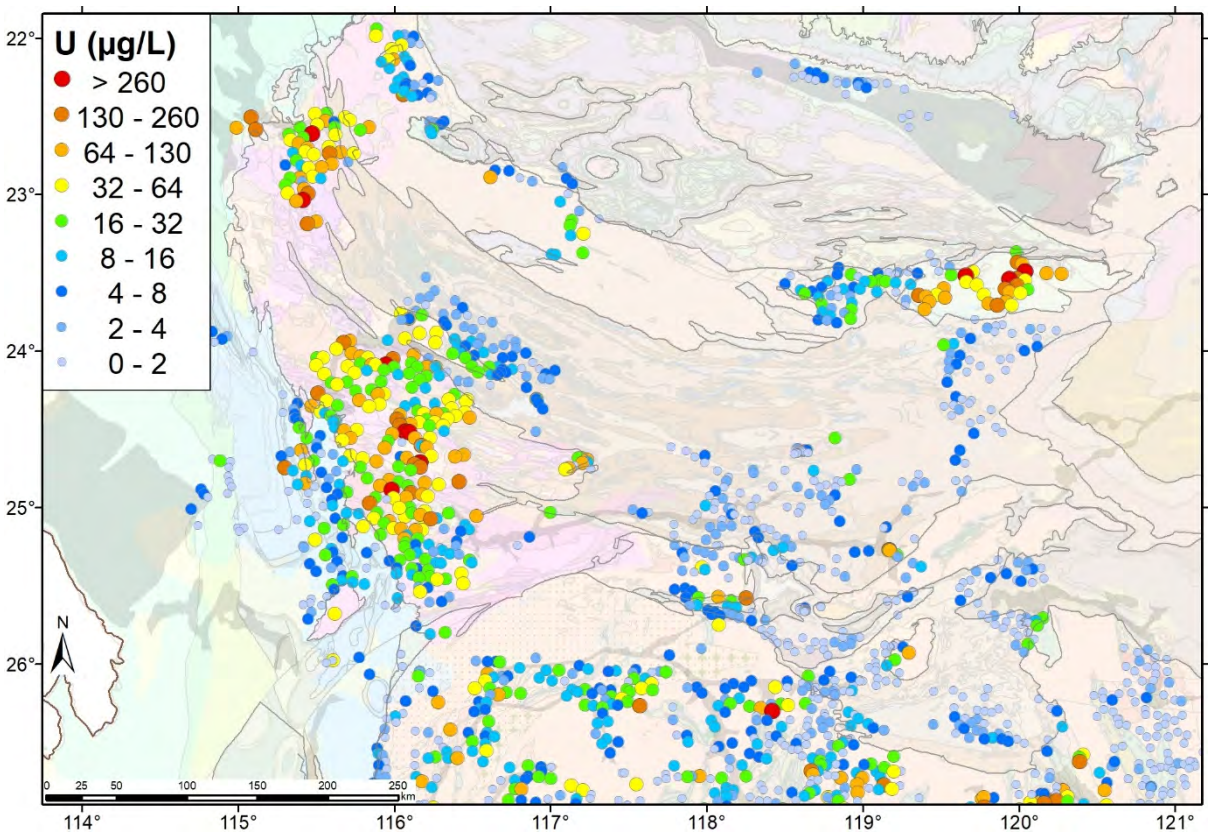

Figure 1.26. Dissolved U distribution for the Capricorn Orogen.

Lithology indices for improved discrimination were created from various element and parameter combinations. The Lithol1 index (V+Cr-2*U; Figure 1.27, Figure 1.28) more robustly separates mafic signatures (blue dots) from granites (red/orange dots) than single element abundances, at this sample spacing of 4-10 km. In previous investigations of the north Yilgarn (Gray et al., 2016a), this groundwater parameter was successful in indicating mafic rocks previously mapped as granites, either due to thin cover sequences or deep weathering. In the Capricorn this still generally holds true and in particular highlights the Sylvania Inlier. However, there is a major split between the north and south Gascoyne which seems to indicate the granitic rocks to the south show up as having a more 'mafic' signature compared to those of the north. This shows up in this index due to the increased U concentrations to the north and increased V to the south. The region with a 'mafic' signature is comprised of the Dalgaringa Supersuite, composed of granites, metatonalite, metagranodiorite and local mafic granulite.

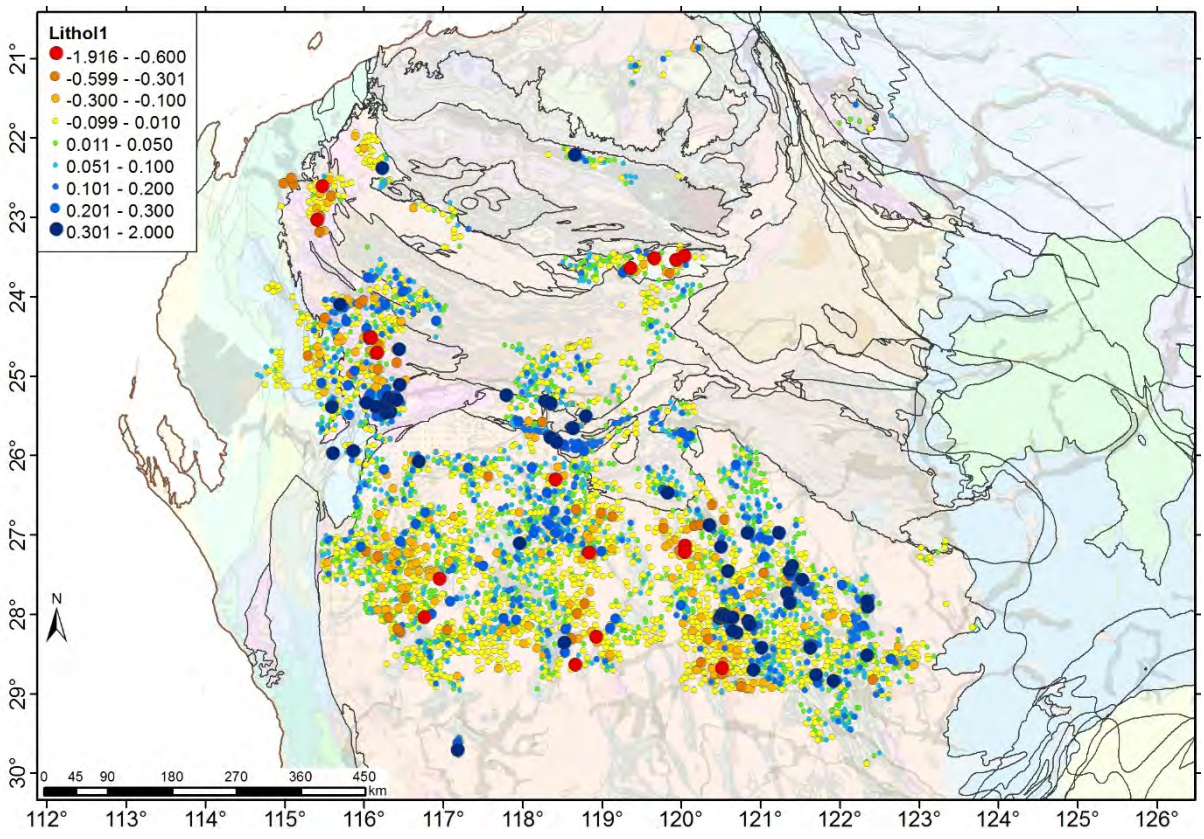

Figure 1.27. The Lithol1 index distribution for the Capricorn Orogen and north Yilgarn.

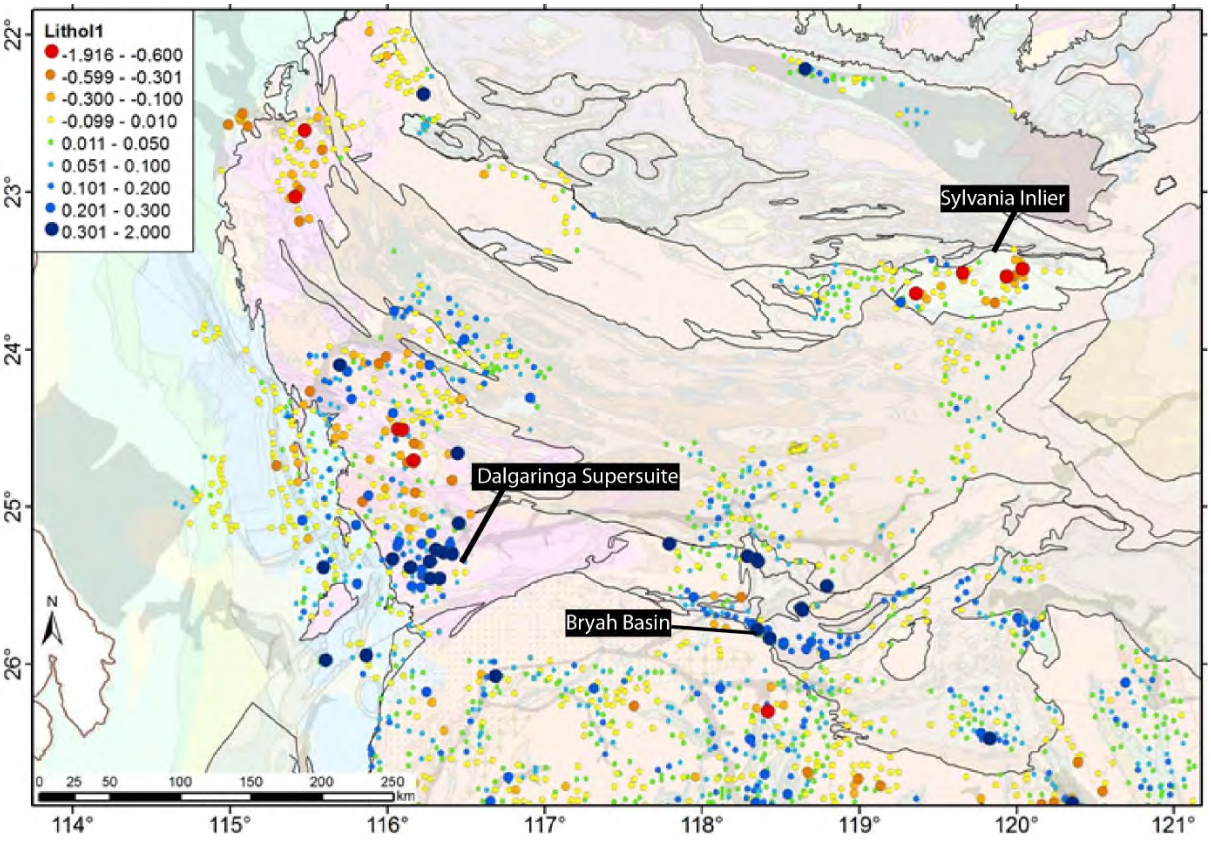

Figure 1.28. The Lithol1 index distribution for the Capricorn Orogen.

Other lithological discriminators use major elements such as Ca, K or Mg, which are constituents of minerals in differing rocks, such as feldspars, chlorites, micas or olivines. Presently, parameters have been derived for which there is minor sea water/evaporation interference and/or dramatic variations in groundwater chemistry, as discussed below. Areas of high Ca (relative to Sr) correlate strongly with mafic belts in the north Yilgarn (Gray et al. 2016a) but in the Capricorn highlight the differences between the granitic rocks and sediment packages (Figure 1.29). In a similar way, areas of high K (relative to Rb) correlate strongly to the granitic rocks in the Capricorn (Figure 1.30).

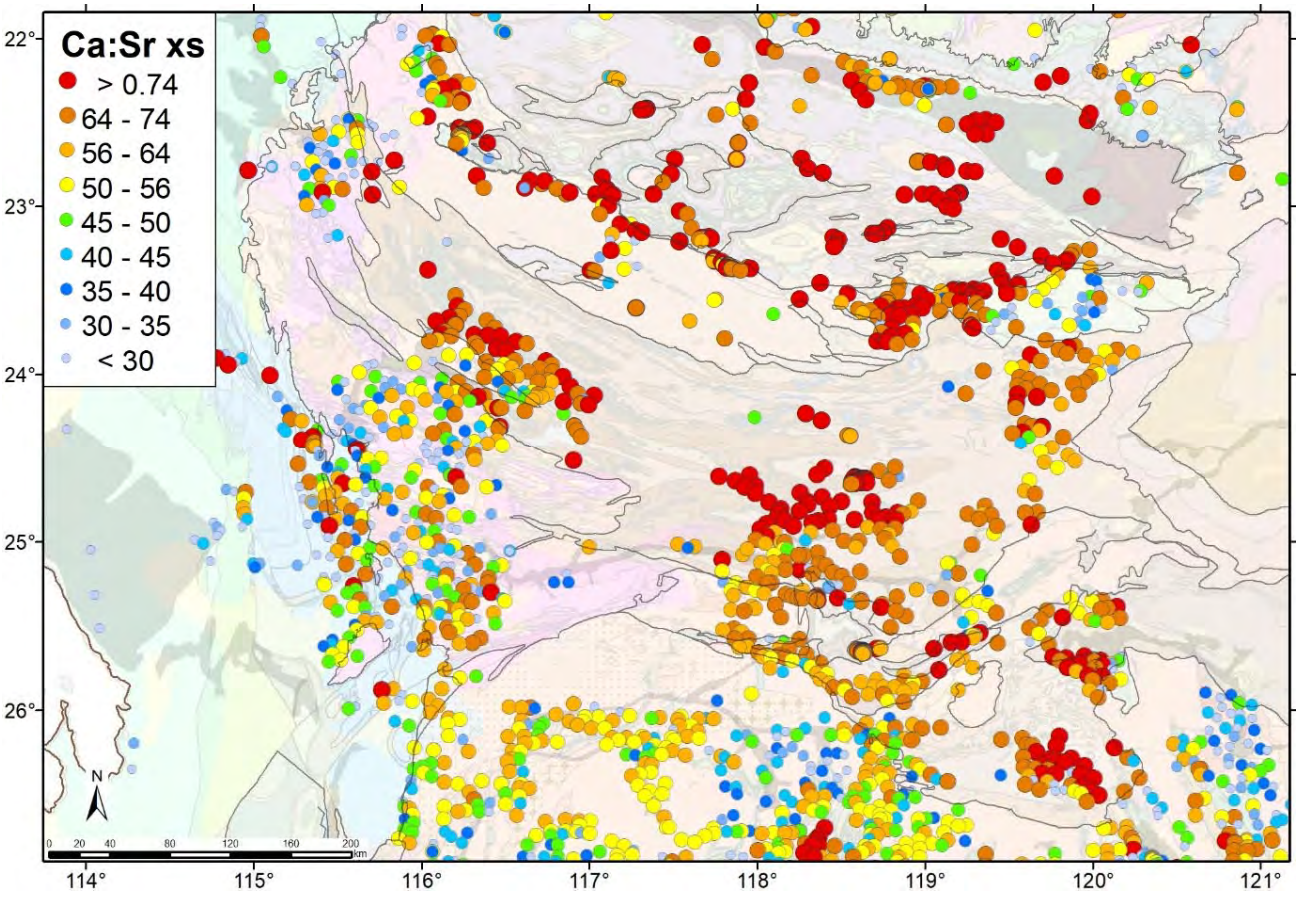

Figure 1.29. Ca excess (relative to Sr) distribution for the Capricorn Orogen.

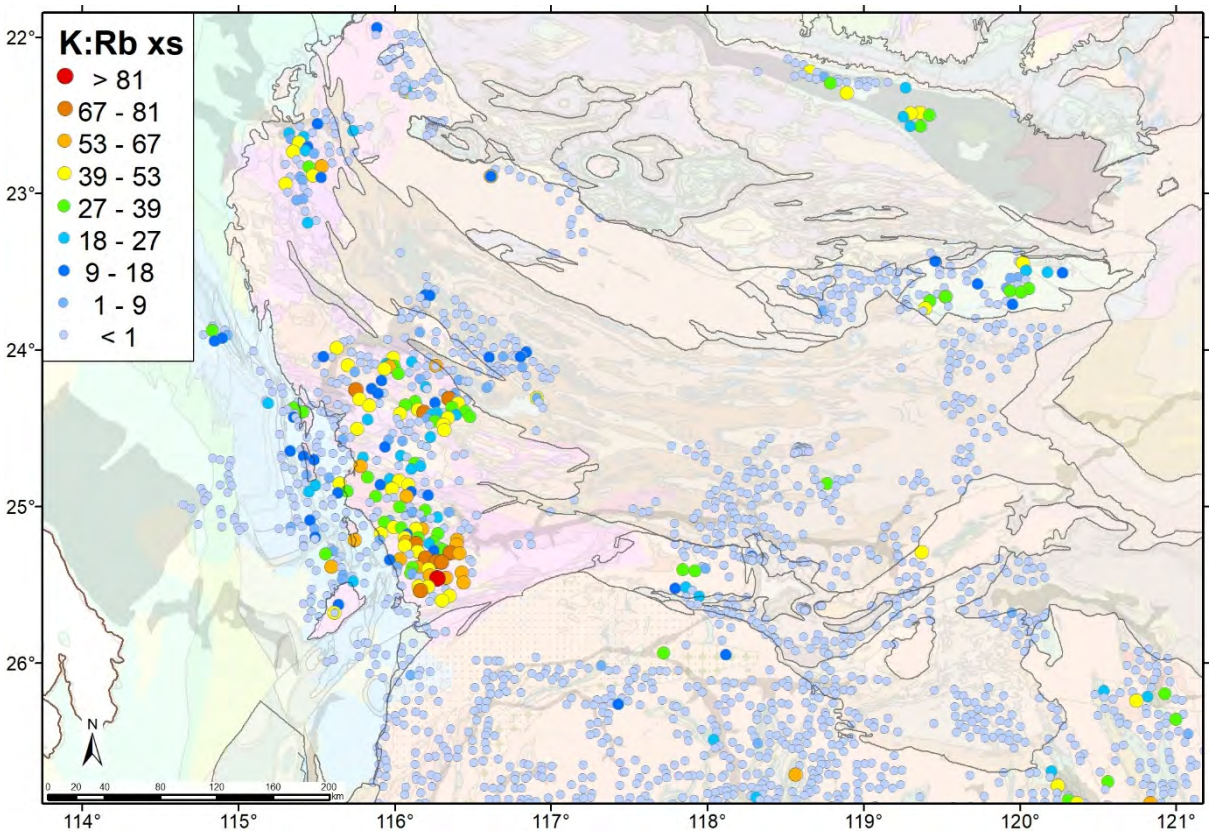

Figure 1.30. K excess (relative to Rb) distribution for the Capricorn Orogen.

1.6.3 Uranium systems

Primary U (U^{4+} as uraninite – UO_2) is highly insoluble and has characteristics similar to other 4+ valence, chemically resistant, elements such as Ti and Th. Uranium is prevalent in the rocks of the Sylvanier Inlier and the Gascoyne Province and once it is eventually mobilised through weathering and subsequent oxidation to U^{6+}, it is highly mobile and the key issue for deposition (i.e. secondary mineralisation) is the chemical reactions required to precipitate U as a solid phase.

However, in the Capricorn the precipitation of U^{6+} is due to an adjustment in pH or Eh as well as a mixing of U with V to precipitate U as carnotite (KUO_2VO_4) and evaporation to form channel and playa deposits. There are no known economic U deposits in the Capricorn Orogen but a number of occurrences are known (Figure 1.3). The carnotite mineral saturation index can be used highlight new areas for exploration (Figure 1.31).

Dissolved V in the 5+ valence state is required for carnotite formation. Virtually all Capricorn groundwaters are expected to have V^{5+} in a hydrated, aqueous, oxy-anion phase that will be mobile in the shallow groundwater system. In the absence of other dissolved metals such as U, Pb or Fe, PO_4 (and to a lesser extent HCO_3) strongly influences U mobility. Without P in the groundwater, U is less mobile in acid to neutral conditions. Ideally the conditions for ore formation (the geochemical barrier zone) are at the interface where U is aqueous and mobile and where it precipitates as an immobile solid. An increase in Eh or pH will precipitate U as carnotite.

Groundwater U concentrations in the Capricorn groundwaters (Figure 1.26) range up to 700 µg/L, and dissolved U alone is a reasonable targeting element. Most of the known deposits in the north Yilgarn occur within close proximity to the larger (>100 µg/L) U groundwater concentrations (Noble et al. 2010) and there are several areas in the Capricorn that have concentrations greater than this. Spatially the carnotite SI predicts most of the known prospects and provides new targets in the Capricorn.

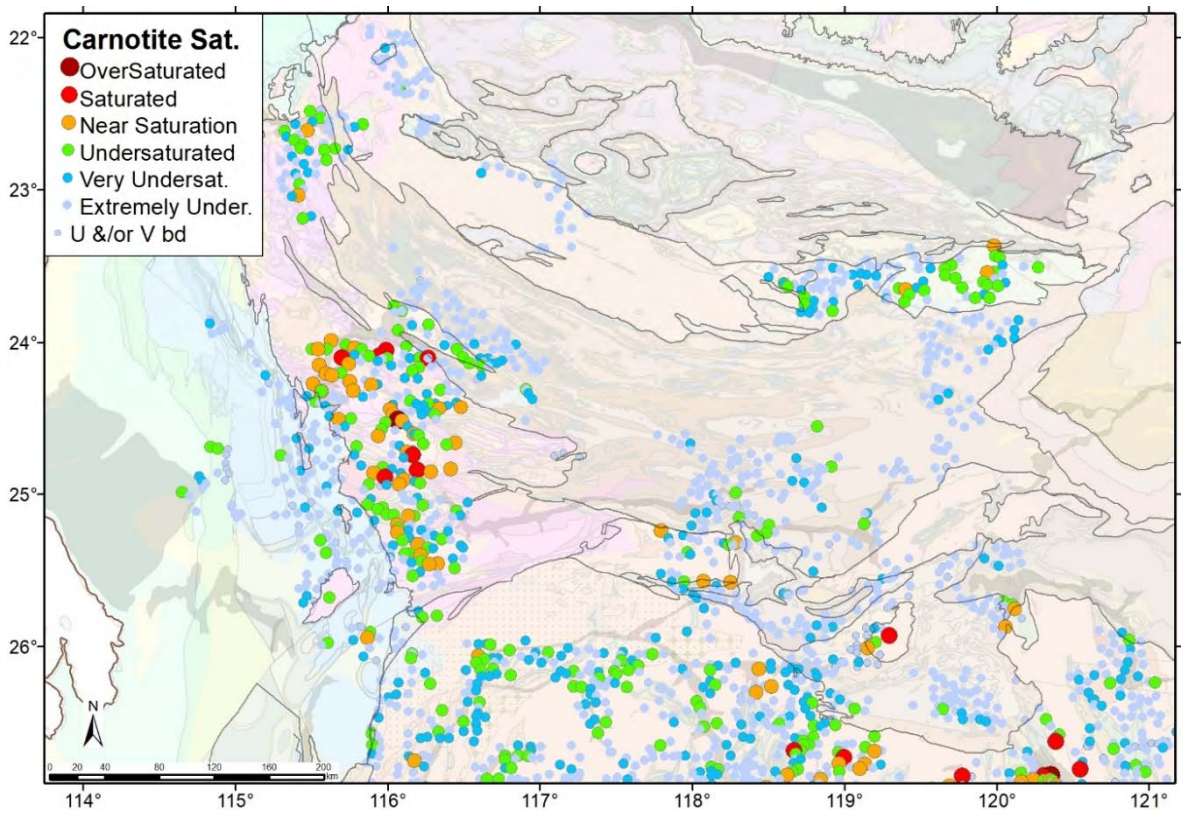

Figure 1.31. Carnotite saturation index distribution for the Capricorn Orogen.

1.6.4 Gold systems

Gold in groundwater is the best target element for Au deposits (Figure 1.32). Many of the larger Au concentrations in groundwater occur near known Au mineralisation, but there are exceptions. Patchy correlations with Au-camps are also observed for Ag (Figure 1.34) and As (Figure 1.33). The Capricorn has several areas with high dissolved concentrations of one or more of these pathfinder elements. In some cases, Mo can be associated with Au systems but this seems to be more complicated in groundwater (Figure 1.35). In the Capricorn, variations in Mo concentration appear to be predominantly controlled by lithology. Antimony is also often associated with Au systems, and in the Capricorn this seems to hold true (Figure 1.36). Arsenic does highlight the deposits sampled in the eastern Capricorn (Abra, Prairie Downs, Peak Hill and Fortnum). These As values are relatively low in the entire dataset, but are significant compared to local background.

To improve the groundwater signature for Au deposits, element indices (rescaled data) were combined to give a better probability of determining major Au camps. The AuMin Index (Au+Ag+As) improves the delineation of larger economic targets (Figure 1.37), and more clearly picks up the major Au camps than dissolved Au, Ag or As alone. However, this index did not take into account the improved Sb results in the Capricorn, so a new index (AuMinC = 2*Au+As+Ag+Sb) was created to enhance the Au results and include Sb (Figure 1.38). This index highlights all known deposits that were sampled and provides some new areas that are not known and warrant further investigation.

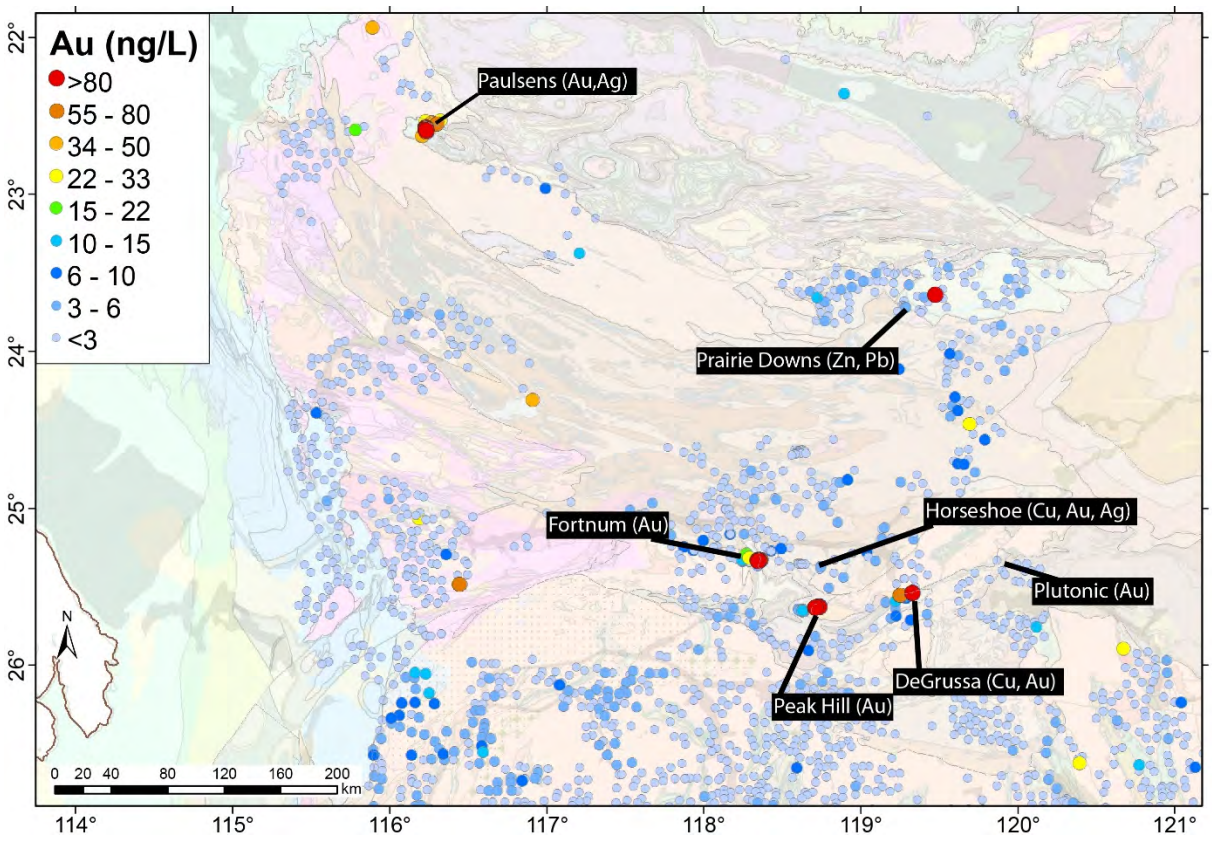

Figure 1.32. Dissolved Au distribution for the Capricorn Orogen.

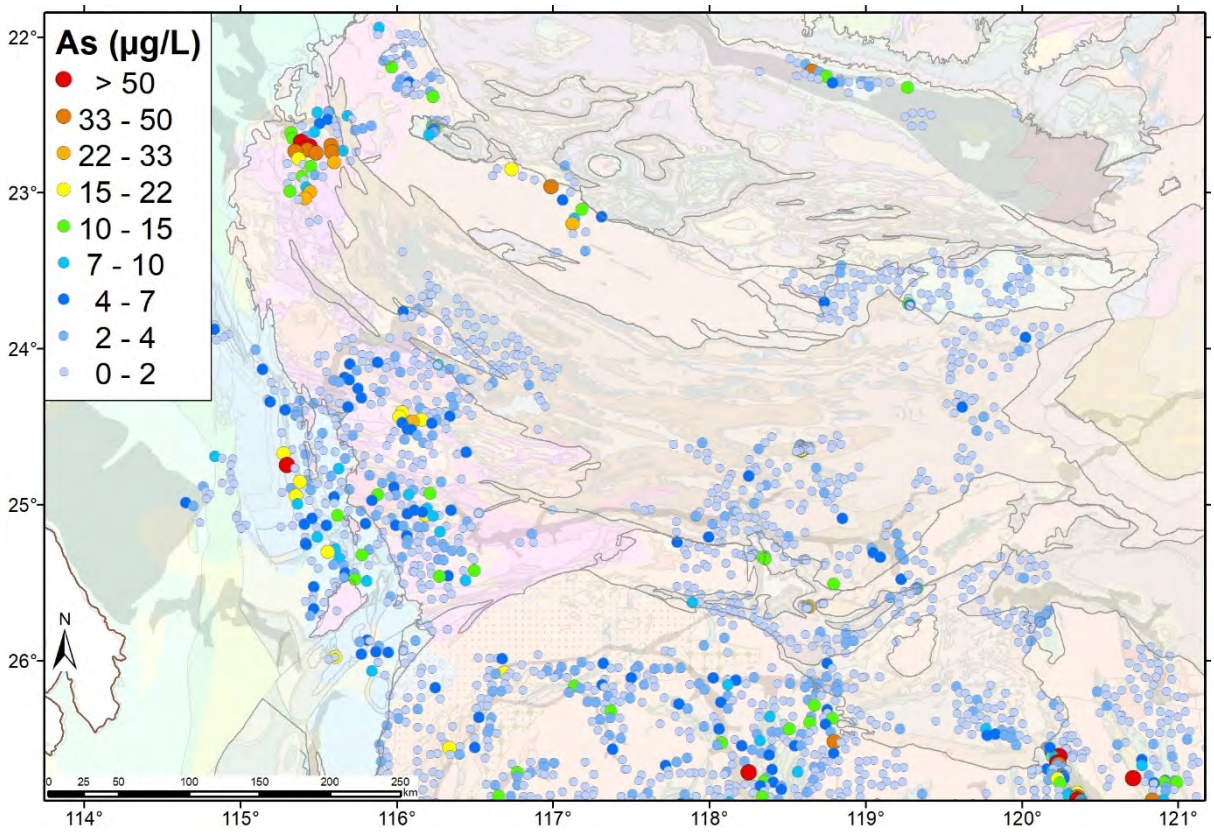

Figure 1.33. Dissolved As distribution for the Capricorn Orogen.

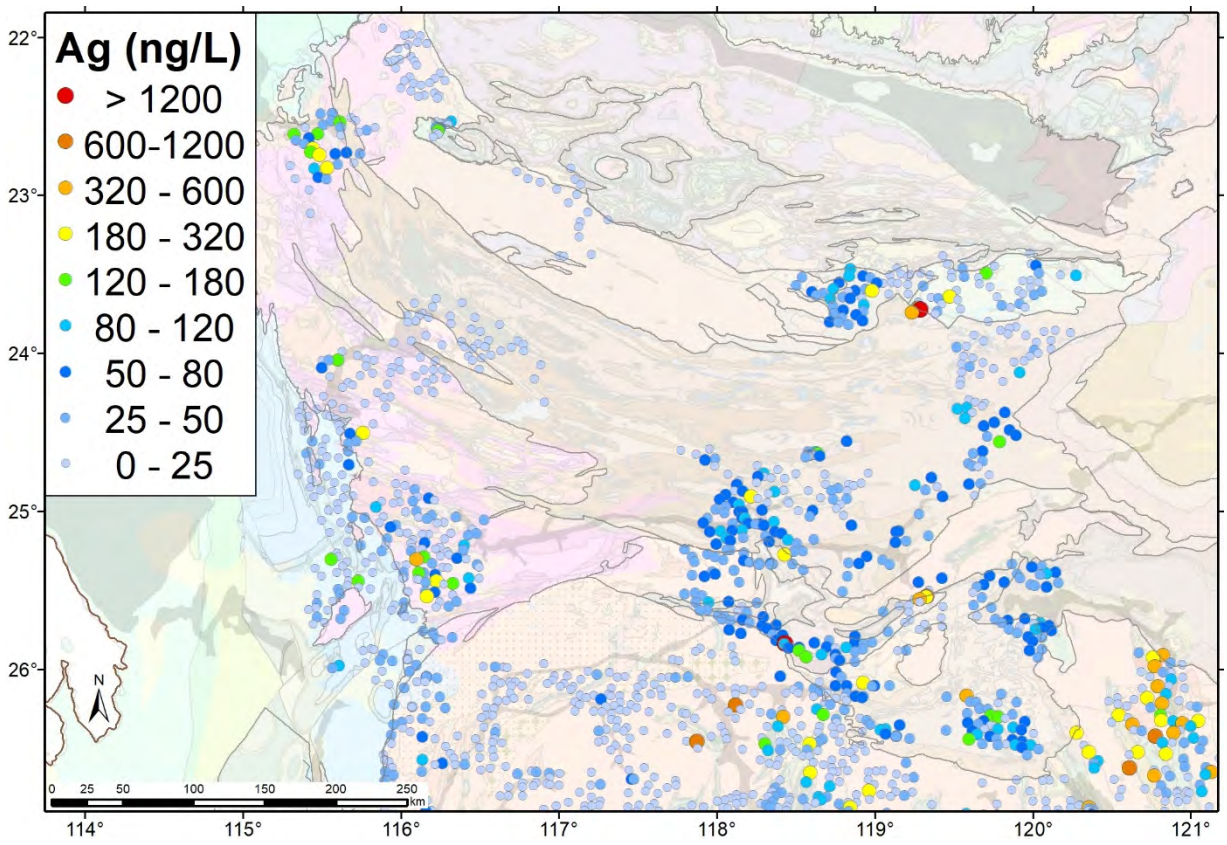

Figure 1.34. Dissolved Ag distribution for the Capricorn Orogen.

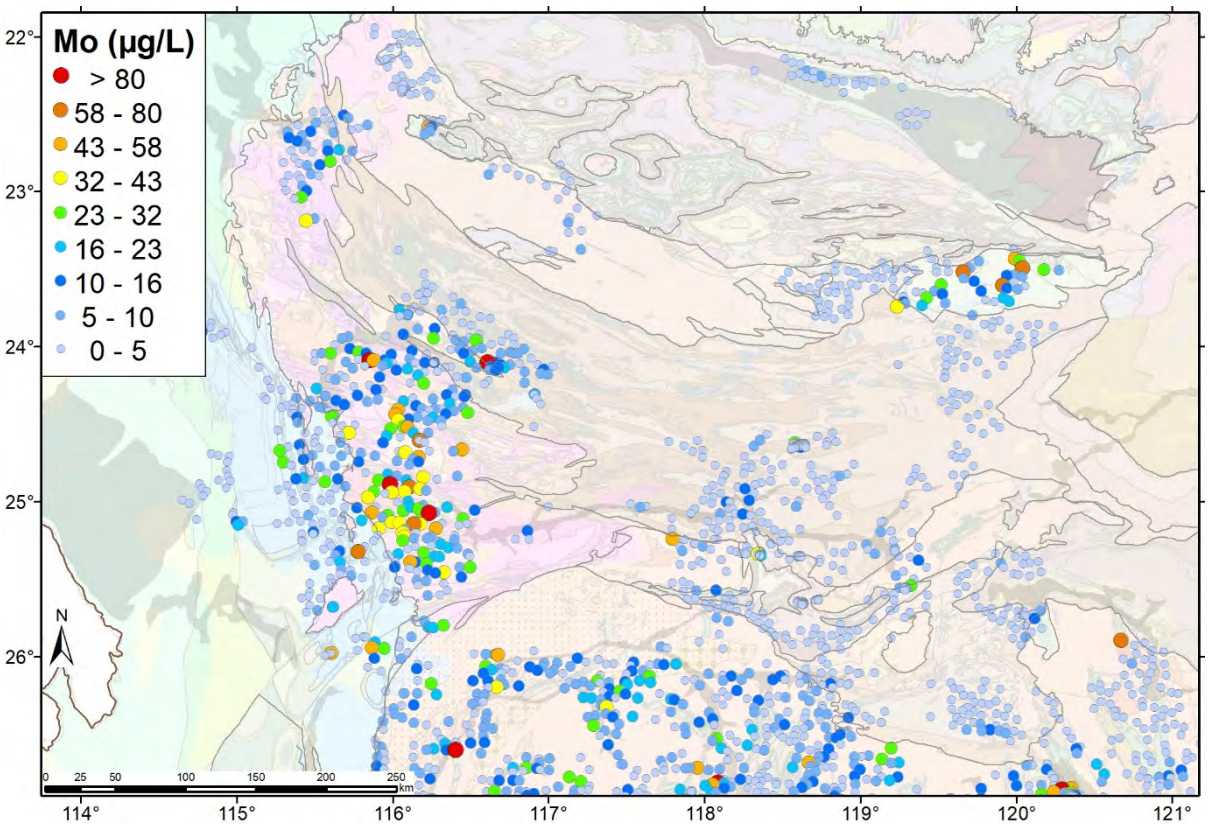

Figure 1.35. Dissolved Mo distribution for the Capricorn Orogen.

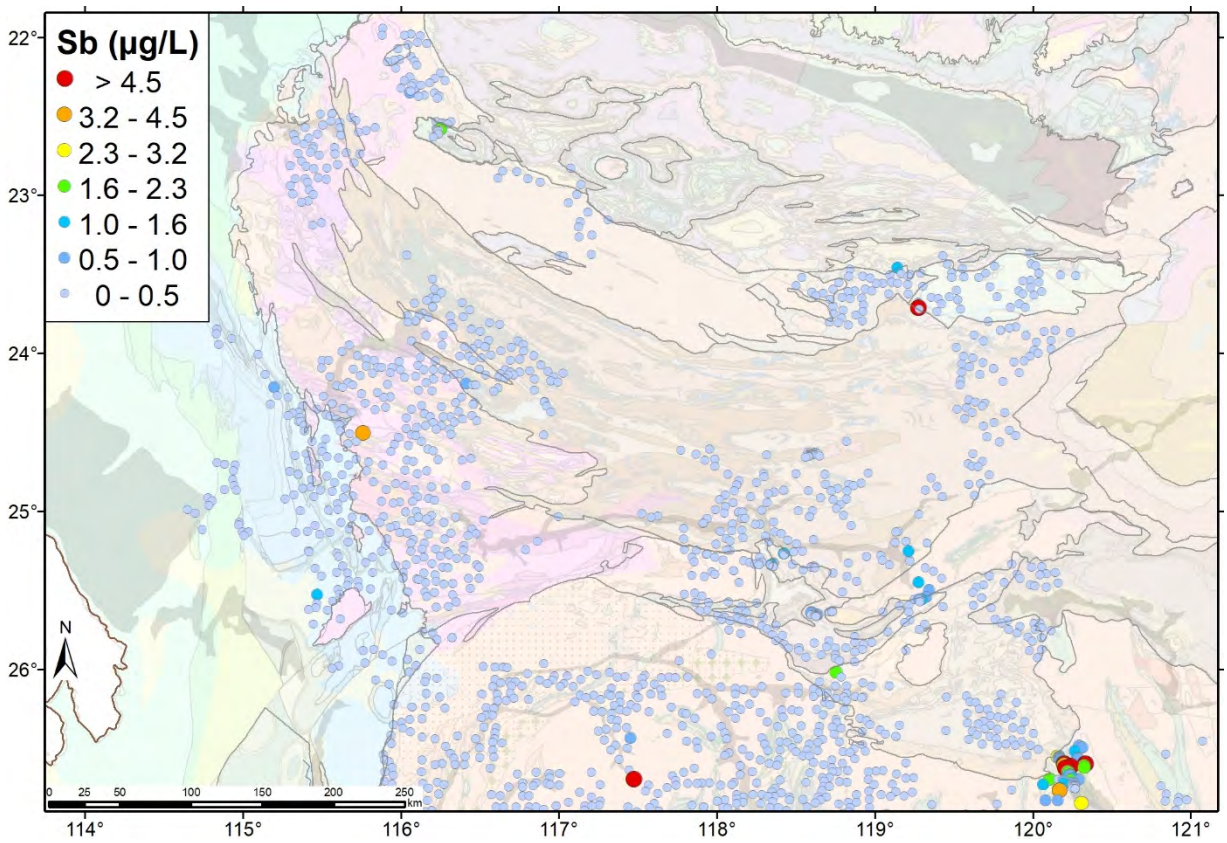

Figure 1.36. Dissolved Sb distribution for the Capricorn Orogen.

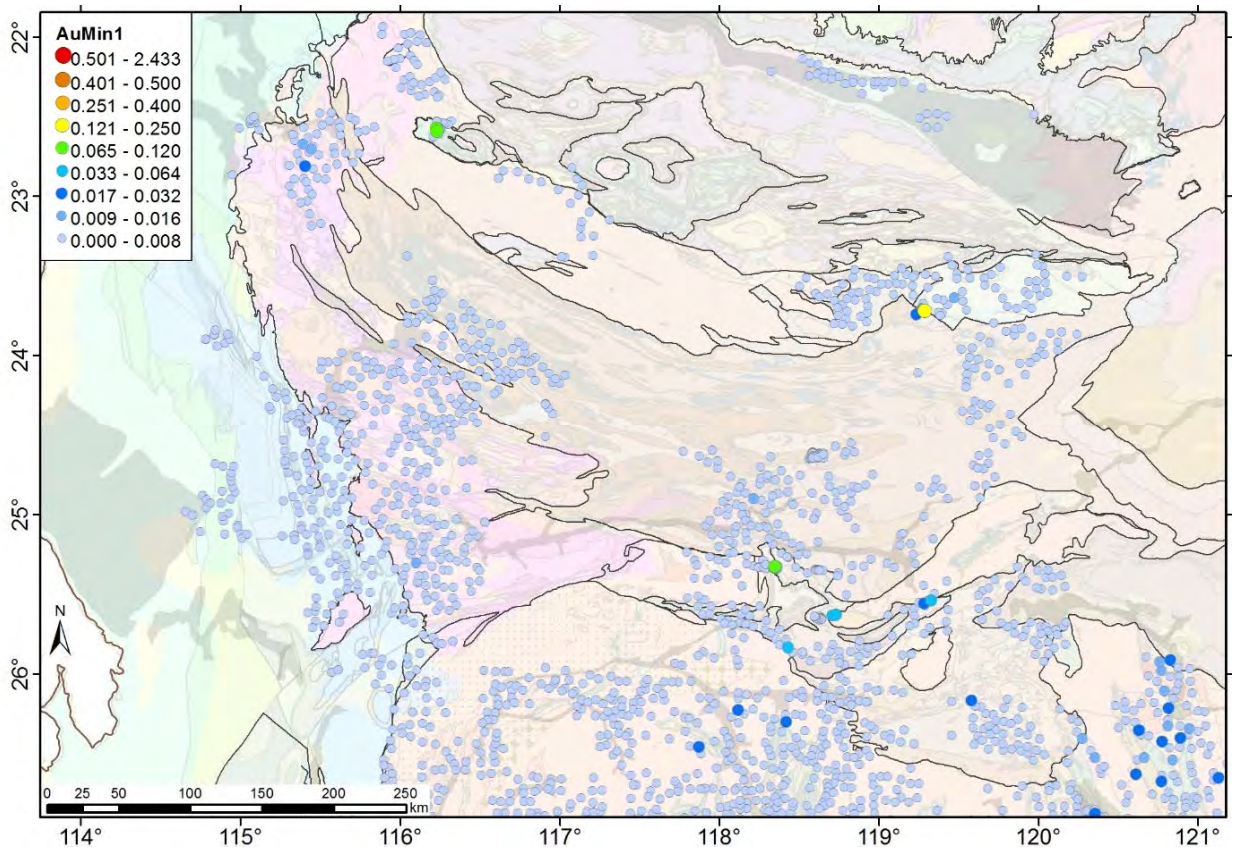

Figure 1.37. AuMin index distribution for the Capricorn Orogen.

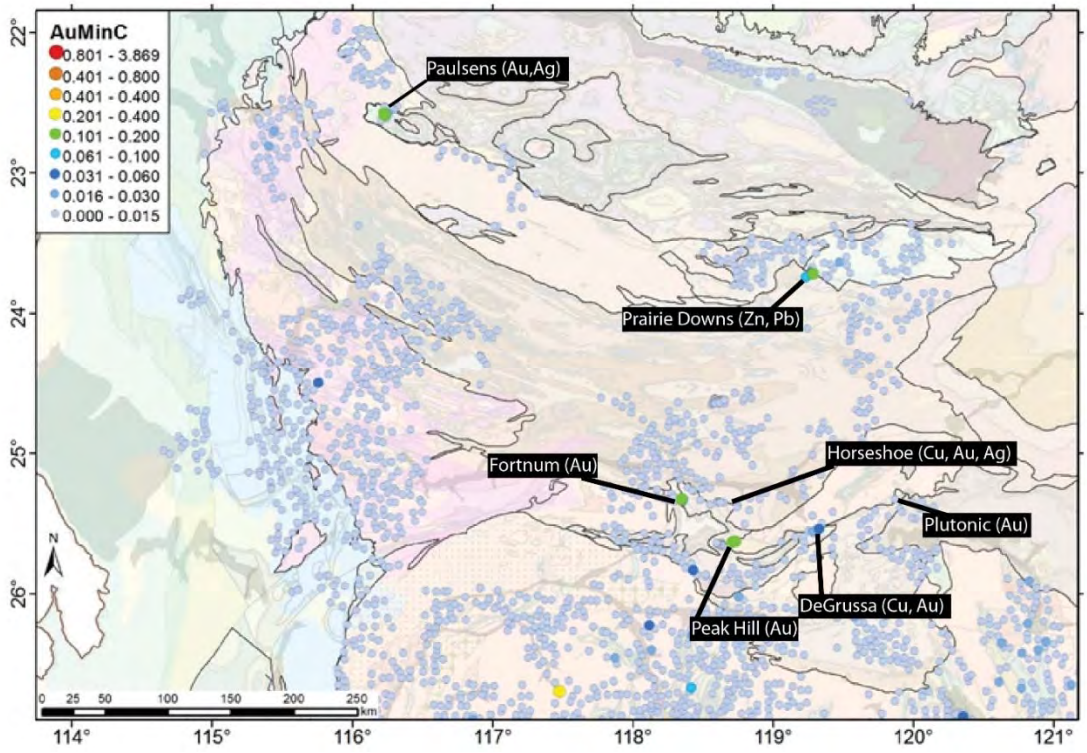

Figure 1.38. AuMinC index distribution for the Capricorn Orogen, mineral deposits of interest are labelled.

1.6.5 Base metals

Regardless of the sulfide style of mineralisation (VHMS, komatiite or sediment hosted) and the target (Ni, Cu/Zn, Cu/Au or Pb/Zn), the groundwater chemistry and the weathering evolution of the groundwater signature in the vicinity of these deposits is similar. However, sedimentary systems are expected to be more disseminated sulfides rather than massive, so their responses are potentially going to be broader and more subtle.

Groundwater in contact with sulfides (mineralised or barren) has highly variable characteristics, but can be distinguished from background water. They generally have one or more of the following properties:

1. Low Eh, and/or low O_2 saturation
2. Moderate to extremely high dissolved Fe content
3. Low pH
4. High concentrations of elements normally characteristic of acid lithologies (Ba, Li, Mn, Mo, V, W)
5. More rarely, detectable Al and REE (La, Ce etc), even in groundwater above pH 6, despite these elements normally only being soluble below pH 5.5.

These results are explained by reference to processes of evolution of groundwater in contact with weathering sulfides (Figure 1.39). Most groundwater in the Capricorn is neutral with moderate Eh (>300 mV) with dissolved sulfur occurring as sulfate (SO_4^{2}). However, groundwater close to weathering sulfides will be controlled by release of reduced phases such as HS^-, leading to Eh values below 150 mV[1]. As these studies

[1] relative to the standard hydrogen potential; equivalent to less than -50 mV on a normal Eh meter (Ag/AgCl cell)

are using shallow, oxidised aquifers, this reducing effect rarely affects the upper groundwater, and such reduced waters are only occasionally observed in the Capricorn (Figure 1.21).

The key point to note with regard to the groundwater expression of sulfide weathering is that SO_4^{2} can actually play the role of the oxidising agent in the weathering of pentlandite to violarite (and pyrrhotite to pyrite, bornite to chalcopyrite). Bicarbonate and nitrate can also be oxidants in these reactions if present. The overall result is that for deep groundwater, weathering of sulfides will actually produce a depletion of HCO_3^-, NO_3^- and SO_4^{2} anions (Figure 1.40; something that initially seems counterintuitive), an effect that will have a larger spatial distribution than the highly localised Eh reduction. The groundwater will also remain neutral to alkaline.

As the groundwater progresses upwards to the surface (oxidised zone), the HS^- is oxidised to SO_4^{2} by the abundant NO_3 (Figure 1.48). In effect, the signature is now a SO_4^{2} excess and a NO_3^- depletion (NO_3^- is reduced to N_2 gas and removed from the groundwater). This SO_4^{2} excess and NO_3^- depletion is the anionic signature expected for shallow groundwater near sulfides for the Capricorn similar to that seen in the north Yilgarn, this concept led to the SEND1 (sulfate enrichment and nitrate depletion) exploration index. The sulfides are eventually weathered to oxides, carbonates and silicates.

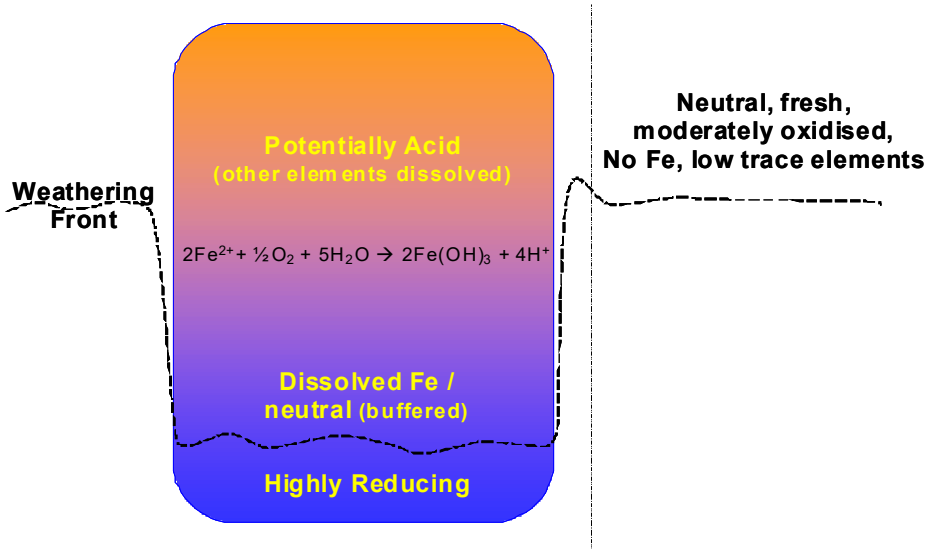

Figure 1.39. Cross section model of groundwater evolution around sulfides showing the distinctive groundwater conditions at varying depths.

Thus, there are complex mineralogical (e.g., presence and chemistry of sulfides and/or carbonates) controls on the groundwater around sulfide deposits; generally, groundwater contacting sulfide mineralisation will tend to be highly reduced at depth, contain dissolved Fe and other base metals at intermediate depths, and in some cases be acidic (<pH 6) closer to the surface. But, pyrite-poor sulfides may have less acid production, whereas more Fe-rich mineralogies are expected to cause greater acidity. Reactive weathering models suggest that the barren (Fe) sulfides will weather more readily than base metal-rich (Ni, Cu, Zn) sulfides (Figure 1.41). Under present day conditions, in much of the Capricorn, these reactions will occur slowly, and any acidity generated is commonly buffered by other minerals such as carbonates, and pH effects are not observed in this regional study. However, it may be possible to distinguish higher concentrations of metals such as Al, base metals and rare earth elements (REE), due to acid attack on wall rocks. This effect will be less in disseminated sulfides. It is possible that in the sedimentary basins, where the mineral buffering potential is less, pH effects may be distinguishable against the regional background and there are a few sites where this is visible. This mechanism is the basis for the AcidS and FeS indices.

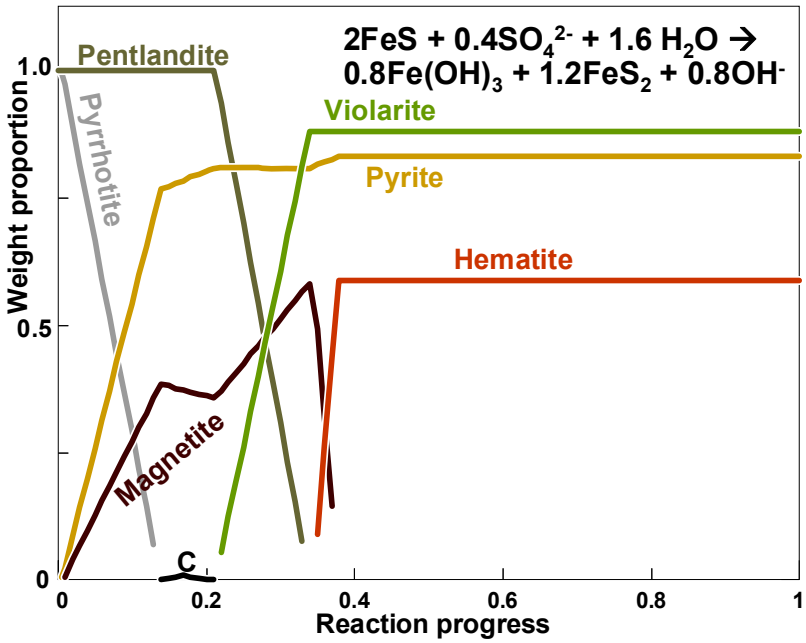

Figure 1.40: Geochemical modelling of the weathering of Ni and Fe sulfides. Conversion of pentlandite/pyrrhotite to violarite/pyrite/hematite uses SO_4^{2-} and HCO_3^- as oxidants. This is representative of deep (reduced Eh) weathering of sulfides. Similar reaction chemistry occurs for Cu and Zn systems. (Geochemists Workbench®, thermo.com.v8.r6+ data and Warner et al., 1996).

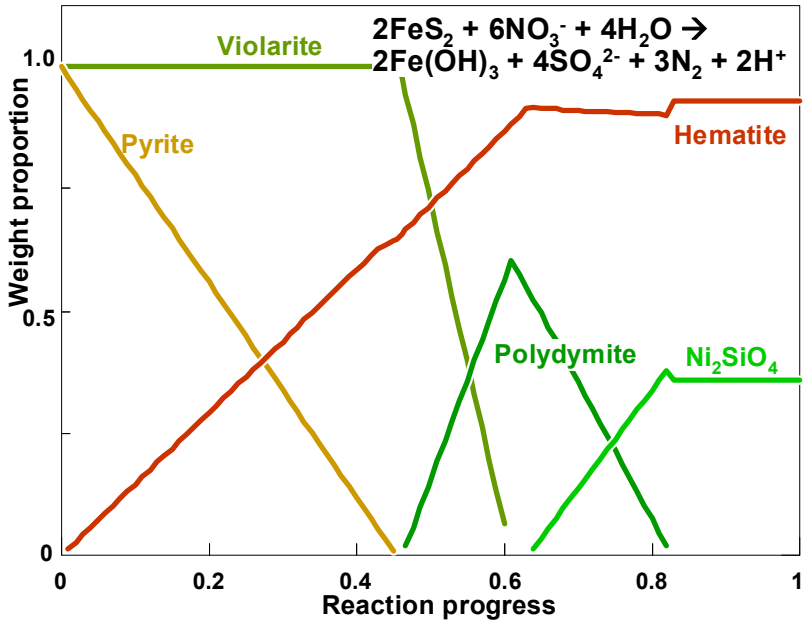

Figure 1.41: Geochemical modelling of shallow (oxidised Eh) weathering of Fe and Ni sulfides. Weathering of violarite/pyrite to hematite/Ni-silicate uses NO_3^- as the oxidant (SO_4^{2-} is produced). Similar reaction chemistry occurs for Cu and Zn systems. (Geochemists Workbench® thermo.com.v8.r6+ data and Warner et al., 1996).

Weathering of sulfides will release target metals like Cu, Pb, Zn, Ni and Se into solution, but these (and particularly Cu, Pb, Zn) are readily adsorbed to clays and/or Fe oxides in the regolith (Figure 1.42, Figure 1.43, Figure 1.44, Figure 1.45 and Figure 1.46). As a result, the dispersion of these elements alone is not normally effective for broad-scale exploration targeting of base metal sulfides. Earlier studies by Gray and Noble (2006) and Gray et al. 2018 suggest useful sample spacing for selecting target metals of approximately 50 to 500 m. A select few samples around sulfide deposits will have large soluble concentrations of the ore metals (mg/L instead of low µg/L), but anomalous values are not spatially consistent.

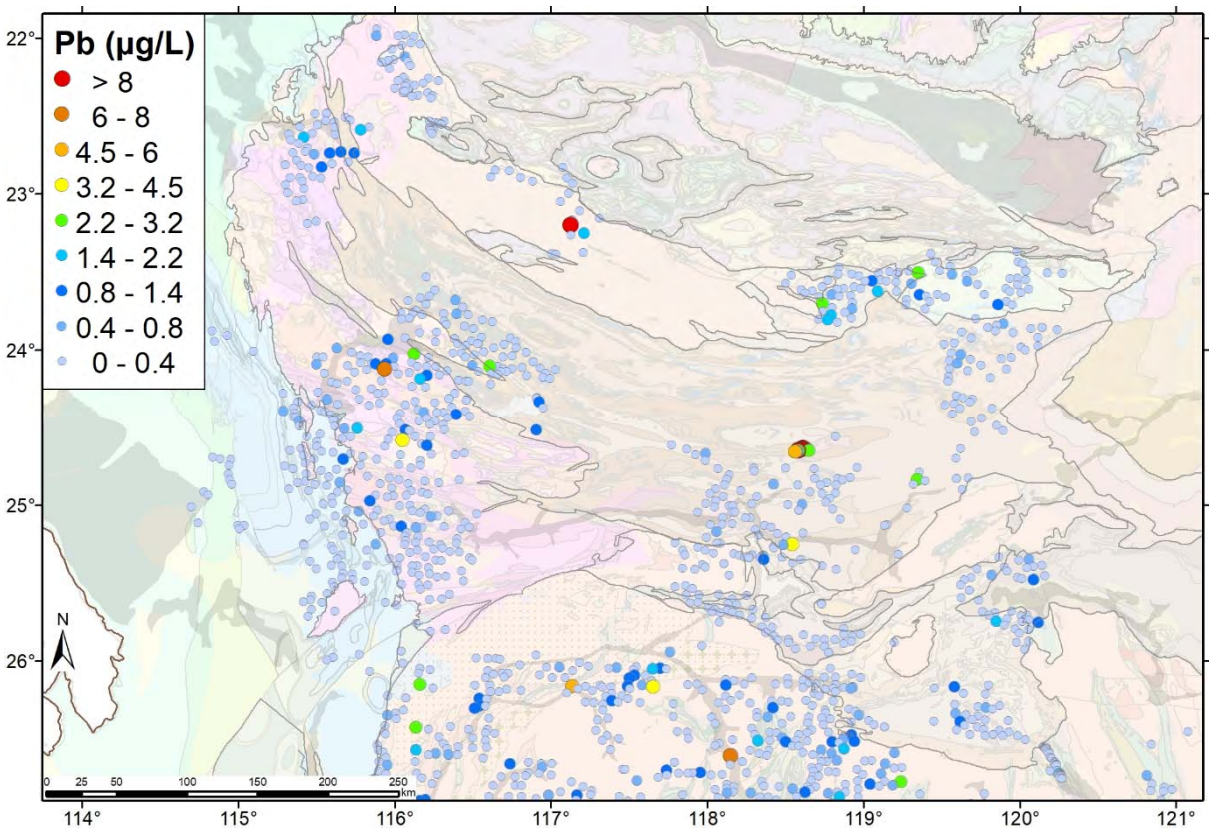

Figure 1.42. Dissolved Pb distribution for the Capricorn Orogen.

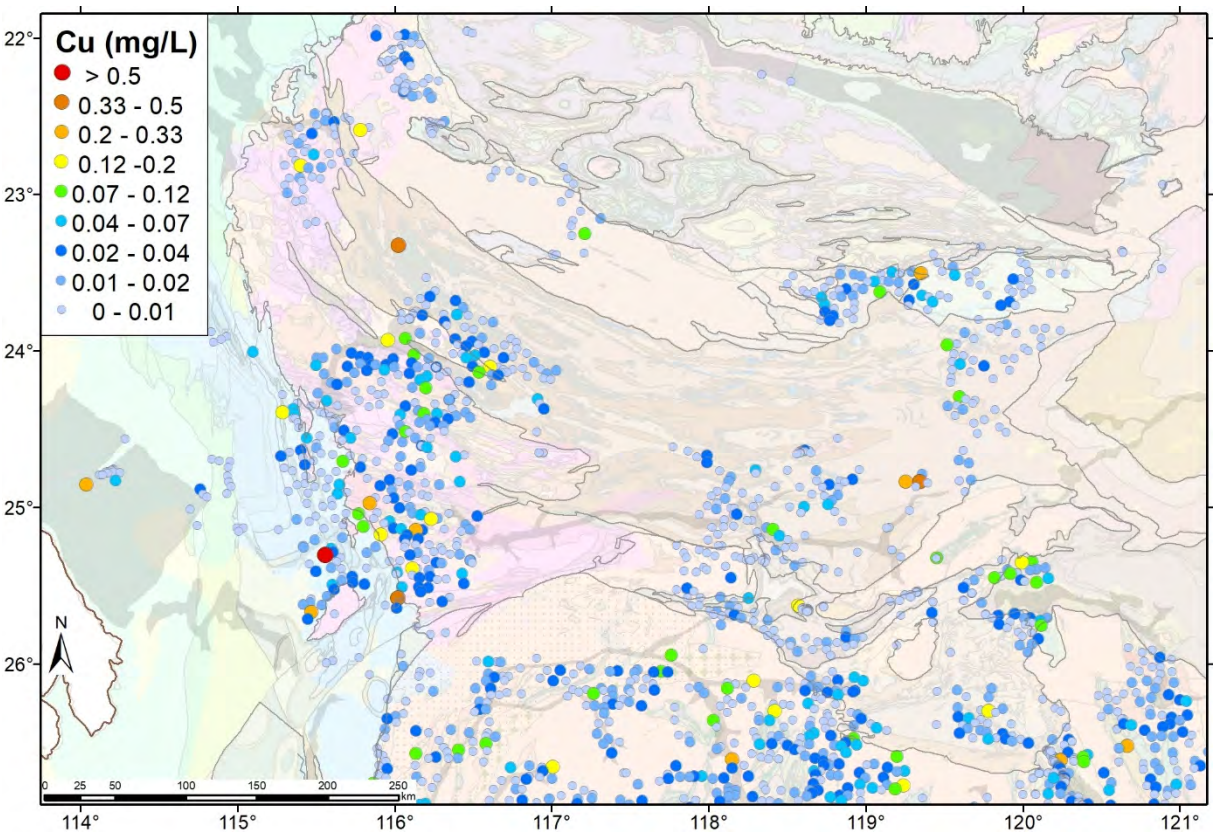

Figure 1.43. Cu distribution for the Capricorn Orogen.

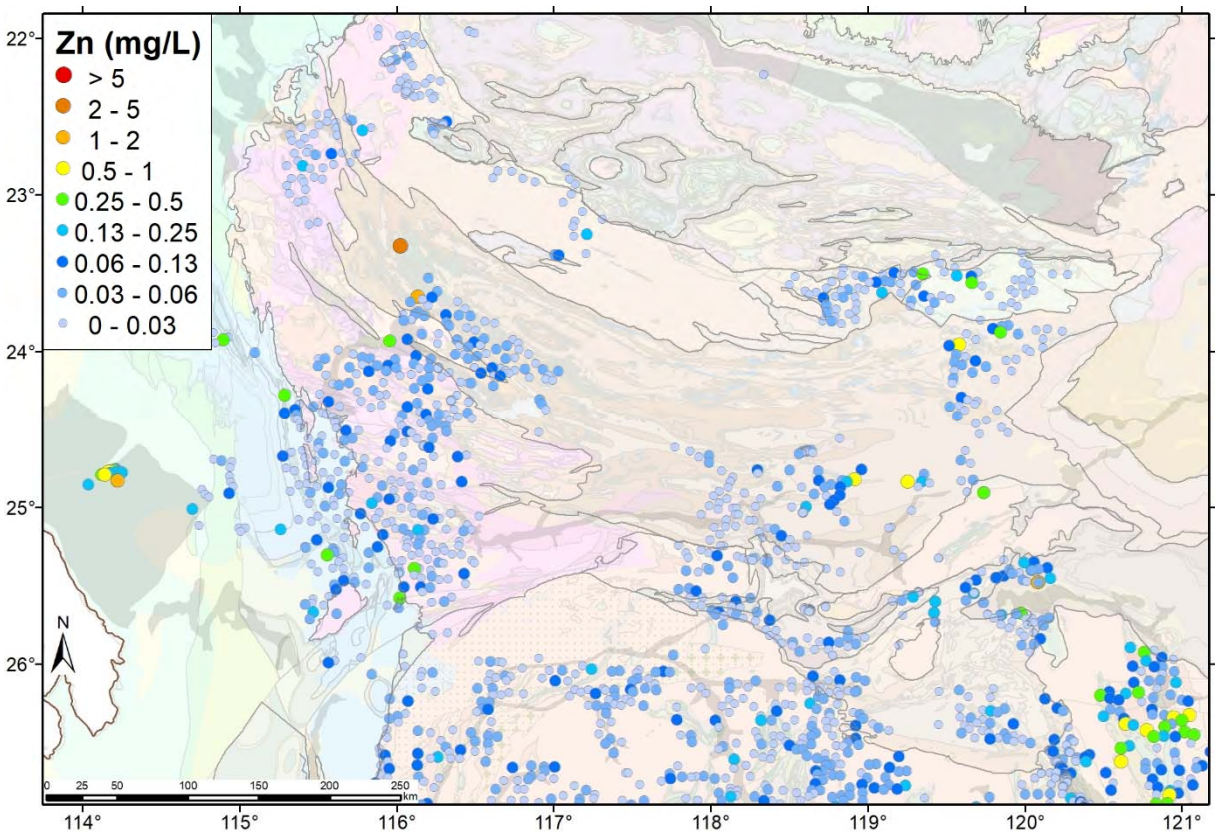

Figure 1.44. Zn distribution for the Capricorn Orogen.

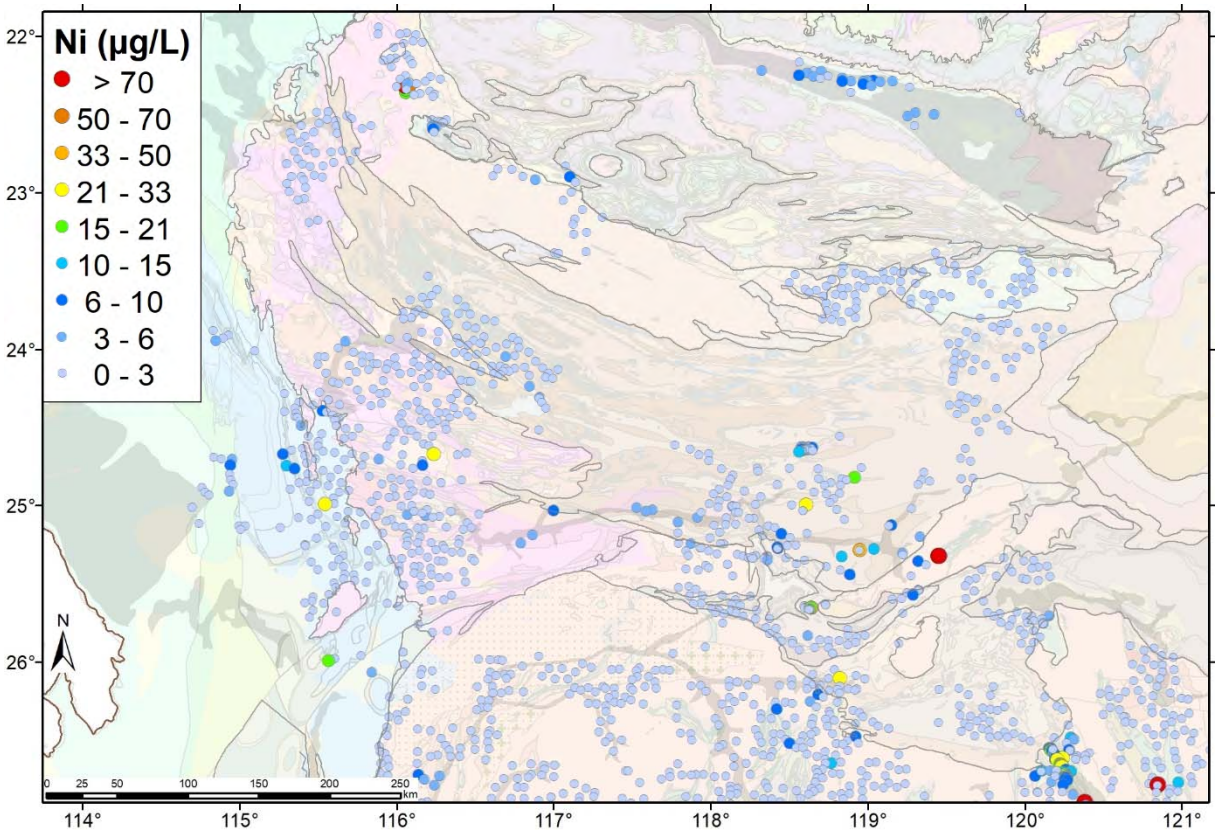

Figure 1.45. Ni distribution for the Capricorn Orogen.

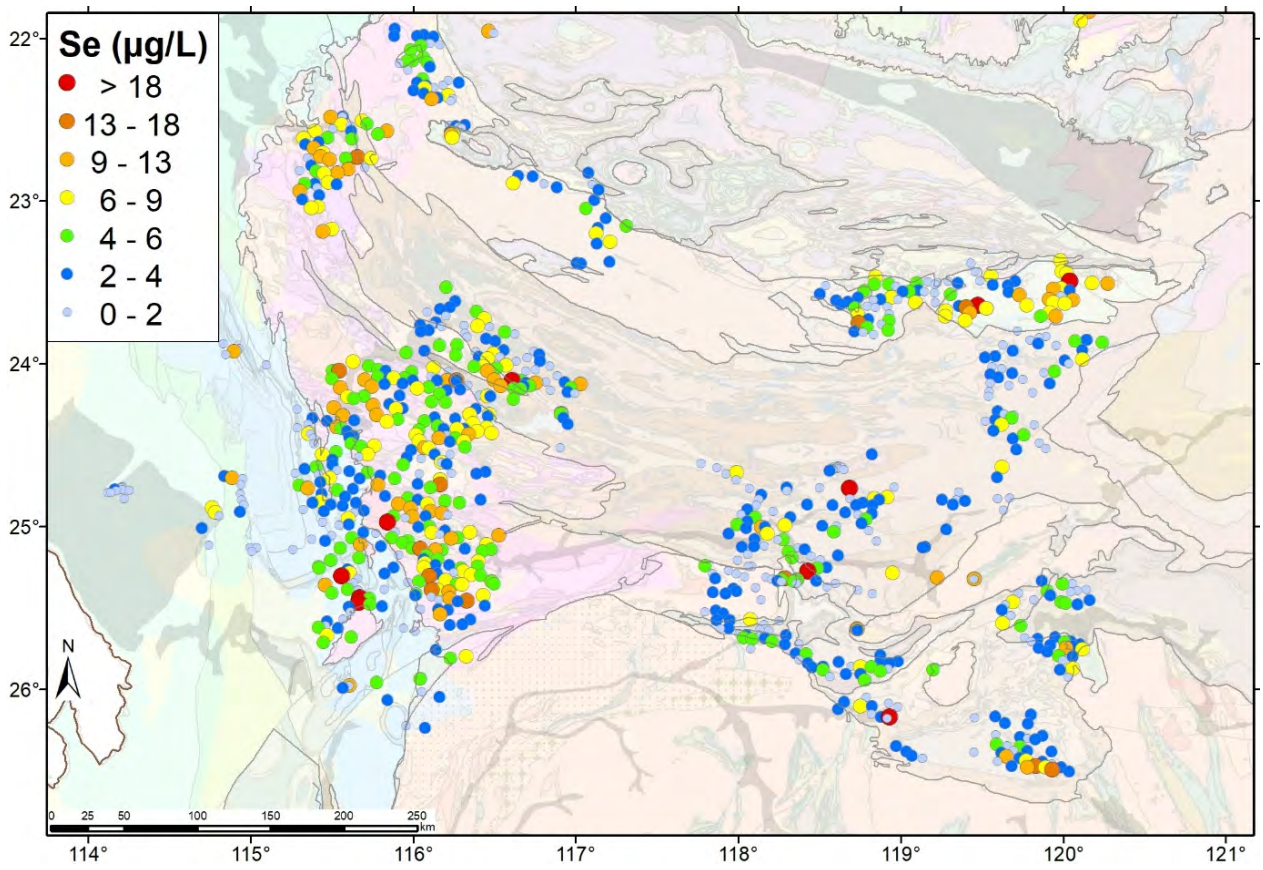

Figure 1.46. Se distribution within groundwaters of the Capricorn Orogen.

Although single base metal concentrations are not consistent pathfinders for sulfides, the weathering model presented in Figure 1.41 indicates that in shallow groundwater excess SO_4^{2} and depleted NO_3^{-} should provide a groundwater signature of weathered, oxidised sulfides.

Using this concept, on a larger scale, some samples have excess SO_4^{2} (relative to the conserved Cl ion) in the Capricorn groundwaters (Figure 1.47). However, closer analysis has indicated that many of these areas of anomalous SO_4^{2} are corresponding to the sedimentary basins, so the reason for these large scale distributions will be better determined by S-isotope research (discussed later; Section 6.7). There are some areas in this region with NO_3^{-} depletion (Figure1.48), though this depletion is relatively weak. Paulsen's deposit in particular shows this sulfate enrichment and nitrate depletion quite strongly (Figure 1.49). Attempting to make an index for this understanding showed mixed success (Figure 1.49), and the reason for this is that the sulfate enrichment and nitrate depletion are in the same areas but are not always the same site. We have created the 'SEND1' index which takes the measure of sulfate enrichment (SO4CLDSW) and subtracts NO_3.

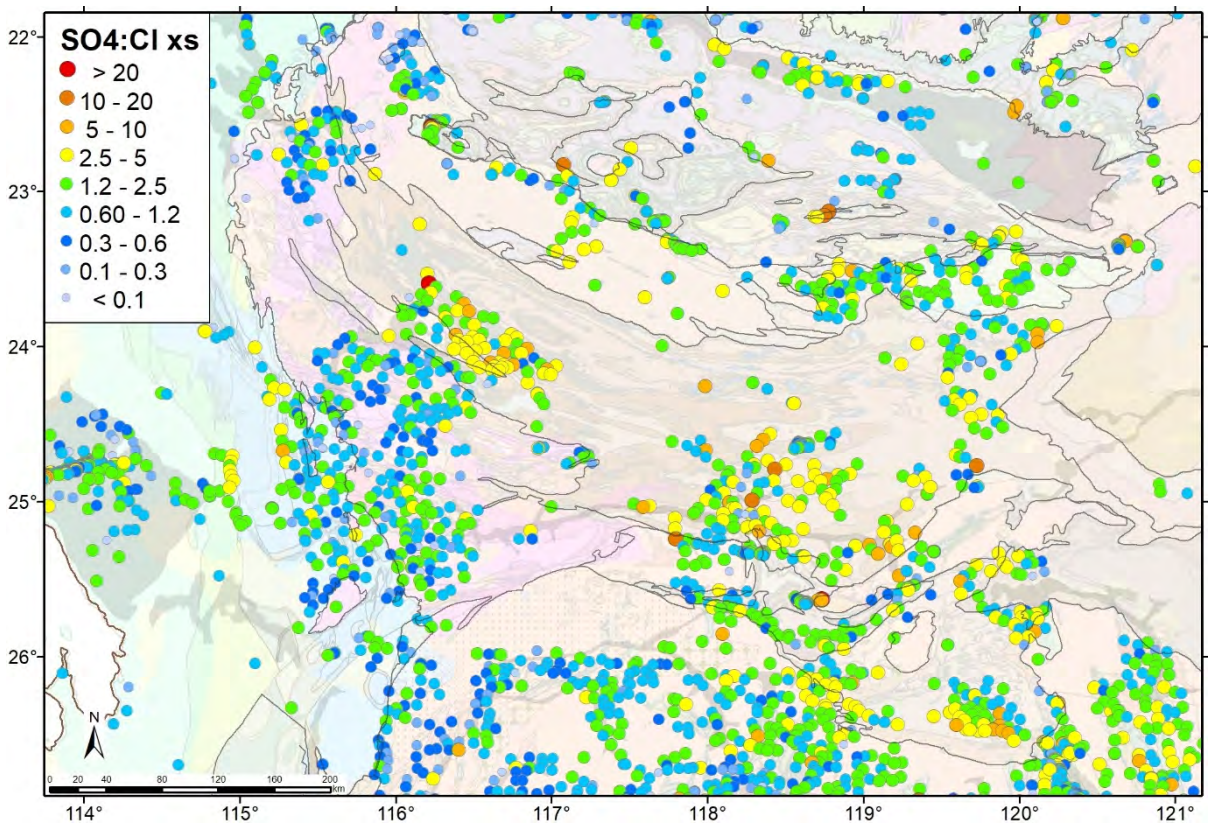

Figure 1.47. SO4:Cl excess ratio distribution for the Capricorn Orogen.

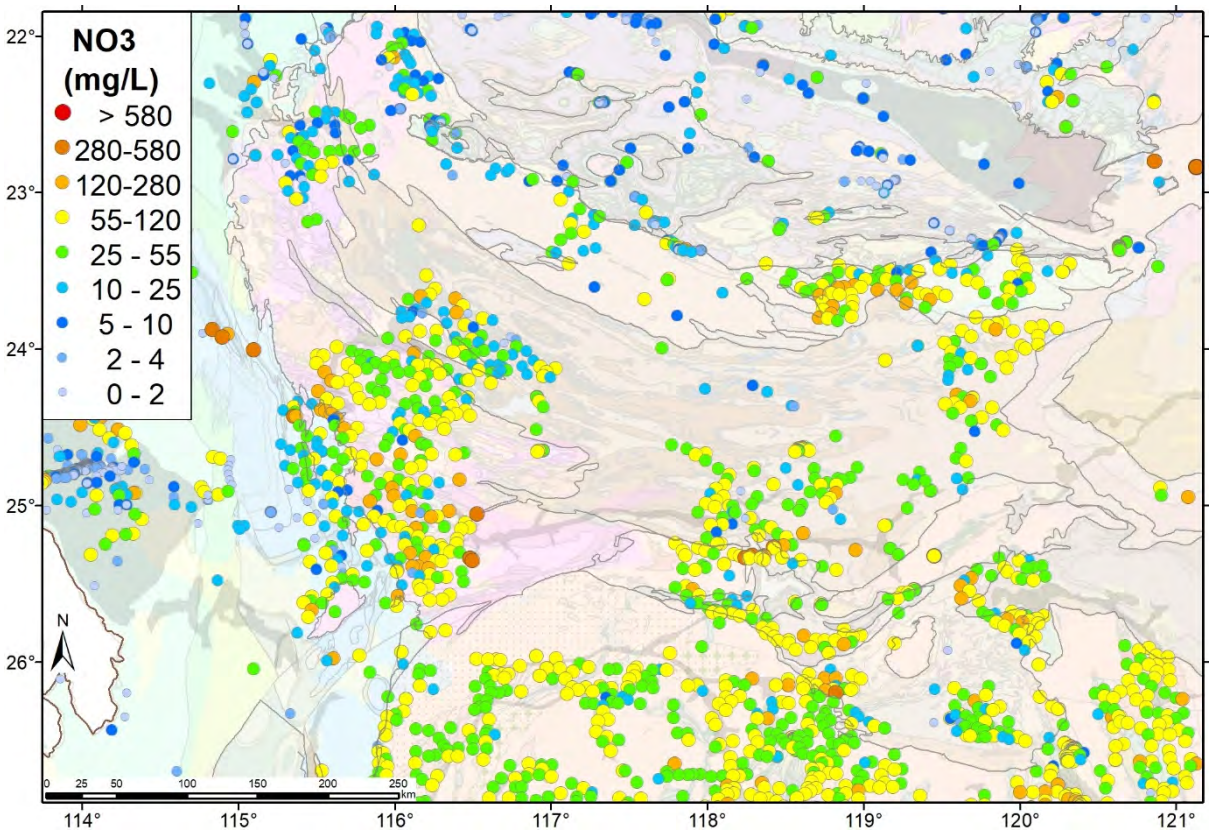

Figure 1.48. Dissolved NO3 distribution for the Capricorn Orogen.

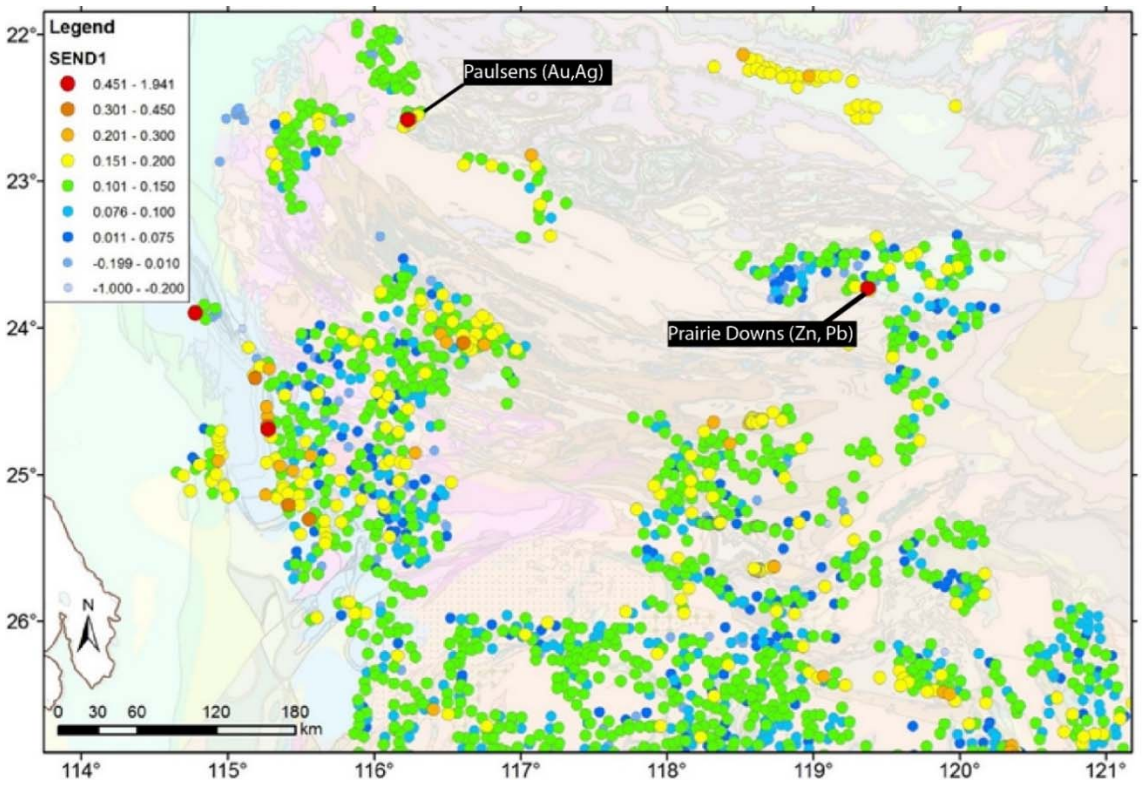

Figure 1.49. SEND1 index distribution for the Capricorn Orogen.

Another potential indicator of excess sulfate released into groundwater is gypsum saturation ($CaSO_4.H_2O$; Figure 1.50). There are few areas where SO_4^2 is high enough to bring groundwaters close to gypsum saturation. The ones that are highlighted (red dots, Figure 1.50), when in conjunction with other metal indicators, may be linked to weathering sulfides.

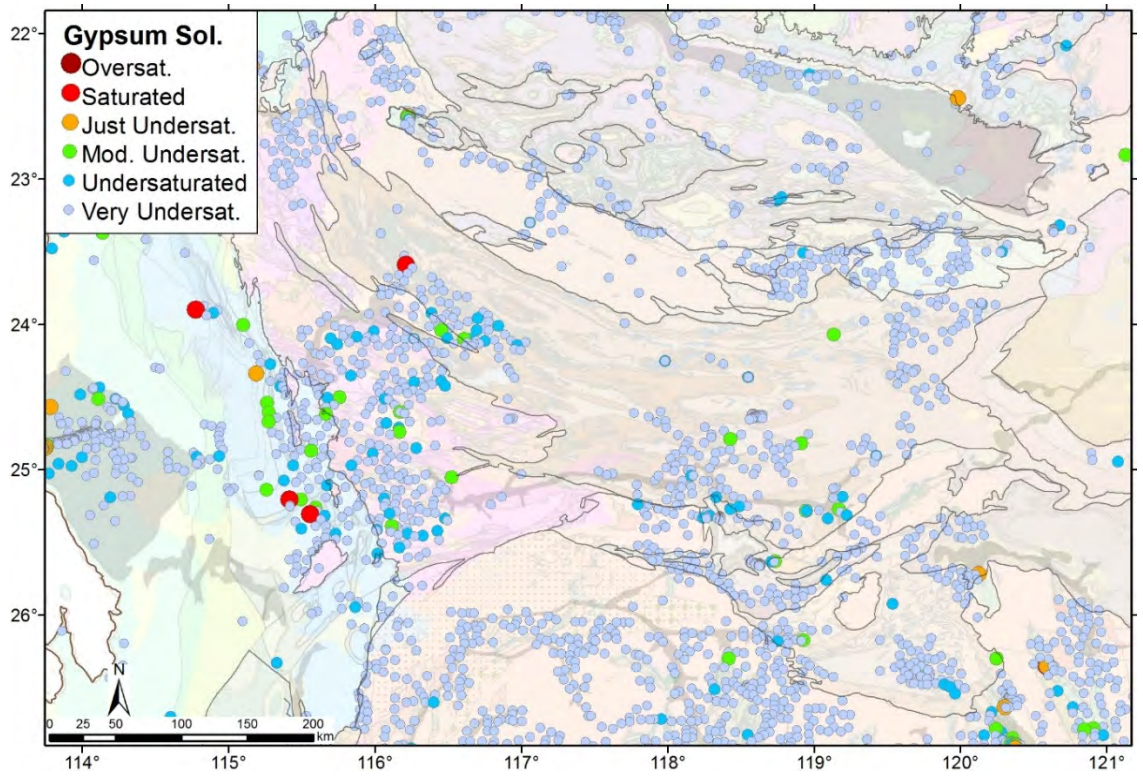

Figure 1.50. Gypsum mineral saturation distribution for the Capricorn Orogen.

The FeS index (pH-Eh+Fe+Mn) is controlled by common parameters associated with the oxidation of Fe-rich sulfides, and the AcidS index (Mo+Ba+Li+Al) relates to higher concentrations of metals due to the acid generation from sulfides. As discussed above, these parameters will be more sensitive to barren Fe-rich (more likely non-economic) sulfides than Ni, Cu or Zn sulfides. The FeS index did not prove to be very effective in the Capricorn, but the AcidS index has anomalism linked to most of the known deposits and provides new areas of interest (Figure 1.51).

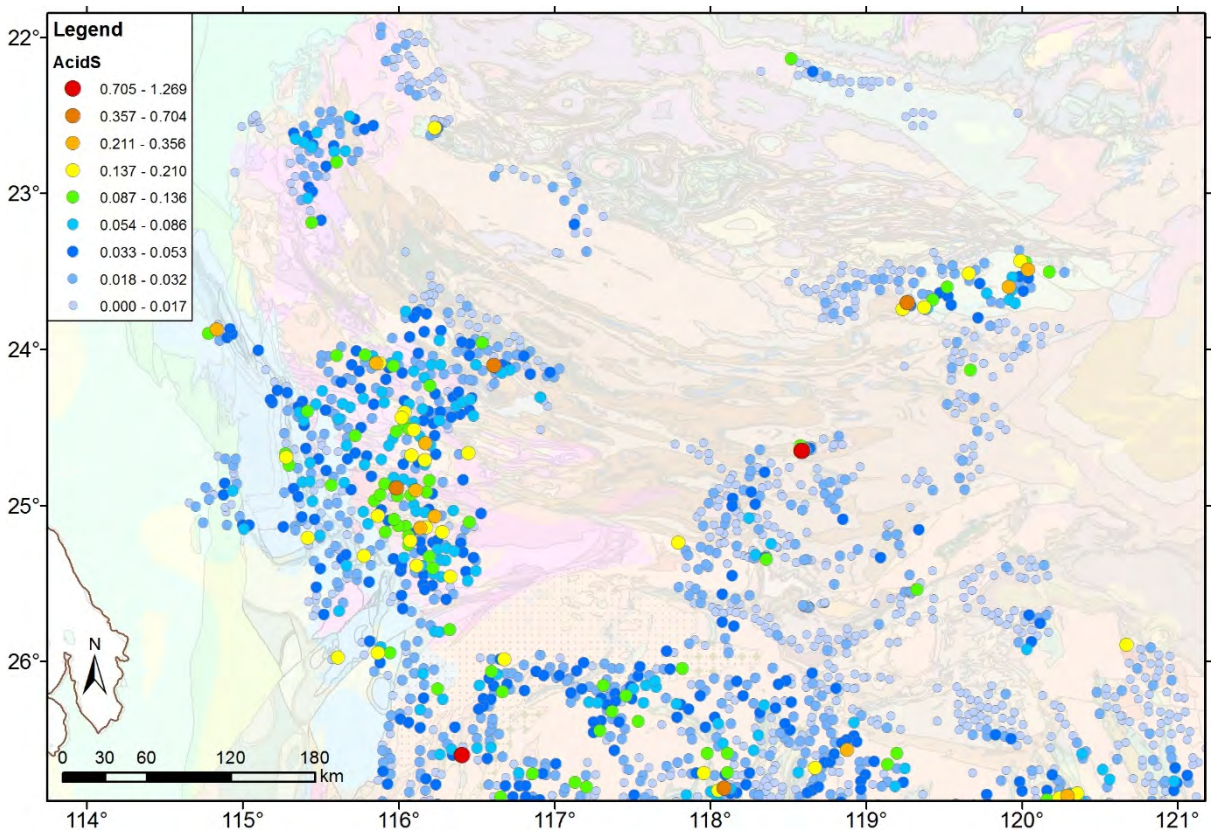

Figure 1.51. AcidS index distribution for the Capricorn Orogen.

As with lithological mapping, targeting of prospective regions is improved by using multielement indices. Derived indices and their linear combinations can be beneficial in defining anomalous samples, particularly for using pathfinder elements such as Co (Figure 1.52), W (Figure 1.53) and PGEs (Figure 1.54) that are not consistently distributed or detectable. The NiS mineralisation index (Ni+Co+W+Pt) developed in the Yilgarn Craton (Gray et al. 2014) utilised several of the individual elements for nickel sulfide exploration (Figure 1.55). In the Capricorn Orogen komatiite style Ni systems are not known, so this index could potentially find new Ni occurrences. The mapping shows that this index does highlight most of the known sulfide systems sampled in the region and presents several new areas of potential mineralisation (Figure 1.56).

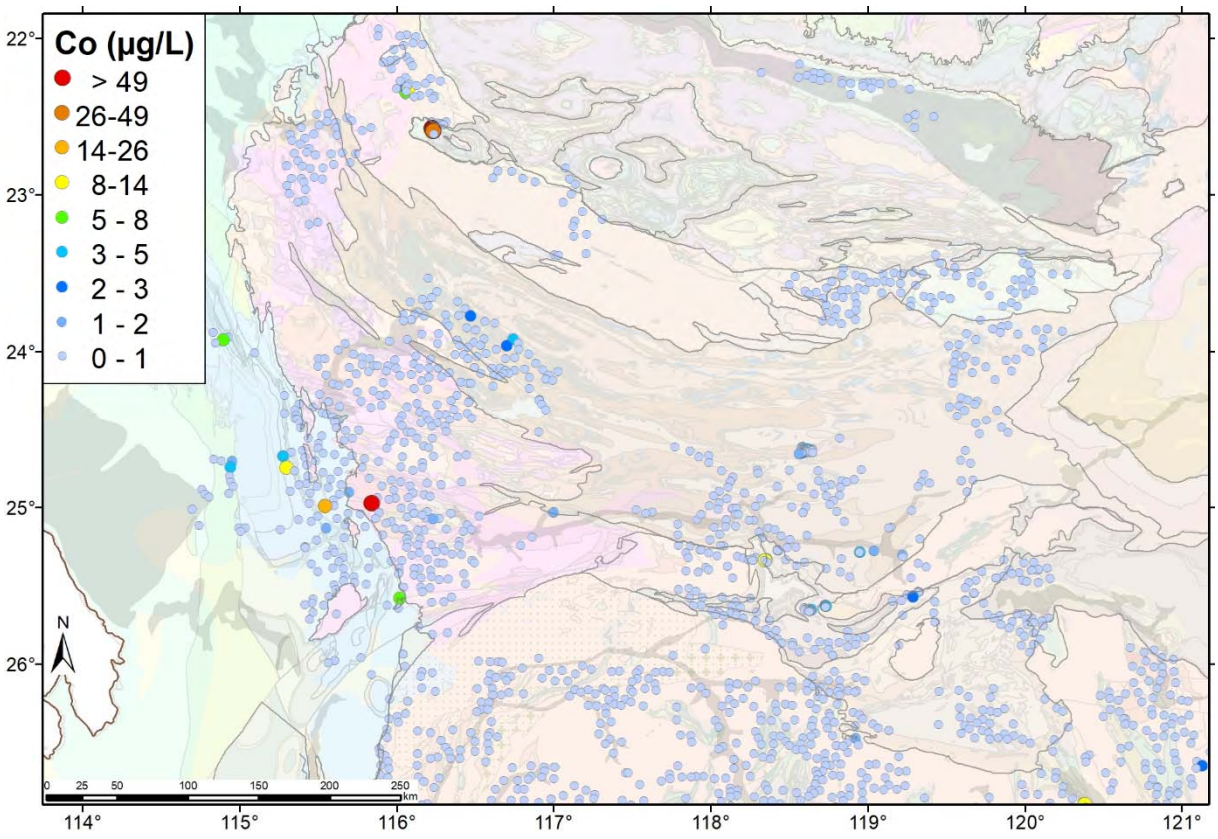

Figure 1.52. Co distribution for the Capricorn Orogen.

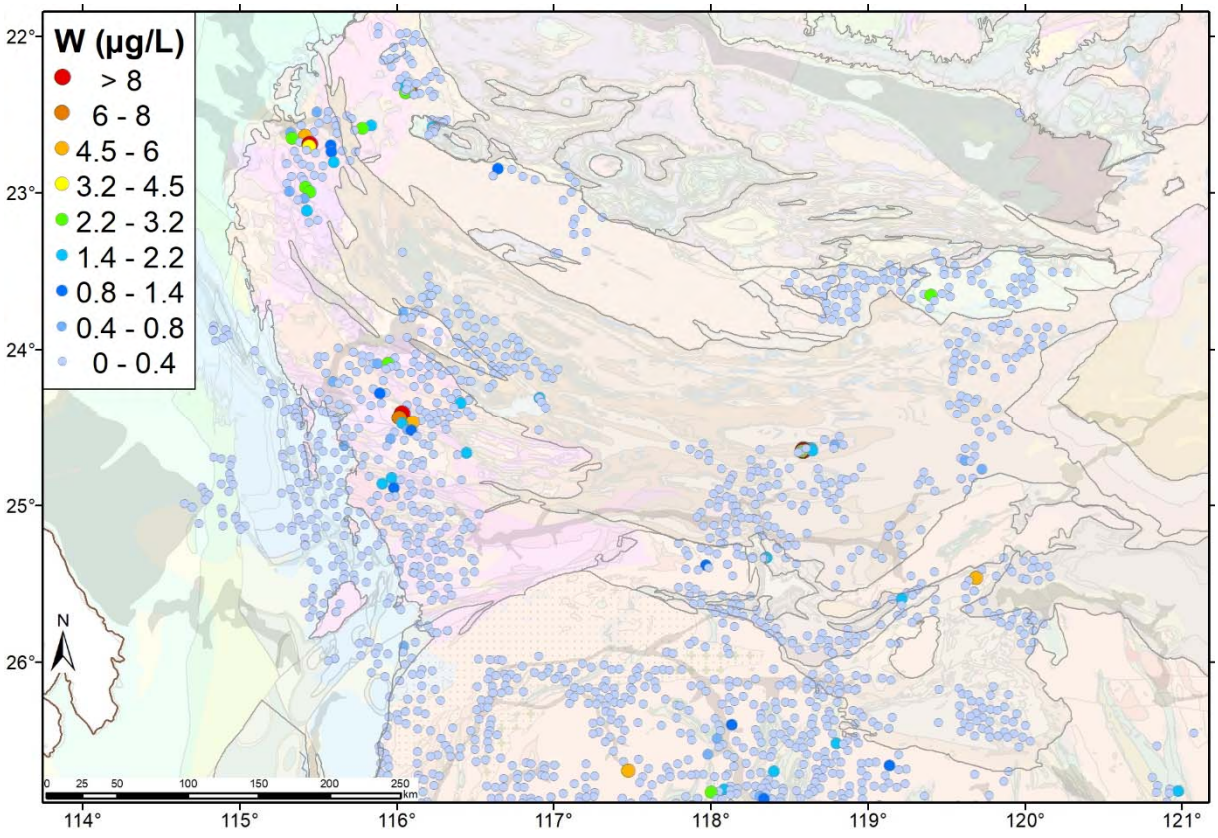

Figure 1.53. W distribution for the Capricorn Orogen.

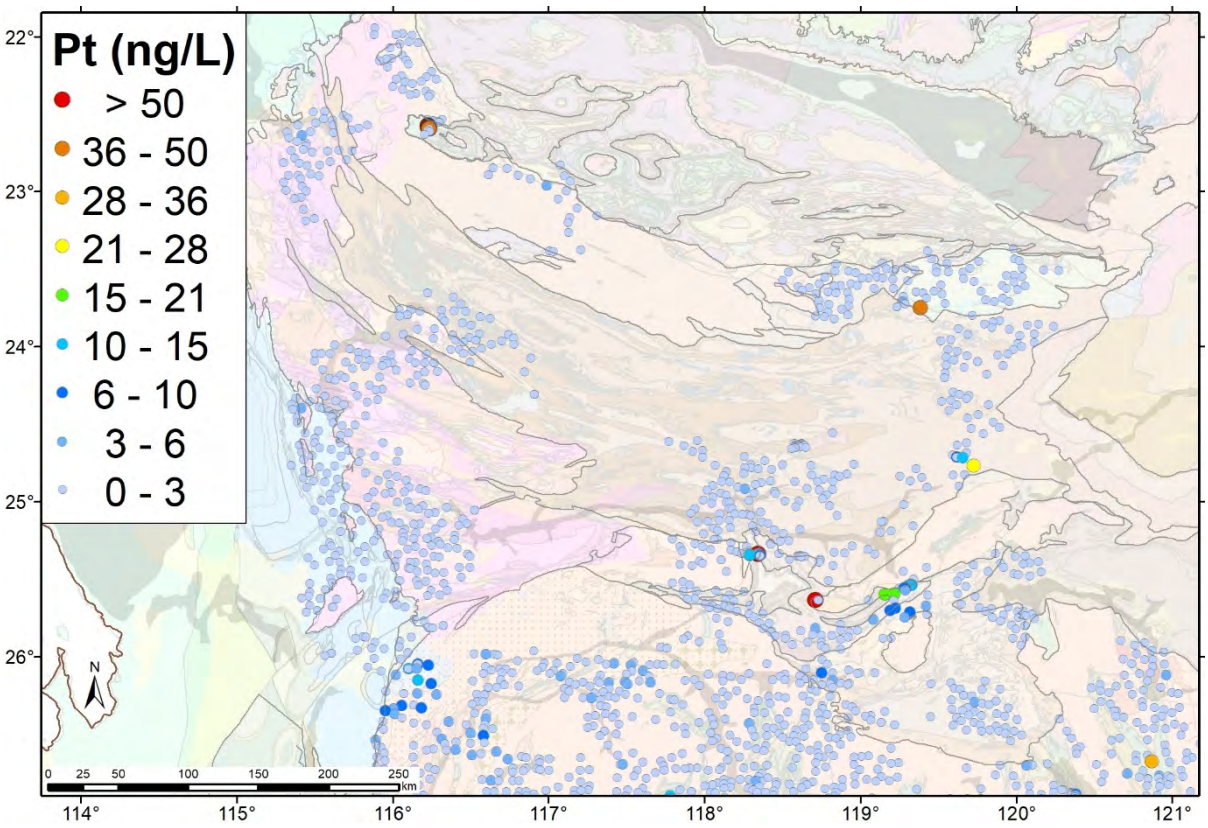

Figure 1.54. Pt distribution for the Capricorn Orogen.

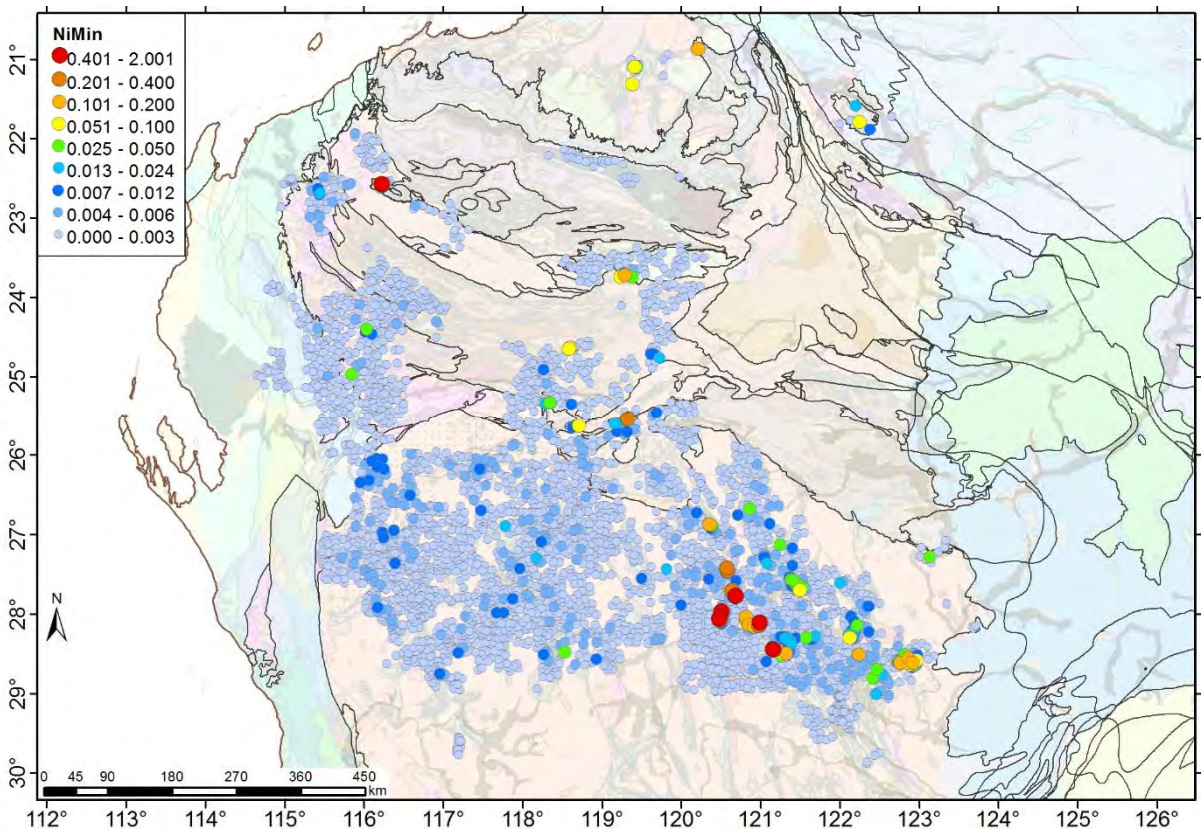

Figure 1.55. NiMin Index distribution for the Capricorn Orogen and north Yilgarn.

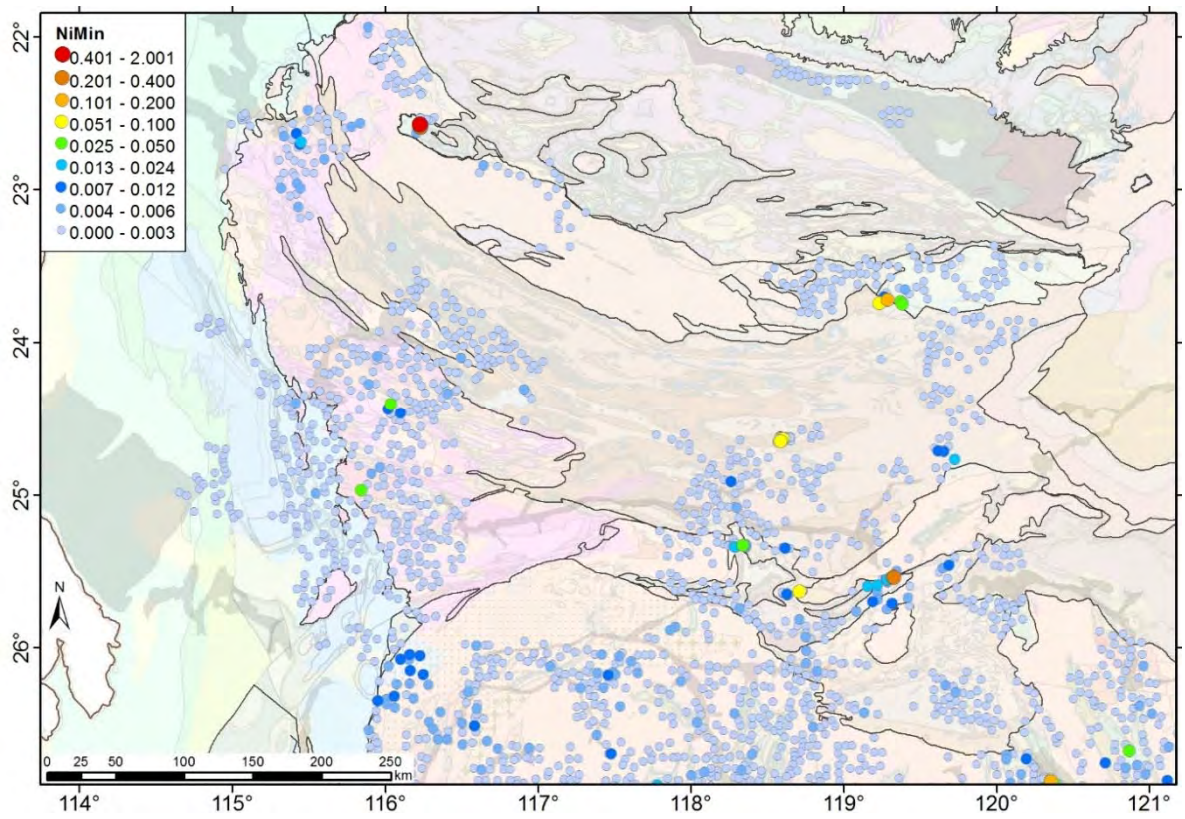

Figure 1.56. NiMin Index distribution for the Capricorn Orogen.

1.6.6 Compounds of environmental concern

Groundwater is a common source of drinking water for humans and livestock in the Capricorn. Significant research has been conducted in other parts of the world investigating toxic concentrations of elements in groundwater. Arsenic (Chen et al., 1992; Alam et al., 2002; ATSDR, 2007a), F (Garciri & Davies, 1993; Saxena & Ahmed, 2003), NO_3 (Johnson & Cross, 1990; NHMRC, 2004), Pb (Kimbrough et al., 1999; ATSDR, 2007b), U, Cu, Zn and Cr (ATSDR, 2000; Gray, 2003) might reach harmful concentrations in Capricorn groundwater.

It is also important for environmental management and mine closure to be aware of the background, natural concentrations of elements of environmental concern to ensure safe use of water resources and also to avoid reclamation requests to reduce concentrations below the levels that naturally occur.

Nitrate is known to be a potential risk in this region: Australian Drinking Water Guidelines (ADWG) state that NO_3 should be below 50 mg/L for infants, 100 mg/L for adults and 400 mg/L for livestock (ANZECC, 2000; NHMRC, 2004) although livestock should only show toxic symptoms above 1500 mg/L). Our data shows that NO_3 is commonly above Australian recommendations for drinking water; in Figure 1.48 groundwater samples that are potentially hazardous for long term NO_3 consumption are coloured yellow (infants only), orange (adults) and red (livestock).

Arsenic is highly toxic in groundwater, as has been well publicised for the Bangladesh delta region. The ADWG recommend that As concentration be <7 µg/L; few groundwater samples of the Capricorn exceed this level (Figure 1.33), with many of these samples around mining infrastructure and major faults, except for one area over the Morrissey Metamorphics to the NW of the Capricorn. Temporal influences of water chemistry may occur and this analysis is not tailored for the most accurate measurement of As, hence further testing is recommended, but this dataset is considered representative of the groundwater conditions at the points sampled. Regional wells, particularly station water supplies, should get a further water assessment if As concentrations are above the ADWG limits from this data set.

Hexavalent (most toxic) Cr naturally occurs in the north Yilgarn groundwater (Gray, 2003), since the Capricorn has similar water conditions it is expected to be the same in this region. The World Health Organization (WHO) provides a drinking water limit of 50 µg/L for Cr^{6+} (IARC, 1990) and only four of the 1000 samples have concentrations approaching or exceeding this level (Figure 1.23), so it is expected that health risks from Cr toxicity are generally minimal.

The Capricorn region does not host known U deposits however, large parts of the region have relatively high concentrations of dissolved U. Unlike most other elements where toxicity is tied to concentration, radioactivity is the most toxic aspect of U in groundwater. The exact concentration is not an accurate measure of toxicity. The radiologically determined health limit is based on Bq/L and is, in terms of concentration, approximately 300 µg/L. Other studies (Moss et al., 1983) have shown no ill health effects with exposure of 700 µg/L U. Only one sample exceeds 700 µg/L in the Capricorn shallow groundwater and only seven out of the 1000 are ≥ 300 µg/L (red dots in Figure 1.26). Consequently health risks from the radioactivity of U in groundwater are probably quite low. However, the ADWG use a concentration of 20 µg/L for safe drinking water (green to red dots in Figure 1.26; NHMRC, 2004) and results in a classification of 14% of groundwater samples being above the recommended guideline value.

Fluoride is often considered beneficial to human health, primarily with the development of teeth. Fluoride deficiency (< 0.5 mg/L) can cause weakened teeth, whereas excess fluoride (F > 1.5mg/L) can cause dental fluorosis (particularly in children), as documented in other regions of the world (Saxena & Ahmed, 2003; Garciri & Davies, 1993). Capricorn groundwater is commonly in this optimal F range of 0.5 – 1.5 mg/L (NHMRC, 2004 Figure 1.57). Excess F is more prevalent in the region (yellow to red dots in Figure 1.57), although many of these samples are more saline, sit in the drainage channels and are not used for human water consumption. As such, F presents only limited health risks associated with dental fluorosis.

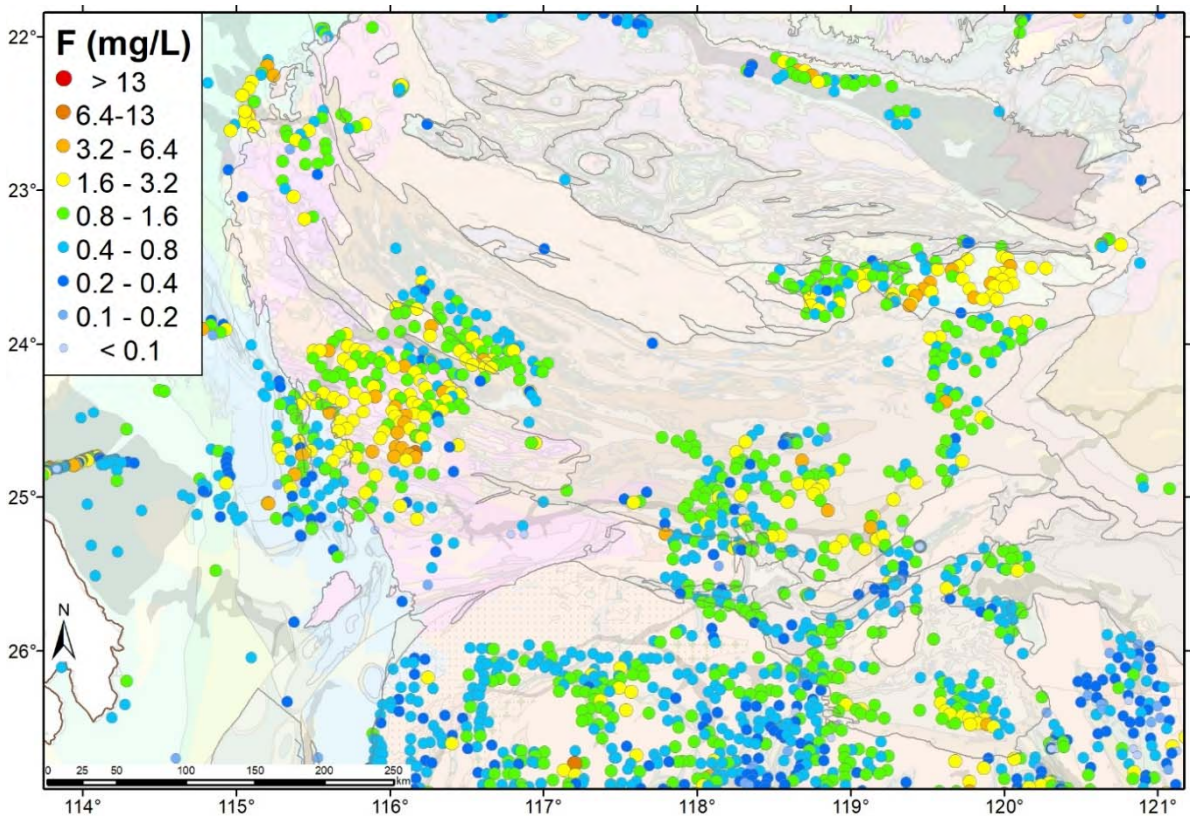

Figure 1.57. Dissolved F distribution for the Capricorn Orogen.

Copper concentrations are all below the ADWG of 2000 µg/L and toxicity from Cu in groundwater supplies is not a concern for humans or livestock. Zinc is also lower than the ADWG of 3000 µg/L.

Lead and Hg are other highly toxic metals that may be found in groundwater. The Capricorn region did not show any detectable dissolved Hg and only a few sites with detectable Pb. Lead is quite immobile in groundwater and is readily adsorbed to clays and Fe oxides, with only four dissolved Pb concentrations above the ADWG of 10 µg/L (NHMRC, 2004) and these, apart from one were all in drillholes above the Abra deposit (Figure.1.42).

Gold in groundwater is the best target element for Au deposits (Figure 1.32). Many of the larger Au concentrations in groundwater occur near known Au mineralisation, but there are exceptions. Patchy correlations with Au-camps are also observed for Ag (Figure 1.34) and As (Figure 1.33). The Capricorn has several areas with high dissolved concentrations of one or more of these pathfinder elements. In some cases, Mo can be associated with Au systems but this seems to be more complicated in groundwater (Figure 1.35). In the Capricorn, variations in Mo concentration appear to be predominantly controlled by lithology. Antimony is also often associated with Au systems, and in the Capricorn this seems to hold true (Figure 1.36). Arsenic does highlight the deposits sampled in the eastern Capricorn (Abra, Prairie Downs, Peak Hill and Fortnum). These As values are relatively low in the entire dataset, but are significant compared to local background.

To improve the groundwater signature for Au deposits, element indices (rescaled data) were combined to give a better probability of determining major Au camps. The AuMin Index (Au+Ag+As) improves the delineation of larger economic targets (Figure 1.37), and more clearly picks up the major Au camps than dissolved Au, Ag or As alone. However, this index did not take into account the improved Sb results in the Capricorn, so a new index (AuMinC = 2*Au+As+Ag+Sb) was created to enhance the Au results and include Sb (Figure 1.38). This index highlights all known deposits that were sampled and provides some new areas that are not known and warrant further investigation.

With the exception of NO_3 and the highly saline groundwater, the majority of the groundwater used for human and livestock consumption is of reasonable quality and should not cause ill health from long term consumption. For livestock, there are very few water samples that are not fit for use; however, those samples that show concentrations above the ADWG for As, Cr, F, NO_3, and TDS should not be used for long term human consumption without further testing and treatment.

1.6.7 Isotope geochemistry

Additional understanding of differing water sources and processes can be developed using isotope geochemistry. Isotope geochemistry is complimentary to “normal” geochemistry in that it is a “fingerprint” of the variations in the relative abundances of isotopes of various elements. Variations in isotopic abundance are measured by isotope ratio mass spectrometry, and can reveal information about the ages and origins of rock, air or water bodies, or processes of mixing between them. Stable isotope geochemistry is largely concerned with isotopic variations arising from isotope fractionation, whereas radiogenic isotope geochemistry is concerned with the products of natural radioactivity.

For most stable isotopes, the magnitude of fractionation from kinetic and equilibrium fractionation is very small; for this reason, enrichments are typically reported in parts per thousand (‰). These enrichments (presented as δ) represent the ratio of heavy isotope to light isotope in the sample over the ratio of a standard. For example:

$$\delta^{34}S = \left(\frac{(^{34}S/_{32}S)sample}{(^{34}S/_{32}S)standard} - 1\right) * 1000‰$$

- **O and H isotopes**

Oxygen has three stable isotopes, ^{16}O, ^{17}O, and ^{18}O, stable H isotopes are ^{1}H, ^{2}H (deuterium), and ^{3}H (tritium). In water samples both H and O isotope ratios are shown relative to Standard Mean Ocean Water (SMOW; Drever 1982). The parameter $\delta^{2}H$ (also noted δD) is a measure of the isotopic enrichment of ^{2}H (over ^{1}H), whereas $\delta^{18}O$ is a similar measure of the isotopic enrichment of ^{18}O (over ^{16}O).

As marine air moves over land it appears to mix and homogenise, this results in precipitation that is closely aligned to specific $\delta^{18}O$: $\delta^{2}H$ mixing relationships termed meteoric water lines (Gat, 1996). These lines are delineated in δ - space by the formula $\delta^{2}H = 8\ \delta^{18}O + d$, where *d* is defined as the deuterium excess ($d = \delta^{2}H - 8\ \delta^{18}O$) (Dansgaard, 1964). The deuterium excess is present because, in addition to the phase changes under equilibrium conditions, a kinetic effect results from a different diffusivity for the isotopically different water molecules in air. Specifically $^{2}H^{1}H^{16}O$ gas a higher diffusivity relative to $^{1}H^{1}H^{18}O$, which results in an additional isotopic separation and therefore a deuterium excess. Humidity relative to saturation at sea surface temperature and wind speed are the major controlling factors of d (Dansgaard, 1964). Dansgaard (1964) documented four factors that affect the isotopic signature of precipitation: distance from the coast (the continental effect); latitude; volume; and altitude. The first continental precipitation will have a similar isotopic composition to seawater, as the distance from the source increases, and consequently rain-out increases, the isotopic values of precipitation will become more depleted. This process is known as Rayleigh distillation, the heavier molecules condense first resulting in precipitation enriched in ^{18}O relative to ^{16}O. The remaining water vapour becomes increasingly depleted as it undergoes successive condensation events and the subsequent precipitation reflects this depletion.

Rayleigh distillation results in precipitation with a significantly lighter isotopic composition (i.e. more negative $\delta^{18}O$ and $\delta^{2}H$) at higher latitudes and on inland regions relative to the evaporative source region. This model portrays the global water cycle in simplified terms: evaporation at warm temperatures in the tropics and subtropics, vapour transport to high latitudes and subsequent condensation (Hoffmann and Heimann, 1997). Although there are many factors affecting the $\delta^{18}O$ values, due to the Rayleigh distillation process the mean annual precipitation at a large number of globally distributed stations is related to mean average temperatures, with warm temperatures corresponding to higher (less negative) $\delta\ ^{18}O$ values (Dansgaard, 1964; Rozanski et al., 1993). This relationship between rain-out and temperature is only observed between -40 and 15 °C, above this temperature range the amount effect dominates. This approximately results in 1.5‰ depletion in $\delta^{18}O$ of precipitation for every 100 mm increase in rainfall and is particularly prevalent in convectively active regions. Finally as water vapour moves over mountains adiabatic expansion causes cooling and condensation of water forming so called orographic precipitation, this produces large isotopic gradients (Quade et al., 2007).

When meteoric water from a particular elevation evaporates prior to recharge, the relationship between $\delta^{2}H$ and $\delta^{18}O$ deviates from the Global Meteoric Water Line (GMWL). Figure 1.58 shows an example of a how the precipitation may vary in different climatic and geographical conditions and how the isotopic composition of the water may change after a rain event. Meteoric water from a given altitude that evaporates forms a linear $\delta^{2}H$ and $\delta^{18}O$ trend, with a different slope and y-intercept compared to the GMWL. Evaporated water samples fall to the right/below the GMWL. If rainfall from a different location was sampled and was evaporated, a different dashed line would likely form around the water samples.

Water may experience evaporation and isotopic enrichment during rainfall through an atmosphere of lower humidity, after reaching the ground but before infiltration, and after reaching the ground but prior to deep infiltration (Ingraham et al. 1998).

The isotopic signature of groundwater may be influenced by a number of processes each of which may have different effect on the δ^2H and $\delta^{18}O$ values (Figure 1.58).

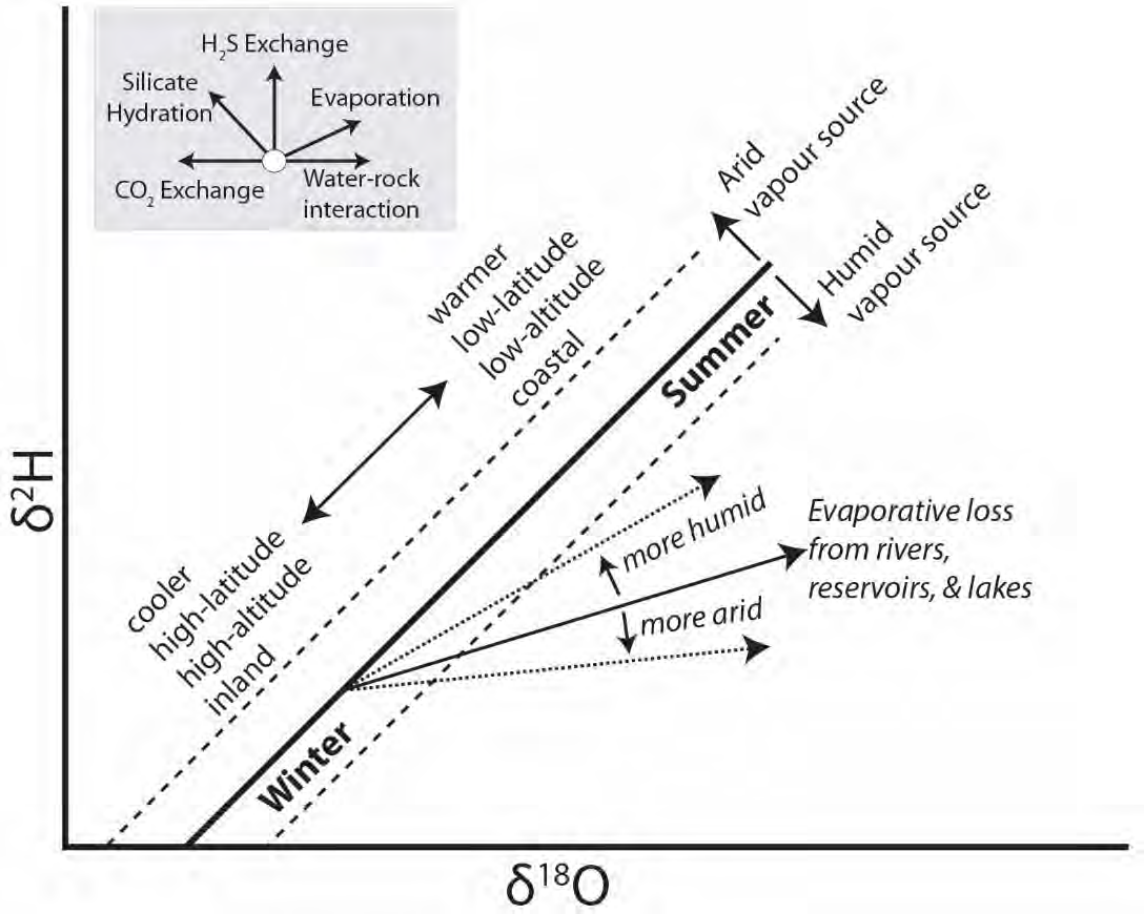

Figure 1.58. Summary figure showing the possible variation of O and H isotopes based on variation before, during and after precipitation.

The δ^2H and $\delta^{18}O$ of the Capricorn groundwaters are plotted in Figure 1.59 and Figure 1.60, these data do not show a well-developed pattern that can be related to the initial isotopic composition of rainwater (e.g. continental effect) potentially due to varying degrees of evaporation leading to variable isotopic compositions. As the evaporation trend is known, the samples can be grouped by their initial isotopic composition effectively, removing the effect of evaporation (Figure 1.61) and, grouping results based on the 'HO difference'. Figure 1.62 shows the HO diff. groups plotted across the Capricorn region.

The variation in the HO difference values in the Capricorn highlights a trend for increasingly isotopically light meteoric waters as rainfall moves away from the coast. The range of sample points along the GMWL and the associated evaporation of these waters is therefore predominantly representative of the 'continental effect'. Isotopically enriched rain forms and falls from a diminishing vapour mass, and residual vapour becomes isotopically depleted with respect to earlier to rains from the same cloud resulting in meteoric waters with increasingly light $\delta^{18}O$ and δ^2H values the further from the coast precipitation occurs.

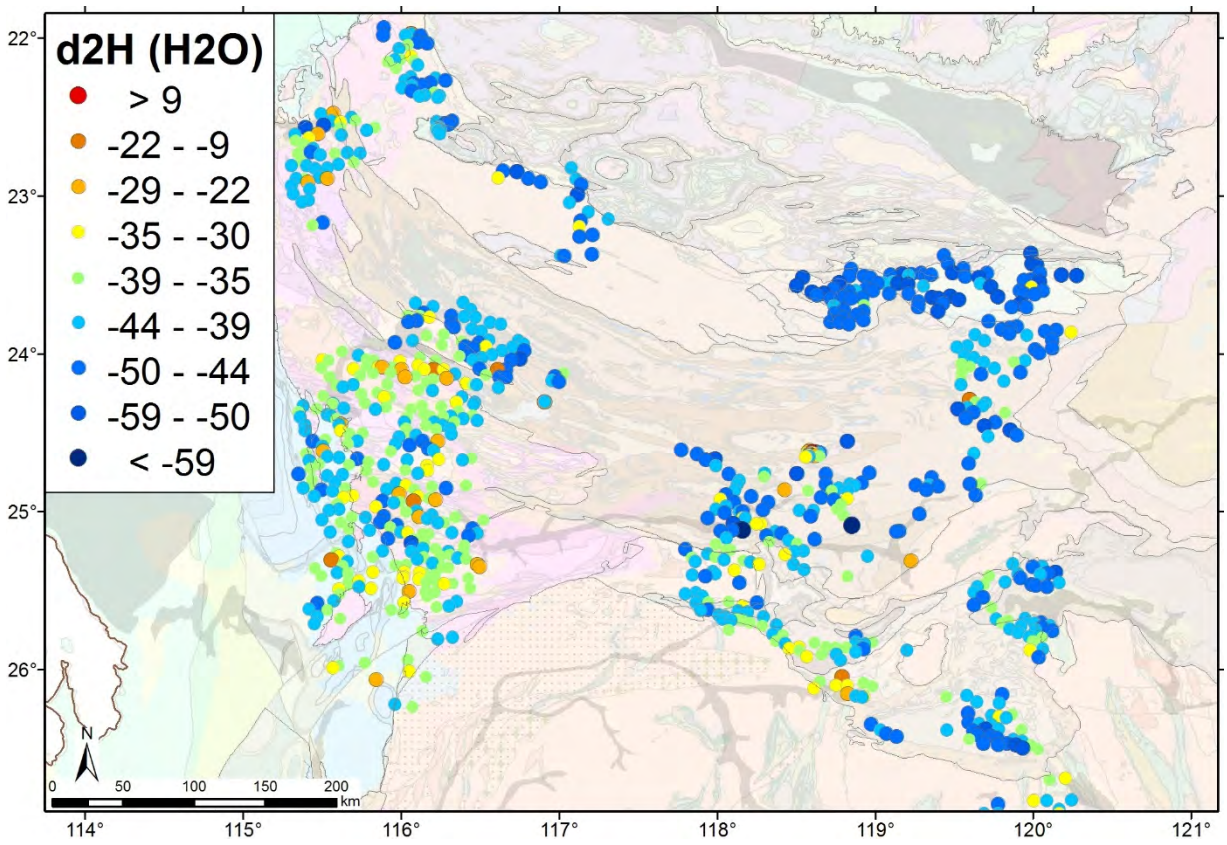

Figure 1.59. δ^2H (d2H) distribution for the Capricorn Orogen.

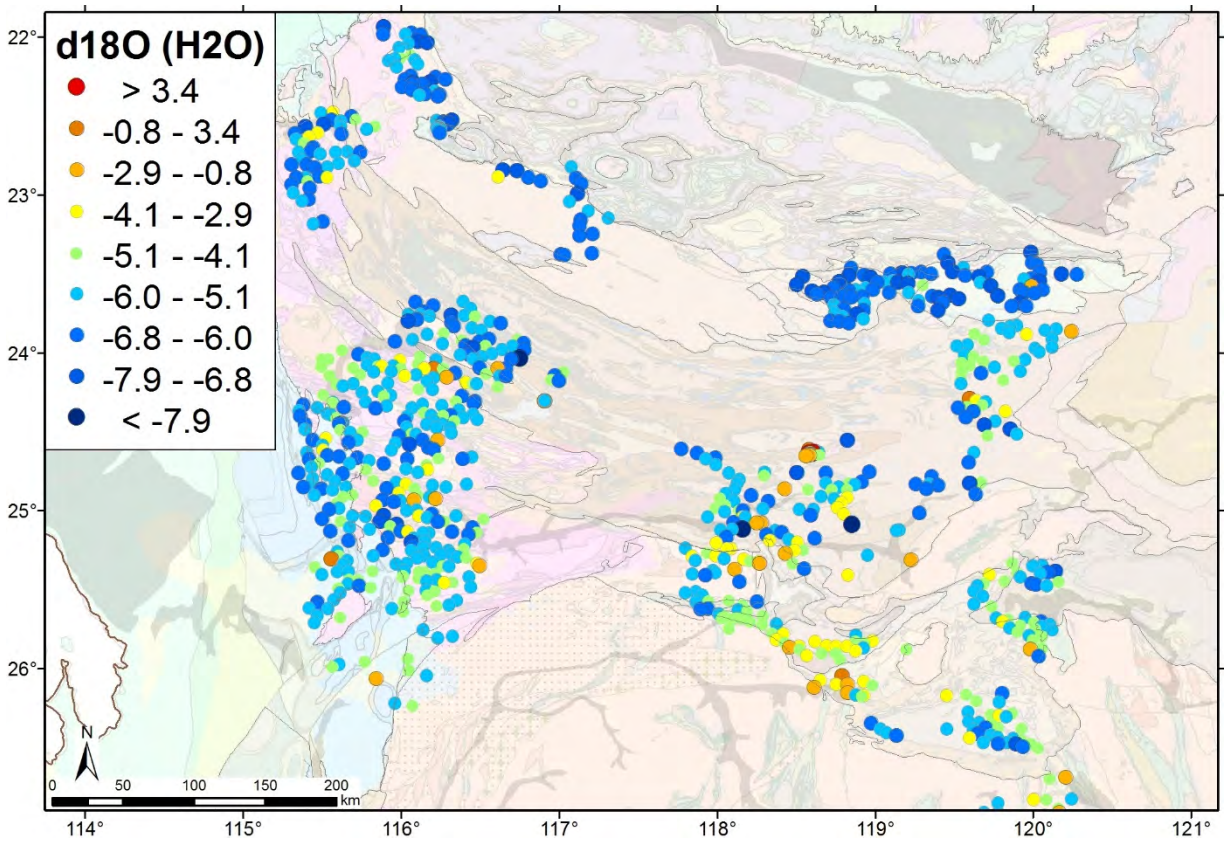

Figure 1.60. $\delta^{18}O$ (d18O) distribution for the Capricorn Orogen.

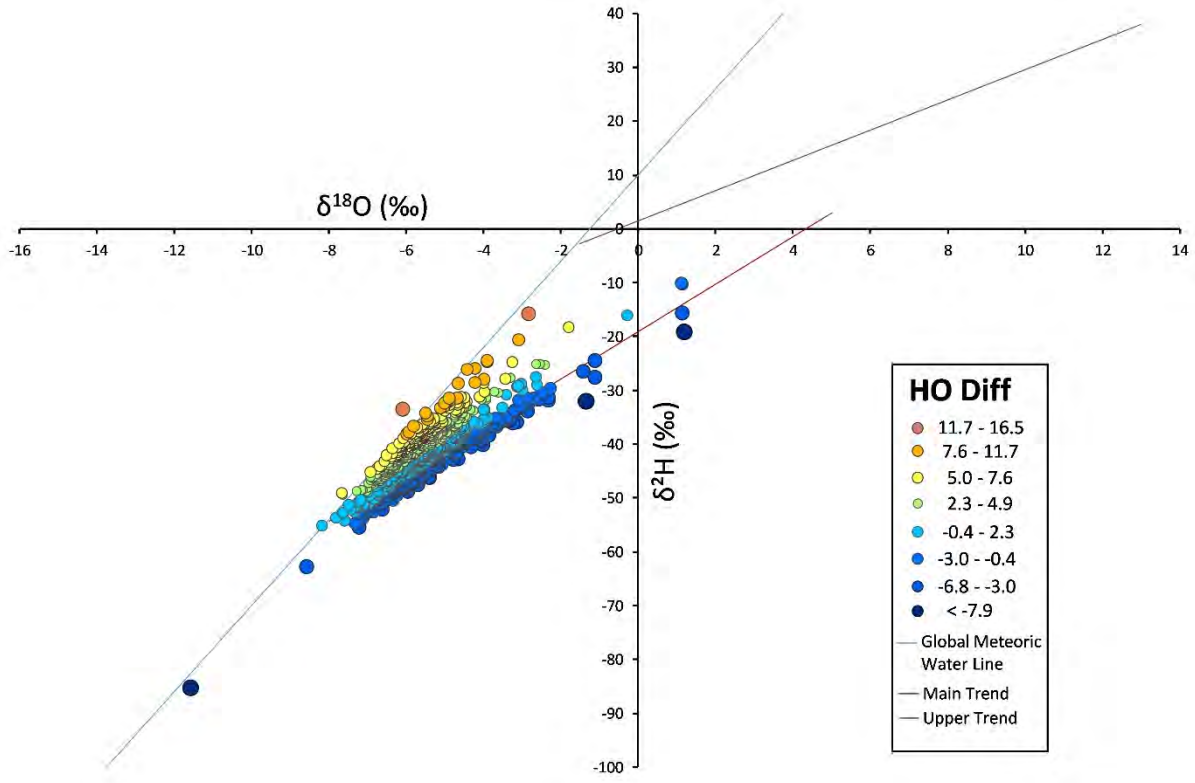

Figure 1.61. Cross plot of δ^2H vs. $\delta^{18}O$ defining HO Diff. groups.

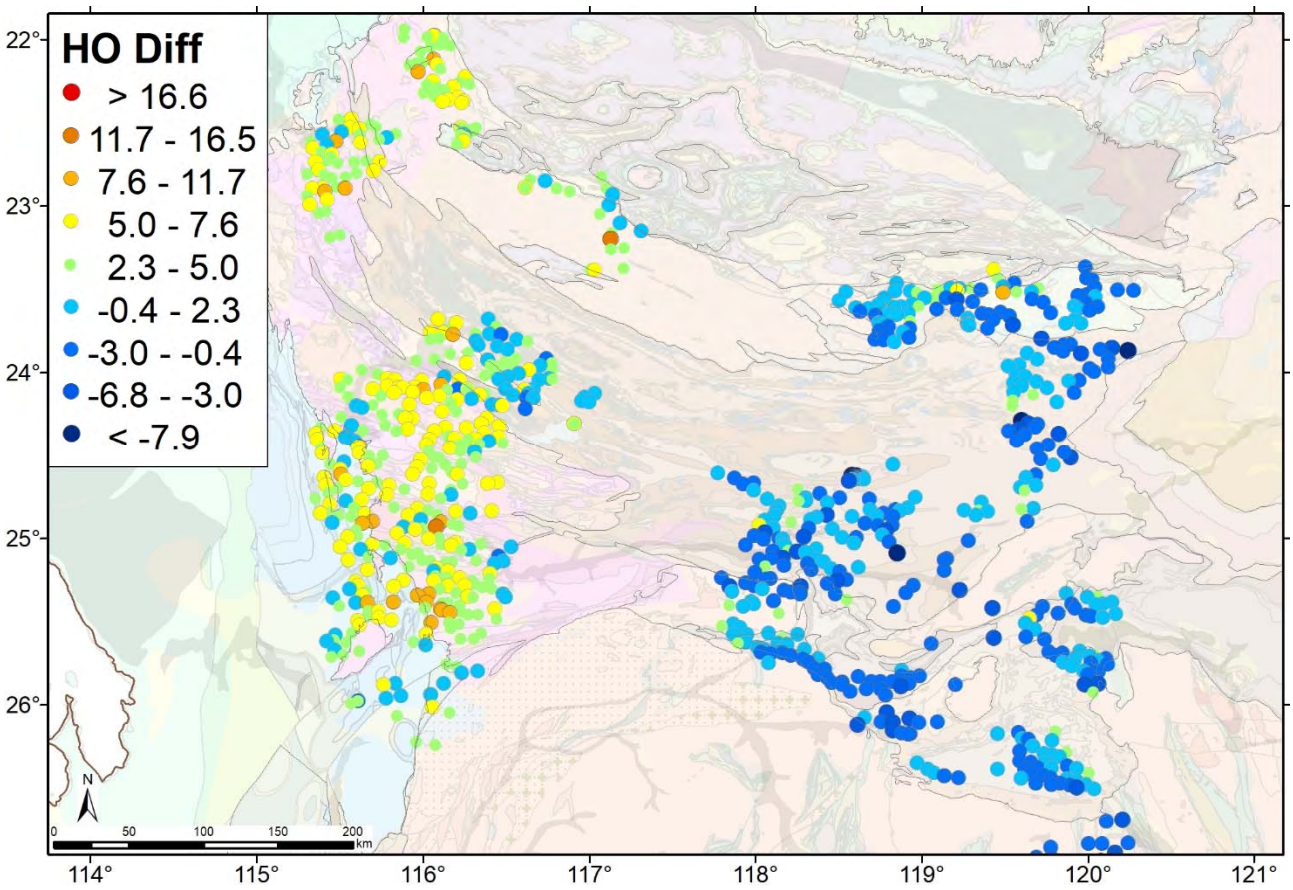

Figure 1.62. HO Diff. distribution for the Capricorn Orogen, based on groups defined in Figure 1.61.

There are range of TDS values recorded for Capricorn waters (Figure 1.22) and it has been suggested that salinity variations are caused by evaporation, if this was the prevailing mechanism for increases in salinity there should be a correlation in this data between increasing TDS values and depleted groundwaters. However, this trend is not observed (Figure 1.63). Alternatively variations in the salinity of groundwater may occur due to: i) evaporation of surface water before deep infiltration, ii) evapotranspiration iii) water-rock interactions. It is suggested that a 3 ‰ increase in $\delta^{18}O$ values is produced by only 15 % evaporation (Gonfiantini 1986), which is far less than required to produce the more elevated TDS values observed in Capricorn waters. Transpiration however has a major influence on water salinity and does not discriminate between isotopes of the water molecule (Zimmerman et al. 1967; Allison et al. 1984), the original $\delta^{18}O$ and $\delta^{2}H$ composition derived from rainfall is essentially preserved, except for a slight enrichment of ^{2}H and ^{18}O due to partial evaporation within the upper few metres of the soil zone during infiltration (Herczeg et al 2001). A combination of evaporation and transpiration has effected the Capricorn groundwater isotopic composition but evaporation has not been sufficient to produce a correlation between TDS and $\delta^{18}O$ values (Figure 1.63).

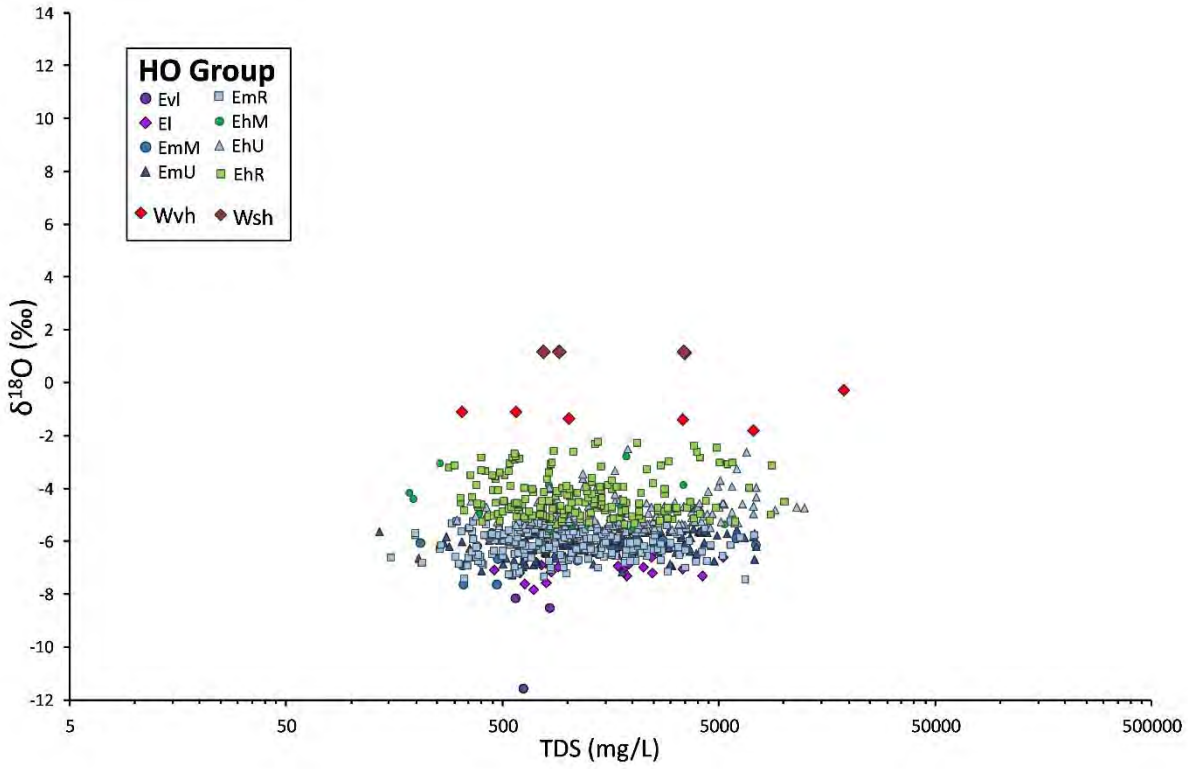

Figure 1.63: $\delta^{18}O$ vs TDS for Capricorn groundwaters. Differing $\delta^{2}H$ / $\delta^{18}O$ groups are discussed in the text.

So as to further aid mapping isotope information, $\delta^{2}H$ / $\delta^{18}O$ is delineated along the evaporation trend from cool (purple, blue) colours (low $\delta^{2}H$ and $\delta^{18}O$) through to warm (red) for highly evaporated (high $\delta^{2}H$ and $\delta^{18}O$) waters (Figure 1.64). Mapping of $\delta^{18}O$ and $\delta^{2}H$ (Figure 1.65), suggests a regional trend, with higher $\delta^{18}O$ values further from the coast suggesting waters have moved further along the evaporation trend in inland regions, either due to a decreased volume of precipitation in this region or increased residence times within reservoirs subject to evaporation. Most notable are the samples of high $\delta^{18}O$, uncorrelated with TDS (i.e. Wvh and Wsh in Figure 1.64). These occur as specific zones that may be correlated with known faults, or with areas previously identified as anomalous in other geochemical parameters Figure 1.66.

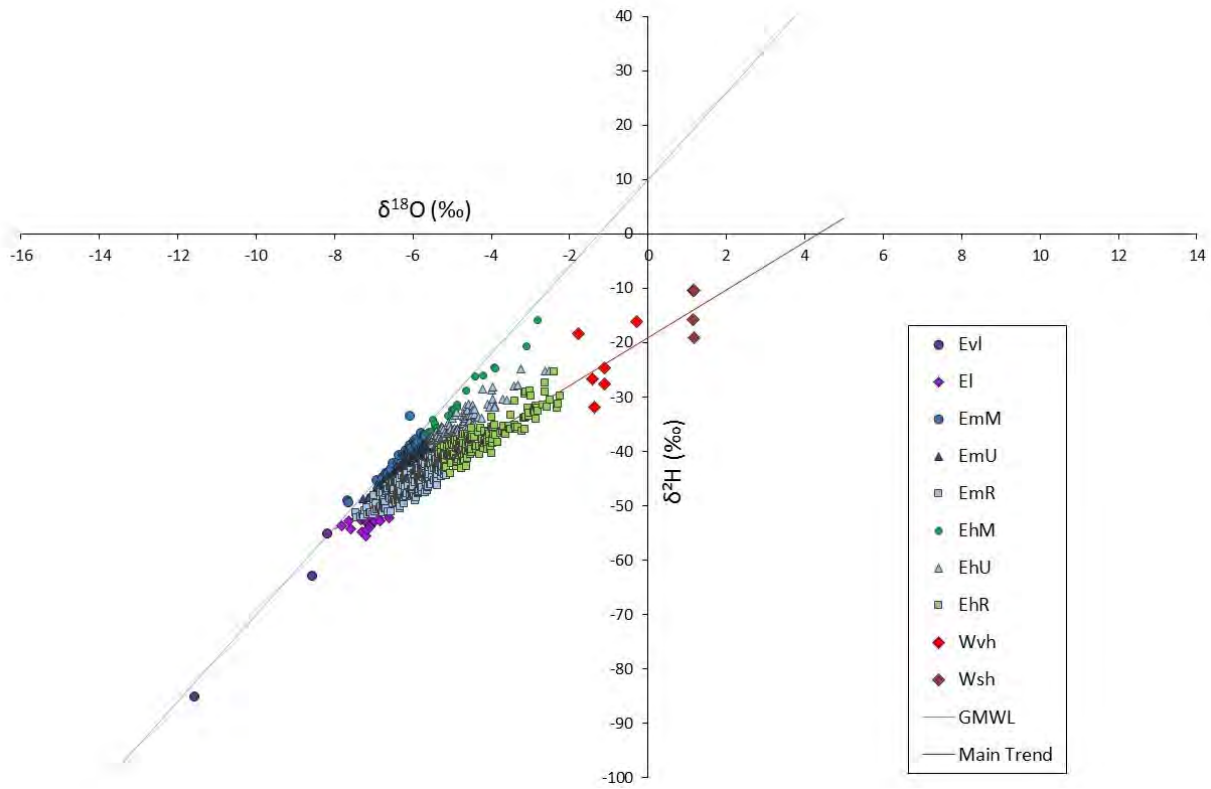

Figure 1.64. δ^2H vs $\delta^{18}O$ for the Capricorn Orogen. Differing δ^2H / $\delta^{18}O$ groups are discussed in the text.

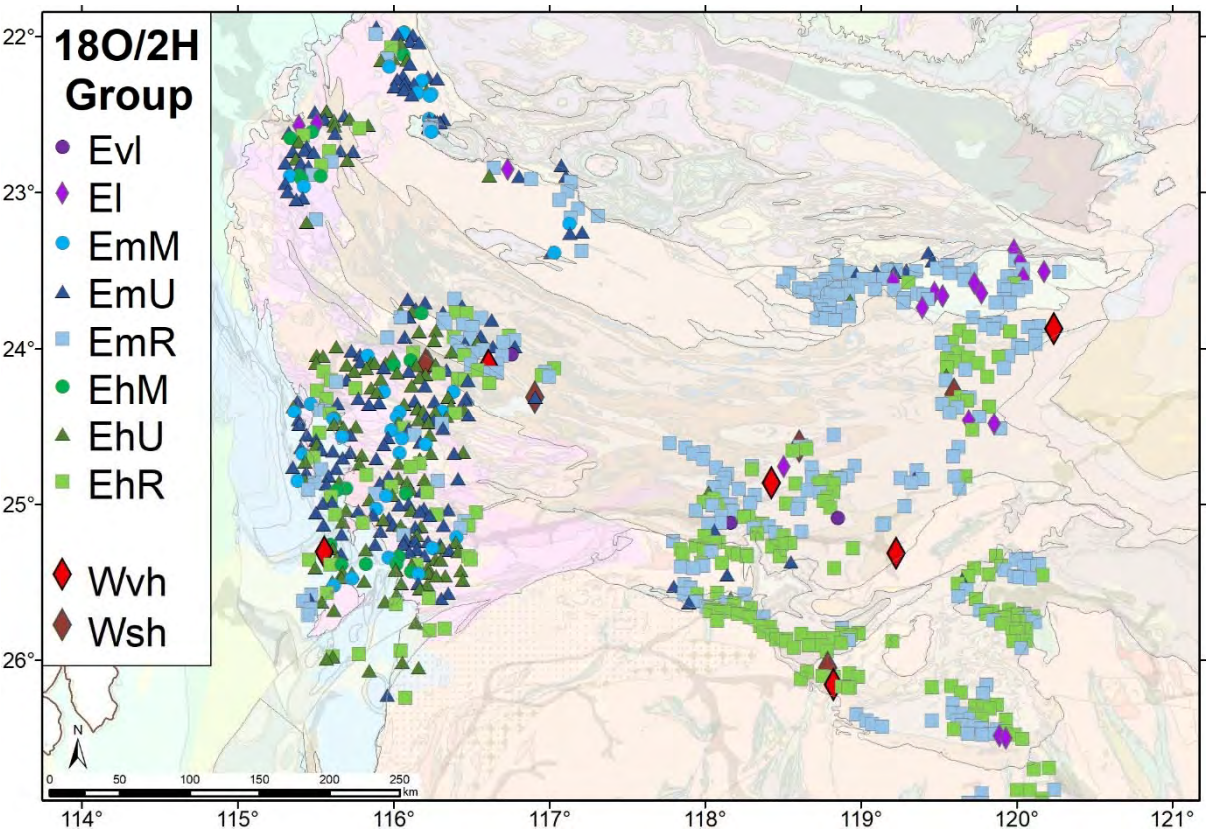

Figure 1.65. $\delta^{18}O$/ δ^2H group distribution for the Capricorn Orogen.

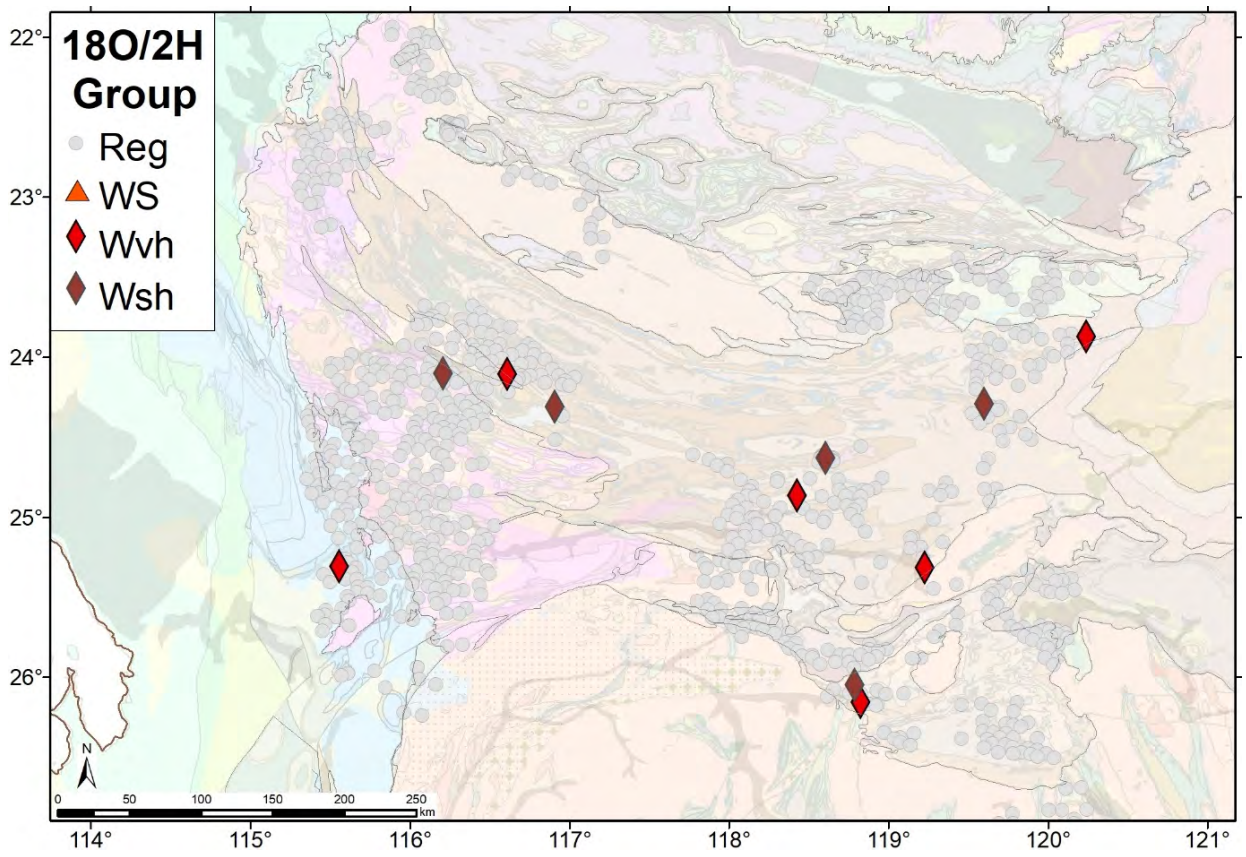

Figure 1.66. Excursion from normal trend for OD groups distribution for the Capricorn Orogen.

The O an H isotope results highlight their ability to identify potentially different water sources that may be related to faults, fractures or mineralisation. When combined with pathfinder chemistry and mineral saturation indices O an H isotope can be used to identify new areas of interest for mineral exploration.

- **S and O combined isotopes**

The $\delta^{34}S$ and associated $\delta^{18}O$ were analysed from SO_4^{2} in three hundred groundwater samples based on samples with the highest SO_4^{2} content. Sulfur has four stable isotopes, with the following terrestrial abundances: ^{32}S (95.02%), ^{33}S (0.75%), ^{34}S (4.21%) and ^{36}S (0.02%). It is well established that $^{34}S/^{32}S$ measurements may be useful in distinguishing rock sulfides from meteoric S (Chivas et al., 1991; de Caritat et al., 2005). Lighter $\delta^{34}S$ measured from SO_4^{2} are more commonly linked with the weathering of sulphides (Gray et al. 2014).

Sulfate in groundwater may be sourced from dissolution of sulfate minerals, precipitation, and dissolution of sulfides. Sulfate derived from the dissolution of sulfate minerals e.g. gypsum will possess heavier $\delta^{18}O\_SO_4^{2}$ values and variable, generally heavier $\delta^{34}S$, whilst data for the $\delta^{34}S$ composition of precipitation in the region is partially dependent on the distance from the coast and the prevailing winds, with coastal regions gaining a higher proportion of ^{34}S (Chivas et al., 1991). Sulfides in the form of pyrite have been shown to react with water and dissolved molecular oxygen to form sulfate and Fe oxyhydroxides. Usher et al. (2004), have shown that water and not dissolved oxygen is the primary source of oxygen in the sulfate product. Similarly Heidel et al. (2009), suggested only a small proportion of molecular oxygen is incorporated into the sulfate during oxidation although this may increase for ultrafine pyrite.

Isotope exchange is slow in the aqueous sulfur system, especially for the ^{18}O-exchange reaction between sulfate and water at normal groundwater temperatures and neutral pH, with the half-time of sulfate-water exchange on the order of 10 million years (Chiba and Sakai, 1985).

Given that the majority of the oxygen in sulfate is derived from water (as opposed to molecular oxygen) and this oxygen is retained over millions of years, the $\delta^{18}O\_SO_4^2$ signature of the sulfate in the Capricorn groundwaters will reflect the isotopic composition of the water at the time of SO_4^- formation.

$\delta^{34}S$ for the Capricorn region range from -2.6 to 29.5 ‰, with a median value of 13.5 ‰. Broadly the major geological terrains appear to be distinguished by varying $\delta^{34}S$ values (Figure 1.68). The Yerrida Basin and Sylvania Inlier possess heavier $\delta^{34}S$ values, whereas the Gascoyne Province and Bryah Basin are defined by relatively light $\delta^{34}S$ values.

In the regional sampling dataset (excluding mineral deposits e.g. Paulsens), the largest grouping of samples with light $\delta^{34}S$ values (Figure 1.71, green points), with the potential to be related to the weathering of sulfides are present in the west of the region within the Phanerozoic Carnarvon Basin sediments. This pattern of anomalous values coincides for the most part with the elevated Li values and samples with elevated TDS found in this area (Figure 1.25). We propose that the elevated Li concentration and low $\delta^{34}S$ in this region are related to the presence of saline brines and gypsum formation in this region, rather than sulfide weathering.

$\delta^{18}O\_SO_4^2$ range from 0.6 to 15.9 ‰ with a median value of 8.6 ‰. Apart from the Sylvania inlier there does not appear to be any major variation in $\delta^{18}O\_SO_4^2$ values with geology (Figure 1.69). There is also no statistically significant correlation between $\delta^{18}O\_SO_4^2$ and $\delta^{18}O$ (Figure 1.67) of the groundwater indicating that for the most part sulfate found in the Capricorn groundwater was not formed in equilibrium with the current groundwater isotopic composition.

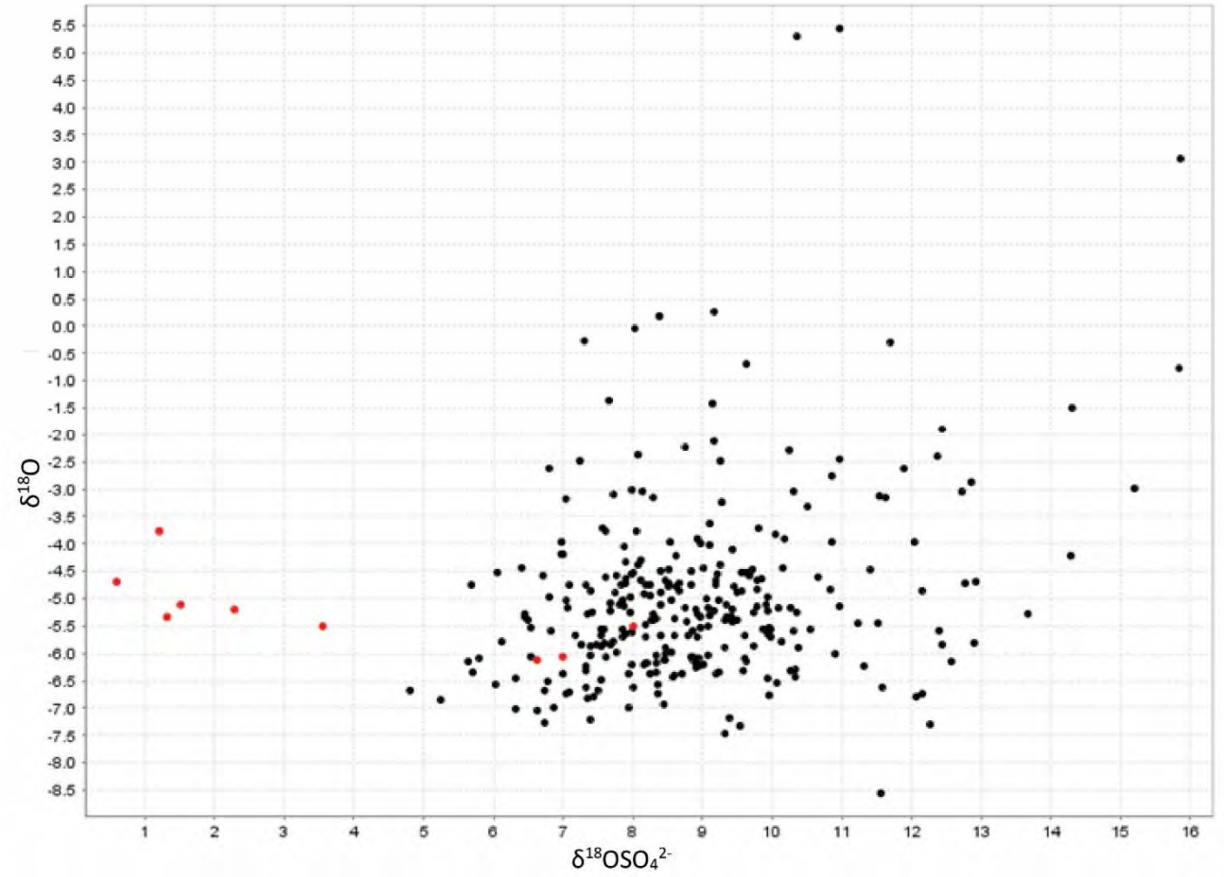

Figure 1.67. Cross plot showing $\delta^{18}O\_SO_4^2$ vs. $\delta^{18}O$ in Capricorn groundwater. Red points are samples are from the area around Paulsens gold deposit.

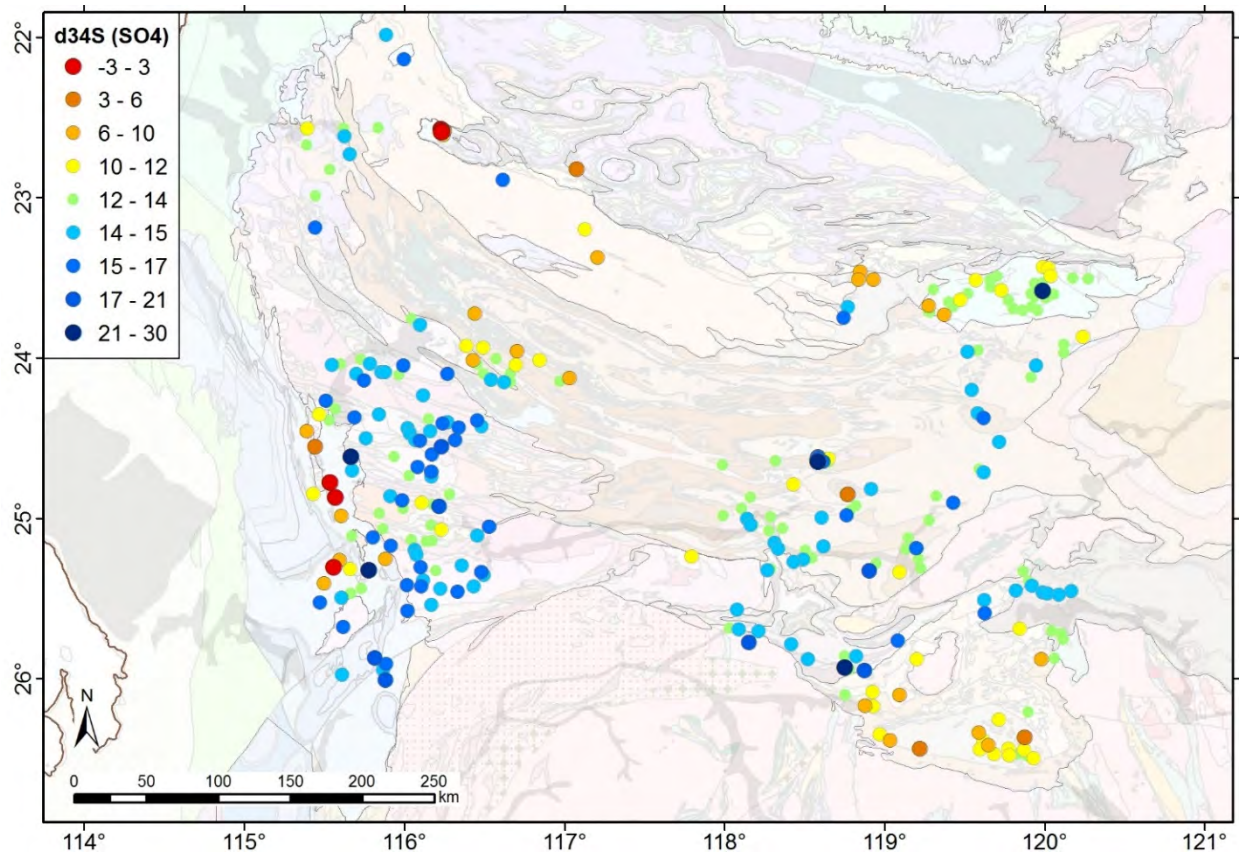

Figure 1.68. $\delta^{34}S$ distribution for the Capricorn Orogen.

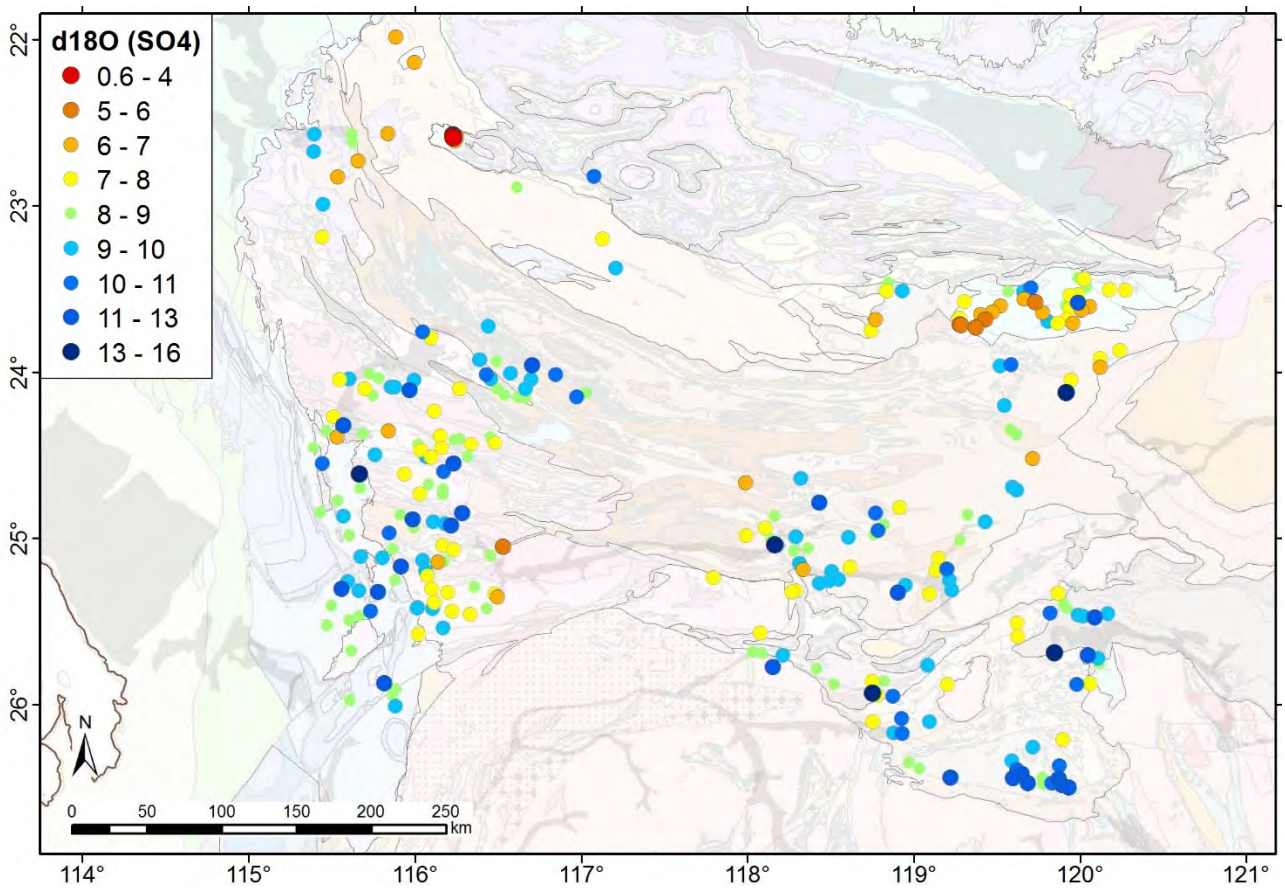

Figure 1.69. $\delta^{18}O\_SO_4^2$ (d18O (SO4)) distribution for the Capricorn Orogen.

Previous studies have suggested that $\delta^{34}S$ values of less than 14 ‰ may be representative of sulfides weathering (Gray et al. 2014) in the Yilgarn Craton. However, this value will vary depending upon background values relating to geology and also the isotopic composition of the weathering sulfides. In this study, Paulsens gold deposit was targeted as a case study location due to the elevated SO_4^2 concentrations within the water and ease of sampling. The $\delta^{34}S$ of sulfides within this deposit have been analysed (Selvaraja et al. 2017).

Paulsens gold deposit

Paulsens ~ 1 million ounce gold deposit is located on the north east edge of the Capricorn Orogen (Figure 1.3) and is hosted in Pilbara Neoarchean sediments and mafic volcanics outcropping in the Wyloo dome. The deposit is comprised of lenses of massive and disseminated sulfides hosted in thick laminated quartz veins that formed contemporaneously with mineralisation.

Groundwaters sampled from around Paulsens are all relatively fresh (median TDS of 1770) and are neutral with a pH between 7 and 7.95. The depth of the water table in the region varies from between 20 and 45 m.

Gold in groundwater has been shown to be a key indicator of gold mineralisation, Au values in water within 1 km of Paulsens reach a maximum concentration of 3070 ng/L in comparison to median of 2 ng/L in regional samples. Groundwater with the highest Au concentrations are found close to a drainage in the west and south of the deposit (Figure 1.70). Although these gold concentrations are exceptional they are close (<2 km) to the mine, however samples up to 5 km away still possess Au concentrations up to 55 ng/L. Cobalt, Pt and Pd concentrations are also elevated near the mine site and show a similar pattern to the highest Au values with the highest concentrations observed to the south and west of the mine (Figure 1.70).

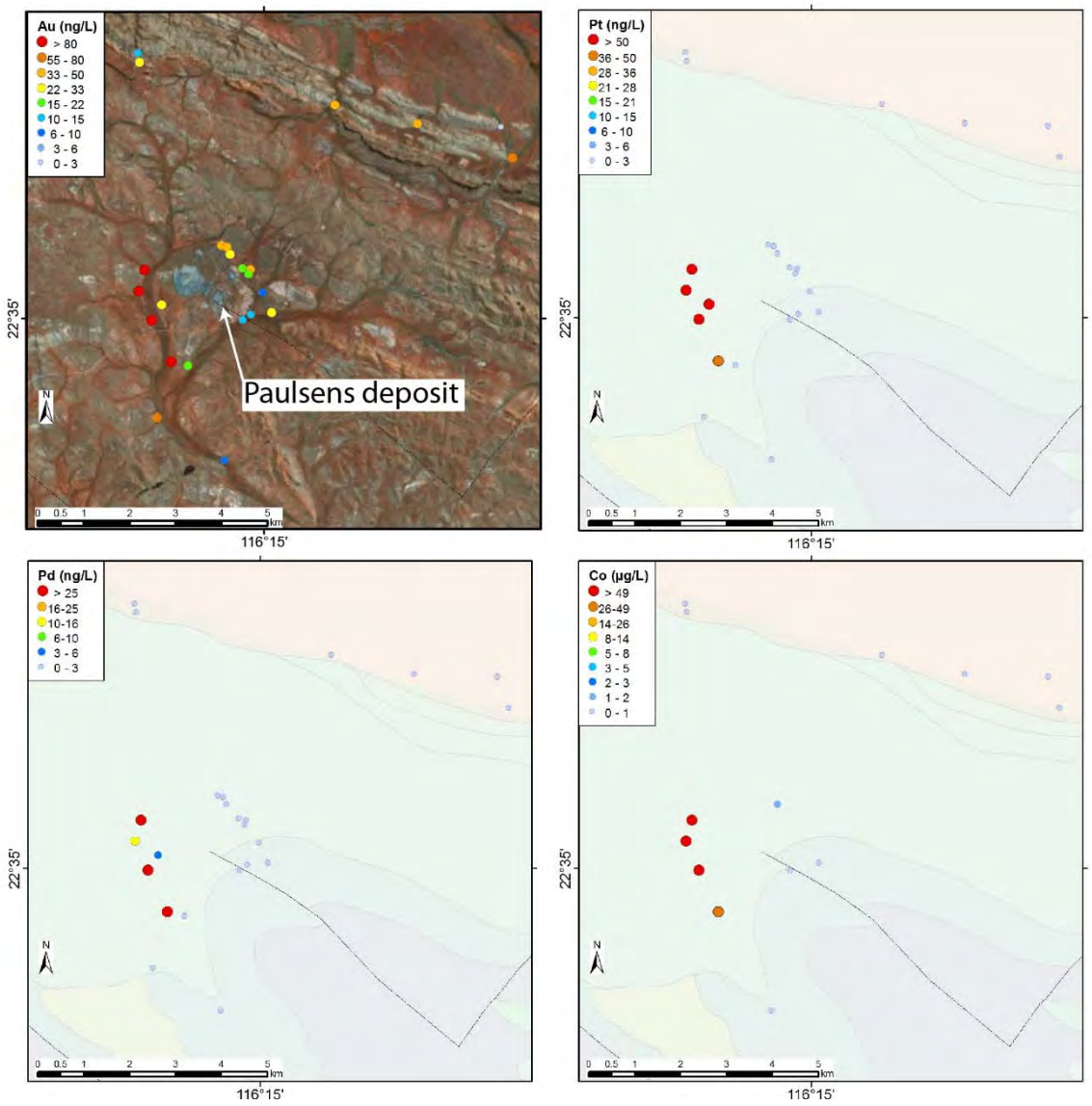

Figure 1.70. Distribution of Au, Pt, Pd and Co around Paulsens gold deposit. The Au distribution map shows aerial imagery and the location of the deposit, all other maps a shown with the same field of view and with the interpreted bedrock geology.

The lightest $\delta^{34}S$ (-2.6 to 2.2 ‰) and particularly $\delta^{18}O\_SO_4^2$ (0.6 to 3.6 ‰) values form a distinct population in the cross plot in Figure 1.71. All these data correspond to samples from the south and west of the Paulsens deposit. The mean $\delta^{34}S$ of two generations of pyrite from the Paulsens deposit are -0.95 ‰ and 0.69 ‰ (Selvaraja et al. 2017). The remainder of the low groundwater $\delta^{34}S$ values (based on an inflection point within the $\delta^{34}S$ probability plot) are shown in green in Figure 1.71. Three of these nine samples are from Paulsens, meaning every sample from Paulsens possesses an anomalously light $\delta^{34}S$, and a range of, but generally light, $\delta^{18}O\_SO_4^2$ values. The isotopic signature of the sulfate in groundwater around Paulsens appears to be geographically controlled, more sampling is required to confirm this (Figure 1.72). One sample falls within the Paulsens data range but is not from this location (Figure 1.71). This sample is located 10 km to the east of the Prairie Downs deposit and was taken from a drill hole, the water possesses low pH, high sulfate and high metal contents all indicative of sulfide weathering, and is therefore considered an area of interest for continued exploration work.

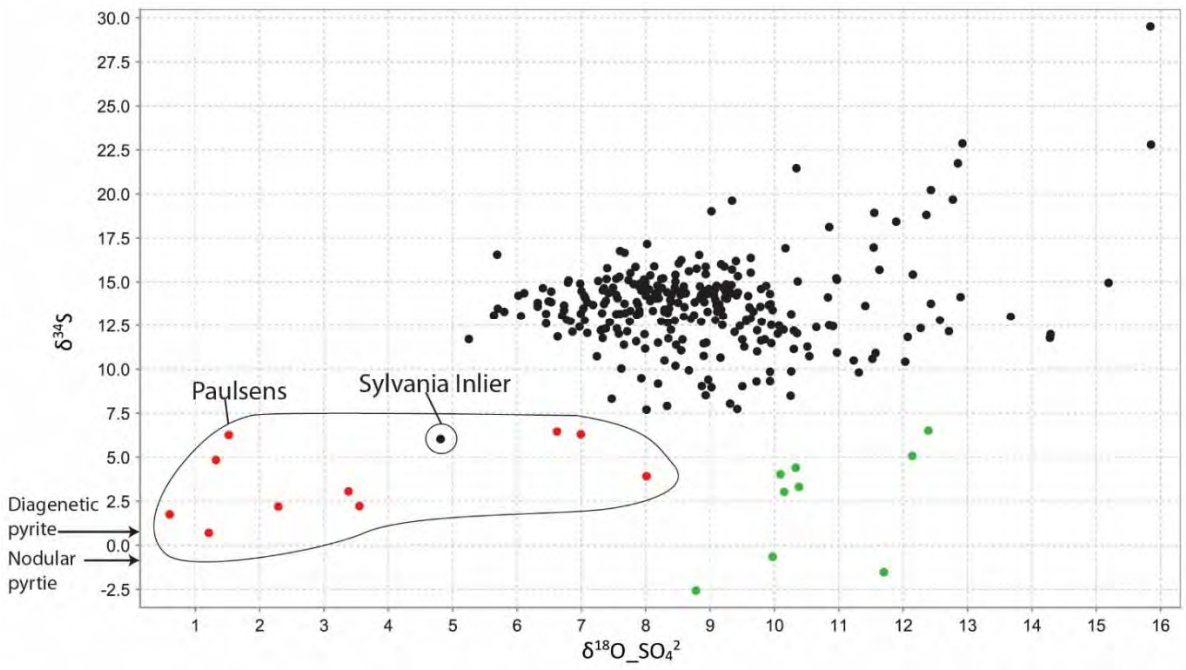

Figure 1.71. Cross plot showing $\delta^{34}S$ vs. $\delta^{18}O\_SO_4^2$, Paulsens samples are shown (red) and mean $\delta^{34}S$ of two pyrite generations from the deposit are indicated. Green = light $\delta^{34}S$.

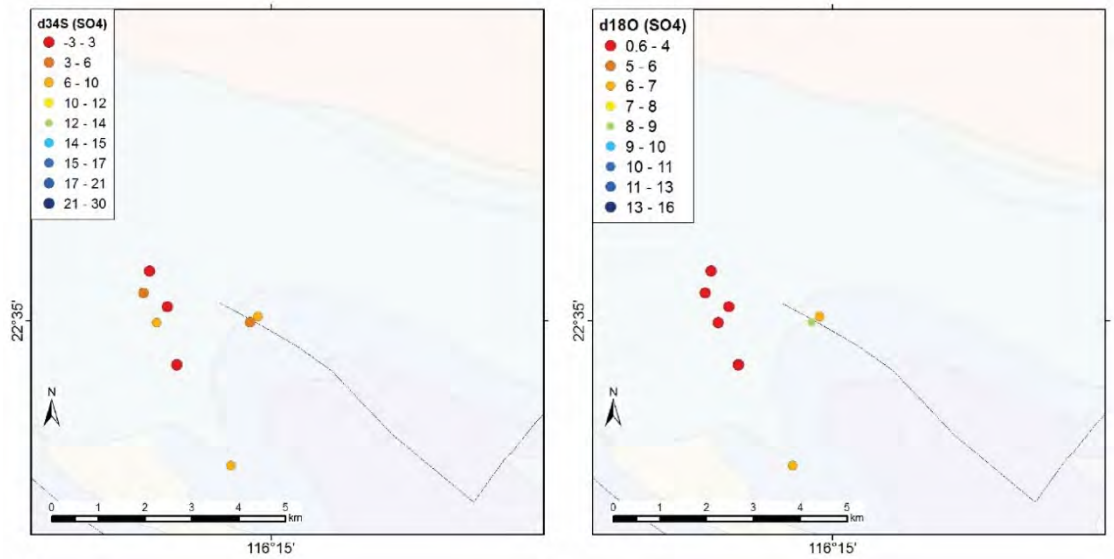

Figure 1.72.Distribution of $\delta^{34}S$ and $\delta^{18}O\_SO_4^2$ around the Paulsens gold deposit.

- **Sr isotopes**

The $^{87}Sr/^{86}Sr$ composition of groundwater originally reflects the composition of percolating rainwater which has a sea spray and dust Sr component. Subsequently this isotopic signature can be modified by interactions with soil and rocks. As there is no measurable fractionation of Sr isotopes during mineral precipitation and dissolution, the Sr isotope composition of groundwater can be used to distinguish between sources of Sr (McNutt, 2000). The Capricorn groundwaters span an extreme range of $^{87}Sr/^{86}Sr$ ratios (nearly 0.070) and even water from the sedimentary basins can, unusually, possess a Sr isotope value of up 0.740 (Harrington and Herczeg, 2003). The groundwater Sr isotope values are significantly higher than the $^{87}Sr/^{86}Sr$ composition

of either seawater during or since the Proterozoic (0.702–0.709; Veizer, 1989) or rainwater. This implies that the higher $^{87}Sr/^{86}Sr$ ratios within the Capricorn groundwaters cannot be explained without an input of radiogenic Sr through water-rock interactions with silicates. This conclusion is further emphasised by the high degree of correlation between geological terrains and variations in $^{87}Sr/^{86}Sr$ ratios (Figure 1.73). The Sr isotope results show that there has been a high degree of interaction between groundwaters and minerals in the basement rocks and this process must have occurred over a relatively long duration due to the relatively resistant nature of the silicate minerals.

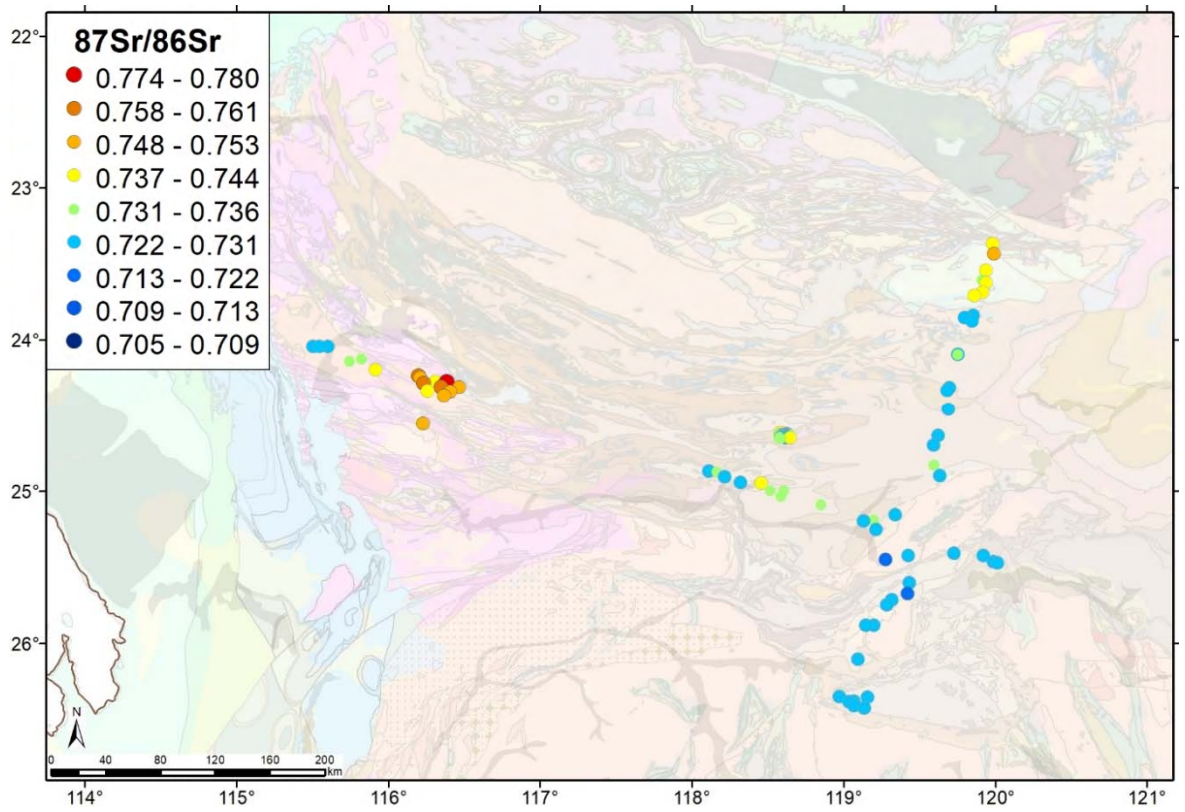

Figure 1.73. Distribution of $^{87}Sr/^{86}Sr$ ratios in groundwater along two transect in the Capricorn Orogen.

1.7 Sampling 'through' cover

Hydrogeochemical analysis of groundwater is presented as a method of 'seeing through' cover sequences in order to gain an understanding of the underlying geology and potential mineralisation (Gray et al. 2016a). Here we present case studies designed to further highlight the potential for hydrogeochemical sampling to provide geochemical data from depth that is otherwise unobtainable from surface sampling.

1.7.1 Bryah Basin

The Proterozoic Bryah Basin in the south of the Capricorn Orogen is comprised of metavolcanics and sediments and lies within the deeply weathered regolith geomorphic province (Figure 1.2). The metabasites of the Narracoota Formation occupy the southern half of the basin (Pirajno and Occhipinti 1998) and extend for 180 km, east to west, across the basin (Figure 1.74). On the basis of field observations, texture, geochemistry, and petrology, Pirajno et al. (2000) subdivided the rocks of the Narracoota formation into metamorphosed peridotitic and high-Mg metabasalt, basaltic hyaloclastite, pyroclastic rocks, intrusive rocks, and mafic and ultramafic schist. Collectively, these subdivisions were referred to as metabasites.

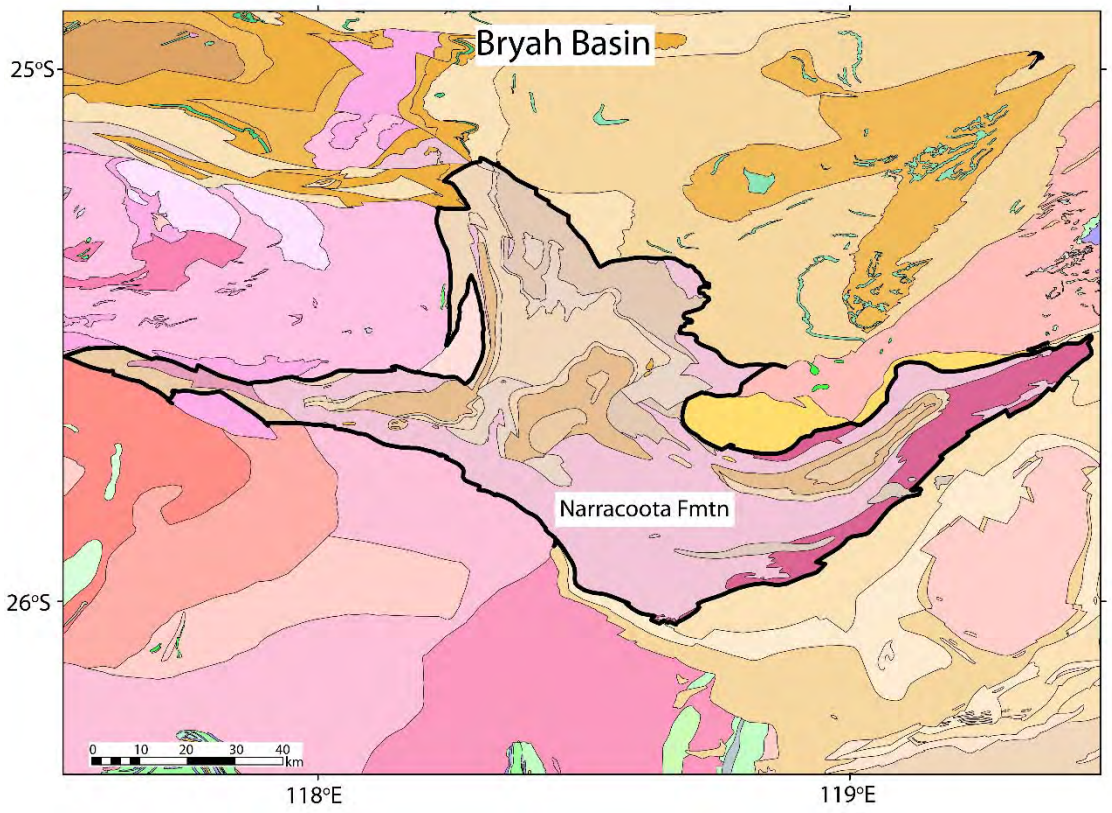

Figure 1.74. Bryah Basin geology, highlighting the Narracoota Formation outcrops.

Geochemical analysis of the Narracoota Formation (Pirajno and Occhipinti, 1998) shows elevated concentration of Cr, up to an average of 2300 ppm, within ultramafic schists. Chromium is generally residually concentrated during the weathering process due to its relative immobility and the stability of chromites in the weathering environment (Anand and Paine 2002). However weathering of the chromites will occur and dissolved Cr is found in high concentrations in the surrounding groundwater. The dissolved Cr in Yilgarn groundwaters is likely naturally occurring hexavalent Cr^{6+}, (Gray, 2003) and due to its similar salinities and pH it is most likely that the groundwaters of the Bryah Basin are the same.

The Geological Society of Western Australia regolith geochemistry database for the Capricorn region was re-plotted and re-processed (Figure 1.75). This database possesses ~10000 samples from surface material across the region and Cr concentrations in the Bryah basin are presented in Figure 1.76. The highest concentrations of Cr (2431-9600 ppm) in regolith material in Capricorn are found within the Bryah Basin and are related to the weathering of the Narracoota mafics.

Groundwaters sampled from within the Bryah Basin are all relatively fresh (average TDS of 985) and are neutral to slightly alkaline with a pH between 7.3 and 8.7. The water table in the region varies from between 20.3 and 3 m.

Chromium concentrations in groundwater are shown to be high within the bores in the southern Bryah Basin with values consistently above 24 µg/L (Figure 1.77, Figure 1.78). These elevated concentrations reflect the outcrop of the Narracoota mafics. However, a comparison between the geochemical expression of the Narracoota Formation in regolith and groundwater shows that these media display different patterns in Cr concentration across the basin. In the regolith data, the highest Cr concentrations are restricted to the central portions of the basin whilst the hydrogeochemistry data shows elevated Cr through the entirety of the southern portion of the basin.

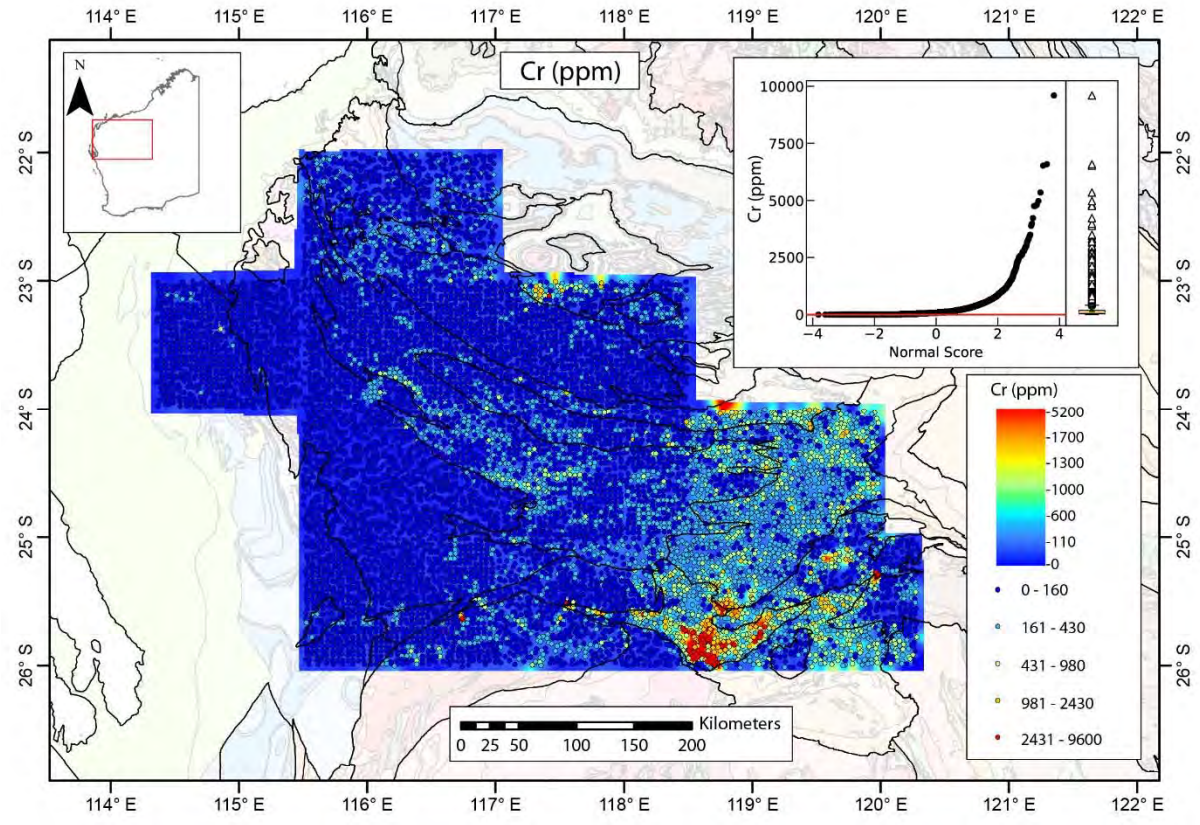

Figure 1.75. Chromium concentrations within GSWA regolith samples. Map data extracted from the Geological Survey of Western Australia *regolith geochemistry* dataset (GSWA 2018b).

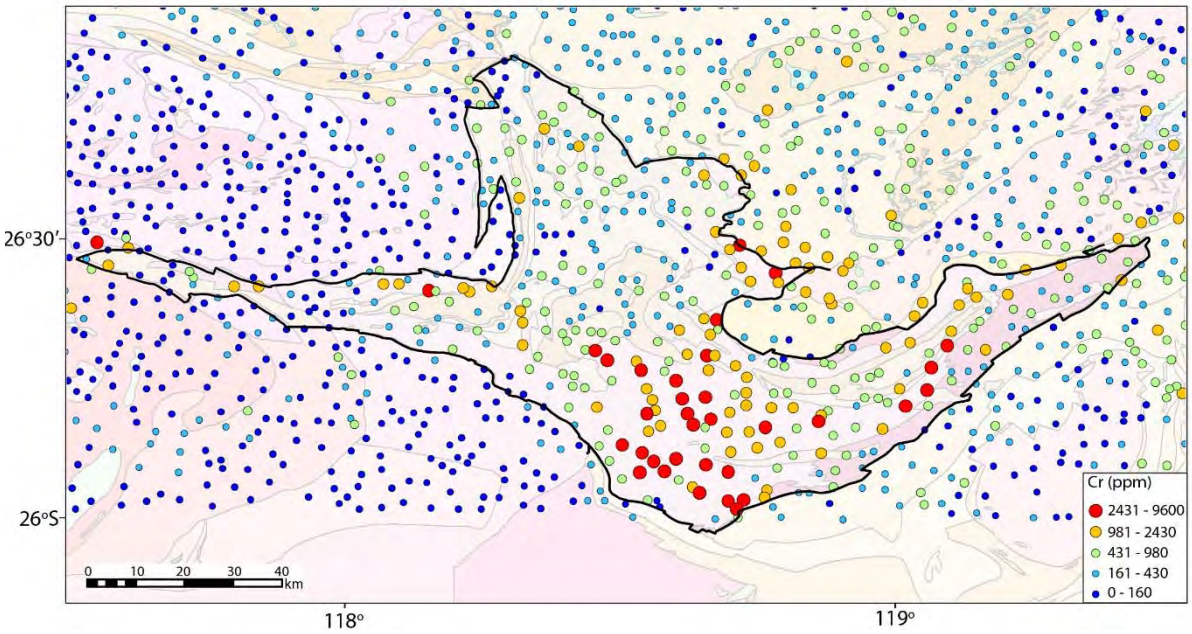

Figure 1.76. Chrmoium concentrations in GSWA regolith samples in the Byah Basin. Map data extracted from the Geological Survey of Western Australia *regolith geochemistry* dataset (GSWA 2018b).

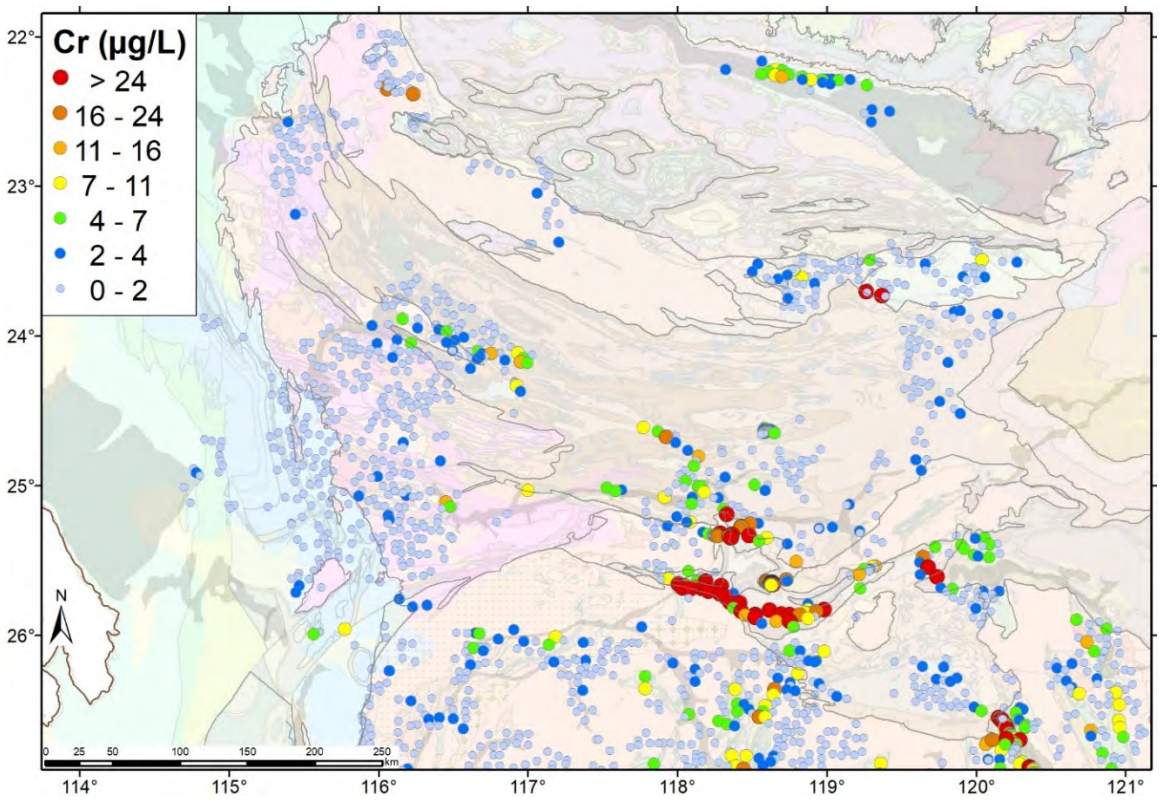

Figure 1.77. Dissolved Cr disribution for the Capricron Orogen.

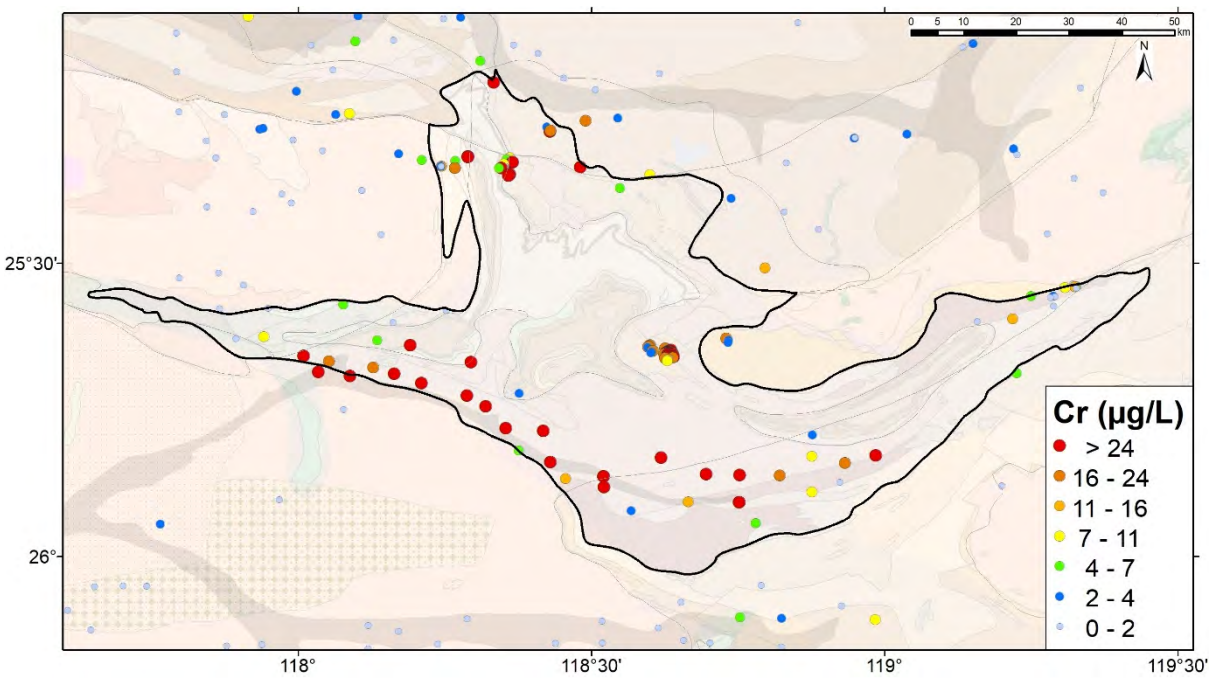

Figure 1.78. Dissolved Cr concentrations in groundwaters of the Bryah Basin.

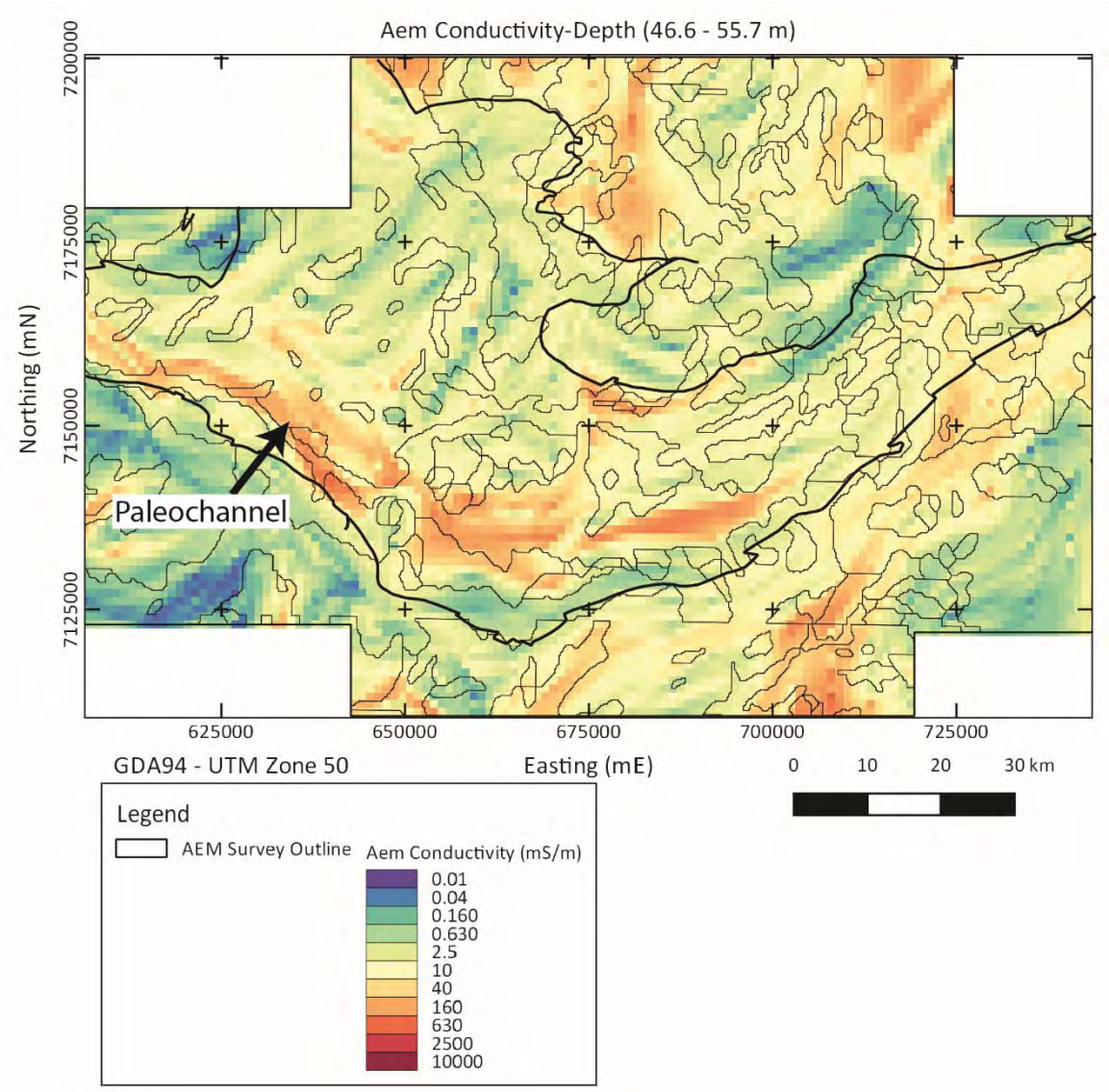

Figure 1.79. Gridded conductiverty depth interval (46.6-55.7 m) from inverted AEM data.

The airborne electromagnetic (AEM) data from the Bryah Basin presents a geo-electric cover map (Figure 1.79) that, with the addition of geological and regolith data, can be interpreted as transported and in-situ weathering cover depth across the basin. The AEM indicates the presence of transported cover in the form of a paleo-drainage channel running from east to west on the southern margin of the Bryah Basin. Modern day drainage follows a similar route. The change in the geochemical expression of the Cr rich Narracoota formation within surface media is interpreted to be due to increasing extent and depth of transported cover from the central to western portions of the Bryah Basin. Groundwaters in the region are able to 'see' through cover due to the volume of water – rock interaction increasing the depth to which geochemical signatures of the underlying rocks are represented in the groundwater compared to surface regolith samples. It has been shown (Anand and Paine 2002) that geochemical signatures from underlying lithologies and mineralisation can be observed at surface in transported cover where the water table is or has been close to surface, providing a pathway for element migration through cover (Anand and Paine 2002). In the Bryah Basin the water table in the west is not sufficiently shallow to allow for the migration of Cr through transported cover to the surface. The combination of a relatively deep water table compared to cover thickness and increased transported cover extent results in negligible Cr concentrations in regolith in the eastern Bryah Basin compared to the central regions. Whereas the groundwater is in direct contact with the Cr bearing mafic rocks allowing for this signature to be detected from the surface.

The Bryah basin case study indicates how groundwater sampling compared to surface sampling can provide an enhanced understanding of geochemical signatures undercover.

1.7.2 Abra deposit

The giant 200 Mt Abra Polymetallic (Fe-Pb-Zn-Ba-Cu ± Au-Ag-Bi-W) deposit is located within the Quartzite Well Fault system in the Mesoproterozoic Edmund Basin (Figure 1.3). Mineralisation is hosted at a disconformity between the Irregully and Kiangi Creek Formations, with stratiform mineralisation rooted by a breccia pipe feeder zone situated beneath ~200 m of silicified siliciclastic lithologies.

Spinks et al. (2017) used ferromanganese crusts as an exploration medium in the region around Abra. The crusts are formed from Fe oxides and Mn (oxyhydr) oxides at surface and adsorb pathfinder elements. Spinks et al. (2017) specifically targeted Zn mineralisation and determined that unlike other deposits (e.g the Prarie Downs, Zn-Pb-Ag deposit), Abra was not geochemically expressed at surface. Soil sampling from two profiles over the deposit subjected to multiple leaches and normalised to Mn similarly do not show any recognisable signature from mineralisation and instead seem to mirror variations in regolith (Thorne et al. 2018b).

Twenty two groundwater samples were taken from drill holes across the Abra deposit region. Waters are fresh (average TDS is 303), and neutral with a pH that ranges from 6.4 to 8.1. The water table is on average 26 m from the surface and reaches a maximum depth of 56 m and a minimum of 14.5 m.

The Pb concentrations from groundwater reach a maximum of 13.1 µg/L from over the Abra deposit, with the majority of higher values between 1 and 6 µg/L, for comparison the greatest Pb concentrations from the regional groundwater samples is a single point at 21 µg/L (Figure 1.80, Figure 1.81), and the median value for the Capricorn as a whole is 0.11 µg/L. The greatest concentration of Pb (82.1 µg/L) sampled from the region is from drill holes intersecting the near surface Prairie Downs Zn-Pb-Ag deposit.

Tungsten concentrations within the groundwater over the Abra deposit reach a maximum of 83 µg/L, the median value for the regional data is 0.1 µg/L (Figure 1.82, Figure 1.83). Tungsten concentrations appear to present a more constrained anomaly, although they are offset from the deposit, whilst Pb concentrations are elevated over a distance of 8 km.

The Abra deposit is a polymetallic deposit and as such, it would be expected, that elements other than Pb and W may be found in elevated concentrations in groundwaters. Zinc especially is known to be highly mobile in the weathering environment (Anand and Paine 2002) and as such may be expected in groundwaters. Zinc has been found in elevated concentrations associated with some deposits e.g. Jaguar/Bentley VHMS Zn-Pb-Cu, but equally can also be absent in areas with known zinc mineralisation (Gray et al. 2018). Zinc has a high compatibility with Fe oxides and Mn (oxyhydr) oxides and therefore when liberated by weathering from primary mineralisation is adsorbed onto secondary Mn and Fe minerals and is therefore may not be found in elevated concentrations around the Abra deposit.

Figure 1.66 shows samples with anomalous O and H isotope values. One of the sample points from Abra possesses an anomalous value indicating that this water sample may have a fluid contribution from a source other than meteoric waters. This could indicate movement of fluid from depth along faults and fractures.

This case study suggests that buried Pb deposits within sedimentary basin systems may be detectable through groundwater sampling even in regions where there is no surface geochemical expression. Given the broad halo and degree to which Pb and W concentrations are elevated, targets similar to Abra could be observed during regional (4 km spacing) sampling campaigns.

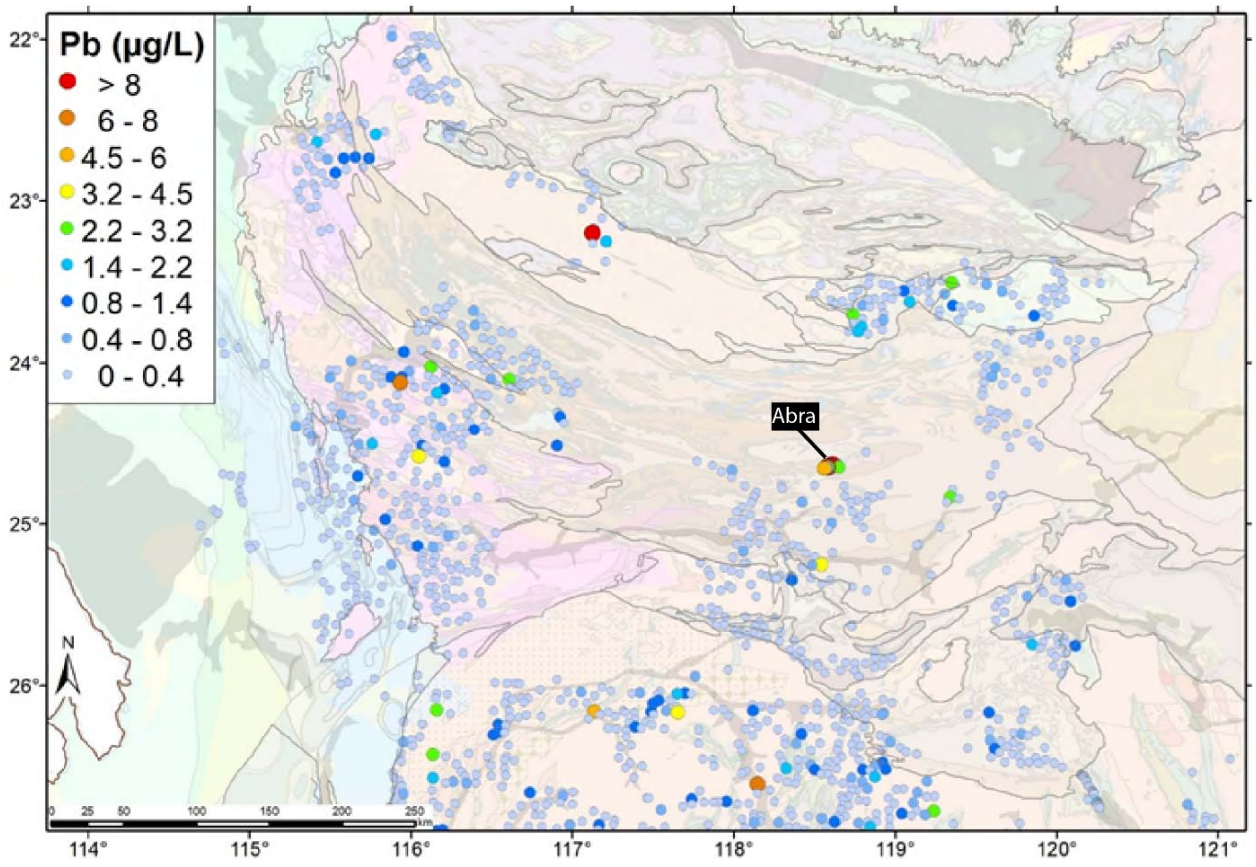

Figure 1.80. Dissolved Pb distribution in groundwaters of the Capricorn Orogen.

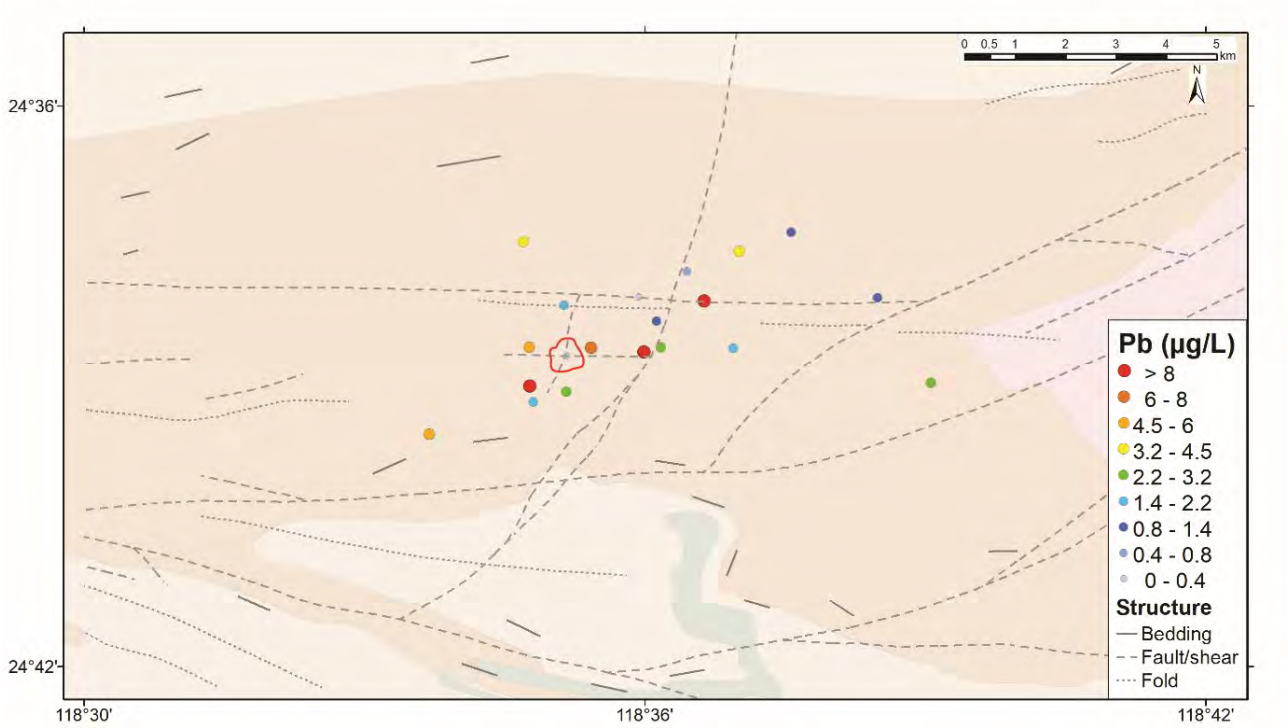

Figure 1.81. Dissolved Pb in groundwaters above the Abra deposit. Red line indicates the high grade ore zone projected to surface.

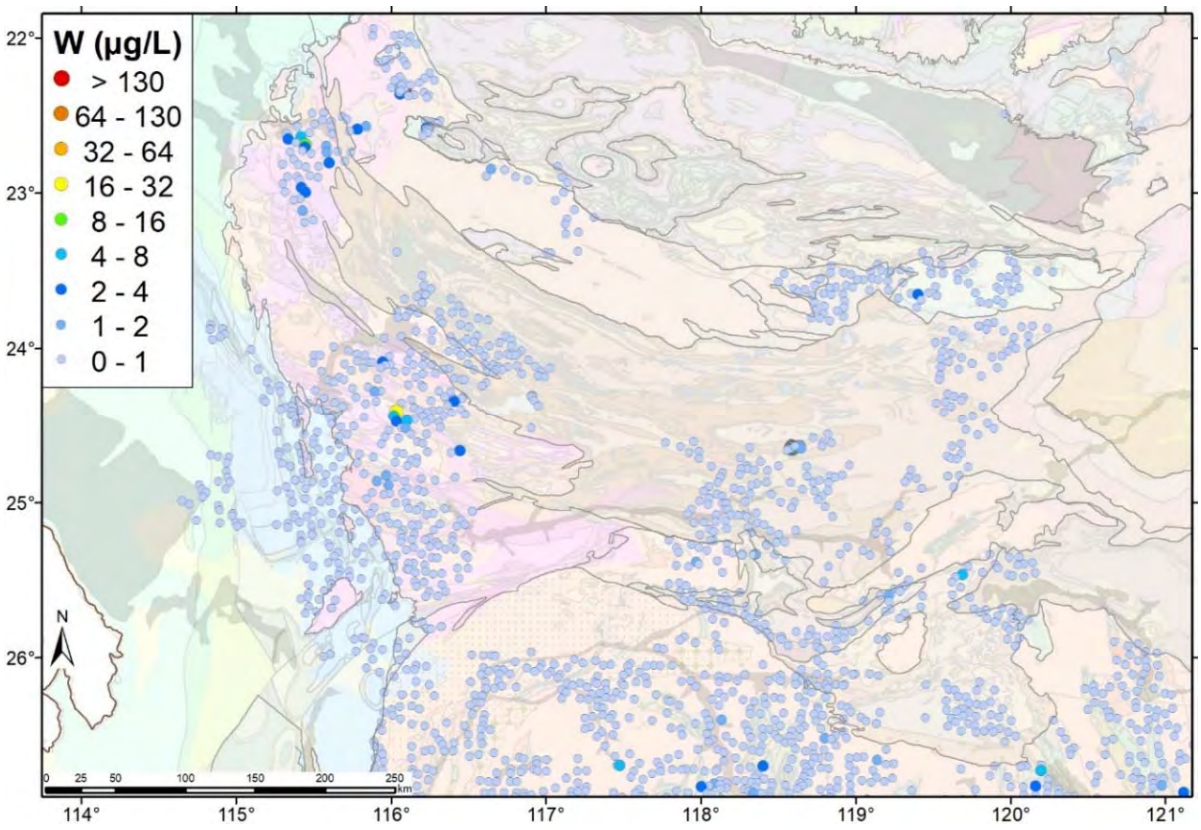

Figure 1.82. Dissolved W distribution in groundwaters of the Capricorn Orogen.

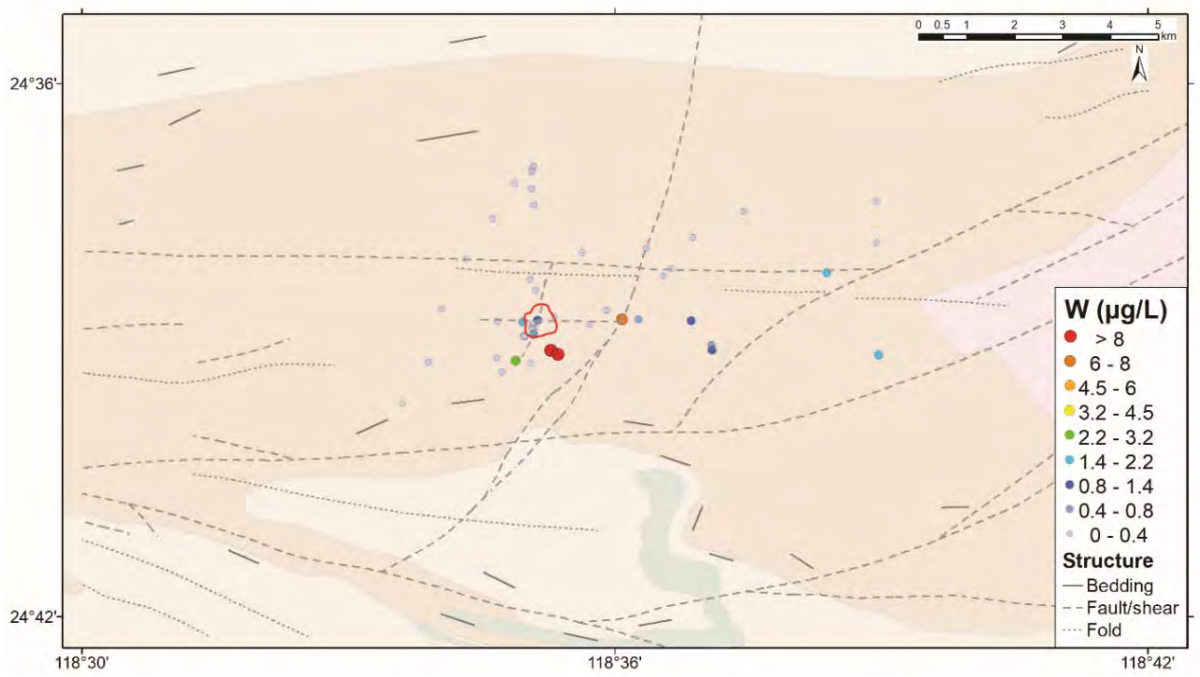

Figure 1.83. Dissolved W in groundwaters above the Abra deposit. Red line indicates the high grade ore zone projected to surface.

1.8 Case studies

1.8.1 DeGrussa

The DeGrussa deposit is located c. 150 km NNW of Meekatharra, (Figure 1.3) in the Capricorn Orogen. DeGrussa is located in the Proterozoic Bryah Basin that lies adjacent to the Archaean Yilgarn Craton to the south and the Archaean granite Marymia Inlier to the north. The dominant underlying lithology is Proterozoic age (c. 2 Ga) sedimentary and volcanic rocks constituting basalts, turbidites of the DeGrussa Formation and argillaceous, sandstone and conglomerate units of the Karalundi Formation (González-Álvarez et al. 2015; Hawke et al. 2015). The DeGrussa deposit is situated on the western flank of a minor plutonic Archaean outlier that protrudes through the basin cover. Locally, the Shiraz Fault is the dominant structure related to mineralisation and strikes in an east–west direction, with the DeGrussa ore zone nearly vertical on the northern side of the fault. In 2009, Sandfire Resources discovered the high grade VHMS Cu-Au mineralisation at DeGrussa by following up anomalous soil Au assays with shallow RAB drilling

As part of a study into surface geochemical signatures Noble et al. (2016) took ten groundwater samples in and immediately adjacent to mineralisation from PVC cased drill holes using a flow-through bailer. Fourteen additional samples were collected from background areas. The groundwater is neutral to alkaline, slightly reduced to slightly oxidised and relatively fresh. The pH range was 6.8 to 12.0, with a median of 7.55, while the Eh range was -154 mV to 375 mV with a median of 321 mV. The EC ranged from 125 to 4490 µS/cm with a median value of 762 µS/cm. Anomalous concentrations of Au, As, Cu, Ag and Mo were present in local groundwater near the DeGrussa site (Figure 1.84). The greatest dissolved Au concentration was just south of the mineralisation with all samples in the shallow supergene enriched Au zone being anomalous (>25 ng/L). The sample in the secondary enriched Cu zone, slightly to the west of the main sampling line, but still in the mineralised zone did not show elevated Au. Molybdenum had one sample with 170 µg/L directly in the mineralised zone. Copper in groundwater also presented an anomalous target. Most Cu concentrations were >4 ppb, with two samples in the mineralised zone with concentrations of 147 and 220 µg/L. Arsenic in groundwater is also an effective pathfinder (Noble et al. 2016).

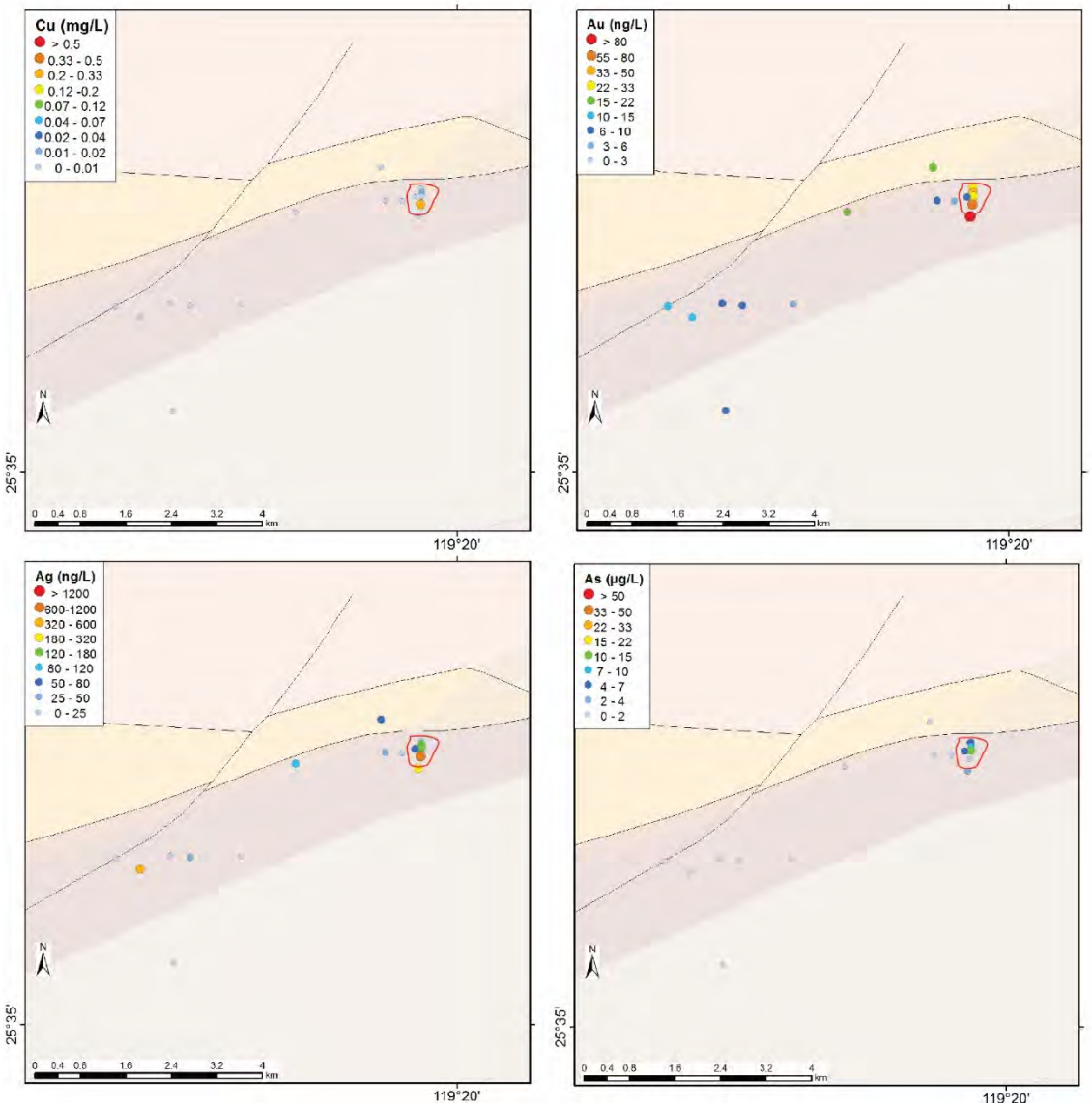

Figure 1.84. Distribution of Cu, Au, Ag and As in and around the DeGrussa deposit. Red outline marks the open pit.

1.8.2 Prairie Downs

The Prairie-Wolfe polymetallic Zn-Pb-Ag±Cu deposits and associated prospects are located within a hydrothermally altered fault breccia zone on the northern margin of the Capricorn Orogen between the Palaeoproterozoic Bresnahan Basin and Neoarchean Fortescue Group (Figure 1.3). Weathered sulfides are visible at surface, and the main mineralized zone is located 10s of metres below the current surface exposure. Soil and vegetation sampling in the region contain pronounced geochemical anomalies close to the deposits.

Groundwater from 11 samples along the Prairie Downs fault and surrounding area were collected. The pH range was 5.8 to 7.7, with a median of 7.28, while the Eh range was 36 mV to 375 mV with a median of 345 mV, and the EC ranged from 340 to 8000 µS/cm with a median value of 1690 µS/cm.

The deposit can be defined by anomalous concentrations of Pb, W, Ag, Sb and As and NO_3^- (Figure 1.85). Arsenic concentrations are relatively low compared to points within the regional dataset. Compared to background values in the surrounding region, concentrations of As are significant in the Prairie Downs samples. This is an important conclusion from this data set, as the geological variation is greater within the Capricorn Orogen than in previous studies, e.g. the Yilgarn Craton (Gray, 2016a), background values will vary more significantly across the study area.

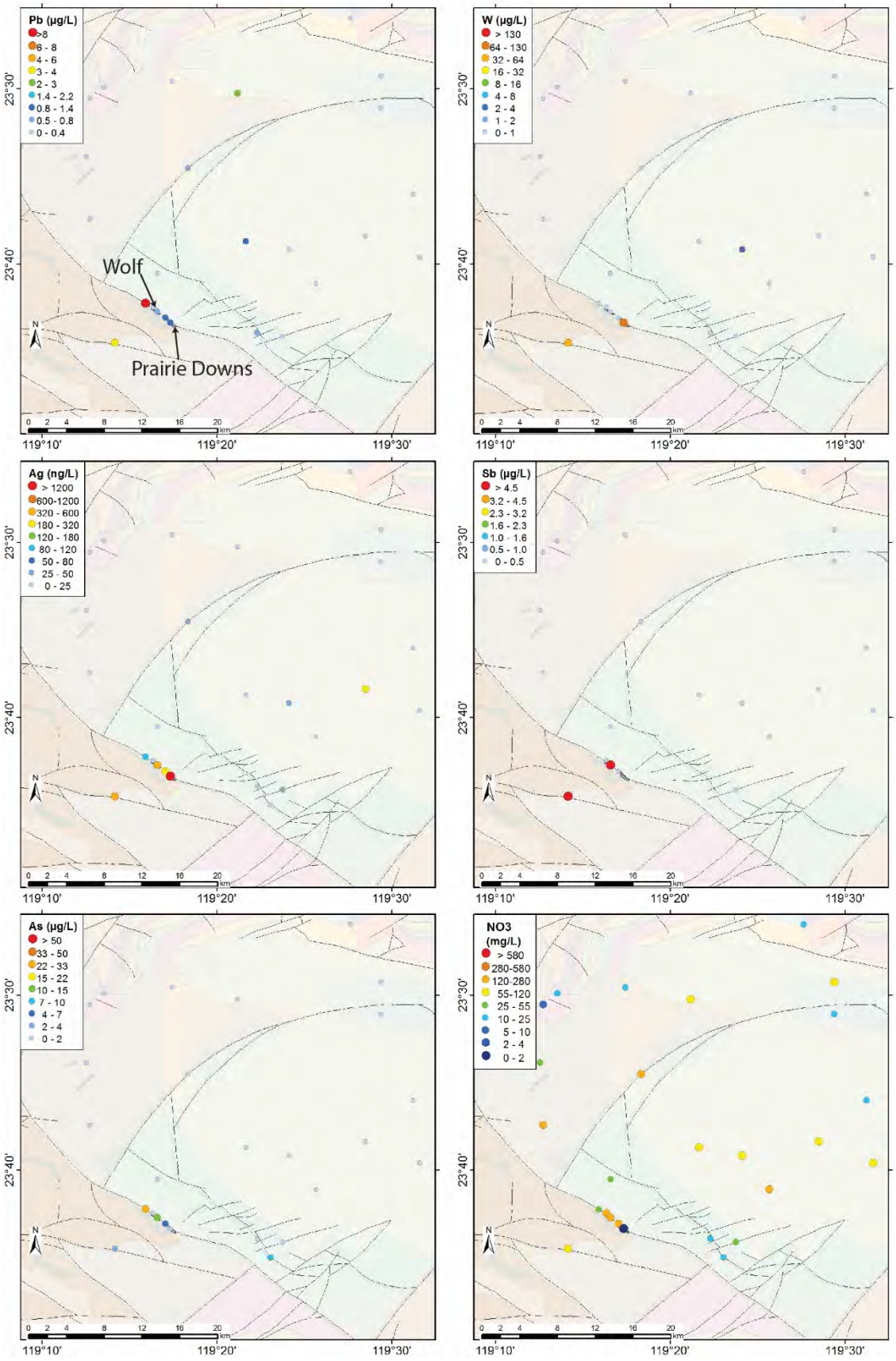

Figure 1.85. Distribution of Pb, W, Ag, Sb and As, and NO_3^- around the Prairie Downs Pb-Zn-Ag deposit.

1.9 Areas of Interest

Several new areas of interest for mineral exploration are suggested based on the results of this study, these are shown in Figure 1.86 and listed below.

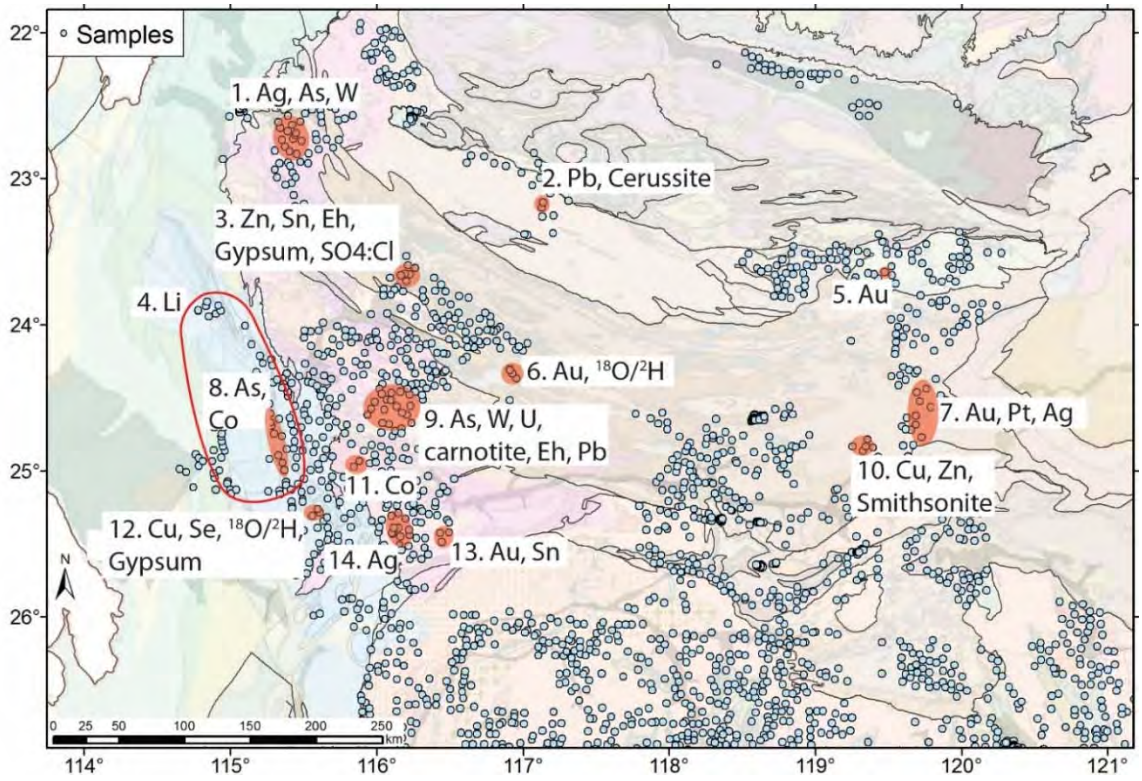

Figure 1.86. New areas of interest in the Capricron Orogen. Red shading highlights individual areas of interest, the red outline shows larger areas of interest that incoporate smaller shaded areas.

Area 1 (Figure 1.87) is a relatively broad area of As, W and Ag anomalism. Arsenic concentrations are the highest in the region (Figure 1.33). The AuMin1 and NiMin indices both suggest this area is prospective for Au and potentially other mineralisation.

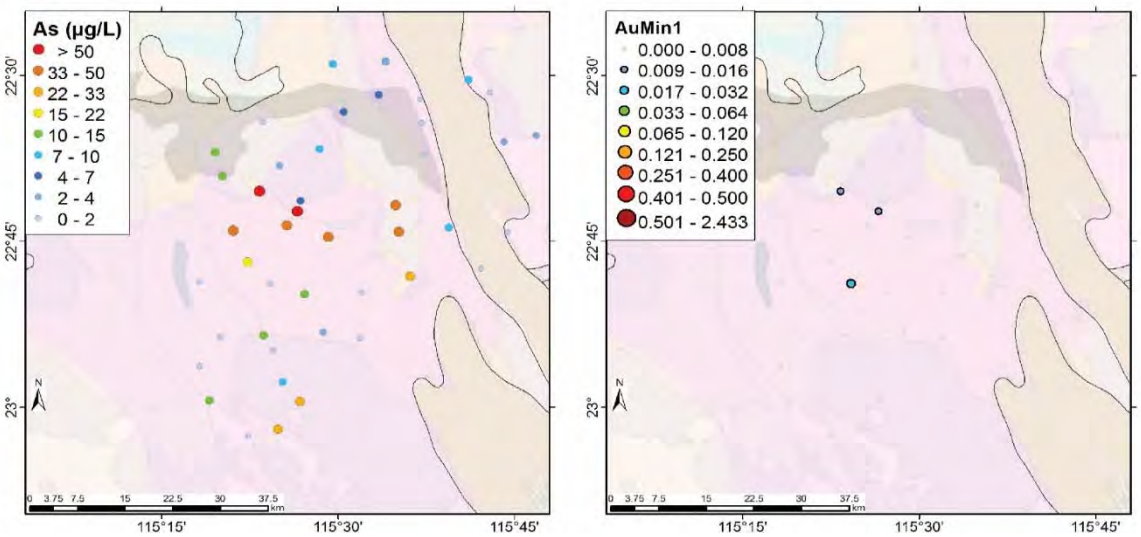

Figure 1.87. Area 1 (Figure 1.86), a broad area of As, W and Ag anomalism.

Area 2 (Figure 1.86, Figure 1.88) is a single point Pb anomaly with waters saturated with respect to cerussite ($PbCO_3$). Although this is only a single sample, a Pb concentration of 21 µg/L is the highest from regional sample and is substantially higher than Pb concentrations (max 13 µg/L) from waters around the Abra Pb deposit.

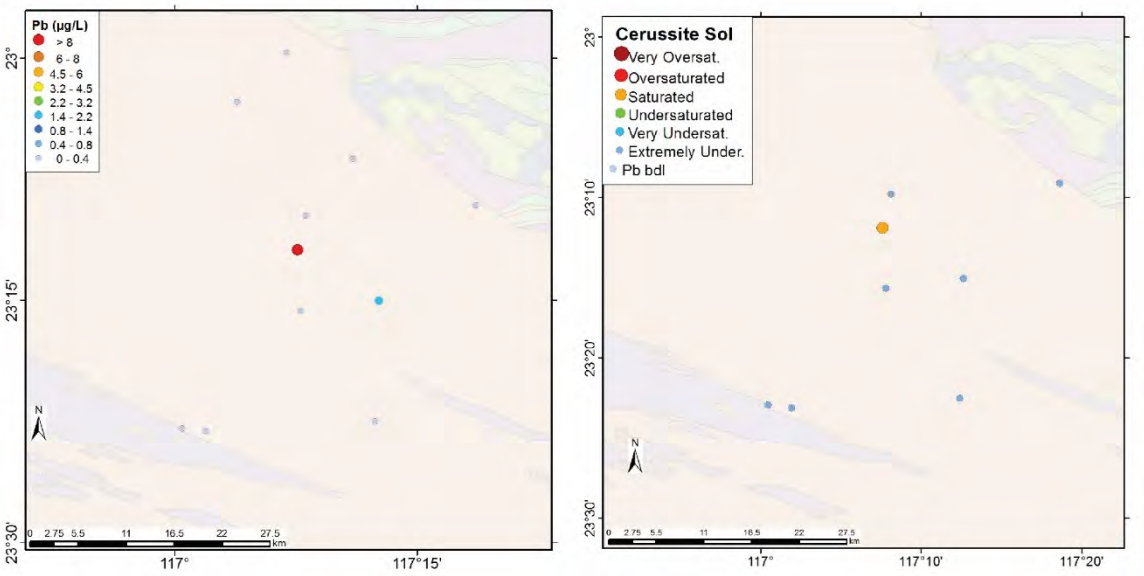

Figure 1.88. Area 2 (Figure 1.86), single point Pb anomaly.

Area 3 (Figure 1.86, Figure 1.89) is a broader area with a number of anomalous values, high SO_4:Cl ratios coincide with waters saturated in gypsum, suggestive of gypsum in the sediments or sulfide weathering. Combined with samples possessing elevated concentrations of Sn, Zn and low Eh values makes this region prospective for base metals.

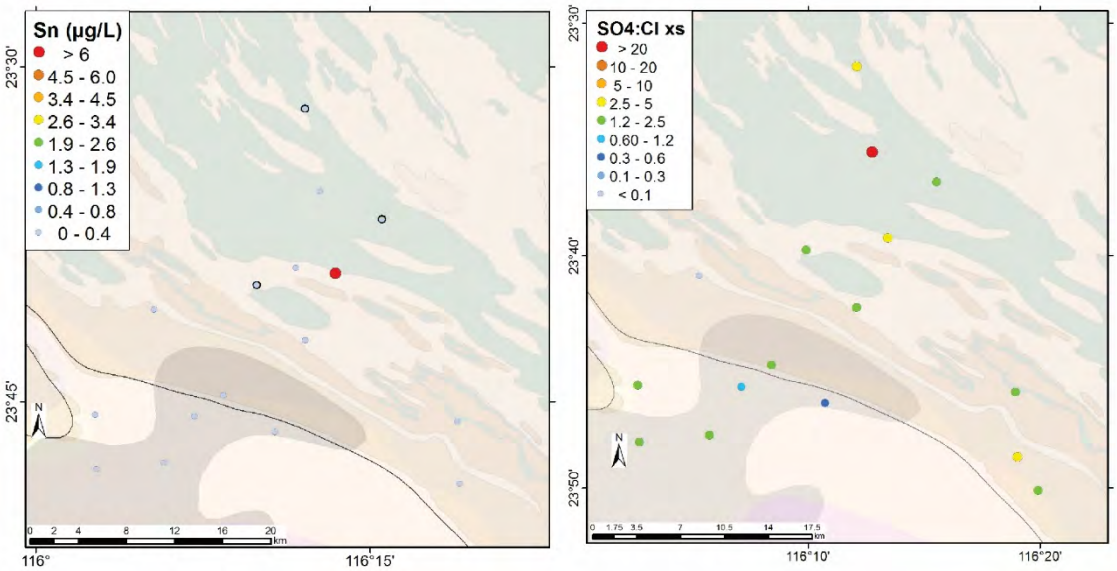

Figure 1.89. Area 3 (Figure 1.86), a broader area with a number of anomalous values including elevated concentrations of Sn and high SO_4:Cl ratios.

Anomalous Li concentrations within samples from the Phanerozoic Southern Canarvon Basin sediments follow the contact with the Gascoyne province (Figure 1.90, Figure 1.86). Lithium concentrations are some of the highest in Western Australia, although the source for Li in these waters is unknown.

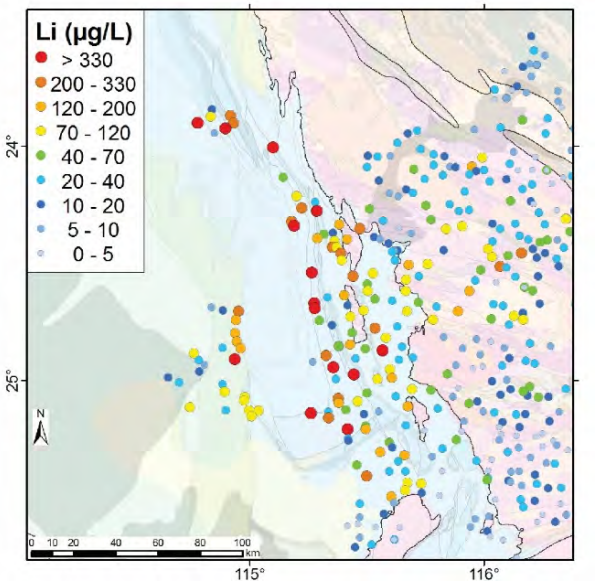

Figure 1.90. Area 4 (Figure 1.86). Anomalous Li concentrations.

Area 5 (Figure 1.86, Figure 1.91) is a single point anomaly located within the Sylvania inlier, with a gold concentration of 198 µ/L it is the highest gold value not associated with known mineralisation.

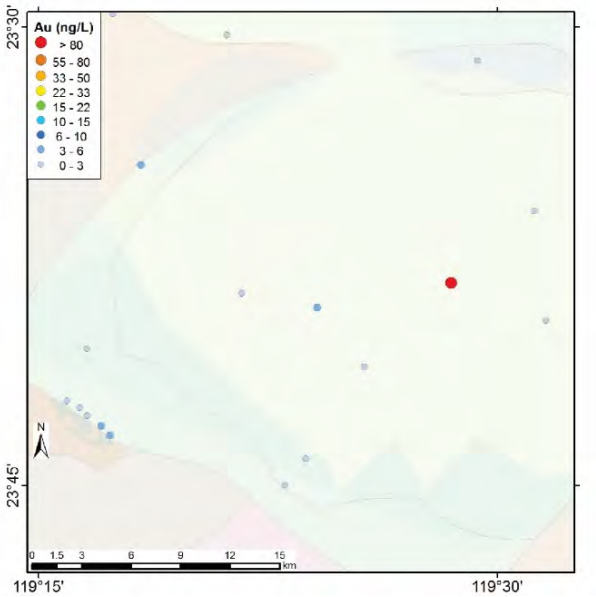

Figure 1.91. Area 5 (Figure 1.86), a single point Au anomaly located within the Sylvania inlier.

Area 6 (Figure 1.86) possesses a moderate single point gold anomaly combined with an anomalous δ^2H and $\delta^{18}O$ signature (Figure 1.92) suggestive of a different fluid source in this area.

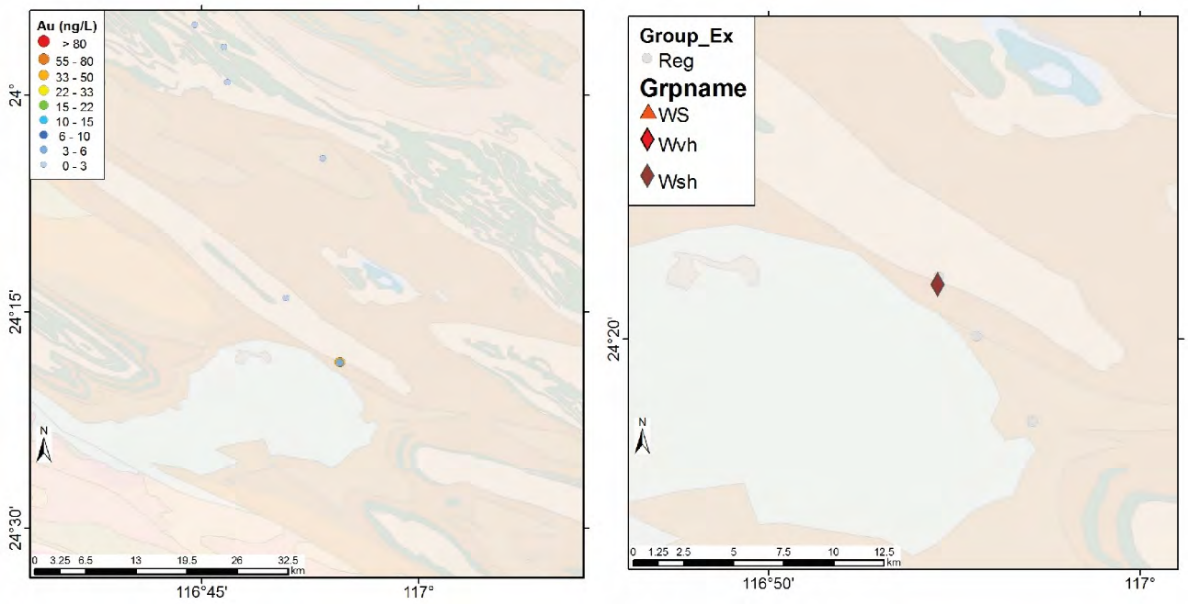

Figure 1.92. Area 6 (Figure 1.86), a single point gold anomaly combined with an anomalous δ^2H and $\delta^{18}O$ signature.

Area 7 (Figure 1.86, Figure 1.93) presents a broad region with moderately elevated concentrations of Au, Pt, Ag spread out in samples across the area. The lack of a clear grouping of samples with anomalous values suggests this region requires more investigation to generate specific targets.

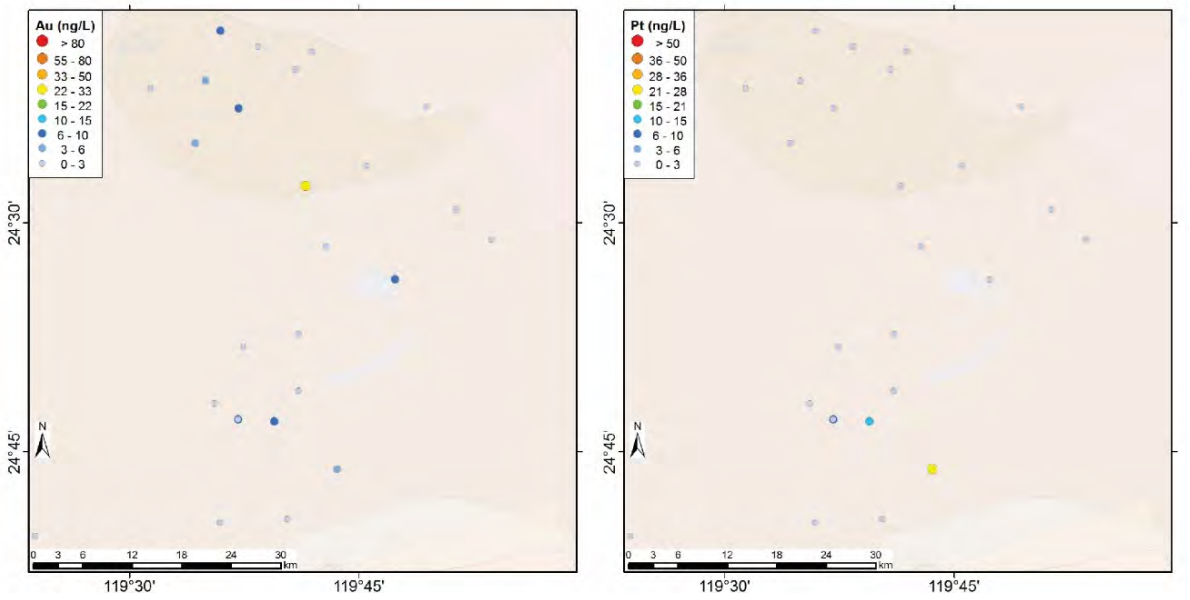

Figure 1.93. Area 7 (Figure 1.86), a broad region with moderately elevated concentrations of Au, Pt, Ag.

Area 8 (Figure 1.86, Figure 1.94) in the margin of the Southern Carnarvon basin possesses elevated As, Co and Mo High SEND1 index values are representative of high SO_4^2 and low NO_3 and therefore potentially sulfate weathering.

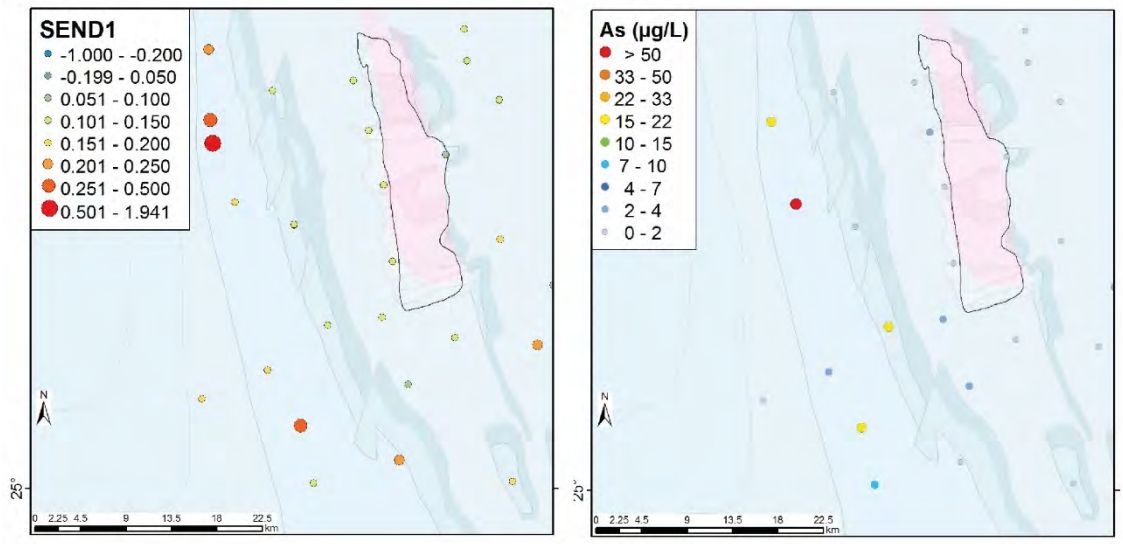

Figure 1.94. Area 8 (Figure 1.86), High SEND1 index values and elevated As.

The groundwaters in the north of area 9 (Figure 1.86) have elevated W (Figure 1.95) and moderate As values as well as possessing a low Eh, suggesting a relatively weak target for gold mineralisation. The region as a whole is prospective for U, with U values or more than 260 µg/L in four samples (Figure 1.95) and samples statured or oversaturated with respect to carnotite in samples spanning a 35 km region.

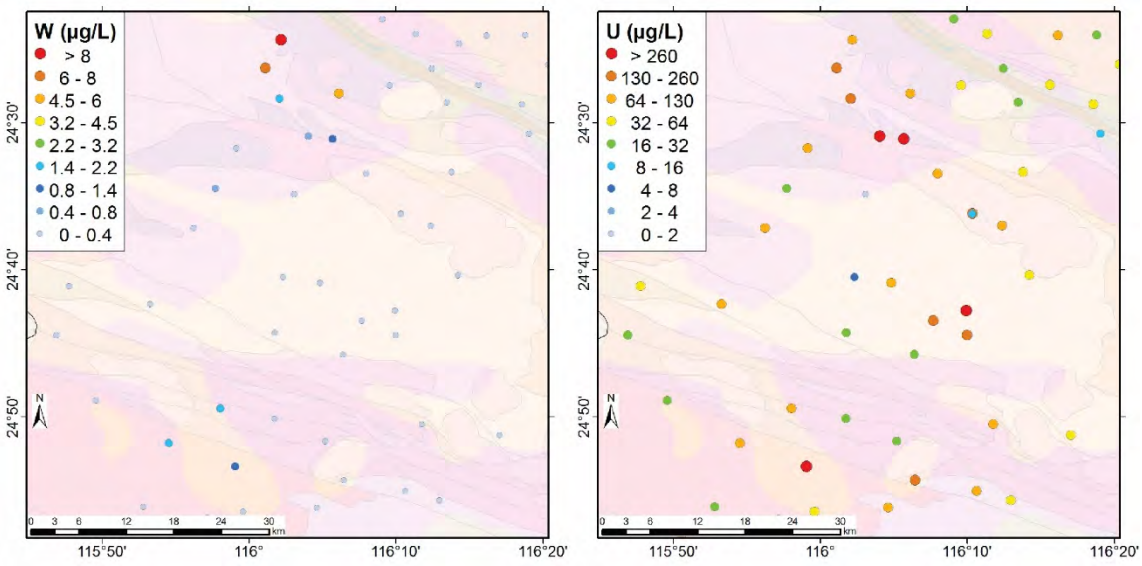

Figure 1.95. Area 9 (Figure 1.86), elevated W and U concentrations.

Anomalous values are generally moderate but are present within multiple elements including Cu, Zn (Figure 1.96), Pb and V. SO_4:Cl ratios are also relatively high. Due to the nature of the multi element anomalies this region is perspective for base metals.

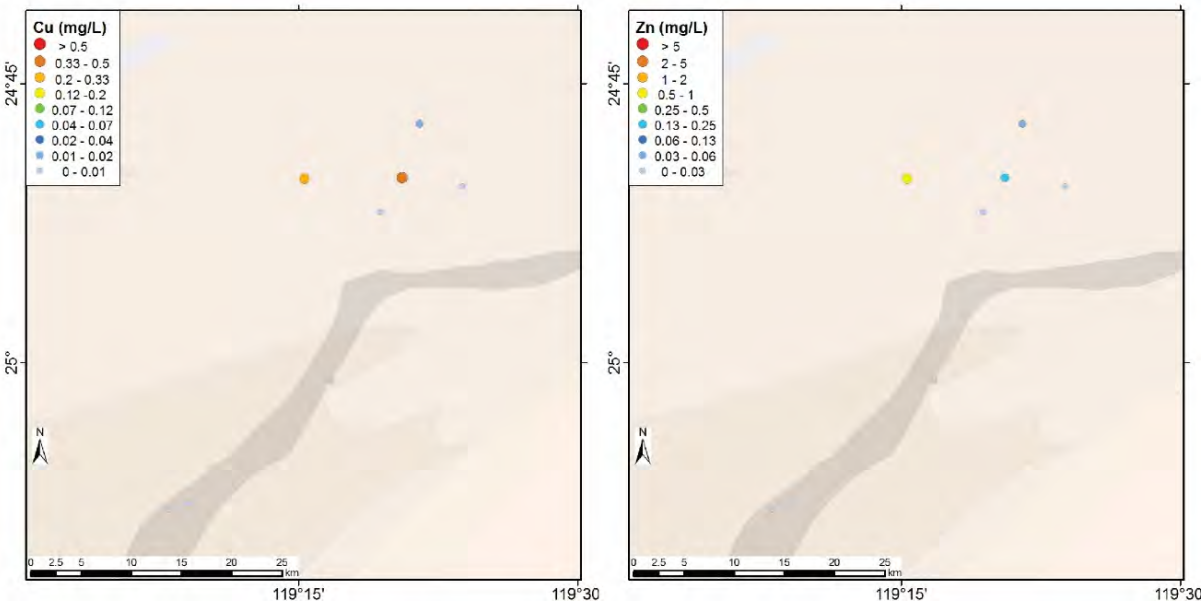

Figure 1.96. Area 10 (Figure 1.86), moderate values in multiple elements including Cu and Zn.

Area 11 (Figure 1.86, Figure 1.97) was identified by a single point Co, Se and minor Cu anomaly. The Co value of 104 µg/L is the fourth highest in the region with the highest three from waters related to mineralisation at Paulsens gold deposit. The Se value of 212 µg/L is the highest in the entire study, Se substitutes for S in sulfides. These results suggest that this regional sample is prospective for sulfide mineralisation.

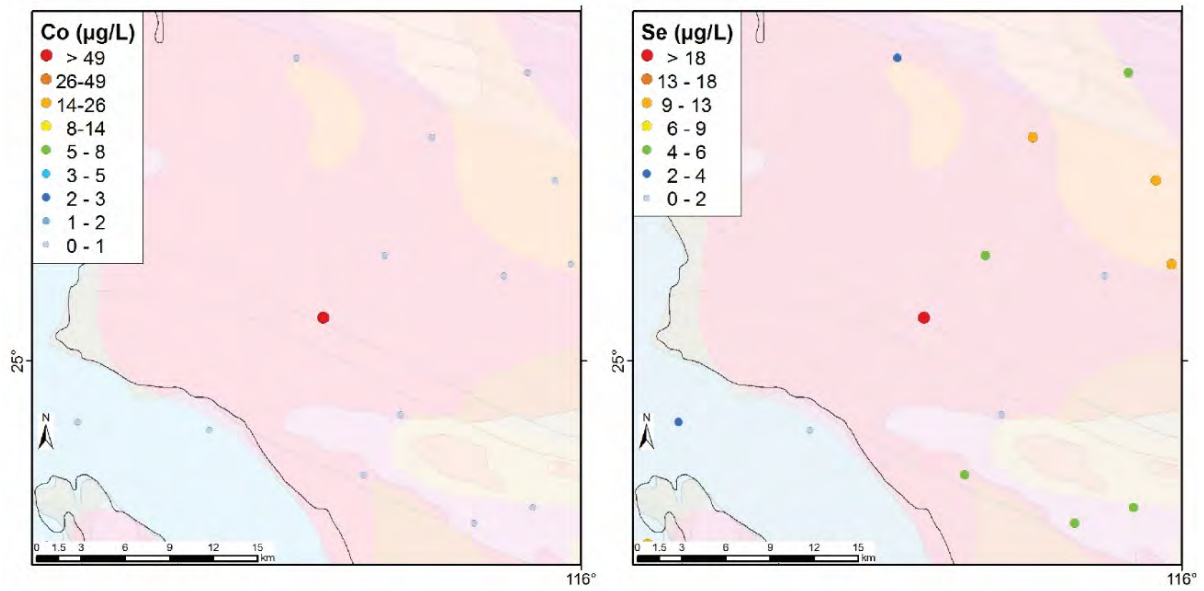

Figure 1.97. Area 11 (Figure 1.86), single point Co and Se anomaly.

Area 12 (Figure 1.86, Figure 1.98) was defined by a single point multi-anomaly sample. Elevated concentrations of Cu and Se, and moderate enrichments of As, Ag and Zn are combined with high SO_4:Cl ratios and modelled oversaturation with respect to gypsum. Anomalous δ^2H and $\delta^{18}O$ values are suggestive of the addition of a separate fluid source (other than meteoric water) into the system.

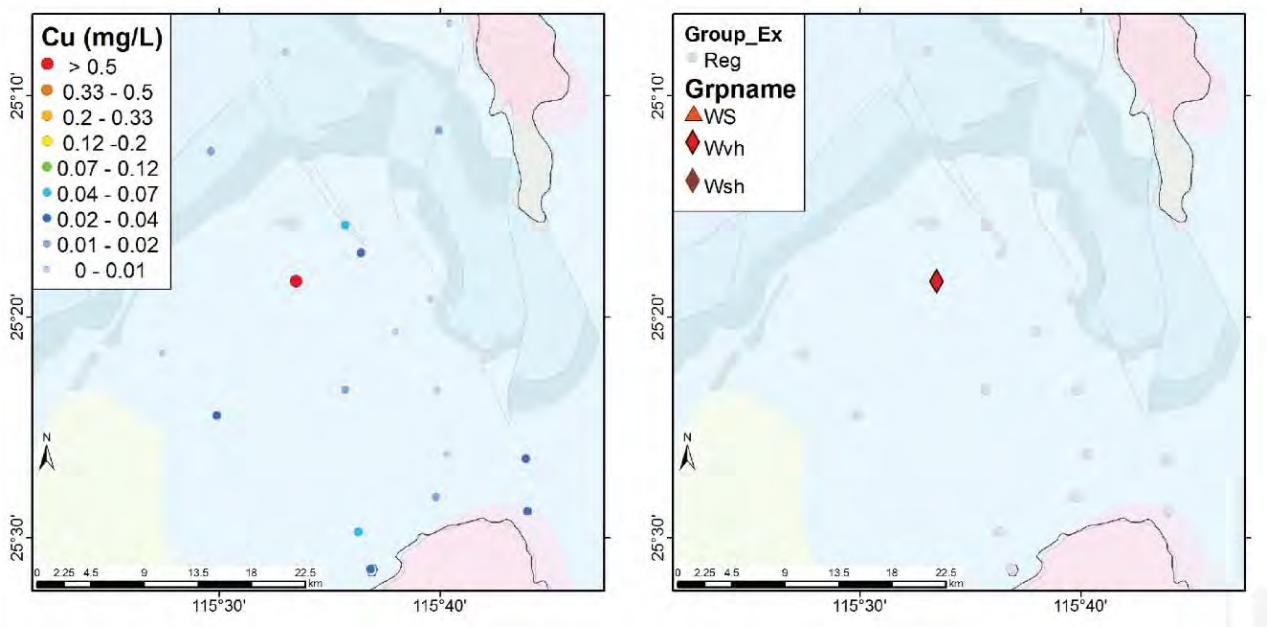

Figure 1.98. Area 12 (Figure 1.86), defined by a single point multi-anomaly sample including Cu and anomalous δ^2H and $\delta^{18}O$ values.

Elevated Au and Sn concentrations from two points in area 13 (Figure 1.86, Figure 1.99) make this region of some interest, but it is less prospective than other areas identified.

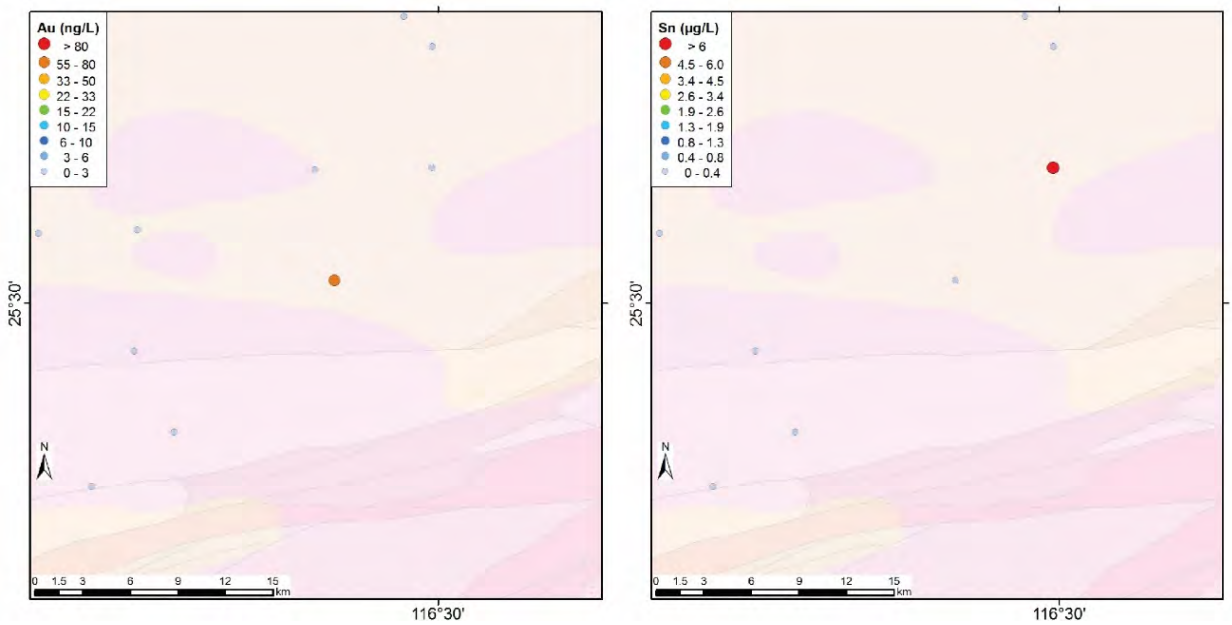

Figure 1.99. Area 13 (Figure 1.86), elevated Au and Sn concentrations.

Low to moderate concentrations in multiple elements including Ag (Figure 1.100), As, Cu and Pb and one high Mo value makes area 14 (Figure 1.86) relatively weakly prospective, much like Area 13.

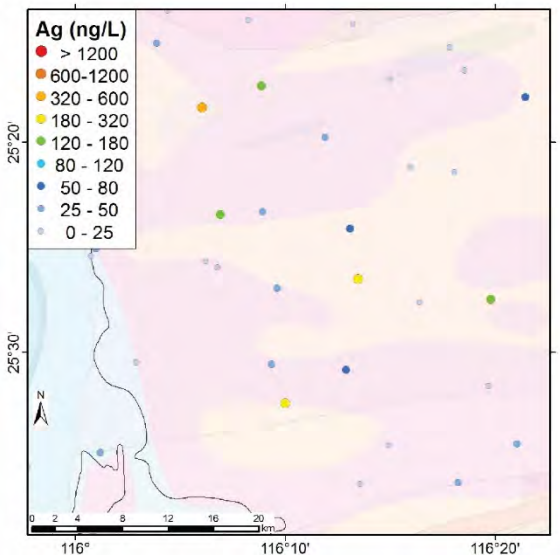

Figure 1.100. Area 14 (Figure 1.86), low to moderate concentrations in multiple elements including Ag.

By combining major geochemical parameters, element concentrations, multielement indices and isotope geochemistry in groundwaters from across the Capricorn Orogen 14 areas of interest for mineral exploration have been identified. These are variably prospective for base metals, Au and uranium.

1.10 Conclusions and Impacts

The Capricorn hydrogeochemistry study has built on the results of the north Yilgarn hydrogeochemistry mapping projects, resulting in a dataset that now covers a significant portion of WA. The Capricorn region groundwaters possess similar characteristics to those in the north Yilgarn but the geology is significantly different and therefore background values vary considerably across the region. However, anomalous samples are still within the ranges defined by earlier studies. Previously defined mapping and mineral exploration indices have been adapted for the Capricorn region and new indices have been created. The utility of various isotope systems in regional hydrogeochemical sampling campaigns have been explored and provide new insights into groundwater chemistry evolution and its association with mineral deposits:

- During the course of this project the hydrogeochemical sampling workflow was analysed and used as basis for designing a field sampling application with in-built integration with the International Geo Sample Number (IGSN). This android app assists with sample collection in remote areas and has been customised for soil, rock and vegetation sampling.
- Lithological indicators have proven successful in separating mafic from granitic and sedimentary rocks. The Sylvania inlier in particular was identified as possessing significantly different groundwater chemistry when compared to other regions within the Capricorn.
- This study has highlighted the greater variation in background values due to the relative complexity of the geology in the study area compared to previous studies (e.g. north Yilgarn). For examples As values that may not be considered anomalous in the dataset as a whole are seen as being indicative of mineralisation compared to local background values.

- The FeS index developed in the north Yilgarn did not prove to be very effective in the Capricorn, but the AcidS index has anomalism linked to most of the known deposits and provides new areas of interest.
- Gold concentrations and the AuMin index delineated known deposits and indicated new areas of potential prospectivity.
- There are several areas in the Capricorn that have U concentrations greater than those in close proximity to known deposits in the north Yilgarn. Spatially, the carnotite saturation index predicts most of the known prospects and provides new targets in the Capricorn.
- With the exception of NO_3 and some highly saline groundwater the majority of the groundwater used for human and livestock consumption is of reasonable quality and should not cause ill health from long term consumption. For livestock there are very few water samples that are not fit for use; however, those samples that show concentrations above the ADWG for As, Cr, F, NO_3, and TDS should not be used for long term human consumption without further testing and treatment.
- Oxygen and H isotopic ratios regionally follow a trend for isotopically light meteoric waters as rainfall moves away from the coast (continental effect). Superimposed on this trend are samples which possess an anomalously light isotopic composition which when combined with anomalous element chemistry provide further confidence in targeting areas of interest for exploration.
- Sulfur and O stable isotopes from sulfate in the Capricorn groundwaters have been able to discriminate sulfide weathering. Low $\delta^{34}S$ (<7.5 ‰) have been shown to be indicative of groundwaters surrounding the Paulsens Au deposit. The O isotopes provide a record of the groundwater composition at the time sulfide weathering occurred and have been shown to vary significantly from the meteoric and associated evaporation trend in some samples.
- Strontium isotopes ($^{87}Sr/^{86}Sr$) show clear evidence of an input of radiogenic Sr through water-rock interactions with silicates. This process must have occurred over a relatively long duration due to the relatively resistant nature of the silicate minerals.
- Case studies in the Bryah Basin and over the Abra deposit have further demonstrated how hydrogeochemistry can provide a way to sample 'through' cover, establishing a pathway for gaining chemical data from rocks and deposits that are not obtainable from surface soil sampling.

1.11 References

Alam, M.G.M., Allinson, G., Stagnitti, F., Tanaka, A., & Westbrooke, M. (2002) Arsenic contamination in Bangladesh groundwater: a major environmental and social disaster. International Journal of Environmental Health Research, 12, 235–253.

Allison, G.B., Barnes, C.J., Hughs, M.W. and Leaney, F.W.J. (1984) Effect of climate and vegetation on oxygen-18 and deuterium profiles in soils. In: Isotope Hydrology 1983, IAEA Symposium 270, September 1983, Vienna, 105-123.

ANZECC (2000) Australian and New Zealand Guidelines for Fresh and Marine Water Quality, 1. Australian and New Zealand Environment and Conservation Council and Agriculture and Resources Management Council of Australia and New Zealand, Canberra, ACT.

ATSDR (2007a) Toxicological profile for arsenic, Agency for Toxic Substances and Disease Registry U.S. Department of Human and Health Services, Atlanta, Georgia

ATSDR (2007b) Toxicological profile for lead, Agency for Toxic Substances and Disease Registry U.S. Department of Human and Health Services, Atlanta, Georgia.

ATSDR (2000) Toxicological profile for chromium, Agency for Toxic Substances and Disease Registry U.S. Department of Human and Health Services, Atlanta, Georgia.

Anand, R.R. & Paine, M. (2002) Regolith geology of the Yilgarn Craton, Western Australia: implications for exploration. Australian Journal of Earth Sciences, 49, 3-262.

Bureau of Meteorology, (2009) Climate data maps online. http://www.bom.gov.au/ accessed June, 2009. Bureau of Meteorology, Canberra, ACT.

Cawood, P.A. and Tyler, I.M. (2004) Assembling and reactivating the Proterozoic Capricorn Orogen: lithotectonic elements, orogenies, and significance. Precambrian Research 128, 201–218.

Chiba, H., and Sakai, H. (1985) Oxygen isotope exchange rate between dissolved sulphate and water at hydrothermal temperatures. Geochemica et Cosmochimica Acta 49, 993-1000.

Chen, C.J., Chen, C.W., Wu, M.M., & Kuo, T.L. (1992) Cancer potential in liver, lung, bladder, and kidney due to ingested inorganic arsenic in drinking water. British Journal of Cancer, 66, 888–892.

Chivas A.K, Andrew A.S., Lyons W.B., Bird M.I. & Donnelly T.H., (1991) Isotopic constraints on the origin of salts in Australian playas. 1. Sulphur. Palaeogeography, Palaeoclimatology, Palaeoecology 84, 309-332.

Cutten, H. N., Johnson, S. P., Thorne, A. M., Wingate, M. T. D., Kirkland, C. L., Belousova, E. A., Blay, O. A. and Zwingmann, H. (2016) Deposition, provenance, inversion history and mineralization of the Proterozoic Edmund and Collier Basins, Capricorn Orogen: Geological Survey of Western Australia, Report 127, 74p.

de Caritat, P., Kirste, D., Carr, G. & McCulloch, M. (2005) Ground water in the Broken Hill region, Australia; recognising interaction with bedrock and mineralisation using S, Sr and Pb isotopes. Applied Geochemistry 20, 767-787.

Dansgaard, W., (1964) Stable isotopes in precipitation. Tellus 5, 46-469.

Drever, J.I. (1982) The Geochemistry of Natural Waters. Prentice-Hall, Inc., Englewood Cliffs, N.J. U.S.A. 388p.

Gaciri, S.J. & Davies, T.C. (1993) The occurrence and geochemistry of fluoride in some natural waters of Kenya. Journal of Hydrology, 143, 395-412.

Gardner C.A. (1959) The Vegetation of Western Australia. In: Keast A., Crocker R.L., Christian C.S. (eds) Biogeography and Ecology in Australia. Monographiae Biologicae. Springer, Dordrecht.

Gat, J.R. (1996) Oxygen and hydrogen isotopes in the hydrologic cycle. Annual Review of Earth and Planetary Sciences 24, 225-262.

Golodoniuc P., Klump J., Reid N., and Gray D., (2015) Mobile data acquisition technology evolution in hydrogeochemical applications: Extended abstract, 21st International Congress on Modelling and Simulation (MODSIM), Broadbeach, Australia.

González-Álvarez, I., Salama,W., Ibrahimi, T. & LeGras, M. (2015) Geochemical dispersion of the DeGrussa deposit within its associated palaeodrainage system. CSIRO technical report, Mineral Resources, Western Australia EP 158718, 87.

Gray, D.J., 2003. Naturally occurring Cr^{6+} in shallow groundwater of the Yilgarn Craton, Western Australia. Geochemistry: Exploration, Environment, Analysis 3, 359-368.

Gray, D.J. & Noble, R.R.P. (2006) Nickel hydrogeochemistry of the northeastern Yilgarn Craton, Western Australia. CRC LEME Open File Report 243R / CSIRO Exploration and Mining Report P2006/524. 133 p.

Gray, D.J., Noble, R.R.P. & Reid, N. (2009) Hydrogeochemical Mapping of the Northeast Yilgarn Craton. CSIRO Exploration and Mining Report P2009/1612. Minerals and Energy Research Institute of Western Australia Report No. 280. 73 p.

Gray, D.J., Reid, N., Noble, R.R.P. (2014) Improved Hydrogeochemical Exploration in the northwest Yilgarn – Adding Value to Underexplored Areas. CSIRO Report EP 143875. 86 p.

Gray, D.J., Noble, R.R.P., Reid, N., Sutton, G.J., and Pirlo, M.C. (2016a) Regional scale hydrogeochemical mapping of the northern Yilgarn, Western Australia: a new technology for exploration in arid Australia. Geochemistry: Exploration, Environment, Analysis. 16, 100-115.

Gray, D. J. (2016b). Hydrogeochemistry dataset obtained from Stygofauna Sampling, Pilbara Region, Western Australia - Data Release: Accompanying Notes. Perth CSIRO: EP162311

Gray, D.J., Yeats, C.J., Noble, R.R.P. and Reid, N. (2018) Hydrogeochemical exploration for volcanic-hosted massive sulfide deposits in semi-arid Australia. Australian Journal of Earth Sciences, 65, 249-274.

GSWA (2017) Geological Survey of Western Australia 2015, Extracted from GeoVIEW.WA. on 23/10/2015 751 Perth, Western Australia: Department of Mines and Petroleum.

GSWA (2018a), Geological Survey of Western Australia 2018, Mines and mineral deposits. Extracted from GeoVIEW.WA. on 23/01/2018 751 Perth, Western Australia: Department of Mines and Petroleum.

GSWA (2018b), Geological Survey of Western Australia 2018, regolith geochemistry. https://dasc.dmp.wa.gov.au/dasc/. Perth, Western Australia: Department of Mines and Petroleum.

Gonfiantini, I R. (1986). Environmental isotopes in lake studies. In: Fritz P. & Fontes J-Ch. (eds). Handbook of Environmental Isotope Geochemistry, Vol. 2, The Terrestrial Environment, Elsevier, Amsterdam. pp. 113 – 168.

Halse, S.A,, Scanlon, M.D., Cocking J.S., Barron, H.J., Richardson, J.B. and Eberhard S.M. (2014) Pilbara stygofauna: deep groundwater of an arid landscape contains globally significant radiation of biodiversity. Records of the Western Australian Museum, Supplement 78, 443-483.

Harrington, G.A., Herczeg, A.L., 2003. The importance of silicate weathering of a sedimentary aquifer in arid Central Australia indicated by very high 87Sr/86Sr ratios. Chem. Geol. 199, 281–292.

Hawke, M.L., Meffre, S., Stein, H., Hilliard, P., Large, R. & Gemmell, J.B. (2015) Geochronology of the DeGrussa volcanic-hosted massive sulphide deposit and associated mineralisation of the Yerrida, Bryah and Padbury Basins, Western Australia. Precambrian Research, 267, 250–284.

Heidel, C., Tichomirowa, M. and Junghans, M. (2008) The influence of pyrite grain size on the final oxygen isotope difference between sulphate and water in aerobic pyrite oxidation experiments. 2nd Joint European Stable Isotope User Meeting. Presquile de Giens, France. AUG 31-SEP 05, 2008.

Herczeg, A.L., Dogramaci, S. and Leaney, F.W.J. (2001) Origin of dissolved salts in a large, semi-arid groundwater system: Murray Basin, Australia. Marine and Freshwater Research, 52, 41-52.

Hoffmann, G., Heimann, M., (1997) Water isotope modelling in the Asian monsoon region. Quaternary International 37, 115-128.

Ingraham, N.L., Caldwell, E.A., Verhagen, B.T. (1998) Arid Catchments In: Kendall, C. and McDonnell (eds). Isotope Tracers in catchment Hydrology. Elsevier. 435-465.

IARC (1990). IARC Monographs on the evaluation of carcinogenic risks to humans: chromium, nickel and welding, 49. World Health Organisation, International Agency for Research on Cancer.

Johnson, C.J. & Kross, B.C. (1990). Continuing importance of nitrate contamination of groundwater and wells in rural areas. American Journal of Industrial Medicine, 18, 449-456.

Johnson, S.P., Thorne, A.M., Cutten, H.N., Tyler, I.M. and Blay, O.A. (2011) Geology of the Gascoyne Province. In Johnson, S.P., Thorne, A.M., Cutten, H.N., Tyler, I.M. (eds) Capricorn Orogen seismic and magneto-telluric (MT) workshop 2011. Geological Survey of Western Australia, Record 2011/25, p. 27–41.

Johnson, S.P., Thorne, A.M., Tyler, I.M., Korsch, R.J., Kennett, B.L.N., Cutten, H.N., Goodwin, J., Blay, O., Blewett, R.S., Joly, A., Dentith, M.C., Aitken, A.R.A., Holzchuh, J., Salmon, M., Reading, A., Heinson, G., Boren, G., Ross, J., Costelloe, R.D. and Fomin, T. (2013) Crustal architecture of the Capricorn Orogen, Western Australia and associated metallogeny. Australian Journal of Earth Sciences 60, 681-705.

Kimbrough, D.E., Cohen, Y., Wilner, A.M., Creelman, L. & Mabuni, C. (1999) A critical assessment of chromium in the environment. Critical Reviews in Environmental Science and Technology, 29, 1–46.

Korhonen, F.J., Johnson, S.P., Fletcher, I.R., Rasmussen, B., Sheppard, S., Muhling, J.R., Dunkley, D.J., Wingate, M.T.D., Roberts, M.P. and Kirkland, C.L. (2015) Pressure–temperature–time evolution of the Mutherbukin Tectonic Event, Capricorn Orogen: Geological Survey of Western Australia, Report 146, 64p.

Klump J., Golodoniuc P., Reid N., Gray D., and Ross S., (2015) Comparative A/B testing a mobile data acquisition app for hydrogeochemistry: Geophysical Research Abstracts, Vol. 17, EGU2015-8332, EGU General Assembly 2015, Vienna, Austria.

Martin, D.M., and Thorne, A.M. (2004) Tectonic setting and basin evolution of the Bangemall Supergroup in the northwestern Capricorn Orogen. Precambrian Research, 128, 385-409.

McNutt, R.H., 2000. Strontium isotopes. In: Cook, P.G., Herczec, A.L. (Eds.), Environmental Tracers in Subsurface Hydrology. Kluwer Academic Publishers, Boston (Chapter 8)

Moss M.A., McCurdy R.F., et al (1983) Uranium in drinking water – report on clinical studies in Nova Scotia. In: Brown S.S. and Savory J. (eds), Chemical Toxicology and Clinical Chemistry of Metals, London, Academic Press, pp 149–152.

NHMRC (2004) Australian Drinking Water Guidelines. National Health and Medical Research Council, Canberra, ACT. http://www.nhmrc.gov.au.

Noble, R.R.P. and Gray, D.J. (2010) Hydrogeochemistry for mineral exploration in Western Australia (I): Methods and equipment. Explore 146, 2-11.

Noble, R.R.P., Anand, R.R., Gray, D.J. and Cleverley, J.S. (2016) Metal migration at the DeGrussa Cu-Au sulphide deposit, Western Australia: Soil, vegetation and groundwater studies. Geochemistry: Exploration, Environment, Analysis IAGS Tuscon.

Noble, R.R.P., Gray, D.J., Reid, N. (2010) Regional exploration for channel and playa uranium deposits in Western Australia using groundwater. Applied Geochemistry 26, 1956-1974.

Parkhurst, D.L., Thorstenson, D.C. & Plummer, L.N. (1980) PHREEQE, a computer program for geochemical calculations. U.S. Geological Survey Water Resources Investigations 80 96, 210p.

Pillans, B. (2005) Geochronology of the Australian regolith. In: Anand, R. R. and de Broekert, P. (eds) Regolith landscape evolution across Australia: a compilation of regolith landscape case studies with regolith landscape evolution models. Perth, W.A.: CRC LEME; 2005.

Pirajno, F. and Occhipinti, S.A. (1998) Geology of the Bryah 1:100000 sheet. Explanatory notes. Geological Survey of Western Australia, Department of Mines and Energy.

Pirajno, F., Occhipinti, S.A. and Swager, C.P. (2000) Geology and Mineralisation of the Palaeoproterozoic Bryah and Padbury Basins, Western Australia. Report 59. Geological Survey of Western Australia, Department of Mines and Energy.

Pirajno, F., Jones, J.A., Hocking R.M. and Halilovic J. (2004) Geology and tectonic evolution of Palaeoproterozoic basins of the eastern Capricorn Orogen, Western Australia. Precambrian Research 128, 315-342.

Quade, J., Garzione, C. and Eiler, J., (2007) Paleoelevation reconstruction using pedogenic carbonates. Paleoaltimetry: Geochemical and Thermodynamic Approaches. Mineralogical Society of America, Chantilly, pp. 53-87.

Reid, N., Gray, D. and Naughton, T., (2012) Hydrogeochemistry Field Data Book. Published by CSIRO as part of the Deep Exploration Technologies CRC.

Reid, N., Klump, J., Ballsun-Stanton, B., White, A., Sobotkova, A., (2015) A mobile app for geochemical field data acquisition. AGU Fall Meeting 2015, San Francisco, California, USA, 14-18 December 2015. American Geophysical Union (AGU).

Rozanski, K., Araguas-Araguas, L., Gonfiantini, R., (1993) Isotopic patterns in modern global precipitation. Climate Change in Continental Isotopic Record. AmericanGeophysical Union, Washington, pp. 1-37.

Saxena, V.K. and Ahmed, S. (2003). Inferring the chemical parameters for the dissolution of fluoride in groundwater. Environmental Geology, 43, 731-736.

Selvaraja, V., Fiorentini, M.L., Jeon, H., Savard, D.D., Laflamme, C., Guagliardo, P., Caruso, S. and Bui, T.H. (2017) Evidence of local sourcing of sulfur and gold in an Archaean sediment-hosted gold deposit. Ore Geology Reviews 89, 909-930.

Spinks, S.C., Uvarova, Y., Thorne, R., Anand, R., Reid, N., White, A., Ley-Cooper, Y., Bardwell, N., Gray, D., Meadows, H. and LeGras, M. (2017) Detection of Zinc deposits using terrestrial ferromanganese crusts. Ore Geology Reviews, 80, 484-503.

Thorne, A.M. (1990) Blair and Mount Minnie Basins. Geology and Mineral Resources of Western Australia. Western Australia Geological Survey, Memoir 3, pp. 220–221.

Thorne, R.L, Spinks, S.C., Anand, R R, Metelka, V., Davis, A., Ibrahimi, T., Reid, N., leGras, M., Brant, F. and Munday, T. (2018a) Regolith landform processes and geochemical exploration of the Capricorn Orogen, Western Australia. EP 183025 CSIRO p. 96.

Thorne, R.L, Spinks, S.C., Reid, N., Gray, D. and, Anand, R. (2018b) 'Seeing through' cover in the Capricorn Orogen. Ore Geology Reviews (draft).

Usher, C.R., Cleveland, C.A., Strongin, D.R., Schoonen, M.A. (2004) Origin of oxygen in sulfate during pyrite oxidation with water and dissolved oxygen: An in situ horizontal attenuated total reflectance infrared spectroscopy isotope study. Environmental Science and Technology 38, 5604-5606.

Veizer, J., (1989) Strontium isotopes in seawater trough time. Ann. Rev. Earth Planet. Sci. 17, 141–167

Warner, T.E., Rice, N.M. and Taylor, N. (1996) Thermodynamic stability of pentlandite and violarite and new Eh-pH diagrams for the iron-nickel sulfur aqueous system. Hydrometallurgy 41, 107-118.

Wingate, M.T.D. and Bodorkos, S. (2007) 156602: granophyric dolerite sill, No. 36 Well; Geochronology Record 695: Geological Survey of Western Australia, 5p.

Zimmerman, U., Münnich, K.O. and Roether W. (1967) Downward movement of soil moisture traced by means of hydrogen isotopes. In: Isotope Techniques in the Hydrologic Cycle, Geophysical Monograph Series 11, American Geophysical Union.

ZoBell, C.E. (1946) Studies on redox potential of marine sediments. Bulletin of the American Association of Petroleum Geologists 30, 477-513.

Theme 5:

Geochemical Mapping for Lithospheric Evolution, Metal Reservoirs and Predictive Targeting

Theme 5A: To See an Orogen in a Grain of Zircon: Crustal Evolution and Source to Sink Sediment Routing in the Capricorn Orogen, a Synthesis of Zircon Geochronology and Geochemistry

M Barham, I Jahn, S Armondola, C Clark, S Reddy, C Kirkland and R Taylor

Theme 5B: Tracing Sulfur Pathways Through the Lithosphere

Crystal LaFlamme, Stefano Caruso, Vikraman Selvaraja, Marco Fiorentini

2 Theme 5A: To See an Orogen in a Grain of Zircon: Crustal Evolution and Source to Sink Sediment Routing in the Capricorn Orogen, a Synthesis of Zircon Geochronology and Geochemistry

M Barham, I Jahn, S Armondola, C Clark, S Reddy, C Kirkland and R Taylor

2.1 Introduction

Accurate regional geological, structural and geodynamic reconstructions become increasingly complex with increasing age, as the geological record becomes progressively obscured by weathering, erosion, sediment cover, crustal re-working and tectono-thermal overprinting. As a result, intricate histories of large regions of Proterozoic and Archean crust remain relatively poorly understood. Fortunately, robust minerals such as zircon are exceptional geochronometers (incorporation of U but exclusion of Pb during crystallization) and proxies for the composition and origin/geological setting of parental melts (distinctive trace element patterns and O- and Hf- isotope ratios), acting to inform broader and deeper records of crustal processes from isolated outcrop, subcrop or even metamorphosed samples (Belousova et al., 2002; Hawkesworth and Kemp, 2006; Johnson et al., 2017; Kirkland et al., 2015; Kirkland et al., 2013; Roberts and Spencer, 2015). Furthermore, the characteristics of sedimentary cover sequences and basins associated with the break-up and assembly of continental fragments are a reflection of the composition of crystalline sediment-source regions, and the tectonic setting and paleoenvironmental conditions of deposition, and thus preserve proxy data of events whose direct products may be completely obscured or otherwise destroyed. In particular, advances in rapid, targeted geochronological and geochemical analytical techniques of detrital mineral phases (such as zircon) are enabling extraction of significant intrinsic (sedimentary system) and extrinsic (crustal scale geological processes) information from cover sequences that is especially important in Proterozoic sequences lacking good biostratigraphic constraints (Barham et al., 2016; Carrapa, 2010; Cawood et al., 2012; Halilovic et al., 2004; Iizuka et al., 2013; Kemp et al., 2006; Martin et al., 2008; Mason et al., 2017; O'Sullivan et al., 2016; Spaggiari et al., 2015; Xu et al., 2016). These data are particularly powerful when crystalline source regions and sedimentary sequences are integrated to capture more holistic views of crustal evolution than is possible from either approach individually (e.g. Belousova et al., 2009; Kemp et al., 2006; Spencer et al., 2014).

Sandwiched between the Archean Yilgarn and Pilbara Cratons in NW Australia, is the broadly east-west trending ~1000 km long Capricorn Orogen (Figure 2.1), which records Proterozoic assembly and reworking of the West Australian Craton component of the supercontinent Nuna (Cawood and Korsch, 2008; Cawood and Tyler, 2004; Johnson et al., 2011a). Subsequent to the multi-stage suturing of the Pilbara and Yilgarn Cratons, the Capricorn Orogen was the site of repeated intra-cratonic reworking due to inherent lithospheric weakness relative to adjacent cratonic blocks – resulting in successive basin formation, magmatic and metamorphic events (Figure 2.2; Cawood and Tyler, 2004; Johnson et al., 2013; Korhonen and Johnson, 2015; Sheppard et al., 2005). As a result of its lithospheric setting, geological history and presence of large-scale crustal conduits (at a suture between two cratons and focus of repeated orogenesis), the Capricorn Orogen is considered to have many of the geological ingredients necessary for the development of large-scale mineral- systems (Begg et al., 2010; Cawood and Tyler, 2004; Groves and Bierlein, 2007; Hronsky et al., 2012; Johnson et al., 2013; Mole et al., 2013; Pirajno, 2004a; Vos et al., 2005). Despite this mineral system prospectivity and vast extent, the Capricorn Orogen hosts a relative paucity of known/worked world-class mineral deposits, likely in part, due to limited exposure and geological complexities hindering exploration.

The Capricorn Orogen is considered relatively complete despite its age (Cawood and Tyler, 2004) with distinct cratonic elements exposed on either side of variously deformed mid- to upper crustal basement and intervening sedimentary basins that collectively have the potential to improve understanding of Paleoproterozoic crustal processes. Given the established links between largescale crustal processes and regional mineral fertility, and growing mineral resource interest in the Capricorn, the "Distal Footprints of Giant Ore Systems" research project was established in 2014 in an attempt to enhance exploration geosciences in the Capricorn and geologically inform over a billion years of continental assembly and reworking. As part of a multi-faceted approach to deconvolute regional geological histories and recognise enigmatic signatures of cryptic mineral systems, this report details geochronological and geochemical analyses of magmatic and detrital zircons from the Capricorn region as part of Theme 5: "*Geochemical Mapping for Lithospheric Evolution, Metal Reservoirs & Predictive Targeting*". Through analysis of the zircons it is hoped to inform the broader geological evolution of the region (contextualizing mineral systems), as well as provide data on sediment transport (relevant for placer deposits) and a database of zircon geochemistry that is increasingly recognized as a potential mineral pathfinder technique (e.g. Gardiner et al., 2017a; Lu et al., 2016).

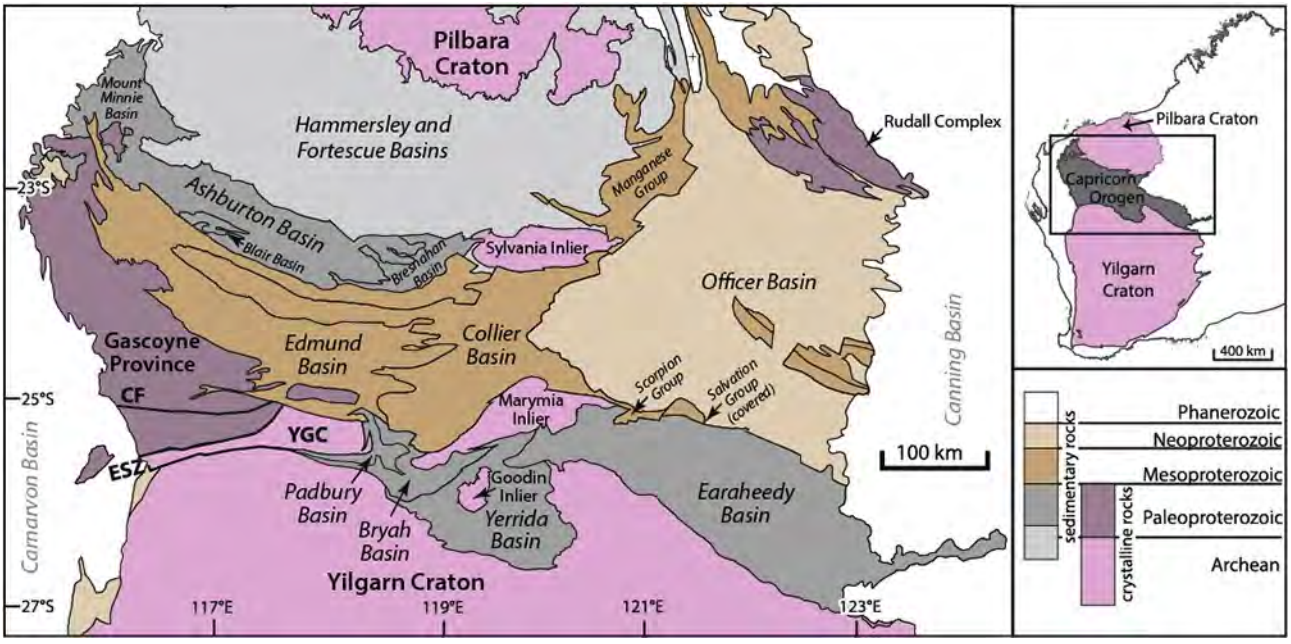

Figure 2.1. Regional geological map of the Capricorn Orogen and bordering basins and tectonic units. CF – Chalba Fault, ESZ – Errabiddy Shear Zone, YGC – Yarlarweelor Gneiss Complex. Modified from Sheppard et al. (2016).

2.2 Geological Background

2.2.1 Regional tectonic assembly

The Capricorn Orogen is a Proterozoic orogenic belt comprising a mosaic of volcano- sedimentary and sedimentary basins overlying and intervening plutonic and medium to high- grade metamorphosed rocks of the Gascoyne Complex and the Yilgarn and Pilbara Cratons (Figure 2.1). As well as the deformed margins of the Archean Pilbara and Yilgarn Cratons, numerous basins within the Capricorn Orogen overlie basement inliers of Archean granite- greenstone: e.g. the Marymia and Goodin Inlier of the Yilgarn Craton, and the Sylvania Inlier of the Pilbara Craton (Dentith et al., 2014; Johnson et al., 2013). Recent studies of the Capricorn Orogen have demonstrated increasing complexity of the protracted multi-phase assembly of the Pilbara and Yilgarn Cratons (into the West Australian Craton – WAC) and later intra-cratonic re-working, which was incompletely captured in older reconstructions (Figure 2.2; Evans et al., 2003; Johnson, 2013; Johnson et al., 2011a; Johnson et al., 2013; Krapez, 1999; Myers et al., 1996; Occhipinti and Reddy, 2009; Sheppard et al., 2016a; Sheppard et al., 2005; Tyler and Thorne, 1990). Current understanding suggests that initially, during the Rhyacian (~2215-2145 Ma), accretion of the Glenburgh Terrane to the southwestern margin of the Pilbara Craton resulted in the Ophthalmian Orogeny (Johnson et al., 2011a). Later, the amalgamated Glenburgh-Pilbara element ("Pilboyne") collided with the northern margin of the Yilgarn Craton to complete cratonic docking during the ~1965-1950 Ma Glenburgh Orogeny (Johnson et al., 2011a). The subsequent ~1820-1770 Ma Capricorn Orogeny, once proposed as signifying oblique collision of the Pilbara and Yilgarn Cratons (Tyler and Thorne, 1990), is now recognized as an interval of intra-cratonic deformation that is broadly coincident with the Yambah (North Australian Craton – NAC), Tanami (NAC), Halls Creek (Kimberley Craton-NAC), and Yapungku (WAC-NAC) Orogenies, and assembly of the WAC and the NAC (Cawood and Korsch, 2008; Johnson, 2013). Focused intracontinental deformation of the Capricorn re-occurred during the Mangaroon Orogeny (~1680-1620 Ma), Mutherbukin Tectonic Event (~1385-1200 Ma) and Edmundian Orogeny (1070-755 Ma), with the latter events lacking significant/widespread coincident magmatism, but being reflected in tectonic overprinting and deformation of Mesoproterozoic basins (Sheppard et al., 2007).

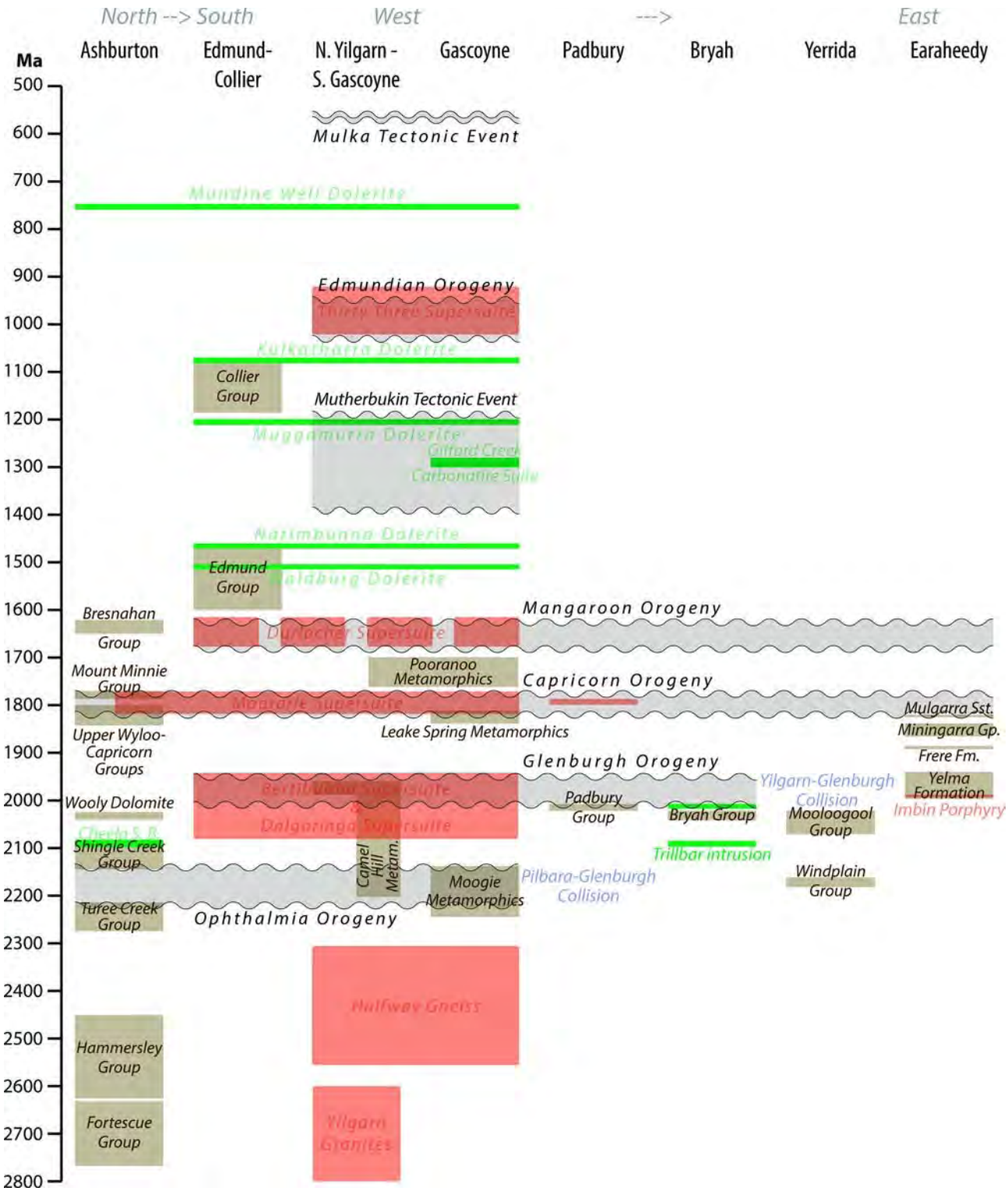

Figure 2.2. Schematic time-space plot of major igneous episodes (red = felsic, green = mafic), orogenic events (grey) and depositional sequences (brown) recorded in the Capricorn Orogen. Compiled from Geoscience Australia and the Australian Stratigraphy Commission (2017); Hawke et al. (2015); Johnson et al. (2013); Sheppard et al. (2016).

2.2.2 Magmatic ages and evolution of crystalline basement within and fringing the Capricorn Orogen

- **Archean Magmatism**

Yilgarn Craton

The Yilgarn Craton, underlying the Capricorn Orogens southern edge, consists of several amalgamated, broadly north-south trending Archean terranes that stabilized in the earliest Paleoproterozoic. The elements comprise the Narryer Terrane, Youanmi Terrane (Murchison and Southern Cross Domains) and Eastern Goldfields Superterrane (Kalgoorlie, Kurnalpi, Burtville and Yamarna Terranes) from west to east (Figure 2.3a & 2.3b; Cassidy et al., 2006; Pawley et al., 2012). The majority of the metasedimentary and metavolcanic rocks of the Yilgarn Craton were formed between 2.6 and 3 Ga, with both the oldest rocks (~3.7 Ga granitic gneisses of the Narryer Gneiss Complex) and minerals (~4.4 Ga zircons) concentrated in the Narryer Terrane in the far northwest (Cassidy et al., 2006). The Narryer Terrane consists of the Archean granitic gneisses with protolith ages between ~ 3.7 Ga and 3.3 Ga (Kinny et al., 1988; Nutman et al., 1991), interleaved with metasedimentary and mafic metaigneous rocks (William and Myers, 1987) that evidence an interval of repeated deformation and high-grade metamorphism between ~3.3 and 3.05 Ga (Nutman et al., 1991). Later, the Narryer Terrane, in particular, was significantly modified during collision with the Glenburgh Terrane and was extensively deformed and intruded by granites during the 1820-1770 Ma Capricorn Orogeny to form the Yarlarweelor Gneiss Complex (Figure 2.1 & 2.3a; Johnson et al., 2013; Sheppard et al., 2003).

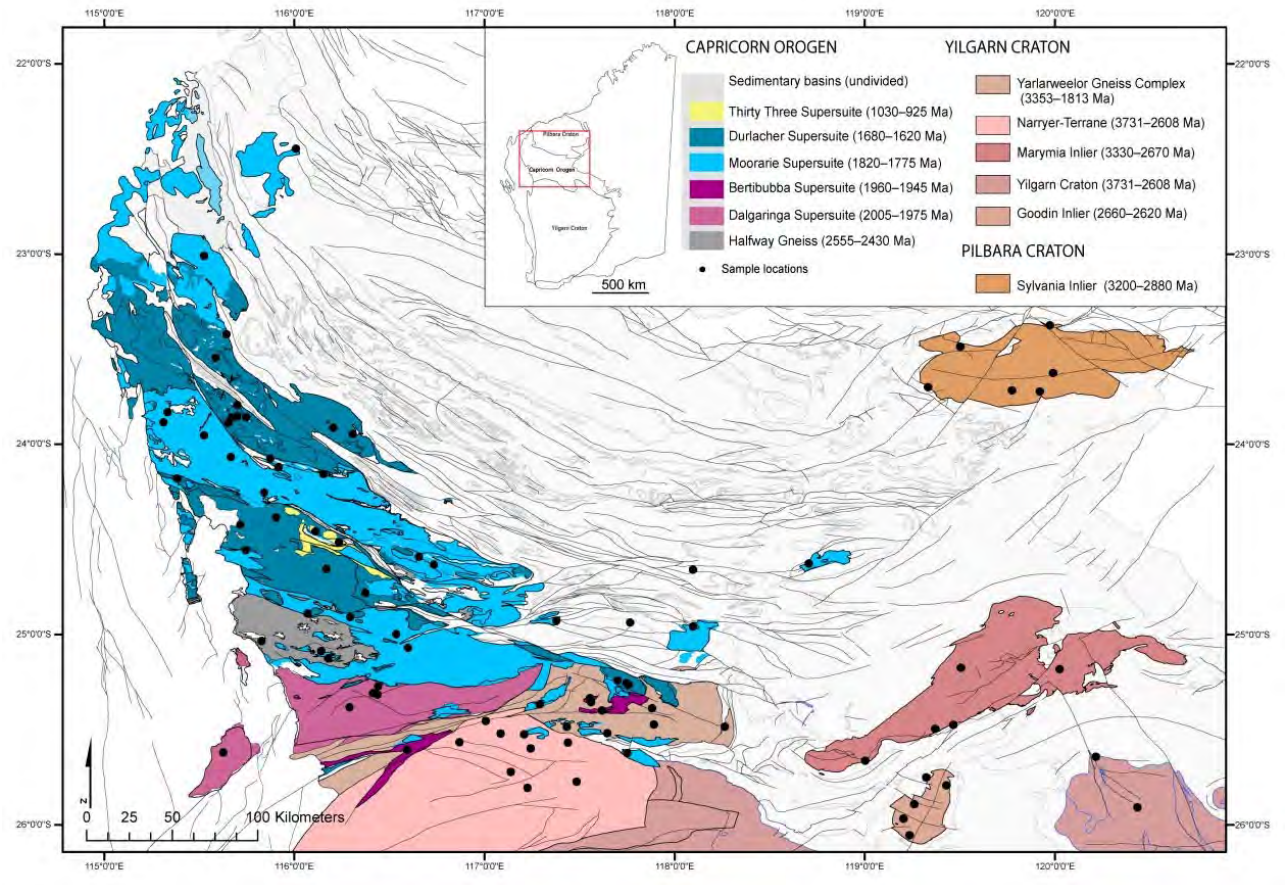

Figure 2.3a. Simplified geological map of the Capricorn Orogen showing the principal magmatic sample locations across Archean inliers and Proterozoic intrusives (black dots).

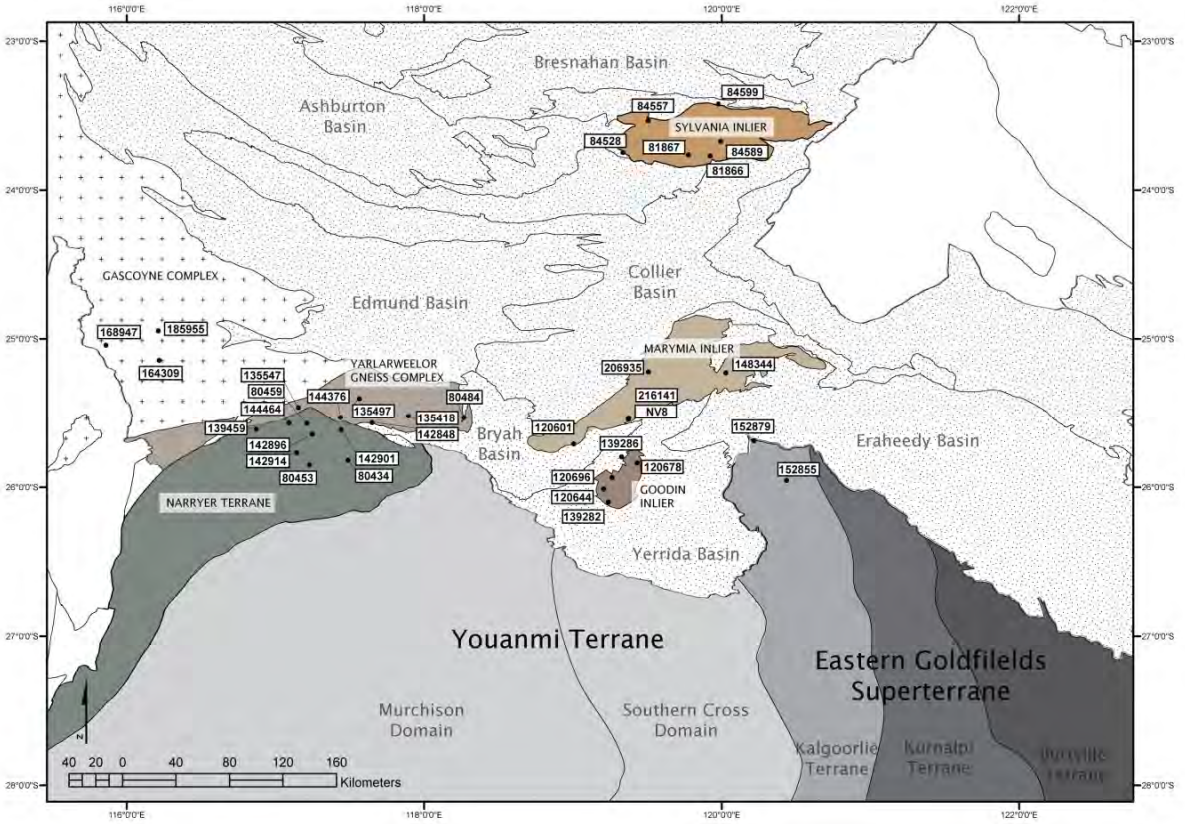

Figure 2.3b. Archean sample locations with corresponding GSWA sample numbers indicated by the black dots.

Between 2750 and 2600 Ma, several generations of granitoids were emplaced throughout the Yilgarn Craton (Nutman et al., 1993). This period of Neoarchean magmatism is associated with cratonic assembly via terrane accretion (Myers, 1995; Wilde et al., 1996), which fundamentally influenced a range of geological processes effecting mineralization, particularly in the eastern Yilgarn Craton (Vielreicher et al., 2015). Further north, collision of the Narryer and Youanmi Terranes caused widespread deformation and high-grade metamorphism (Myers, 1993; Myers, 1990; Spaggiari et al., 2008). This northwestern region was further modified during the Glenburgh Orogeny, with the Yilgarn Craton (Narryer Terrane) now separated from the Gascoyne Province by the Errabiddy Shear Zone (Occhipinti et al., 2004). Elsewhere, the northern margin of the Yilgarn is obscured by sedimentary basins (Figure 2.1; Pirajno et al., 2004).

Marymia and Goodin Inliers

Isolated inliers of Archean, dominantly granitoid, basement (principally the Marymia and Goodin) crop out within the Capricorn Orogen to the north of the Younami Terrane and Eastern Goldfields Superterrane of the Yilgarn Craton (Figure 2.1, 2.3a&b). The nature of the boundaries potentially separating the Archean Yilgarn Craton to the south and the rocks that make up the inliers, as well as the tectonised unconformable contacts between the Proterozoic rocks that envelope the Marymia and Goodin Inliers, are relatively poorly known (Bagas, 1999). As a result, the provenance, age and nature of emplacement of the rocks in the Marymia Inlier are not yet fully resolved, with various proposals suggesting the Marymia Inlier could consist of Archean and/or Proterozoic rocks akin to the Gascoyne Complex, Narryer Gneiss Terrane, Yilgarn Craton and/or another Archean basement terrane (Bagas, 1998, 1999). The Marymia Inlier comprises two greenstone belts intruded by c. 2720 Ma monzogranite (Vielreicher and McNaughton, 2002) and is most widely interpreted to represent a portion of the Yilgarn Craton that was uplifted, rotated and reworked during the Proterozoic (Krapez and Martin, 1999; Myers, 1993; Occhipinti et al., 1998; Pirajno et al., 2004; Pirajno and Occhipinti, 2000). Bagas, (1999) interpreted the inlier to include two components separated by the Jenkins Fault, one inferred to be an eastern or northern extension of the Narryer Terrane, Murchison Domain or Southern Cross Domain, and the other a northwestern extension of the Eastern Goldfields Superterrane. Recent compilations

of stratigraphic, geochronological and isotopic data have been used to correlate the Marymia Inlier to the Eastern Goldfields Superterrane of the Yilgarn Craton (Bagas, 1999; Dentith et al., 2014; Gazley, 2011; Gazley et al., 2011; Griffin et al., 2004; Vielreicher and McNaughton, 2002; Vielreicher et al., 2002).

The Goodin Inlier is smaller, situated closer to the Yilgarn Craton and comprises monzogranite and syenogranite that have been dated (2.6 Ga; Nelson, 1996) as distinctly younger than the granitoid rocks of the Marymia Inlier (Bagas, 1999). Pirajno (2004b) suggested that a mantle plume at 2.0 Ga caused uplift, rifting and massive volcanism, resulting in the fragmentation of the northwestern margin of the craton, which split into a number of fragments, now represented by the Goodin and Marymia Inliers. More recently, Paleoproterozoic thinning and rifting of the northern margin of the Yilgarn Craton has been discussed by Occhipinti et al. (2017) and associated with basin formation (Yerrida and Bryah Basins) that now isolates the Marymia and Goodin Inliers from the Yilgarn Craton.

Pilbara Craton and related inliers

The Pilbara Craton comprises ~3.7-2.8 Ga low grade volcano-sedimentary greenstone belts, granitic bodies and younger coarse clastic-dominated basins, all unconformably overlain by volcanics and sediments of the Fortescue and Hammersley Basins to the south (Hickman, 2012; Van Kranendonk et al., 2007). Revised mapping and geochronology have recognized several discrete greenstone belts that attest to exotic terrane accretion during cratonic evolution; the c. 3.5-3.2 Ga East Pilbara Terrane, the 3.3-3.1 Ga West Pilbara Superterrane (Regal, Sholl and Karratha Terranes) that crops out in the northwest of the craton, and the ≥ 3.2 Ga Kurrana Terrane in the southeast of the Craton, interpreted as a rifted fragment of the East Pilbara Terrane (Van Kranendonk et al., 2010). Magmatic zircons produced throughout the Paleo- Meso-Archean interval are reflected in fringing sedimentary basins to the north of the craton (Sheppard et al., 2016b). To the south, the Fortescue, Hamersley and Turee Creek Groups were deposited between ~2.7 and 2.2 Ga (Geoscience Australia and the Australian Stratigraphy Commission, 2017) during the evolution from a rifted (Fortescue Group), to passive (Hammersley Group) to active continental margin (Turee Creek Group; Blake and Barley, 1992; Krapež et al., 2017; Martin and Morris, 2010). Paleoproterozoic intracontinental reactivation is thought to be responsible for renewed deposition of Ashburton Basin sediments in a possible foreland basin setting, subsequent to the assembly of the West Australian Craton (Johnson et al., 2013).

Inliers of Granite-greenstone Archean basement affiliated with the Pilbara Craton are exposed across the northern Capricorn Orogen in the Wyloo, Rocklea and Milli Milli Domes, as well as, the Sylvania Inlier (Johnson et al., 2013). The Sylvania Inlier crops out to the south of the Bresnahan Basin and comprises granitoids and minor discontinuous greenstone belts. Early geochemical and isotopic studies interpreted the inlier as part of an allochthonous terrane accreted to the Pilbara Craton between 3000–2760 Ma (Tyler, 1991; Tyler et al., 1992). More recent studies integrating SHRIMP U–Pb zircon data have identified the terrane as a rifted crustal fragment of the Pilbara Craton (Van Kranendonk et al., 2010). The Sylvania Inlier is overlain unconformably by the Hammersley Basin in the north, and the Mesoproterozoic Edmund and Collier Basins to the south.

- **Proterozoic orogenic magmatism**

The Gascoyne Province in the western Capricorn consists of Neoarchean to Paleoproterozoic gneisses and metasediments of an exotic terrane (Glenburgh Terrane) in the south, and medium to high-grade metamorphic rocks in the north that have been extensively intruded during regional orogenic events (Figure 2.3a-d). The Glenburgh Terrane comprises variably deformed and metamorphosed granitic rocks with c. 2660–1970 Ma protolith ages interleaved with metasedimentary rocks (Johnson et al., 2011b; Occhipinti et al., 2004). Basement gneisses (Halfway Gneiss) of the Glenburgh Terrane are a distinctive component of the Gascoyne Complex, with the area later intruded by younger granitoids associated with assembly of the WAC (granitic rocks of the ~2005-1970 Ma Dalgaringa Supersuite; Johnson, 2013; Johnson et al., 2011a; Occhipinti et al., 2004; Sheppard et al., 2004). The entire Gascoyne Province was successively intruded, metamorphosed and deformed to varying degrees during intracratonic reworking events (Figure 2.2).

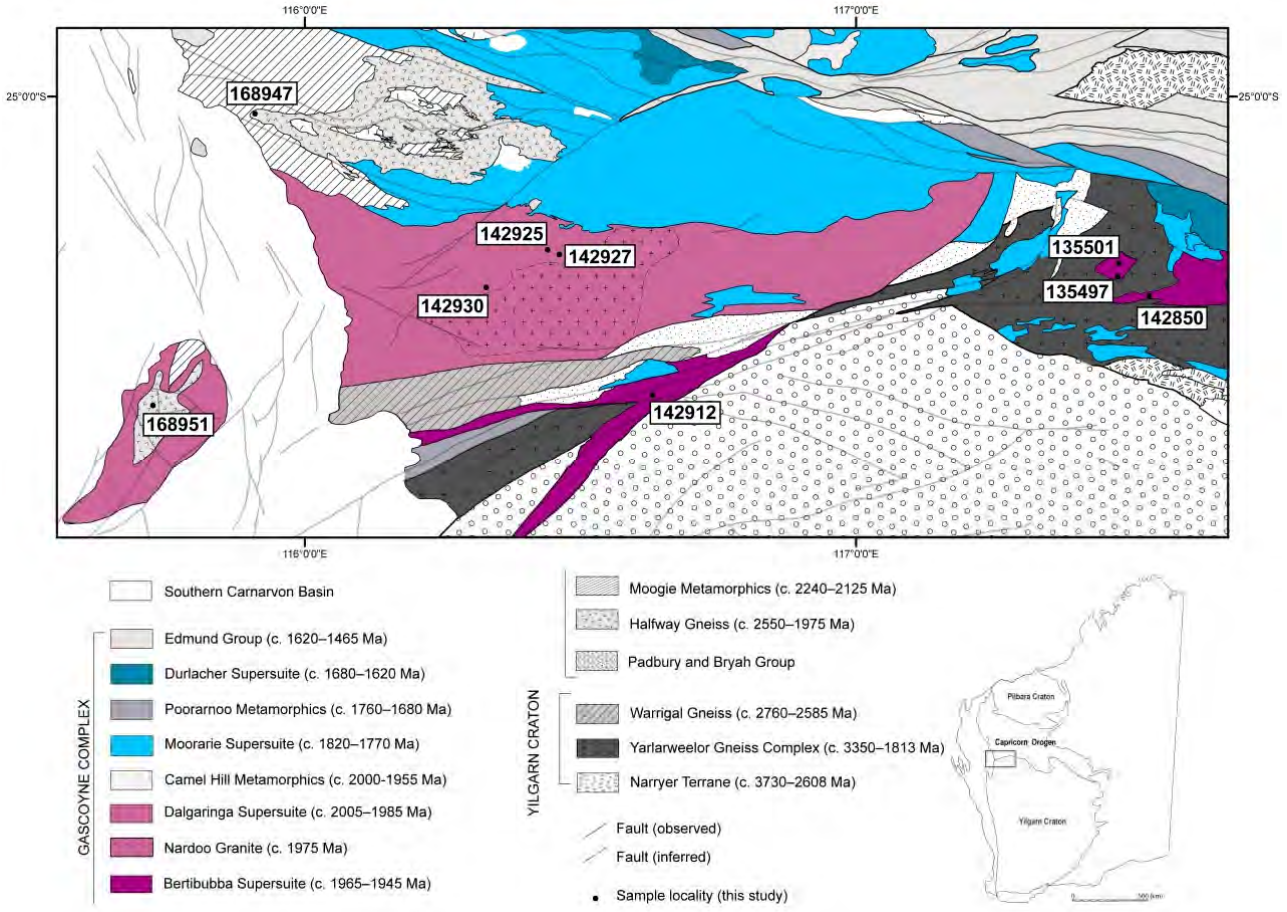

Figure 2.3c. Gascoyne Complex locations with corresponding GSWA sample numbers indicated.

Paleoproterozoic magmatism of the Dalgaringa Supersuite was generated in a continental arc setting along the southern margin of the Glenburgh Terrane (Johnson et al., 2017; Johnson et al., 2011a) during the accretion of the southern Gascoyne Complex onto the passive northwestern margin of the Yilgarn Craton (Sheppard et al., 2004). Subsequent intrusion of the Bertibubba Supersuite (~1965-1945 Ma) across the northern Yilgarn and through the Glenburgh Terrane effectively sutured the crustal-scale boundary during the Glenburgh Orogeny (Occhipinti et al., 2004). The 1820-1770 Ma Capricorn Orogeny is associated with low- to medium-grade metamorphism and intense structural reworking, the intrusion of voluminous granitic magmas of the 1830-1775 Ma Moorarie Supersuite across the orogeny, and deposition of the 1840-1810 Ma Leake Spring Metamorphics in the Gascoyne Province (Johnson et al., 2011a; Johnson et al., 2011b; Johnson et al., 2013; Sheppard et al., 2010).

Granitic rocks of the Moorarie Supersuite intruded across the Gascoyne Province and into adjacent Yarlarweelor Gneiss Complex and Ashburton Basin during the Capricorn Orogeny (Figure 2.2, 2.3a & 2.3d). Extensive whole-rock trace element and isotopic work has been directed towards identifying the sources of the Moorarie Supersuite granites in the Capricorn Orogen, and has revealed that all granites in the supersuite reflect reworking of older crust (Johnson et al., 2017; Sheppard et al., 2010; Sheppard et al., 2003, 2004). However, the nature of the recycling and distinction between possible infracrustal and supracrustal components has not been established. The later Durlacher Supersuite (~1700-1620 Ma) was largely contemporaneous with the Mangaroon Orogeny (Geoscience Australia and the Australian Stratigraphy Commission, 2017) but largely restricted to the Gascoyne Province and parts of the northern Yilgarn Craton margin (Figure 2.3a & 2.3d).

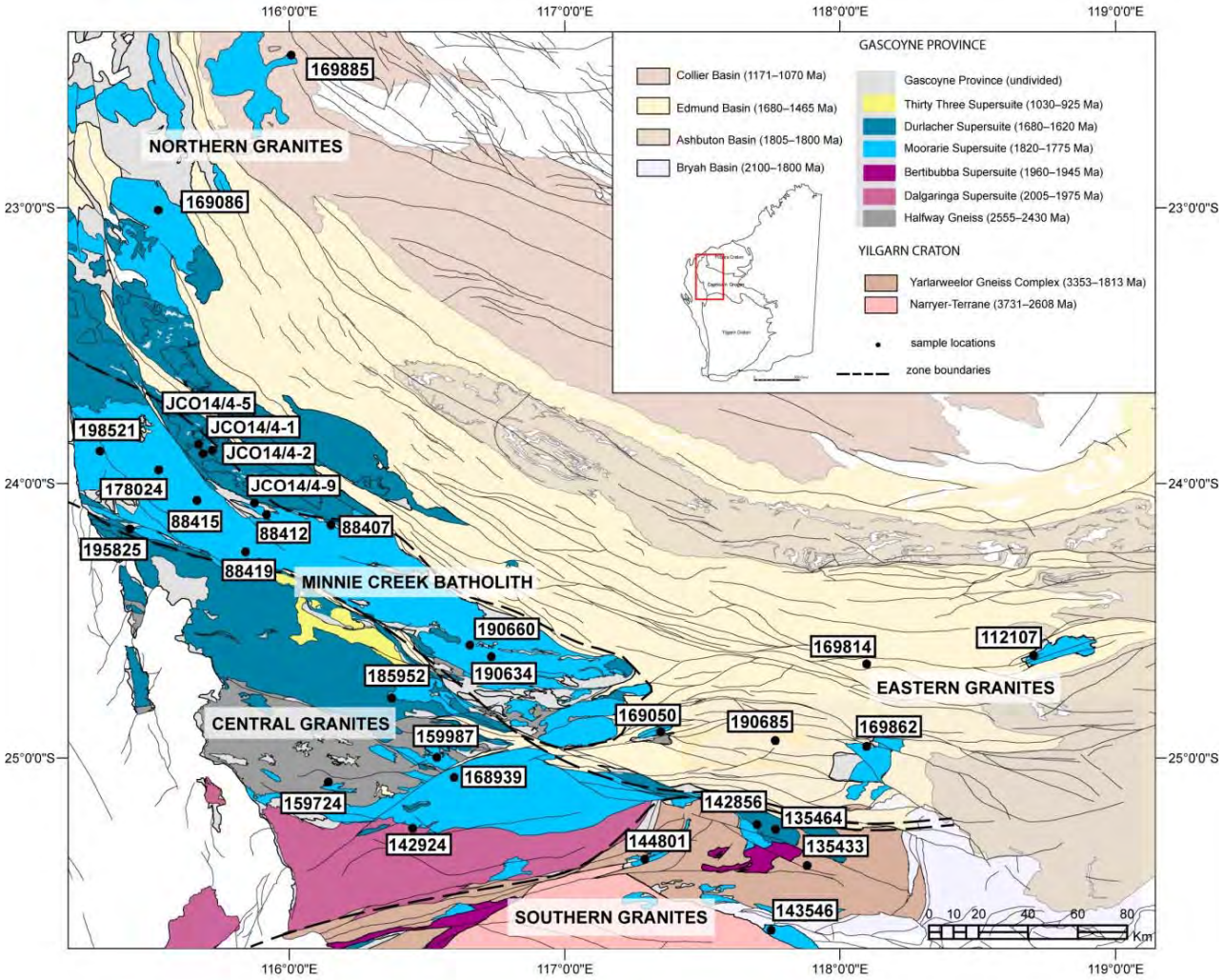

Figure 2.3d. Intracratonic granitic supersuite sample locations with corresponding GSWA sample numbers.

2.2.3 Regional depo-center evolution

Paleoproterozoic sedimentary basins of the Capricorn Orogen fringe the borders of the Yilgarn and Pilbara Cratons, while the Mesoproterozoic Edmund and Collier Basins, which are ~1 Ga younger than the oldest sediments associated with the orogeny, crop out through central regions in an east-west trending belt (Figure 2.1). With increasing chronological constraints from isotopic ages (tuffs, cross-cutting intrusions or mineralization events) the relationship of basin-formation and fill to regional tectonics is improving (e.g., Cutten et al., 2016; Occhipinti et al., 2017; Sheppard et al., 2016a, and references therein). It is becoming clear that Paleoproterozoic basins along the bounding cratonic margins formed in intimate association with early orogenic events, with later Mesoproterozoic basins largely reflecting a more quiescent period post cratonic-assembly (Figure 2.2). The Capricorn Orogen is overlain in the west by the Paleozoic Carnarvon Basin and the Neoproterozoic to Paleozoic Officer Basin in the east (Figure 2.1).

- **Northern Capricorn Orogen margin (Ashburton province)**

The Ashburton Basin sits on the southern edge of the Pilbara Craton (unconformably overlying the Archean to Paleoproterozoic Hammersley and Turee Creek Groups) and marks the northern margin of the Capricorn Orogen (Cawood and Tyler, 2004). The broader Ashburton Province preserves an ~30 km thick unconformity-bound sequence of variably deformed metasediments and metavolcanics of the Shingle Creek, Wyloo, Mount Minnie, Capricorn and Bresnahan Groups, variously interpreted to represent different basin episodes (Krapež

et al., 2015; Thorne and Seymour, 1991). The Ashburton Basin itself is represented by the Shingle Creek Group (previously Lower Wyloo, comprising the Beasley River Quartzite and Cheela Springs Basalt), Wooly Dolomite and the Wyloo Group (including the Mt. McGrath Formation), which are collectively and successively succeeded by the Mount Minnie Group of the Mount Minnie Basin in the northwest, the Capricorn Group (including the Mooline Formation) of the Blair Basin centrally, and the Bresnahan Group of the Bresnahan Basin in the east (Figure 2.4; Geoscience Australia and the Australian Stratigraphy Commission, 2017; Thorne and Seymour, 1991). Deposition occurred in discrete episodes over a protracted ~0.5 Ga interval in the Paleoproterozoic (Rhyacian-Statherian) with evolving depositional environments interpreted in terms of regional tectonostratigraphic forcings. Most recently, Krapež et al. (2015) continued supporting an intracontinental rift setting for the development of the Shingle Creek Group after the Opthalmian Orogeny, tracking fluvial and tidally influenced sandstones of the Beasley River Quartzite to terrestrial and shallow marine flood basalts and volcaniclastics of the Cheela Springs Basalt and shelfal shaly dolostone of the Wooly Dolomite (Krapez, 1999).These sediments are separated from the overlying sedimentary sequence by an unconformity associated with the Panhandle Event (Tyler and Thorne, 1990). The Mount McGrath Formation is interpreted to correspond to a period of gradual subsidence, with deltaic shallow marine to sub-aerial sedimentation replaced by deeper water pro-delta to deeper-water mudstone and siltstone (Thorne and Seymour, 1991). Overlying sediments have been attributed to a foreland basin associated with the ultimate assembly of the West Australian Craton with shallowing indicated from the deeper submarine deposits of the Ashburton Formation through to the paralic and fluvio- deltaic sediments of the Capricorn Formation derived from the SW (Hall et al., 2001). Post-collisional extension was later inferred to explain the deposition of dominantly terrestrial siliciclastic sediments of the Mt. Minnie and Bresnahan Basins (Thorne and Seymour, 1991).

Figure 2.4. Simplified lithostratigraphy of the southern Pilbara Craton, and overlying northern Capricorn Orogen, sedimentary basins. Modified from Johnson et al. (2013).

- **Southern Capricorn Orogen margin**

Along the southern margin of the Capricorn Orogen, volcano-sedimentary and sedimentary basins formed between ~2.2 and 1.8 Ga in response to specific thermal, extensional and contractional events that occurred during the amalgamation of the WAC. The present-day outcrop of these basins are an incomplete reflection of their original extent due to complex reworking and erosion over ~2 Ga. In the northwest, the Paleoproterozoic basins are unconformably overlain by the Mesoproteozoic Bangemall Supergroup (i.e, the Edmund and Collier Basins), and are unconformably succeeded by Neoproterozoic to Paleozoic sediments of the Officer Basin in the northeast and Paleozoic Canning Basin in the east (Figure 2.1).

Paleoproterozoic sediments along the southern margin of the Capricorn Orogen were originally assigned to the "Nabberu Basin", comprising (from west to east) the Padbury, Glengarry and Earaheedy Sub-basins (Hall and Goode, 1978). These were subsequently revised and individual sedimentary basins recognized in their own right, with the Glengarry Basin being further divided into an eastern Yerrida Basin and western Bryah Basin (Occhipinti et al., 1997; Pirajno et al., 2004; Pirajno and Occhipinti, 2000; Pirajno et al., 1998). Most recently, lateral equivalence of units has been recognized between the Mooloogool Group of the Yerrida Basin and upper levels of the Bryah Basin and younger units in the Padbury Basin with basal units of the Earaheedy Basin (Figure 2.2 & 2.5; Occhipinti et al., 2017).

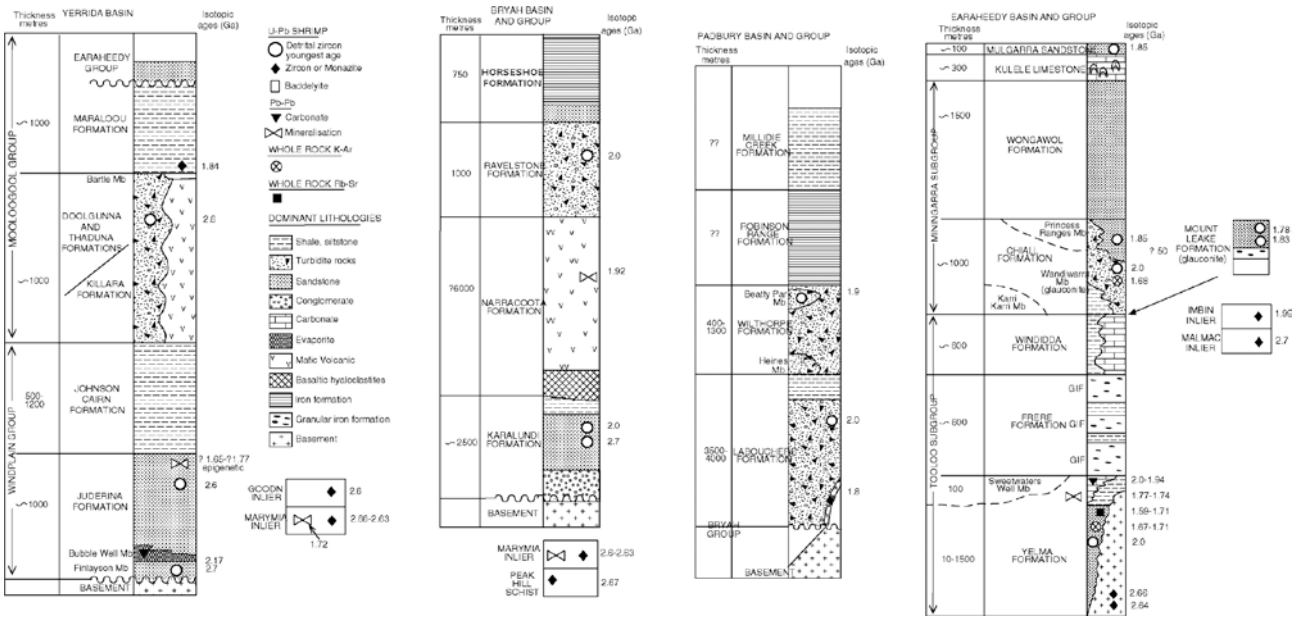

Figure 2.5. Lithostratigraphy of the Palaeoproterozoic sedimentary basins of the southern Capricorn Orogen. Reproduced from Pirajno et al. (2004).

The Yerrida Basin represents the oldest in a succession of related sedimentary basins (Bryah and Padbury) that progressively young to the northwest (Figure 2.1). Sedimentation (Windplain Group) in the Yerrida Basin was initiated during crustal thinning, contemporaneous with, but apparently unrelated to, the collision of the Glenburgh Terrane and the Pilbara Craton (Ophthalmian Orogeny) to the north (Figure 2.2). Continued rifting led to the intruded basin fill of intercalated sediments and extrusive volcanics in the Mooloogool Group of the Yerrida Basin and coeval Bryah Group sediments in the Bryah Basin to the northwest (Occhipinti et al., 2017). Extensional processes were terminated preceding the collision of the "Pilboyne" (united Pilbara and Glenburgh Terrane) with the northern margin of the Yilgarn Craton, withthe clastics of the Padbury Basin now considered to have been deposited in a pro-foreland basin associated with the Glenburgh Orogeny (Occhipinti et al., 2017).

As a result of Glenburgh orogenesis, depocenters subsequently migrated to the east, with the largely unconformable development of the Earaheedy Basin in the Orosirian, which variously overlies parts of the northeastern margin of the Yilgarn Craton and the Yerrida Basin (Sheppard et al., 2016a). Revised dating of the Earaheedy Basin succession has suggested coeval deposition of its oldest sediments and the youngest Padbury Basin sediments further west (Sheppard et al., 2016a). Northeast facing passive margin sedimentation in the Earaheedy Basin was terminated by ~1.8 Ga and the Yapungku and Capricorn Orogenies associated with the collision of the North Australian Craton and WAC (Johnson, 2013; Pirajno et al., 2009), with any evidence of later sedimentation across the northern Yilgarn Craton margin subsequently eroded.

Yerrida Basin

The Yerrida Basin is developed unconformably over the northern Yilgarn Craton margin, although the contact is faulted against the same Archean basement in places at the present day (Occhipinti et al., 2017). The Windplain Group, comprising the Juderina Formation and overlying Johnson Cairn Formation, is the oldest depositional sequence in the Yerrida Basin (Figure 2.5). The Juderina Formation is characterized by cross-stratified quartz sandstone to siltstone and conglomerate and locally significant volcanics, all of which thicken to the north (Occhipinti et al., 1997). Two distinctive members in the lower Juderina Formation have been defined; a basal quartzite Finlayson Member and an overlying stromatolitic carbonate with occasional evaporates known as the Bubble Well Member (Figure 2.5; Geoscience Australia and the Australian Stratigraphy Commission, 2017). The Johnson Cairn Formation conformably overlies and is in parts transitional from the Juderina Formation. The Johnson Cairn Formation is dominated by pyritic, finely laminated dark mudstone and shale with local graded silts, soft-sediment deformation, and dolomitic siltstoneand mudstone.

The Mooloogool Group disconformably overlies the Windplain Group and consists of (from oldest to youngest) the Thadunna, Doolgunna, Killara and Maraloou Formations (Figure 2.5; Occhipinti et al., 2017). The coarser clastics of the Thadunna and Doolgunna Formations are thought to have been derived from Archean basement, as well as local mafic volcanics (Killara Formation), with which the formations interdigitate (Pirajno et al., 2004). Emplacement of the mafic volcanics continued during deposition of the finely laminated carbonaceous shales of the overlying Maraloou Formation, as indicated by peperite textures and geochronology of thermal metamorphic mineral phases (Rasmussen and Fletcher, 2002).

Bryah Basin

The Bryah Group is represented by the conformable Karalundi, Narracoota, Ravelstone and Horseshoe Formations, which were deposited a few tens of millions of years prior to the Glenburgh Orogeny (~2030-2010 Ma) and are interpreted to represent continental rifting along the northern Yilgarn Craton margin (Figure 2.5; Occhipinti et al., 2017; Pirajno et al., 2004; Pirajno and Occhipinti, 2000). The basal Karalundi Formation is dominated by siliciclastics that interdigitate and are succeeded by mafic volcanics and volcanosedimentary units with subordinate clastic horizons of the Narracoota Formation (Hawke et al., 2015). The Narracoota Formation is in turn conformably overlain and interfingered by the Ravelstone Formation, which marks a return to siliciclastic deposition and dominance of quartz wacke, siltstone and mudstone with isolated felsic volcanics (Occhipinti et al., 2017). Capping the sequence, a succession of dominantly fine-grained manganiferous mudstone with banded iron-formation is attributed to the Horseshoe Formation. This youngest unit is conformable and transitional from the underlying Ravelstone Formation.

Padbury Basin

The Padbury Group (Figure 2.5) is variously faulted against Bryah Group sediments or Archean Yilgarn Craton basement, or rests unconformably over the Horseshoe Formation of the Bryah Group (Pirajno et al., 1998). Up to 10 km of clastics within the Padbury Group are inferred to have accumulated in a foreland basin and

derived from northward shedding from the Yilgarn Craton margin (Martin, 1998; Occhipinti et al., 2004). The basal turbiditic Labouchere Formation is dominated by an upward-coarsening clastic succession that grades into the overlying Wilthorpe Formation (Pirajno et al., 2004). Deposition of the finer clastics and ironstones of the Robinson Range and Millidie Creek Formations are interpreted to have occurred in shallower conditions (Krapez and Martin, 1999).

Earaheedy Basin

The Earaheedy Basin unconformably overlies the Yilgarn Craton and Yerrida Basin, and accumulated a total ~3 km of sediments in dominantly shallow marine and coastal settings that deepened towards the north and northeast (Jones et al., 2000; Pirajno et al., 2009; 2004). Paleocurrent indicators(Sheppard et al., 2016a; and references therein) suggest derivation of clastics from the south and west, with detrital zircon geochronology indicating the Yilgarn Craton (Narryer Terrane and Murchison Province) and the Glenburgh Terrane were the dominant source regions (Halilovic et al., 2004; Matonia, 2009). Traditionally the Earaheedy Basin sequence has been divided into the Tooloo Group and overlying Miningarra Group (Figure 2.5). However, recent work has suggested the basin succession comprises a greater number of distinct predominantly coastal to shallow-marine unconformity-bound packages deposited over the course of almost 200 Ma (Figure 2.2; ~1990-1820 Ma; Sheppard et al., 2016a).

The basal Tooloo Group was previously considered to consist, from oldest to youngest, ofthe Yelma, Frere and Windidda Formations. New age constraints (Sheppard et al., 2016a) and reinterpretation of the nature of unit boundaries (Frere Formation is unconformable on the Yelma Formation; Akin et al., 2013) has seen the Frere Formation excluded from the Tooloogoo Group, and the Windidda Formation relegated to member status. The Yelma Formation thickens towards the NW and variably consists of fluvial to shallow marine clastics and lagoonal carbonates (Sweetwaters Well Member; Hocking et al., 2000). The now independent overlying Frere Formation comprises granular iron beds deposited in a shallow marine setting with intervening shales, siltstones and carbonates driven by sea-level change. The Windidda Member at the top of the Frere Formation (formally considered an independent formation) is similarly composed of ferruginous shale and siltstone, but also stromatolitic carbonate, and was deposited in a shallower supra-tidal setting (Halilovic et al., 2004; Pirajno et al., 2009).

The overlying Miningarra Group contains the Chiall Formation, Wongawol Formation, Kulele Limestone and Mulgarra Sandstone. The Chiall Formation comprises three members (Karri Karri, Wandiwarra and Princess Ranges Members) that grade from intercalated shale, siltstone and sandstone into coarser sandstone and breccias. The relatively thick overlying Wongawol Formation comprises a mixture of ferruginous shale, coarser clastics and glauconitic carbonates with thin distal volcaniclastic horizons, all associated with shallow marine to terrestrial deposition (Matonia, 2009). The Kulele Limestone consists of shallow marine cyclical alternations of carbonates and fine clastics deposited in a sub-tidal to inter- tidal environment (Jones et al., 2000).

The sandstone, shale and minor carbonate facies of the overlying Mulgarra Sandstone are thought to have been deposited in a coastal environment experiencing fluctuations in sea- level driving periodic exposure and submergence. Although disputed (Pirajno et al., 2009), the Mulgarra Sandstone has been inferred to be separated from the underlying Kulele Limestone by an interpreted disconformity, as well as available age constraints (Sheppard et al., 2016a).

Outliers of the sandstone-dominated Mount Leake Formation overlie the Goodin Fault that locally juxtaposes the Bryah and Padbury Groups, and has thus been interpreted to indicate a far greater original extent for sedimentation associated with the Earaheedy Basin (Pirajno et al., 2009; and references therein).

- **Central Capricorn Bangemall Supergroup**

The Mesoproterozoic Bangemall Supergroup comprises the youngest preserved sedimentary successions of the Capricorn Orogen and is developed nonconformably across stabilized and exhumed Archean and Paleoproterozoic basement, and unconformably across Paleoproterozoic sedimentary basins along the Pilbara and Yilgarn cratonic margins (Martin and Thorne, 2004). In the east, Neoproterozoic to Paleozoic sediments of the Officer Basin succeed sediments of the Bangemall Supergroup. Between four and 12 km of mixed siliciclastic and carbonate deposits are preserved within six major depositional packages (DP) within the Edmund (DP 1-4) and Collier Basins (DP 5-6; Figure 2.6). The older (Calymmian) Edmund Basin is temporally constrained by the older Durlacher Supersuite and Mangaroon Orogeny (1680-1620 Ma) and modification from the Mutherbukin Tectonic Event (~1385- 1200 Ma), as well as intrusion by a number of dolerite units (Kulkatharra ~1080 Ma, Narimbunna ~1450 Ma, Waldburg ~1510 Ma; Figure 2.2). The overlying Collier Basin was not affected by the Mutherbukin Tectonic Event but was deformed during the ~1030-950 Ma Edmunduan Orogeny and was intruded by the ~1080 Ma Kulkatharra Dolerite (Figure 2.2). Intracratonic extensional reactivation of basement faults is implicated for generation of accommodation space in the Edmund Basin, with syndepositional fault activity driving considerable lateral thickness and facies variations along the pronounced NW-SE trend of the basin (Figure 2.6; Cutten et al., 2016; Martin and Thorne, 2004). Although most of the Bangemall Supergroup sediments were deposited distal to their original basin margins, paleocurrent data suggest a broadly northern transport origin for sediments in DP 1-3, a southeastern derivation in DP4 and mixed south-eastern and northern sourcing in DP5 (Figure 2.6; Martin et al., 2008; Martin and Thorne, 2004). Existing detrital zircon data suggest significant recycling of sedimentary units to the north, as well as, derivation from the Gascoyne Complex to the west (Cutten et al., 2016; Martin et al., 2008). Further east, the Scorpion (lower Edmund Group), Manganese (Collier Group) and Salvation Groups (Collier Group) are all considered correlatives of the Edmund and Collier Basins (Figure 2.1), while to the south, the Mt. Augustus Sandstone outlier, has been correlated with the basal Collier Group (Yilgatherra Formation; Martin et al., 2008).

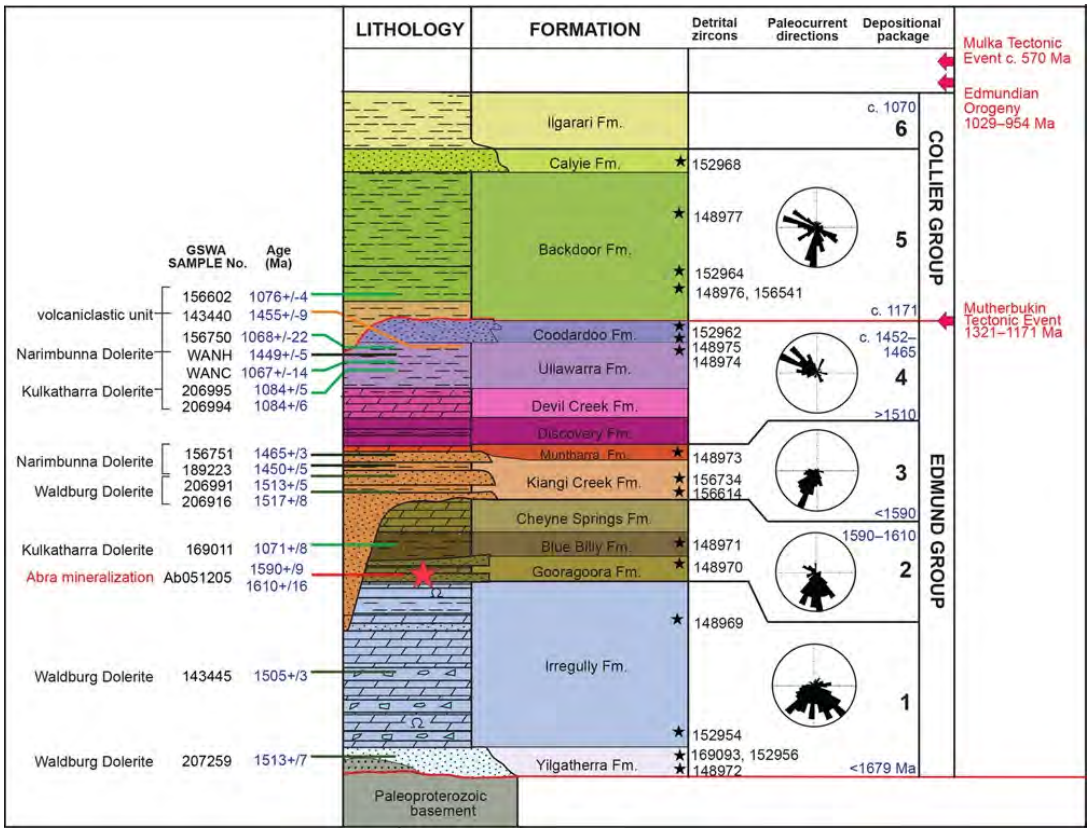

Figure 2.6. Lithostratigraphy of the Mesoproterozoic sedimentary basins of the Bangemall Supergroup. Reproduced from Cutten et al. (2016).

The Edmund Group comprises a basal sequence of the Yilgatherra and Irregully Formations of DP1, which record deepening from fluvial dominated sandstones to shallow marine clastics and stromatolitic dolostones (Martin and Thorne, 2004). The Gooragoora Formation of DP2 conformably overlies the Irregully Formation, marking the progradation of deltaic sandstone and the start of another transgressive sequence with overlying deeper water carbonaceous siltstones of the Blue Billy Formation. The overlying intercalated dolostone-clastic sequence of the Cheyne Springs Formation are interpreted to represent a return to shallower-water shelf conditions (Martin et al., 2008). The base of DP3 is erosional, marking a distinct disconformity, with overlying mixed deeper shelf carbonaceous siltstone, turbiditic and mass-flow sandstone (Kiangi Creek Formation) giving way to occasionally stromatolitic dolostone (Muntharra Formation) as a result of reduced clastic supply to the deeper shelf (Martin and Thorne, 2004). Renewed transgression is represented by the sediments of DP4 and, in particular, the deposition of anoxic basinal siltstones of the Discovery Formation across the northern margin of the Edmund Basin. This is in turn conformably succeeded by the Devil Creek and Ullawarra Formations tracking shallowing through stromatolitic dolostones to rippled silt and sandstones, prior to renewed deepening to turbiditc facies in the Coodardoo Formation (Martin and Thorne, 2004).

Sediments of the Collier Basin rest on a distinct unconformity that in parts has completely eroded the uppermost unit of the underlying Edmund Basin (Coodardoo Formation). The thick Backdoor Formation comprises laminated siltstone and interbedded thin sandstone, and together with the shallow-marine sandstones of the overlying Calyie Formation constitutes DP5 in an upward shallowing progradational shelfal sequence (Martin and Thorne, 2004).

The Ilgarari Formation is the sole constituent unit of DP6 and conformably overlies the Calyie Formation. The characteristic laminated pyritic and carbonaceous siltstones of the Ilgarari Formation indicate a final major transgressive episode across the region (Cutten et al., 2016).

2.3 Methodology

This report combines data obtained via Secondary Ion Mass Spectrometry (SIMS, specifically Sensitive High Resolution Ion Microprobe, i.e. SHRIMP) and LA-ICPMS, which have been demonstrated to be equivalent through comparable standard analyses and technique integration (Jahn, 2018). New age and geochemical data reported herein were collected using SIMS (secondary ion mass spectrometry; O-isotopes) and laser based mass spectrometer systems (U/Pb ages, Hf-isotopes and trace-element geochemistry). Over 4000 split-stream U/Pb and trace-element analyses were conducted on zircons from 91 samples of igneous and metamorphic crystalline rocks (~50 analyses/sample) focussed on the northern margin of the Yilgarn Craton, Archean Inliers on the southern and northern margins of the Capricorn Orogen, as well as the major intrusive units of the Gascoyne Complex associated with cratonic assembly. Selected ~850 zircons (of the ~2000 that produced concordant data) were analysed for additional Hf- and O-isotope data. A comprehensive database of detrital zircon geochronology has been compiled from across the Capricorn Orogen (totalling 5610 analyses). A further 6046 new, split-stream integrated geochronological and trace-element geochemical analyses of detrital zircons have been undertaken from outcrop and core samples across the Paleoproterozoic Yerrida, Bryah and Padbury Basins and through the Mesoproterozoic Edmund and Collier Basins. These new data have targeted previously unworked stratigraphy, as well as, more continuous sections around critical intervals of basin development.

2.3.1 Sample acquisition and processing

Selected rocks were variously crushed or disaggregated (Selfrag electro-pulse- disaggregation) to reduce samples to their sand-gravel grade mineral components. Coarser (> ~350 µm) and finer (< ~30 µm) components were removed using a combination of sieves and elutriation with resulting residues subjected

to heavy liquid separation (typically alkali metal- polytungstate @ ~2.9 g/cm^3 and methylene iodide @ ~3.3 g/cm^3). Depending on volumes of resulting concentrates, residues were further subjected to Frantz magnetic susceptibility separation to concentrate zircons.

Zircon grains were hand-picked from heavy mineral concentrates under a reflected light binocular microscope and mounted in rows on double-sided tape with standard reference materials for both U-Pb geochronology and Hf isotope characterization, including: 91500 (Wiedenbeck et al., 1995), GJ-1 (Jackson et al., 2004), OGC-1 (Stern et al., 2009), BR266 (Stern, 2001), Mud Tank (Griffin et al., 2007), MU31 (Fisher et al., 2014) and Plešovice (Sláma et al., 2008). For analyses conducted at Curtin University, standard mounts exist for use with the laser system and so are unnecessary to mount with unknowns. For magmatic zircon samples, typically 50-100 representative crystals were picked, while for detrital zircon samples >150 representative grains were picked (where available). Standard epoxy resin was poured over the samples to make 25 mm rounds, which were left to cure before grinding/cutting to ~5mm thickness and polishing the mounted surface to half-grain thickness to expose the internal structure of the zircons. Mount faces were polished to a 1 µm finish using successively finer diamond paste abrasives.

Mounts were preliminarily imaged using reflected light microscopy in order to identify cracks and inclusions that should be avoided during analysis. Mounted zircons were then imaged using electron microscopy (back-scattered-electrons, BSE and cathodoluminescence, CL) to better constrain compositional variations and the growth history of individual zircons in terms of growth history, cores, rims, metamict zones etc. that could affect analyses and therefore dictate the position of analytical spots (Hanchar and Miller, 1993; Nasdala et al., 2003). All electron microscopy was undertaken at the John de Laeter Centre using a Tescan Mira3 field emission scanning electron microscope (FESEM) fitted with a KE Developments CL detector using a 12 kV beam current.

2.3.2 Laser Ablation Split Stream Inductively Coupled Plasma Mass Spectrometry (LASS-ICPMS) Analyses

Two separate LASS-ICPMS systems were utilized during data collection. Data reduction, including baseline, instrument-drift and mass-bias correction, error propagation and downhole fractionation calculations, were undertaken using Iolite v. 2.5 (Paton et al., 2011; Paton et al., 2010). Uncertainties are quoted at the 2σ level and include errors from counting statistics, as well as U–Pb calibration errors based on the reproducibility of U–Pb measurements of the primary standard. Where appropriate, REE values were normalized to chondritic values (Anders and Grevesse, 1989), given as X_N values (X= relevant element).

All data are reported as $^{207}Pb/^{206}Pb$ ages where grains are >1500 Ma and $^{206}Pb/^{238}U$ for the limited analyses < 1500 Ma (Spencer et al., 2016). For the purpose of calculating crystallisation ages of magmatic zircons, single populations (where multiple analyses are considered together to define the age of a geological event) were identified using the reduced chi-squared statistic (Wendt and Carl, 1991) following the procedures outlined in Spencer et al. (2016). Uncertainties of weighted mean values for pooled analyses and concordia ages are at the 95% confidence level, with MSWD calculated for concordance and equivalence on concordia ages. Data >10% discordance are excluded from Concordia diagrams. Concordia diagrams were constructed using Isoplot 3.75 (Ludwig, 2012). The term 'inherited zircon' will be used to define any zircon that is interpreted not to have newly crystallised from the melt in the rock of interest (i.e. it is older that the crystallisation of the magmatic host rock). Detrital data are considered concordant within 10% of age agreement between the $^{207}Pb/^{206}Pb$ and $^{206}Pb/^{238}U$ systems.

- **U-Pb geochronology integrated with trace-element geochemistry analyses LASS-ICPMS**

The LASS analytical set-up at the University of California, Santa Barbara (UCSB) consists of a Photon Machines Analyte 193ArF laser ablation system coupled to an Agilent 7700x quadrupole ICP and a Nu Plasma high

resolution multi-collector (MC)-ICPMS. The detailed outline of the LASS instrumentation and techniques is given in Kylander-Clark et al. (2013). Operating conditions for the instrument were routine (e.g. Cottle et al., 2012), with a 25-30 µm ablation spot size, a fluence of ~ 1-4 J/cm^{-2}, and a repetition rate of 3-4 Hz (for a 30-second total of 120 shots), which ablates at a rate of 0.05–0.15 µm/pulse. Data acquisition consists of (1) two laser pulses at the start of measurement to remove surface contamination, (2) 15-second washout period during which the background signal is collected, (3) 25- seconds of continuous ablation during which data are collected, and (4) ~three seconds with no laser firing to allow dispersal of all sample material before the next analysis. The ablated material is carried by He gas from the sample cell and then mixed with Ar to stabilize the aerosol before input to the plasma. Immediately after mixing, the ablation stream is split approximately evenly and directed into each mass spectrometer. The detection system on the Nu Plasma at UCSB allows for simultaneous measurement of ^{232}Th and ^{238}U on Faraday cups equipped with 1011 ohm resistors and ^{208}Pb, ^{207}Pb, ^{206}Pb and ^{204}Pb and ^{204}Hg on four ETP discrete dynode electron multipliers. Data for magmatic zircon analyses were collected over two separate analytical sessions over two years (2014 and 2015). During the second analytical session the detection system was set up for measurement of ^{208}Pb, ^{207}Pb ^{206}Pb, ^{232}Th and ^{238}U on Faraday cups equipped with 1011 ohm resistors and ^{204}Pb + Hg and ^{202}Hg on two ETP discrete dynode electron multipliers. A sample-standard bracket approach was used, with 91500 zircon used as the primary reference material to monitor and correct for mass fractionation and instrumental drift. Secondary reference zircons GJ1 and Plešovice were used to monitor data accuracy and precision. The accuracy of ^{207}Pb/^{206}Pb ratios was verified by comparison with the Archean OGC-1 zircon standard (Stern et al., 2009).

Accuracy is within 0.01–1.16% for secondary reference materials GJ1, Plešovice, OGC-1 and BR266 analysed. Precision on individual analyses depends on the volume and concentrations of U, Th and Pb. Secondary standards after normalisation to the primary standard yield <3% precision on ^{206}Pb/^{238}U ratios and typically 5-11% precision on ^{207}Pb/^{206}Pb ratios. During the 2015 session the accuracy of the secondary reference material was within 0.02–0.81% of the published reference value.

At UCSB, trace element concentrations in magmatic zircons were measured simultaneously with U-Pb geochronology determination on the Agilent 7700x quadrupole ICP-MS. GJ1 zircon was used as a calibration standard to monitor and correct for mass fractionation and instrumental drift. Any zircon analyses that sampled inclusions were removed (e.g. Lu et al., 2016). GJ1 was run every 8-10 unknowns per sample, with three analyses at the beginning and end of each run. Stoichiometric major elements were used for calibration of trace elements in each phase. Stoichiometric Zr was used as the internal standardisation element for zircon (43.14 wt %). Measured trace elements comprise, ^{28}Si, ^{90}Zr, ^{31}P, ^{49}Ti, ^{89}Y, ^{93}Nb, ^{139}La, ^{140}Ce, ^{141}Pr, ^{146}Nd, ^{147}Sm, ^{153}Eu, ^{157}Gd, ^{159}Tb, ^{163}Dy, ^{165}Ho, ^{166}Er, ^{169}Tm, ^{172}Yb, ^{176}Lu, ^{179}Hf, ^{232}Th, and ^{238}U. Uncertainties on individual spot measurements are cited at 2σ level and include the internal uncertainties associated with counting statistics only.

Detrital zircons were analysed at the Geohistory facility of the John de Laeter Center at Curtin University, Western Australia. U-Pb and trace element analyses were performed simultaneously with a LASS-ICPMS. The LASS is fitted with a Resonetics S-155-LR 193 nm excimer laser ablation system coupled to an Agilent 7700x quadrupole ICPMS and a Nu Instruments Plasma HR multi-collector ICPMS. Isotopic data pertaining to the U–Pb system were collected in time resolved mode for a total of 90 s for each analysis.

Operating conditions followed those set out by Kylander-Clark et al. (2013), where ion counters were used to measure Pb isotopes and a Faraday cup was used for ^{238}U. For older grains, or those with high Pb concentrations, (i) laser energies were reduced, (ii) spot sizes were reduced) or (iii) Faraday cups were used to measure both U and Pb isotopes, in order to prevent overloading and tripping of the ion-counters. Spot sizes was adapted from 23 µm to 33 µm, depending on the size of zircon grains in the samples and Pb concentrations in the grains. Every 20 analyses, the accuracy of the data was checked by analysing zircon standards, including GJ1, Plešovice, Z91500 and OG1. The 1σ output errors calculated with the Iolite software

were integrated with additional uncertainties obtained from OG1 and Plešovice standards to produce final propagated errors at a 2σ level. Trace-elemental abundances of the analysed zircons were measured on the quadrupole using GJ1 as a primary standard.

- **Lu-Hf isotope analyses LA-ICPMS**

Lu–Hf isotope data were collected using a NuPlasma high resolution MC-ICPMS at UCSB coupled with the same laser and ablation cell as described above. Hafnium isotope measurements were performed on ten Faraday cups (also with 1011 ohm resistors) in a central array at 1 atomic mass unit (amu) spacing. Instrument settings were established first by analysis of 10 ppb solutions of JMC475 and a Spex Hf solution, and then by analysis of 10 ppb solutions containing Spex Hf, Yb, and Lu. Laser ablation analyses were conducted with a laser beam diameter of ~50 µm; yielding approximately 0.8 volts/ppm Hf. Ablation pits were located on top of the LASS analysis pits. Data acquisition consists of (1) two laser pulses at the start of measurement to remove surface contamination, (2) 40-second of baseline acquisition by the on-peak-zero (OPZ) method, (3) 30-seconds of continuous ablation during which data are collected (laser frequency - 10 Hz; spot size - 44 µm), and (4) ~three seconds with no laser firing to allow decay of the previous signal before the next analysis. The best estimate of analytical uncertainty (external precision and accuracy) is represented by the total deviation of $^{176}Hf/^{177}Hf$ from values determined by ID-TIMS dissolution methods. Mud Tank zircon was used as the primary reference material. A combination of 91500, Plešovice, GJ1 and MU31 were used as secondary standards to monitor the precision and accuracy of each analytical session. Analyses of secondary standards yield $^{176}Hf/^{177}Hf$ within uncertainty of published values; 0.282310 ± 0.000115 (n = 34, 2014) and 0.282286 ± 0.000092 (n = 24, 2015) for 91500 (0.282308 ± 0.000006; Blichert-Toft, 2008); 0.282493 ± 0.000052 (n = 12, 2014) and 0.282498 ± 0.000089 (n = 27, 2015) for Plešovice (0.282482 ± 0.000013; Sláma et al., 2008); 0.281979 ± 0.000110 (n =12, 2014) and 0.282001± 0.000073 (n = 18, 2015) for GJ1 (0.282000 ± 0.000005; Morel et al., 2008).

- **Secondary Ion Mass Spectrometry O-isotope analyses**

Oxygen isotope ratios ($^{18}O/^{16}O$) of magmatic zircons were determined using a Cameca IMS 1280 multi-collector ion microprobe located at the Centre for Microscopy, Characterisation and Analysis (CMCA) at the University of Western Australia. Analytical conditions were similar to those outlined in detail by Kita et al. (2009). Analyses were performed within the same CL zones of zircon grains as used for U–Pb and Lu–Hf analyses.

Oxygen secondary ions are sputtered from the sample by bombarding its surface with a 10 kV, Gaussian Cs+ beam with a 3 nA intensity and a total impact energy of 20 keV. This primary beam was rastered over a 10 × 10 µm area at the surface of the sample. Secondary ions are admitted in the double focusing mass spectrometer within a 110 µm entrance slit and are focused in the centre of a 4000 µm field aperture (×130 magnification). Secondary ions are energy filtered using a 40 eV band pass with a 5 eV gap toward the high-energy side.

Isotopes ^{16}O and ^{18}O were collected simultaneously in Faraday cup detectors fitted with 1010 Ω (L'2) and 1011 Ω (H'2) resistors, respectively, and operating at a mass resolution of ∼2430. The magnetic field was regulated using NMR control.

Each analysis includes a pre-sputtering step over a 15 × 15 µm area during 30 s and the automatic centering of the secondary ions in the field aperture, contrast aperture and entrance slit. Each analysis then consists of 20 four-second cycles. Penglai zircon (5.31‰; Li et al., 2010) was used as the primary reference material to monitor and correct for mass fractionation and instrumental drift. Secondary reference zircon Temora-2 (8.2‰; Black et al. 2004) was used to monitor data accuracy and precision. Analyses of secondary standards yield average $\delta^{18}O$ values of 8.32 ± 0.54‰ (2σ), in good agreement to the published value (8.2 ± 0.1‰; Black et al., 2004). The external precision based on analyses of the standard was 0.52‰ (2σ) across the total of 13

analytical sessions. All oxygen isotope values reported here are in per mil (‰) relative to VSMOW (Vienna Standard Mean Ocean Water).

2.4 Magmatic zircon geochronology and geochemistry

Geochronological and isotopic data can constrain the relationships between crystalline crustal rocks in the Capricorn Orogen whether part of intrusive bodies, basement inliers or the bordering Yilgarn and Pilbara Cratons. The data reported herein are used to identify regions with a shared history of magmatic emplacement corresponding to a common geological and crustal evolution.

Zircon trace element compositions can provide insight to the minerals original protolith and tectonic environment. Numerous studies have identified systematic correlations between elemental ratios in zircon and the tectono-magmatic provenance and magmatic composition of parent rocks (Belousova et al., 2002; Grimes et al., 2007; Grimes et al., 2015; Guo et al., 2017; Pearce, 2008). Generally trace element abundances increase from mantle derived rocks, toward evolved granitoids and pegmatites (Belousova et al., 2002). Yttrium can be used as an indicator of the overall abundance and enrichment of REE into a zircon. The elements U and Th are enriched in syenite, pegmatites, granitoids and larvikites, less abundant in dolerite and lamproites and depleted in carbonatite and kimberlite rocks. Similarly, Nb/Yb ratios plotted against U/Yb ratios have proven useful in constraining the tectono-magmatic setting of zircon crystallisation, distinguishing Continental Arc from Ocean Island and Mid Oceanic Ridge Basalt (Grimes et al., 2007; 2015; Pearce, 2008).

2.4.1 Narryer Terrane

- **U–Pb geochronology**

The dataset from the Narryer Terrane consists of nine samples, and the analysed zircon cover a period of 1209 Myr, with individual $^{207}Pb/^{206}Pb$ ages ranging between c. 3766 and c. 2557 Ma (Figure 2.7; Table 2.1). Most of the granites were generated during magmatic episodes at c. 3350 Ma, c. 2720 Ma and c. 2620 Ma. The zircon geochronology of these samples is dominated by >50% inherited material, and although granites and gneisses older than c. 3400 Ma are not preserved, the inherited zircon record shows that granite magmatism of this age and older is well documented.

- **Zircon trace-element composition**

Zircon grains from the Narryer Terrane samples have trace-element compositions typical of continental zircon, with both magmatic and inherited populations plotting within continental arc-type zircon fields (Figure 2.8).

Chondrite-normalised REE element patterns of the magmatic zircon from the Narryer Terrane granites are characterised by strong positive Ce and negative Eu anomalies and a positive heavy REE (HREE) slope (Figure 2.8). Magmatic zircon trace element signatures indicate no evidence of co-crystallisation with garnet (i.e. flat HREE pattern with Lu/Gd <3 coupled with no negative Eu anomaly, Eu/Eu* >0.75). The zircon record a range of Yb_N/Gd_N of 6-59 and Eu/Eu* of 0.01-0.81, indicating formation in lower pressures than eclogitic minerals (<1.2 GPa, <45 km depth; Rubatto and Hermann, 2007).

All Narryer Terrane samples record zircon Ti crystallisation temperatures with averages between 726 and 832°C. These temperatures are comparable with the low-T inheritance-rich granitoids with T_{Zr} <800°C of Miller et al. (2003) that are interpreted as forming in regions of crustal thickening.

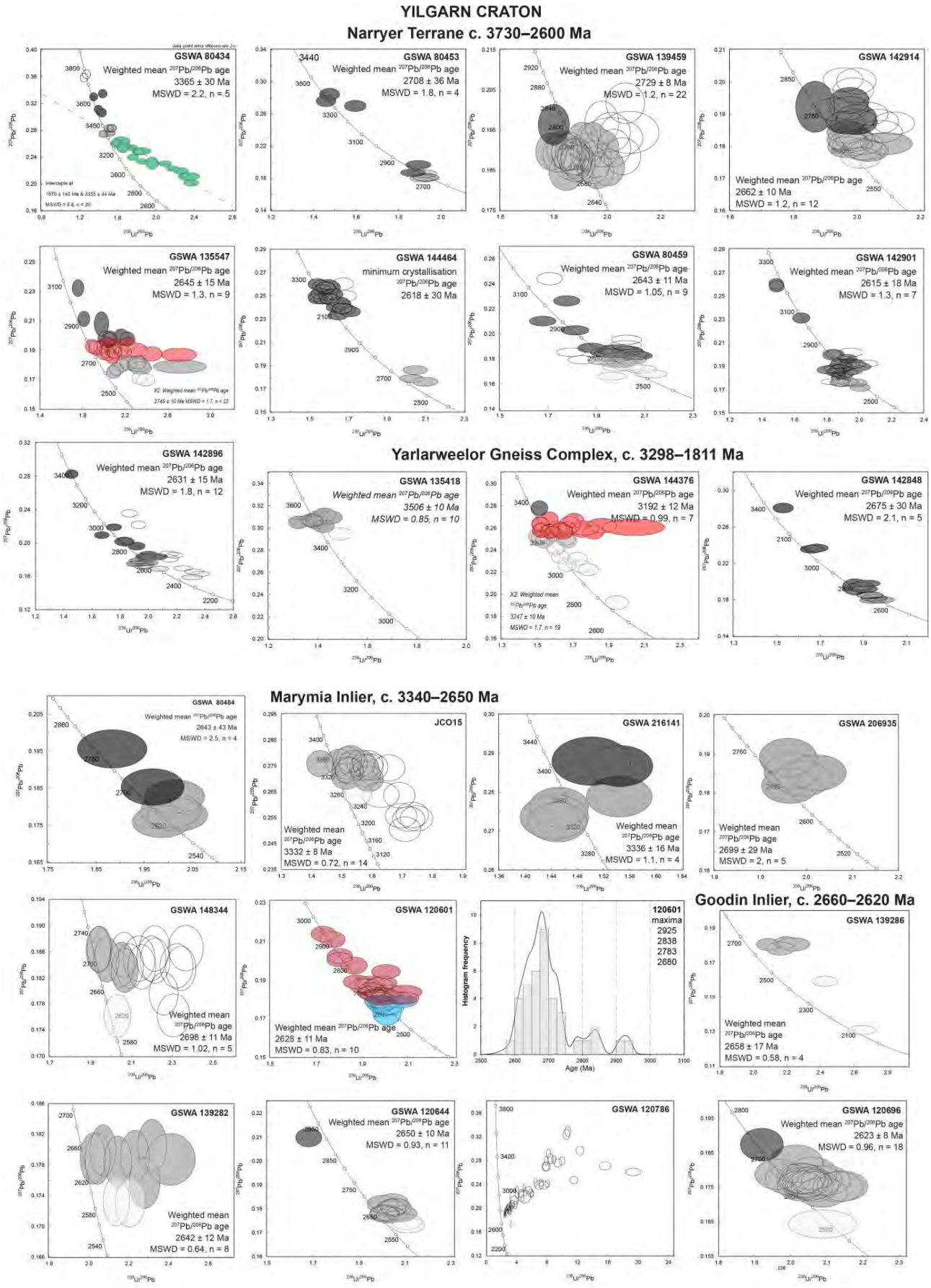

Figure 2.7 continues with caption overleaf.

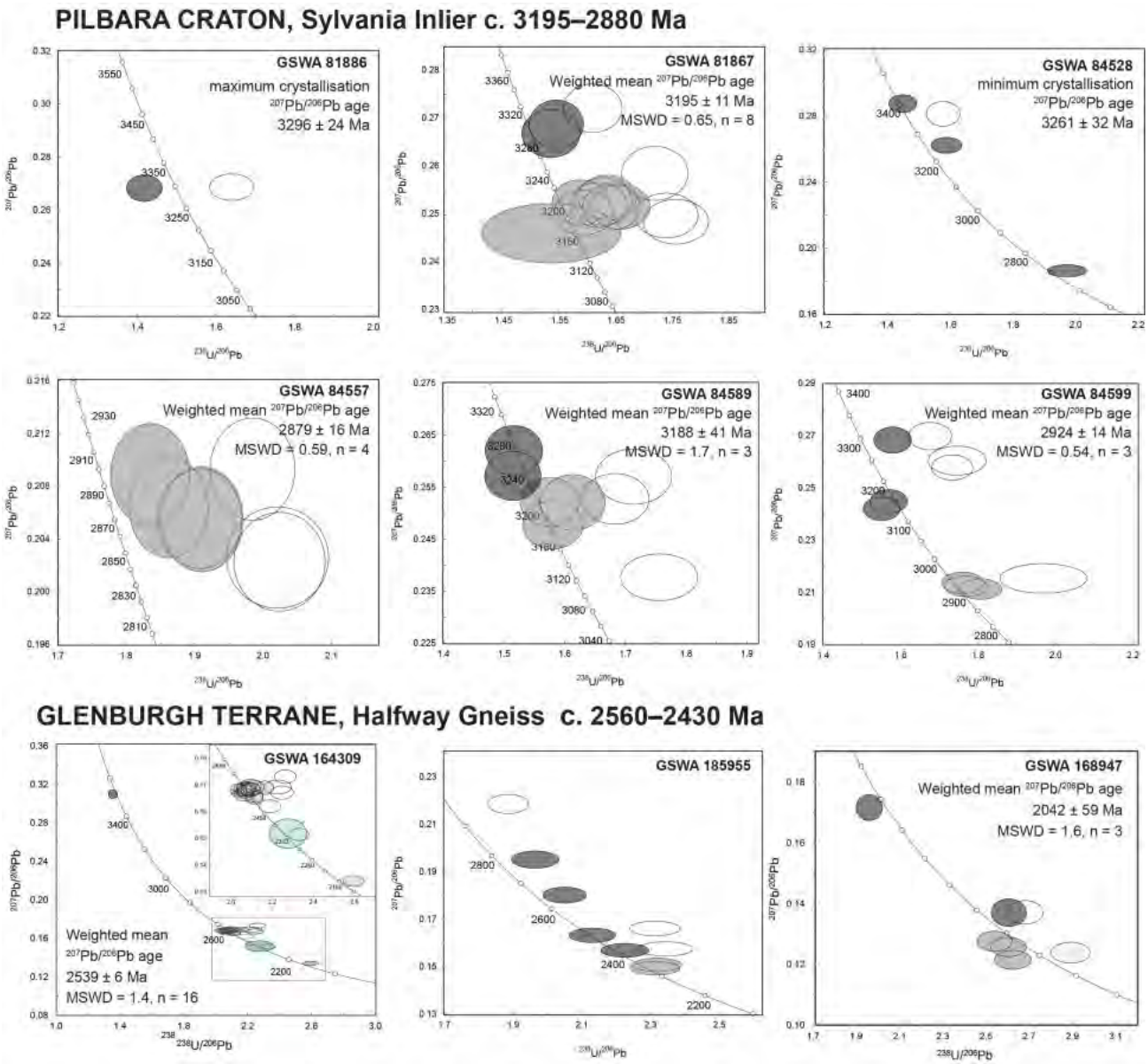

Figure 2.7. Concordia diagram showing the subset of Archean zircon with <10% discordance. Grey ellipses indicate analyses used to calculate Group 1 (crystallisation age). Black ellipses indicate inherited zircon (Group X). Red ellipses indicate analyses used to calculate Group 2 (inherited zircon group). Green ellipses indicate younger (metamorphic) zircon (Group M). Light grey ellipses indicate radiogenic Pb-loss (Group P). Hollow ellipses indicate outside discordance threshold (Group D). Blue ellipses indicate Group Y (youngest detrital zircon). Dark red ellipses indicate Group S (older detrital zircon).

Table 2.1 Summary of sample descriptions and U–Pb LASS data for Archean samples.

Sample	unit[1]	Lithology[2]	Pb–Pb age (Ma)[2]	Inheritance (Ma)	Pb–Pb age (Ma)[3]	T_{ZR} (°C)	Lat	Long
80434	NT	granodiorite	3365 ± 30	3766–3529	-	832	-25.773	117.484
80453	NT	metamonzo-granite	2708 ± 36	3400–2752	-	739	-25.806	117.226
139459	NT	monzogranite	2728 ± 8	2785	2738 ± 5	765	-25.567	116.867
142914	NT	monzogranite	2662 ± 10	2779–2719	2615 ± 2	724	-25.723	117.139
133547	NT	granitic gneiss	2645 ± 15	2916–2702	-	816	-25.455	117.007
144464	NT	metgranite	(2618 ± 37)	3233–3078	-	-	-25.522	117.086
80459	NT	felsic gneiss	2643 ± 11	3027–2678	-	739	-25.525	117.21
142901	NT	monzogranite	2615 ± 18	3249–2678	-	726	-25.567	117.438
142896	NT	gneiss	2631 ± 15	3378–2685	2576 ± 11	744	-25.599	117.243
135418	YGC	granitic gneiss	*3506 ± 10*	-		760	-25.474	177.889
144376	YGC	metagranite	3187 ± 10	3351	-	-	-25.484	117.434
142848	YGC	monzogranite	2691 ± 39	2654–2648	-	676	-25.521	117.645
80484	YGC	metagranite	2643 ± 43	2790–2702	-	808	-25.621	115.626
JC15	MI	granitic rock	3332 ± 8	-	-	724	-25.476	119.465
216141	MI	granitic rock	3336 ± 16	3406–3400		735	-25.496	119.370
148344	MI	metagranite	2698 ± 11	-	-	698	-25.181	120.024
206935	MI	granitic gneiss	2699 ± 29	-	-	762	-25.175	119.505
120601	MI	metasediment	2588 ± 53	2936–2655	-	756	-25.664	119.002
139286	GI	granitic rock	2658 ±17	-	-	814	-25.752	119.323
139282	GI	granitic rock	2642 ± 9	-	-	787	-26.056	119.236
120644	GI	granitic rock	2650 ± 11	2905	-	827	-25.968	119.203
120678	GI	granitic rock	-	-	-	850	-25.793	119.429
120696	GI	granitic rock	2623 ± 8	2720	-	815	-25.891	119.260
152855	EGST	granitic rock	2668 ± 31	2778–2726	-	639	-25.908	120.433
152879	EGST	granitic rock	-	2892–2531	-	-	-25.643	120.215
81886	SI	granitic rock	(3296 ± 34)	-	-	-	-23.723	119.920
81867	SI	monzogranite	3195 ± 11	3299–3288	-	-	-23.716	119.773
84528	SI	granitic rock	(3261 ± 32)	3405–2710	-	-	-23.700	119.333
84557	SI	granitic rock	2879 ± 14	-	-	-	-23.486	119.502
84589	SI	Granodiorite	3188 ± 41	3259–3230	-	773	-23.625	119.991
84599	SI	monzogranite	2924 ± 14	3296–3133	-	751	-23.375	119.973
185955	HG	granitic gneiss	-	2788–2341	2527 ± 9	689–871	-24.909	116.294
164309	HG	granodiorite gneiss	2539 ± 6	3521	2548 ± 8	-	-25.086	116.142
168947	HG	monzogranite gneiss	2042 ± 59	2574–2188	2006 ± 6	600–631	-25.033	115.828

[1]NT= Narryer Terrane, YGC= Yarlarweelor Gneiss Complex, MI= Marymia Inlier, GI= Goodin Inlier, EGST = Eastern Goldfields Superterrane, SI= Sylvania Inlier, HG= Halfway Gneiss. [2]Crystallisation age ($^{207}Pb/^{206}Pb$) established by LASS, ages in brackets() indicate maximum crystallisation age. [3]Crystallisation age ($^{207}Pb/^{206}Pb$) established by SHRIMP (GSWA). (-) indicates no value obtained.

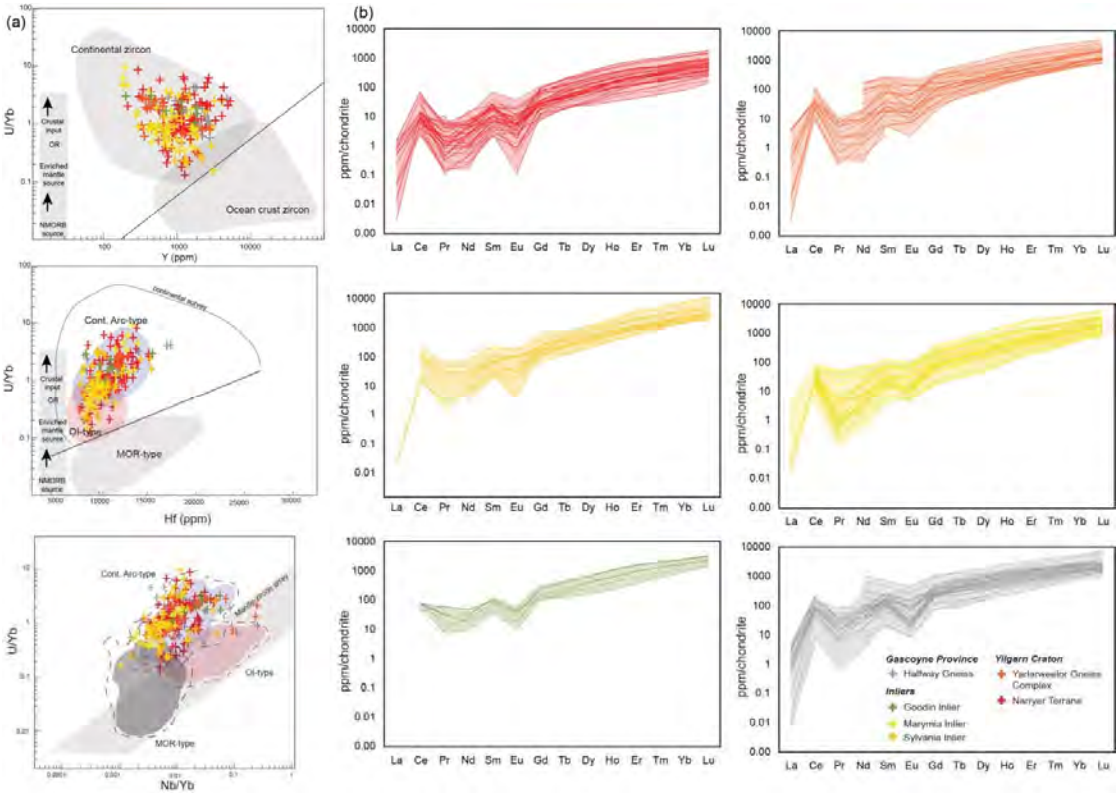

Figure 2.8. (a) Discrimination diagrams for magmatic zircon trace elements in Archean samples (Jahn, In prep). Fields after Grimes et al. (2007; 2015). (b) Chondrite-normalised REE plots showing data from magmatic zircons analysed from Archean samples.

- **Lu-Hf isotopic data**

A total of 110 magmatic and inherited zircon grains were analysed from nine samples. Initial $^{176}Hf/^{177}Hf$ ratios of all analysed zircon grains range between 0.280399 and 0.280978, corresponding to εHf values of -13.3 and +3.6 (Figure 2.9; Table 2.2). Magmatic grains (n = 56) yield a range of initial $^{176}Hf/^{177}Hf$ ratios between 0.280428 and 0.280963 (εHf -13.3 and - 0.6), with median εHf values from each sample ranging between -11.7 ± 4.6 and -2.4 ± 2.9, 2σ. Inherited zircon grains (n = 54) with $^{207}Pb/^{206}Pb$ ages ranging between 3619 to 2678 Ma yield a range of εHf values between -10.2 and +3.6.

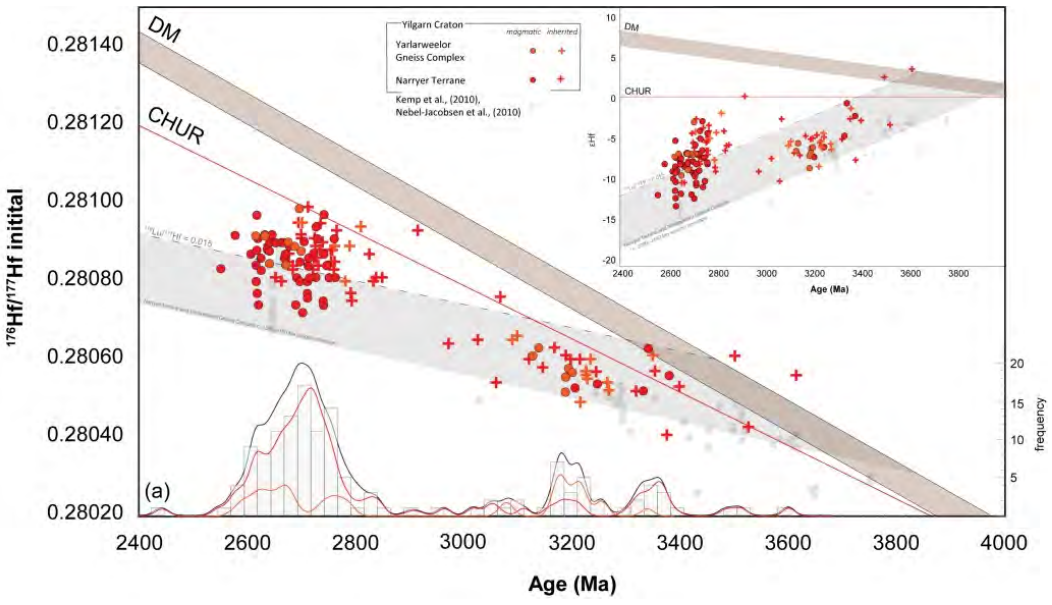

Figure 2.9 continues with caption overleaf

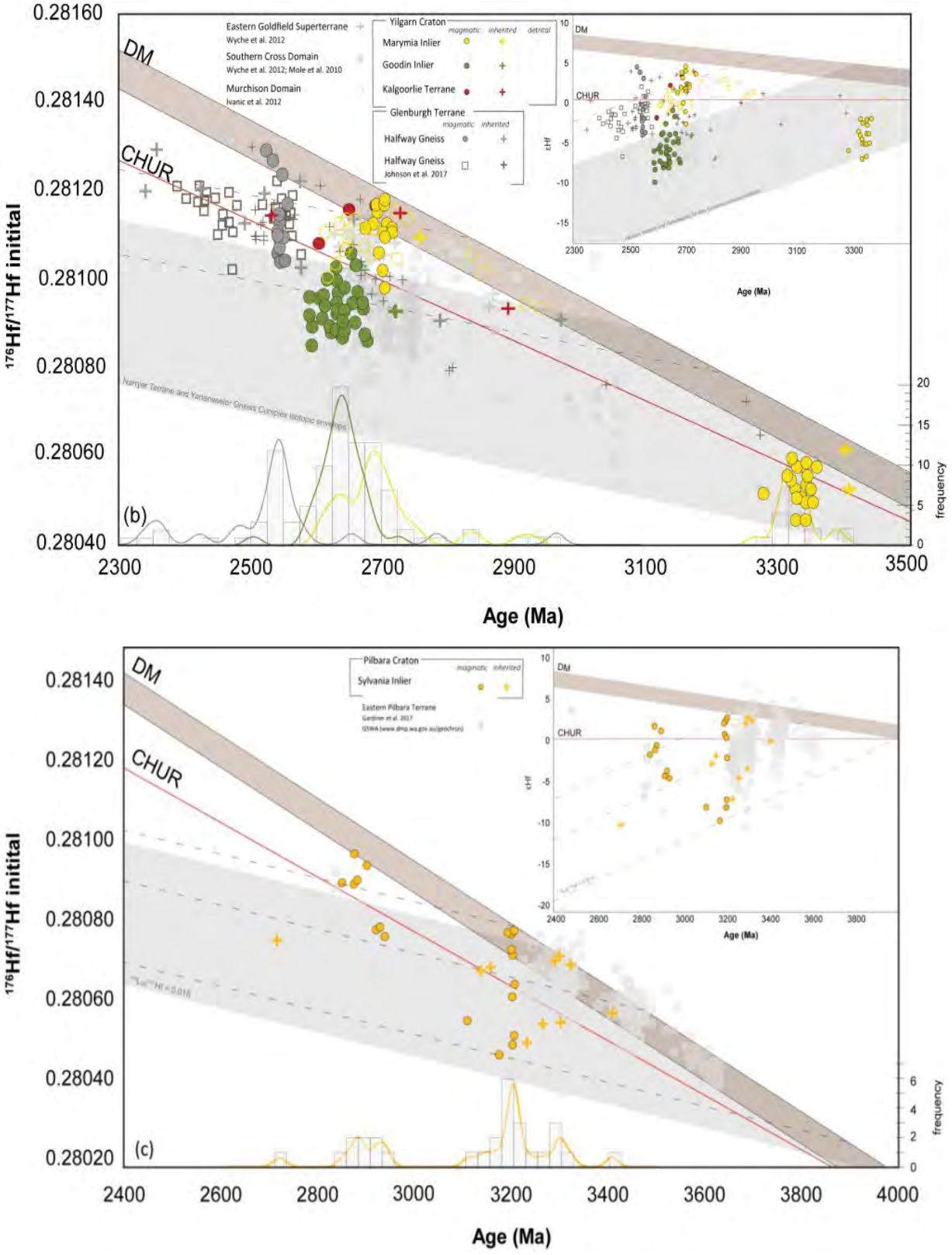

Figure 2.9. Evolution diagram of $^{176}Hf/^{177}Hf$ initial ratios for zircon from individual samples (a) Yilgarn Craton (Yarlarweelor Gneiss Complex and Narryer Terrane), (b) Yilgarn Craton (Kalgoorlie Terrane, Marymia and Goodin Inliers) and Glenburgh Terrane (Halfway Gneiss) (c) Pilbara Craton (Sylvania Inlier).

Table 2.2. Summary of zircon hafnium and oxygen isotope data for Archean samples.

Sample	Unit	Pb-Pb age (Ma)	εHf[1]	εHf range	TDMC[2]	$\delta^{18}O$[3] (‰)	$\delta^{18}O$ range (‰)
80434	NT	3365 ± 30	-2.4 ± 2.9 (4)	-4.7 to -0.6	3938–3712	6.49 ± 1.24 (7)	5.90–7.92
80453	NT	2710 ± 67	-10.4 ± 2.7 (7)	-12.3 to -7.9	3985–3861	6.4 ± 0.24 (2)	6.28–6.43
139459	NT	2728 ± 8	-6.8 ± 4.3 (16)	-10.9 to -2.6	3903–3378	6.19 ± 0.77 (13)	5.71–7.12
142914	NT	2661 ± 10	-7.5 ± 1.4 (10)	-12.3 to -6.4	3680–3531	5.93 ± 1.13 (10)	5.09–6.23
133547	NT	2645 ± 15	-9 ± 0.1 (2)	-9 to -8.9	3665–3328	6.81 (1)	5.42–7.77
80459	NT	2643 ± 13	-7.0 ± 1.6 (9)	-7.3 to -5.2	-	6.94 ± 0.44 (6)	6.71–7.36
144464	NT	2618	-	-16.7 to -4.5	4189–3873	6.39 (1)	5.96–6.74
142896	NT	2614 ± 13	-11.7 ± 4.6 (5)	-13.7 to -8.4	3964–3653	6.23 ± 0.44 (3)	5.93–6.43
142901	NT	2615 ± 18	-	-10.2 to +0.5	4106–3147	-	5.86–7.59
135418	YGC	3506 ± 10	-	-	-	6.05 ± 1.48 (8)	5.21–7.81
144376	YGC	3187 ± 10	-6.8 ± 3.4 (7)	-10.7 to -5.3	3966–3940	6.52 ± 1.55 (7)	6.2–8.13
142848	YGC	2691 ± 39	-6.3 ± 4.3 (4)	-8.8 to -0.4	3716–3361	6.19 ± 1.06 (5)	5.16–6.45
80484	YGC	2643 ± 43	-7.2 ± 2.8 (4)	-9.5 to -6.6	3587–3572	5.64 ± 0.94 (3)	5.23–6.3
Jc15	MI	3332 ± 8	-4.7 ± 2.6 (13)	-7.1 to -2.9	4113–3830	6.38 ± 0.8 (10)	5.65–7.20
216141	MI	3336 ± 27	-2.2 ± 2.6 (5)	-5.2 to -2.1	3812	6.46 ± 0.7 (2)	6.11–6.81
148344	MI	2698 ± 11	+1.4 ± 3.8 (10)	-2.7 to +3.8	3076–3042	6.35 ± 0.55 (9)	6.0–6.94
206935	MI	2699 ± 29	+2.3 ± 2.6 (4)	+1.1 to +4.0	3087–2925	5.94 ± 0.93 (4)	5.6–6.73
120601	MI	2628 ±11	-0.3 ± 3.1 (12)	-3.9 to +1.5	3216–3137	6.55 ± 1.71 (7)	5.39–7.9
139286	GI	2658 ±13	-6.4 ± 1.7 (3)	-6.9 to -4.7	-	-	6.4–7.02
139282	GI	2642 ± 9	-6.5 ± 5.5 (6)	-10 to -1.2	3653–3516	5.73 ± 1.55 (5)	4.73–6.89
120644	GI	2649 ± 11	-6.5 ± 3.4 (13)	-8 to -2	3638–3276	5.34 ± 0.83 (13)	4.52–5.76
120678	GI	-	-	-	-	6.42 ± 0.88 (4)	5.99–7.12
120696	GI	2622 ± 8	-6.4 ± 3.2 (14)	-8.4 to -2.9	3632–3378	6.15 ± 1.01 (11)	5.42–6.94
152855	EGST	2668 ± 31	+2.7 ± 1.2 (2)	+2.1 to +3.3	2955	5.04 ± 2.92 (2)	3.58–6.93
152879	EGST	2594	-	-1.9 to +0.0	3107–2809	6.93 (1)	5.84–6.93
81866	SI	3296	-	-	-	-	5.04–6.76
81867	SI	3196 ± 9	+1.2 ± 3.2 (8)	-2.3 to +2.5	3716–3414	6.55 ± 1.55 (10)	4.17–6.83
84528	SI	3405-2710	-	-9.9 to -0.3	-	-	6.31–6.79
84557	SI	2879 ±12	+0.1 ± 2.2 (4)	-1.3 to +1.3	3393–3269	5.03 ± 2.64 (5)	2.72–6.03
84589	SI	3188 ± 41	-7.4 ± 4.9 (4)	-9.4 to -3.6	-	-	-
84599	SI	2924 ± 14	-4.3± 2.4 (3)	-4.4 to -3.9	-	7.1 ± 0.6 (2)	6.86–7.42
164309	HG	2539 ± 6	-1.5 ± 5.7 (12)	-4.2 to +4.3	3312–2771	6.19 ± 0.84 (13)	5.56–7.12
185955	HG	2788-2341	-	-3.9 to +1.6	-	-	5.11–6.43
168947	HG	2042 ± 59	-10.3 ± 3.9 (3)	-13.3 to -8.6	-	-	7.07

[1]εHf values of magmatic zircon are expressed as median values in, ±2SD. Number of analyses donated in brackets. [2] TDMC will only be quoted where $\delta^{18}O$ indicate magmatic values. [3]$\delta^{18}O$ values of magmatic zircon are expressed as mean averages, ±2SD. Number of analyses donated in brackets. (-) indicates no value obtained. Where no value is obtained for magmatic zircon, the range reflects values from inherited zircon.

- **Oxygen isotopic data**

One hundred and five analyses were conducted on magmatic and inherited zircon grains from nine samples from the Narryer Terrane. Zircon $\delta^{18}O$ values of all analysed samples range between 5.09 and 8.32‰ (Figure 2.10; Table 2.2). Magmatic grains (n = 46) yield a range of $\delta^{18}O$ values between 5.09 to 7.94‰, with the average $\delta^{18}O$ of magmatic zircon from each sample varying from +5.93 ± 1.13 to 6.94 ± 0.44 ‰, 2σ.

Inherited zircon grains (n = 59) with $^{207}Pb/^{206}Pb$ ages ranging between 3766 to 2653 Ma yield a range of $\delta^{18}O$ values between 5.23 to 8.32‰.

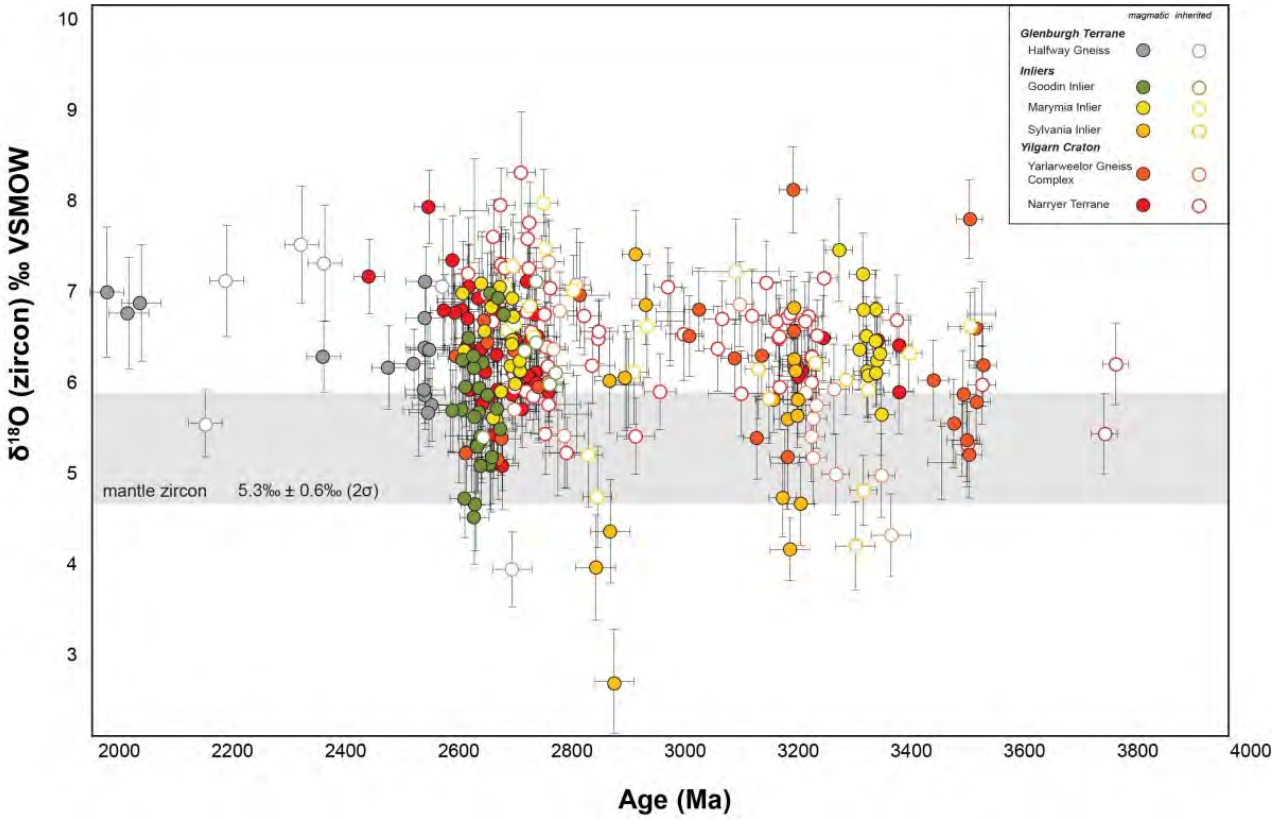

Figure 2.10. Oxygen isotope results from Archean zircon samples analysed.

2.4.2 Yarlarweelor Gneiss Complex

- **U–Pb geochronology**

The dataset from the Yarlarweelor Gneiss Complex consists of three samples, and the analysed zircon crystals cover a period of 800 Myr, with ages between c. 3192 and c. 2390 Ma (Figure 2.7; Table 2.1). Granites were generated during magmatic episodes at c. 3500 Ma and c. 2660 Ma.

- **Zircon trace-element composition**

Zircon grains from the Yarlarweelor Gneiss Complex (YGC) samples have trace-element compositions typical of continental zircon, with both magmatic and inherited populations plotting within continental arc-type zircon fields (Figure 2.8).

Chondrite-normalised REE element patterns of the magmatic zircon from the YGC granites are characterised by strong positive Ce and weakly negative Eu anomalies and a positive heavy REE (HREE) slope (Figure 2.8). The magmatic zircon record a range of Yb_N/Gd_N of 5-39 and Eu/Eu* of 0.06-1.04, indicating formation in lower pressures than eclogitic minerals (<1.2 GPa, <45 km depth; Rubatto and Hermann, 2007). Three inherited zircon exhibit flat HREE and no negative Eu anomaly, indicating formation in equilibrium with eclogitic minerals. Yarlarweelor Gneiss Complex samples record zircon Ti crystallisation temperatures with averages between 676 and 760°C.

- **Lu-Hf isotopic data**

A total of 29 zircon grains were analysed from three samples (Figure 2.9; Table 2.2). Initial $^{176}Hf/^{177}Hf$ ratios of all analysed zircon grains range between 0.280484 and 0.280979, corresponding to εHf values of -9.5 and -1.2. Magmatic grains (n = 15) yield a range of initial $^{176}Hf/^{177}Hf$ ratios between 0.280506 and 0.280979 (εHf -9.5 and -2.9). Median values (magmatic) range between -7.2 ± 2.8 and -6.3 ± 4.3 (2σ). Inherited zircon grains (n = 14) with $^{207}Pb/^{206}Pb$ ages ranging between 3351 to 2702 Ma yield a range of εHf values between -8.4 and -1.2.

- **Oxygen isotopic data**

Forty-eight analyses were conducted on magmatic, metamorphic and inherited zircon grains from three samples. Zircon $\delta^{18}O$ values of all analysed samples range between 3.95 and 8.96‰ (Figure 2.10; Table 2.2). Magmatic grains (n = 31) yield a range of $\delta^{18}O$ values between 5.09 to 8.13‰, with the average $\delta^{18}O$ of magmatic zircon from each sample varying from 6.05 ± 1.48 to 6.52 ± 1.55‰, 2σ. Inherited zircon grains (n = 17) with $^{207}Pb/^{206}Pb$ ages ranging between 3368 to 2702 Ma yield a range of $\delta^{18}O$ values between 3.95 and 6.87‰.

2.4.3 Marymia Inlier

- **U–Pb geochronology**

The dataset from the Marymia Inlier consists of five samples, and the analysed zircon cover a period of 820 Myr, with ages between c. 3406 and c. 2620 Ma (Figure 2.7; Table 2.1). Granites were generated during magmatic episodes at c. 3300 Ma, and c. 2700 Ma. One metasediment indicates a maximum depositional age of c. 2630 Ma.

- **Zircon trace-element composition**

Zircon grains from the Marymia Inlier samples have trace-element compositions typical of continental zircon, with both magmatic and inherited populations plotting within continental arc-type zircon fields, with minor overlap with OI-type zircon field (Figure 2.8).

Chondrite-normalised REE element patterns of the magmatic zircon from the Marymia Inlier granites are characterised by strong positive Ce and negative Eu anomalies and a positive heavy REE (HREE) slope (Figure 2.8). The magmatic zircon record a range of Yb_N/Gd_N of 7-46 and Eu/Eu* of 0.04-1.14, indicating formation in lower pressures than eclogitic minerals (<1.2 GPa, <45 km depth; Rubatto and Hermann, 2007).

Marymia Inlier samples record zircon Ti crystallisation temperatures with averages between 698 and 756°C. These temperatures are comparable with the low-T inheritance-rich granitoids with T_{Zr} <800°C of Miller et al. (2003) that are interpreted as forming in regions of crustal thickening.

- **Lu-Hf isotopic data**

Fifty-seven analyses were conducted on magmatic, inherited and detrital zircon grains from five samples. Initial $^{176}Hf/^{177}Hf$ ratios of all analysed zircon grains range between 0.280447 and 0.281168, corresponding to εHf values of -7.1 and +5.7 (Figure 2.9b; Table 2.2). Magmatic grains (n = 31) yield a range of initial $^{176}Hf/^{177}Hf$ ratios between 0.280447 and 0.281180 (εHf -7.1 and +4.0). Median values (magmatic) range between -4.7 ± 2.6 and +2.3 ± 2.6 (2σ). Inherited zircon grains (n = 4) with $^{207}Pb/^{206}Pb$ ages ranging between 3406 and 2753 Ma yield a range of εHf values between -2.7 and +5.7. Detrital zircon (n = 22) with $^{207}Pb/^{206}Pb$ ages ranging between 2936 to 2610 Ma yield a range of εHf values between -3.9 and +3.4.

- **Oxygen isotopic data**

Fifty analyses were conducted on magmatic, inherited and detrital zircon grains from five samples (Figure 2.10; Table 2.2). Magmatic grains (n = 26) yield a range of $\delta^{18}O$ values between 5.6 to 7.47‰, with the average $\delta^{18}O$ of magmatic zircon from each sample varying from 5.94 ± 0.93 to 6.4 ± 0.9‰, 2σ. Inherited zircon grains (n = 2) with $^{207}Pb/^{206}Pb$ ages of c. 3508 and 3400 Ma yield a range of $\delta^{18}O$ values between 6.33 to 6.63‰. Detrital zircon grains (n = 22) with $^{207}Pb/^{206}Pb$ ages ranging between 3093 to 2610 Ma yield a range of $\delta^{18}O$ values between 4.75 to 7.29‰.

2.4.4 Goodin Inlier

- **U–Pb geochronology**

The dataset from the Goodin Inlier consists of five samples, and the analysed zircon cover a period of 315 Myr, with individual $^{207}Pb/^{206}Pb$ ages between c. 2905 and c. 2592 Ma (Figure 2.7; Table 2.1). Granites were generated during one major magmatic episode at c. 2650 Ma.

- **Zircon trace-element composition**

Zircon grains from the Goodin Inlier samples have trace-element compositions typical of continental zircon, with both magmatic and inherited populations plot within continental arc- type zircon fields (Figure 2.8).

Chondrite-normalised REE element patterns of the magmatic zircon from the Goodin Inlier granites are characterised by strong positive Ce and negative Eu anomalies and a positive heavy REE (HREE) slope (Figure 2.8). The magmatic zircon record a range of Yb_N/Gd_N of 5-13 and Eu/Eu* of 0.17-0.66, indicating formation in lower pressures than eclogitic minerals (<1.2 GPa, <45 km depth; Rubatto and Hermann, 2007). Goodin Inlier samples record zircon Ti crystallisation temperatures with averages between 787 and 850°C.

- **Lu-Hf isotopic data**

Thirty-seven zircon grains were analysed from four samples. Magmatic grains (n = 36) yield a range of initial $^{176}Hf/^{177}Hf$ ratios between 0.280859 and 0.281238 (εHf -10 and -1.2; Figure 2.9b; Table 2.2). Median values (magmatic) range between -6.6 ± 3.4 and -6.2 ± 4.9 (2σ).

One inherited zircon grain with a $^{207}Pb/^{206}Pb$ age of c. 2720 Ma returned a εHf value of -4.2.

- **Oxygen isotopic data**

Thirty-seven analyses were conducted on magmatic and inherited zircon grains from five samples (Figure 2.10; Table 2.2). Magmatic grains (n = 29) yield a range of $\delta^{18}O$ values between 4.52 and 7.05 ‰, with the average $\delta^{18}O$ of magmatic zircon from each sample varying from 5.34 ± 0.83 to 6.15 ± 1.01 ‰, 2σ. One inherited zircon grain with a $^{207}Pb/^{206}Pb$ age of c. 2720 Ma returned a $\delta^{18}O$ value of 6.36‰. Seven analyses with no reliable U–Pb ages yield $\delta^{18}O$ values between 5.99 and 7.12‰.

2.4.5 Sylvania Inlier

- **U–Pb geochronology**

The dataset from the Sylvania Inlier consists of six samples, and the analysed zircon cover a period of 695 Myr, with individual $^{207}Pb/^{206}Pb$ ages between c. 3405 and c. 2710 Ma (Figure 2.7; Table 2.1). The analyses had a high number of discordant analyses, with only 20% of the analyses indicating <10% discordance.

- **Zircon trace-element composition**

Zircon grains from the Sylvania Inlier samples indicate trace-element compositions typical of continental zircon, with both magmatic and inherited populations plot within continental arc- type zircon fields (Figure 2.8).

Chondrite-normalised REE element patterns of the magmatic zircon are characterised by strong positive Ce and negative Eu anomalies and a positive heavy REE (HREE) slope. The magmatic zircon record a range of Yb_N/Gd_N of 6–35 and Eu/Eu* of 0.05–1.16, indicating formation in lower pressures than eclogitic minerals (<1.2 GPa, <45 km depth; Rubatto and Hermann, 2007). Sylvania Inlier samples record zircon Ti crystallisation temperatures with averages between 773 and 751°C.

- **Lu-Hf isotopic data**

A total of 28 zircon grains were analysed from five samples. Magmatic grains (n = 19) yield a range of initial $^{176}Hf/^{177}Hf$ ratios between 0.280487and 0.280984 (εHf -9.4 and +2.4; Figure 2.9c; Table 2.2). Median values (magmatic) range between -7.4 ± 4.9 and +1.2 ± 3.8 (2σ). Inherited zircon grains (n = 9) with $^{207}Pb/^{206}Pb$ ages ranging between c. 3405 and 2710 Ma returned a εHf value ranging from -9.9 to +2.5.

- **Oxygen isotopic data**

Thirty-four zircon grains were analysed from six samples. Zircon $\delta^{18}O$ values of all analysed samples range between 2.72 and 7.42‰ (Figure 2.10; Table 2.2). Magmatic grains (n = 18) yield a range of $\delta^{18}O$ values between 2.72 and 7.42‰, with the average $\delta^{18}O$ of magmatic zircon from each sample varying from 5.03 ± 2.64 to 7.1 ± 0.6 ‰, 2σ. Inherited zircon grains (n = 6) with $^{207}Pb/^{206}Pb$ ages ranging between 3305 and 3133 Ma yield a range of $\delta^{18}O$ values between 4.21 and 6.23‰. Analyses with no reliable U–Pb ages associated with them (n = 10) yield a range of $\delta^{18}O$ values between 5.04 to 6.79‰.

2.4.6 Glenburgh Terrane

- **U–Pb geochronology**

The dataset from the Glenburgh Terrane (principally the Halfway Gneiss) consists of three samples, and the analysed zircon cover a period of 1209 Myr, with individual $^{207}Pb/^{206}Pb$ ages between c. 3521 and c. 2557 Ma (Figure 2.7; Table 2.1). Magmatic ages recorded in the individual sample range from c. 2539 Ma to 2042 Ma.

- **Zircon trace-element composition**

Zircon grains from the Halfway Gneiss samples indicate trace-element compositions typical of continental zircon, with both magmatic and inherited populations plot within continental arc-type zircon fields, with minor overlap with OI-type zircon field (Figure 2.8; Grimes et al., 2007; Grimes et al., 2015). Chondrite-normalised REE element patterns of the magmatic zircon are characterised by strong positive Ce and negative Eu anomalies and a positive heavy REE (HREE) slope (Figure 2.8).

- **Lu-Hf isotopic data**

Twenty-seven zircon grains were analysed from three samples. Magmatic grains (Archean protoliths, n = 15) yield a range of initial $^{176}Hf/^{177}Hf$ ratios between 0.281042 and 0.281293 (Figure 2.9b; Table 2.2; εHf -4.2 and +4.3, median εHf -1.5 ± 5.7, 2σ). Neoproterozoic protoliths (n = 3) yield a range of initial $^{176}Hf/^{177}Hf$ ratios between 0.281110 and 0.281227 (εHf -13.3 and -8.6, median εHf -10.6 ± 3.9, 2σ). Inherited zircon grains (n = 12) with $^{207}Pb/^{206}Pb$ ages between c. 2971 and 2188 Ma yield a range of εHf values between -4.8 and +2.7.

One analyses with $^{207}Pb/^{206}Pb$ age of c. 1979 Ma, interpreted as having undergone ancient radiogenic-Pb loss, returned εHf values of –8.6.

- **Oxygen isotopic data**

A total of 24 zircon grains were analysed from three samples. Zircon $\delta^{18}O$ values of all analysed samples range between 5.11 and 7.12.‰ (Figure 2.10; Table 2.2). Magmatic grains (Archean protoliths, n = 13) yield a range of $\delta^{18}O$ values between 5.58 and 7.12‰, average $\delta^{18}O$ of magmatic zircon 6.24 ± 0.84‰, 2σ. Two zircon grains from younger pegmatite intrusions with $^{207}Pb/^{206}Pb$ ages of c. 2360 and 2150 Ma yield $\delta^{18}O$ values of 5.56 and 6.45‰. Magmatic grains (Neoproterozoic protoliths, n = 3) yield a range of $\delta^{18}O$ values between 6.77 and 7‰, with an average $\delta^{18}O$ of magmatic zircon of 6.85 ± 0.18 ‰, 2σ.

Inherited zircon grains (n = 4) with $^{207}Pb/^{206}Pb$ ages ranging between 2574 and 2191 Ma yield a range of $\delta^{18}O$ values between 7.07 to 7.53‰. Inherited zircon grains (n = 3). Sample 185955 (n = 3), which has no associated U–Pb ages, yields a range of $\delta^{18}O$ values between 5.11 and 6.43‰.

2.4.7 Dalgaringa Supersuite

- **U–Pb geochronology**

The dataset from the Dalgaringa Supersuite consists of four samples, and the analysed zircon cover a period of 580 Myr, with individual $^{207}Pb/^{206}Pb$ ages ages between c. 2539 and c. 1959 Ma (Figure 2.11; Table 2.3). The granites were emplaced during one main period at c. 2000 Ma.

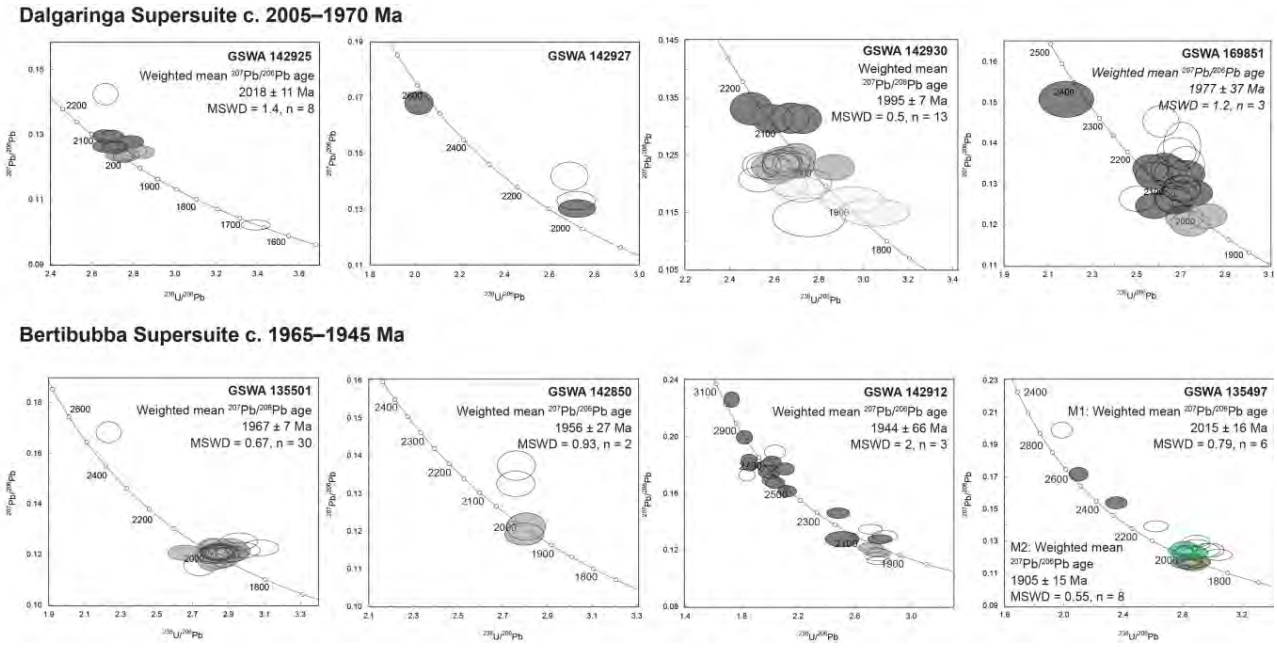

Figure 2.11. Concordia diagram showing the subset of Dalgaringa and Bertibubba Supersuites zircon with <10% discordance. Colour scheme follows that of Figure 2.7.

Table 2.3. Summary of sample descriptions and U–Pb LASS data for Glenburgh Orogeny associated magmatism.

Sample	Unit[1]	lithology	Pb–Pb age (Ma)[2]	Inheritance (Ma)	Pb–Pb age (Ma)[3]	T_{ZR}(°C)	Lat	Long
168947	HG	monzogranite gneiss	2042 ± 59	2574–2188	2006 ± 6	-	-25.03388	115.82858
142925	DS	monzogranite	2018 ± 11	2093–2044	2002 ± 3	680	-25.3077	116.4132
142927	DS	granodiorite	-	2539–2102	1999 ± 5	-	-25.3165	116.4369
142930	DS	pegmatite	1995 ± 7	2128–2104	1994 ± 52	773	-25.38185	116.29083
168951	DS	monzogranite	1976 ± 20	2353–2023	2007 ± 3	691	-25.62111	115.62623
135501	BS	granodiorite	1967 ± 7	-	-	800	-25.3343	117.55646
142850	BS	monzogranite	1956 ± 27	-	1958 ± 4	698–781	-25.39979	117.61641
142912	BS	monzogranite	1944 ± 66	3025–2066	1961 ± 3	710	-25.60764	116.59326
135497	BS	metagranite	2014, 1905	2574–2390	-	698, 627	-25.35544	117.6132

[1]DS = Dalgaringa Supersuite, BS = Bertibubba Supersuite, HG = Halfway Gneiss.
[2]Crystallisation age ($^{207}Pb/^{206}Pb$) established by LASS, ages in brackets () indicate maximum crystallisation age.
[3]Crystallisation age ($^{207}Pb/^{206}Pb$) established by SHRIMP (GSWA).
(-) indicates no value obtained.

- **Zircon trace-element composition**

Magmatic zircons have a strong association with continental arc fields, with a steep positive M-HREE slope (Yb_N/Gd_N = 12–113) and highly negative Eu anomaly (Eu/Eu* = 0.01–0.52; Figure 2.12). Inherited zircon have a slightly flatter M–HREE slope (Yb_N/Gd_N = 7–26) and small Eu anomalies (Eu/Eu* = 0.27–0.52). All Dalgaringa Supersuite samples record zircon Ti crystallisation temperatures with averages between 680 and 773°C.

- **Lu–Hf isotopes**

A total of 35 magmatic and inherited zircon grains were analysed from three samples. Magmatic grains (n = 20) yield a range of initial $^{176}Hf/^{177}Hf$ ratios between 0.281307 and 0.281511 (εHf -7.2 and 0; Figure 2.13; Table 2.4). T_{DM}^{C} values range between 3094 Ma and 2668 Ma. Median values (magmatic) range between -6.1 ± 2 and -3.3 ± 4.5 (2σ). Inherited zircon grains (n = 9) with $^{207}Pb/^{206}Pb$ ages ranging between c. 2353 and 2064 Ma returned a εHf value ranging from -7 to +4.5, corresponding to T_{DM}^{C} values between 3122 and 2616 Ma. One analyses with $^{207}Pb/^{206}Pb$ age of c. 1930 Ma, interpreted as having undergone ancient radiogenic-Pb loss, returned εHf values of –4.7.

- **Oxygen isotopes**

Forty zircon grains were analysed from three samples. Zircon $\delta^{18}O$ values of all analysed samples range between 3.93 and 7.55 ‰ (Figure 2.14-2.15; Table 2.4). Magmatic grains (n = 25) yield a range of $\delta^{18}O$ values between 4.31 and 7.55 ‰, with the average $\delta^{18}O$ of magmatic zircon from each sample varying from 4.93 ± 1.05 to 6.44 ± 1.1 ‰, 2σ. Inherited zircon grains (n = 12) with $^{207}Pb/^{206}Pb$ ages ranging between 2784 and 2087 Ma yield a range of $\delta^{18}O$ values between 3.93 and 6.48‰. Analyses of zircon cores with no concordant U–Pb data associated with them (n = 3) yield a range of $\delta^{18}O$ values between 5.9 and 6.19‰.

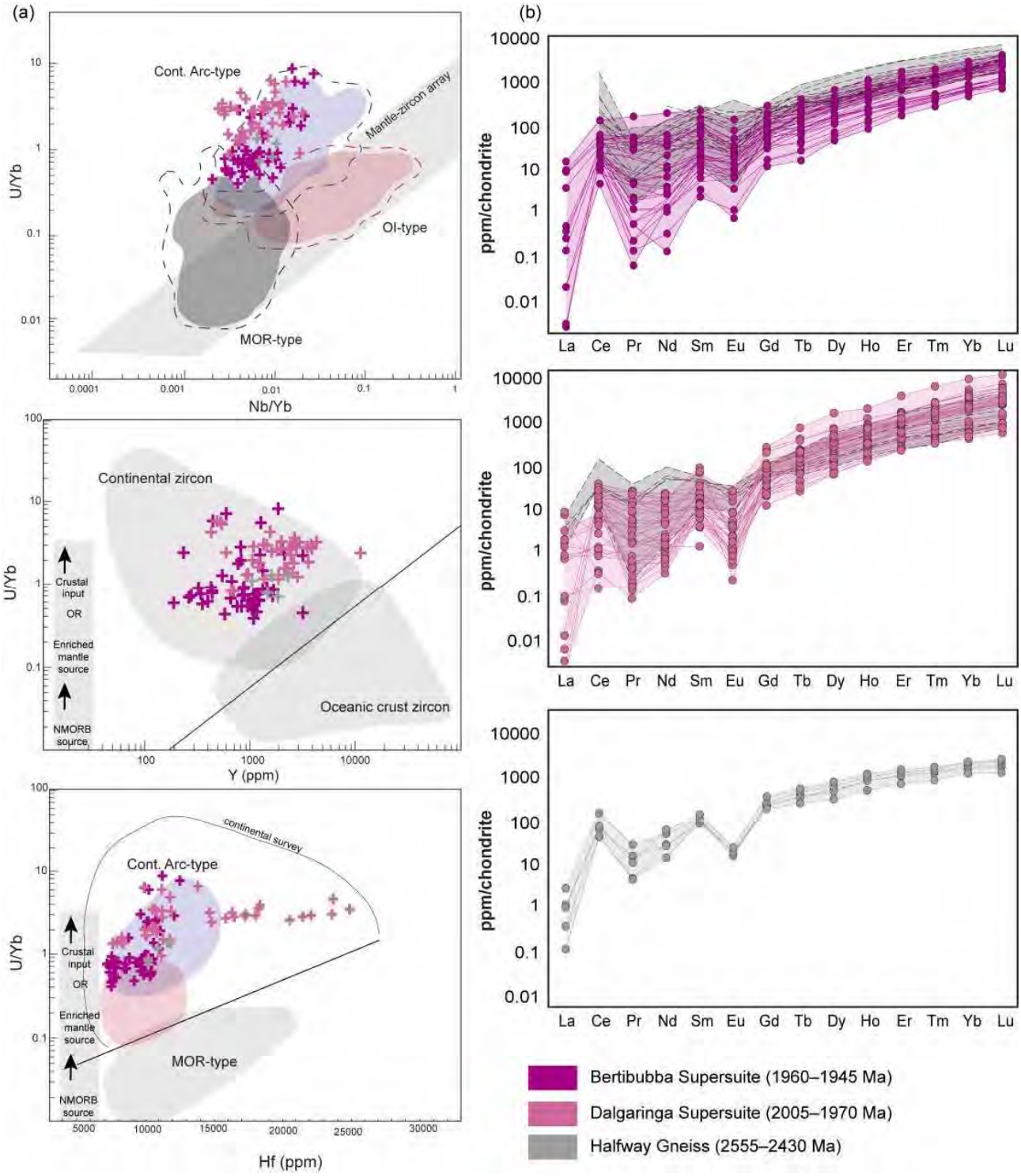

Figure 2.12. (a) Discrimination diagrams for Glenburgh Orogeny magmatic zircon trace elements in Archean samples (Jahn, In prep). Fields after Grimes et al. (2007; 2015). (b) Chondrite-normalised REE plots showing data from magmatic zircons analysed from Dalgaringa and Bertibubba Supersuite samples.

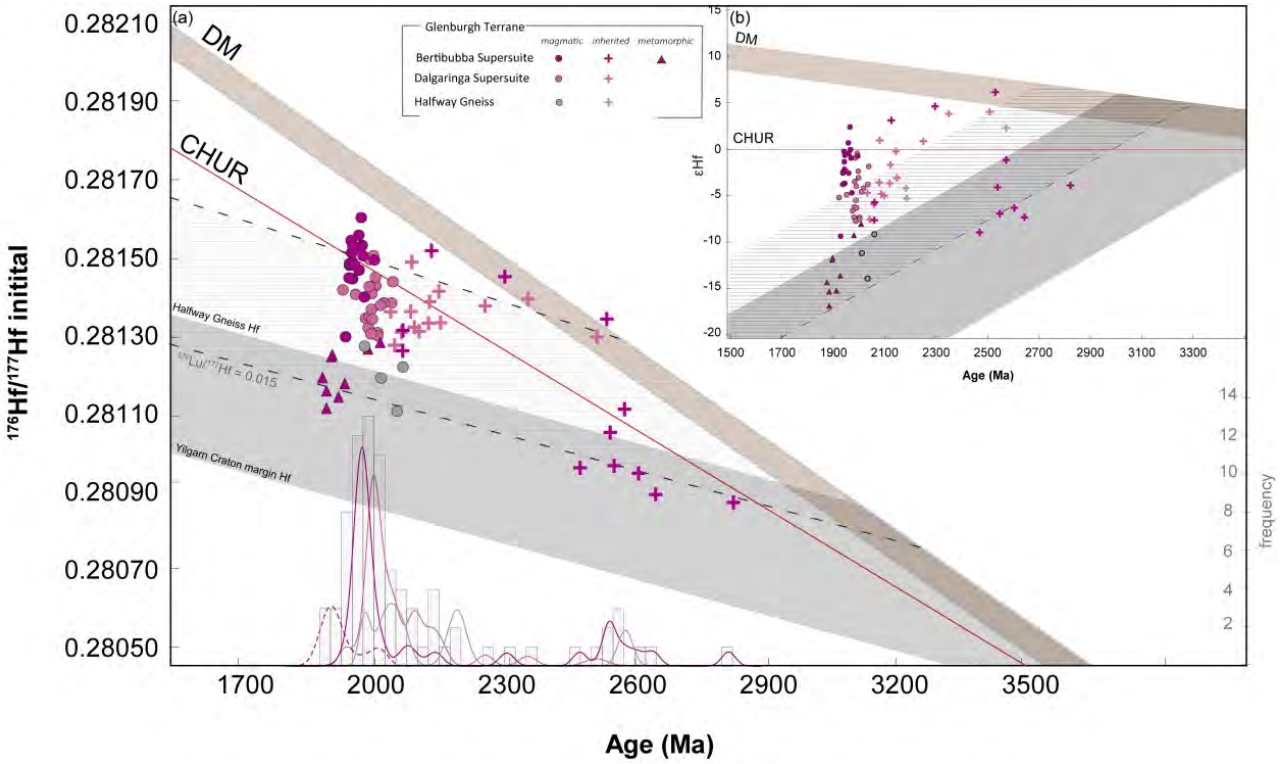

Figure 2.13. Evolution diagrams of (a) $^{176}Hf/^{177}Hf$ initial ratios versus age, and (b) εHf versus age for zircon from samples from the Dalgaringa and Bertibubba Supersuite and Proterozoic Halfway Gneiss. The dashed line is a reference evolution line corresponding to a Lu/Hf ratio of 0.015.

Table 2.4. Summary of zircon hafnium and oxygen isotope data for Glenburgh Orogeny associated magmatism.

Sample	Unit	Pb-Pb age (Ma)	εHf[1]	εHf range	TDMC[2]	$\delta^{18}O$[3] (‰)	$\delta^{18}O$ range (‰)
168947	HG	2042 ± 59	-10.6 ± 3.9 (3)	-13.3 to -8.6	-	6.9 ± 0.2 (3)	6.77–7.0
142925	DS	2018 ± 11	-3.7 ± 3.7 (7)	-6.7 to -1.4	3077–2895	5.99 ± 0.36 (10)	5.73–6.3
142927	DS	-	-	-	-	-	-
142930	DS	1995 ± 7	-3.3 ± 4.5(11)	-7.2 to 0	3093–2668	6.44 ± 1.1 (11)	5.88–7.55
168951	DS	1976 ± 20	-6.1 ± 2 (3)	-6.8 to -4.4	3063–2890	4.93 ± 1.05 (3)	4.31–5.32
135501	BS	1967 ± 7	-1.3 ± 2.5 (16)	-3.2 to +1.1	2807–2598	5.81 ± 0.85 (14)	4.86–6.37
142850	BS	1956 ± 27	-0.2 ± 6.1 (2)	-3.3 to +2.8	2440	5.79 ± 0.39 (1)	-
142912	BS	1944 ± 66	-6.5 ± 4.6 (2)	-8.8 to -4.4	3142	5.8 ± 0.49 (2)	5.55–6.04
135497	BS	2014, 1905	-7.5 (1), -10.6 ± 3.4 (7)	-7.5, -16.2 to -11.1	3127, 3582–3127	5.93, 5.84 ± 0.83(6)	5.17–6.52

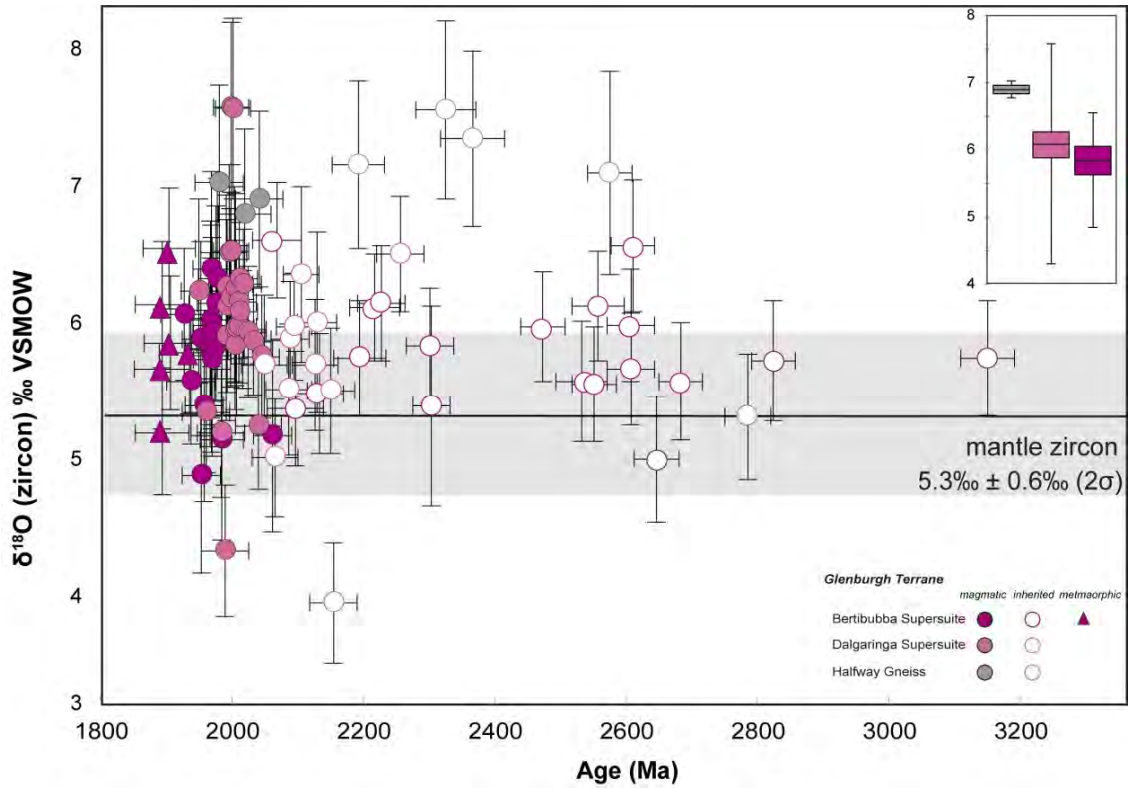

Figure 2.14. $\delta^{18}O$ versus age (Ma). The compositional field for zircon in equilibrium with mantle-derived melts has a $\delta^{18}O_{VSMOW}$ value of 5.3 ± 0.6‰ (2σ; Valley, 2003), (b) Box-and-whisker plots showing the range and median values of $\delta^{18}O_{VSMOW}$ compositions.

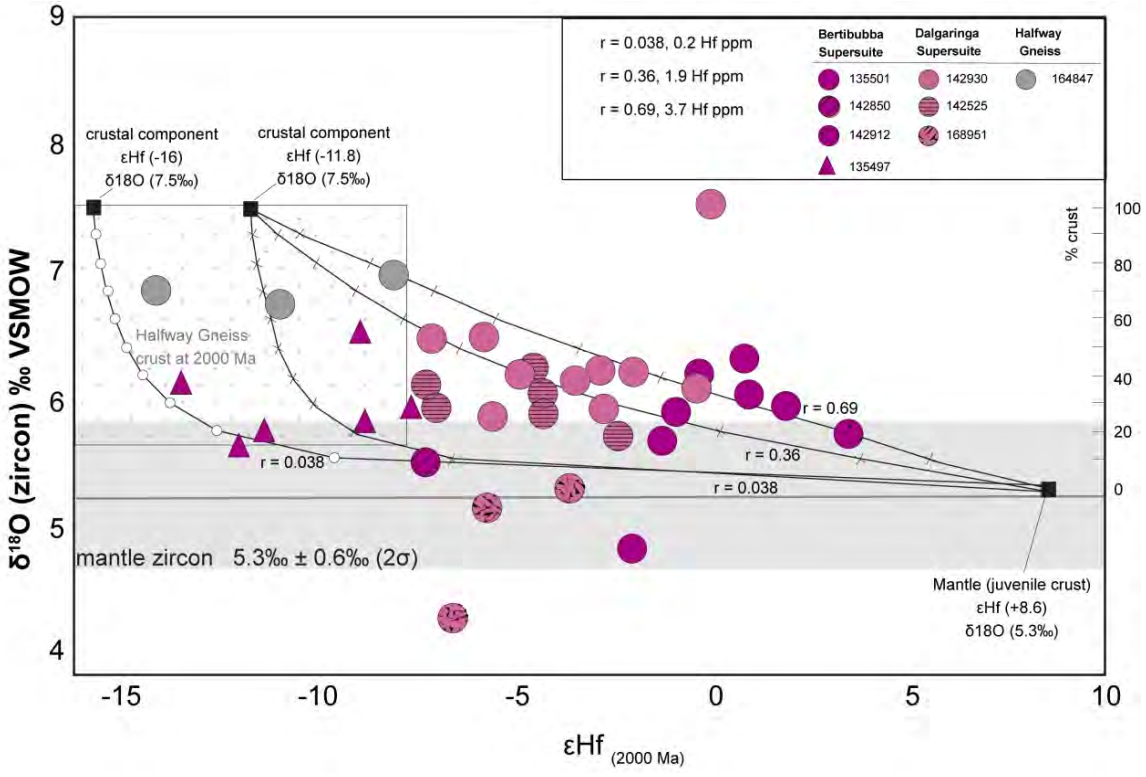

Figure 2.15. Plot of $\delta^{18}O$ versus εHf for zircon from the Glenburgh Terrane with bulk mixing model between depleted mantle and crustal source component. The parameters of end members are discussed in text. Bulk mixing curves are marked at 10% increments.

2.4.8 Bertibubba Supersuite

- **U–Pb geochronology**

The dataset from the Bertibubba Supersuite consists of four samples, with the analysed zircons covering a period of 580 Myr (individual $^{207}Pb/^{206}Pb$ ages between c. 2539 and c. 1959 Ma; Figure 2.11, Table 2.3.). The granites were emplaced during one main period at c. 1960 Ma.

- **Zircon trace-element composition**

Magmatic zircon are associated with the continental field and have a steep positive M-HREE slope (Yb_N/Gd_N = 13–38; Figure 2.12) and small negative Eu anomaly (Eu/Eu* = 0.13–0.80).

Inherited zircon display a similar M–HREE slope and Eu anomaly (Yb_N/Gd_N = 6–36; Eu/Eu* = 0.31–0.76). Zircon rims display a similar M–HREE slope and Eu anomaly (Yb_N/Gd_N = 6– 23; Eu/Eu* = 0.38–0.63). All Bertibubba Supersuite samples record zircon Ti crystallisation temperatures with averages between 680 and 773°C.

- **Lu–Hf isotopes**

A total of 30 magmatic, metamorphic and inherited zircon grains were analysed from four samples. Magmatic grains (n = 20) yield a range of initial $^{176}Hf/^{177}Hf$ ratios between 0.281304 and 0.281607 (εHf -8.8 and +2.8; Figure 2.13; Table 2.4). T_{DM} values range between 3148 and 2440 Ma. Median εHf values (magmatic) range between -6.5 ± 4.6 and -0.2 ± 6.1 (2σ). Inherited zircon grains (n = 11) with $^{207}Pb/^{206}Pb$ ages ranging between c. 2823 and 2066 Ma returned a εHf value ranging from -8.4 to +6.5, corresponding to T_{DM} values between 3569 and 2520 Ma. Metamorphic zircon grains (n = 9) with $^{207}Pb/^{206}Pb$ ages ranging between c. 2015 and 1934 Ma returned a εHf value ranging between -14.7 and -7.5.

- **Oxygen isotopes**

Forty-four zircon grains were analysed from four samples. Zircon $\delta^{18}O$ values of all analysed samples range between 4.86 and 6.58 ‰ (Figure 2.14 & 2.15; Table 2.4). Magmatic grains (n = 25) yield a range of $\delta^{18}O$ values between 4.86 and 6.52 ‰, with the average $\delta^{18}O$ of magmatic zircon from each sample varying from 5.79 ± 0.39 to 5.81 ± 0.85 ‰, 2σ. Inherited zircon grains (n = 19) with $^{207}Pb/^{206}Pb$ ages ranging between 3149 and 2067 Ma yield a range of $\delta^{18}O$ values between 4.98 and 6.52‰.

2.4.9 Moorarie Supersuite

- **U–Pb geochronology**

The dataset from the Moorarie Supersuite consists of twenty-nine samples. The analysed zircon from the Moorarie Supersuite samples cover a period of 1755 Myr, with individual $^{207}Pb/^{206}Pb$ ages ranging from 3506 to 1751 Ma (Figure 2.16; Table 2.5). Magmatic ages recorded in the individual Moorarie Supersuite samples range from c. 1846 to 1754 Ma.

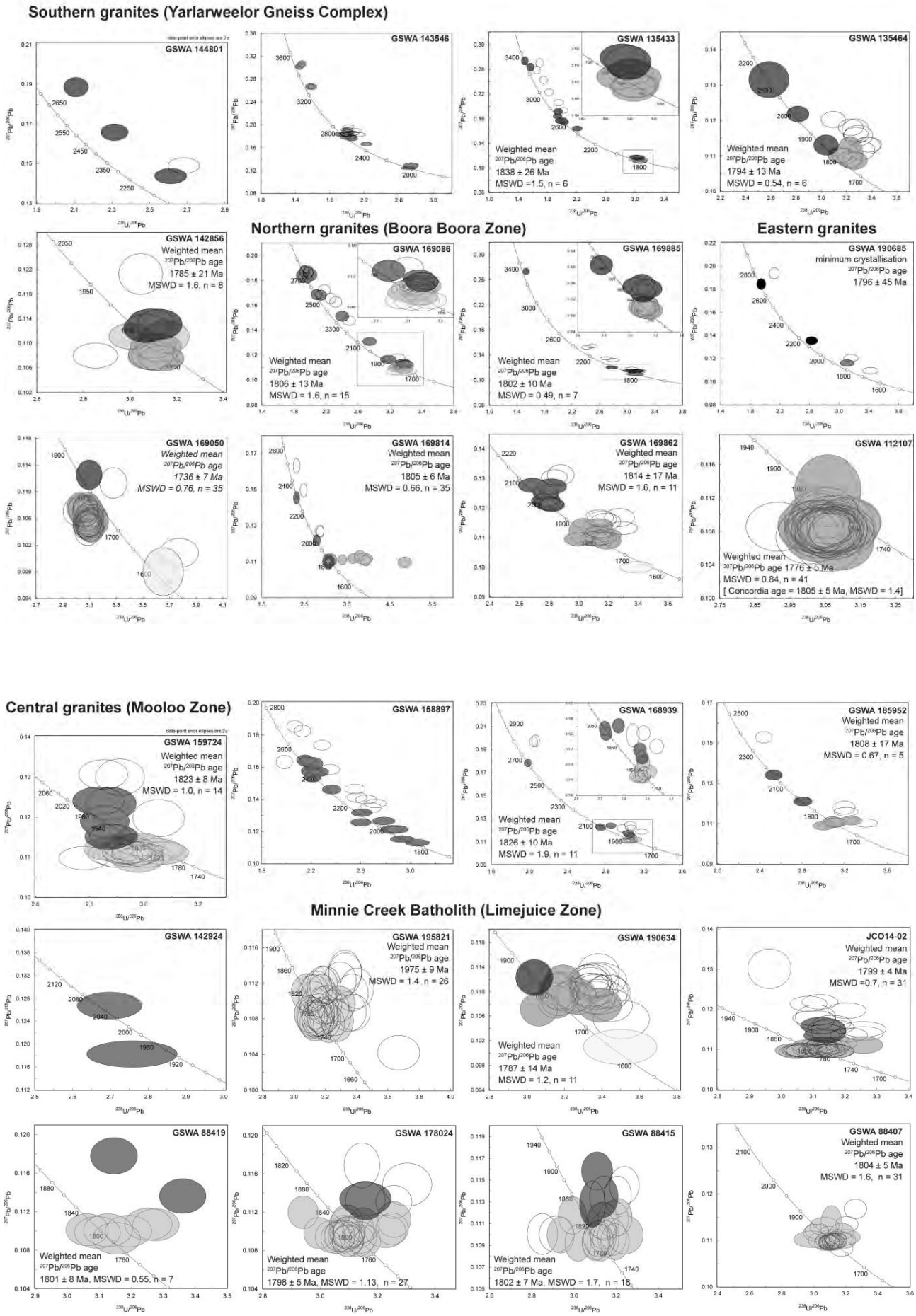

Figure 2.16 continues with caption overleaf.

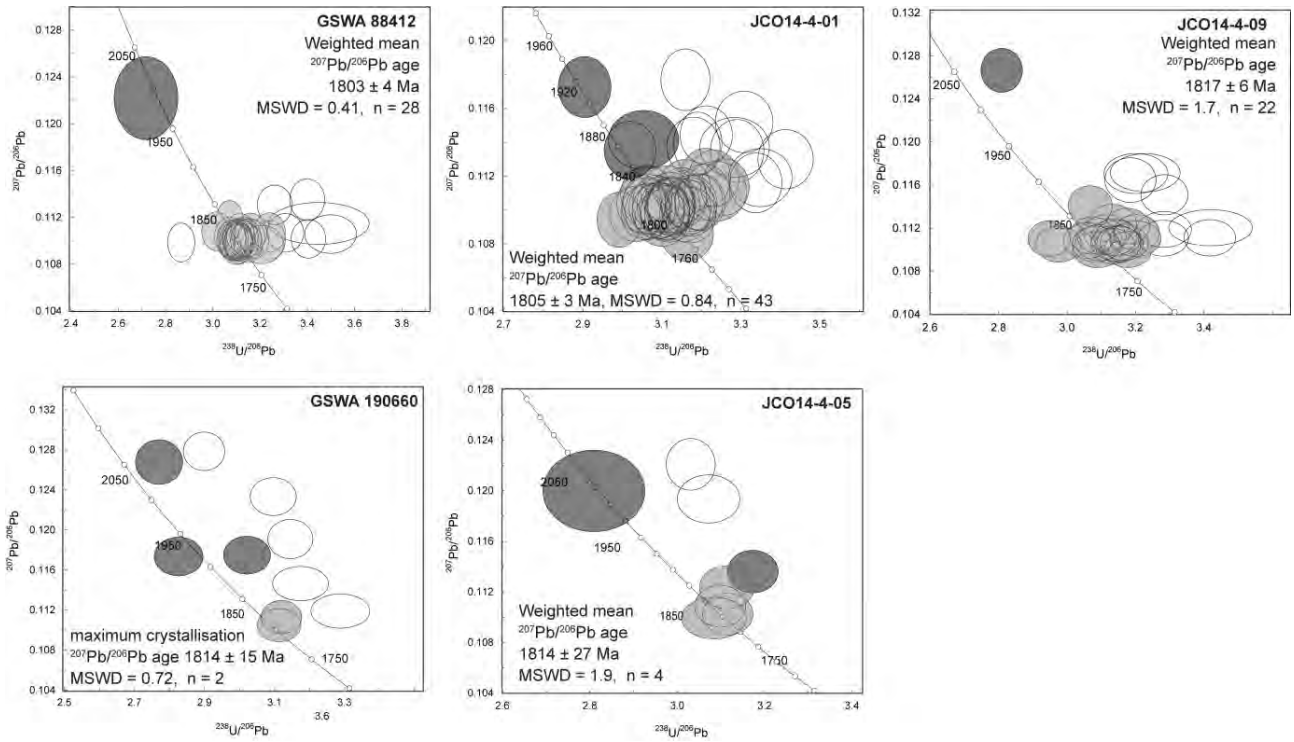

Figure 2.16. Concordia diagram for Moorarie Supersuite zircon with <10% discordance. Colour scheme follows that of Figure 2.7. Figure continues overleaf for the Minnie Creek Batholith samples.

Inherited zircons recovered indicate that significant proportions of crust of Paleoproterozoic age (c. 1860 Ma; Figure 2.17) is present within, or was involved in the formation of the Moorarie Supersuite. The existing data for igneous and sedimentary rocks within the Capricorn Orogen indicate that 1950-1820 Ma crustal components are currently unexposed. This suggests that the most likely crustal source(s) of the abundant Paleoproterozoic inherited material are at deeper crustal levels.

- **Zircon trace-element composition**

All of the Moorarie Supersuite samples show similar REE patterns, which suggests that all the granites were derived from a source of similar composition and/or a similar degree of partial melting. Zircon grains have trace-element compositions typical of continental zircon, with both magmatic and inherited populations plot within continental arc-type zircon fields (Figure 2.16).

Table 2.5. Summary of sample descriptions and U–Pb LASS data for Capricorn Orogeny magmatism.

Sample	Unit[1]	Lithology	Pb–Pb age (Ma)[2]	Inheritance (Ma)	Pb–Pb age (Ma)[3]	TZR (°C)	Lat	Long
144801	SG	metamonzogranite	–	2730–2272	-	775–853	–25.36743	117.29085
143546	SG	metagranite	-	3506–2023	-	688–849	–25.6243	117.7502
135433	SG	metagranite	1838 ± 26	3331–1903	-	733	–25.38876	117.88123
135464	SG	monzogranite	1794 ± 13	2112–1853	-	759	–25.26451	117.75733
142856	SG	monzogranite	1785 ± 21	1857–1839	1801 ± 7	728	–25.24085	117.69802
169086	NG	monzogranite	1806 ± 13	2722–1846	1784 ± 5	729	–23.00884	115.52444
169885	NG	granodiorite	1802 ± 10	3329–1858	1796 ± 9	744	–22.4466	116.0077
190685	EG	metatonalite	-	2693–1898	1811 ± 5	-	–24.93638	117.76473
169050	EG	tonalite	n/a	-	1806 ± 5	828	–24.92847	117.37784
169814	EG	granitic rock	1805 ± 6	2294–1984	-	719	–24.65851	118.09598
169862	EG	granitic rock	1814 ± 17	2067–1973	-	718	–24.95796	118.09544
112107	EG	granodiorite	1773 ± 6	-	1797 ± 8	742	–24.6279	118.70389
159724	CG	monzogranite	1823 ± 8	2016–1882	1815 ± 4	760	-25.1264	116.1787
159987	CG	granodiorite	-	2507–1849	1810 ± 9	810	-24.9983	116.5352
168939	CG	monzogranite	1826 ± 10	2639–1988	1800 ± 7	689	-25.0699	116.5982
185952	CG	monzogranite	1808 ± 17	2153–1973	1799 ± 5	758	-24.78183	116.37321
142924	CG	granodiorite	-	2054–1930	1827 ± 14	–	-25.2717	116.4398
195821	MCB	metagranodiorite	1785 ± 9	-	1794 ± 5	690	-23.88417	115.31163
190634	MCB	metamonzogranite	1787±14	1837	1777 ± 5	695	-24.63234	116.73361
JCO14/4–02	MCB	metagranite	1799 ± 4	1893–1863	-	728	-23.857945	115.74535
88419	MCB	monzogranite	1801 ± 8	-	1781 ± 6	676	-24.2535	115.8416
178024	MCB	granodiorite	1798 ± 5	-	1783 ± 5	678	-23.9531	115.5255
88415	MCB	granodiorite	1802 ± 7	1893–1844	1777 ± 8	693	-24.0668	115.6653
88407	MCB	monzogranite	1801 ± 5	1848	1794 ± 8	723	-24.1568	116.1523
88412	MCB	monzogranite	1803 ± 4	1876	1801 ± 5	718	-24.1185	115.917
JCO14/4–01	MCB	metagranite	1805 ± 3	1915–1857	-	720	-23.857773	115.74537
JCO14/4–09	MCB	metagranite	1817 ± 6	1865	-	708	-24.075952	115.87397
190660	MCB	felsic intrusive	1814 ± 15	2053–1808	1791 ± 4	-	-24.5902	116.655
JCO14/4–05	MCB	metagranite	1814 ± 27	1956–1858	-	564	-23.855011	115.70045

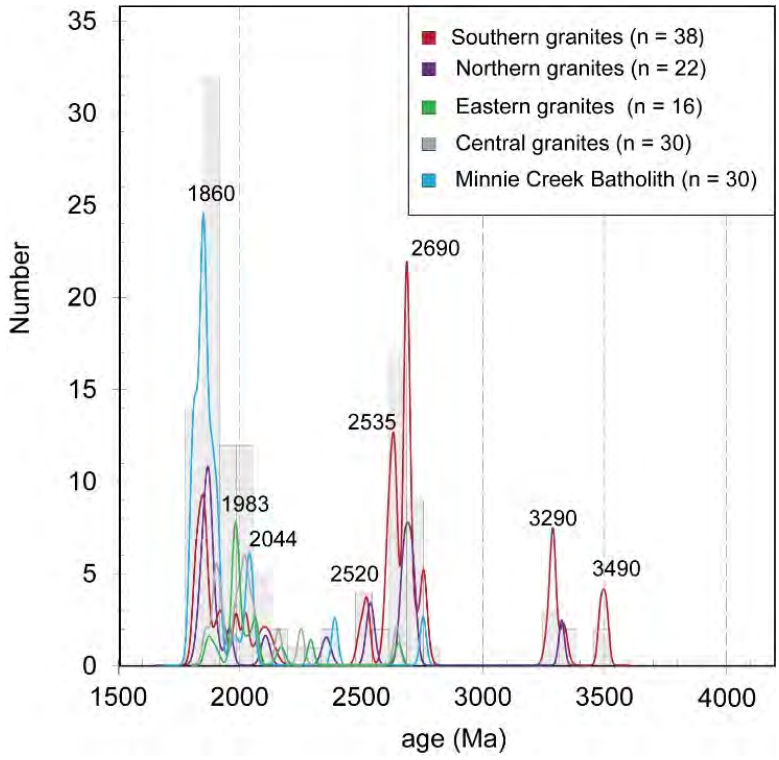

Figure 2.17. Probability density plot of inherited zircon U– Pb age data for Moorarie Supersuite analyses.

Trace-element ratios display a continental signature (Figure 2.18), while chondrite-normalised REE element patterns of the magmatic zircon from the Moorarie Supersuite granites are characterised by strong positive Ce and negative Eu anomalies and a positive heavy REE (HREE) slope (Figure 2.19). Magmatic zircon trace element signatures indicate no evidence of co-crystallisation with garnet (i.e. flat HREE pattern with Lu/Gd <3 and no negative Eu anomaly, Eu/Eu* >0.75). Magmatic zircon trace element signature indicate no evidence of co-crystallisation with garnet (Yb_N/Gd_N = 3-69, Eu/Eu* = 0.01-0.69), indicating formation in lower pressures than eclogitic minerals (<1.2 GPa, <45 km depth; Rubatto and Hermann, 2007).

All Moorarie Supersuite samples record zircon Ti crystallisation temperatures with averages between 682 and 828°C (Ferry and Watson, 2007). These temperatures are comparable with the low-T inheritance-rich granitoids with T_{Zr} <800°C of Miller et al. (2003) that are interpreted as forming in regions of crustal thickening.

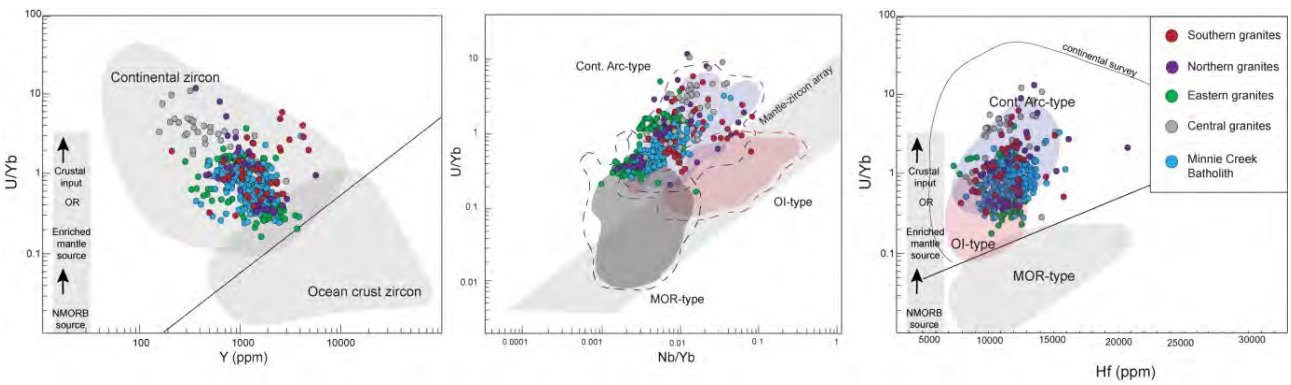

Figure 2.18. Discrimination diagrams for trace elements in Moorarie Supersuite samples, after Grimes et al. (2007; 2015).

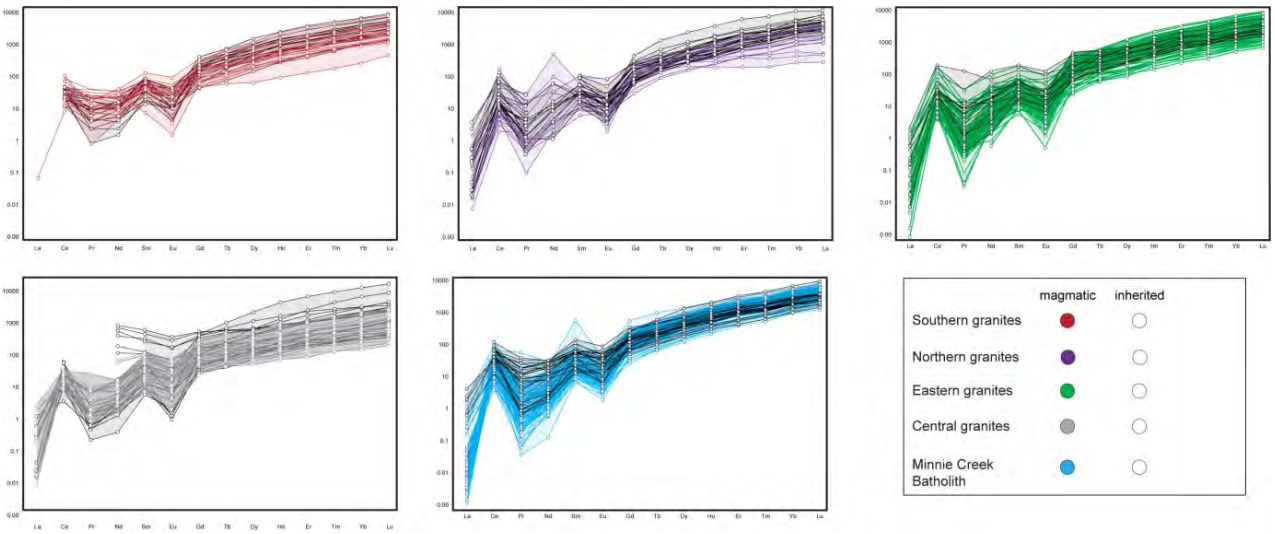

Figure 2.19. Chondrite-normalised REE plots showing data from the Moorarie Supersuite samples.

- **Lu-Hf isotopic data**

Three hundred and three analyses were conducted on magmatic and inherited zircon grains from 27 samples from the Moorarie Supersuite granites (Figure 2.20 & 2.21; Table 2.6). Initial $^{176}Hf/^{177}Hf$ ratios of all analysed zircon grains range between 0.280408 and 0.281732, corresponding to εHf values of -18.6 and +5. Magmatic grains (*n* = 215) yield a range of initial $^{176}Hf/^{177}Hf$ ratios between 0.281287 and 0.281732 (εHf -12.7 and +3.3), with median εHf values from each sample ranging between -11.1 ± 3.4 and +0.5 ± 1.2, 2σ. Inherited zircon grains (*n* = 88) with $^{207}Pb/^{206}Pb$ ages ranging between 3506 and 1808 Ma yield a range of εHf values between -18.6 and +5.

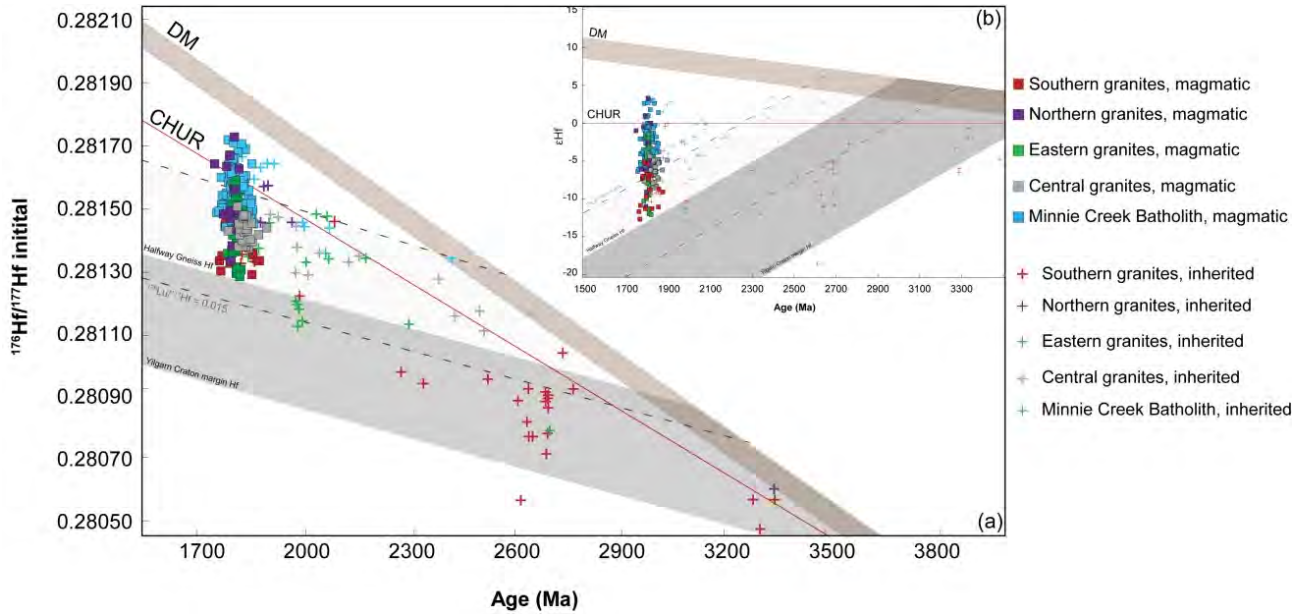

Figure 2.20. Lu–Hf isotope results from the Moorarie Supersuite. Grey shaded area: isotopic envelope for the Yilgarn Craton margin Hf (magmatic) analyses (Narryer Terrane and Yarlarweelor Gneiss Complex) and striped area: isotopic envelope for the Halfway Gneiss Hf analyses. The dashed line is a reference evolution line corresponding to a Lu/Hf ratio of 0.015. (a) Initial Hf evolution plot for the Moorarie Supersuite (n = 290). (b) Hf evolution diagram for zircon grains from the Moorarie Supersuite, deviations of Hf ($^{176}Hf/^{177}Hf$) isotopic composition from the chondrite uniform reservoir (CHUR) standard are expressed in epsilon units, εHf.

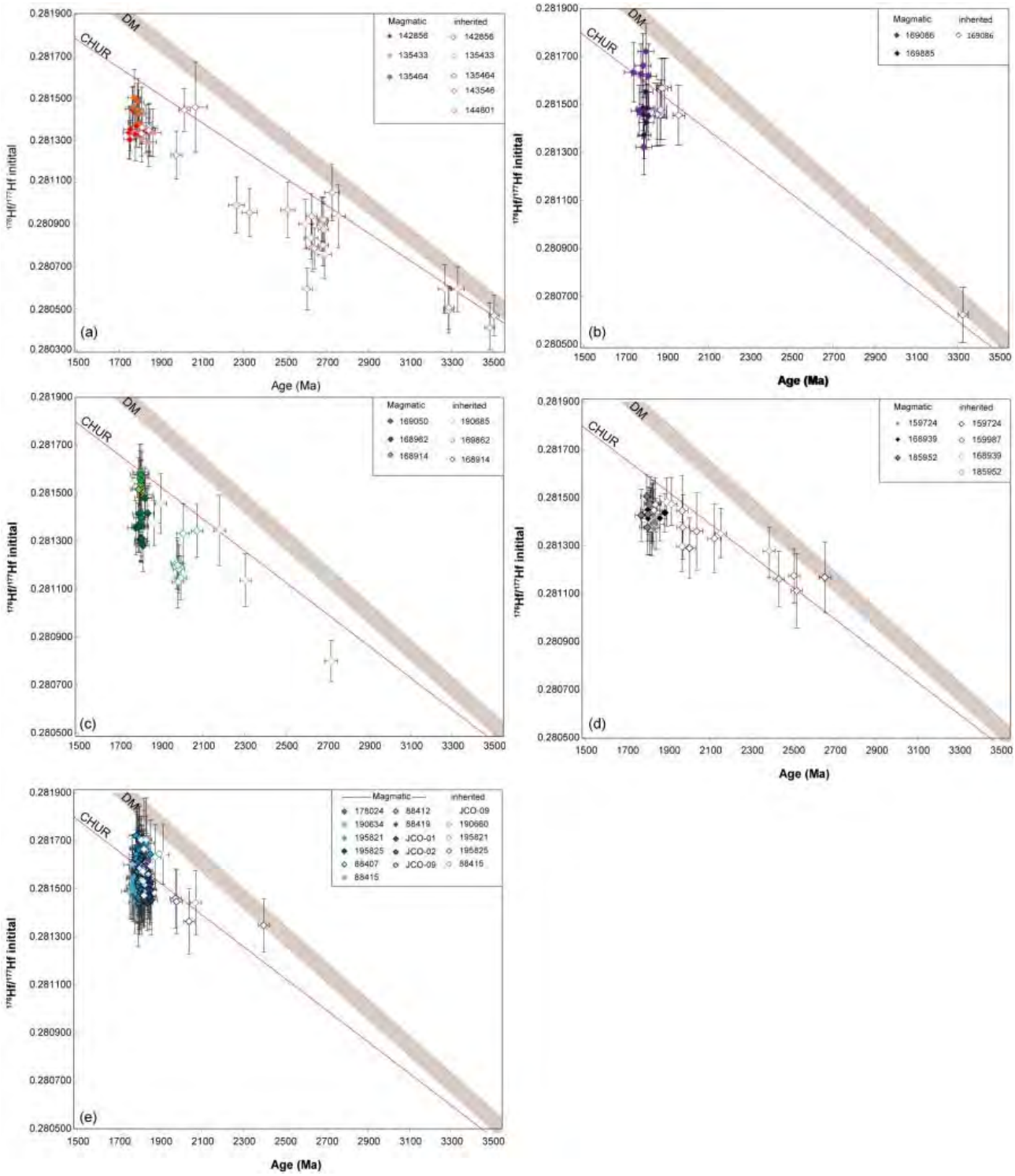

Figure 2.21. Evolution diagram of $^{176}Hf/^{177}Hf$ initial ratios for zircon from individual samples of the Moorarie Supersuite (a) southern granites, (b) northern granites, (c) eastern granites, (d) central granites (e) Minnie Creek Batholith.

Table 2.6. Summary of zircon hafnium and oxygen isotope data for Capricorn Orogeny magmatism.

Sample	Unit	Pb-Pb age (Ma)	εHf[1]	εHf range	TDMC[2]	$\delta^{18}O$[3] (‰)	δ18O range (‰)
144801	SG	-	-	-12.2 to +0.5	3621	-	4.93-6.51
143546	SG	-	-	-11.4 to 0	4093–3767	-	5.03-8.77
135433	SG	1838 ± 26	-9.1 ± 3.2 (5)	-11.3 to-6.9	3221	7.18 ± 0.42 (3)	7.03-7.42
135464	SG	1791 ± 11	-6.9 ± 2.4 (6)	-8.8 to -5.2	3053–2803	6.79 ± 0.79 (6)	6.34-7.47
142856	SG	1774 ± 12	-11.1 ± 3.4 (6)	-12.7 to -7.3	3192	6.92 ± 0.43 (5)	6.66-7.24
169086	NG	1806 ± 13	-0.8 ± 8.2 (8)	-11.0 to +3.3	2822–2360	6.29 ± 1.73 (9)	5.45-7.95
169885	NG	1802 ± 10	-5.9 ± 3.7 (7)	-9.1 to-2.6	n/a	9.01± 1.63 (7)	7.79-9.63
190685	EG	-	-3.5 (1)	-	n/a	-	6.71-7.59
169050	EG	-	-9.5 ± 4.8 (15)	-11.8 to -2.8	3298–2977	5.47 ± 0.41 (13)	5.11-5.8
169814	EG	1806 ± 5	-3.3± 5.8 (9)	-11.3 to -1.5	n/a	9.42 ± 0.53 (7)	9.04-9.76
169862	EG	1808 ± 13	-9.7 ± 4.5 (8)	-12.1 to -4.9	3265	6.29 ± 0.96 (3)	5.22-7.07
112107	EG	1773 ± 5	-	-	n/a	7.54± 0.96 (13)	5.75-9.0
159724	CG	1838 ± 7	-7.3 ± 2 (12)	-8.6 to -5.3	3055–2873	6.51 ± 0.45 (7)	6.17-6.83
159987	CG	-	-	-5.0 to -0.3	n/a	-	-
168939	CG	1826 ± 11	-5.7 ± 1.9 (8)	-7.4 to -4.8	n/a	8.1 ± 0.6 (7)	7.82-8.72
185952	CG	1808 ± 13	-6.8 ± 3.3 (5)	-8.8 to -4.4	n/a	-	-
142924	CG	-	-	-	-	-	-
195821	MCB	1785 ± 9	-4.3 ± 2.6(15)	-7.4 to -2.5	n/a	7.94 ± 0.52 (11)	7.52-8.45
190634	MCB	1787±14	-3.7 ± 2.9 (14)	-6.4 to -1.7	n/a	8.63 ± 0.73 (10)	8.19-9.23
JCO14-02	MCB	1799 ± 4	-3.9 ± 2.1 (15)	-7.2 to +0.8	n/a	9.42 ± 0.8 (13)	8.66-10.06
88419	MCB	1801 ± 10	+0.5 ± 1.2 (6)	-0.7 to +1.8	n/a	7.04 ± 0.62 (6)	6.66-7.37
178024	MCB	1798 ± 5	-0.5 ± 4.2 (15)	-4.6 to +2.7	n/a	7.22 ± 0.64 (11)	6.78-7.82
88415	MCB	1802 ± 7	-1.8 ± 0.6 (6)	-2.3 to -0.6	n/a	7.36 ± 0.85 (8)	6.86-8.17
88407	MCB	1803 ± 6	-2.2 ± 1.5 (11)	-5.9 to -0.3	n/a	7.87 ± 0.82 (12)	6.94-8.35
88412	MCB	1803 ± 4	-2.0 ± 1.1 (12)	-2.3 to -0.6	n/a	8.3 ± 1.1 (16)	7.97-10.23
JCO14-01	MCB	1806 ± 4	-3.9 ± 1.9 (11)	-5.4 to 0.0	n/a	9.12 ± 0.76 (7)	8.72-9.92
JCO14-09	MCB	1817 ± 6	-2.1 ± 2 (11)	-5.5 to +3.0	n/a	8.03 ± 0.4 (11)	7.61-8.26
JCO14-05	MCB	1814 ± 27	-	-	-	9.07 ± 1.11 (4)	8.3-9.48
190660	MCB	--	2 ± 1.4 (2)	+1.5 to +2.5	n/a	-	7.22-8.42

[1]SG= Southern granites, NG = Northern granites, EG = Eastern granites, CG = Central granites, MCB = Minnie Creek Batholith. [2]εHf values of magmatic zircon are expressed as median values in, ±2SD. Number of analyses donated in brackets. [3]TDMC will only be quoted where δ18O indicate magmatic values. 3δ18O values of magmatic zircon are expressed as mean averages, ±2SD. Number of analyses donated in brackets. (-) indicates no value obtained. Where no value is obtained for magmatic zircon, the range reflects values from inherited zircon.

- **Oxygen isotopic data**

Two hundred and ninety-six analyses were conducted on magmatic and inherited zircon grains from 27 granitic rocks (Figure 2.22; Table 2.6). Magmatic zircon $\delta^{18}O$ values of all analysed samples range between 3.91 and 10.23‰. Magmatic grains (n = 203) yield a range of $\delta^{18}O$ values between 5.11 and 10.23‰, with the average $\delta^{18}O$ of magmatic zircon from each sample varying from +5.47 ± 0.41 to +9.42 ± 0.53‰, 2σ. Inherited zircon grains (n = 93) with $^{207}Pb/^{206}Pb$ ages ranging between 3506 and 1818 Ma yield a range of $\delta^{18}O$ values between 3.9 and 10.1‰.

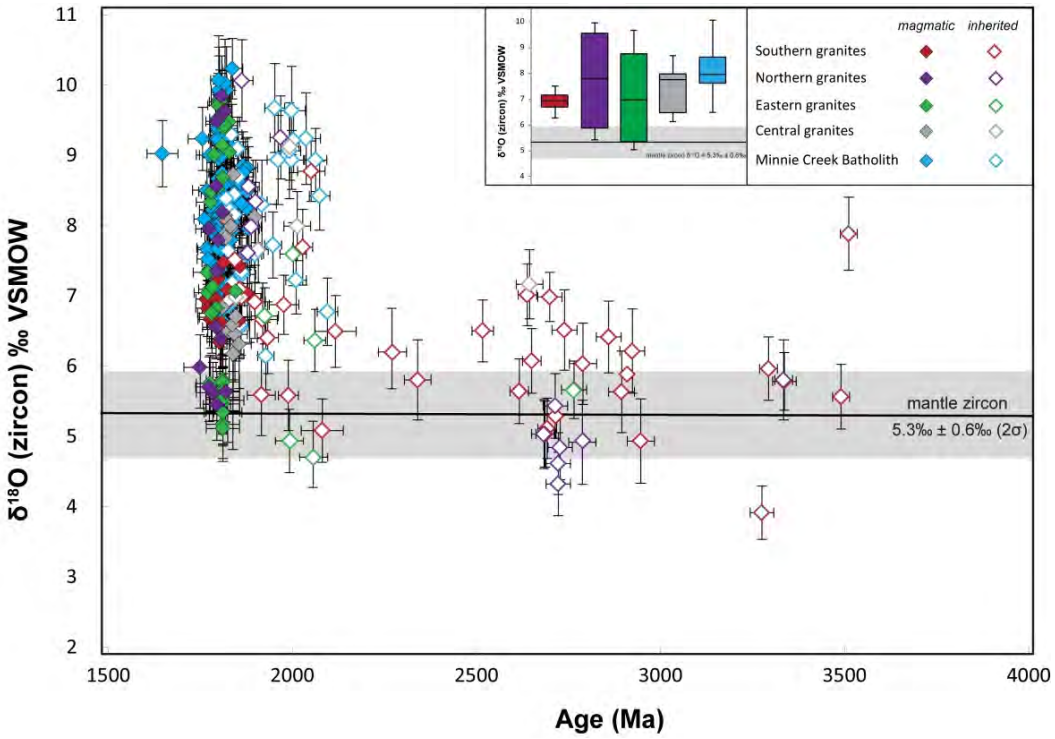

Figure 2.22 Oxygen isotope results from magmatic zircons in the Moorarie Supersuite.

2.4.10 Durlacher Supersuite

- **U–Pb geochronology**

The dataset from the Durlacher Supersuite consists of fourteen samples, and the analysed zircon cover a period of 1570 Myr, with ages between c. 2778 and c. 1209 Ma (Figure 2.23; Table 2.7). Granites were generated during one main magmatic episode at c. 1695–1645 Ma.

Table 2.7. Summary of sample descriptions and U–Pb LASS data for Durlacher Supersuite samples.

Sample	Unit[1]	lithology	Pb–Pb age (Ma)[2]	Inheritance (Ma)	Pb–Pb age (Ma)[3]	T_{ZR} (°C)	Lat	Long
168751	SG	monzogranite	1651 ± 13	2061–1705	1644 ± 6	753	-25.25506	117.74676
183212	DWB	granitic gneiss	1684 ± 9	2409–1739	1666 ± 5	746	-24.42339	115.71645
183215	DWB	metamonzogranite	1666 ± 6	1742–1721	1667 ± 3	772	-24.38626	115.90343
185944	DWB	monzogranite	1665 ± 8	2246–1706	1653 ± 10	803	-24.8899	116.0697
191993	DWB	metamongranite	1658 ± 5	1724–1713	1666 ± 7	784	-24.4572	116.1106
195826	DWB	metamonzogranite	1674 ± 5	2565–1738	1664 ± 8	741	-24.5575	115.745
195819	NG	metamonzogranite	1682 ± 11	1765–1748	1670 ± 7	781	-23.83188	115.33255
169054	MG	metatonalite	1667 ± 15	2778–1746	1674 ± 4	708	-23.94653	116.30706
169060	NG	syenogranite	(1692 ± 23)	2265	1673 ± 15	-	-23.9129	116.2055
178027	NG	granodiorite	-	2222–1748	1677 ± 5	-	-23.88722	115.65568
178030	NG	granodiorite	1689 ± 5	2320–1747	1678 ± 6	716	-23.5456	115.5853
178026	NG	syenogranite	(1690 ± 16)	1920–1805	1691 ± 9	613	-23.8601	115.67
JCO14-06	NG	metagranite	(1683 ± 19)	1798	-	590	-23.792716	115.70107
169092	NG	monzogranite	-	-	1681 ± 10	-	-23.42301	115.64358
TTSZ14	33SS	metagranite	(1665 ± 5)	2233–1712	-	764	-24.5156	116.2357
185946	33SS	pegmatite	*1035 ± 7	1749–1634	*1030 ± 6	600	-24.6547	116.1677
185945	33SS	pegmatite	(*1028 ± 26)	1738–1558	*1000 ± 8	712	-24.65474	116.16774

[1]SG = southern granites, DWB = Davey Well Batholith, NG = northern granites. [2]Crystallisation age ($^{207}Pb/^{206}Pb$) established by LASS, ages in brackets () indicate maximum crystallisation age, [*] indicates $^{206}Pb/^{238}U$ age. [3]Crystallisation age ($^{207}Pb/^{206}Pb$) established by SHRIMP (GSWA). (-) indicates no value obtained.

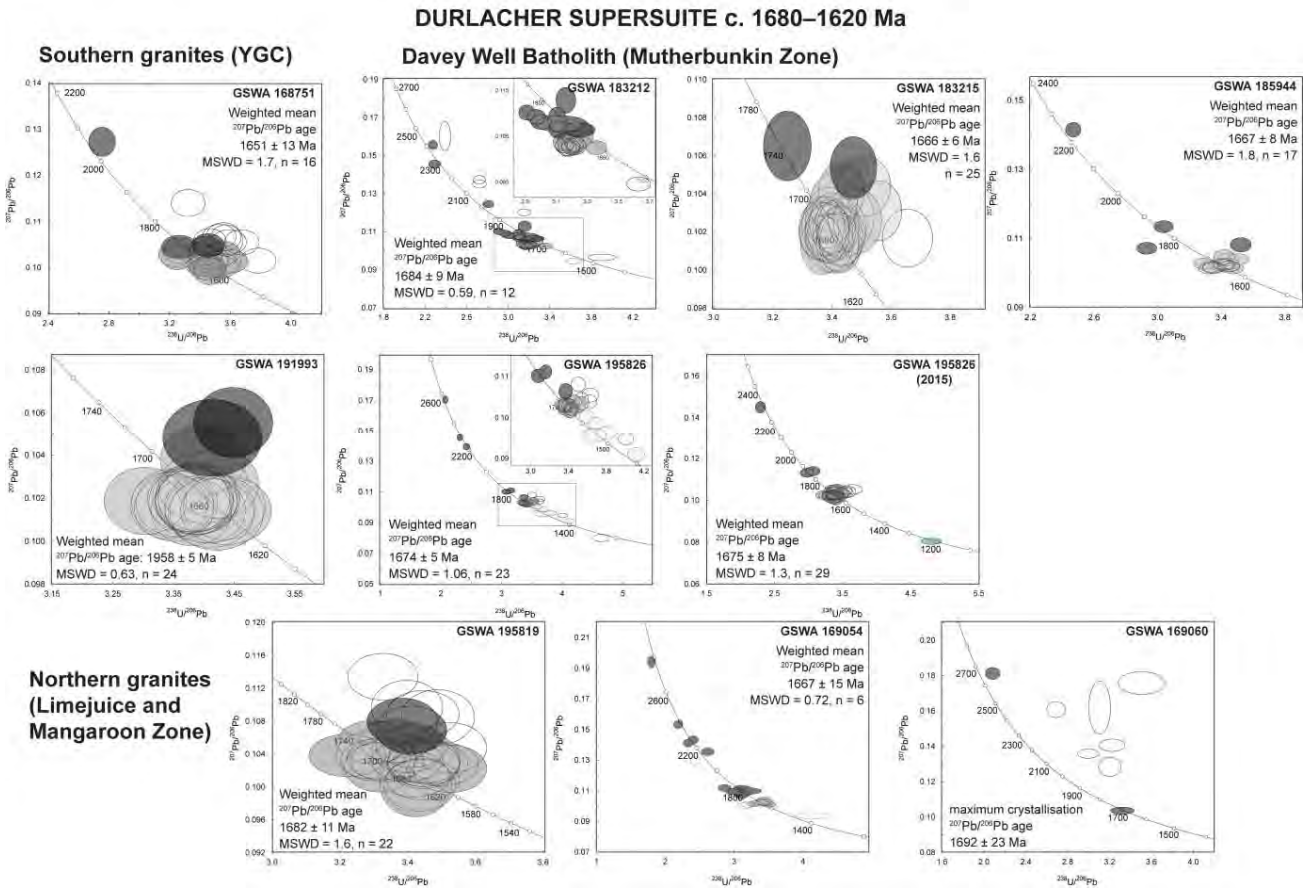

Figure 2.23. Concordia diagram for Durlacher Supersuite zircon with <10% discordance. Colour scheme follows that of Figure 2.7.

- **Zircon trace-element composition**

Durlacher Supersuite samples from the Gascoyne Province show similar REE patterns, which suggests that all the granites were derived from a source of similar composition (continental) and/or a similar degree of partial melting (Figure 2.24). Magmatic zircon trace element signatures indicate no evidence of co-crystallisation with garnet (Yb_N/Gd_N = 2–43, Eu/Eu* = 0.04– 0.74), indicating formation pressures lower than around 1.2 GPa (<45 km depth; Rubatto and Hermann, 2007).

All Durlacher Supersuite samples record zircon saturation temperatures with averages between 613 and 803°C (Ferry and Watson, 2007). These temperatures are comparable with the low-T inheritance-rich granitoids with T_{Zr} <800°C of Miller et al. (2003) that are interpreted as forming in regions of crustal thickening.

- **Lu–Hf isotopes**

A total of 149 analyses were conducted on magmatic and inherited zircon grains from 12 samples from the Durlacher Supersuite granites. Initial $^{176}Hf/^{177}Hf$ ratios of all analysed zircon grains range between 0.281002 and 0.281873, corresponding to εHf values of -19.8 and +5.6 (Figure 2.25; Table 2.8). Magmatic grains (*n* = 113) yield a range of initial $^{176}Hf/^{177}Hf$ ratios between 0.281347 and 0.281677 (εHf -13and -1.3), with median εHf values from each sample ranging between -10.7 ± 2.7 and -3.2 ± 1.8, 2σ. Inherited zircon grains (*n* = 61) with $^{207}Pb/^{206}Pb$ ages ranging between 2565 and 1646 Ma yield a range of εHf values between -9.3 and -0.7. One analysis of a rim dated at c. 1217 Ma returned an initial $^{176}Hf/^{177}Hf$ ratio of 0.281456 (εHf -19.8).

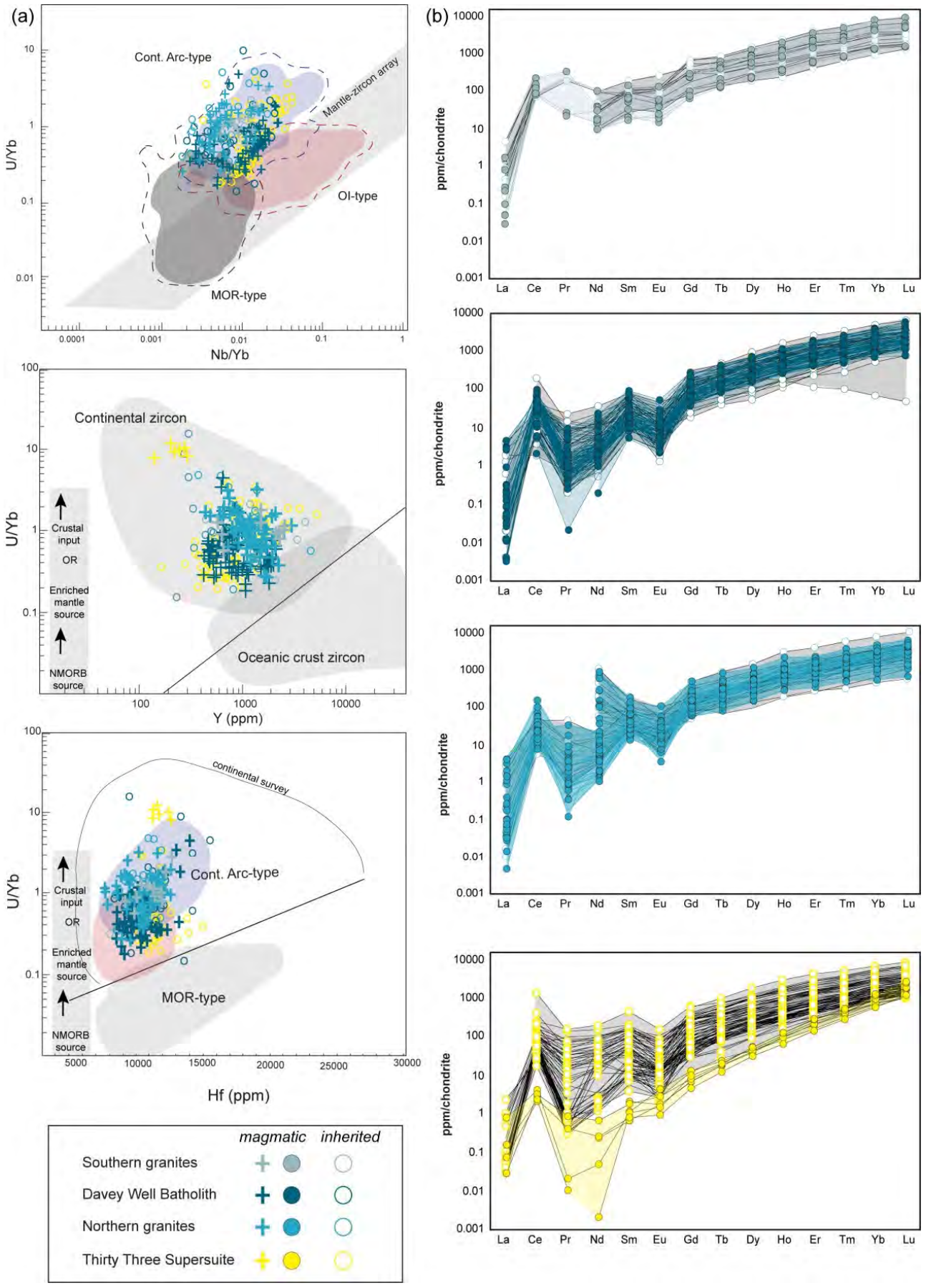

Figure 2.24. Discrimination diagrams and chondrite-normalised plots for trace elements recorded in Durlacher and Thirty-three supersuites zircons. Discrimination fields after Grimes et al. (2007; 2015).

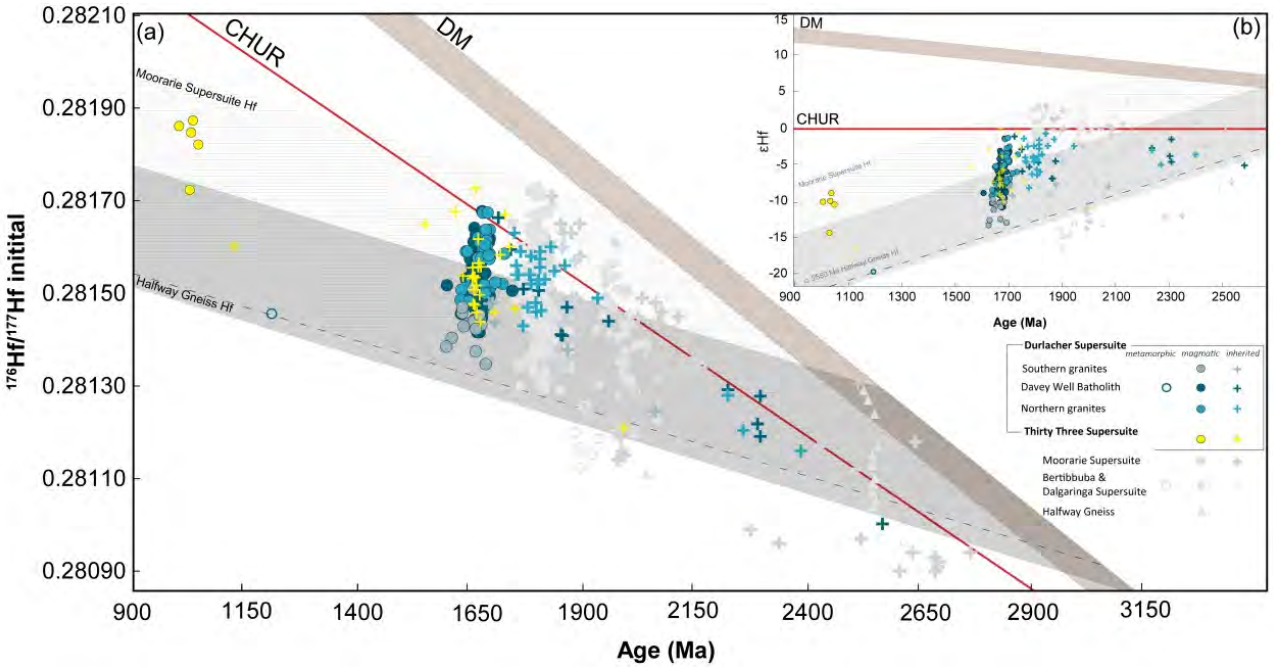

Figure 2.25. Lu–Hf isotope results from the Durlacher Supersuite. Grey shaded area: isotopic envelope for the Halfway Gneiss Hf (work presented herein) and striped area: isotopic envelope for the Moorarie Supersuite Hf (work presented herein). The dashed line is a reference evolution line corresponding to a Lu/Hf ratio of 0.015. (a) Initial Hf evolution plot for the Durlacher and Thirty Three Supersuite (n = 149), (b) εHf evolution diagram for zircon from the Duralcher Supersuite.

Table 2.8. Summary of hafnium and oxygen isotope data for Durlacher Supersuite samples.

Sample	Unit[1]	Pb-Pb age[2] (Ma)	εHf[3]	εHf range	TDMC[4]	$\delta^{18}O$[4] (‰)	$\delta^{18}O$ range (‰)
168751	SG	1651 ± 13	-10.7 ± 2.7 (13)	-13 to -7.8	3169–3046	6.38 ± 1.39 (12)	5.46–7.39
183212	DWB	1684 ± 9	-3.2 ± 1.8 (3)	-3.4 to -1.4	n/a	8.96 ± 0.82 (7)	8.49–9.85
183215	DWB	1664 ± 5	-6.3 ± 3.2 (12)	-9.2 to -3.6	n/a	-	-
185944	DWB	1665 ± 8	-8.5 ± 4.3 (6)	-10.2 to -3.5	n/a	-	-
191993	DWB	1658 ± 5	-6.4 ± 2.7 (14)	-8.4 to -3.1	n/a	8.65 ± 0.38 (10)	8.29–8.98
195826	DWB	1675 ± 8	-8.1 ± 3.3 (22)	-10.9 to -5.1	n/a	7.85 ± 1.01 (13)	6.95–9.02
195819	NG	1682 ± 11	-6.9 ± 3.9(13)	-9.8 to -3.9	n/a	8.97 ± 0.72 (14)	8.33–9.64
169054	NG	1667 ± 15	-5.2 ± 3.2 (3)	-7.4 to -3.5	n/a	-	-
169060	NG	*1692±23*	-	-	n/a	-	-
178027	NG	-	-4 ±2.7 (11)	-5.7 to -1.4	2702	*9.59 ± 0.49 (1)*	-
178030	NG	1689 ± 5	-3.9 ±2.6 (14)	-6.2 to -1.3	n/a	-	-
178026	NG	*1690 ± 16*	*-2.5 ± 3 (1)*	-	n/a	-	6.74–9.82
JCO14-06	NG	*1683 ± 19*	-	-	n/a	8.31 ± 0.05 (2)	8.28–8.33
169092	NG	-	-	-	n/a	-	6.87–10.41
TTSZ14	33SS	*1665 ± 5*	-	-10.9 to -0	n/a	-	5.59–8.92
185946	33SS	*1035 ± 7	-10 ± 1.2 (4)	-10.5 to -8.9	n/a	8.32 ± 0.96 (3)	7.93–8.99
185945	33SS	*1028 ± 26*	-15.4 ± 2.1(2)	-16.5 to -14.4	n/a	*8.84 ± 0.96 (1)*	-

[1]SG= Southern granites, DWB = Davey Well Batholith, NG = Northern granites. [2][*] indicates $^{206}Pb/^{238}U$ age, [3]εHf values of magmatic zircon are expressed as median values in, ±2SD. Number of analyses donated in brackets. [4]TDMC will only be quoted where $\delta^{18}O$ indicate magmatic values. [4]δ18O values of magmatic zircon are expressed as averages, ±2SD. Number of analyses donated in brackets. (-) indicates no value obtained. Where no value is obtained for magmatic zircon, the range reflects values from inherited zircon. n/a indicates not available.

- **Oxygen isotopes**

A total of 104 zircon grains were analysed from 9 samples. Zircon $\delta^{18}O$ values of all analysed zircon grains range between 5.46 and 10.95‰ (Figure 2.26 & 2.27; Table 2.8). Magmatic grains (n = 59) yield a range of $\delta^{18}O$ values between 5.46 and 9.85‰, with median εHf values from each sample ranging between 6.38 ± 1.39 and 8.97 ± 0.72‰ 2σ. Inherited zircon grains (n = 37) with $^{207}Pb/^{206}Pb$ ages ranging between 2288 and 1713 Ma yield a range of $\delta^{18}O$ values between 5.46 and 10.95‰. Analyses with no corresponding age data have $\delta^{18}O$ values between 6.87 and 10.41‰.

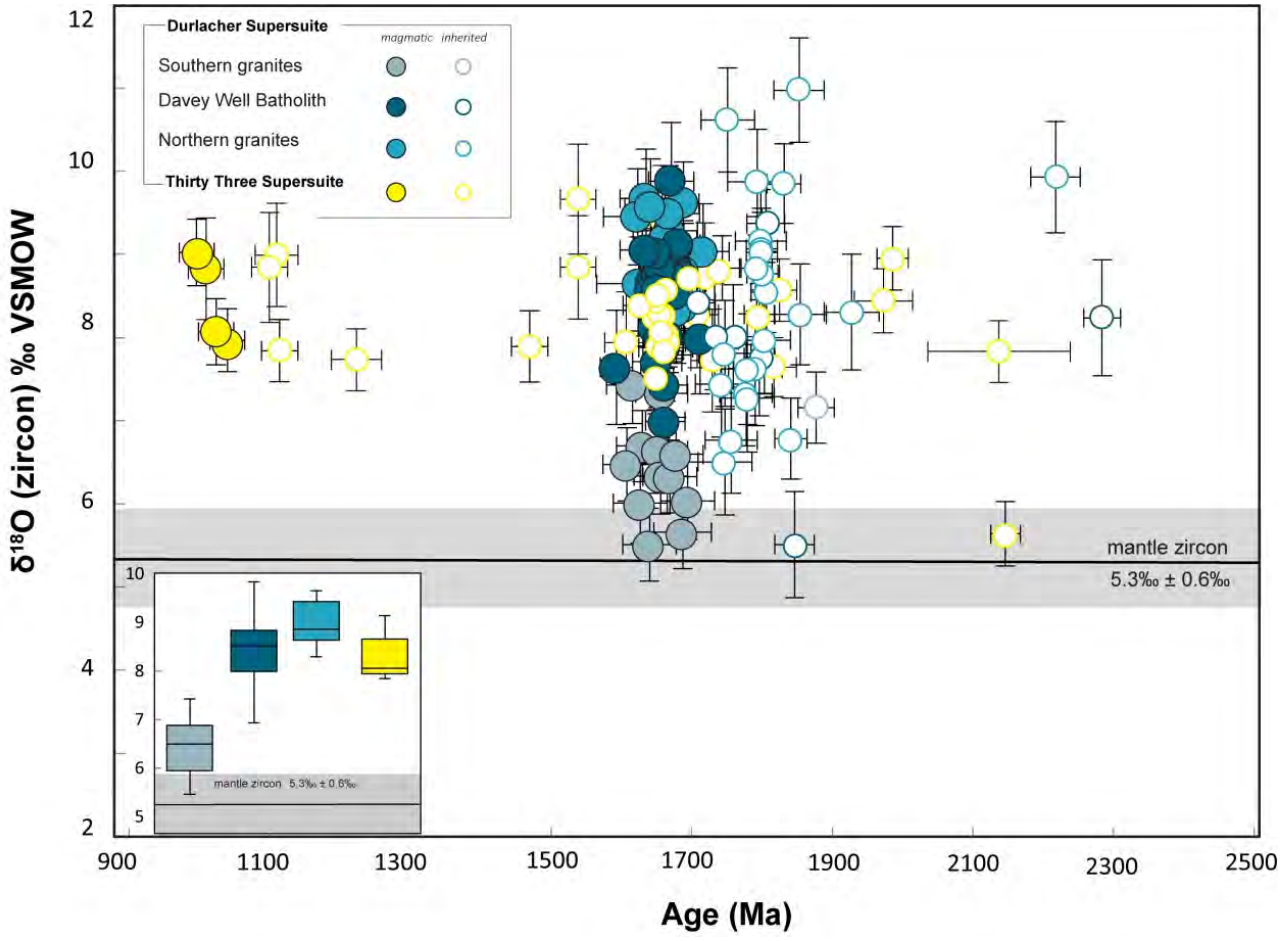

Figure 2.26. Oxygen isotope results from magmatic zircons in the Durlacher and Thirty-three Supersuites.

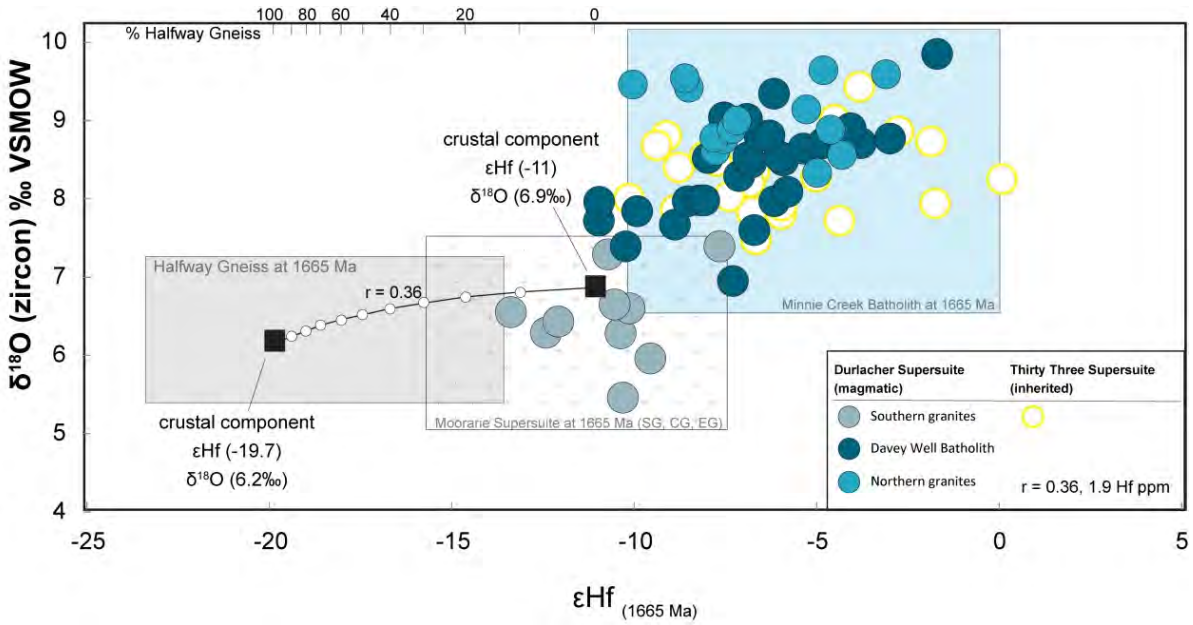

Figure 2.27. Plot of $\delta^{18}O$ versus εHf for magmatic zircon from the Durlacher Supersuite and inherited zircon from the Thirty Three Supersuite. The blue box represents the Minnie Creek Batholith at c. 1665 Ma, the stippled (crosses) box represents the Southern, Central and Eastern Granites of the Moorarie Supersuite at c. 1665 Ma, grey box represents the Halfway Gneiss granitoids at c. 1665 Ma (based on Hf–O data presented herein). The parameters of end members are discussed in text. Bulk mixing curves are marked at 10% increments.

2.4.11 Thirty Three supersuite

- **U–Pb geochronology**

The dataset from the Thirty Three Supersuite consists ofthree samples, and the analysed zircon cover a period of 1229 Myr, with ages between c. 2233 and c. 1004 Ma (Figure 2.28). Granites were generated during one main magmatic episode at c. 1050–1015 Ma.

- **Zircon trace-element composition**

Magmatic zircon trace element signatures plot within the continental field and display no evidence of co-crystallisation with garnet (Yb_N/Gd_N = 31–36, Eu/Eu* = 0.46–1.13), indicating formation pressures lower than around 1.2 GPa (Figure 2.24; <45 km depth; Rubatto and Hermann, 2007). Inherited zircon have a steep M–HREE slope (Yb_N/Gd_N = 5–51) and slightly more pronounced Eu anomalies (Eu/Eu* = 0.02–0.82), similar to that of the Durlacher Supersuite. Zircon Ti crystallisation temperatures range between 600 and 764°C.

- **Lu–Hf isotopes**

A total of 31 zircon grains were analysed from three samples. Magmatic grains (n = 4) yield a range of initial $^{176}Hf/^{177}Hf$ ratios between 0.281723 and 0.281873 (εHf -14.4 and -8.9; Figure 2.25). One sample returned a median εHf value of -10 ± 1.2, 2σ. Inherited zircon grains (n = 26) with $^{207}Pb/^{206}Pb$ ages ranging between 1991 and 1127 Ma yield a range of εHf values between -16.5 and 0.

- **Oxygen isotopes**

A total of 44 analyses were obtained from three samples. Zircon $\delta^{18}O$ values of all analysed zircon grains range between 5.46 and 9.69‰. Magmatic grains (n = 4) yield a range of $\delta^{18}O$ values between 7.93 and 8.99‰ (average 8.32 ± 0.96‰, 2σ; Figure 2.26 & 2.27). Inherited zircon grains (n = 28) with $^{207}Pb/^{206}Pb$ ages ranging between 2151 and 1147 Ma yield a range of $\delta^{18}O$ values between 5.59 and 9.69‰.

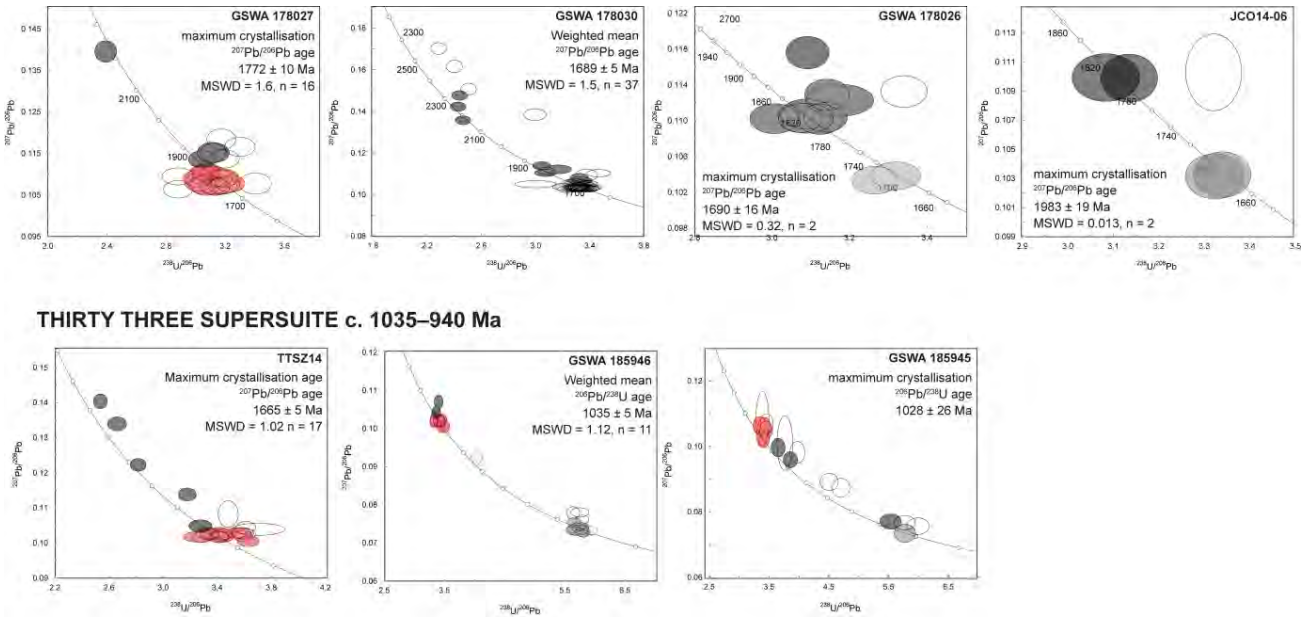

Figure 2.28. Concordia diagram for Thirty-three Supersuite zircon with <10% discordance. Colour scheme follows that of Figure 2.7.

2.5 Detrital zircon geochronology and geochemistry

In total, 5610 detrital zircon analyses have been compiled from the literature (Supplementary Table 2.1 for data sources). A further 1500 detrital zircon analyses were obtained from the Yerrida Basin, 1930 analyses from the Bryah and Padbury Basins, 1965 from the Edmund Basin and 832 from the Collier Basin. Published data were screened to remove any analyses that were performed on metamorphic overgrowths.

For data display and analysis, the software *isoplot 4.15* (Ludwig, 2012) was used to produce Tera-Wasserburgh concordia diagrams, with Excel macros available from the Arizona Laserchron Centre website (http://www.geo.arizona.edu/alc) used to produce detrital zircon age probability density plots (PDP). Peak ages were assessed with the *AGE PICK* analytical tool (Gehrels et al., 2008), while kernel density plots of detrital zircon age populations, and comparisons of detrital zircon age populations between samples (multidimensional scaling - MDS) were performed in the R statistical provenance analysis package (Vermeesch et al., 2016).

2.5.1 Depositional age constraints and primary sources

Only zircon analyses within 10% of concordance were considered when identifying significant youngest age components and characteristic subpopulation ages.

- **Ashburton province**

The Beasley River Quartzite has a youngest detrital zircon age component at ~2.25 Ga. The detrital zircon age spectrum is polymodal with a dominant age peak at ~2.5 Ga corresponding to Halfway Gneiss crystallisation ages, distinct subordinate age sub-populations at ~2.45, 2.7 and 2.8 Ga and an Archean tail (Figure 2.29).

Intercalated sediments within the Cheela Springs Basalt yield detrital zircons with a broadly bimodal age spectrum (Figure 2.29). The Cheela Springs Basalt have a youngest age component at ~2.1 Ga and approximately equivalent dominant age peaks at ~2.2 Ga and 2.5 Ga that correspond to proposed magmatism of the Ophthalmian Arc (Johnson et al., 2011a) and Halfway Gneiss, respectively. A minor, poorly defined subpopulation age peak is also apparent at ~2.7 Ga.

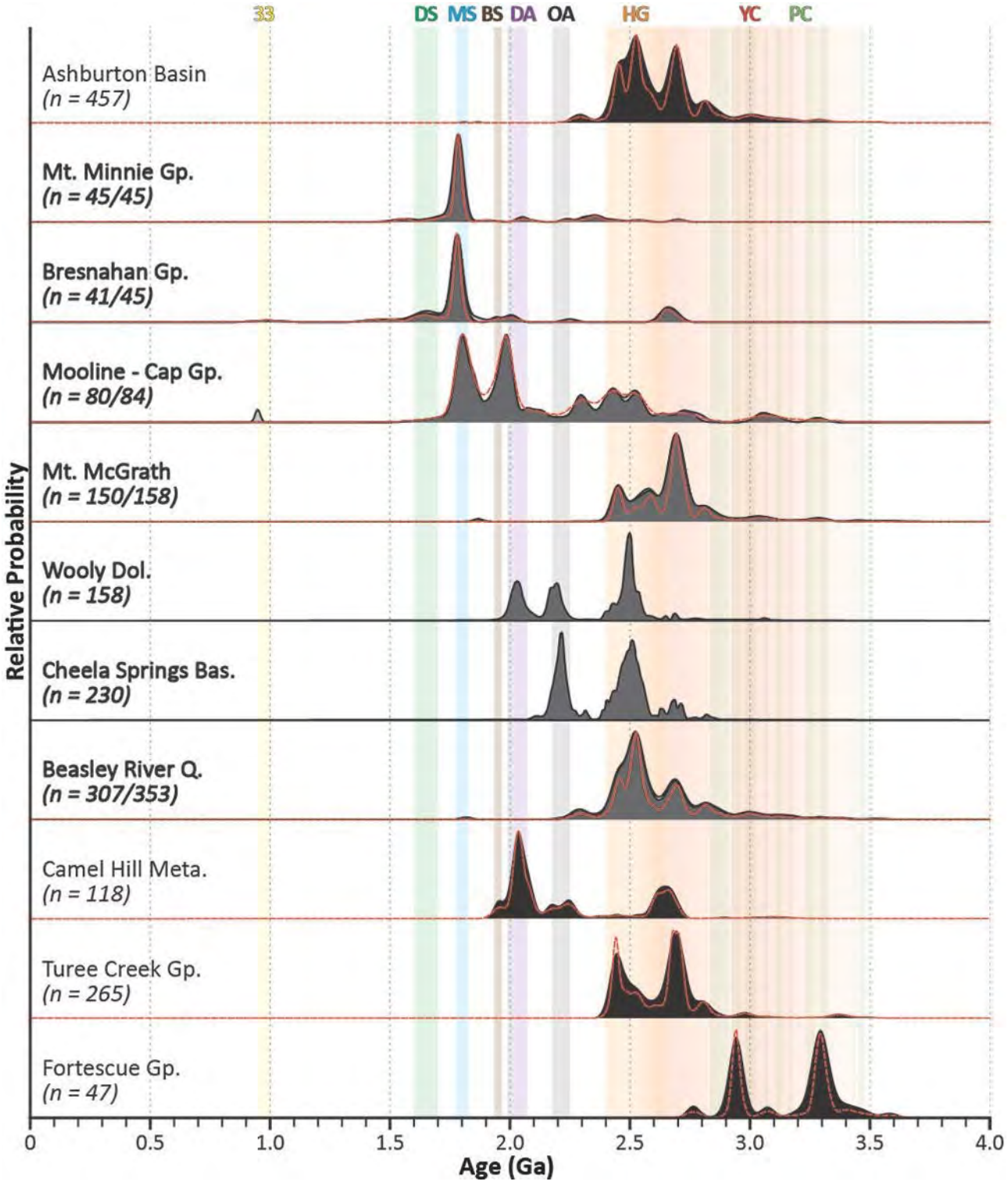

Figure 2.29. Stacked probability plot of detrital zircon ages from the Ashburton Basin and potential sediment source regions. Red dashed lines represent kernel density estimates for the zircon populations. Black spectra correspond to normalised probability density diagrams for pooled concordant analyses (± 10%) from specific regions, dark grey spectra represent concordant zircon analyses (± 10%) of a particular lithostratigraphic unit and are overlain on pale grey spectra representing all zircon ages derived for the same unit. Vertical coloured bars correspond to ages of major regional magmatic events – 33 = Thirty-three Supersuite; DS = Durlacher Supersuite; MS = Moorarie Supersuite; BS = Bertibubba Supersuite; DA = Dalgaringa Arc; OA = Opthalmian Arc; HG = Halfway Gneiss; YC = Yilgarn Craton; PC = Pilbara Craton.

Detrital zircons from the Wooly Dolomite are clustered in three discrete age peaks (Figure 2.29). The youngest detrital zircon sub-population component is at ~2.0 Ga, with a dominant 2.5 Ga (Halfway Gneiss) age spectrum peak and subordinate subpopulations centred at ~2.05 and 2.2 Ga, which correlate with hypothetical arc magmatism in the Dalgaringa and Ophthalmian Arcs, respectively (Johnson et al., 2011a).

Mount McGrath detrital zircons have a youngest significant age component at ~2.4 Ga and a dominant age peak at ~2.7 Ga (Figure 2.29). Subordinate subpopulation age peaks at ~2.45 and 2.6 Ga (Halfway Gneiss) and ~2.8 Ga are also apparent.

Detrital zircons in the Mooline Fm. (Capricorn Group, Blair Basin) have a youngest zircon grain of ~1.65 Ga (subpopulation at ~1.75 Ga) and two dominant age peaks at ~1.8 Ga and ~2.0 Ga, corresponding to the Moorarie Supersuite and the Glenburgh Orogeny (Dalgaringa and Bertibubba Supersuites), respectively (Figure 2.29). The detrital zircon age spectrum exhibits a tail of older grains to ~3.3 Ga with subordinate age subpopulations peaks at ~2.3, 2.45 and 2.55 Ga that in part correspond to the Halfway Gneiss.

Limited data from the Bresnahan Group (Bresnahan Basin) demonstrate a youngest coherent age component at ~1.6 Ga and an almost unimodal dominant age peak at ~1.8 Ga that corresponds with Moorarie Supersuite magmatism (Figure 2.29). Less defined subordinate subpopulation peaks in the age spectrum are at 1.65 Ga (Durlacher Supersuite) and 2.65 Ga.

Limited detrital zircon analyses in the Mt Minnie Group sediments (Mt. Minnie Basin) are essentially unimodal with a dominant age peak at ~1.8 Ga corresponding to the Moorarie Supersuite (Figure 2.29). A youngest age component is defined by two grains at ~1.55 Ga.

- **Southern Paleoproterozoic basins**

Yerrida Basin

A large detrital zircon dataset compiled for the Juderina Formation indicates a youngest significant age component at ~2.1 Ga and an otherwise essentially unimodal dominant age population centred on ~2.7 Ga corresponding to the Yilgarn Craton (Figure 2.30). Overall analyses were significantly discordant with older ages increasingly represented by discordant analyses. Very minor sub-populations are expressed in the Paleoarchean. More detailed sampling within the formation demonstrates an evolution of the dominant age peak up through the section from ~2.6 Ga in TD10 to ~2.7-2.75 Ga in samples TD6 to TD1 (Figure 2.31). The youngest age component is relatively consistent through the samples though there is a concurrent increase in the contribution of older Mesoarchean and Paleoarchean detrital grains in samples TD6 to TD1.

A very limited detrital zircon population is currently available from supposed rocks of the Killara Formation with a number of discrete age spectra peaks represented by a few grains only ranging from ~1.3 Ga to ~3.3 Ga (Figure 2.30).

A small population of detrital zircons from the Doolgunna Formation define a tightly defined unimodal peak at ~2.65 Ga corresponding to widespread Yilgarn Craton magmatism (Figure 2.30).

Bryah Basin

Previously acquired detrital zircon age data (Halilovic, 2002) for the Karalundi Formation exhibits a broadly bimodal spectrum (Figure 2.32). The youngest age component at ~1.9 Ga forms part of a subordinate sub population centred at ~2.0 Ga (Dalgaringa Supersuite). The dominant broad age peak is centred at ~2.7 Ga and has defined shoulders at ~2.6 Ga and ~2.8 Ga (Yilgarn Craton magmatism). New data obtained herein are broadly in agreement with peak population ages of ~2.7 Ga, but with less significant Glenburgh Orogeny associated zircon contribution and greater Mesoarchean zircon contribution in RBSH03-04 (Figure 2.32).

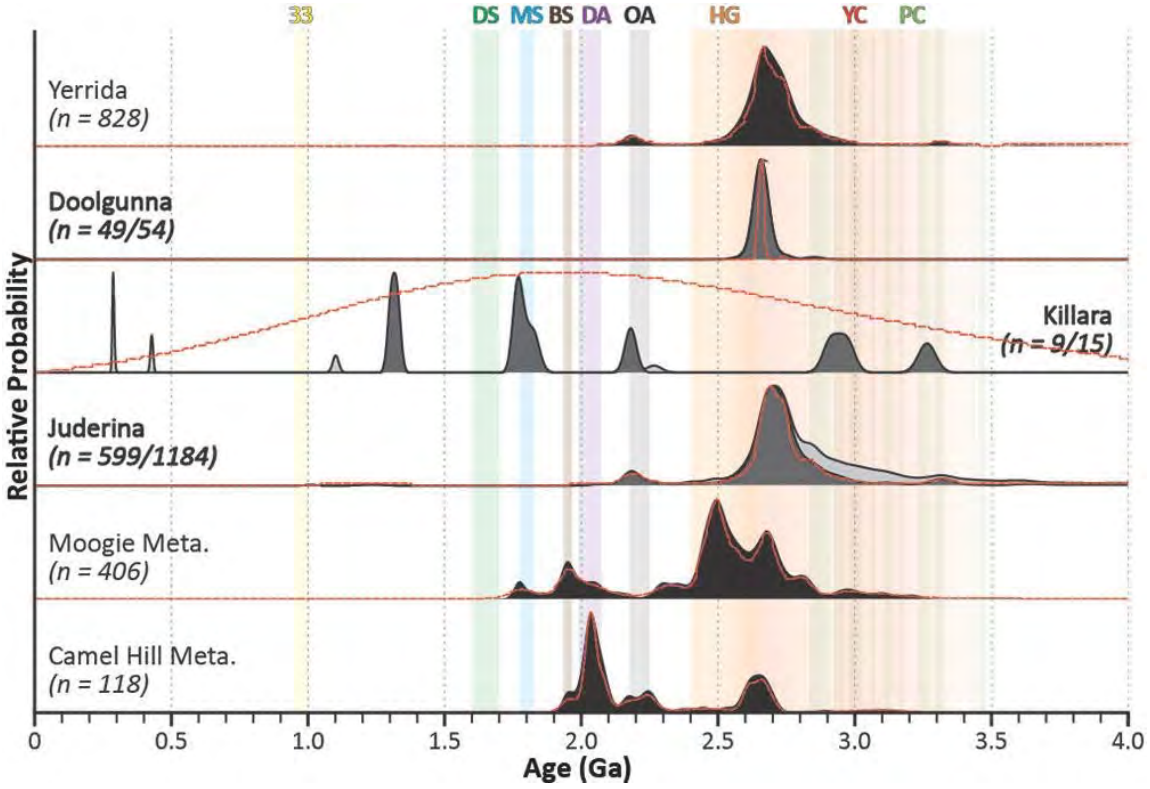

Figure 2.30. Stacked probability plot of detrital zircon ages from the Yerrida Basin and potential sediment source regions. Red dashed lines represent kernel density estimates for the zircon populations. Black spectra correspond to normalised probability density diagrams for pooled concordant analyses (± 10%) from specific regions, dark grey spectra represent concordant zircon analyses (± 10%) of a particular lithostratigraphic unit and are overlain on pale grey spectra representing all ages for the same unit. Vertical coloured bars correspond to ages of major regional magmatic events (see caption to Fig. 2.29). New analyses for the Juderina Formation combined with published data.

Newly acquired detrital zircon age data for the Narracoota Formation display a well-defined unimodal population with a youngest age component at ~2.1 Ga and dominant peak age centred at ~2.7 Ga, which corresponds with widespread Yilgarn Craton magmatism (Figure 2.32).

Previously dated (Halilovic, 2002) detrital zircons from the Ravelstone Formation define an almost unimodal age spectrum with a dominant peak at ~2.7 Ga corresponding to significant Yilgarn Craton magmatism (Figure 2.32). The youngest significant zircon sub-population is centred at ~2.0 Ga (Dalgaringa Supersuite), with additional very minor age components at ~2.55 Ga and 3.6 Ga resolvable in the age spectrum. Newly acquired detrital zircons from material mapped as Ravelstone Formation (BP10) display a significantly different polymodal age spectrum with a dominant 2.0 Ga peak and multiple subordinate peaks ranging from 1.2 to 3.4 Ga (Figure 2.32).

Padbury Basin

Previously acquired (Halilovic, 2002) detrital zircon analyses from the Labouchere Formation define a polymodal population (Figure 2.33). The youngest age sub-population peak is defined at ~1.8 Ga and corresponds to the age of the Moorarie Supersuite. A defined dominant age peak is centred at ~2.05 Ga (Dalgaringa Supersuite magmatism), with a second broader significant peak subpopulation at ~2.7 Ga (Yilgarn Craton magmatism). Subordinate subpopulations are further apparent at ~2.15 and ~2.3 Ga. Newly acquired data from the Labouchere Formation demonstrate lateral/stratigraphical variation that corresponds to the mixed age spectrum signal previously identified (Halilovic, 2002). Samples BP3 and BP11 are dominated by detrital zircons of ~2.6-2.8 Ga age with only minor Paleoproterozoic contributions, while sample BP2 has a subordinate ~2.65 Ga peak to dominant ~2.0, ~2.2and ~2.3 Ga peaks (Figure 2.33).

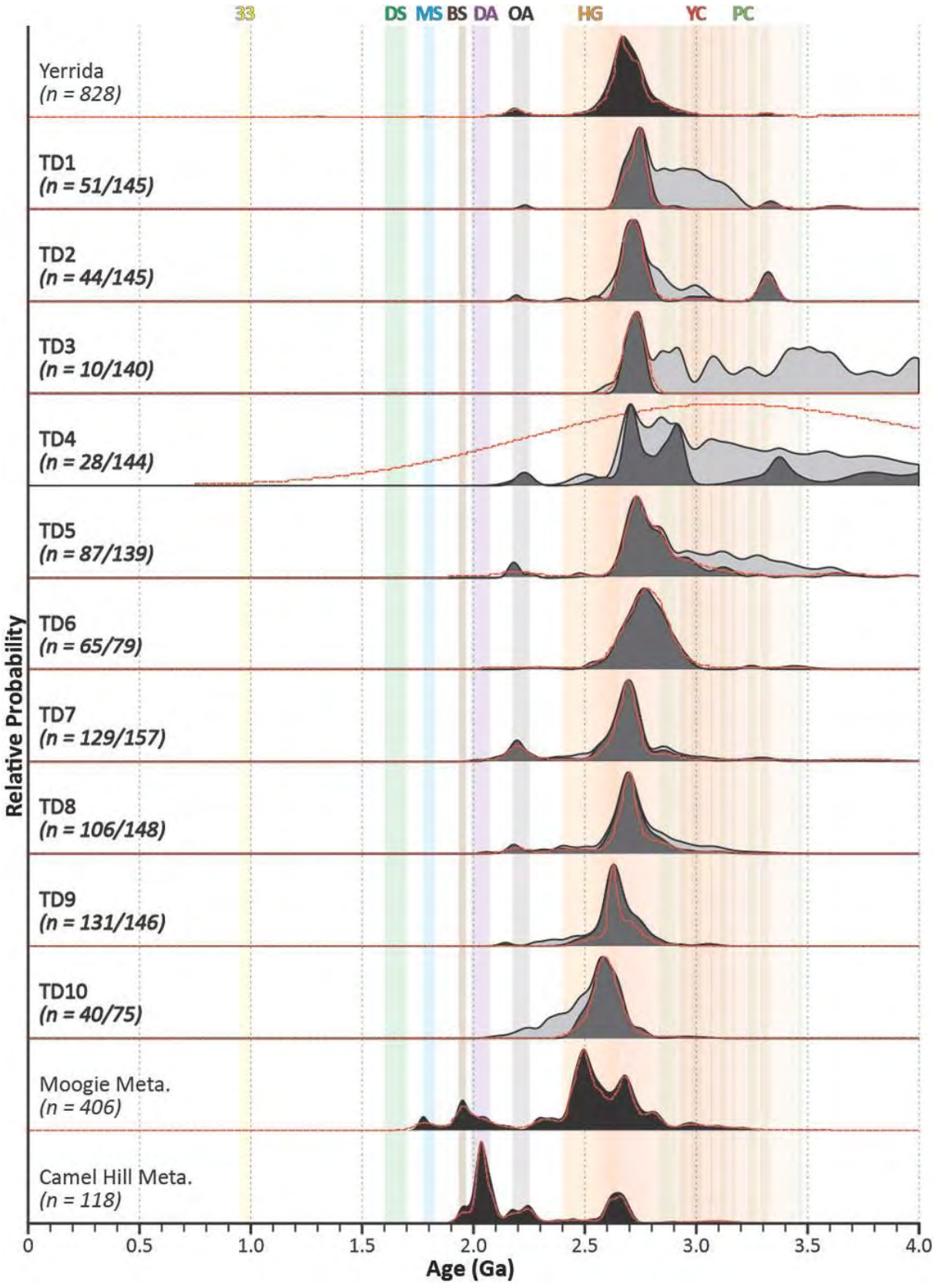

Figure 2.31. Stacked probability plot of detrital zircon ages from the Juderina Formation in the Yerrida Basin and potential sediment source regions. Red dashed lines represent kernel density estimates for the zircon populations. Black spectra correspond to normalised probability density diagrams for pooled concordant analyses (± 10%) from specific regions, dark grey spectra represent concordant zircon analyses (± 10%) of a particular lithostratigraphic unit and are overlain on pale grey spectra representing all ages for the same unit. Vertical coloured bars correspond to ages of major regional magmatic events (see caption to Figure 2.29).

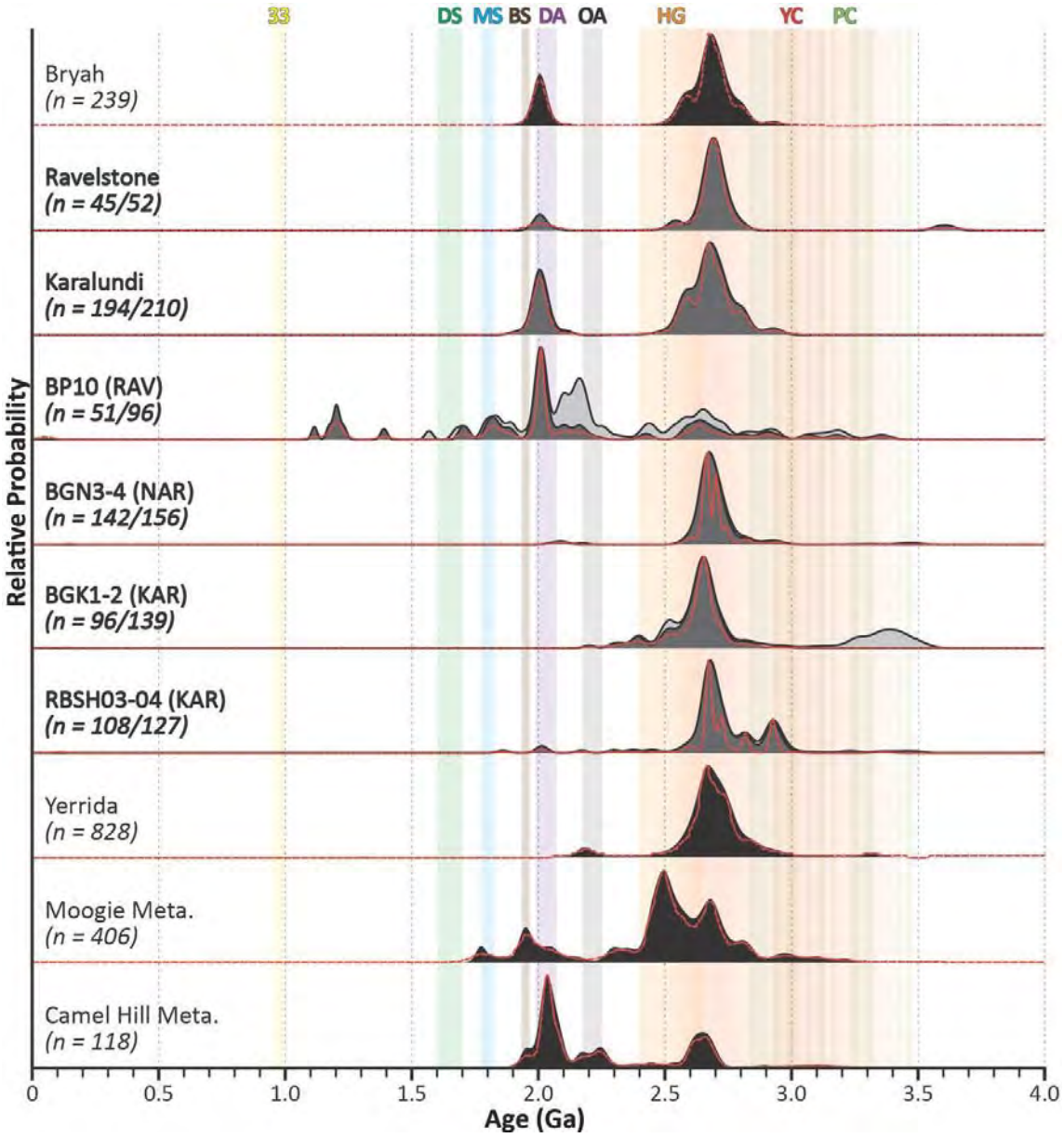

Figure 2.32. Stacked probability plot of detrital zircon ages from the Bryah Basin and potential sediment source regions. Red dashed lines represent kernel density estimates for the zircon populations. Black spectra correspond to normalised probability density diagrams for pooled concordant analyses (± 10%) from specific regions, dark grey spectra represent concordant zircon analyses (± 10%) of a particular lithostratigraphic unit and are overlain on pale grey spectra representing all ages for the same unit. Vertical coloured bars correspond to ages of major regional magmatic events (see caption to Figure 2.29). Sample numbers indicate new analyses conducted herein. KAR – Karalundi Formation; NAR – Narracoota Formation; RAV – Ravelstone Formation.

The Wilthorpe Formation detrital zircon population has a youngest significant age component defining a subordinate sub-population centred at 2.0 Ga (Dalgaringa Supersuite magmatism) and an otherwise unimodal dominant age peak at ~2.6 Ga that correlates to voluminous Yilgarn Craton magmatism (Figure 2.33). Minor age contributions from ~2.8-3.1 Ga concordant zircons form a minor tail to the age spectrum. Newly acquired detrital zircon geochronology here is in broad agreement with that previously available (Halilovic, 2002), with a clear Neoarchean dominance and minor Paleoproterozoic contributions. Sample BP8 in the Wilthorpe Formation also displays a prominent ~3.3 Ga subordinate age peak in its detrital zircon age spectrum.

Newly acquired detrital zircon geochronological data from the Milliddie Creek Formation inidicate a unimodal age population centred on ~2.7 Ga, with minor Paleoproterozoic and older Archean contributions (Figure 2.33).

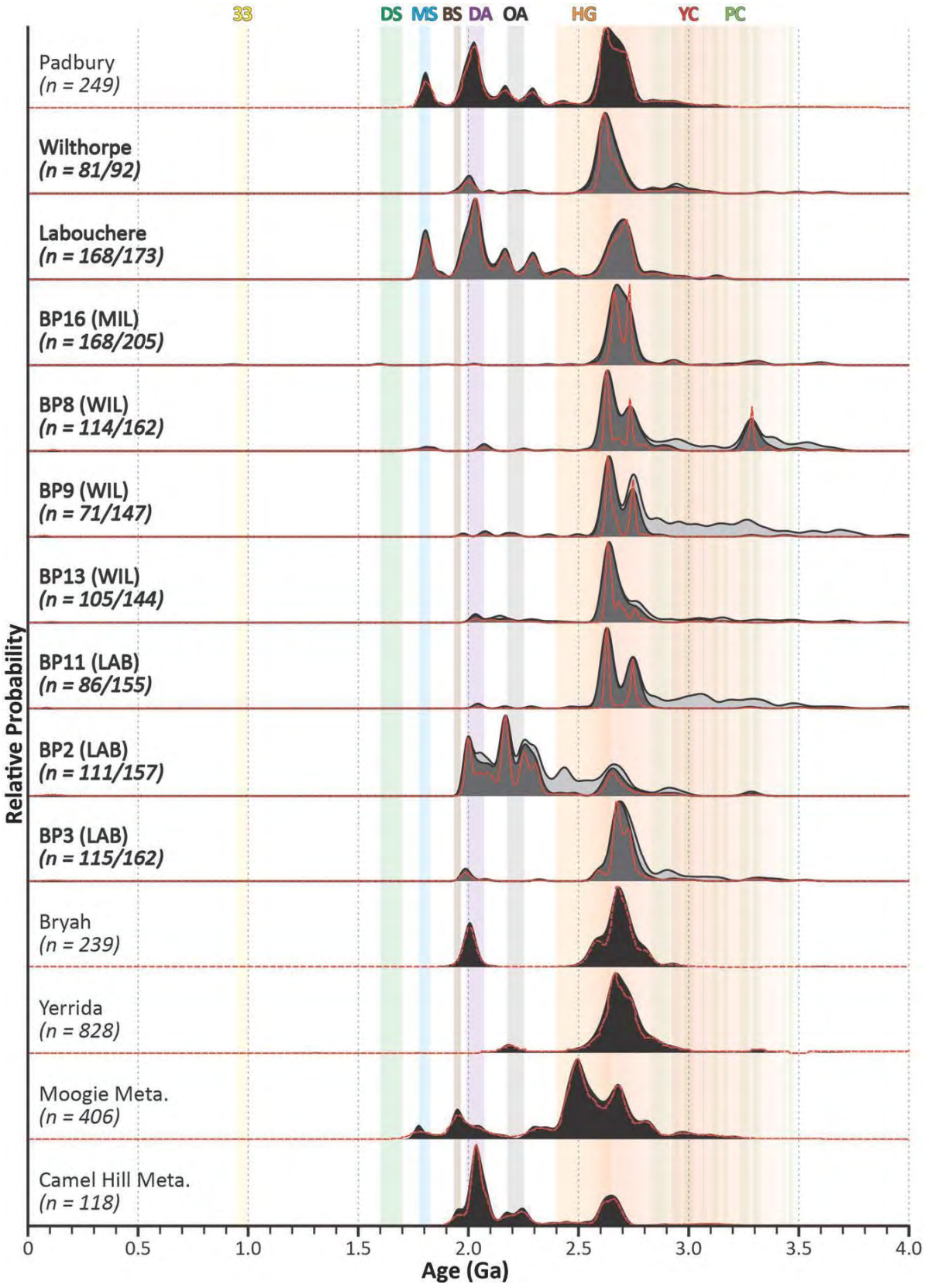

Figure 2.33. Stacked probability plot of detrital zircon ages from the Padbury Basin and potential sediment source regions. Ornament and arrangement follows that in Figure 2.29. Sample numbers indicate new analyses conducted herein. LAB – Labouchere Formation; WIL – Wilthorpe Formation; MIL – Millidie Creek Formation.

Earaheedy Basin

Significant numbers of discordant analyses are recorded the Yelma Formation (Figure 2.34). The youngest concordant detrital zircon age component is at ~1.95 Ga. The formation has a dominant detrital age peak centred at 2.65 Ga (Yilgarn Craton magmatism) and subordinate age components around ~2.05 and ~ 2.2 Ga, corresponding to hypothesised Dalgaringa and Ophthalmian arc magmatism, respectively. A limited detrital zircon population from the Frere Formation displays a youngest age component at ~2.0 Ga corresponding to Dalgaringa Supersuite magmatism in a polymodal age spectrum (Figure 2.34). The formation exhibits a dominant age peak at ~2.65 Ga (Yilgarn Craton magmatism) and a subordinate subpopulation centred at ~2.25 Ga, which corresponds to hypothesised magmatism associated with the Ophthalmian Orogeny.

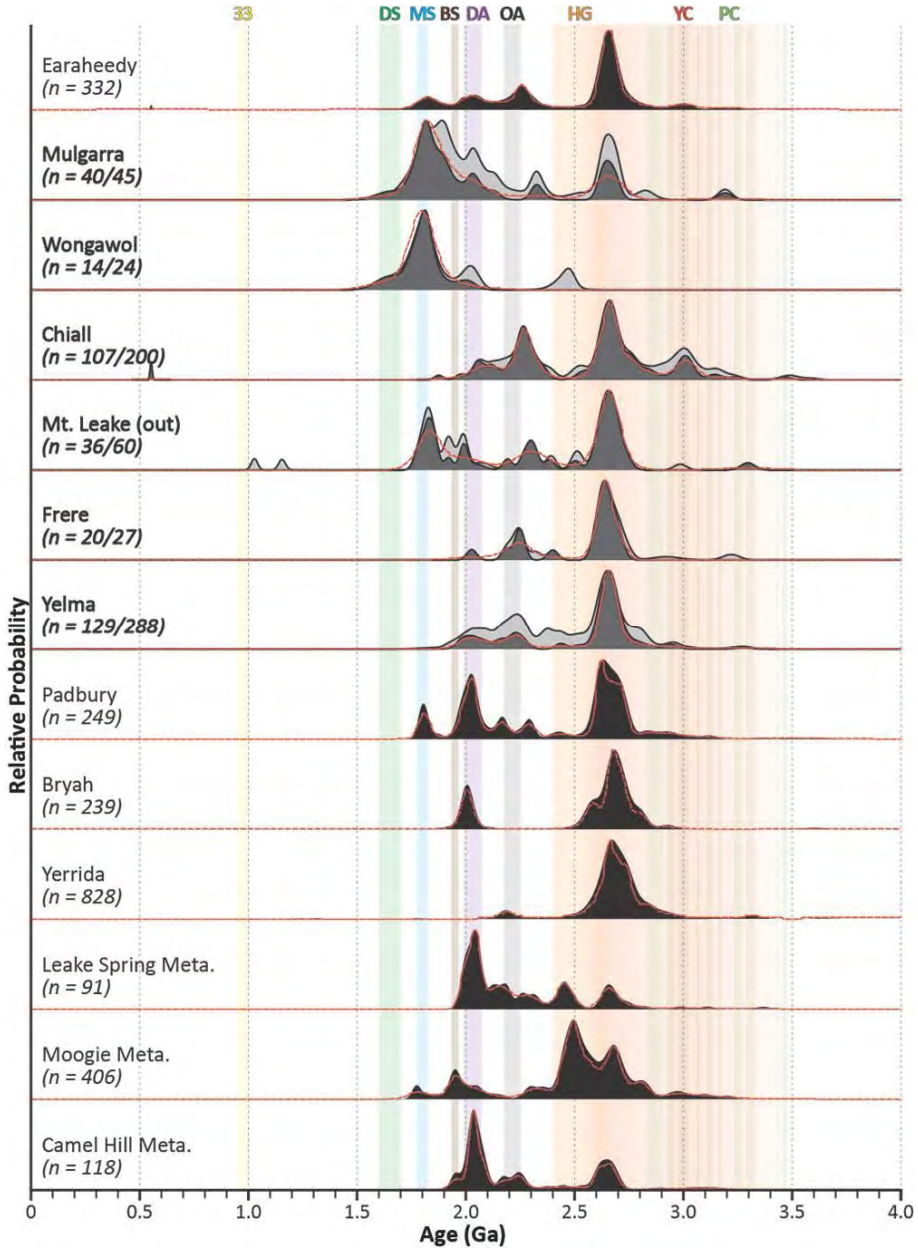

Figure 2.34. Stacked probability plot of detrital zircon ages from the Earaheedy Basin and potential sediment source regions. Red dashed lines represent kernel density estimates for the zircon populations. Black spectra correspond to normalised probability density diagrams for pooled concordant analyses (± 10%) from specific regions, dark grey spectra represent concordant zircon analyses (± 10%) of a particular lithostratigraphic unit and are overlain on pale grey spectra representing all ages for the same unit. Vertical coloured bars correspond to ages of major regional magmatic events (see caption to Figure 2.29).

Detrital zircons analysed from the Chiall Formation (Miningarra Group) display a significant number of discordant grains, though $^{207}Pb/^{206}Pb$ ages of discordant grains largely match those of concordant analyses (Figure 2.34). The age spectrum of detrital grains from the Chiall Formation is polymodal with a youngest age component at ~2.0 Ga and a dominant peak age of ~2.65 Ga (Yilgarn Craton magmatism). Subordinate age subpopulations are centred at ~2.1, ~2.75 and 3 Ga.

The very limited number of detrital zircon analyses available from the Wongawol Formation (Miningarra Group) define a shouldered unimodal age spectrum (Figure 2.34). The youngest zircons are dated ~1.65 Ga with the dominant age component centred at 1.8 Ga corresponding to the Moorarie Supersuite.

The detrital zircon age spectrum of the limited analyses from the Mulgarra Sandstone (Miningarra Group) is polymodal (Figure 2.34). The youngest zircon sub-population corresponds to the dominant age peak at ~1.8 Ga (Moorarie Supersuite), with an extended tail of older grains to ~2.2 Ga and a discrete subordinate age peak at ~2.65 Ga (Yilgarn Craton).

- **Bangemall Supergroup**

Edmund Basin

A large dataset of detrital zircon analyses have been compiled for the Edmund Basin, totalling >2000 concordant data points from nine constituent formations (Figure 2.35).

The Yilgatherra Formations (DP1) detrital zircon age spectrum is essentially bimodal, with its youngest age component at ~1.7 Ga forming part of a continuum with the dominant age peak centred at ~1.8 Ga (Moorarie Supersuite, Figure 2.35). A subordinate secondary peak is centred at ~2.0 Ga.

A large detrital zircon population was analysed from the Irregully Formation (DP1) with a broad spread of ages from ~1.65 Ga to 2.8 Ga (scattered grains up to ~4.1 Ga; Figure 2.35). A single well-defined peak dominates the spectrum centred at ~1.8 Ga, corresponding to the Moorarie Supersuite.

The detrital zircon age spectrum of the Gooragoora Formation (DP2) is essentially unimodal with a single major age peak centred at ~1.8 Ga corresponding with ages of magmatism in the Moorarie Supersuite (Figure 2.35). An almost negligible subordinate subpopulation is apparent at ~2.0 Ga.

A large dataset of detrital zircon ages, with a high degree of discordant analyses was compiled for the Blue Billy Formation (DP2). The youngest component of the detrital population at ~1.5 Ga marks the start of a wide spread of ages extending to ~2.85 Ga (Figure 2.35). A broad peak characterised by ages from ~1.65 to ~1.8 Ga dominates the spectrum and spans magmatism of the Durlacher and Moorarie Supersuites.

A similarly large detrital zircon geochronological dataset for the Kiangi Creek Formation (DP3) yields an almost unimodal age spectrum (Figure 2.35). The youngest zircons at ~1.5 Ga form part of a minor subpopulation marking one end of a background suite of low abundance grains extending to ~2.8 Ga, with a final low-abundance component at ~3.5 Ga. The age spectrum is dominated by a ~1.8 Ga peak, which corresponds to Moorarie Supersuite magmatism. A less well-defined subordinate age subpopulation at ~1.9 to 2.0 Ga spans Bertibubba and Dalgaringa Supersuite activity.

The Muntharra Formation (DP3) detrital zircon age spectrum is essentially unimodal with several very minor subpopulations spanning from ~1.5 Ga to ~3.1 Ga (Figure 2.35). The youngest significant detrital component is dated at ~1.5 Ga with a dominant age peak at ~1.8 Ga corresponding to the Moorarie Supersuite.

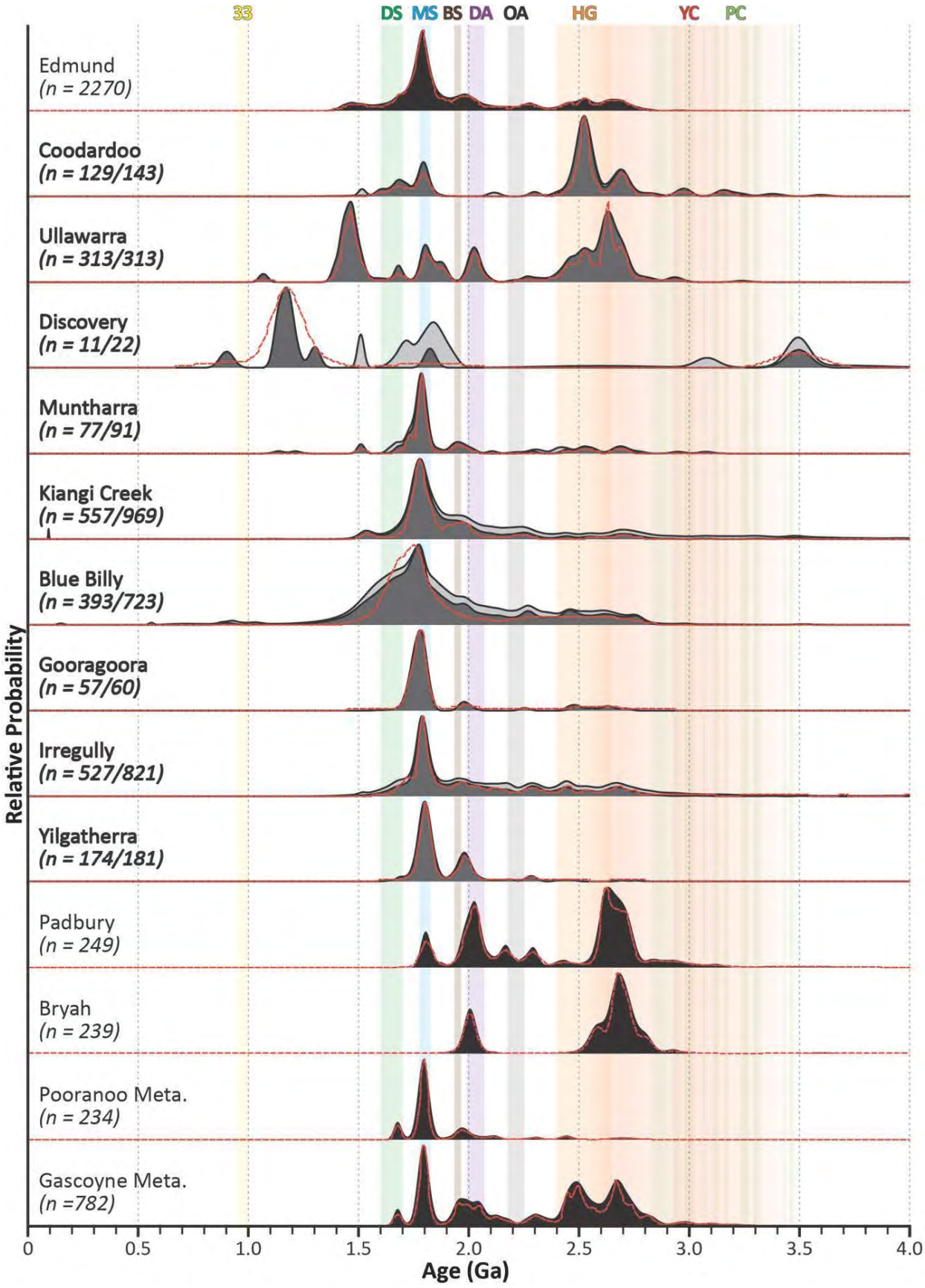

Figure 2.35. Stacked probability plot of detrital zircon ages from the Edmund Basin and potential sediment source regions. Red dashed lines represent kernel density estimates for the zircon populations. Ornament follows Figure 2.29. New analyses are combined with published data.

Extremely limited detrital zircons have been analysed from the Discovery Formation (DP4), with poor results and remaining analyse apparently reflecting disturbance during the Mutherbukin Tectonic event and Edmundian Orogeny (Figure 2.35).

Detrital zircons from the Ullawarra Formation (DP4) define a polymodal age spectrum with the youngest minor subpopulation defined at ~1.1 Ga considered metamorphic in origin (Figure 2.35). The youngest detrital zircon component is taken at ~1.4 Ga, forming part of the dominant age peak centred at 1.45 Ga. A secondary dominant peak in the age spectrum is less well defined at ~2.65 Ga and merges with a subordinate age subpopulation at ~2.5 Ga (corresponding to magmatism in both the Halfway Gneiss and Yilgarn Craton). Additional subordinate age subpopulations are centred at ~1.7, ~1.8 and 2.05 Ga, corresponding to the Durlacher, Moorarie and Dalgaringa Supersuites.

Detrital zircons from the Coodardoo Formation (DP4) define a polymodal age spectrum with a youngest component at ~1.55 Ga (Figure 2.35). The dominant age peak at ~2.5 Ga corresponds with Halfway Gneiss magmatism, while subordinate age subpopulations are expressed at ~1.7 (Durlacher Supersuite), ~1.8 (Moorarie Supersuite) and 2.5-2.7 Ga (Yilgarn Craton).

Collier Basin

The Backdoor Formation (DP5) detrital zircon age spectrum can be described as bimodal with broad dominant subpopulations centred at ~1.8 Ga and ~2.5 Ga, corresponding to the Moorarie Supersuite and Halfway Gneiss magmatism (Figure 2.36). Subordinate subpopulations are poorly resolved at ~1.9-2.0, ~2.25-2.35 and ~2.7 Ga, with the latter tailing off to ~3.15 Ga. The youngest age component of the Backdoor Formation is particularly minor in volume at ~1.35 Ga. A single sample from the upper Backdoor Formation (GSWA 148977) demonstrates a significantly simpler unimodal age spectrum dominated by ~1.8 Ga zircons.

Detrital zircons from the Calylie Formation (DP5) yield a polymodal age spectrum ranging from ~1.55 to ~3.6 Ga (Figure 2.36). Broad dominant age peaks are exhibited from ~1.75-1.95 Ga (primary peak), ~2.2-2.35 Ga, ~2.7-2.85 Ga and ~3.35-3.55 Ga.

A large, dominantly discordant population of detrital zircons were analysed from the Ilgarari Formation (DP6). Remaining concordant analyses define a unimodal age spectrum at ~1.25 Ga, with a ~1.05 Ga youngest component (Figure 2.36).

- **Basin outliers**

Limited data exist from previous work on detrital zircons from the inferred Mt. Leake Formation outlier of the Earaheedy Basin. Existing work yield a polymodal age spectrum, with two major peaks separated by a scattering of intervening ages (Figure 2.34 & 2.37). The youngest component corresponds to the ~1.8 Ga Moorarie Supersuite, while the dominant age subpopulation is dated at ~2.65 Ga (Yilgarn Craton magmatism). Limited new detrital zircon geochronological data were obtained from the Mt. Leake Formation (ML11, Figure 2.37). These data are dominated by a peak age dominance at ~2.65 Ga with subordinate Archean subpopulations at ~3.15 and 3.3 Ga.

A robust population of detrital zircons were dated as part of this work from the Mt. Augustus Sandstone. The resulting age spectrum is bimodal with a well-defined strongly dominant age peak at ~1.7 Ga and a subordinate peak at 1.8 Ga.

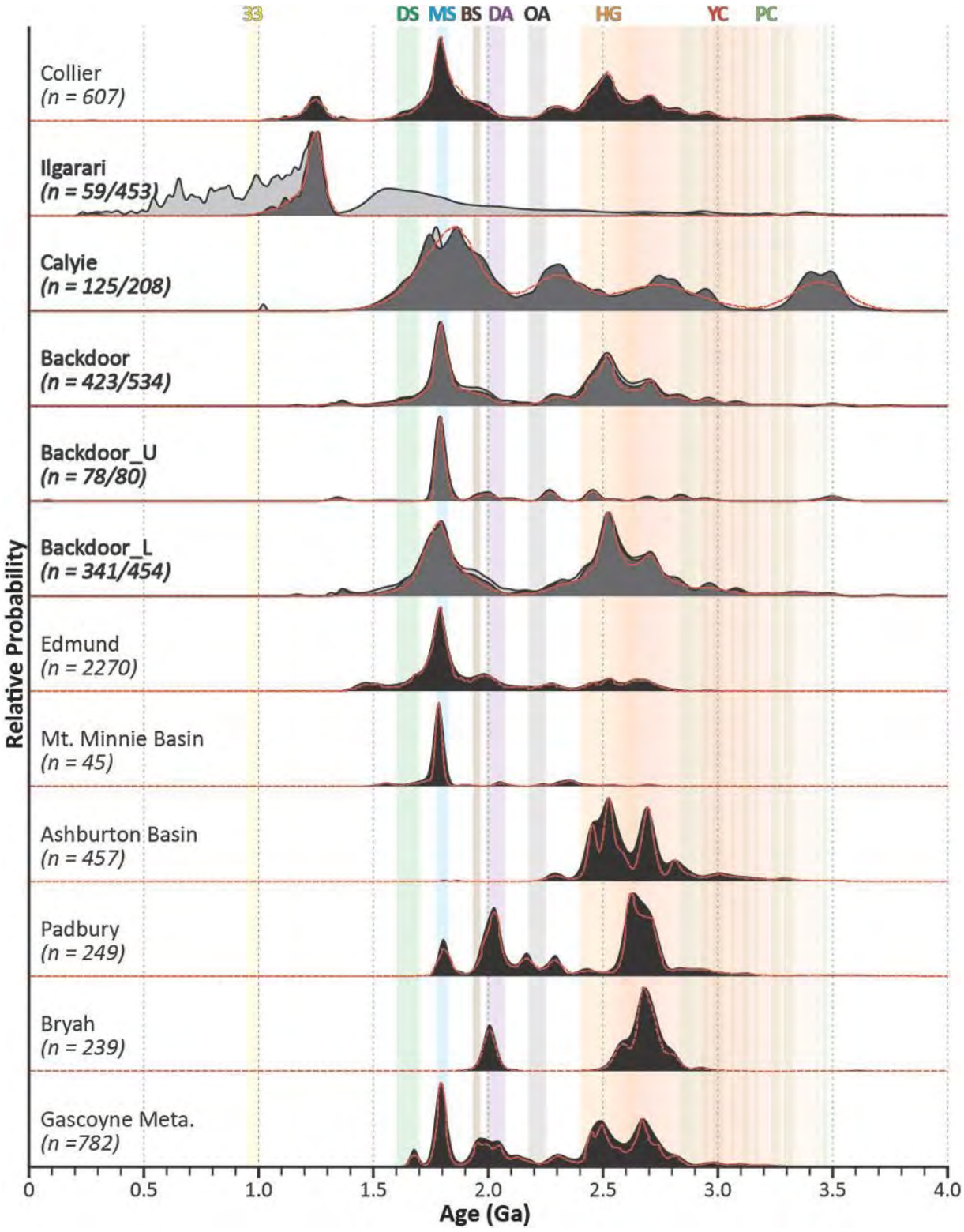

Figure 2.36. Stacked probability plot of detrital zircon ages from the Collier Basin and potential sediment source regions. Red dashed lines represent kernel density estimates for the zircon populations. Black spectra correspond to normalised probability density diagrams for pooled concordant analyses (± 10%) from specific regions, dark grey spectra represent concordant zircon analyses (± 10%) of a particular lithostratigraphic unit and are overlain on pale grey spectra representing all ages for the same unit. Vertical coloured bars correspond to ages of major regional magmatic events (see caption to Figure 2.29). New analyses combined with published data. Upper Backdoor Formation sample corresponds to GSWA 148977.

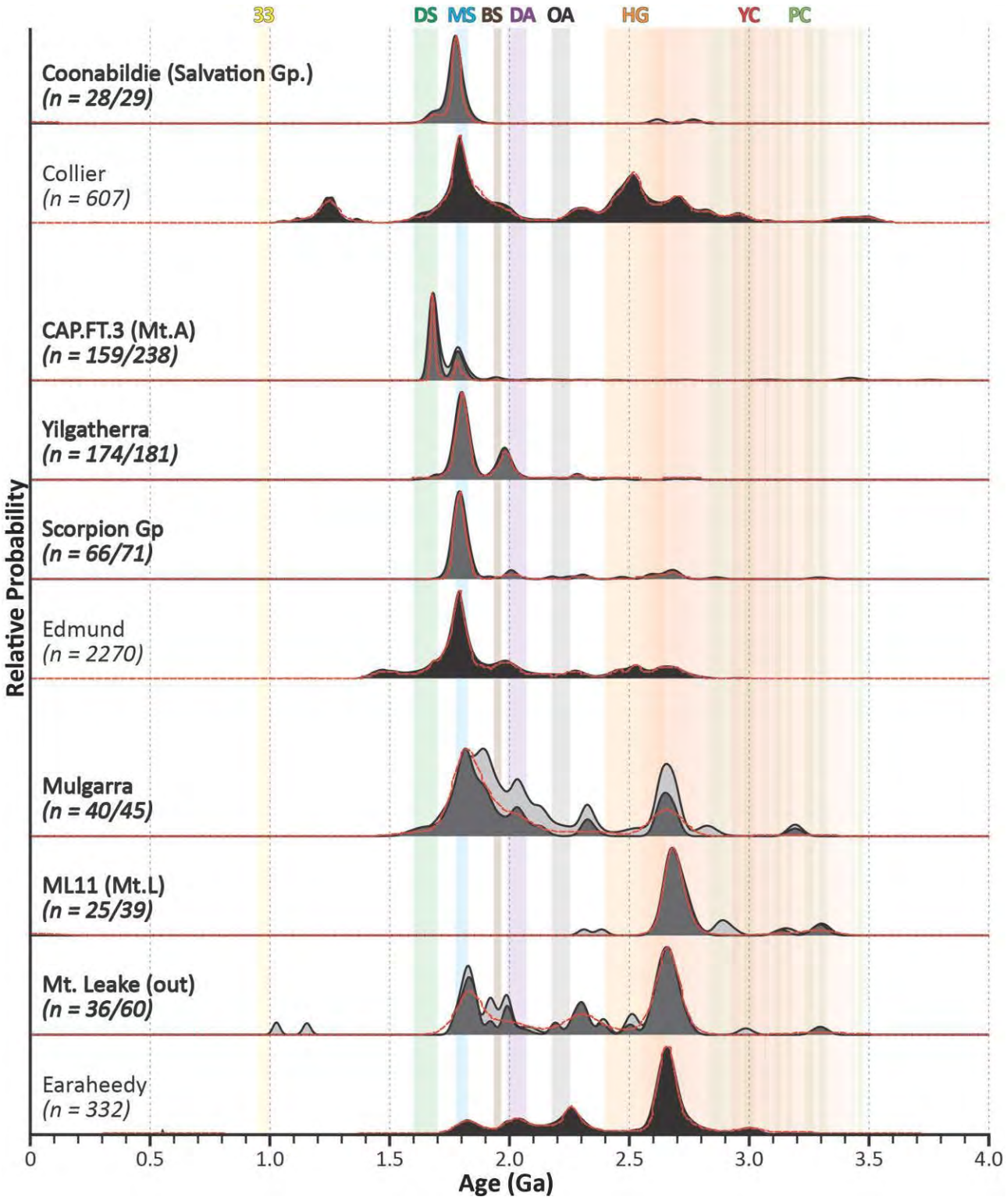

Figure 2.37. Stacked probability density plot of detrital zircon ages from outlier depositional packages and their hypothesised equivalent basins. Red dashed lines represent kernel density estimates for the zircon populations. Black spectra correspond to normalised probability density diagrams for pooled concordant analyses (± 10%) from specific regions, dark grey spectra represent concordant zircon analyses (± 10%) of a particular sedimentological unit and are overlain on pale grey spectra representing all ages for the same unit. Vertical coloured bars correspond to ages of major regional magmatic events (see caption to Figure 2.29). Mt.L – Mount Leake Formation; Mt.A – Mount Augustus Sandstone.

2.5.2 Detrital zircon geochemistry – source region composition and setting

- **Yerrida Basin**

The vast majority of the analysed detrital zircons have (i) high Th/U ratios (>0.07), (ii) fractionated chondrite-normalized rare earth element (REE) patterns with HREE enrichment and a steep positive slope from the LREE to the HREE, and (iii) positive Ce anomalies [$(Ce/Ce^*)_N$ = 0.13–647, where $Ce^* = (La_N+Pr_N)/2$] and pronounced negative Eu anomalies [$(Eu/Eu^*)_N$ =0.007–3.51, where $Eu^* = (Sm_N+Gd_N)/2$]. All these factors point to a magmatic origin for the majority of zircon crystals (Anders and Grevesse, 1989; Hoskin and Ireland, 2000; Hoskin and Schaltegger, 2003; Liu et al., 2002; Rubatto, 2002). A minor proportion of grains (less than 3%) show a smooth REE slope, with less pronounced Eu anomalies (Hoskin and Schaltegger, 2003; Liu et al., 2002) that, in some cases, are associated with Th/U <0.07, implying a metamorphic origin.

Trace-element ratio (e.g. U/Yb versus Hf and Y, U/Yb vs Nb/Yb) plots (Figure 2.38) suggest that almost all Yerrida Basin detrital zircon grains crystallized in continental settings. Exceptions include younger grains, particularly between 2100 and 2200 Ma, which have a more significant mantle influence. Trace element compositions of the Yerrida Basin detrital zircons examined suggest the grains were sourced from several different protolith types consistent with granitoids, carbonatites, syenitic rocks and lamproites (Figure 2.39; Belousova et al., 2002). Less well represented are grains with chemistries associated with mafic rocks and syenites- pegmatites.

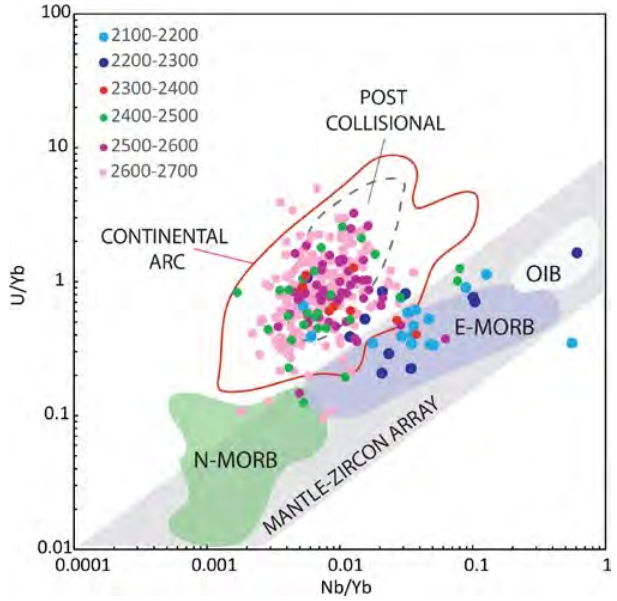

Figure 2.38. Zircon U/Nb tectono-magmatic source region discrimination diagram for detrital zircons from the Yerrida Basin. Protolith compositional fields are overlain in colour after Klein (2003); Rudnick and Gao (2003); Sun and McDonough (1989). The mantle zircon array of Grimes et al. (2015) encloses MORB, Oceanic

- **Edmund Basin**

The Th/U ratios for the analysed zircons from the Edmund Basin span from 0.046 to 4.13, with the majority having Th/U higher than > 0.07, fractionated chondrite normalized REE patterns, with depleted HREE, and LREE relatively enriched by two to four orders of magnitude (Yb/Sm)N = 3.25-1976.69. Analysed zircons exhibit positive Ce anomalies, with content ranging between 2.51 and 420 ppm and Eu is characterized by a negative anomaly and varies from 0.18 to 134 ppm. The trace-element patterns and Th/U indicate a magmatic origin for the majority of the zircon grains (Hoskin and Schaltegger, 2003; Rubatto, 2002; Rubatto and Hermann, 2007). Zircon grains with conspicuously young ages, low Th/U ratio, and complex CL overgrowth textures indicating a metamorphic origin (Rubatto, 2002; Rubatto and Hermann, 2007), were not included in the chemical diagrams for protolith discriminations and maximum depositional age discussion. Compositionally, Edmund Basin zircons are associated with granitoid and lamproitic fields in a relatively evolved tectonic setting (Figure 2.40).

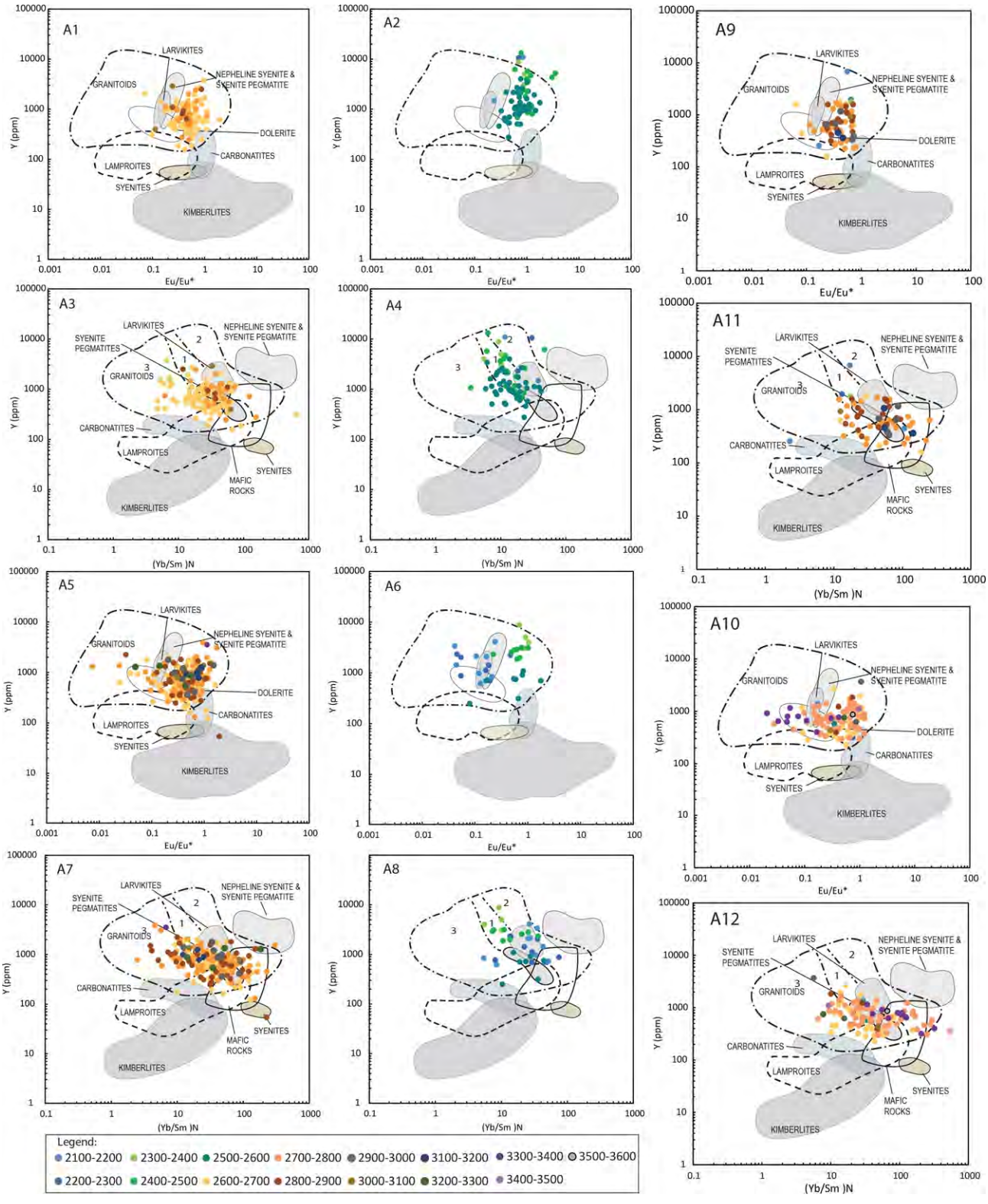

Figure 2.39. Discrimination diagrams showing like parental compositions for Yerrida Basin detrital zircons. Legend indicates detrital zircon crystallisation age. Compositional fields modified from Belousova et al. (2002).

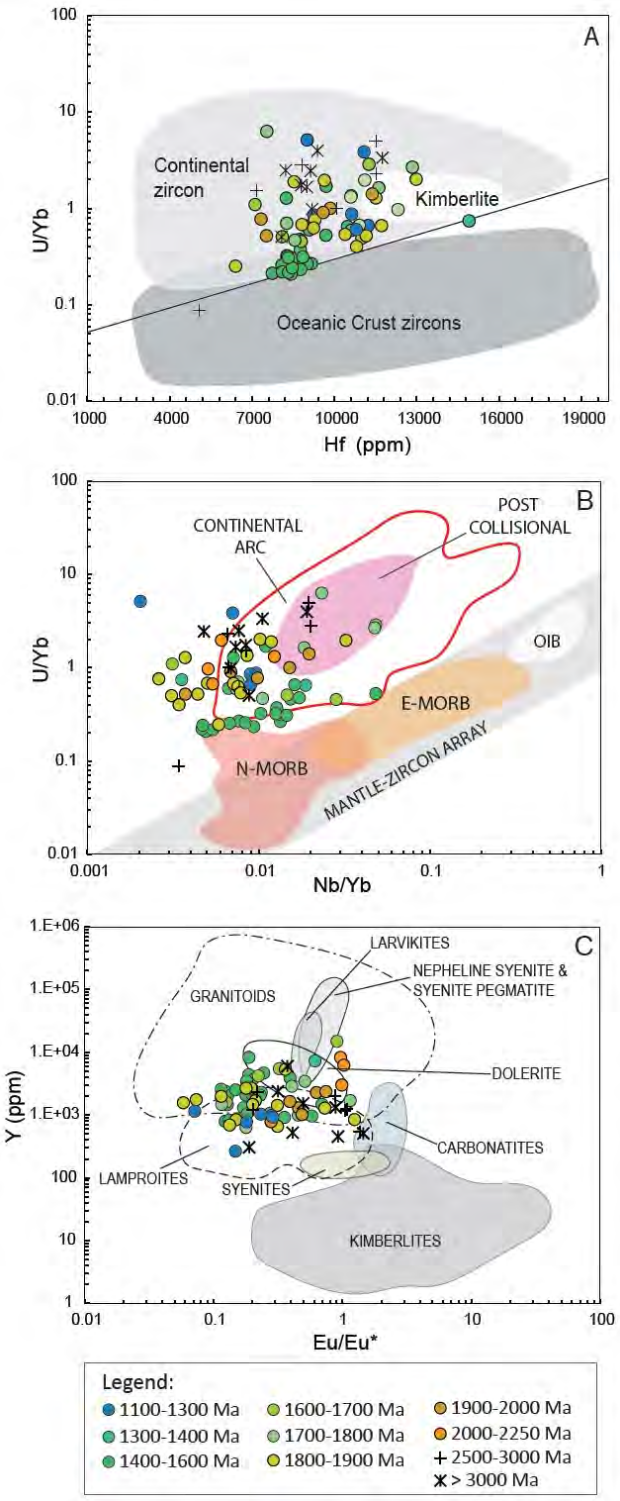

Figure 2.40. Trace element discrimination diagrams for detrital zircons from the Edmund Basin. Compositional fields modified from Belousova et al. (2002). Protolith compositional fields are overlain in colour after Klein (2003); Rudnick and Gao (2003); Sun and McDonough (1989). The mantle zircon array of Grimes et al. (2015) encloses MORB, Oceanic Island and kimberlite zircons. Modified from Grimes et al. (2015).

- **Collier Basin**

Chondrite Normalized REE patterns of detrital zircons from the Collier Basin are characterized by depleted LREE and enriched HREE $(Gd/Yb)_N$ = 0.26 to 6751), a pronounced negative Eu anomaly (Eu/Eu* < 1.3) and a positive Ce anomaly. Virtually all the analysed zircons have Th/U ratios (> 0.1; Figure 2.41). The youngest group of zircons with ages ranging between ~1.2 and 1.4 Ga (samples DD1 to 5 – Ilgarari Formation and CAP.FT28 – Backdoor Formation), have fractionated REE patterns and relatively high Th/U ratios (>0.7) compared with older grains. These characteristics indicate a magmatic origin for the older detrital grains (Fu et al., 2009; Hoskin and Ireland, 2000; Hoskin and Schaltegger, 2003), and a potential volcanic origin for the youngest group.

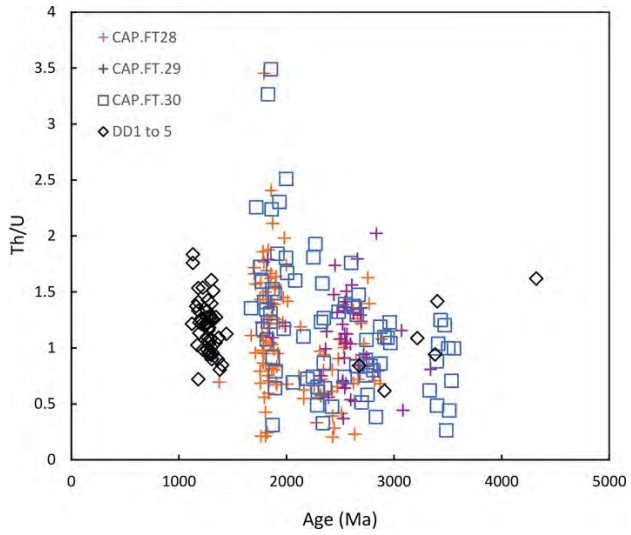

Figure 2.41. Th/U vs age plot for detrital zircons from the Collier Basin. CAP.FT28 and 29 correspond to the Backdoor Formation, CAP. FT30 samples the Calyie Formation and samples DD1 To 5 are from the Ilgarari Formation.

Detrital zircons from the Collier Basin have variable U/Yb and Nb/Yb ratios but mainly plot above the mantle-zircon array defined by Grimes et al. (2015) with a more continental signature (Figure 2.42). Collier Basin detrital zircons have Y values ranging between 116 and 4160 ppm, Eu/Eu* values between 0.017 and 1.265, with Eu/Eu*=Eu/((Sm+Gd)/2)) and $(Yb/Sm)_N$ ranging between 3.31 and 400 (Figure 2.43). These trace element concentrations predominantly overlap the granitoid (granodiorites and tonalities), lamproite and mafic rock compositional fields identified by Belousova et al. (2002), with grains plotting within the syenite, pegmatite carbonatite fields with decreasing frequency (Figure 2.43).

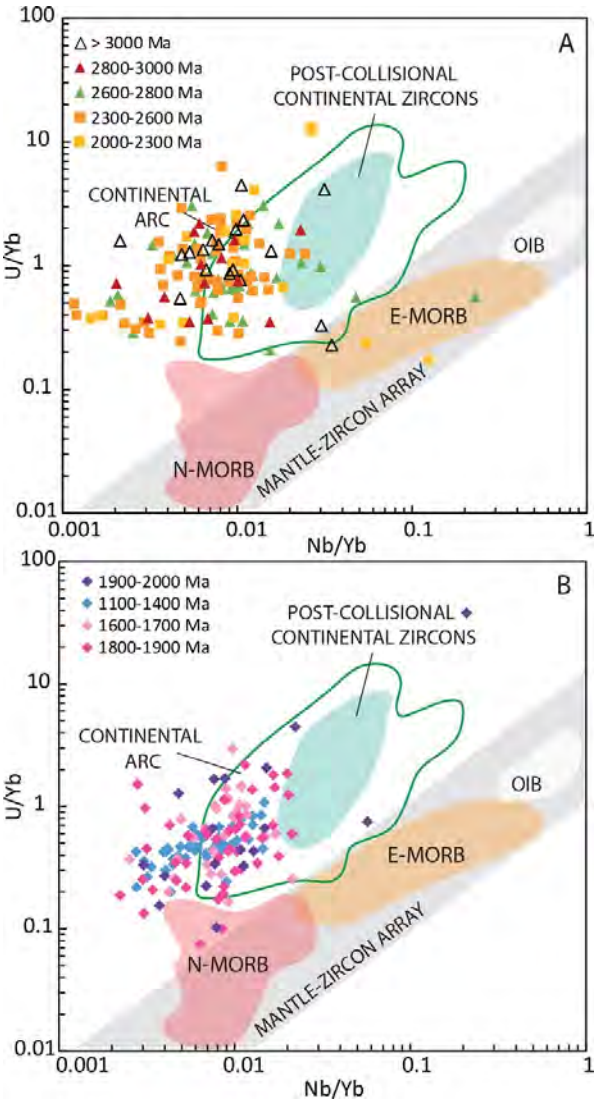

Figure 2.42. U/Yb vs Nb/Yb discrimination diagram of detrital zircons from the Collier Basin. Analysed grains have been divided into groups according to the ages of the main igneous units known across the Capricorn. Compositional fields and diagrams following Grimes et al. (2015).

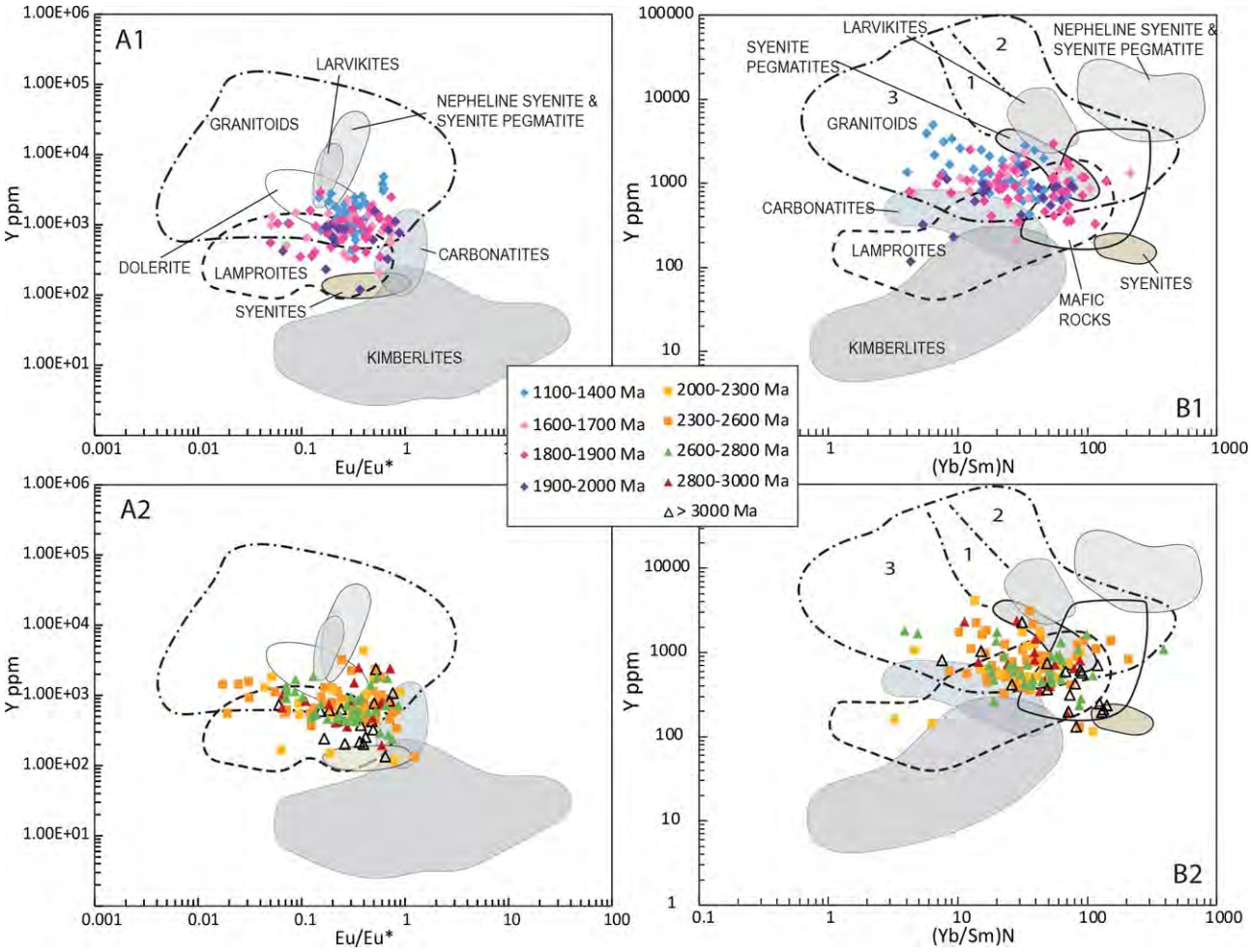

Figure 2.43. Trace-element discrimination diagrams for Collier Basin detrital zircons. Analysed grains have been divided into groups according to the ages of the main igneous units known across the Capricorn. Protolith fields from Belousova et al. (2002).

2.6 Basin associations and evolution of sediment routing

2.6.1 Ashburton Basin

Peak sub-population ages largely correspond to the ~2.5 Ga Halfway Gneiss with distinct subordinate age peaks corresponding to interpreted arc magmatism associated with the Ophthalmian Orogeny (~2.2 Ga) and the Dalgaringa Arc (~2.05 Ga), as well as granitic intrusions (~2.7 and 2.8 Ga) in the Gascoyne Province (Figure 2.29; Johnson et al., 2011a; Krapež et al., 2017).

The zircon age spectra of units within the Shingle Creek Group evolves through time, with decreasing dominance of the ~2.5 Ga peak (and overall contribution of older zircons), and progressively younger max depositional age peaks up through the sequence (Figure 2.29). This increasing contribution of younger zircon age sub-populations is interpreted to represent contributions from successive magmatic events associated with the Glenburgh Terrane's collision with the Pilbara and Yilgarn Cratons and suggest (i) unroofing of intrusive rocks through the Gascoyne Province, (ii) enlargement of catchment areas or temporal changes in catchments up through the Shingle Creek Group, (iii) increasing sourcing of sediment from the south up section (Dalgaringa Supersuite in the Wooly Dolomite and potential Yilgarn Craton-derived ~2.7 Ga zircons in the Mount McGrath Formation), and/or (iv) decreasing recycling of older sediments.

Sediments are depauperate of distinctive zircon age populations of the Pilbara Craton, and are more aligned with events in the Gascoyne Province (c.f. Moogie Metamorphics) despite the Shingle Creek Group being derived predominantly from the north and northeast according to paleocurrent data (Krapež et al., 2017). These data suggest that Shingle Creek Zircons were likely partially derived from intermediate sediment reservoirs during reworking events rather than solely direct sourcing from crystalline source regions. This recycling could have involved underlying Turee Creek Group sediments (Figure 2.29) or material that was eroded from the Glenburgh Terrane and transported northwards into a foreland basin of the Ophthalmian Orogeny (that is no longer preserved), before being recycled back southwards into the Shingle Creek Group sediments (Krapež et al., 2017). Archean age components at ~2.7 Ga in the Beasley River Quartzite and Mt. McGrath Formation (Fig. 2.29) may alternatively be derived from reworking of Turee Creek Group sediments or reworking of volcanics from the Fortescue and Hammersley Basins to the north (Cutten et al., 2016).

Later deposition in the Blair, Bresnahan and Mt. Minnie Basins are relatively distinct from the underlying Ashburton Basin, with clear derivation from the Gascoyne Province to the south. Detrital zircon data from the Bresnahan and Mt. Minnie Basins suggest equivalent sediment derivation and approximate depositional age, younger than the Blair Basin, which is more similar to the underlying Ashburton Basin sediment spectrum (Figure 2.29). Given the exclusive dominance of ~1.8 Ga zircons in the Bresnahan and Mt. Minnie Basins sediments, the Moorarie Supersuite must have been well exposed and subject to extensive weathering and erosion at the time of deposition.

2.6.2 Yerrida Basin

Detrital zircons from the Yerrida Basin are dominated by those obtained in this study through the Juderina Formation. Although dominated by ~2.65-2.8 Ga zircons that have a broad potential source region across the northern Yilgarn Craton margin to the south, nuanced variations in the peak ages (Figure 2.31) may be correlated with component terranes/provinces within the craton that track changes in sediment supply as the Yerrida Basin opened (Armondola, In prep). Paleoarchean components within the basin are suggested as having derived from the Marymia Inlier (Figure 2.7) given similarities with the distinctive ~3.3 Ga zircon subpopulation and the sampling location from drillcore on the flank of the inlier. Increasing recognition of contemporaneous volcanism with sedimentation in the Yerrida Basin (Occhipinti et al., 2017), in conjunction with trace-element geochemistry indicative of greater mantle influence, and mafic volcaniclastics within the sequence, all suggest that the distinctive ~2.2 Ga detrital zircon population within the Yerrida Basin, was locally derived.

Therefore despite temporal overlap with magmatism further north, associated with the Opthalmian Orogeny, the Yerrida Basin was principally sourced from combined denudation of the northern margin of the Yilgarn Craton, Marymia Inlier and local volcanics, which provide a useful age constraint that is essentially contemporaneous with deposition.

2.6.3 Bryah Basin

Detrital zircons from the Bryah Basin are dominated by ~2.7 Ga and 2.0 Ga age components that are interpreted to represent the Archean Yilgarn Craton (and associated inliers) and the Dalgaringa Supersuite associated with arc magmatism and Glenburgh-Yilgarn collision.

These sources are consistent with trace-element geochemistry and imply a connected routing from the magmatic arc into basins on the northern margin of the Yilgarn Craton. Similar age peaks are also exhibited in the Camel Hill Metamorphics further west, where even greater amounts of northerly derived detritus is preserved, implying convergence from the west to the east and relatively homogeneous regional sediment generation.

Similarities in the dominant ages of detrital zircons in the Bryah and Yerrida Basin may be interpreted to represent a degree of sediment recycling. However, given (i) temporal equivalence now recognised between parts of the sequences, and (ii) conspicuous differences in the spectra, e.g. appearance of a ~2.0 Ga subpopulation, as well as, reduction of any ~2.2 Ga component in the Bryah Basin, it seems more likely that the basins shared similar Yilgarn Craton crystalline source regions. Direct sourcing from the norther margin of the Yilgarn Craton, in addition to the volcanic arc associated with the impending Glenburgh Orogeny, likely drown out a recycling signal from the Yerrida Basin.

New data from sample BP10, mapped as Ravelstone Formation, yielded a distinct detrital zircon age spectrum with numerous concordant analyses younger than supposed depositional age (~1980-2000 Ma; Occhipinti et al., 2017). These grains are interpreted as igneous in origin and do not correspond in all instances with known periods of metamorphism and zircon re-growth/re-setting. Instead, it is possible that the sediments are instead stratigraphically younger and associated with the Collier Basin, sharing a distinctive Mesoproterozoic zircon subpopulation with younger depositional packages in the Bangemall Supergroup (Figure 2.32).

2.6.4 Padbury Basin

Detrital zircon spectra for the Padbury Basin sediments are dominated by Neoarchean ages (Figure 2.33) attesting to a dominance of sediment supply from the Yilgarn Craton. Distinct bimodality to the Neoarchean ages suggest that distinct crustal components of the Yilgarn may be discernible, with the Marymia Inlier, at least contributing to the Wilthorpe Formation based on a distinctive 3.3 Ga subpopulation (BP8; Figure 2.33; Figure 2.7). Similarities in the age spectra of the Padbury Basin and the Moogie Metamorphics support attribution of Paleoproterozoic detrital zircons to derivation from the Gascoyne Province in the west.

Significant facies variations in the detrital zircon cargo are recognised in the basal unit of the basin (Labouchere Formation), resulting in an overall polymodal zircon population for the formation (Figure 2.33). Although only sampled ~50 m apart, samples BP2 and BP3, exhibit very distinct detrital zircon age spectra. Given support from other samples analysed herein or previously (Halilovic, 2002), it is thought the differences are real and reflecting dramatic switches in catchment/provenance. Given the Labouchere Formations inferred depositional setting, it is likely that turbidites from different feeder canyons are responsible for switching between a dominantly southern-derived (Archean – Yilgarn Craton) sediment and western-derived (Paleoproterozoic–Gascoyne Province) sediment. The apparent contribution of Moorarie Supesuite (~1.8 Ga) zircons to the Labouchere Formation (Halilovic, 2002) seems unusual given it is younger than the supposed depositional age and if real, requires significant reinterpretation of the stratigraphic position or sample attribution.

The Wilthorpe and Millidie Creek Formations appear to represent a return to simpler Neoarchean-dominated sediment derivation and potential recycling of Bryah Basin stratigraphy (Figure 2.33).

2.6.5 Earaheedy Basin

Limited paleocurrent data (Halilovic et al., 2004) suggest derivation of sediments from the southwest for the Chiall Formation, which is likely true also for the underlying formations too given broad similarities in the detrital zircon age spectrum of the Yelma, Frere and Chiall Formations (Figure 2.34). Despite apparent unconformities separating the Yelma, Frere and Chiall Formations, no significant differences are apparent in their respective zircon age spectra (bar additional ~3.0 Ga component in the youngest Chiall Formation sample). This strongly suggests recycling and stability of sediment routing during the early Earaheedy Basin history, with sediments largely derived from the Yilgarn Craton (to the south) and Gascoyne Province (Dalgaringa Supersuite and unknown source) to the west. Hafnium isotopes of Neoarchean zircons derived from the Earaheedy Basin have been correlated with magmatic zircons from the Narryer Terrane and Murchison Province specifically (Matonia, 2009).

An overall increase in Paleoproterozoic detritus derived from the Gascoyne Province is evident up section through the Earaheedy Basin and a relatively dramatic switch to Paleoproterozoic detritus dominance is observed in the limited data available from the Wongawol Formation and Mulgarra Sandstone (Figure 2.34). Incorporation of Moorarie Supersuite aged detrital zircons into the upper Miningarra Group (Wongawol Formation and Mulgarra Sandstone) suggests this stratigraphy may be younger than previously appreciated (Sheppard et al., 2016a). These zircons are unlikely to be metamorphic since they are not represented in underlying units in a similar area. Furthermore, this relatively pronounced provenance change between Chiall Formation and overlying units suggests a change in basin structure and sediment sourcing, with a greater western influence perhaps driven by the Capricorn Orogeny.

Enigmatic zircons between ~2.1 and ~2.3 Ga are relatively common in the Earaheedy Basin and do not have a readily identifiable source, despite overlap with the Opthalmian Orogeny, which occurred further north. Metasedimentary rocks in the southern Gascoyne Province and northern Yilgarn Craton (Leake Spring Metamorphics and Camel Hill Metamorphics) also show evidence of these ages but no outcrops of crystalline rocks of this age remain (Figure 2.34; Halilovic et al., 2004). Zircons partially overlapping with this age are recovered in the Yerrida Basin and are associated with rift-associated igneous activity, which may partially explain these ages.

2.6.6 Edmund Basin

Detrital zircon age data for the Edmund Basin demonstrate relatively consistent signatures dominated by ~1.8-2.0 Ga sources in DP1-3 (Yilgatherra-Muntharra Formations) that are interpreted to have derived ultimately from the Moorarie Supersuite in the Gascoyne Province to the west (Figure 2.35). Accompanying paleocurrent readings consistently record southward-directed transport and either are only a local environmental signal, or, more likely given their consistency, are a reflection of persistent northern derivation or recycled Gascoyne Province detritus from intermediate reservoirs on the southern Pilbara Craton margin (Cutten et al., 2016; Martin et al., 2008). Similarities with the detrital zircon age spectra of the Bresnahan and Mt. Minnie Basins, support a larger sediment pool of this nature across the southern margin of the Pilbara Craton that could have been denuded during deposition of DP1-3 (Figure 2.29, 2.35, 2.36 & 2.44). Significant quantities of Gascoyne Province detritus (in particular the Moorarie Supersuite) were distributed across the Capricorn region during the late Paleoproterozoic given the same detrital age spectra identified in the Pooranoo Metamorphics deposited across the northern Yilgarn and southern Gascoyne Province (Figure 2.35).

A distinct shift in the detrital zircon age spectra of sediments in DP4 (Discovery-Coodardoo Formations) is correlated with a change in paleocurrent directions (from the SE) and a distinctive regional transgression (Figure 2.6). Sediments in DP4 yield more complex detrital zircon age spectra, typically dominated by Neoarchean ages. Given southerly-directed paleocurrent domination through the basin, Martin et al. (2008) attributed these age components to Neoarchean volcanics interbedded with the Fortescue and Hammersley Basins. However, considerable age overlap exists with potential crystalline sources in the southern Gascoyne Province (Halfway Gneiss) and Yilgarn Craton to the south. It has been argued (Cutten et al., 2016) based on slight differences in the degree of Hf-isotope evolution of source regions, that recycling of southern Pilbara Craton volcanics contributed to sediments in DP4, while low concentrations of older Paleoproterozoic and Neoarchean zircons in DP1-3 were more likely derived originally from the Gascoyne Province. Overall, the detrital zircon age spectrum of a combined DP4 shares similarities with the Ashburton Basin and Gascoyne Province metamorphics, as well as the Bryah and Padbury Basins (bar Mesoproterozoic component; Figure 2.44).

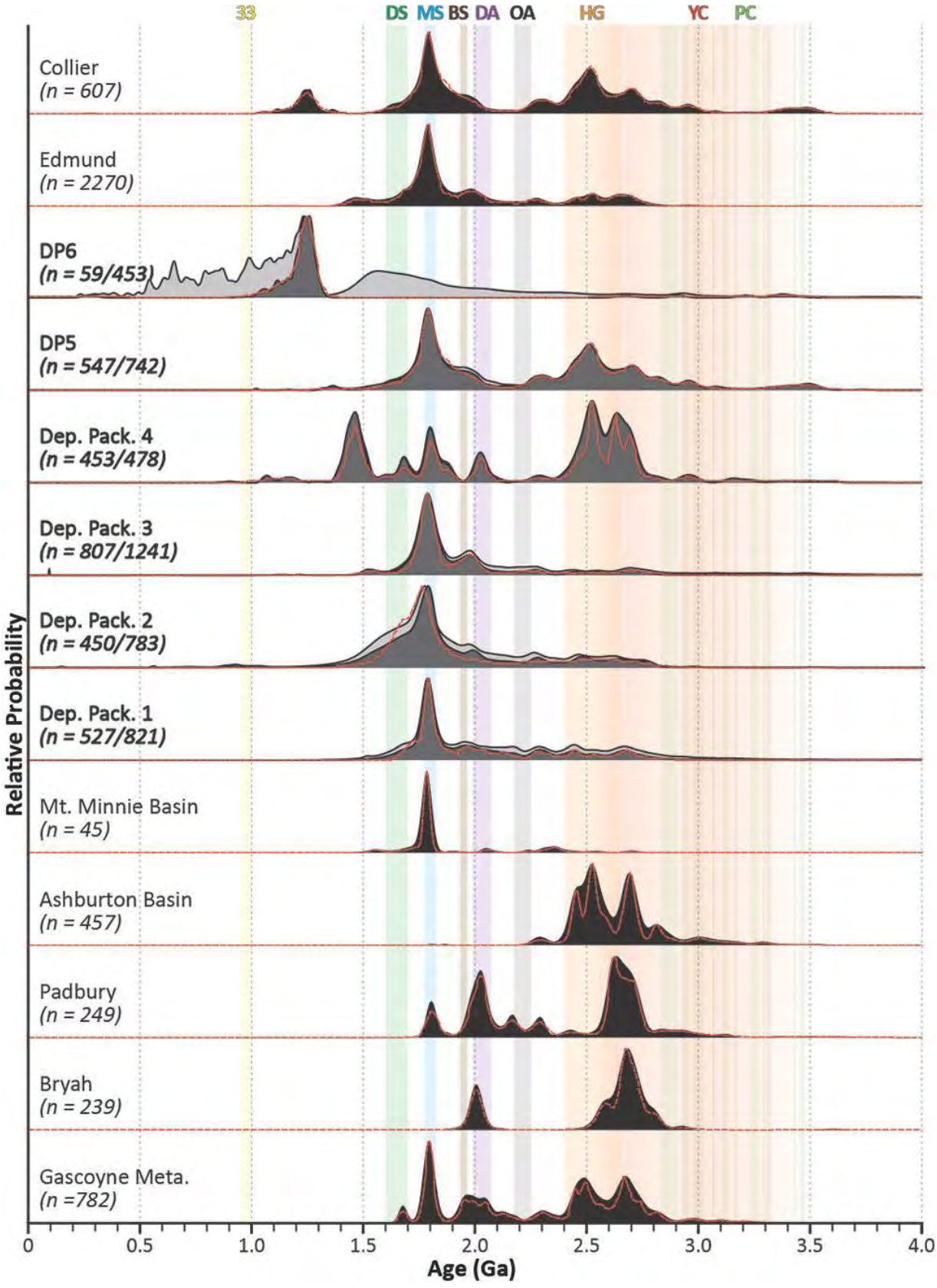

Figure 2.44. Stacked probability plot of detrital zircon ages from major depositional packages of the Edmund and Collier Basins. Red dashed lines represent kernel density estimates for the zircon populations. Black spectra correspond to normalised probability density diagrams for pooled concordant analyses (± 10%) from specific regions, dark grey spectra represent concordant zircon analyses (± 10%) of a particular sedimentological unit and are overlain on pale grey spectra representing all ages for the same unit. Vertical coloured bars correspond to ages of major regional magmatic events (see caption to Figure 2.29).

Distinctive younger Mesoproterozoic detrital zircon ages throughout the Edmund Basin, but in particular in the Discovery and Ullawarra Formations provide useful maximum depositional age constraints on the stratigraphy. Dominant ~1.45 Ga zircons in the Ullawarra Formation may correlate with doleritic intrusions that are common in the underlying stratigraphy (Narimbunna and Waldburg Dolerites; Figure 2.6). Zircons of this age have a relatively distinctive more primitive trace-element chemistry may support this. Limited zircon analyses form the MJGD2 core attributed to the Discovery Formation are dominated by Mesoproterozoic ages that are younger than constraints on the formations' depositional age (Figure 2.6 & 2.35). However, similarities are apparent with detrital zircon data from the Ilgarari Formation in the overlying Collier Basin and imply incorrect assignment of local stratigraphy.

2.6.7 Collier Basin

Detrital zircon age spectra from the Collier Basin are variable, in correspondence with basin partitioning and paleocurrent readings that dominantly suggest southeastern and northern derivation (Martin et al., 2008; Martin and Thorne, 2004). The Backdoor Formation is dominated by Paleoproterozoic and Neoarchean zircons that correspond to the ~1.8 Ga Moorarie Supersuite and the ~2.5 Ga Halfway Gneiss (Figure 2.36 & 2.44). A sample in the upper Backdoor Formation (GSWA 148977) yields a simpler almost unimodal detrital zircon age spectrum centred on ~1.8 Ga that closely parallels sediments in the Mt. Minnie and Bresnahan Basins to the north, and may correspond to a switch to sediment recycling from these northern reservoirs. This reduction in the variety of sediment sourcing argues for changes in sediment derivation and a stronger influence of more focused erosion of a defined source vs. recycling of intermediate sediments that tends to homogenise and mix source signals. Similarities in the detrital zircon age spectra of a single sample from the Coonabildie Formation in the Mesoproterozoic Salvation Group (eastern Capricorn Orogen) with the sample in the upper Backdoor Formation may suggest contemporaneous sedimentation of these units and regional shedding ofdistinct Moorarie Supersuite-derived material at this time (Figure 2.36-2.44). This interpretation is based on the expectation for incorporation of other detritus across this geographic area if both Collier Basin and Salvation Group samples were derived from recycling of the Mt. Minnie or Bresnahan Basins (or equivalents), and the fact that the signal is relatively isolated in the Collier Basin, rather than more pervasive, as expected from a regional sediment recycling event. The overlying Calyie Formation yields broad, poorly-defined age peaks that are poor matches with known regional source rock ages, includinga ~2.3 Ga sub-population. Overall, Hf-isotopes of the majority of samples from DP5 are similar to those of depositional packages (DP3-4) in the underlying Edmund Basin, and together with the overall similarities in dominant detrital ages, suggest either derivation from the same regions or recycling of the Edmund Basin during uplift to the south (Cutten et al., 2016; Martin et al., 2008).

The overlying Ilgarari Formation of DP6 is dominated by discordant zircon grains. However, through multiple samples, a consistent and relatively unique ~1.1-1.3 Ga zircon source is suggested that is unrecognized in regional geology. Mesoproterozoic magmatism of this age are well known from orogenic systems (Albany-Fraser Orogen and Musgrave Province) developed during assembly of the combined WAC-NAC and South Australian Craton (Johnson, 2013; Kirkland et al., 2015; Kirkland et al., 2013; Spaggiari et al., 2015).

Paleoslopes in the Ilgarari Formation dipped towards the northwest, with sediment transport, at least locally, in the same direction (Martin and Thorne, 2004). Mesoproterozoic detritus matching this age (1.1-1.3 Ga) has been suggested as being shed northward from the Albany- Fraser Orogen and incorporated into the Northampton Complex on the western margin of Australia (Ksienzyk et al., 2012). However, large regions of the present day Albany-Fraser Orogen comprise older Meso- to Paleoproterozoic crystalline rocks that are not reflected in the defined Ilgarari Formation detrital zircon signature. A more promising match is recognized with crystalline rocks in the Musgrave Province, with further support of extensive shedding of this age material evident in intervening sedimentary basins (Officer Basin; Haines et al., 2016; and references therein), as well as paleocurrent directions (Martin and Thorne, 2004). Alternatively, these zircons, given

their persistence through the sampled core and exclusion of any other significant detritus, may represent an unknown local source, with associated implications for thermal history and fluid generation. Detrital zircon geochemistry suggests that at least some of the ~1.1-1.3 Ga detritus was eroded from granitic parents that are currently unknown but may be broadly coeval with the Mutherbukin Tectonic event (Figure 2.43).

2.6.8 Basin outliers and modern sediment

New geochronological analyses of detrital zircons from the Mt. Leake Formation outlier (ML11) support those undertaken previously (Halilovic et al., 2004), which confirm stratigraphic correlation with the Earaheedy Basin based on similarities in sediment source signals (Figure 2.37). Archean detrital zircons (in particular a subordinate ~3.3 Ga subpopulation) indicate derivation from the Marymia Inlier, with contributions from the Gascoyne Province variable between the samples currently available for the formation, indicative of distinct catchment areas. Incorporation of Moorarie Supersuite aged detritus in the Mount Leake Formation suggests deposition equivalent to younger units in the basin and changing sediment dispersal patterns with a greater western provenance, or reflects greater proximity to the Gascoyne Province in the west. The Mulgarra Sandstone at the top of the Earaheedy Basin stratigraphy has been suggested as being separated by a disconformity from the underlying sequence (Bunting, 1986), but this was rejected by Pirajno et al. (2009). Detrital zircon populations differ in the relative proportions of peak contributors between the Mulgarra Sandstone and the remaining Earaheedy Basin (with a spectrum more similar to the younger Edmund Basin) but are insufficient to demonstrate complete stratigraphic distinction (Figure 2.37).

Detrital zircon age spectra acquired for the Mount Augustus Sandstone matches that previously published (Martin et al., 2008) with a bimodal detrital zircon age spectrum with a dominant peak at ~1.65 Ga and a subordinate peak at 1.8 Ga (Figure 2.37). This age spectrum is relatively unique in the samples analysed across sedimentary basins in the Capricorn Orogen and suggests relatively defined sediment sourcing from Durlacher Supersuite basement in the west. Furthermore, the Mount Augustus Sandstone is unlikely to be age equivalent to the Yilgatherra Formation of the Edmund Basin as has been suggested (Martin et al., 2008).

Detrital zircon geochronology for the Scorpion Group in the eastern Capricorn Orogen evidence a dominance of Moorarie Supersuite derived material and minor older grains spreading into the Archean (Figure 2.37). This detrital zircon age spectrum is a close match to those in DP1-3 of the Edmund Basin, as well as the Mt. Minnie and Bresnahan Basins, and suggest homogeneity of regional late Paleoproterozoic to early Mesoproterozoic sediment, as well as broad stratigraphic equivalence of the units.

Detrital zircon age spectra of outliers in the Salvation Group (Coonabildie Formation) are relatively distinct to sediments of the Collier Basin to which it has been equated (Figure 2.37). The detrital age spectrum is unimodal corresponding to the ~1.8 Ga Moorarie Supersuite peak and lacks distinctive Paleoproterozoic and Archean grains characteristic of most samples in the Collier Basin (bar a single sample in the Backdoor Formation). Instead it is more similar to nearby Scorpion Group sediments, which are a close match to prosed equivalent sediments in the Edmund Basin.

Sampling of modern sediment in river systems overlying or draining the Capricorn region (Figure 2.45) provide an indication of the fidelity of regional sediment pools separated by billions of years as a result of recycling and continued erosion of preserved source regions. Recent stream sediment sampling overlying the Edmund Basin, Marymia Inlier and Earaheedy Basin (Griffin et al., 2004), demonstrate (i) relative consistency of characteristic Paleoproterozoic signals with undetectable contamination from more recent orogenic events, (ii) Marymia Inlier-derived sediments are not always endowed with a distinctive 3.3 Ga age component, making distinction from other Archean source rocks on the northern Yilgarn margin problematic and probably requiring Hf- or O-isotope analysis, and (iii) complete loss of signals and effective “drowning” of underlying sedimentary detrital age spectra is possible, with the sampled stream in the Earaheedy Basin dominated by Paleozoic to late Neoproterozoic peak ages (potentially reflecting central Australian

orogenesis). New data reported herein for the mouth of the Gascoyne River (Figure 2.45) broadly reflect dominant ages through the Gascoyne Province, but is unusually dominated by Durlacher Supersuite aged zircons and also includes a suite of Meso- to Neoproterozoic sub-populations, likely associated with modification of the western margin of the WAC.

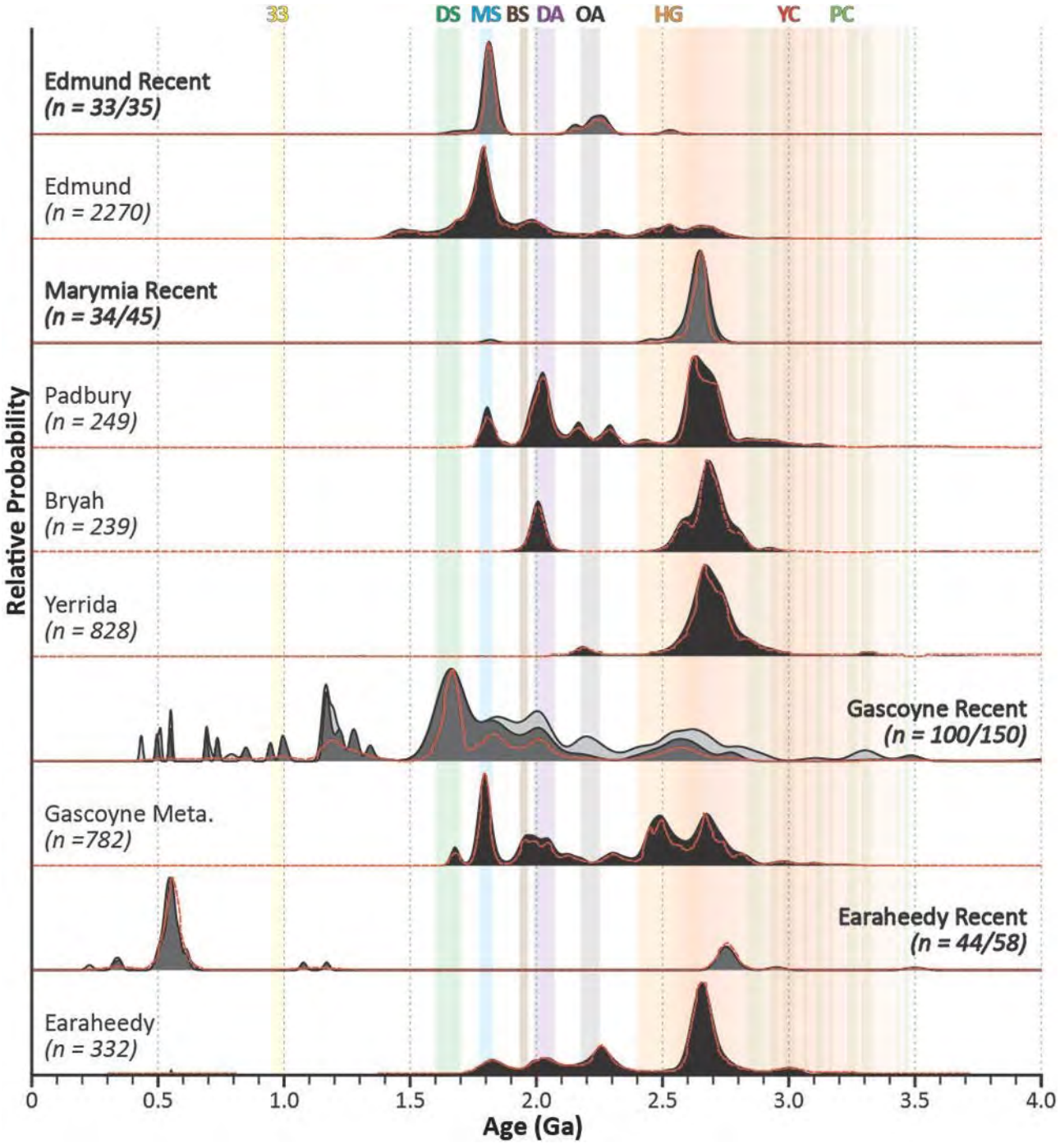

Figure 2.45. Stacked probability plot of detrital zircon ages from modern fluviatile system sediment draining the Capricorn Orogen and potential sediment source regions. Red dashed lines represent kernel density estimates for the zircon populations. Black spectra correspond to normalised probability density diagrams for pooled concordant analyses (± 10%) from specific regions, dark grey spectra represent concordant zircon analyses (± 10%) of a particular sedimentological unit and are overlain on pale grey spectra representing all ages for the same unit. Vertical coloured bars correspond to ages of major regional magmatic events (see caption to Figure 2.29).

2.7 Implications and constraints for crustal evolution from magmatic zircon geochronology and geochemistry

2.7.1 Narryer Terrane and Yarlarweelor Gneiss Complex

Dominance of evolved εHf values in the Narryer Terrane and YGC samples suggests that these granites were formed mainly from the reworking of isotopically evolved pre-existing crustal components with little/no significant mantle input (Figure 2.46). Magmatic zircon U–Pb age data reveals three main periods of granite emplacement at c. 3380, 3190, and a younger main c. 2740–2625 Ma event. The c. 3380 Ma zircons exhibit a large range in εHf values (-7.4 to +0.2), which corresponds to T_{DM}^{C} ages of 4145 and 3687 Ma, respectively. This suggests that a juvenile component underwent variable mixing with older Hadean to Eoarchean material.

Magmatic zircon O-isotope analysis in the Narryer Terrane and YGC indicate average $\delta^{18}O$ of 6.49 ± 1.24‰ (2σ), with the most radiogenic εHf value (+0.2) corresponding broadly with a mantle-like $\delta^{18}O$ value (6.47 ± 0.47, 2σ; Figure 2.46). This suggests the c. 3380 Ma granite was generated during a period of crustal growth, with a c. 3687 Ma juvenile component undergoing variable mixing with older, early Archean material, resulting in the large Hf- isotope array. The subsequent. 3190 Ma and c. 2740–2625 Ma groups appear to be reworking of this source. Zircons from the Mesoarchean granites display dominantly unradiogenic $^{176}Hf/^{177}Hf$ ratios between 0.280554 and 0.280620 (εHf -8.2 to -5.3). The c. 2740–2625 Ma granites have median εHf values (-11.7 to -6.7) that are more evolved than the c. 3380 Ma and the c. 3190 Ma granites (median εHf: -3.3 to -6.1). Evolution lines defined by a source $^{176}Lu/^{177}Hf$ value of 0.015, show that the younger granites lie within the older granites isotopic envelope (Figure 2.9). Therefore, these isotopic arrays indicate that the melts were formed by reworking of an infracrustal source possessing a broadly similar $^{176}Lu/^{177}Hf$ ratio, such as the c. 3380 Ma granites. Inherited zircon grains have compositions that plot along this evolution line, and are consistent with the interpretation that the c. 2700–2600 Ma granites were sourced from reworking of the 3380 Ma granites. This conclusion is supported by the occurrence of c. 3400–3320 Ma inherited zircon with model ages of 4110–3830 Ma in the younger granites (Figure 2.9).

Zircons from the Narryer Terrane and YGC granites that contain analyses with $\delta^{18}O$ values within error of the of mantle zircon field indicate that the parent magmas contained significant low-$\delta^{18}O$ material representing an infracrustal source component with mantle-like $\delta^{18}O$ (i.e. a meta-igneous crustal component that has not interacted significantly with shallow crustal material), and negligible amounts of supracrustal (metasedimentary) material. These data (Figure 2.46) indicate derivation from an old or evolved crustal component that has not interacted significantly with shallow crustal material, with inherited material incorporated into the host magma from surrounding crust during magma ascent and/or emplacement within the mid- to low-crust. This is consistent with the U–Pb and Hf data, which suggest derivation from reworking of Paleoarchean granites.

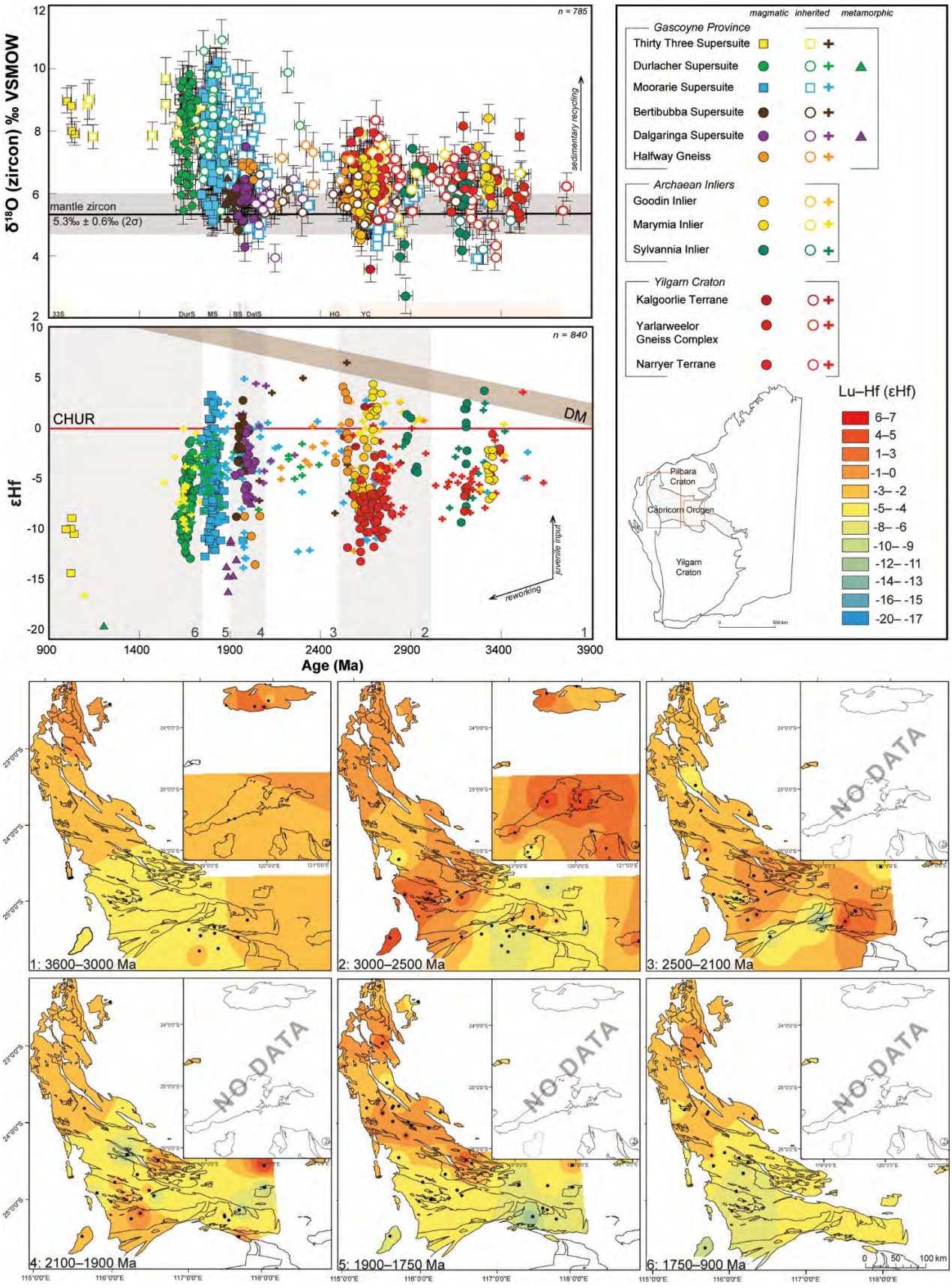

Figure 2.46. Lu-Hf and O-isotope data from magmatic zircons of the Capricorn Orogen and associated cratonic margins/inliers. Data record the reworking of crustal material, as well as intervals of juvenile mantle input during the geological evolution of the region, which may be associated with enhanced mineral endowment. More negative εHf values indicate more evolved magmatic sources, with more positive values suggesting more recent mantle interactions. More positive O-isotope values suggest greater reworking of crustal material in melts.

2.7.2 Marymia Inlier

The Marymia Inlier closely resembles, and is interpreted to be part of the granite-greenstone terranes of the Yilgarn Craton. It is not clear to which part of the Yilgarn Craton the inlier relates to given its position where the Narryer Terrane, the Murchison and Southern Cross Domains (Youanmi Terrane) and Eastern Goldfields Superterrane converge under Proterozoic cover sequences (Figure 2.3b).

Analysed magmatic zircons from the Marymia Inlier have U–Pb ages of c. 3330–2700 Ma, with two well-defined events at c. 3330 and 2700 Ma. The c. 3300 Ma samples are the first to date magmatism of this age in the Marymia Inlier (Figure 2.7). Magmatic crystallisation U–Pb ages >c. 3010 Ma are rare in the Yilgarn Craton. However, c. 3730–3300 magmatism is recorded in the Narryer Terrane (Kinny et al., 1988; Nutman et al., 1993; Nutman et al., 1991), suggesting a correlation between the two regions.

Analyses of magmatic zircon with $^{207}Pb/^{206}Pb$ ages between c. 3360–3320 Ma indicate εHf values between -7.1 and -2.1, corresponding to T_{DM}^{C} ages between 4113 and 3812 Ma (Figure 2.9b). The dominance of evolved (unradiogenic) εHf values in the c. 3330 Ma samples suggests that these granites were formed mainly from the reworking of isotopically evolved crustal components with little/no significant juvenile input. The magmatic zircon form homogenous oxygen isotope populations with $\delta^{18}O$ values between 5.65 and 7.20‰, and inherited zircon show $\delta^{18}O$ values ranging from 5.93 to 8.09‰ (Figure 10). This Hf–O array (unradiogenic εHf coupled with mantle to slightly enriched $\delta^{18}O$ values) indicates that the magmas that the zircon crystallised from contained both significant low-$\delta^{18}O$ material representing an infracrustal source component (i.e. a meta-igneous crustal component that has not interacted significantly with shallow crustal material), and negligible amounts of high-$\delta^{18}O$ supracrustal (metasedimentary or volcanic-igneous) material. Both crustal assimilation and melting of older high-$\delta^{18}O$ crust are concluded to be possible processes to produce this array. This is consistent with derivation from reworking of crustal components with Eo- to Paleoarchean T_{DM}^{C} ages. The Hf-O isotope data from these samples are comparable to that of the Narryer Terrane and Yarlarweelor Gneiss granites of equivalent age (εHf values -7.4 to +0.2, T_{DM}^{C} ages 4145-3687 Ma, and average $\delta^{18}O$ values 5.93 ± 1.13‰ to 6.94± 0.44‰; Figure 9 & 10). It is not clear whether the c. 3330 Ma crust now part of the Marymia Inlier is a rifted fragment or extension of the Narryer Terrane.

In contrast to the c. 3330 Ma granites, the zircon Hf-isotope data for the c. 2700 Ma granites show a change to much more radiogenic $^{176}Hf/^{177}Hf$ ratios between 0.281022 and 0.281168 (εHf -1.6 to +4) corresponding to younger T_{DM}^{C} ages between 3270 and 2925 Ma (average c. 3060 Ma). The dominance of positive εHf values indicates that crustal growth occurred largely through the input of juvenile mantle-derived magmatic components (Figure 2.9b). The Hf- isotope array extends to negative εHf values, suggesting variable degrees of mixing with more evolved crustal components. These U–Pb ages and Hf-isotope data are similar in age and Hf-isotope signature to those from the Eastern Goldfields Superterrane (EGST; Griffin et al., 2004). The c. 2700 Ma granites of the Marymia Inlier show a range of $\delta^{18}O$ values between 5.6 and 6.94‰, with average $\delta^{18}O$ values of 6.35 ± 0.55 and 5.94 ± 0.93‰ (2σ; Figure 2.10). This suggests that the melts that these zircon crystallised from were sourced from an infracrustal source component with mantle-like $\delta^{18}O$, and negligible amounts of supracrustal (metasedimentary) material. The juvenile input at c. 2700 Ma observed in the Marymia Inlier and EGST is contemporaneous with komatiite volcanism recorded in the Kalgoorlie and Kurnalpi Terrane (Barley et al., 2003; Kositcin et al., 2008). The O-isotope data support interpretations based on geochronology and Hf-isotopes that the eastern part of the Marymia Inlier is a northwestern extension of the EGST (Dentith et al., 2014; Gazley, 2011; Gazley et al., 2011; Griffin et al., 2004; Vielreicher and McNaughton, 2002; Vielreicher et al., 2002).

The isotopic data clearly record the presence of Paleoarchean crust in the south-eastern region of the Marymia Inlier (Figure 2.46). The U–Pb and Hf-isotopic data suggests a Narryer Terrane/YGC association, with

part of the Marymia Inlier and the Narryer Terrane contiguous for a part of their history. It is therefore possible that the western region of the Marymia Inlier represents an extension of the Narryer Terrane. While no crystallisation ages >c. 2670 Ma are recorded east of the c. 3330 Ma granitoids, inherited zircon from a granite gneiss located 40 km to the west returned $^{207}Pb/^{206}Pb$ ages between c. 3800 and 2980 Ma (Lu et al., 2016), indicating the presence of Narryer Terrane aged crust in the area. However, U– Pb ages of inherited zircons cannot be considered clear evidence of underlying basement, as the inherited zircon may represent some sediment derived from the Narryer Terrane.

2.7.3 Goodin Inlier

Magmatic zircon U–Pb data from the Goodin Inlier reveal one main period of granite emplacement at c. 2660–2620 Ma, contemporaneous with the c. 2760–2620 Ma voluminous granite emplacement observed in the Narryer Terrane, Marymia Inlier and Yilgarn Craton (Figure 2.7). Previous zircon geochronology has dated magmatism in the Goodin Inlier at 2624 ± 8 Ma (Nelson, 1997, 1998).

The Goodin Inlier samples indicate evolved Hf-isotope signatures, with median εHf values between -6.4 ± 3.2 and -4.7 ± 7.9 (2σ; Figure 2.9b). εHf values from individual magmatic zircon range between -8.4 and -1.2 (median -6.4), and indicate T_{DM}^{C} ages between 3638 and 3276 Ma (median 3514 Ma). The unradiogenic εHf values indicate that the melts were sourced from reworked crust with a mean model age of c. 3500 Ma. Oxygen isotope data for the individual magmatic range from 4.73 to 7.12‰, (average $\delta^{18}O$ = 5.34 ± 0.83 to 6.42 ± 0.88‰, 2σ; Figure 2.10). These oxygen values are consistent with the interpretation that the zircons crystallised from a magma generated by melting of pre-existing igneous rocks mixed with evolved sources at lower- to mid- crustal levels. The U–Pb age and Lu-Hf isotope composition of the zircon from the Goodin Inlier zircon and the Youanmi Terrane are similar (Figure 2.9). The c. 2680–2580 Ma Youanmi Terrane granites are dominated by unradiogenic zircon (εHf -14 to +2.4, median -5.5) and T_{DM}^{C} ages ages 4191–2880 Ma (median 3527 Ma; Ivanic et al., 2012; Mole et al., 2012; Wyche et al., 2012). The similarities in U–Pb and Hf-isotopic composition suggest that the Goodin Inlier closely resembles, and is therefore interpreted to be part of, the Youanmi Terrane of the Yilgarn Craton. However, there is some overlap in the isotopic signature of the zircon from the Murchison and Southern Cross Domains, which precludes further correlation to either domain.

2.7.4 Sylvania Inlier

Zircon U–Pb geochronology has identified two main episodes of granite crystallisation in the Sylvania Inlier at c. 3190 and 2900 Ma (Figure 2.9c). The c. 3190 Ma granites have εHf values ranging from -9.4 to +2.4, and those with mantle like $\delta^{18}O$ values return T_{DM}^{C} ages between c. 3716 and 3440 Ma. This pattern suggests melt production from mixed sources: an older crustal component and an additional juvenile component extracted from the mantle at c. 3400 Ma (Figure 2.9c). The c. 2900 Ma granites also show a large range in εHf values (-4.3 to +1.3) and those with mantle like $\delta^{18}O$ values return T_{DM}^{C} ages between c. 3406 and 3393 Ma. Inherited zircon with ages ranging between 3405 and 3133 Ma show a large range in εHf values (-6.9 to +2.5), and those with mantle like $\delta^{18}O$ values return T_{DM}^{C} ages between c. 3692 and 3522 Ma. The Hf-isotope data from the inherited component are comparable to that of the East Pilbara Terrane (EPT) granites of similar age (εHf values -9.3 to +3.7; Gardiner et al., 2017b). The majority of analyses indicate values that lie within the isotopic evolution line of the EPT, indicating that the rocks of the Sylvania Inlier may have formed from the reworking of crustal material with Hf-isotopic signature similar to that of the EPT. However, these data also indicate radiogenic values that lie above the isotopic evolution line of the EPT, indicating that the Hf composition of the Sylvania Inlier requires an input of material with more radiogenic Hf signature. Similarly, the c. 2900 Ma granites indicate a more radiogenic Hf isotope signature, with values plotting above the Hf

evolution line of c. 3190 Ma granites, and therefore requiring an input of additional juvenile material to produce these arrays (Figure 2.9c).

U–Pb ages indicate the main period of granitic magmatism in the Sylvania Inlier occurred c. 3190 Ma, granites of similar ages are not found in the EPT, but are recorded in the West Pilbara Superterrane. Inherited components indicate EPT-like ages (c. 3400–3200 Ma), with similar Hf-isotope compositions. The overlap in the isotopic signatures of the Sylvania Inlier and the EPT suggests a shared crustal source. U–Pb ages and Hf-isotope compositions of Sylvania Inlier granites suggests a separate evolution to the EPT after c. 3200 Ma. Similar ages are recorded in the Kurrana Terrane in the southeastern part of the craton (c. 3178 Ma, Nelson, 2004), interpreted as a rifted fragment of the EPT separated between 3200 and 3150 Ma (Van Kranendonk et al., 2010).

2.7.5 Halfway Gneiss

The c. 2600–2430 Ma Halfway Gneiss is considered to be exotic to the adjacent Pilbara and Yilgarn Cratons based on the absence of late Paleoprotoerozoic magmatism within the Yilgarn Craton, lack of similarities in tectonomagmatic history with the Yilgarn Craton, and contrasting Hf-isotope signatures (Johnson et al., 2011b; Occhipinti et al., 2004; Sheppard et al., 2004). The crustal evolution of the Halfway Gneiss is attributed to the reworking of older c. 2730–2600 Ma gneiss components, and major, trace and REE compositions of these rocks were interpreted as reflecting c. 2730–2600 Ma recycled components rather than source materials, and therefore did not reflect the tectonic setting of the younger c. 2600–2430 Ma rocks (Johnson et al., 2011b).

The Archean protoliths of the Halfway Gneiss samples have εHf values ranging from -4.2 to +4.3, and those with mantle like $\delta^{18}O$ values return T_{DM}^{C} ages between 3312 and 2771 Ma (Figs. 2.9-2.10 & 2.46). The magmatic zircons form a homogenous O-isotope population with $\delta^{18}O$ values between 5.56 and 7.12‰ (av. 6.19 ± 0.84‰, 2σ). The range in εHf values reflects a heterogeneous magma at the time of crystallisation, and suggests melt production from mixed sources: an older crustal component with T_{DM}^{C} ages of > c. 3320 Ma and an additional juvenile component extracted from the mantle at c. 2770 Ma. Analyses that indicate εHf values more radiogenic than CHUR have mantle-like $\delta^{18}O$ values, consistent with derivation from juvenile, mantle-derived magmas mixing with additional crustal sources.

Inherited zircons in the Halfway Gneiss with $^{207}Pb/^{206}Pb$ ages between c. 2971 and 2339 Ma have εHf values ranging from -3.5 to +2.7 (Figure 2.9). The T_{DM}^{C} ages of the inherited zircon range between 3473 and 2900 Ma, similar to the c. 2550 Ma protoliths (T_{DM}^{C} = 3312–2771 Ma), suggesting they were sourced from reworking of a crustal component with the same model age. The inherited zircon indicate elevated $\delta^{18}O$ values (7.07-7.53‰), indicating that the older crustal component consisted of supracrustal (metasedimentary) sources. The T_{DM}^{C} ages of the most radiogenic Halfway Gneiss analyses are <300 Ma older than the crystallisation ages, indicating a short crustal residence time. Contamination with older crustal material reduces the $^{176}Hf/^{177}Hf$ of mantle-derived magmas, and the short crustal residence times combined with the strongly juvenile signatures (εHf +2.9 to +4.3) suggests that the magma source was closely related to mantle material, i.e. remelting of a juvenile mantle-derived mafic lower crust. The range in $\delta^{18}O$ values and εHf values requires: (i) input of material into the source that was previously affected by low-temperature alteration at or near Earth's surface, (i) input of an old infracrustal material into the source, and (iii) input of juvenile mantle-derived material.

Taking into account zircon and whole-rock geochemistry, possible tectonic settings for these criteria includes supra-subduction zones, likely a continental-margin arc environment (Figure 2.8).

While no magmatism is recorded in the Yilgarn Craton younger than c. 2600 Ma, a significant proportion of inherited zircon from the Halfway Gneiss samples yield ages between c. 2730–2600 Ma and have εHf values between -4.4 and +3.8 (Johnson et al., 2011b). This period of magmatic activity is contemporaneous with the widespread c. 2760– 2620 Ma granitic magmatism observed in the Yilgarn Craton and Marymia and Goodin Inliers (Fig. 2.9). Hf-isotope data from the adjacent Narryer Terrane indicate unradiogenic εHf values (-13.3 to -2.8) during the c. 2730–2600 period, while the Halfway Gneiss indicates significant juvenile-like input (εHf values -4.4 to +3.8; Johnson et al., 2017; Johnson et al., 2011a). Similarly, Hf-isotope data from the Youanmi Terrane are dominated by unradiogenic εHf values; however, the Murchison Domain indicates some juvenile mantle-derived input during this period (εHf values between -11.4 and +1.9; Ivanic et al., 2012). Crustal evolution lines show that there is overlap in the most unradiogenic components of the Halfway Gneiss and the most juvenile values of the Narryer Terrane/YGC (Figure 2.9b). Evolution lines suggest crustal components could include equivalents of the c. 2730–2600 Ma Murchison Domain, and is supported by the occurrence of inherited zircon with comparable εHf and T_{DM}^{C} ages. Furthermore, zircon from the Eastern Goldfields Superterrane (Kalgoorlie Terrane) show evidence of significant juvenile input at c. 2700–2640 Ma, with εHf values between -4.9 and +2.2 (Wyche et al., 2012). Consequently, as the Halfway Gneiss and the Yilgarn Craton have some degree of isotopic similarity, the Yilgarn Craton should not be ruled out as a possible crustal source. It is possible that the Halfway Gneiss represents a rifted fragment of the Yilgarn Craton that separated during widespread magmatism initiated at c. 2700 Ma, and subsequent magmatism at c. 2550 Ma involved the addition of a juvenile component, which resulted in the 'dilution' of the isotopic signature of the unradiogenic Archean crustal components.

2.7.6 Glenburgh Orogeny magmatism

The analysed zircon from the Glenburgh Terrane samples cover a period of 1142 Myr, with individual $^{207}Pb/^{206}Pb$ ages ranging from c. 3025 to c. 1883 Ma, with peaks at c. 2655–2545 Ma, c. 2100 Ma, c. 1995 and c. 1965 Ma. The Dalgaringa Supersuite samples are dominated by inherited material, with a total of 53% of concordant analyses indicating Paleoproterozoic ages, ranging between c. 2539 and c. 2023 Ma (Figure 2.11). Inherited ages from the Bertibubba Supersuite are significantly older than those reported for the Dalgaringa Supersuite, with ages ranging between c. 3025 Ma and c. 2066 Ma. The Bertibubba Supersuite intruded the northern margin of the Yilgarn Craton (Narryer Terrane), and inherited zircons are mainly Archean in age and reflect 3300–2640 Ma protolith ages established for the granitic gneisses of the Yarlarweelor Gneiss Complex (Nutman et al., 1991). Samples from both the Dalgaringa and Bertibubba Supersuites contain inherited zircon with ages similar to the c. 2550–2430 Ma protolith ages established for orthogneisses of the Halfway Gneiss (Johnson et al., 2011b). However, the majority of the inherited zircons yield $^{207}Pb/^{206}Pb$ ages that are between c. 2353 Ma and c. 2023 Ma, with a major peak at c. 2095 Ma. In summary, the dominance of the inherited U–Pb ages, and the paucity of dated granitoids of this age, indicates that granitic magmatism in the Dalgaringa Arc likely started prior to ages indicated by currently exposed rocks. This supports the U–Pb and Hf isotopic evidence of (Johnson et al., 2011b) of a proto-Dalgaringa arc.

Magmatic zircon with crystallisation ages between c. 2044–1959 Ma display dominantly unradiogenic initial $^{176}Hf/^{177}Hf$ ratios between 0.2813069 and 0.2815109 (εHf -7.2 to 0; Figure 2.13). Magmatic zircons with mantle like $\delta^{18}O$ values yield T_{DM}^{C} ages between 3094 and 2668 Ma. Crustal evolution lines defined by source $^{176}Lu/^{177}Hf$ values of 0.015 (Griffin et al., 2002) are plotted from analyses of the Halfway Gneiss (Archean protolith) and the Yilgarn Craton (Figure2.13). The Dalgaringa Supersuite zircons lie within the Halfway Gneiss isotopic envelope. This suggests that parental magmas of the c. 2044–1959 Ma granites interacted with, or were derived from reworking of a source possessing broadly similar $^{176}Lu/^{177}Hf$ ratios to, the Halfway Gneiss. Inherited zircon grains have compositions that plot along this evolution line, and are consistent with the interpretation that the Dalgaringa Supersuite was sourced from reworking of the Halfway Gneiss.

In contrast to the Dalgaringa Supersuite granites, Hf-isotope data for the c. 2002–1936 Ma granites from the Bertibubba Supersuite show much more radiogenic initial $^{176}Hf/^{177}Hf$ ratios of 0.2813040–0.2816071 (εHf -8.8 to +2.8). Those with mantle like $\delta^{18}O$ values have T_{DM}^{C} ages between 3148 and 2440 Ma (Figure 2.13-2.14). The range in εHf values reflects a heterogeneous magma at the time of crystallisation, and suggests melt production from mixed sources: an older crustal component with T_{DM}^{C} ages of 3148 Ma and an additional juvenile component extracted from the mantle at c. 2440 Ma. The Hf-isotope array extends to highly negative εHf values, suggesting variable degrees of mixing with more evolved crustal components. As the Hf-isotope array lies within the Halfway Gneiss isotopic envelope, it would be possible to produce magmas of apparent chondritic compositions by mixing high Lu/Hf mantle sources and enriched crustal sources with compositions similar to the Halfway Gneiss and/or the Dalgaringa Supersuite. However, inherited zircon with $^{207}Pb/^{206}Pb$ ages between c. 2823 and 2066 Ma have Hf-isotope compositions (εHf -6.8 to +6.5) that lie within both the Halfway Gneiss and Yilgarn Craton granites Hf–U–Pb field. This suggests that the Bertibubba Supersuite sourced a range of Yilgarn Craton and Halfway Gneiss material and mixed with an additional juvenile component at the time of emplacement. Therefore, the likely sources for the Bertibubba Supersuite are the Glenburgh Terrane granites, with minor amounts of Yilgarn Craton granites.

Dalgaringa Supersuite zircons can be modelled with bulk-mixing of a depleted mantle component with a 15-55% contribution from an older crustal component (comparable with a Halfway Gneiss composition; Figure 2.15). The Halfway Gneiss protoliths indicate a 65–75% contribution and 10–40% for Bertibubba Supersuite magmatic zircon.

2.7.7 Intracratonic recycling – Capricorn Orogeny

- **Timing of post-assembly magmatism and significance of inherited ages**

Individual 207Pb/206Pb ages of inherited grains range from 3506 to 1808 Ma, with major peaks at c. 2690, 2535, 1983 and 1860 Ma, and minor peaks at 3490, 3290, 2520, 2150 and 2044 Ma (Figure 2.17). The presence of Neoarchean and Paleoarchean inherited zircon components can be attributed to respective samples spatial location. The southern granites intruded the Yarlarweelor Gneiss Complex, and the inherited material have mainly Neoarchean ages, which reflect the 3300-2640 Ma protolith ages established for the granitic gneisses of the Yarlarweelor Gneiss Complex (Nutman et al., 1991). Within the Gascoyne Province, the Moorarie Supersuite intrudes metasedimentary rocks (Leake Spring Metamorphics) and igneous rocks (Glenburgh Terrane: Halfway Gneiss, Dalgaringa Supersuite). The Neoarchean-aged inherited material from the central granites reflect ages similar to the c. 2550– 2430 Ma protolith ages established for orthogneisses of the Halfway Gneiss (Johnson et al., 2011a; 2011b). The eastern granites intrude metasedimentary rocks, with the Yilgarn Craton margin likely contributing the contaminating sedimentary components.

The inherited zircon from all samples indicate that significant proportions of crust of Paleoproterozoic age (c. 1860 Ma) is present within, or was involved in the formation of, the Moorarie Supersuite. The existing data for igneous and sedimentary rocks within the Capricorn Orogen indicate that 1950–1820 Ma crustal components are currently unexposed (Figure 2.3a). This suggests that the most likely crustal source(s) of the abundant Paleoproterozoic inherited material are at depths beneath the current exposure level.

- **Development of crustal components – evidence from hafnium isotopes**

Granites that intrude the Yarlarweelor Gneiss Complex (southern granites) and those from the central portion of the Gascoyne Province indicate Hf-isotope compositions that are all more evolved than CHUR (Figure 2.20). All display a similar range of evolved εHf values of -12.7 to - 1.4, and the dominance of unradiogenic εHf values suggests that these granites were formed mainly from the reworking of pre-existing isotopically evolved crustal components with little/no mantle input. By contrast, the Hf-isotope data for the northern

samples (Minnie Creek Batholith and those that lie north of it) record more radiogenic εHf values (-11 to +3.3) that suggest mixing between a pre-existing crustal component and a juvenile component.

These data suggest that the magmas that the zircon grains crystallised from were sourced from different, spatially discrete, crustal components (Figure 2.21). Evolution lines defined by source $^{176}Lu/^{177}Hf$ values of 0.015 (Griffin et al., 2002) are plotted from analyses of Yilgarn Craton granites (Narryer Terrane and Yarlarweelor Gneiss Complex) and the Glenburgh Terrane granites (Halfway Gneiss, Dalgaringa Supersuite and Bertibubba Supersuite; Figure 2.20). These represent isotope arrays along which the Moorarie Supersuite may have evolved. Zircon Lu–Hf data for samples from the Halfway Gneiss yield a clearly-defined initial Hf-isotope array with crystallisation ages of c. 2689–2387 Ma, which correspond and T_{DM}^{C} ages of 3434–2771 Ma (Johnson et al., 2017). Crustal evolution lines show that the granites of the central granite samples lie within the Halfway Gneiss isotopic envelope (Figure 2.20). Therefore, these isotopic arrays indicate that the parental magmas were formed by reworking of a source possessing broadly similar $^{176}Lu/^{177}Hf$ ratios, such as the Halfway Gneiss. Inherited zircon grains have compositions that plot along this evolution line, and are consistent with the interpretation that the central granites was sourced from reworking of the Halfway Gneiss. The southern granites have unradiogenic εHf values of -12.7 to -6.8 that, like the central granite samples, lie within the Halfway Gneiss isotopic envelope. In addition, inherited zircon grains with $^{207}Pb/^{206}Pb$ ages between c. 3506 and 2335 Ma have Hf compositions (εHf -12.2 to -1.9) that lie within the Yilgarn Craton granites Hf– U–Pb field. Sources for the southern granites are the Paleoproterozoic granites of the southern Gascoyne Complex (with minor amounts of Archean Yilgarn Craton granites). This indicates that crustal components of the Glenburgh Terrane were present under the margin of the Yilgarn Craton during the c. 1820–1770 Ma Capricorn Orogeny. The presence of the Glenburgh Terrane below the Narryer Terrane is consistent with seismic reflection lines, which show south dipping crustal-scale thrusting, and indicate the existence of the Glenburgh Terrane below the Narryer Terrane at depths of 45–48 km (Johnson et al., 2013).

By contrast, Hf-isotope data for Minnie Creek Batholith magmatic zircons define an array that includes values that are representative of more radiogenic (juvenile) crust (εHf -7.4 to +2.7; Figure 2.20-2.21). Inherited zircon grains with $^{207}Pb/^{206}Pb$ ages between c. 2069 and 1831 Ma have εHf values of -2.8 to +3.1. The range in isotopic composition in the Minnie Creek Batholith is more radiogenic than can be explained by reworking of the Glenburgh Terrane alone, and is compatible with melt sourced from two compositionally and isotopically distinct sources; an evolved component with an isotopic composition similar to that of the southern Gascoyne Province and a juvenile component. This interpretation is supported by the presence of mafic-ultramafic intrusions and mafic inclusions within the batholith, as well as field evidence of magma mingling (Sheppard et al., 2010). This interpretation is essentially similar to that based on whole-rock geochemistry, which led Sheppard et al. (2010) to suggest that the Minnie Creek Batholith granites were generated by a mantle-derived mafic underplating beneath thinned lithosphere.

The eastern granite samples (those that lie east of the main portion of the Gascyone Province, intruding the Edmund Basin) have εHf values of -12.1 to -1.5, and those with mantle- like $\delta^{18}O$ values have corresponding T_{DM}^{C} ages that range from 3265 to 2977 Ma. These evolved Hf-isotope compositions imply that the magmas from which these zircon crystallised were derived, at least in part, from remelting of more evolved crustal sources with lower Lu/Hf than CHUR. The Hf-isotopic range of this material overlaps the Glenburgh Terrane granites and suggests that the Glenburgh Terrane or its reworked equivalents were present as basement when magmatic rocks of the eastern granites were emplaced. This has implications for the interpretation of magnetotelluric studies of Dentith et al. (2014) that suggest the central part of the Collier Basin is underlain by rocks of the Glenburgh Terrane.

All the granitic rocks of the Moorarie Supersuite appear to share common source components, with variable mixing between upper and mid-to lower crustal components, with some depleted-mantle components, depending on the portion of the crust intruded.

- **Development of crustal components – evidence from oxygen isotopes**

Oxygen isotope data for magmatic zircons from the individual Moorarie Supersuitegranites range from 5.11 ± 0.43‰ to 10.23 ± 0.43‰, 2σ (Figure 2.22). The magmatic zircons show systematic variations in $\delta^{18}O$ with respect to spatial distribution of host granites, with the lowest $\delta^{18}O$ values observed in the southern granites within the Yarlarweelor Gneiss Complex (average $\delta^{18}O$: 6.79-7.15‰), increasing towards the northwest towards the central granites (average 6.48-8.09‰), and the Minnie Creek Batholith (average 7.04-9.42‰). The eastern and the northern granites show a larger range in $\delta^{18}O$, with averages between 5.47- 9.42‰ and 6.29-9.01‰, respectively. The northern granites, eastern granites, southern granites and central granites have $\delta^{18}O$ values that are within error of the field of mantle zircon. This indicates that the parent magmas that these zircon crystallised in contained significant amounts of low-$\delta^{18}O$ material representing an infracrustal source component with mantle-like $\delta^{18}O$ (i.e. a meta-igneous crustal component that has not interacted significantly with shallow crustal material), and negligible amounts of supracrustal (metasedimentary) material. In contrast, the Minnie Creek Batholith is dominated by higher $\delta^{18}O$ (7-10‰; average 8.12 ± 1.6‰ 2σ). These high $\delta^{18}O$ zircon values are typical of magmas with a dominant metasedimentary component (~8-12‰; Appleby et al., 2010). The diversity of the data indicates that the magmas that the zircon grains crystallised from were sourced from multiple, isotopically distinct, crustal components.

Southern granites: Individual samples display a narrow range of average $\delta^{18}O$ values (6.72 ± 1.87‰ to 6.92 ± 0.43‰) coupled with variably evolved εHf compositions (-12.7 to -5.2). Together, these data indicate derivation from an old or evolved crustal component that did not interact significantly with shallow crustal material, but host magma incorporated material from surrounding crust during ascent and/or emplacement within the mid- to lower-crust. This is consistent with the U–Pb and Hf data that suggest reworking of Paleoproterozoic granites of the southern Gascoyne Complex, and emplacement of magmas into the Yilgarn Craton margin.

Central granites: Characterised by contrasting average $\delta^{18}O$ of 6.51 ± 0.45‰ and 8.1 ± 0.6‰, coupled with moderately evolved εHf compositions (-8.6 to -4.8). The origin of these low $\delta^{18}O$ magmas can be attributed to an infracrustal source component (igneous rock solidified at depth with limited interaction with shallow crustal material) and is consistent with the U– Pb and Hf data that suggest derivation from reworking of granites of the southern Gascoyne Complex. The higher $\delta^{18}O$ values observed in GSWA 168939 indicates incorporation of a high $\delta^{18}O$ material into the melt source and may represent an additional metasedimentary source component. Assuming an average Paleoproterozoic sediment value of ~10-15‰, and an average magmatic value of ~8‰, implies an input of ~20-50% high-$\delta^{18}O$ material in the GSWA 168939 magmas relative to average Glenburgh Terrane granite $\delta^{18}O$ values (~6.1‰). For sample GSWA 159724 an input of ~5-11% high $\delta^{18}O$ material is implied.

Eastern granites: The eastern granites display similar Hf-O arrays, with samples indicating average $\delta^{18}O$ that range from mantle-like values 5.47 ± 0.41‰ to high $\delta^{18}O$ values of 9.42 ± 0.53‰, coupled with variably evolved εHf compositions (-11.8 to -1.5). This Hf-O isotope array can be accounted for by progressive contamination of magma batches due to crustal assimilation and wall-rock interaction, i.e. the granites were formed from melts generated from mixing of low-$\delta^{18}O$ magmas (partial melts of a Halfway Gneiss-like component) with a minor metasedimentary component, while other broadly coeval granites formed from melts that incorporated larger amounts of metasedimentary components during their path to emplacement.

Minnie Creek Batholith: Typified by variably evolved εHf compositions (-7.4 to +3.0) coupled with high $\delta^{18}O$ values (7-10‰), indicating assimilation of buried sediments or other supracrustal material within the mid to upper crust. For the granites, an input of ~30-62% high-$\delta^{18}O$ material could have been incorporated into the

magmas, suggesting a voluminous magma originating from mixing differentiated mantle melts with melts generated in the upper crust. It is possible that the intrusion of mantle-derived magmas induced crustal anatexis in the lower- to middle-crust (<45km, constrained by the absence of a garnet signature in the granites), producing hybrid magmas. Extraction and subsequent migration of these melts could have occurred along deep-seated lithospheric structures into upper crustal reservoirs, where mixing may have occurred between different melt batches. In combination with partial melting of metasediments, this could precipitate zircon with high $\delta^{18}O$ values and low εHf values (e.g. Kemp et al., 2007). Metasedimentary enclaves (metre to kilometre-scale) in the Minnie Creek Batholith (Johnson et al., 2017) are interpreted as evidence for bulk assimilation.

Most of the samples have $\delta^{18}O$ values between 7 and 9‰, a characteristic consistent with derivation of granite magmas from a source containing a significant component of weathered materials. Some samples have mantle like $\delta^{18}O$ values implying that not all magmas involved supracrustal contributions. This variation in $\delta^{18}O$ values may be explained if the zircon derived from magmas formed at different crustal levels.

2.7.8 Intracratonic recycling – Durlacher and Thirty-three Supersuites

The analysed zircon from the Durlacher Supersuite samples cover a period of 1570 Myr, with individual $^{207}Pb/^{206}Pb$ ages ranging between c. 2778 and c. 1209 Ma (Figure 2.23). Granites were generated during one main magmatic episode at c. 1685–1645 Ma. The northern granites have older crystallisation ages (c. 1690–1667 Ma) than magmatism recorded in the Davey Well Batholith granites in the central part of the study area (c. 1674–1658 Ma). The youngest magmatism is recorded in a southern granite sample (c. 1651 Ma). Individual ages for the samples from the Thirty Three Supersuite range between c. 2233 and 1004 Ma, with magmatic crystallisation constrained at c. 1030 Ma. The magmatic ages established are in broad agreement with the c. 1682–1619 Ma age range established for the Durlacher Supersuite (Sheppard et al., 2005) and the c. 1030–889 Ma age range of the Thirty Three Supersuite (Piechocka et al., 2017; Sheppard et al., 2007).

Inherited zircon grains from the Durlacher Supersuite indicate $^{207}Pb/^{206}Pb$ ages of c. 2778– 1700 Ma, with two main magmatic events identified at 1805 and 1762 Ma, and a minor peak at c. 2290–2225 Ma. In the Gascoyne Province, the Durlacher Supersuite intruded the Pooranoo Metamophics, and the major group of inherited material at c. 1762 Ma reflects the c. 1760–1680 Ma depositional ages established for the metasediments (Sheppard et al., 2005; 2007). The main group of inherited zircon grains at c. 1805 and c. 1762 Ma have ages that reflect the ages of the Moorarie Supersuite and Pooranoo Metamorphics, and indicate that the Durlacher Supersuite granitoids assimilated these rocks during emplacement and crystallisation.

U–Pb data reveals three main periods of magmatic activity at c. 1850–1770, 1663, and 1030 Ma, and a minor c. 2295–2225 event. Zircon from these samples yield initial $^{176}Hf/^{177}Hf$ ratios between 0.281160 and 0.281873 (εHf -14.4 to 0). The majority of analyses indicate evolved εHf values (median = -6.3), indicating that these granites were formed mainly from the reworking of crustal components with little to no significant mantle input.

The c. 2295–2225 Ma zircon form a small group indicate moderately evolved εHf compositions (-5 to -1.5) and $\delta^{18}O$ values between 5.59 and 9.9‰. The Durlacher Supersuite extensively intruded rocks of the 1740–1680 Ma Pooranoo Metamorphics, and the age range of these inherited zircon are comparable to the detrital components identified in metasedimentary rocks of the Pooranoo Metamorphics (Bodorkos et al., 2006; Wingate et al., 2010a, 2010b, 2017). This suggests that the zircons are likely to have been sourced from host metasedimentary country rocks during magma ascent and emplacement. Zircon with elevated $\delta^{18}O$ values (8.2–9.9‰) are characteristic of a metasedimentary component (~8-12‰; Appleby et al., 2010), and are consistent with an interpretation of inherited zircon being incorporated from assimilated Pooranoo Metamorphics. The c. 1850–1770 Ma zircon indicate a large range in εHf values (-8.2 to -0.7) and $\delta^{18}O$ values

ranging between 5.56 and 10.95‰. These U–Pb ages and Hf-O isotope data are identical to the c. 1820–1775 Ma Moorarie Supersuite (Figure 2.46), and imply that the Moorarie Supersuite was incorporated into host magma, either during magma ascent or crustal anatexis.

The c. 1030 Ma magmatic zircon from the Thirty Three Supersuite have unradiogenic initial $^{176}Hf/^{177}Hf$ ratios that range between 0.281723 and 0.281873 (εHf -14.4 to -8.9). The $\delta^{18}O$ values range between 7.93–8.99‰. Crustal evolution lines defined by a source a $^{176}Lu/^{177}Hf$ value of 0.015, show that the younger granites lie within the Durlacher Supersuite and Moorarie Supersuite granites isotopic envelope. Therefore, these isotopic arrays indicate that the melts were formed by reworking of an infracrustal source possessing broadly similar $^{176}Lu/^{177}Hf$ ratios, such as the c. 1800–1600 Ma granites. Inherited zircon have U–Pb ages and Hf–O isotope compositions comparable to the Durlacher Supersuite, consistent with the interpretation that the c. 1035 Ma granites were sourced from reworking of the c. 1663 Ma granites. The Thirty Three Supersuite zircon have εHf values that are more radiogenic than can be explained by remelting of the Durlacher Supersuite alone, and instead suggests mixing with an alternative end-member.

2.8 Summary and Conclusions

A large geochronological and geochemical dataset has been assembled for the mineral zircon across crystalline basement and overlying sedimentary sequences in order to temporally and geodynamically constrain the geological history of the Capricorn Orogen. Analyses from the crystalline basement inform major magmatic events and the relative contributions of juvenile vs reworked material during regional crustal evolution and its development from isolated continental fragments in the Archean, to a stabilized West Australian Craton in the Proterozoic. In concert with this, analyses of detrital zircons from the overlying sedimentary basins enable reconstruction of the denudation histories of various basement components and the tracking of sediment fingerprints through successive contractional and extensional episodes. While known mineral deposits in the Gascoyne Complex are associated with major structural trends, there also appears to be a correlation between juvenile input and mineral deposits around the Marymia Inlier (Figure 2.46).

Overall, Hf- and O-isotopic data from magmatic zircons indicate relatively limited juvenile input during orogenic events in the Gascoyne Complex, with regions of crustal growth in the south along the Yilgarn Craton margin from 3000-2100 Ma, and in the north during 2100- 1750 Ma (Figure 2.46). The Hf-isotope data trend towards more evolved εHf values with decreasing age, indicating that the zircons parent magmas were predominantly derived by melting pre-existing crustal rocks. The O-isotopes show a progressive increase of $\delta^{18}O$ over time, in agreement with the reworking trend seen in the Lu-Hf data, and indicate the progressive incorporation of supracrustal and sedimentary rocks into melt sources.

The Narryer Terrane and Yarlarweelor Gneiss Complex are characterised by evolved εHf and mantle-derived to slightly elevated mean $\delta^{18}O$ compositions that indicate derivation from the progressive reworking of Paleoarchean granites (Figure 2.46). Zircon U-Pb geochronology from the Marymia Inlier indicate two periods of granite generation, at c. 3330 Ma and c. 2700 Ma. The U–Pb and Hf–O isotope data of the c. 3330 Ma granites (which have not previously been recognised) are comparable to granitoids from the Narryer Terrane, suggesting that the Marymia Inlier is an extension of the Narryer Terrane. Furthermore, Hf-O isotope data of c. 2700 Ma Marymia Inlier granitoids indicate correlation with the western part of the ESGT (Kalgoorlie Terrane). The Goodin Inlier exhibits evolved Hf-isotope signatures coupled with mantle-derived $\delta^{18}O$ compositions, with melts sourced from the reworking of isotopically evolved pre-existing crustal components with little/no significant mantle input. Hf-isotope data shows that the Goodin Inlier closely resembles, and is interpreted to be part of, the Youanmi Terrane of the Yilgarn Craton. Magmatism in the Sylvania Inlier has been dated to between c. 3196 and 2879 Ma, which together with Hf-isotopic data suggests correlation to

the East Pilbara Terrane. Hafnium and oxygen isotope data from the Halfway Gneiss suggest that it is comparable to the Yilgarn Craton, and is not an exotic micro-continent as previously thought. This would imply that the Glenburgh Terrane represents an ultimately recombined block that had previously rifted free from the margin of the Yilgarn Craton to collide with the Pilbara Terrane. Similar rift, re-assembly events are considered important in the development of mineralisation at Tropicana (eastern Yilgarn Craton) and may inform mineral potential in the Gascoyne Province.

Paleoproterozoic orogenic granites in the Glenburgh Terrane contain zircons spanning over 1 Ga, with peaks at c. 2670–2545 Ma, c. 2100 Ma and c. 1970 Ma, indicating that significant proportions of crust were generated during the Paleoproterozoic (c. 2353–2030 Ma), and that granitic magmatism during the Glenburgh Orogeny extends to ages older than those indicated by current exposed rocks and involved recycling of continental crust. Hafnium and oxygen isotope data from Glenburgh Orogeny magmatism support significant recycling of previously formed continental crust, and overall progressive reworking of Archean granites mixing with juvenile melts.

Granitic samples associated with the Capricorn Orogeny exhibit similar hafnium and oxygen isotopic indicators of crustal re-working with only limited contributions of juvenile depleted- mantle like sources. Increasing spread in the isotopic composition of zircons in Moorarie Supersuite attributed samples reflect incorporation of multiple local, isotopically distinct, crustal components: (1) reworked meta-igneous rocks with compositions similar to that of the Halfway Gneiss protoliths and (2) metasedimentary rocks. All Capricorn Orogeny granites record a c. 1860 Ma component, which does not match any metasedimentary successions in the region, suggesting that they were derived in large part from melting of crust that is not currently exposed.

Successive reworking of the crust is further evidenced through later magmatism in the Capricorn Orogen. Hafnium and oxygen isotopic data indicate reworking of the Halfway Gneiss and Moorarie Supersuite in southern granites of the Durlacher Supersuite, remelting of the Moorarie Supersuite and mid to upper crustal components to produce Durlacher Supersuite magma further north in the Gascoyne Province, while inherited zircon geochronology and Hf-O geochemistry in the younger Thirty-three Supersuite are consistent with the reworking of c. 1663 Ma Durlacher Supersuite granites during the youngest major magmatic episode in the region at ~1.0 Ga.

Overall, the sedimentary sequences of the Capricorn Orogen are dominated by zircons from granitoid magmatism of the Archean Yilgarn Craton in the south and Paleoproterozoic detritus from the Gascoyne Province through central and northern basins (Figure 2.47 & 2.48).

Limited zircons from the Archean Pilbara Craton proper are not recognised in any of the Capricorn Orogen basins, despite their occurrence in Fortescue Basin sediments to the north of the Capricorn Orogen. This is interpreted to be a result of drowning of any Pilbara Craton signal by more local sediment sources and topography. Evolution in the major sediment sources through time track the assembly of the West Australian Craton and associated intrusion of various magmatic supersuites (Figure 2.49), with the Moorarie Supersuite being a particularly prominent source of zircons in all younger basins, likely as a result of its extensive spatial development across the region.

During deposition of the Ashburton Basin, sediments were principally derived from reworking of the Turee Creek Group with increasing influence from the Gascoyne Complex through younger sedimentary units (Figure 2.29) in response to the Pilbara-Glenburgh Terrane collision. Palaeocurrents from the north imply that sediments may have been recycled from earlier northward shedding from the Gascoyne Complex. Later depocenter development in the form of the Mt. Minnie and Bresnahan Basins are simpler and indicate significant denudation of the Moorarie Supersuite subsequent to the Capricorn Orogeny.

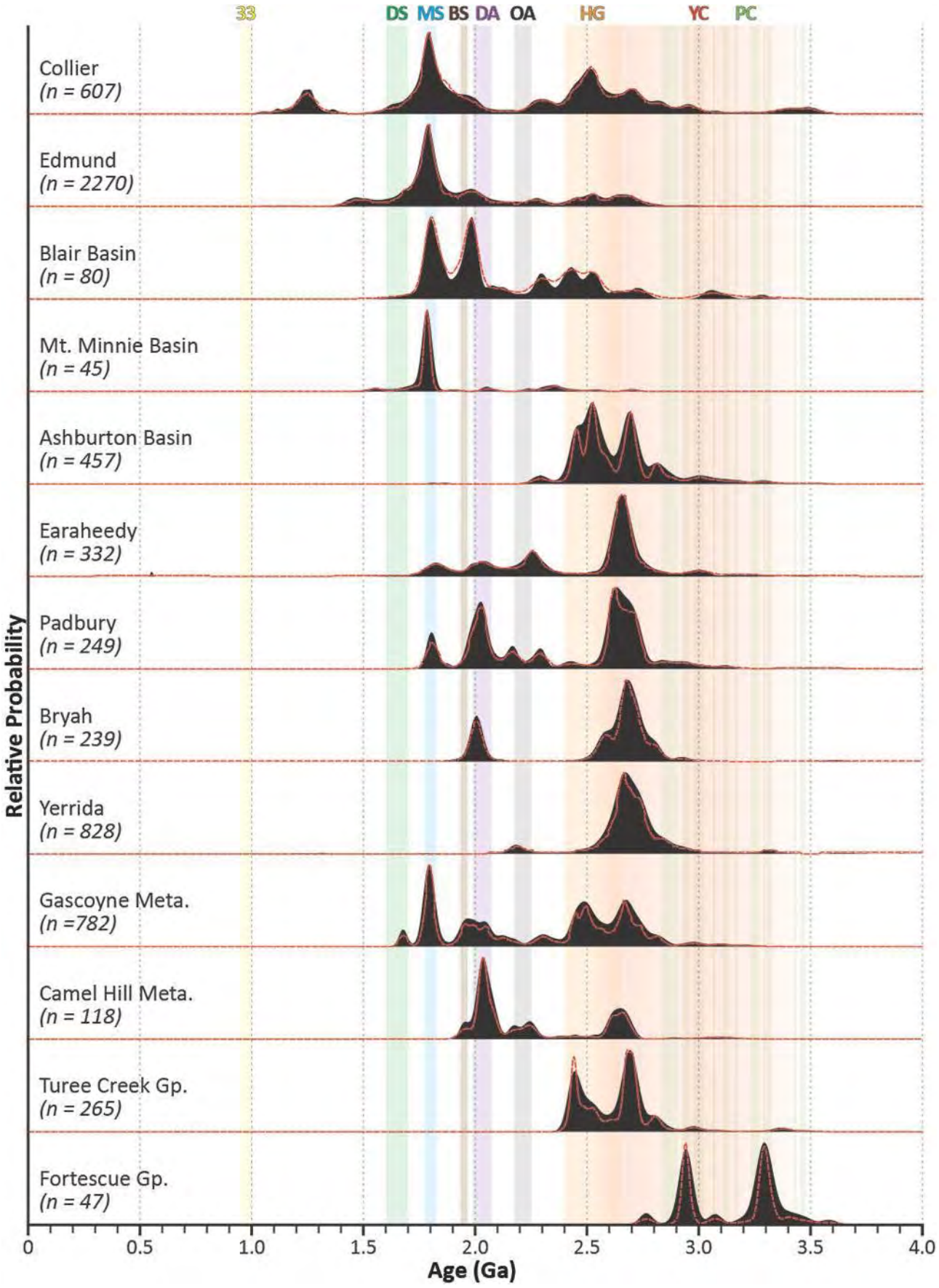

Figure 2.47. Stacked probability plot of detrital zircon ages from all the major depositional sequences of the Capricorn Orogen. Red dashed lines represent kernel density estimates for the zircon populations. Black spectra correspond to normalised probability density diagrams for pooled concordant analyses (± 10%) from specific regions. Vertical coloured bars correspond to ages of major regional magmatic events (see caption to Figure 2.29).

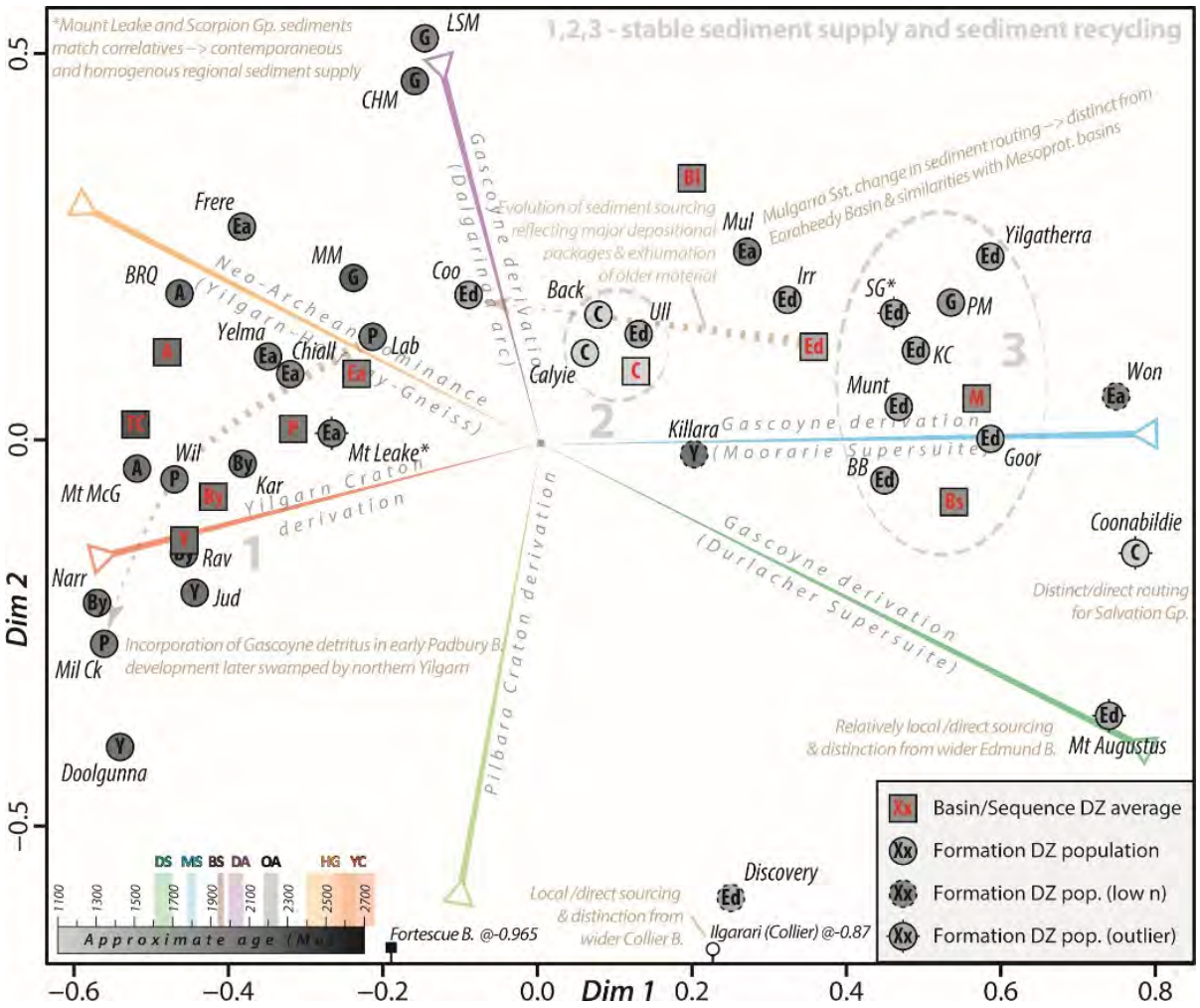

Figure 2.48. Multi-dimensional scaling plot of Capricorn Orogen detrital zircon geochronology data. Data points represent the detrital zircon age populations of stratigraphic units across the Capricorn with greyscale colour coding according to depositional age. The proximity of the points indicates the similarity of the populations and suggests similar source regions or recycling. The overall array is dominated by Archean (Yilgarn) to late Palaeoproterozoic (Moorarie) provenance. Squares = pooled basin data, circles = formations. A – Ashburton, Bl – Blair, BS – Bresnahan, By – Bryah, C – Collier, Ea – Earaheedy, Ed – Edmund, G – Gascoyne, P – Padbury, Y – Yerrida. Coloured vectors indicate the dominant sources that cause dispersion of the data.

Between ~2.2 and 2.0 Ga, thinning of the crust on the northern margin of the Yilgarn Craton facilitated the progressive development of the Yerrida, Bryah and Padbury Basins. Mafic volcanism is reflected in the age and geochemistry of the detrital zircon population and support rift-related magmatism and some degree of local sourcing. All units are dominated by zircons from the northern Yilgarn Craton with subtle changes in peak ages reflecting the progressive opening of the basins across different tectonic domains. Parts of the upper Bryah and lower Padbury Basin sequences demonstrate sediment pathways to the approaching Dalgaringa Arc to the northwest, constraining the magnitude of separation. Gross similarities in the zircon populations along the northern margin of the Yilgarn Craton represents sediment recycling, as well as homogeneity of regional supply prior to the Glenburgh Orogeny.

Sediment provenance was relatively stable through deposition of the Earaheedy Basin between the Glenburgh and Capricorn Orogenies, despite the recognition of stratigraphic breaks. Yilgarn Craton-derived zircons dominate the sediments but several components from the Gascoyne Complex are also represented. Towards the top of the succession, zircons from the Moorarie Supersuite (distinct from underlying sediments) suggest a younger age of sedimentation and relatively rapid exhumation and exposure of the granitic units after emplacement.

The Edmund and Collier Basins are dominated by zircons derived from the Moorarie Supersuite but exhibit sediment source region complexity associated with changes in paleocurrents during fault-reactivation. Collectively, pooled data for the basins correspond with the appearance of a broader polymodal Archaean through Proterozoic zircon sub- population reflecting recycling of Yilgarn Craton, Gascoyne Province and southern Pilbara Craton volcanics suggesting overall reduced dominant topographies and homogenising of the regional sediment signature. Distinct ~1.45 Ga zircons suggest local sourcing from doleritic intrusives in the Edmund Basin and provide a new useful maximum depositional age constraint. The lower Collier Basin sequence appears recycled from the underlying Edmund Basin, while limited data from the uppermost formation in the Collier Basin provide a maximum depositional age constraint of ~1.11-1.3 Ga. These youngest grains attest to previously unknown crystalline rocks in the region, or, more likely, reflect continental-scale transport of detritus from the Musgrave Province, since the distinctive age is also recognised in intermediate Neoproterozoic basins as well as the modern Gascoyne River catchment.

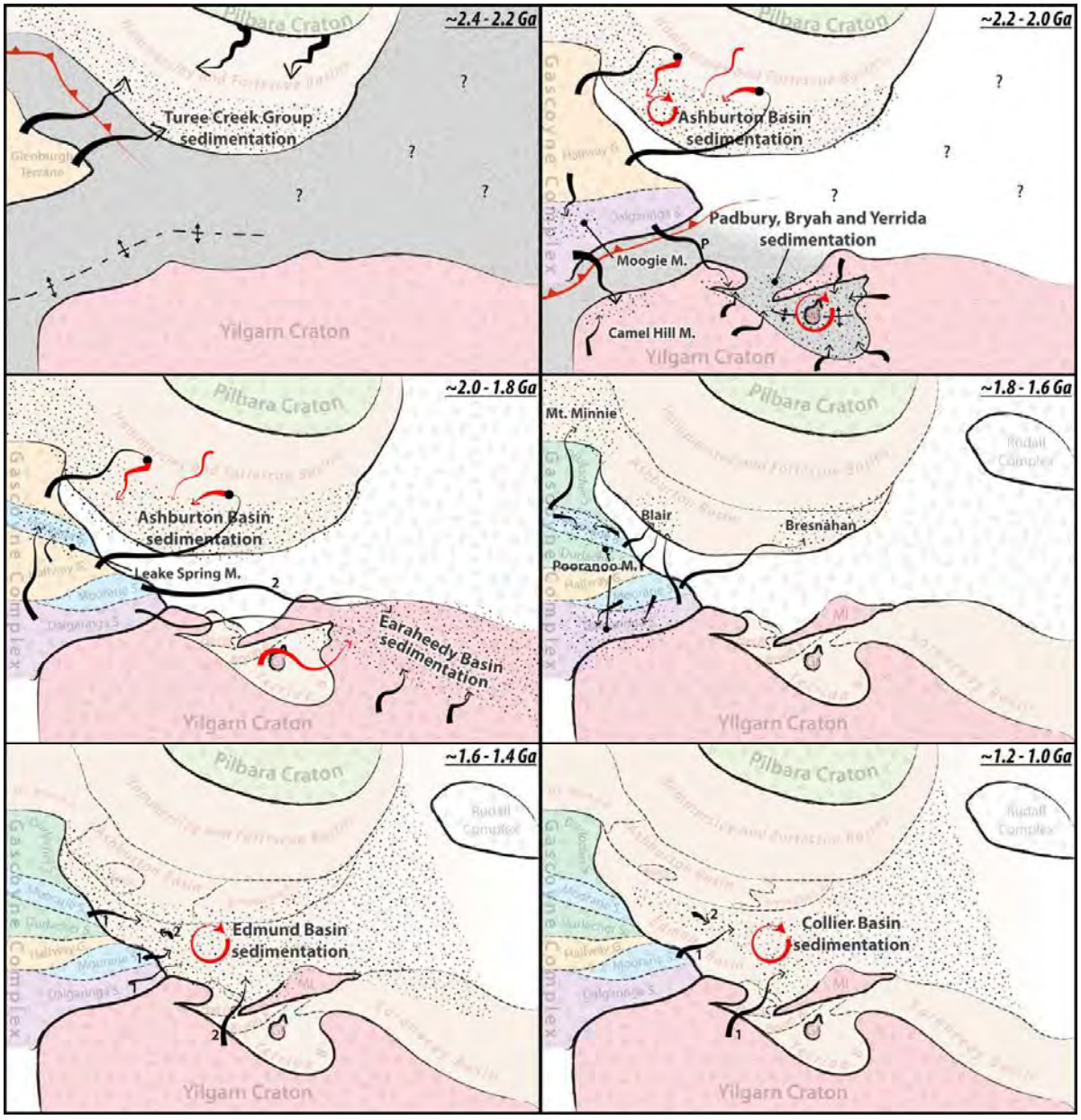

Figure 2.49. Schematic sediment routing evolution diagram for major depositional intervals within the Capricorn Orogen. Stippled areas indicate areas of sedimentation, black arrows indicate erosion from crystalline source regions, red arrows indicate recycling of sediments. Numbers indicate progressive changes in sourcing through the interval – higher numbers indicating younger sediments in the sequence. Line thicknesses are indicative of significance of source. Arrows are illustrative only of provenance connections, not of exact routing pathways.

2.9 References

Akin, S. J., Pufahl, P. K., Hiatt, E. E., and Pirajno, F., 2013, Oxygenation of shallow marine environments and chemical sedimentation in Palaeoproterozoic peritidal settings: Frere Formation, Western Australia: Sedimentology, v. 60, no. 7, p. 1559-1582.

Anders, E., and Grevesse, N., 1989, Abundances of the elements: Meteoritic and solar: Geochimica et Cosmochimica Acta, v. 53, no. 1, p. 197-214.

Appleby, S. K., Gillespie, M. R., Graham, C. M., Hinton, R. W., Oliver, G. J. H., and Kelly, N. M., 2010, Do S-type granites commonly sample infracrustal sources? New results from an integrated O, U–Pb and Hf isotope study of zircon: Contributions to Mineralogy and Petrology, v. 160, no. 1, p. 115-132.

Armondola, S., In prep, TBC - Detrital zircon geochronology and geochemistry from the Capricorn Orogen [PhD: Curtin University.

Bagas, L., 1998, The Archaean Marymia Inlier - a review of its tectonic history and relationships to the Yilgarn Craton, Western Australia: Western Australia Geological Survey, Annual Review 1997-1998.

Bagas, L., 1999, Early tectonic history of the Marymia Inlier and correlation with the Archaean Yilgarn Craton, Western Australia: Australian Journal of Earth Sciences, v. 46, no. 1, p. 115-125.

Barham, M., Kirkland, C. L., Reynolds, S., O'Leary, M. J., Evans, N. J., Allen, H., Haines, P. W., Hocking, R. M., McDonald, B. J., Belousova, E., and Goodall, J., 2016, The answers are blowin' in the wind: Ultra-distal ashfall zircons, indicators of Cretaceous super-eruptions in eastern Gondwana: Geology, v. 44, no. 8, p. 643-646.

Barley, M. E., Brown, S. J. A., Cassidy, K. F., Champion, D. C., and Krapez, B., 2003, An integrated geological and metallogenic framework for the eastern Yilgarn Craton: developing geodynamic models of highly mineralised Archaean granite-greenstone terranes: Australasian Minerals Industry Association Report, v. P624.

Begg, G. C., Hronsky, J. A. M., Arndt, N. T., Griffin, W. L., O'Reilly, S. Y., and Hayward, N., 2010, Lithospheric, Cratonic, and Geodynamic Setting of Ni-Cu-PGE Sulfide Deposits: Economic Geology, v. 105, no. 6, p. 1057-1070.

Belousova, E., Griffin, W., O'Reilly, S. Y., and Fisher, N., 2002, Igneous zircon: trace element composition as an indicator of source rock type: Contributions to Mineralogy and Petrology, v. 143, no. 5, p. 602-622.

Belousova, E. A., Reid, A. J., Griffin, W. L., and O'Reilly, S. Y., 2009, Rejuvenation vs. recycling of Archean crust in the Gawler Craton, South Australia: Evidence from U– Pb and Hf isotopes in detrital zircon: Lithos, v. 113, no. 3–4, p. 570-582.

Black, L. P., Kamo, S. L., Allen, C. M., Davis, D. W., Aleinikoff, J. N., Valley, J. W., Mundil, R., Campbell, I. H., Korsch, R. J., Williams, I. S., and Foudoulis, C., 2004, Improved $^{206}Pb/^{238}U$ microprobe geochronology by the monitoring of a trace-element- related matrix effect; SHRIMP, ID–TIMS, ELA–ICP–MS and oxygen isotope documentation for a series of zircon standards: Chemical Geology, v. 205, no. 1, p. 115-140.

Blake, T. S., and Barley, M. E., 1992, Tectonic evolution of the Late Archaean to Early Proterozoic Mount Bruce Megasequence Set, Western Australia: Tectonics, v. 11, no. 6, p. 1415-1425.

Blichert-Toft, J., 2008, The Hf isotopic composition of zircon reference material 91500: Chemical Geology, v. 253, no. 3, p. 252-257.

Bodorkos, S., Love, G. J., Nelson, D. R., and Wingate, M. T. D., 2006, 149695: quartz sandstone, Quadrio Lake; Geochronology dataset 616, Compilation of geochronology data, June 2006 update, Western Australia Geological Survey.

Bunting, J. A., 1986, Geology of the eastern part of the Nabberu Basin, Geological Survey of Western Australia. Bulletin 131.

Carrapa, B., 2010, Resolving tectonic problems by dating detrital minerals: Geology, v. 38, no. 2, p. 191-192.

Cassidy, K. F., Champion, D. C., Krapež, B., Barley, M. E., Brown, S. J. A., Blewett, R. S., Groenewald, P. B., and Tyler, I. M., 2006, A revised geological framework for the Yilgarn Craton, Western Australia, Western Australia Geological Survey Record 2006/8.

Cawood, P. A., Hawkesworth, C. J., and Dhuime, B., 2012, Detrital zircon record and tectonic setting: Geology, v. 40, no. 10, p. 875-878.

Cawood, P. A., and Korsch, R. J., 2008, Assembling Australia: Proterozoic building of a continent: Precambrian Research, v. 166, no. 1–4, p. 1-35.

Cawood, P. A., and Tyler, I. M., 2004, Assembling and reactivating the Proterozoic Capricorn Orogen: lithotectonic elements, orogenies, and significance: Precambrian Research, v. 128, no. 3–4, p. 201-218.

Cottle, J. M., Kylander-Clark, A. R., and Vrijmoed, J. C., 2012, U–Th/Pb geochronology of detrital zircon and monazite by single shot laser ablation inductively coupled plasma mass spectrometry (SS-LA-ICPMS): Chemical Geology, v. 332-333, no. Supplement C, p. 136-147.

Cutten, H. N., Johnson, S. P., Thorne, A. M., Wingate, M. T. D., Kirkland, C. L., Belousova, E., Blay, O. A., and Zwingmann, H., 2016, Deposition, preovenance, inversion history and mineralization of the Proterozoic Edmund and Collier Basins, Capricorn Orogen: Geological Survey of Western Australia, Report 127.

Dentith, M. C., Johnson, S. P., Evans, S., Aitken, A. R. A., Joly, A., Thiel, S., and Tyler, I. M., 2014, A magnetotelluric traverse across the eastern part of the Capricorn Orogen, Geological Survey of Western Australia, Report 135.

Evans, D. A. D., Sircombe, K. N., Wingate, M. T. D., Doyle, M., McCarthy, M., Pidgeon, R. T., and Van Niekerk, H. S., 2003, Revised geochronology of magmatism in the western Capricorn Orogen at 1805-1785 Ma: Diachroneity of the Pilbara-Yilgarn collision: Australian Journal of Earth Sciences, v. 50, no. 6, p. 853-864.

Ferry, J. M., and Watson, E. B., 2007, New thermodynamic models and revised calibrations for the Ti-in-zircon and Zr-in-rutile thermometers: Contributions to Mineralogy and Petrology, v. 154, no. 4, p. 429-437.

Fisher, C. M., Vervoort, J. D., and DuFrane, S. A., 2014, Accurate Hf isotope determinations of complex zircons using the “laser ablation split stream” method: Geochemistry, Geophysics, Geosystems, v. 15, no. 1, p. 121-139.

Fu, B., Mernagh, T. P., Kita, N. T., Kemp, A., and Valley, J. W., 2009, Distinguishing magmatic zircon from hydrothermal zircon: A case study from the Gidginbung high- sulphidation Au-Ag-(Cu) deposit, SE Australia: Chemical Geology, v. 259, p. 131- 142.

Gardiner, N. J., Hawkesworth, C. J., Robb, L. J., Whitehouse, M. J., Roberts, N. M. W., Kirkland, C. L., and Evans, N. J., 2017a, Contrasting Granite Metallogeny through the Zircon Record: A Case Study from Myanmar: Scientific Reports, v. 7, no. 1, p. 748.

Gardiner, N. J., Hickman, A. H., Kirkland, C. L., Lu, Y., Johnson, T., and Zhao, J. X., 2017b, Processes of crust formation in the early Earth imaged through Hf isotopes from the East Pilbara Terrane: Precambrian Research, v. 297, p. 56-76.

Gazley, M. F., 2011, Metamorphism, Geochronology and Stratigraphy of an Amphibolite- Facies Greenstone-Hosted Gold Deposit: Plutonic Gold Mine, Marymia Inlier, Western Australia [PhD: Victoria University of Wellington, 176 p.

Gazley, M. F., Vry, J. K., and Boorman, J. C., 2011, P–T evolution in greenstone-belt mafic amphibolites: an example from Plutonic Gold Mine, Marymia Inlier, Western Australia: Journal of Metamorphic Geology, v. 29, no. 6, p. 685-697.

Gehrels, G. E., Valencia, V. A., and Ruiz, J., 2008, Enhanced precision, accuracy, efficiency, and spatial resolution of U-Pb ages by laser ablation–multicollector–inductively coupled plasma–mass spectrometry: Geochemistry, Geophysics, Geosystems, v. 9, no. 3, p. n/a.

Geoscience Australia and the Australian Stratigraphy Commission, 2017, Australian Stratigraphic Units Database, Geoscience Australia and Australian Stratigraphy Commission.

Griffin, W. L., Belousova, E. A., Shee, S. R., Pearson, N. J., and O'Reilly, S. Y., 2004, Archean crustal evolution in the northern Yilgarn Craton: U–Pb and Hf-isotope evidence from detrital zircons: Precambrian Research, v. 131, no. 3–4, p. 231-282.

Griffin, W. L., Pearson, N. J., Belousova, E. A., and Saeed, A., 2007, Reply to "Comment to short-communication 'Comment: Hf-isotope heterogeneity in zircon 91500' by W.L. Griffin, N.J. Pearson, E.A. Belousova and A. Saeed (Chemical Geology 233 (2006) 358–363)" by F. Corfu: Chemical Geology, v. 244, no. 1–2, p. 354-356.

Griffin, W. L., Wang, X., Jackson, S. E., Pearson, N. J., O'Reilly, S. Y., Xu, X., and Zhou, X., 2002, Zircon chemistry and magma mixing, SE China: In-situ analysis of Hf isotopes, Tonglu and Pingtan igneous complexes: Lithos, v. 61, no. 3, p. 237-269.

Grimes, C. B., John, B. E., Kelemen, P. B., Mazdab, F. K., Wooden, J. L., Cheadle, M. J., Hanghøj, K., and Schwartz, J. J., 2007, Trace element chemistry of zircons from oceanic crust: A method for distinguishing detrital zircon provenance: Geology, v. 35, no. 7, p. 643-646.

Grimes, C. B., Wooden, J. L., Cheadle, M. J., and John, B. E., 2015, "Fingerprinting" tectono-magmatic provenance using trace elements in igneous zircon: Contributions to Mineralogy and Petrology, v. 170, no. 5-6, p. 1-26.

Groves, D. I., and Bierlein, F. P., 2007, Geodynamic settings of mineral deposit systems: Journal of the Geological Society, v. 164, no. 1, p. 19-30.

Guo, L., Zhang, H.-F., Harris, N., Xu, W.-C., and Pan, F.-B., 2017, Detrital zircon U–Pb geochronology, trace-element and Hf isotope geochemistry of the metasedimentary rocks in the Eastern Himalayan syntaxis: Tectonic and paleogeographic implications: Gondwana Research, v. 41, p. 207-221.

Haines, P. W., Kirkland, C. L., Wingate, M. T. D., Allen, H., Belousova, E. A., and Gréau, Y., 2016, Tracking sediment dispersal during orogenesis: A zircon age and Hf isotope study from the western Amadeus Basin, Australia: Gondwana Research, v. 37, p. 324- 347.

Halilovic, J., 2002, SHRIMP geochronology of southern Capricorn Orogen detrital zircons, Curtin University.

Halilovic, J., Cawood, P. A., Jones, J. A., Pirajno, F., and Nemchin, A. A., 2004, Provenance of the Earaheedy Basin: implications for assembly of the Western Australian Craton: Precambrian Research, v. 128, no. 3–4, p. 343-366.

Hall, C. E., Powell, C. M., and Bryant, J., 2001, Basin setting and age of the Late Palaeoproterozoic Capricorn Formation, Western Australia: Australian Journal of Earth Sciences, v. 48, no. 5, p. 731-744.

Hall, W. D. M., and Goode, A. D. T., 1978, The Early Proterozoic Nabberu Basin and associated iron formations of Western Australia: Precambrian Research, v. 7, no. 2, p. 129-184.

Hanchar, J. M., and Miller, C. F., 1993, Zircon zonation patterns as revealed by cathodoluminescence and backscattered electron images: Implications for interpretation of complex crustal histories: Chemical Geology, v. 110, no. 1, p. 1-13.

Hawke, M. L., Meffre, S., Stein, H., Hilliard, P., Large, R., and Gemmell, J. B., 2015, Geochronology of the DeGrussa volcanic-hosted massive sulphide deposit and associated mineralisation of the Yerrida, Bryah and Padbury Basins, Western Australia: Precambrian Research, v. 267, p. 250-284.

Hawkesworth, C. J., and Kemp, A. I. S., 2006, Using hafnium and oxygen isotopes in zircons to unravel the record of crustal evolution: Chemical Geology, v. 226, no. 3–4, p. 144- 162.

Hickman, A. H., 2012, Review of the Pilbara Craton and Fortescue Basin, Western Australia: Crustal evolution providing environments for early life: Island Arc, v. 21, no. 1, p. 1- 31.

Hocking, R. H., Jones, J. A., Pirajno, F., and Grey, K., 2000, Revised lithostratigraphy for Proterozoic rocks in the Earaheedy Basin and nearby areas.

Hoskin, P. W. O., and Ireland, T. R., 2000, Rare earth element chemistry of zircon and its use as a provenance indicator: Geology, v. 28, no. 7, p. 627-630.

Hoskin, P. W. O., and Schaltegger, U., 2003, The Composition of Zircon and Igneous and Metamorphic Petrogenesis: Reviews in Mineralogy and Geochemistry, v. 53, no. 1, p. 27-62.

Hronsky, J. M. A., Groves, D. I., Loucks, R. R., and Begg, G. C., 2012, A unified model for gold mineralisation in accretionary orogens and implications for regional-scale exploration targeting methods: Mineralium Deposita, v. 47, no. 4, p. 339-358.

Iizuka, T., Campbell, I. H., Allen, C. M., Gill, J. B., Maruyama, S., and Makoka, F., 2013, Evolution of the African continental crust as recorded by U–Pb, Lu–Hf and O isotopes in detrital zircons from modern rivers: Geochimica et Cosmochimica Acta, v. 107, p. 96-120.

Ivanic, T. J., Van Kranendonk, M. J., Kirkland, C. L., Wyche, S., Wingate, M. T. D., and Belousova, E. A., 2012, Zircon Lu–Hf isotopes and granite geochemistry of the Murchison Domain of the Yilgarn Craton: Evidence for reworking of Eoarchean crust during Meso-Neoarchean plume-driven magmatism: Lithos, v. 148, no. Supplement C, p. 112-127.

Jackson, S. E., Pearson, N. J., Griffin, W. L., and Belousova, E. A., 2004, The application of laser ablation-inductively coupled plasma-mass spectrometry to in situ U–Pb zircon geochronology: Chemical Geology, v. 211, no. 1–2, p. 47-69.

Jahn, I., 2018, In-situ zircon geochronological and geochemical insights to the evolution of the Capricorn Orogen: Curtin University.

Johnson, S. P., 2013, The birth of supercontinents and the Proterozoic assembly of Western Australia, Geological Survey of Western Australia, 78 p.:

Johnson, S. P., Korhonen, F. J., Kirkland, C. L., Cliff, J. B., Belousova, E. A., and Sheppard, S., 2017, An isotopic perspective on growth and differentiation of Proterozoic orogenic crust: From subduction magmatism to cratonization: Lithos, v. 268–271, p. 76-86.

Johnson, S. P., Sheppard, S., Rasmussen, B., Wingate, M. T. D., Kirkland, C. L., Muhling, J. R., Fletcher, I. R., and Belousova, E. A., 2011a, Two collisions, two sutures: Punctuated pre-1950 Ma assembly of the West Australian Craton during the Ophthalmian and Glenburgh Orogenies: Precambrian Research, v. 189, no. 3–4, p. 239-262.

Johnson, S. P., Sheppard, S., Wingate, M. T. D., Kirkland, C. L., and Belousova, E., 2011b, Temporal and Hafnium Isotopic Evolution of the Glenburgh Terrane Basement: An Exotic Crustal Fragment in the Capricorn Orogen, Geological Survey of Western Australia, Report 110.

Johnson, S. P., Thorne, A. M., Tyler, I. M., Korsch, R. J., Kennett, B. L. N., Cutten, H. N., Goodwin, J., Blay, O., Blewett, R. S., Joly, A., Dentith, M. C., Aitken, A. R. A., Holzschuh, J., Salmon, M., Reading, A., Heinson, G., Boren, G., Ross, J., Costelloe, R. D., and Fomin, T., 2013, Crustal architecture of the Capricorn Orogen, Western Australia and associated metallogeny: Australian Journal of Earth Sciences, v. 60, no. 6-7, p. 681-705.

Jones, J. A., Pirajno, F., Hocking, R. H., and Grey, K., 2000, Revised statigraphy for the Earaheedy Group: implications for the tectonic evolution and mineral potential of the Earaheedy Basin.

Kemp, A. I. S., Hawkesworth, C. J., Foster, G. L., Paterson, B. A., Woodhead, J. D., Hergt, J. M., Gray, C. M., and Whitehouse, M. J., 2007, Magmatic and Crustal Differentiation History of Granitic Rocks from Hf-O Isotopes in Zircon: Science, v. 315, no. 5814, p. 980-983.

Kemp, A. I. S., Hawkesworth, C. J., Paterson, B. A., and Kinny, P. D., 2006, Episodic growth of the Gondwana supercontinent from hafnium and oxygen isotopes in zircon: Nature, v. 439, no. 7076, p. 580-583.

Kinny, P. D., Williams, I. S., Froude, D. O., Ireland, T. R., and Compston, W., 1988, Early archaean zircon ages from orthogneisses and anorthosites at Mount Narryer, Western Australia: Precambrian Research, v. 38, no. 4, p. 325-341.

Kirkland, C. L., Smithies, R. H., and Spaggiari, C. V., 2015, Foreign contemporaries – Unravelling disparate isotopic signatures from Mesoproterozoic Central and Western Australia: Precambrian Research, v. 265, p. 218-231.

Kirkland, C. L., Smithies, R. H., Woodhouse, A. J., Howard, H. M., Wingate, M. T. D., Belousova, E. A., Cliff, J. B., Murphy, R. C., and Spaggiari, C. V., 2013, Constraints and deception in the isotopic record; the crustal evolution of the west Musgrave Province, central Australia: Gondwana Research, v. 23, no. 2, p. 759-781.

Kita, N. T., Ushikubo, T., Fu, B., and Valley, J. W., 2009, High precision SIMS oxygen isotope analysis and the effect of sample topography: Chemical Geology, v. 264, no. 1–4, p. 43-57.

Klein, E. M., 2003, Geochemistry of the igneous oceanic crust, *in* Rudnick, R. L., ed., The crust, Volume Treatise on Geochemistry, v. 3: Oxford, Elsevier-Pergamon, p. 433– 464.

Korhonen, F. J., and Johnson, S. P., 2015, The role of radiogenic heat in prolonged intraplate reworking: The Capricorn Orogen explained?: Earth and Planetary Science Letters, v. 428, p. 22-32.

Kositcin, N., Brown, S. J. A., Barley, M. E., Krapež, B., Cassidy, K. F., and Champion, D. C., 2008, SHRIMP U-Pb zircon age constraints on the Late Archaean tectonostratigraphic architecture of the Eastern Goldfields Superterrane, Yilgarn Craton, Western Australia: Precambrian Research, v. 161, no. 1, p. 5-33.

Krapez, B., 1999, Stratigraphic record of an Atlantic-type global tectonic cycle in the Palaeoproterozoic Ashburton Province of Western Australia: Australian Journal of Earth Sciences, v. 46, no. 1, p. 71-87.

Krapez, B., and Martin, D. M., 1999, Sequence stratigraphy of the Palaeoproterozoic Nabberu Province of Western Australia: Australian Journal of Earth Sciences, v. 46, no. 1, p. 89-103.

Krapež, B., Müller, S. G., and Bekker, A., 2015, Stratigraphy of the Late Palaeoproterozoic (~2.03 Ga) Wooly Dolomite, Ashburton Province, Western Australia: A carbonate platform developed in a failed rift basin: Precambrian Research, v. 271, p. 1-19.

Krapež, B., Müller, S. G., Fletcher, I. R., and Rasmussen, B., 2017, A tale of two basins? Stratigraphy and detrital zircon provenance of the Palaeoproterozoic Turee Creek and Horseshoe basins of Western Australia: Precambrian Research, v. 294, p. 67-90.

Ksienzyk, A. K., Jacobs, J., Boger, S. D., Košler, J., Sircombe, K. N., and Whitehouse, M. J., 2012, U–Pb ages of metamorphic monazite and detrital zircon from the Northampton Complex: evidence of two orogenic cycles in Western Australia: Precambrian Research, v. 198–199, p. 37-50.

Kylander-Clark, A. R. C., Hacker, B. R., and Cottle, J. M., 2013, Laser-ablation split-stream ICP petrochronology: Chemical Geology, v. 345, no. Supplement C, p. 99-112.

Li, X.-H., Long, W.-G., Li, Q.-L., Liu, Y., Zheng, Y.-F., Yang, Y.-H., Chamberlain, K. R., Wan, D.-F., Guo, C.-H., Wang, X.-C., and Tao, H., 2010, Penglai Zircon Megacrysts: A Potential New Working Reference Material for Microbeam Determination of Hf–O Isotopes and U–Pb Age: Geostandards and Geoanalytical Research, v. 34, no. 2, p. 117-134.

Liu, F., Xu, Z., Juhn G., L., Ikuo, K., Hideki, M., Shigenori, M., and Yang, J., 2002, Ultrahigh-pressure mineral inclusions in zircons from gneissic core samples of the Chinese Continental Scientific Drilling Site in eastern China: European Journal of Mineralogy, v. 14, no. 3, p. 499-512.

Lu, Y.-J., Loucks, R. R., Fiorentini, M., McCuaig, C., Evans, N. J., Yang, Z.-M., Hou, Z.-Q., Kirkland, C. L., Parra-Avila, L. A., and Kobussen, A., 2016, Zircon compositions as a pathfinder for porphyry Cu ± Mo ± Au deposits, *in* Richards, J. P., ed., Tectonics and Metallogeny of the Tethyan Orogenic Belt, Society of Economic Geologists Special Publication No. 19, p. 329-347.

Ludwig, K. R., 2012, User's Manual for Isoplot/Ex, v.3.75, A Geochronological Toolkit for Microsoft Excel, Berkeley Geochronological Center Special Publications, 5.

Martin, D. M., 1998, Lithostratigraphy and structure of the Palaeoproterozoic lower Padbury group, Milgun 1:100,000 sheet, Western Australia.

Martin, D. M., and Morris, P. A., 2010, Tectonic setting and regional implications of ca 2.2 Ga mafic magmatism in the southern Hamersley Province, Western Australia: Australian Journal of Earth Sciences, v. 57, no. 7, p. 911-931.

Martin, D. M., Sircombe, K. N., Thorne, A. M., Cawood, P. A., and Nemchin, A. A., 2008, Provenance history of the Bangemall Supergroup and implications for the Mesoproterozoic paleogeography of the West Australian Craton: Precambrian Research, v. 166, no. 1–4, p. 93-110.

Martin, D. M., and Thorne, A. M., 2004, Tectonic setting and basin evolution of the Bangemall Supergroup in the northwestern Capricorn Orogen: Precambrian Research, v. 128, no. 3–4, p. 385-409.

Mason, C. C., Fildani, A., Gerber, T., Blum, M. D., Clark, J. D., and Dykstra, M., 2017, Climatic and anthropogenic influences on sediment mixing in the Mississippi source- to-sink system using detrital zircons: Late Pleistocene to recent: Earth and Planetary Science Letters, v. 466, p. 70-79.

Matonia, K. J., 2009, U-Pb and Hf analysis of detrital zircons: Implications for provenance of the Earaheedy Basin, Capricorn Orogen: Geological Survey of Western Australia, Record 2009/19.

Miller, C. F., McDowell, S. M., and Mapes, R. W., 2003, Hot and cold granites? Implications of zircon saturation temperatures and preservation of inheritance: Geology, v. 31, no. 6, p. 529-532.

Mole, D. R., Fiorentini, M. L., Cassidy, K. F., Kirkland, C. L., Thebaud, N., McCuaig, T. C., Doublier, M. P., Duuring, P., Romano, S. S., Maas, R., Belousova, E. A., Barnes, S. J., and Miller, J., 2013, Crustal evolution, intra-cratonic architecture and the metallogeny of an Archaean craton: Geological Society, London, Special Publications, v. 393.

Mole, D. R., Fiorentini, M. L., Thebaud, N., McCuaig, T. C., Cassidy, K. F., Kirkland, C. L., Wingate, M. T. D., Romano, S. S., Doublier, M. P., and Belousova, E. A., 2012, Spatio-temporal constraints on lithospheric development in the southwest–central Yilgarn Craton, Western Australia: Australian Journal of Earth Sciences, v. 59, no. 5, p. 625-656.

Morel, M. L. A., Nebel, O., Nebel-Jacobsen, Y. J., Miller, J. S., and Vroon, P. Z., 2008, Hafnium isotope characterization of the GJ-1 zircon reference material by solution and laser-ablation MC-ICPMS: Chemical Geology, v. 255, no. 1, p. 231-235.

Myers, J., S., 1993, Precambrian History of the West Australian Craton and Adjacent Orogens: Annual Review of Earth and Planetary Sciences, v. 21, no. 1, p. 453-485.

Myers, J. S., 1990, Precambrian tectonic evolution of part of Gondwana, southwestern Australia: Geology, v. 18, no. 6, p. 537-540.

Myers, J. S., 1995, The generation and assembly of an Archaean supercontinent: evidence from the Yilgarn craton, Western Australia: Geological Society, London, Special Publications, v. 95, no. 1, p. 143-154.

Myers, J. S., Shaw, R. D., and Tyler, I. M., 1996, Tectonic evolution of Proterozoic Australia: Tectonics, v. 15, no. 6, p. 1431-1446.

Nasdala, L., Zhang, M., Kempe, U., Panczer, G., Gaft, M., Andrut, M., and Plötze, M., 2003, Spectroscopic methods applied to zircon: Reviews in Mineralogy and Geochemistry, v. 53, no. 1, p. 427-467.

Nelson, D. R., 1996, Compilation of SHRIMP U-Pb zircon geochronology data, 1995, Western Australia Geological Survey, Record 1996/5.

Nelson, D. R., 1997, Evolution of the Archaean granite-greenstone terranes of the Eastern Goldfields, Western Australia: SHRIMP U-Pb zircon constraints: Precambrian Research, v. 83, no. 1, p. 57-81.

Nelson, D. R., 1998, Compilation of SHRIMP U-Pb zircon geochronology data, 1997.

Nutman, A. P., Bennett, V. C., Kinny, P. D., and Price, R., 1993, Large-scale crustal structure of the Northwestern Yilgarn Craton, western Australia: Evidence from Nd isotopic data and zircon geochronology: Tectonics, v. 12, no. 4, p. 971-981.

Nutman, A. P., Kinny, P. D., Compston, W., and Williams, I. S., 1991, SHRIMP U-Pb zircon geochronology of the Narryer Gneiss Complex, Western Australia: Precambrian Research, v. 52, no. 3, p. 275-300.

O'Sullivan, G. J., Chew, D. M., and Samson, S. D., 2016, Detecting magma-poor orogens in the detrital record: Geology.

Occhipinti, S., Hocking, R., Lindsay, M., Aitken, A., Copp, I., Jones, J., Sheppard, S., Pirajno, F., and Metelka, V., 2017, Paleoproterozoic basin development on the northern Yilgarn Craton, Western Australia: Precambrian Research, v. 300, p. 121- 140.

Occhipinti, S. A., Grey, K., Pirajno, F., Adamides, N. G., Bagas, L., Dawes, P., and Le Blanc Smith, G., 1997, Stratigraphic revision of Palaeoproterozoic rocks of the Yerrida, Bryah and Padbury Basins (former Glengarry Basin), Geological Survey of Western Australia Record 1997/3.

Occhipinti, S. A., and Reddy, S. M., 2009, Neoproterozoic reworking of the Palaeoproterozoic Capricorn Orogen of Western Australia and implications for the amalgamation of Rodinia, Geological Society Special Publication, Volume 327, p. 445-456.

Occhipinti, S. A., Sheppard, S., Nelson, D. R., Myers, J. S., and Tyler, I. M., 1998, Syntectonic granite in the southern margin of the Palaeoproterozoic Capricorn Orogen, Western Australia: Australian Journal of Earth Sciences, v. 45, no. 4, p. 509- 512.

Occhipinti, S. A., Sheppard, S., Passchier, C., Tyler, I. M., and Nelson, D. R., 2004, Palaeoproterozoic crustal accretion and collision in the southern Capricorn Orogen: the Glenburgh Orogeny: Precambrian Research, v. 128, no. 3, p. 237-255.

Paton, C., Hellstrom, J., Paul, B., Woodhead, J., and Hergt, J., 2011, Iolite: Freeware for the visualisation and processing of mass spectrometric data: Journal of Analytical Atomic Spectrometry, v. 26, no. 12, p. 2508-2518.

Paton, C., Woodhead, J. D., Hellstrom, J. C., Hergt, J. M., Greig, A., and Maas, R., 2010, Improved laser ablation U-Pb zircon geochronology through robust downhole fractionation correction: Geochemistry, Geophysics, Geosystems, v. 11, no. 3.

Pawley, M. J., Wingate, M. T. D., Kirkland, C. L., Wyche, S., Hall, C. E., Romano, S. S., and Doublier, M. P., 2012, Adding pieces to the puzzle: episodic crustal growth and a new terrane in the northeast Yilgarn Craton, Western Australia: Australian Journal of Earth Sciences, v. 59, no. 5, p. 603-623.

Pearce, J. A., 2008, Geochemical fingerprinting of oceanic basalts with applications to ophiolite classification and the search for Archean oceanic crust: Lithos, v. 100, no. 1, p. 14-48.

Piechocka, A. M., Gregory, C. J., Zi, J.-W., Sheppard, S., Wingate, M. T. D., and Rasmussen, B., 2017, Monazite trumps zircon: applying SHRIMP U–Pb geochronology to systematically evaluate emplacement ages of leucocratic, low-temperature granites in a complex Precambrian orogen: Contributions to Mineralogy and Petrology, v. 172, no. 8, p. 63.

Pirajno, F., 2004a, Metallogeny in the Capricorn Orogen, Western Australia, the result of multiple ore-forming processes: Precambrian Research, v. 128, no. 3-4, p. 411-439.

Pirajno, F., 2004b, Oceanic plateau accretion onto the northwestern margin of the Yilgarn Craton, Western Australia: implications for a mantle plume event at ca. 2.0 Ga: Journal of Geodynamics, v. 37, no. 2, p. 205-231.

Pirajno, F., Hocking, R. M., Reddy, S. M., and Jones, A. J., 2009, A review of the geology and geodynamic evolution of the Palaeoproterozoic Earaheedy Basin, Western Australia: Earth-Science Reviews, v. 94, no. 1, p. 39-77.

Pirajno, F., Jones, J. A., Hocking, R. M., and Halilovic, J., 2004, Geology and tectonic evolution of Palaeoproterozoic basins of the eastern Capricorn Orogen, Western Australia: Precambrian Research, v. 128, no. 3–4, p. 315-342.

Pirajno, F., and Occhipinti, S. A., 2000, Three Palaeoproterozoic basins—Yerrida, Bryah and Padbury—Capricorn Orogen, Western Australia: Australian Journal of Earth Sciences, v. 47, no. 4, p. 675-688.

Pirajno, F., Occhipinti, S. A., and Swager, C. P., 1998, Geology and tectonic evolution of the Palaeoproterozoic Bryah, Padbury and Yerrida Basins (formerly Glengarry Basin), Western Australia: implications for the history of the south-central Capricorn Orogen: Precambrian Research, v. 90, no. 3, p. 119-140.

Rasmussen, B., and Fletcher, I. R., 2002, Indirect dating of mafic intrusions by SHRIMP U– Pb analysis of monazite in contact metamorphosed shale: an example from the Palaeoproterozoic Capricorn Orogen, Western Australia: Earth and Planetary Science Letters, v. 197, no. 3, p. 287-299.

Roberts, N. M. W., and Spencer, C. J., 2015, The zircon archive of continent formation through time: Geological Society, London, Special Publications, v. 389, no. 1, p. 197- 225.

Rubatto, D., 2002, Zircon trace element geochemistry: partitioning with garnet and the link between U–Pb ages and metamorphism: Chemical Geology, v. 184, no. 1, p. 123-138.

Rubatto, D., and Hermann, J., 2007, Experimental zircon/melt and zircon/garnet trace element partitioning and implications for the geochronology of crustal rocks: Chemical Geology, v. 241, no. 1, p. 38-61.

Rudnick, R. L., and Gao, S., 2003, 3.01 - Composition of the Continental Crust A2 - Holland, Heinrich D, *in* Turekian, K. K., ed., Treatise on Geochemistry: Oxford, Pergamon, p. 1-64.

Sheppard, S., Bodorkos, S., Johnson, S. P., Wingate, M. T. D., and Kirkland, C. L., 2010, The Paleoproterozoic Capricorn Orogeny: Intracontinental Reworking Not Continent- Continent Collision, Geological Survey ofWestern Australia, Report 108.

Sheppard, S., Fletcher, I. R., Rasmussen, B., Zi, J.-W., Muhling, J. R., Occhipinti, S. A., Wingate, M. T. D., and Johnson, S. P., 2016a, A new Paleoproterozoic tectonic history of the eastern Capricorn Orogen, Western Australia, revealed by U–Pb zircon dating of micro-tuffs: Precambrian Research, v. 286, p. 1-19.

Sheppard, S., Krapež, B., Zi, J. W., Rasmussen, B., and Fletcher, I., 2016b, The 1320 Ma intracontinental Wongawobbin Basin, Pilbara, Western Australia: A far-field response to Albany–Fraser–Musgrave tectonics: Precambrian Research, v. 285, p. 58-79.

Sheppard, S., Occhipinti, S. A., and Nelson, D. R., 2005, Intracontinental reworking in the Capricorn Orogen, Western Australia: The 1680-1620 Ma Mangaroon Orogeny: Australian Journal of Earth Sciences, v. 52, no. 3, p. 443-460.

Sheppard, S., Occhipinti, S. A., and Tyler, I. M., 2003, The relationship between tectonism and composition of granitoid magmas, Yarlarweelor Gneiss Complex, Western Australia: Lithos, v. 66, no. 1-2, p. 133-154.

Sheppard, S., Occhipinti, S. A., and Tyler, I. M., 2004, A 2005-1970 Ma Andean-type batholith in the southern Gascoyne Complex, Western Australia: Precambrian Research, v. 128, no. 3-4, p. 257-277.

Sheppard, S., Rasmussen, B., Muhling, J. R., Farrell, T. R., and Fletcher, I. R., 2007, Grenvillian-aged orogenesis in the Palaeoproterozoic Gascoyne complex, Western Australia: 1030-950Ma reworking of the Proterozoic Capricorn Orogen: Journal of Metamorphic Geology, v. 25, no. 4, p. 477-494.

Sláma, J., Košler, J., Condon, D. J., Crowley, J. L., Gerdes, A., Hanchar, J. M., Horstwood, S. A., Morris, G. A., Nasdala, L., Norberg, N., Schaltegger, U., Schoene, B., Tubrett, M. N., and Whitehouse, M. J., 2008, Plešovice zircon — A new natural reference material for U–Pb and Hf isotopic microanalysis: Chemical Geology, v. 249, no. 1–2, p. 1-35.

Spaggiari, C. V., Kirkland, C. L., Smithies, R. H., Wingate, M. T. D., and Belousova, E. A., 2015, Transformation of an Archean craton margin during Proterozoic basin formation and magmatism: The Albany–Fraser Orogen, Western Australia: Precambrian Research, v. 266, p. 440-466.

Spaggiari, C. V., Wartho, J. A., and Wilde, S. A., 2008, Proterozoic deformation in the northwest of the Archean Yilgarn Craton, Western Australia: Precambrian Research, v. 162, no. 3-4, p. 354-384.

Spencer, C. J., Cawood, P. A., Hawkesworth, C. J., Raub, T. D., Prave, A. R., and Roberts, M. W., 2014, Proterozoic onset of crustal reworking and collisional tectonics: Reappraisal of the zircon oxygen isotope record: Geology, v. 42, no. 5, p.451-454.

Spencer, C. J., Kirkland, C. L., and Taylor, R. J. M., 2016, Strategies towards statistically robust interpretations of in situ U–Pb zircon geochronology: Geoscience Frontiers, v. 7, no. 4, p. 581-589.

Stern, R. A., 2001, A new isotopic and trace-element standard for the ion microprobe: preliminary thermal ionization mass spectrometry (TIMS) U-Pb and electron- microprobe data, Ressources naturelles Canada.

Stern, R. A., Bodorkos, S., Kamo, S. L., Hickman, A. H., and Corfu, F., 2009, Measurement of SIMS Instrumental Mass Fractionation of Pb Isotopes During Zircon Dating: Geostandards and Geoanalytical Research, v. 33, no. 2, p. 145-168.

Sun, S.-s., and McDonough, W. F., 1989, Chemical and isotopic systematics of oceanic basalts: implications for mantle composition and processes: Geological Society, London, Special Publications, v. 42, no. 1, p. 313-345.

Thorne, A. M., and Seymour, D. B., 1991, Geology of the Ashburton Basin, Western Australia, Perth, Geological Survey of Western Australia Bulletin 139.

Tyler, I. M., 1991, The geology of the Sylvania Inlier and the southeast Hammersley Basin, Geological Survey of Western Australia, Bulletin 138.

Tyler, I. M., Fletcher, I. R., de Laeter, J. R., Williams, I. R., and Libby, W. G., 1992, Isotope and rare earth element evidence for a late archaean terrane boundary in the southeastern pilbara craton, western australia: Precambrian Research, v. 54, no. 2, p. 211-229.

Tyler, I. M., and Thorne, A. M., 1990, The northern margin of the Capricorn Orogen, Western Australia—an example of an Early Proterozoic collision zone: Journal of Structural Geology, v. 12, no. 5, p. 685-701.

Van Kranendonk, M. J., Hugh Smithies, R., Hickman, A. H., and Champion, D. C., 2007, Review: secular tectonic evolution of Archean continental crust: interplay between horizontal and vertical processes in the formation of the Pilbara Craton, Australia: Terra Nova, v. 19, no. 1, p. 1-38.

Van Kranendonk, M. J., Hugh Smithies, R., Hickman, A. H., Wingate, M. T. D., and Bodorkos, S., 2010, Evidence for Mesoarchean (~3.2 Ga) rifting of the Pilbara Craton: The missing link in an early Precambrian Wilson cycle: Precambrian Research, v. 177, no. 1–2, p. 145-161.

Vermeesch, P., Resentini, A., and Garzanti, E., 2016, An R package for statistical provenance analysis: Sedimentary Geology, v. 336, no. Supplement C, p. 14-25.

Vielreicher, N., Groves, D., McNaughton, N., and Fletcher, I., 2015, The timing of gold mineralization across the eastern Yilgarn craton using U–Pb geochronology of hydrothermal phosphate minerals: Mineralium Deposita, v. 50, no. 4, p. 391-428.

Vielreicher, N. M., and McNaughton, N. J., 2002, SHRIMP U-Pb geochronology of magmatism and thermal events in the Archaean Marymia Inlier, central Western Australia: International Journal of Earth Sciences, v. 91, no. 3, p. 406-432.

Vielreicher, N. M., Ridley, J. R., and Groves, D. I., 2002, Marymia: An Archean, amphibolite facies-hosted, orogenic lode-gold deposit overprinted by Palaeoproterozoic orogenesis and base metal mineralisation, Western Australia: Mineralium Deposita, v. 37, no. 8, p. 737-764.

Vos, I. M. A., Bierlein, F. P., Heithersay, P. S., and Lister, G. S., 2005, Geodynamic controls on giant metallogenic provinces: Insights from gold provinces in southeast Australia, *in* Mao, J., and Bierlein, F. P., eds., Mineral Deposit Research: Meeting the Global Challenge: Proceedings of the Eighth Biennial SGA Meeting Beijing, China, 18–21 August 2005: Berlin, Heidelberg, Springer Berlin Heidelberg, p. 61-64.

Wendt, I., and Carl, C., 1991, The statistical distribution of the mean squared weighted deviation: Chemical Geology: Isotope Geoscience section, v. 86, no. 4, p. 275-285.

Wiedenbeck, M., AllÉ, P., Corfu, F., Griffin, W. L., Meier, M., Oberli, F., Quadt, A. V., Roddick, J. C., and Spiegel, W., 1995, Three natural zircon standards for U-Th-Pb, Lu-Hf, trace element and REE analyses: Geostandards Newsletter, v. 19, no. 1, p. 1- 23.

Wilde, S. A., Middleton, M. F., and Evans, B. J., 1996, Terrane accretion in the southwestern Yilgarn Craton: evidence from a deep seismic crustal profile: Precambrian Research, v. 78, no. 1, p. 179-196.

William, I. R., and Myers, J. S., 1987, Archaean geology of the Mount Narryer region, Western Australia, Western Australian Geological Survey Report 22.

Wyche, S., Kirkland, C. L., Riganti, A., Pawley, M. J., Belousova, E., and Wingate, M. T. D., 2012, Isotopic constraints on stratigraphy in the central and eastern Yilgarn Craton, Western Australia: Australian Journal of Earth Sciences, v. 59, no. 5, p. 657-670.

Xu, J., Snedden, J. W., Stockli, D. F., Fulthorpe, C. S., and Galloway, W. E., 2016, Early Miocene continental-scale sediment supply to the Gulf of Mexico Basin based on detrital zircon analysis: Geological Society of America Bulletin.

3. Theme 5B: Tracing Sulfur Pathways Through the Lithosphere

Crystal LaFlamme, Stefano Caruso, Vikraman Selvaraja, Marco Fiorentini

3.1 Introduction and Project Aims

Sulfur can act as a volatile component of many geological reservoirs on Earth. Consequently, the complex sulfur cycle plays a critical role in a variety of fundamental Earth processes such as regulating the global climate, the living cell, and ore deposit formation. In ore deposit formation, sulfur plays a key role in the formation of numerous world-class mineral systems, including gold, nickel, copper and the platinum group elements. Sulfur is a critical ligand that complexes, transports and concentrates gold in hydrothermal fluids (Loucks and Mavrogenes 1999). Similarly, base metals such as nickel, cobalt, copper, zinc, arsenic and lead, due to their chalcophile nature in sulfur-saturated magmatic and hydrothermal systems, may be concentrated in sulfides. However, the extremely important cycle of sulfur, reflected in the lithospheric-scale transport mechanism of this element among different geochemical reservoirs, is incompletely understood.

This knowledge gap is addressed by examining the indelible nature of the mass-independent fractionation of sulfur (MIF-S), which was imparted to different sulfur-bearing reservoirs prior to 2.4 billion years ago, in the Archean eon. This fractionation process led to the unique preservation of this anomalous sulfur isotope signature (as $\Delta^{33}S$) in the Archean sedimentary rock record (Farquhar et al. 2000). Subsequently, as this signature was recycled through different geological processes operating at various scales in space and time, we are now in the privileged position to be able to use it as an indelible tracer and marker of different geological processes. So, just as radio-isotope dyes are used in the medical sciences to map the intricate pathways of the inner human body, we have used the MIF-S signature to illuminate the pathways of sulfur.

Here we seek to understand cycling of the volatile sulfur through the lithosphere. To do so, we approach this research through the following questions.

- How does sulfur cycle through the lithosphere and can we trace its pathways?
- What is the background concentration of sulfur?
- How is sulfur recycled to mineral systems?
- Can we use the isotopic signature of sulfur-bearing minerals as vectors to metals?

Importantly, these questions are addressed at multiple spatial and temporal scales in different tectonic settings. Further, this project necessitated a significant amount of method development in the collection and interpretation of multiple sulfur isotopes as applied to tracing the pathway of sulfur through the lithosphere and its application to mineral deposits. Further, we compiled 5500 published multiple sulfur isotope analyses from sediments through time and around the world (Figure 3.1). This database was used to develop a fundamental understanding of the primary MIF-S record. The database is maintained here: http://www.cet.edu.au/research-projects/special-projects/gssid-global-sedimentary-sulfur-isotope-database.

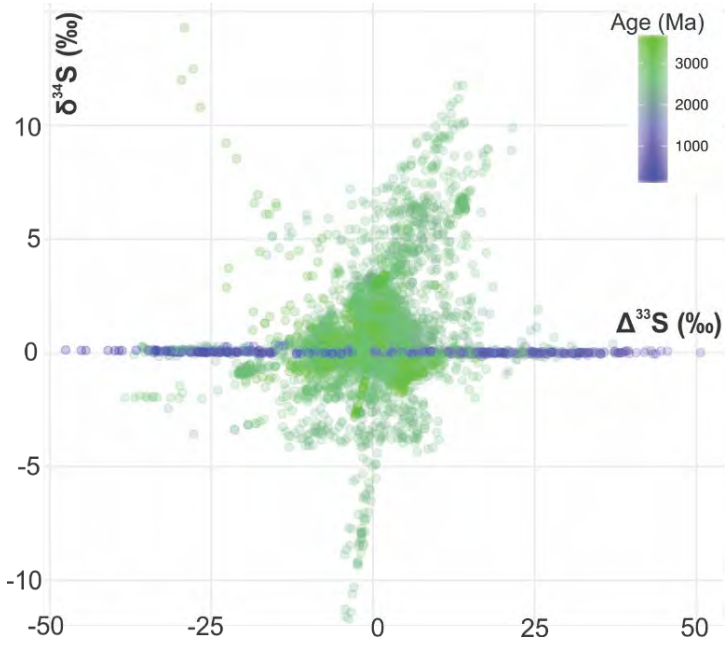

Figure 3.1. Multiple sulfur isotope signature of the sedimentary rock record through time to demonstrate the presence of MIF-S (as Δ33S) as unique to the Archean record.

We split this report into two parts. In Part 1, we focus on the nature of the geological processes that recylce sulfur in the Archean and discuss the background sulfur isotope signature of the Yilgarn Craton, focussing on the multi-scale remobilisation and recycling of sulfur to orogenic gold, VMS and Ni-komatiite deposits. These processes have fundamental bearing on our understanding of how volatiles move through the lithosphere and what that means for processes (including sulfur degassing and plate tectonics) that are not only critical for focussing of metals into ore deposits but also life supporting elements like an atmosphere. In Part 2, we investigate multi-scale remobilisation of sulfur from the metal- and sulfur-endowed Archean Yilgarn craton to its Proterozoic margin – the Capricorn Orogen.

3.2 Background

The sulfur cycle is extremely sensitive to physico-chemical changes in the Earth's reservoirs, changes which are preserved by the sulfur isotope signature of sulfides throughout the rock record. As organic and inorganic sulfur molecules break to form new bonds, the isotopes of sulfur undergo mass dependent fractionation (MDF-S) during chemical exchange between different sulfur-bearing reservoirs through its planetary cycle. MDF-S, expressed as $\delta^{34}S$, has enabled understanding of the redox evolution of the oceans and atmosphere through the Precambrian (Kump et al. 2012 and references therein).

Prior to the Great Oxygenation Event at ca. 2.4 Ga, sulfur also underwent MIF-S in the atmosphere by photodissociation of SO_2 (Farquhar et al. 2000). These molecules were transported to the surface and preserved as MIF-S in the sedimentary rock record as sulfate and sulfide minerals (Farquhar and Wing 2003). The discovery of MIF-S in Archean supracrustal rocks has significantly improved our understanding of the early Earth's surface processes by, in particular, elucidating the link between the emergence of life and the development of an oxygenated atmosphere (Kaufman et al. 2007). MIF-S is quantified as $\Delta^{33}S$ or $\Delta^{36}S$ to represent a deviation from normal MDF-S. The distinct process is a highly effective tracer of a specific reservoir because it is chemically conservative and mostly indelible. Large $\Delta^{33}S$ (and $\Delta^{36}S$) dispersions were created prior to ca. 2.4 Ga (Figure 3.2). Once formed, these signatures were preserved during subsequent normal equilibrium and kinetic reactions.

However, small $\Delta^{33}S$ values can also be generated by MDF-S. With the improved ability to precisely measure ^{33}S and ^{36}S, the paleomicrobiology community demonstrated that kinetic reactions involving mostly organic compounds can impart small $\Delta^{33}S$ and $\Delta^{36}S$ values. This allowed for a greater understanding of interaction of biotic sulfur reactions through time (Johnston et al. 2007) and their importance in oxygenation of the hydrosphere.

The sulfur cycle is and has been, however, not only part of Earth's surface processes. In addition to tracking sulfur cycling in the surface environment, atmospheric MIF-S signatures can also be used to track sulfur sources and mobility between surface and subsurface reservoirs. The research program carried out within the framework of this MRIWA project focussed on ore deposits to better understand how sulfur is transported from the Earth's surficial reservoir into the subsurface, and recycled through the lithosphere. In fact, ore deposits, leaving aside their economic significance, are loci where mass and energy concentrative processes take place and are, therefore, the ideal natural laboratories to study the cycling of sulfur.

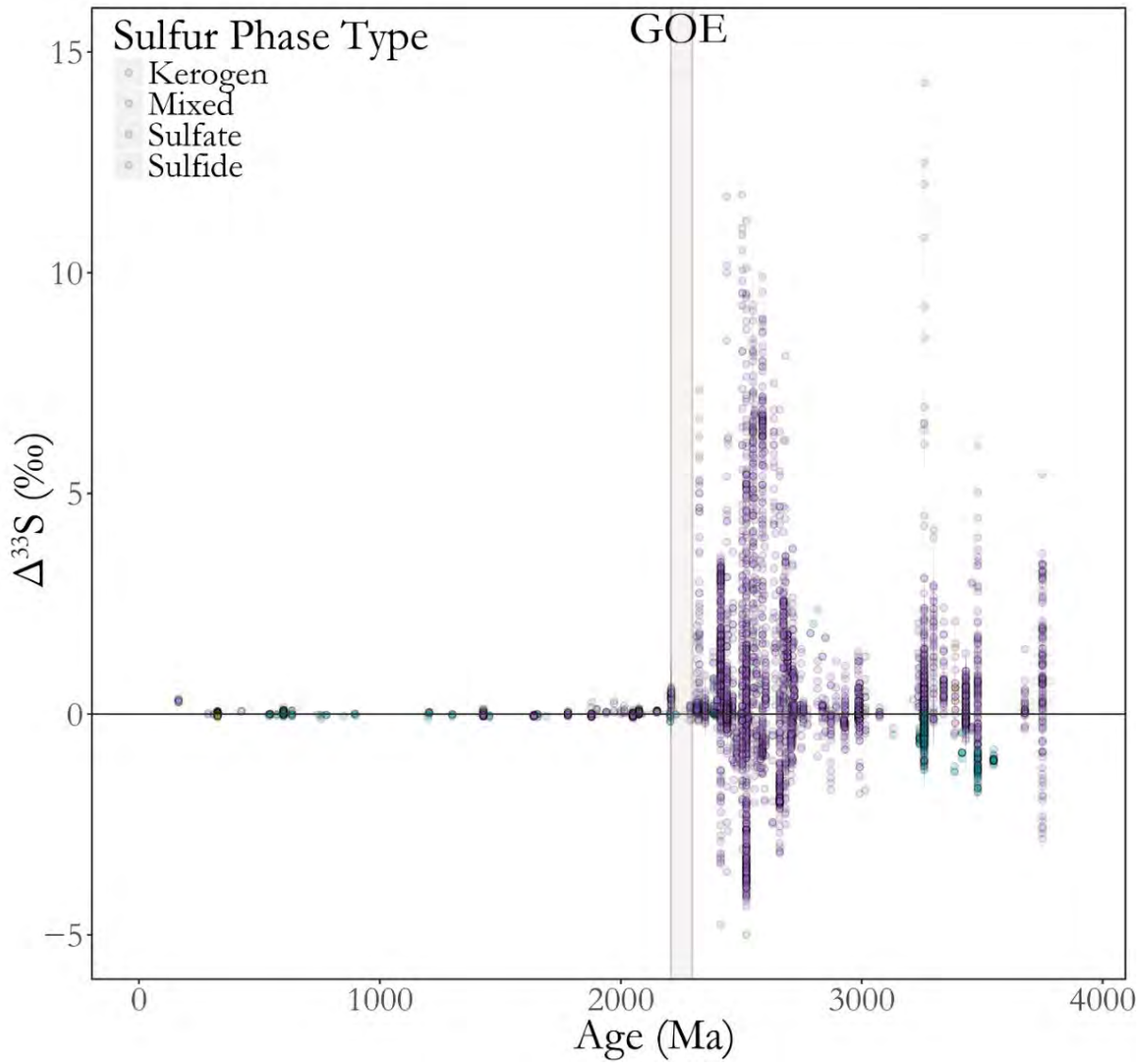

Figure 3.2. The evolution of the global sedimentary Δ33S record through time produced from the sulfur isotope through time database1. GOE – Great Oxygenation Event.

Specific mineral systems are the geological expression of distinct tectonic regimes (McCuaig et al. 2010); therefore, by understanding the source of sulfur in their formation, it is possible to infer geological processes that control sulfur exchange pathways in the surface and subsurface environments. By applying the study of MIF-S to ore deposits, it has been demonstrated that Precambrian mineral systems may source sulfur from Archean supracrustal reservoirs in magmatic ore deposits associated with komatiites (Bekker et al. 2009; Fiorentini et al. 2012) and hydrothermal systems associated with volcanic-hosted massive sulfides (Jamieson et al. 2006). These are near-surface processes. What is not understood well is how sulfur may track through the lithosphere and be recycled into deposits forming within the crust in orogenic settings (Agangi et al. 2016).

Although the genetic association between sulfur and metal enrichment is well established, it is generally difficult to fingerprint and spatially localise the sulfur and metal sources that play a role in ore genesis. In these systems the source of sulfur is commonly difficult to fingerprint using $\delta^{34}S$ (e.g., Hodkiewicz et al. 2009) for two reasons: different sulfur reservoirs can have the same $\delta^{34}S$ and, more importantly, fluids/magmas travel great distances and record changes in their thermochemistry that modify the isotopic composition of the fluid. Conversely, MIF-S cannot be modified, other than by dilution by mixing with non MIF-S-bearing sulfur reservoirs (e.g., Selvaraja et al. 2017a,b; LaFlamme et al. 2018a,b). Therefore, the ability to quickly and reliably map different sulfur reservoirs in terms of their isotopic signatures will impact on targeting criteria at the deposit, camp and regional scale, in both brownfield and greenfield settings.

3.3 Geological Background

3.3.1 Natural laboratory to study sulfur cycling and recycling

Our natural laboratory to trace volatile movement within and across tectonic boundaries is the Archean and Proterozoic terrains of Western Australia. The Proterozoic Capricorn Orogen developed between two volatile-rich and metal-endowed Archean crustal blocks: the Yilgarn and Pilbara cratons that formed during the amalgamation of cratons worldwide to form the 2.0–1.8 Ga supercontinent Nuna/Columbia (Cawood and Tyler, 2004; Evans and Mitchell, 2011).

The Yilgarn Craton is metal-rich and preserves terranes that were amalgamated in the Neoarchean. It is at the margins of these ancient terranes that Au and Ni endowment is especially rich (Mole et al. 2014). The Capricorn Orogen contains numerous mineral occurrences of various commodities; however, the orogenic belt is poorly exposed and the extent of its metal endowment is unknown. Further, the Capricorn Orogen preserves many lithological features that document various stages in its formation; it is dominantly composed of variably deformed and metamorphosed Paleoproterozoic to Neoproterozoic magmatic and supracrustal rocks with overlying sedimentary basins (Johnson et al. 2013). Whereas many Proterozoic orogens consist mainly of reworked Archean gneisses and younger plutonic suites (see Trans-Hudson Orogen of Canada, Limpopo belt of South Africa), the basement to the Capricorn Orogen is only exposed as fragments in the west. The southern margin of the orogen preserves Paleoproterozoic volcanosedimentary basins, arc plutonism and ophiolites.

In addition, the timespans of crust formation and geodynamism preserved in this area of Western Australia are prolonged. The Yilgarn Craton ranges in age from the Eoarchean to the Neoarchean. The Capricorn Orogen saw a billion years of intercontinental reworking, magmatism and sedimentation following ca. 2 Ga multi-stage collision between the Pilbara and Yilgarn Cratons that resulted in the amalgamation of the West Australian Craton (Occhipinti et al. 2004). This long time span saw a secular change in the type of and preservation of mineral occurrences, making this area a key locality for studying sulfur cycling. This next section describes in more detail the geology of the three sulfur reservoirs that dynamically interacted during the amalgamation of the West Australian Craton: the Pilbara Craton, Yilgarn Craton and Capricorn Orogen.

- **Pilbara Craton**

The Pilbara Craton is dominantly composed of granite-greenstone basement rocks older than ca. 2.77 Ga (Van Kronendonk et al. 2007). Within the Capricorn Orogen, the Pilbara Craton is exposed in several inliers, the Sylvania, Rocklea, Milli Milli and Wyloo Inliers, along the northern margin of the orogen. The craton is overlain by mafic volcanic, volcaniclastic and sedimentary rocks of the Fortescue and Hamersley Basins, which formed during protracted rifting between ca. 2.77 and 2.44 Ga. Rifting began with mafic and felsic volcanism and siliciclastic sedimentation and continued with the deposition of banded iron formation, shale and carbonate in a passive margin or back arc basin. The Neoarchean basins outboard from the Pilbara Craton are important to the formation of some of the localities studied here, but otherwise our discussion of the Pilbara Craton ends here.

- **Yilgarn Craton**

The Yilgarn Carton is an extensive region of Archean crust dominated by granite-greenstone belts (Cassidy et al. 2006). The craton has been subdivided into several tectonic units, including the Narryer, Youanmi, and Yamarna Terranes and the Eastern Goldfields Superterrane, many of which have margins that intersect the Capricorn Orogen. These units generally contain north-south-striking greenstone belts separated by granite and gneiss. Extensive tectonometamorphic reworking and magmatic intrusion occurred at the margins of these terranes prior to, and during, the 1.82–1.77 Ga Capricorn Orogeny. Ongoing work funded by the Geological Survey of Western Australia and MRIWA, through the work of PhD students Stefano Caruso and Eunjoo Choi, is currently integrating existing sulfur isotope data with new results from sulfide-bearing sedimentary units from greenstone belts as well as from granite batholiths and alkaline mafic and ultramafic units to image the multiple sulfur isotope architecture of the craton, thus implementing the existing framework put forward by Selvaraja et al. (2017; see below) as part of this MRIWA study.

- **Capricorn Orogen**

The geological packages of the Capricorn Orogen have been previously described in detail (Johnson et al. 2013) and are briefly detailed below and presented in Figure 3.3. The ~1000 km-long, ~500 km-wide belt underwent at least two collisional events known as the 2.22–2.15 Ga Ophthalmia Orogeny and the 2.01–1.95 Ga Glenburgh Orogeny in which the Glenburgh Terrane was accreted to the Pilbara and Yilgarn cratons, respectively (Occhipinti et al. 2004). The oldest crustal fragment in the Capricorn Orogen is the Neoarchean-Paleoproterozoic Glenburgh Terrane, which is composed of 2.55–2.43 Ga granitoid gneisses intruded by Proterozoic plutonic suites. The Glenburgh Terrane is also host to ca. 2.2 Ga metasedimentary rocks that were deposited in a foreland basin during accretion of the Pilbara and Glenburgh Terranes during the 2.22–2.15 Ga Ophthalmia Orogeny (Johnson et al. 2013). The Glenburgh Orogeny, on the southern margin of the composite Pilbara Craton–Glenburgh Terrane, resulted in the emplacement of arc-related granitic rocks of the 2.00–1.97 Ga Dalgaringa Supersuite (Occhipinti et al. 2004; Sheppard et al. 2004; Martin and Morris, 2010; Johnson et al. 2011).

Associated with, and following this tectonic event, siliciclastic and mafic volcano-sedimentary rocks were deposited in the Yerrida, Earaheedy, Bryah and Padbury basins to the east (Pirajno and Occhipinti, 2001). These basins formed between ca. 2.20 and 1.80 Ga, recording periods of sedimentation and volcanism associated with rifting, accretion, and passive margin tectonism. The 2.26–2.17 Ga Yerrida Basin is composed of siliciclastic, stromatolitic carbonate, and evaporitic rocks at the base which are derived from the Yilgarn Craton, and are overlain by ca. 1.76 Ga ferruginous clastic mafic volcanic rocks. The 2.02–1.85 Ga Earaheedy Basin is comprised of shallow-marine turbiditic sandstones, siltstone and carbonate rocks that have been deformed into an asymmetric east-plunging regional syncline. The 2.05–1.99 Ga Bryah Basin is comprised of mafic to ultramafic intrusive and volcaniclastic rocks that were formed, or deposited, in a rift environment. These units are overlain by high-energy, siliciclastic metasedimentary rocks of the 2.01–1.80 Ga Padbury

Basin that form rift-fill successions. At the top of the succession extensive banded iron formations and ferruginous sedimentary rocks are present that were deposited sometime between ca. 1.80 and 1.60 Ga.

The Capricorn Orogen is also host to felsic magmatic rocks of the 1.82–1.77 Ga Moorarie and 1.68–1.62 Ga Durlacher Supersuites, which were generated during intracratonic reworking events of the Capricorn and Mangaroon Orogenies, respectively (Evans et al. 2003; Johnson et al. 2013; Sheppard et al. 2005; 2010). The Capricorn Orogeny also resulted in deposition of siliciclastic sedimentary rocks into the Ashburton Basin, along the southern margin of the Pilbara Craton. Following the Mangaroon Orogeny, sedimentation took place in the 1.68–1.07 Ga Edmund and Collier Basins, which consist of 4–10 km of siliciclastic and carbonate rocks that were deposited under fluviatile to deep-marine conditions (Martin and Thorne, 2004). The Edmund Basin forms four major sequences of dominantly silisticlastic sedimentary rocks including siltstone, mudstone, sandstone, and conglomerate with minor carbonate rocks. The basin formed in an intracontinental extensional setting and was deposited between 1.68 and 1.45 Ga in a series of half grabens. The 1.17–1.07 Ga Collier Basin forms two major depositional sequences that are composed of shale, mudstone, siltstone, sandstone, and minor dolostone. Both these basins were intruded by numerous dolerite sills between 1.51–1.07 Ga. The youngest rocks in the region, which overlie the Capricorn Orogen, are a succession of mixed carbonate-clastic-evaporite rocks (Grey et al. 2005) that form part of the Neoproterozoic to Cambrian Officer Basin. Subsequently, the Capricorn Orogen experienced over a billion years of magmatism, intracontinental reworking and basin development (Johnson et al. 2013).

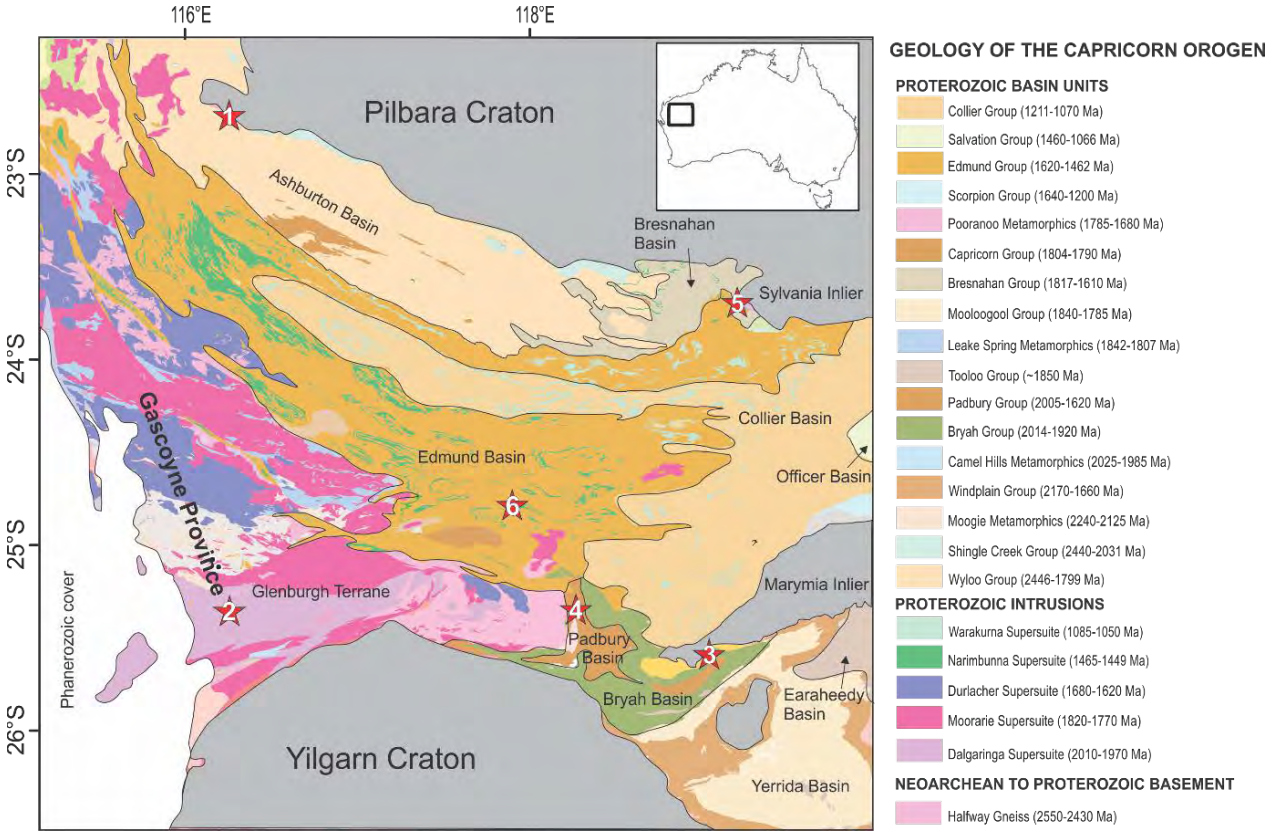

Figure 3.3. Geology of the Capricorn Orogen highlighting the mineral systems focused on in this report. 1 – Paulsens', 2 – Glenburgh, 3 – Degrussa, 4 – Padbury orogenic gold deposits, 5 – Prairie Downs, 6 – Abra.

3.3.2 Metallogenesis of the Study Area

- **Archean Yilgarn Craton**

The Yilgarn Craton is metal endowed and hosts a number of precious and base metal occurrences; it is anomalously endowed in gold and nickel world-class systems. These mineral occurrences are primarily associated with greenstone successions near ancient tectonic boundaries (i.e., Mole et al., 2014). Specific lithospheric blocks within the Yilgarn Craton seem to be more metal-rich than others, pointing to an early metallogenic fertility that is currently being investigated within the framework of the MRIWA-funded PhD project of Eunjoo Choi. Broadly, many orogenic gold deposits were analysed across the Yilgarn Craton as part of Selvaraja et al. (2017a) and LaFlamme et al. (2018b). Specifically, the deposits and camps that were investigated in detail as part of this study are the Wannaway and Black Swan komatiite-hosted nickel-sulfide deposits, the Nimbus Ag-Zn-Pb volcanogenic massive sulfide deposit, the Agnew gold camp and the Lady Bountiful orogenic gold deposit. These deposits are located on Figure 3.4.

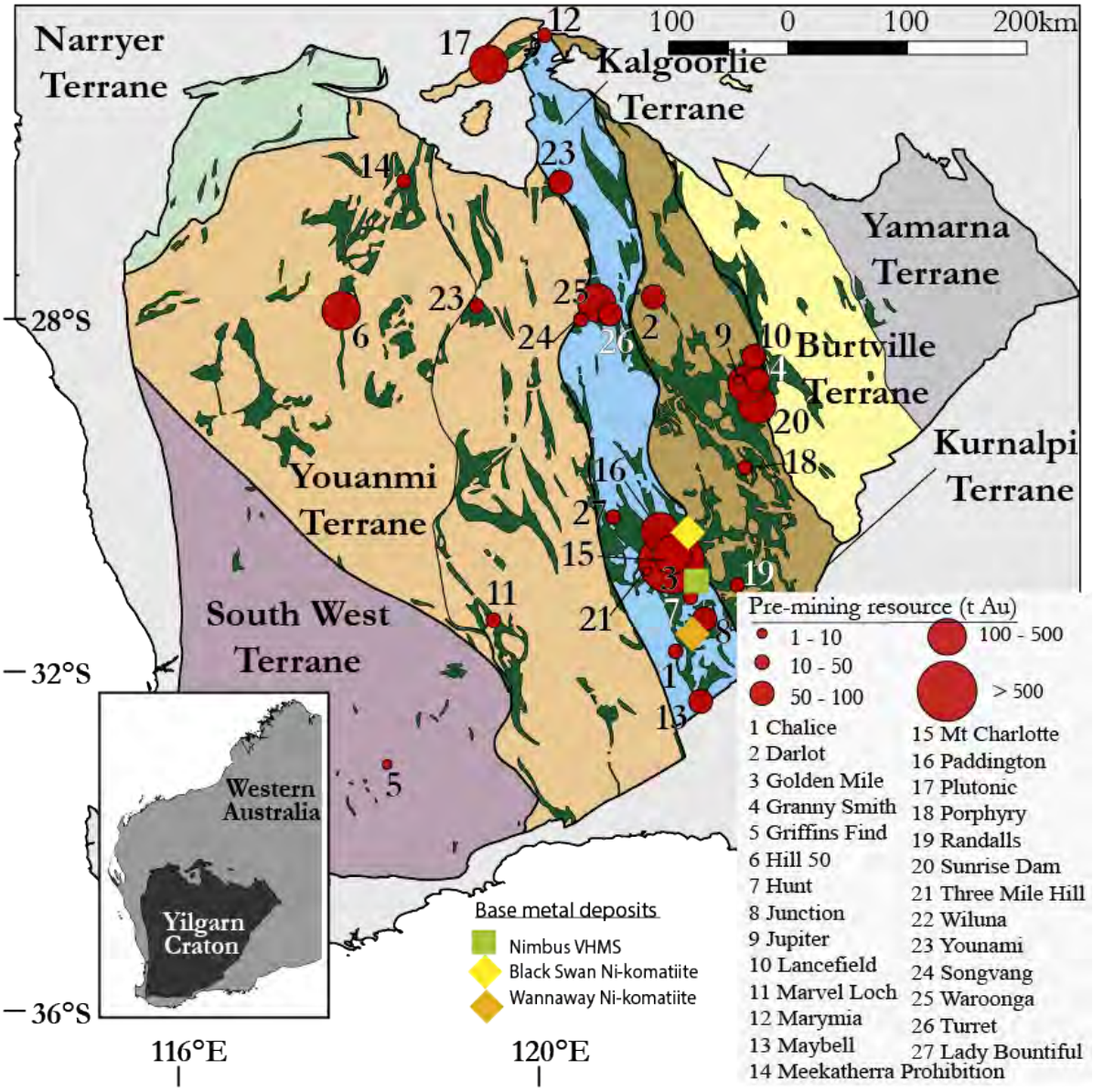

Figure 3.4. Locations of base and gold deposits studied in the Yilgarn Craton for multiple sulfur isotopes.

Wannaway komatiite-hosted nickel-sulfide deposit

The Wannaway nickel-sulfide deposit occurs in the Widgiemooltha Dome mining district, where a well preserved supracrustal sequence consists of three stratigraphically distinct ultramafic-rich zones where ore-bearing komatiite lava units alternate with sulfidic sediments and tholeiitic basalts. In spite of regional deformation and amphibolite facies metamorphism the sequence still preserves some of the original, magmatic textures and sulfide assemblages. Magmatic mineralisation at Wannaway displays features analogous to Kambalda-style Ni ore intersections, having basal massive sulfide accumulation grading to matrix and disseminated ore upward in the komatiite (Caruso et al., 2017; Moroni et al., 2017).

Black Swan komatiite-hosted nickel-sulfide deposit

The Black Swan Succession is a bimodal association of dacite and komatiite volcanic units forming part of the regional greenstone stratigraphy of the 2.7 Ga Eastern Goldfields Province. The komatiites of the sequence host a number of sulfide deposits displaying either massive (Type-I) or disseminated (Type-II) sulfide textures. The Black Swan Complex as a whole displays a concentric zonation from serpentinite cores to talc-carbonate margins, with an intermediate zone of serpentine-carbonate rocks (Barnes, 2004).

Nimbus Ag-Zn-Pb volcanogenic massive sulfide deposit

The Nimbus VHMS deposit is located in the Kurnalpi Terrane, approximately 10 km east of Kalgoorlie. It displays an unusually enriched Ag-Zn-Pb signature associated with low Cu and minor Au. The Nimbus resource of primary sulfide mineralization currently stands at 12.1 Mt at 52 g/t Ag, 0.9% Zn and 0.2 g/t Au (including measured, indicated and inferred resources; April 2015). Several lodes of high grade silver-zinc (1.22 Mt at 175 g/t Ag and 3.5% Zn) and anomalous gold (2.45 Mt at 0.8 g/t Au) mineralization have been identified (Hollis et al., 2017). The orebody consists of a series of stacked sulfide-bearing lenses hosted in a NW-trending and steeply-dipping bimodal felsic package of largely coherent volcanic rocks. The ore mineralogy typically consists of a pyrite-sphalerite assemblage associated with abundant galena, Ag-Sb sulfosalts. Hydrothermal alteration is pervasive showing a predominant quartz-sericite-carbonate assemblage in the felsic rocks, and a quartz-carbonate-chlorite assemblage in the basaltic rocks. These features, largely preserved after lower greenschist-facies metamorphism, suggest that the Nimbus deposit formed in shallow water from relatively low temperature hydrothermal fluids with epithermal characteristics (Hollis et al., 2017)

Agnew Gold Camp

The Agnew Gold Camp sits in the southwest corner of the Agnew–Wiluna belt in the Eastern Goldfields Superterrane in a district referred to as the Agnew-Mt White district (Duuring et al. 2012). The Agnew Gold Camp host numerous gold deposits including the New Holland–Genesis, the Waroonga, the Crusader, the Songvang and the Turret deposits. Recent field investigation has demonstrated that mineralisation in all four was controlled by the formation of the Lawlers Antiform during regional E-W contraction. Geochronological constraint for the systems interpreted in the context of structural and paragenetic relationships indicate mineralisation developed during two discrete episodes (at. 2.66 and 2.63 Ga) with contrasting fluid sources (Thébaud et al. 2018).

Lady Bountiful orogenic gold deposit

The Lady Bountiful deposit is in the northern section of the Mount Pleasant complex of the Eastern Goldfields Superterrane of the Yilgarn Craton. Gold mineralisation is hosted along quartz-veined fault zones that transect the late-tectonic Neoarchean granitoids (Cassidy and Bennett, 1993). Historically the deposit was mined as shallow open pits, and underground workings, but the workings now are largely abandoned. The mine produced 4.79 Mt at 1.75 g/t yielding 269 000 ounces of gold.

- **Proterozoic Capricorn Orogen**

The Capricorn Orogen is not well exposed and so the overarching theme to the Capricorn distal footprints project is to understand whether the orogenic belt is host to large mineral occurrences. Mineral occurrences that are known in the Capricorn Orogen are diverse and reflet the various tectonic environments that have evolved during the formation and evolution of the orogenic belt (Pirajno, 2004). Some of the larger occurrences are the focus of studies within this report. They include:

Paulsens' sediment-hosted gold deposit

Paulsens is a ~1 million ounce gold deposit (Bland et al. 2014) located at the southern edge of the Pilbara Craton, which is a major mineral province for iron ore but hosts very few known gold deposits. The deposit itself is hosted in a sequence of mafic volcanic and sedimentary rocks of the Hardey Formation in the Wyloo Dome, which preserves a complete stratigraphic succession from the Paleoarchean to the Proterozoic (Fig. 1; Thorne and Trendall 2001). Mineralisation is interpreted to have occurred at 2.4 Ga (Fielding et al. 2017). Mining began in this deposit in the 1930s with an estimated 742,000 ounces of gold extracted from 3.7 million tonnes of ore at an average grade of 6.3 g/t by 2014 (Bland et al. 2014).

Glenburgh orogenic gold deposit

The Glenburgh sulfide-bearing gold deposit, is hosted within <2.04 Ga metasedimentary rafts in the ~2.0 Ga Dalgaringa Supersuite, which intrudes the ~2.5 Ga Glenburgh Terrane (Sheppard et al. 2005) at the southernwestern edge of the Capricorn Orogen. The deposit formed between 2.04 Ga and 1.99 Ga (Roche, 2014), synchronous with subduction and arc magmatism. Although not being presently mined, a feasibility study demonstrates 21.1 Mt of ore at 1.5 g/t Au for 1.0 million ounces gold.

Degrussa Cu-Au VMS deposit

The DeGrussa VHMS deposit is located in the southeastern Capricorn Orogen and is hosted within the Narracoota Formation of the Bryah Basin. It is syngenetic to the surrounding stratigraphy, having formed at ~2.0 Ga (Hawke et al. 2015). The mineralisation is interpreted to be Besshi-type (Pirajno et al. 2016). Degrussa was discovered in 2009 and has produced 1.5 Mt per year since 2013.

Orogenic gold deposits of the Padbury Basin

Small orogenic, shear-hosted gold lodes occur in the volcano-sedimentary rocks of the Padbury Basin and the Peak Hill schist (a mylonitic tectonic unit). These lodes formed during the tectonic assembly of the Glenburgh Orogeny in which fluids were focused along shear zones. Mines are or have been developed at Peak Hill, Harmony, Fortnum, Labouchere, and Horseshoe (Pirajno, 2004). Fortnum deposit is known to contain 5.4 million tonnes of 1.95 g/t Au in reserve.

Prairie Downs Zn-Pb-Ag mineral system

The Prairie Downs Zn-Pb-Ag system is located as multiple occurrences along the Prairie Downs fault, a long-lived structure that juxtaposes the ca. 2.55 Ga Hamersley Basin outboard from the Sylvania Inlier of the Pilbara Craton against the <2.0 Ga Edmund Basin. The Prairie Downs system is a multi-sulfide mineral system that is structurally controlled as it is hosted in vein and breccia arrays within the fault zone. Mineralisation has been reported to be ca. 1.77 Ga (Davaadorj, 2015). The deposit was discovered in 1963 during 1:250000 scale mapping by the Geological Survey of Western Australia but has yet to be mined. According to the project evaluation report of Prairie Downs, compiled by Reynolds and Wilson (2012), the estimated resource at the Prairie Downs deposit is 2.98 Mt at 5.22% Zn, 1.59% Pb, and 15 g/t Ag, with minor Cu, Au, As, Sb anomalies near the deposit.

Abra stratabound Pb-Ag-Cu-Au deposit

Abra is one of the largest undeveloped Pb-Ag-Cu-Au deposits in the world. It is a blind deposit discovered in 1981 that is estimated to contain approximately 150 Mt of base metals. Abra is hosted in the Edmund Basin and is interpreted by Pirajno et al. (2016) to have been formed in a SEDEX environment that was then reworked. Mineralising hydrothermal events had mean temperatures of about 300°C, enveloping the deposits with a kaolinite-chlorite-siderite alteration halo (Lampinen et al., 2017 and references therein).

3.3.3 Understanding Sulfur Transfer Undercover

Western Australia is plagued by a thick overburden and/or thick weathering profile as highlighted by the Uncover project driven by Australian Academy of Sciences (AAS, 2012). The Capricorn orogenic belt of Western Australia formed during the Paleoproterozoic collision of the nickel- and gold-rich Yilgarn and iron- and base metal-rich Pilbara Archean cratons. The belt is flat, altered and poorly exposed, owing to a relatively inactive tectonic history since its formation. However, for this same reason, it is one of few preserved Paleoproterozoic orogenic belts worldwide. This belt requires advanced geochemical techniques to see through overburden and altered outcrop to unravel is tectonic history and mineral wealth. To better assess the mineral potential of the poorly exposed Capricorn orogen, and to better understand tectonic processes linked with ore deposits at cratonic margins in general, we utilise these sophisticated isotopic tracers paired with detailed mapping and geophysical interpretations.

With this in mind, we guided our research to better understand how sulfur isotopes can be used for predictive targeting undercover. To do so, we worked to apply sulfur isotopes at multiple scales, from the orogen- (e.g., Selvaraja et al. 2017b; LaFlamme et al. 2018b; LaFlamme et al. in review a), to the camp- (e.g., Sugiono, 2016; Thébaud et al. 2018), to the deposit (e.g., Selvaraja et al. 2017a, c; LaFlamme et al. 2018a), to the ore shoot-scale (e.g., Bell, 2016; LaFlamme et al. in review b).

To undertake this study we worked closely with mine site geologists for a better understanding of controls on mineralisation. We also worked with survey geologists from the Geological Survey of Western Australia (GSWA) to understand the geodynamic evolution of the Yilgarn Craton and Capricorn Orogen. To complete this study fieldwork was undertaken to understand the geology and knowledge gaps of the areas. Samples were collected by the authors at surface, from the GSWA archives, and from drill core and above/underground workings.

3.4 Materials and Methods

3.4.1 Sampling and preparation

Samples were collected at mine sites and in the field, in the GSWA core storage facilities, and at the archive collections of the University of Western Australia (UWA). The key challenge is to place the existing mineralisation and associated alteration into a spatial and temporal context that can guide sample selection. This requires an intimate understanding of the structural and hydrothermal architecture at the deposit-scale. Techniques include geological mapping, pit mapping and core logging which lead to informed sample selection.

Selected samples underwent detailed petrography by transmitted and reflected light microscopy; images were taken using high resolution camera attachments. From there, selected samples were cored to a diameter of around 3 mm using a drill press and were cast in epoxy to form 25 mm diameter mounts. After casting, the mounts were mechanically ground (1200 grit), and polished in three successive steps (9, 3, and 1 µm) with medium nap diamond polishing compound. Mounts were imaged in reflected light and carbon

coated (10 nm thickness) for Secondary Electron Microscope (SEM) and analysis at the Centre for Microscopy, Characterisation and Analysis (CMCA), UWA. Characterisation of small (<50 µm) sulfides by Energy-dispersive X-ray spectroscopy (EDS), and identification of fractures, inclusions and elemental zoning by backscatter electron (BSE) imaging occurred using a FEI Verios 460 XHR SEM or a Tescan Vega-3 SEM. Compositional analyses by wavelength dispersive spectrometry were acquired using a JEOL 8530F hyperprobe EPMA equipped with five tuneable wavelength dispersive spectrometers at the CMCA, UWA.

3.4.2 Multiple sulfur isotope systematics

Sulfur naturally occurs as four stable isotopes, 32S, 33S, 34S, and 36S with terrestrial abundances of 94.99%, 0.75%, 4.25%, and 0.01%, respectively (DeLaeter et al. 2003). By convention, sulfur isotope data are standardised to the Vienna-Cañon Diablo Troilite (V-CDT; Ding et al. 2001) and as the relative shift in ‰ using the delta-notation (δ) as follows,

$$(1)\ \delta^{x}S_{V-CDT} = \left[\frac{\left(\frac{^{x}S}{^{32}S}\right)_{measured}}{\left(\frac{^{x}S}{^{32}S}\right)_{V-CDT}} - 1\right] \times 1000$$

where x is 33, 34, or 36. The most widely employed sulfur isotope ratio has been the $^{34}S/^{32}S$, because it involves the two most abundant isotopes. More importantly, it was also previously thought that the $^{33}S/^{32}S$ and $^{36}S/^{32}S$ ratios provided little additional information because they had consistent linear relationships with $^{34}S/^{32}S$, obeying mass dependent fractionation (MDF) laws. However, significant work completed in the past ~15 years demonstrates that the relationship between $\delta^{33}S$ and $\delta^{34}S$, and $\delta^{36}S$ and $\delta^{34}S$ may depart from the MDF line in rocks older than ca. 2.45 Ga (e.g., Farquhar et al. 2000). Most deviations are due to MIF processes triggered by the presence an oxygen-poor atmosphere that existed before the Great Oxidation Event at ca. 2.4 Ga (Farquhar and Wing, 2003). In this environment, ultraviolet radiation was the driver for mass independent photochemical separation of sulfur isotopes. For this reason, the measure of ^{33}S has become essential to evaluate the full suite of isotopic features of Archean rocks (e.g., Bühn et al. 2012; Farquhar et al. 2013), and those from younger terranes that might be sourcing Archean rocks (e.g., Selvaraja et al. 2017b; LaFlamme et al. in review b). The lowest abundance stable isotope of sulfur, ^{36}S, behaves similarly to ^{33}S, and has also become increasingly important for fingerprinting Archean source rocks and understanding early Earth processes. The mass independent relationship is denoted by the $\Delta^{33}S$ and $\Delta^{36}S$ notation to represent the deviation between the isotopic ratios measured and those predicted according to mass dependent fractionation. The $\Delta^{33}S$ and $\Delta^{36}S$ values are calculated to approximate high temperature conditions (Farquhar and Wing, 2003),

$$(2)\ \Delta^{x}S_{i} = \delta^{x}S_{i} - 1000 \times \left[\left(\frac{\delta^{34}S_{V-CDT}}{1000} + 1\right)^{\lambda} - 1\right]$$

where x is either 33 or 36 and λ is the slope of the mass dependent fractionation line (~0.515 for δ33S and ~1.91 for δ36S; Hulston and Thode, 1965; Ono et al. 2006).

3.4.3 Measurement of multiple sulfur isotopes

LaFlamme, C, Martin, L, Jeon, H, Reddy, S, Selvaraja, V, Caruso, S, Bui, TH, Roberts, M, Littman, S, Voute, F, Hagemann, S, Wacey, D, Wing, B, Fiorentini, ML and Kilburn, M 2016, In situ multiple sulfur isotope analysis by SIMS of pyrrhotite, pentlandite and chalcopyrite to refine magmatic ore genetic models: Chemical Geology, v. 444, p. 1-15.

Multiple sulfur isotope research has previously focused on understanding changes in the evolution of the Earth's atmosphere, biosphere and hydrosphere and so has concentrated on analysis of pyrite. However, ore deposit research necessitates the analysis of a number of sulfide minerals that precipitate from magmas and hydrothermal fluids. So far, ore deposit research has focused on multiple sulfur isotope in bulk analyses, however, this prevents the analysis of a paragenetic sequence to monitor the isotopic evolution of a hydrothermal fluid or magma. During this project we developed five new reference materials for multiple sulfur isotope analysis by in situ analysis – pyrite, pyrrhotite, pentlandite, arsenopyrite and chalcopyrite (Figure 3.5). These standards have been distributed to ion probe labs around the world. The work presented in LaFlamme et al. (2016) - Chemical Geology – and has been cited 14 times in just over a year, as well as LaFlamme et al. (2018a). It has been the basis to understanding sulfur reservoirs in a variety of mineral systems including Ni-komatiite, Ni-PGE, orogenic gold and VMS deposits.

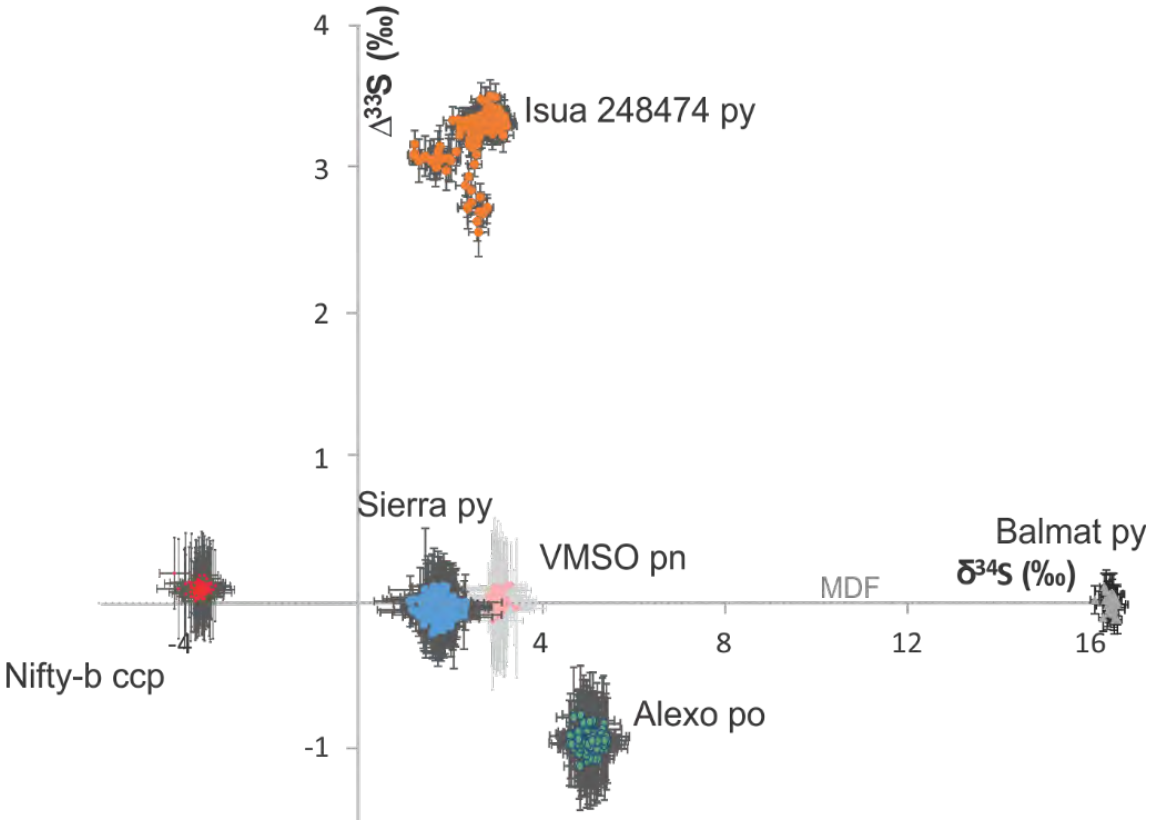

Figure 3.5. Five new reference materials for in situ multiple sulfur isotope analysis by SIMS as applied to ore deposit analysis – Nifty-b chalcopyrite, Sierra pyrite, Alexo pyrrhotite, VMSO pentlandite, and ASP200 arsenopyrite. Plotted against known Balmat and Isua 248474 pyrite reference materials.

3.4.4 In situ techniques

Multiple sulfur isotopic ratios (33S/32S, 34S/32S, and 36S/32S) on pyrite were determined in situ using a CAMECA IMS1280 large-geometry ion microprobe located at the CMCA, UWA, following the procedures and using the reference materials defined in LaFlamme et al. (2016). Trimmed mounts (to a 4.5 mm width) were coated with 30 nm of gold were loaded with a standard block into the sample holder as described in LaFlamme et al. (2016). A 3.7–4.6 nA focused (Gaussian mode) Cs+ primary beam interacted with the sample at the total impact energy of 20 keV. The analysis area was pre-sputtered using a 25 × 25 µm raster for 30 s followed by secondary beam centering and analysis using a using a 15 × 15 µm rastered beam. The secondary sulfur ions from the target sample were extracted and admitted to the mass spectrometer with a field magnification of 100×, with automated centering of the secondary beam in the field aperture (both x and y;

aperture size 4000 µm) and entrance slit (x direction only; slit width 60 µm). The NMR magnetic field controller locked the axial mass at the beginning of each session, and the mass spectrometer operated at a nominal mass resolution (M/ΔM) of about 5000 with an exit slit width of 250 µm on the multi-collector, which is adequate to off centre the 33S peak from the 32S1H peak.

Isotopes 32S, 33S and 34S were simultaneously detected by three Faraday Cups using amplifiers with 1010 Ω (L'2), 1011 Ω (L1), and 1011 Ω (H1) resistors, respectively. Count rates on 32S were between 1-4 × 109 counts per second. The 36S was detected using a low-noise ion counting Electron Multiplier (EM) in the H2 position of the multicollector axis. The count rates on 36S typically cause a significant gain drift for the EM. Hence, the EM high voltage was optimized using a Pulse Height Amplitude (PHA) distribution curve at the start of each session, and the gain drift was measured three times during each analysis (at the beginning, middle and end) and corrected by the CAMECA CIPS software (Schuhmacher et al. 2004). Data were collected over 20 integration cycles with 4 s counting time for each cycle. In the case of unknown material, measurements were interspersed with Sierra pyrite (δ34S = +2.17‰, Δ33S = −0.02‰) to correct for drift, monitor internal sample repeatability, and to calibrate isotope ratios. As well, analyses of matrix-matched reference material were used to calibrate isotope ratios for chalcopyrite using Nifty-b (δ34S = −3.58‰, Δ3fac3S = +0.06‰), pyrrhotite using Alexo (δ34S = +5.23‰, Δ33S = −0.96‰), and arsenopyrite using in house ASP200 (δ34S = +1.50‰, Δ33S = −0.50‰; see below). Measurements of Isua pyrite (see Whitehouse, 2013) were interspersed to act as a quality control standard. Data reduction followed procedures described in LaFlamme et al. (2016).

3.4.5 Bulk extraction techniques

Bulk multiple sulfur isotope analysis was completed in two manners. Firstly, by fluorination coupled with gas chromatography isotope ratio mass spectrometry (IRMS) was completed at the Stable Isotope Laboratory of the Department of Earth and Planetary Sciences at McGill University, Montreal, Canada as described in Wing and Farquhar (2015). For whole rock samples without visible sulfur-bearing phases, sulfur was chemically extracted from 5–15 g powders to form Ag_2S by Cr reduction and follow previously defined methods (Wing and Farquhar, 2015). Depending on the lithology, ~0–15 mg of Ag_2S was yielded from the extraction process. An additional 32 whole rock samples yielded <0.5 mg of Ag_2S (the minimum for analysis) and could not be analysed. For samples with 0.5–1.0 mg of yielded Ag_2S, a microanalytical method utilised a microvolume and modified resistor capacities (Au Yang et al. 2016). The $\delta^{34}S$, $\Delta^{33}S$, and $\Delta^{36}S$ values of the Ag_2S reference material, IAEA-S-1, are taken to be −0.3‰, +0.094‰, and −0.7‰, respectively. The precision and accuracy of the bulk fluorination system is evaluated by repeat analyses that return uncertainty (2SD) on $\delta^{34}S$, $\Delta^{33}S$, and $\Delta^{36}S$ values as better than ±0.15‰, ±0.02‰ and ±0.3‰, respectively.

Secondly, by using an Isoprime continuous flow IRMS, coupled with an Elementar Vario isotope cube for the elemental analyse at the Stable Isotope Geochemistry Laboratory at the University of Queensland, Brisbane, Australia as described in Baublys et al. (2004). Samples are calibrated via three point normalisation using IAEA-S1, S2, and S2. Samples which have a $\Delta^{33}S$ equal or greater than ±0.3‰ are counted as exhibiting MIF-S.

3.4.6 Trace elements in sulfides

Trace elements in pyrite and sphalerite were acquired by EPMA and Laser Ablation Inductively Coupled Mass Spectrometry (LA-ICPMS). Compositional analyses were acquired using a JEOL 8530F hyperprobe EPMA equipped with five tunable wavelength dispersive spectrometers at the CMCA, UWA. The operating conditions were 40 degrees take-off angle, and a beam energy of 20 keV. The beam was fully focused to give a spot size of about 1 µm with a 50 nA beam current. Elements were acquired using analyzing crystals LiF for V kα, Fe kα, Ti kα, Au lα, Te lα, Cu kα, Ni kα, Zn kα, Co kα, PETJ for S kα, Ag lα, Cd lα, PETH for Sb lα, Pb mα, Bi mα and TAP for As lα, Se lα. The standards employed were an assortment of commercially available metals,

oxides, sulfides and tellurides. Count times were 20 s for S kα, Fe kα, 60 s for Cu kα, Ni kα, Zn kα, Co kα, 80 s for V kα, Ti kα, Se lα, Te lα, 100 s for As lα, 120 s for Pb mα, Sb lα, Ag lα, Cd lα, Bi mα, and 200 s for Au lα. Mean atomic number background corrections were employed throughout (Donovan and Tingle, 1996). Unknown and standard intensities were corrected for deadtime and the ZAF algorithm utilised for matrix absorption (Armstrong, 1988). Standard intensities were corrected for standard drift over time. On peak interference corrections were applied as appropriate (Donovan et al. 1993). Detection limits ranged from 0.005 wt.% for Sb to 0.033 wt.% for Au. Quantitative chemical map acquisition utilised an 80 nA beam current with a 2 x 2 µm pixel dimension and 200 ms dwell time per pixel. Data were processed using the Calcimage software package and output to Surfer® for further processing and enhancement.

LA-ICPMS analyses were performed at UQAC-LabMaTer (Université du Québec à Chicoutimi, Canada). An excimer 193 nm laser system (RESOlution – Australian Scientific Instruments Pty. Ltd.) equipped with a dual-volumes cell (S-155 Laurin Technic, Australia) was coupled to a 7900 Agilent mass spectrometer. Helium flow in the ablation cell was 350 mL/min and mixed to the ICP-MS argon carrier gas (~1.0 mL/min), and 2 mL/min nitrogen was added to the line. A tiny flow of helium (1 mL/min) was injected in the collision cell of the ICP-MS to reduce the formation poly-atomic interferences without affecting the sensitivity and stability of mid- and high-range masses. Instrument was tuned daily to maximize sensitivity and ensure oxide formation level being <1% based on 248/232 mass ratio. Typical short term stability shows <5% RSD. Spot analyses were performed on the samples using varying beam size (25–55 µm) with a pulsing rate of 20 Hz and a fluence of 2.0 J/cm2. Data reduction was performed using IOLITE software (Paton et al. 2011) using 57Fe as internal standard which was fixed to pyrite stoichiometric values (46.55%, Webmineral.org). Isotopes studied to generate a fully quantitative dataset are: ^{34}S, ^{49}Ti, ^{51}V, ^{53}Cr, ^{55}Mn, ^{59}Co, ^{60}Ni, ^{65}Cu, ^{66}Zn, ^{69}Ga, 74Ge, ^{75}As, ^{77}Se, ^{85}Rb, ^{88}Sr, ^{90}Zr, ^{95}Mo, ^{107}Ag, ^{111}Cd, ^{118}Sn, ^{121}Sb, ^{125}Te, ^{137}Ba, ^{157}Gd, ^{178}Hf, ^{181}Ta, ^{182}W, ^{195}Pt, ^{197}Au, ^{202}Hg, ^{205}Tl, ^{206}Pb, ^{207}Pb, ^{208}Pb, ^{209}Bi, ^{232}Th, ^{238}U. A combination of 3 reference materials (RM) was necessary to cover the elements ranges: GSE-1g, MASS-1, and PO-727. Three more RMs were used for quality control: AI-3 (UQAC house RM), JB5 (James Brenan house-RM) and G-Probe-6 (USGS). Limits of detection as calculated by IOLITE typically range between 0.001 ppm and 1 ppm for elements of interest.

3.5 Results and Discussion

3.5.1 The Multiple Sulfur Isotope Signature of the Archean Yilgarn Craton

- **Defining the threshold of tracing MIF-S**

LaFlamme, C, Jamieson, J, Fiorentini, M, Thébaud, N, Caruso, S and Selvaraja, V 2018, Tracing sulfur pathways through the lithosphere by tracing mass independent fractionation of sulfur in orogenic gold deposits, Gondwana Research, v. 58, p. 27-38.

It is widely accepted that $\Delta^{33}S$ anomalies ($\Delta^{33}S > \pm 0.2‰$) were formed in the Archean eon, largely through mass independent fractionation of sulfur (MIF-S) in an oxygen-poor atmosphere and imparted to the Archean supracrustal rock record (as MIF-S) (Farquhar and Wing 2003). Here, we harness the indelible MIF-S signature to trace sulfur pathways to orogenic gold deposits. Through this recycling process, the original MIF-S signal ($\Delta^{33}S \neq 0‰$) may be diluted by mixing between sulfur reservoirs to such an extent to yield near-zero values ($\Delta^{33}S = 0\pm0.5‰$). In such cases, interpretation of the geological significance of such isotopic signatures may be compromised as it is known that mass dependent fractionation of sulfur (MDF-S, recorded as $\delta^{34}S$) can yield small $\Delta^{33}S$ values (±0.2‰), often owing to biological reactions involving sulfur. Therefore, to address these shortcomings we reassessed the quantification of $\Delta^{33}S$ due MDF-S from the traditionally accepted 0±0.2‰ value (Farquhar and Wing 2003), to demonstrate that its magnitude is not constant but rather directly linked to the degree of $\delta^{34}S$ fractionation. The old and new MDF-S thresholds are presented in Figure 3.6.

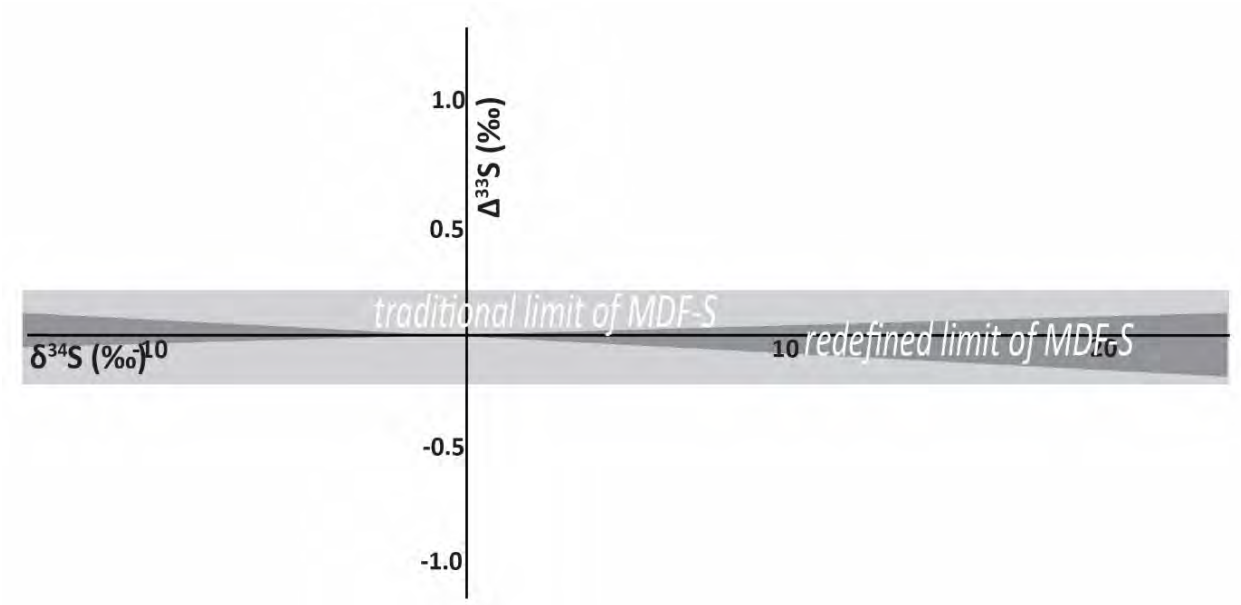

Figure 3.6. Threshold of MDF-S processes in δ34S-Δ33S space. Traditional limit was defined in Farquhar and Wing (2003), and the new limit is presented in LaFlamme et al. 2018b.

- **Insight into Archean interaction between reservoirs by multiple sulfur isotope data**

Caruso, S, Fiorentini, ML, Moroni, M and Martin, LAJ 2017, Evidence of magmatic degassing in Archean komatiites: insights from the Wannaway nickel-sulfide deposit, Western Australia. Earth and Planetary Science Letters, v. 479, p. 252-262.

LaFlamme, C, Martin, L, Jeon, H, Reddy, S, Selvaraja, V, Caruso, S, Bui, TH, Roberts, M, Littman, S, Voute, F, Hagemann, S, Wacey, D, Wing, B, Fiorentini, ML and Kilburn, M 2016, In situ multiple sulfur isotope analysis by SIMS of pyrrhotite, pentlandite and chalcopyrite to refine magmatic ore genetic models: Chemical Geology, v. 444, p. 1-15.

Caruso, S, Fiorentini, ML, Hollis, SP, LaFlamme, C, Baumgartner, RJ, Steadman, JA, Savard, D. The fluid evolution of the Nimbus Ag-Zn-(Au) deposit: an interplay between mantle plume and microbial activity. Precambrian Research (submitted).

Caruso, S., Fiorentini, K.L., Barnes S.J., LaFlamme C, 2018, Insights into the magmatic and hydrothermal evolution of the Black Swan complex, Yilgarn Craton: Evidence from textural and sulfur isotope. In prep.

Insights into the Earth's Archean processes are investigated by monitoring the multiple sulfur isotope systematics of Ni-komatiite and VHMS deposits in the Yilgarn Craton. Multiple sulfur isotope systematics lend insight into the interactions between the atmosphere, hydrosphere, biosphere and hydrothermal fluids and magmas (Bekker et al. 2009). Spatially constrained sulfur isotope signatures enables us to observe assimilation of distal sulfidic shales (+Δ33S) into the komatiitic flows at the Kambalda (LaFlamme et al., 2016; Appendix A) and the Wannaway (Caruso et al. 2017; Appendix B) deposits. Alternatively, proximal VHMS hydrothermal mineralisation (-Δ33S) is assimilated into at the Black Swan deposit (Caruso et al. in prep; Appendix C). Further, Caruso et al. (2017) demonstrate that a δ34S depletion up-stratigraphy indicates a loss of heavy sulfur isotope by degassing of SO2 during ultramafic volcanism in the Archean.

Multiple sulfur isotopes (presented in Appendix D) were also applied to the Nimbus VHMS deposit to monitor the evolving sulfur isotope signature of the mineralising fluids in Caruso et al. (in review). In the first stage, the hydrothermal system - powered by plume-related magmatism and deposited a series of barren pyrite lenses with colloform textures. Their variable but consistently negative MIF-S signature ($\Delta^{33}S$ = -0.81‰) reflects the interaction between magmatic fluids and Archean seawater. The ubiquitous presence of C-rich porous textures and the remnants of carbonaceous "nests" in colloform pyrite also indicate a significant contribution of microbial sulfate reducers during the incipient stages of sulfide precipitation. The gradual formation of colloform lenses eventually sealed the hydrothermal system establishing a physical barrier that limited the interaction with seawater. This process promoted the onset of higher temperature and pressure conditions required to form the high-grade Zn-Ag mineralization, sourcing sulfur and fluids largely from a magmatic reservoir ($\Delta^{33}S$ = +0.09‰). Whereas the identification of a predominantly magmatic sulfur source is supported by sulfur isotope signatures, the recognition of a magmatic origin of the fluid may only be inferred indirectly. Indeed, this ore-forming scenario is commonly favoured by high confining pressures, which at Nimbus were established following the deposition of the colloform pyrite lenses that progressively sealed the hydrothermal system creating the favourable conditions for mineralization.

- **Source of sulfur in Archean orogenic gold deposits across the Yilgarn Craton**

LaFlamme, C, Jamieson, J, Fiorentini, M, Thébaud, N, Caruso, S and Selvaraja, V 2018b, Tracing sulfur pathways through the lithosphere by tracing mass independent fractionation of sulfur in orogenic gold deposits, Gondwana Research, v. 58, p. 27-38.

Selvaraja, V, Caruso, S, Fiorentini, ML, LaFlamme, C and Bui, TH 2017b, Atmospheric sulfur in the orogenic gold deposits of the Archaean Yilgarn Craton: Geology, v. 45, p. 691-694

Sulfur forms the main complexing ligand for Au transport in aqueous fluid (Loucks and Mavrogenes 1999; Pokrovski et al. 2015). However, the source of sulfur in orogenic gold deposits remains a contentious scientific debate. The proposed sulfur sources are attributed to: recrystallisation of diagenetic pyrite derived from seawater (Chang et al. 2008), interaction with the surrounding supracrustal host rocks (e.g., Palin and Xu 2000), devolatilisation of oceanic crust (e.g., Phillips and Groves 1983; Phillips and Powell 2010) and/or sediments (Large et al. 2011; Tomkins 2010; 2013; Selvaraja et al. 2017b; LaFlamme et al. 2018a), mid crustal magmatic hydrothermal systems (e.g., Mueller et al. 2008; Xue et al. 2013) or sourcing deeper reservoirs such as the lower crust or the mantle (e.g., Hronsky et al. 2012). The debate continues at what depth these processes occurred and whether the source of sulfur was constant or evolving through Earth's history (Goldfarb and Groves 2015) reflecting changes in geodynamic processes.

The application of $\delta^{34}S$ can indicate the source reservoir of sulfur; however, many orogenic gold deposits report a large spread (~>10‰) in $\delta^{34}S$ leading to ambiguous interpretations (Hodkiewicz et al. 2009 and references therein). However, $\Delta^{33}S$ values can be traced to a specific reservoir. At the craton-scale, many Archean orogenic gold deposits in the Yilgarn Craton contain MIF-S ($\Delta^{33}S$ = -1.9‰ to +2.0‰), sourcing at least some of their sulfur from the Archean supracrustal rock record (Selvaraja et al. 2017a). The analysis of these results, as well as of a data compilation from ~2.65 Ga orogenic gold deposits of the Yilgarn Craton presented in LaFlamme et al. 2018b (Figure 3.7), indicates that $\Delta^{33}S$ values are too large to be the result of purely MDF-S processes and indicate sourcing of sulfur (at least partially) from the Archean sedimentary rock record. To address this, we have compared with our compilation of >3400 $\Delta^{33}S$ measurements of Archean sedimentary rocks, which shows highly variable positive and negative signals, the remarkably constant positive MIF-S signature of gold deposits from the Yilgarn Craton, with $\Delta^{33}S$ values generally between 0 and +0.6‰, is evidence that the source of the auriferous fluids equilibrated at depth by mixing sulfur from Archean sedimentary rocks with a non MIF-S-bearing sulfur reservoir. The outcomes will greatly enhance the application of MIF-S ($\Delta^{33}S$) as a powerful tracer of sulfur pathways through the lithosphere. Data was collected by bulk and in situ methods and are presented in Appendices E and F.

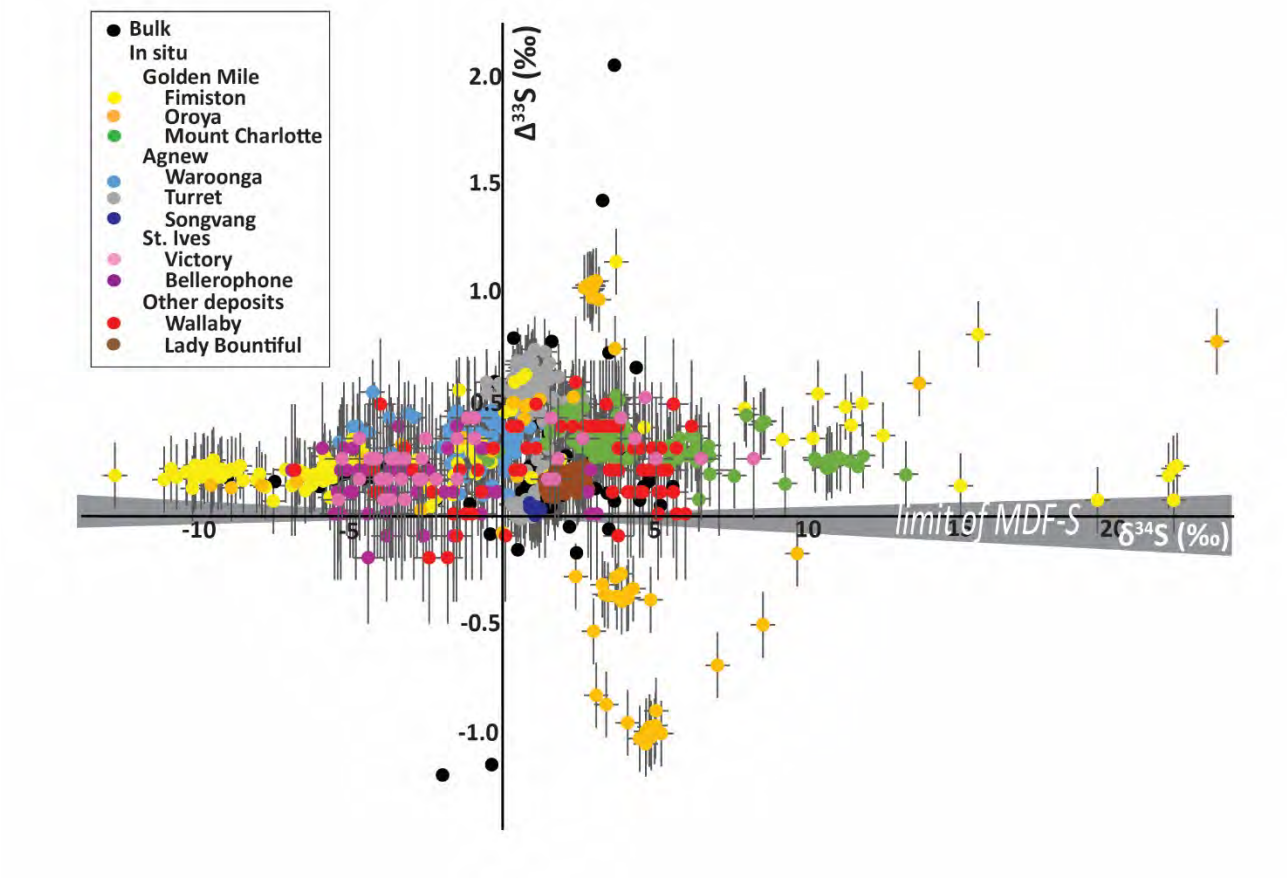

Figure 3.7. Compilation of multiple sulfur isotopes from ~2.65 Ga orogenic gold deposits of the Yilgarn Craton. Data are from two different methods: high precision fluorination of 19 deposits (Selvaraja et al. 2017a) and in situ methods. In situ methods included SHRIMP-SI of the St. Ives camp Xue et al. (2013) and SIMS of the Agnew camp (LaFlamme et al. 2018a; Thébaud et al. 2018), Golden Mile Godefroy-Rodríguez et al. (2017) and Lady Bountiful deposit (LaFlamme et al. 2018b).

- **Monitoring isotopic composition of auriferous hydrothermal fluids**

LaFlamme C, Hollis S, Jamieson J, Fiorentini M. Spatially-constrained multiple sulfur isotopes highlight processes controlling sulfur cycling in the near surface of sedimented hydrothermal systems. Geochemistry, Geophysics and Geosystems, submitted.

LaFlamme, C, Sugiono, D, Thébaud, N, Caruso, S, Fiorentini, M, Selvaraja, V, Voute, F, Jeon, H, and Martin, L 2018a, Multiple Sulfur Isotopes Monitor Fluid Evolution in MIF-S-bearing Orogenic Gold Deposit. Geochimica et Cosmochimica Acta, v. 222, p. 436-446

Thébaud, N, Sugiono, D, LaFlamme, C, Miller, J, Fisher, L, Voute, F, Tessalina, S, Sonntag, I and Fiorentini, M 2018, The protracted and polyphased formation of the Agnew Gold Camp (Yilgarn Craton, Western Australia). Precambrian Research, v. 310, p. 291-304.

Sugiono, D 2016, Sulfur isotope analysis at Archean gold deposits in Agnew Camp, Yilgarn Craton. University of Western Australia, MSc unpublished thesis. 66 p.

Hydrothermal systems generally report a large spread in $\delta^{34}S$ because sulfur isotopes are sensitive to changes in pH, P, T, f_{O_2}, f_{S_2}. This work focusses on harnessing this variation in a spatially- and temporally-constrained hydrothermal architecture to understand the precipitation mechanisms of metals carried in fluids. By monitoring the isotopic evolution of a hydrothermal fluid in space and time, we can better understand the changes in thermochemistry of a fluid that lead to metal precipitation and consequently apply this to vector toward mineralisation.

We first investigate the spatial variability of $\delta^{34}S$ in a modern seafloor hydrothermal system in LaFlamme et al. (in review a). Here, we present sulfur isotope results from laterally- and vertically-constrained hydrothermal pyrite from the Iheya North hydrothermal system in the Okinawa Trough, which was investigated during the Integrated Ocean Drilling Program Expedition 331. A change to lighter and more scattered sulfur isotopic signature is interpreted to indicate mixing with local biogenic sulfides from the surrounding sedimentary strata. As the most significant metal enrichments (Fe, Zn, Cu, Bi, Tl, Cd) are associated with samples that contain average pyrite $\delta^{34}S$ values of the vent fluid, we demonstrate that sulfur isotopes can vector toward metals in seafloor massive sulfide deposits.

We investigate whether hydrothermal fluid sources are variable in space and time in the Agnew orogenic gold camp in Thébaud et al. (2018). A detailed structural and geochronological study of auriferous-fluids at the Agnew camp within the Yilgarn Craton has identified two generations of mineralising events separated by 30 million years: the older 2.66 Ga event does not show evidence for sourcing of a MIF-S reservoir whereas the younger 2.63 Ga event preserves MIF-S ($\Delta^{33}S$ = +0.3–0.6‰). This time-dependent isotopic variation at the gold camp scale indicates that throughout the progression of an orogenic event, multiple mineralising events can source sulfur reservoirs with different $\Delta^{33}S$ values (Thébaud et al. 2018). This isotopic evolution may be important for our understanding of changes (or not) of sulfur reservoirs during the Neoarchean orogenic cycle, but more detailed studies are necessary.

The development of techniques to measure a number of sulfide phases in situ (LaFlamme et al. 2016) allows for the thermochemical evolution of an ore fluid to be monitored in space and time. At the ~6 Moz Waroonga orogenic gold deposit in the Agnew camp, detailed in situ sulfur isotope analysis of the sulfide-bearing petrogenetic sequence yields an invariant MIF-S signature ($\Delta^{33}S$ = +0.3‰) that coincides with $\delta^{34}S$ values that range from -12 to +3‰. These results aid to 1) fingerprint a specific sulfur reservoir (see Figure 3.8) and 2) constrain the thermochemical evolution of the auriferous hydrothermal fluid leading to gold precipitation (LaFlamme et al. 2018a). We utilise sulfide chemistry to argue that Au precipitation is driven by an abrupt change in redox state of the ore fluid (captured in the $\delta^{34}S$ values of the mineralisation sequence). Therefore, this multi-scale and multi-dimensional isotopic approach to understanding the source of sulfur in orogenic gold deposits lends insight into the regional- to grain-scale ore forming processes that control gold transport and precipitation.

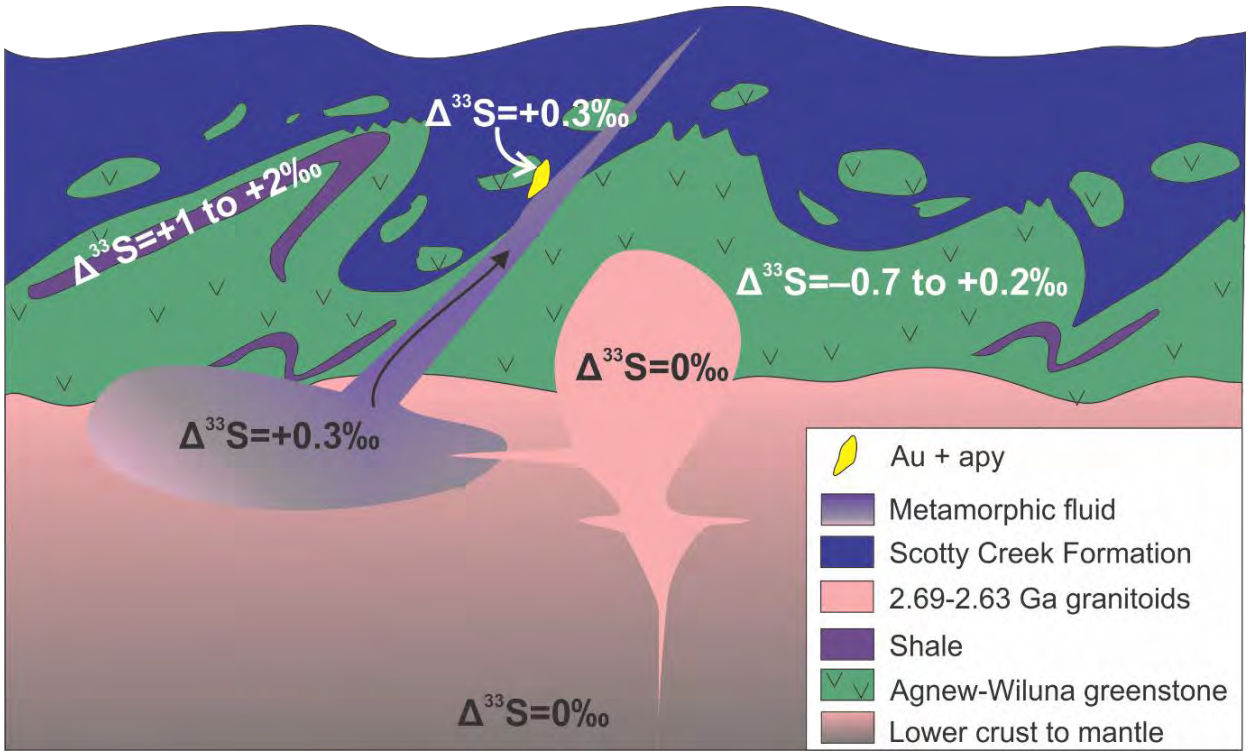

Figure 3.8. Schematic diagram demonstrating known sulfur reservoirs and their corresponding MIF-S components and hypothesised metamorphic fluid reservoir. MIF-S constraints on the Agnew-Wiluna greenstone belt are from Bekker et al. (2009) in nearby but structurally separate domains. MIF-S composition of pluton is based on results presented in Labidi et al. (2013).

- **Tracing Sulfur from an Archean Craton to its Proterozoic Margin**

Sulfur pathways through the lithosphere at convergent margins

LaFlamme C, Fiorentini ML, Wing B., Lindsay M, Bui TH The fate of Archean sulfur through a Proterozoic supercontinent cycle. Geochemical Prospective Letters, submitted.

Selvaraja V, Fiorentini ML, LaFlamme C, Wing BA, Bui TH, 2017a, Anomalous isotope signatures trace sulfur pathways in magmatic arcs: Geology, v. 45, p. 419-422.

Volatile pathways through the lithosphere are an understudied part of the supercontinent cycle but are a powerful tool to understand mechanisms that 1) generate crust and 2) focus deposits at craton margins. While the sulfur cycle is studied readily at the Earth's surface, an understanding of how sulfur is transported through the lithosphere and where it is concentrated in the Earth's crust and mantle has been obscured by a lack of clear markers to uniquely fingerprint this element. Lithospheric-scale Neoarchean tectonic boundaries that suture ancient terranes are known to host an abundance of Ni and Au occurrences (Mole et al. 2014), indicating that sulfur and metals are preferentially recycled along these structures. We built on this knowledge by investigating how sulfur is recycled from these metal endowed cratons to their margins, specifically the Capricorn Orogen. So, just as radio-isotope dyes are used in the medical sciences to map the intricate pathways of the inner human body, we have used the MIF-S signature to illuminate the pathways of sulfur through the lithosphere and across lithospheric blocks.

High-precision bulk multiple sulfur isotope analyses were collected by fluorination coupled with gas chromatography IRMS and are presented in Appendix G. Results from a suite of samples across the Capricorn Orogen yield $\Delta^{33}S$ values that range from −0.07‰ to +0.80‰. The units hosting Archean-sourced MIF-S are

dominantly magmatic (granitoids associated with collision and intraplate reworking) and hydrothermal (mineralised samples associated with faulting and veining) in nature. Spatially, data from this study show that MIF-S anomalies in the Capricorn Orogen occur in localised areas, preferentially located near to the margins with Archean cratons (Figure 3.9). Rather than a primary MIF-S signature, it is interpreted that the spatially localised anomalous $\Delta^{33}S$ values in Proterozoic samples reflect a recycled MIF-S component. Therefore, we propose that magmatic and hydrothermal events associated with collision and intracontinental reworking processes are large-scale mechanisms responsible not only for recycling sulfur across terrain boundaries, but also for potentially transferring metals from endowed Archean reservoirs into their younger orogenic margins. These results indicate that Archean sedimentary sulfur is transported from the surface, through the mantle and recycled for over 300 million years of punctuated magmatism (LaFlamme et al. In review a). This is in agreement with the findings of Selvaraja et al. (2017a) who determine that the Paleoproterozoic magmatic arc-hosted Glenburgh orogenic gold deposit also recycles MIF-S.

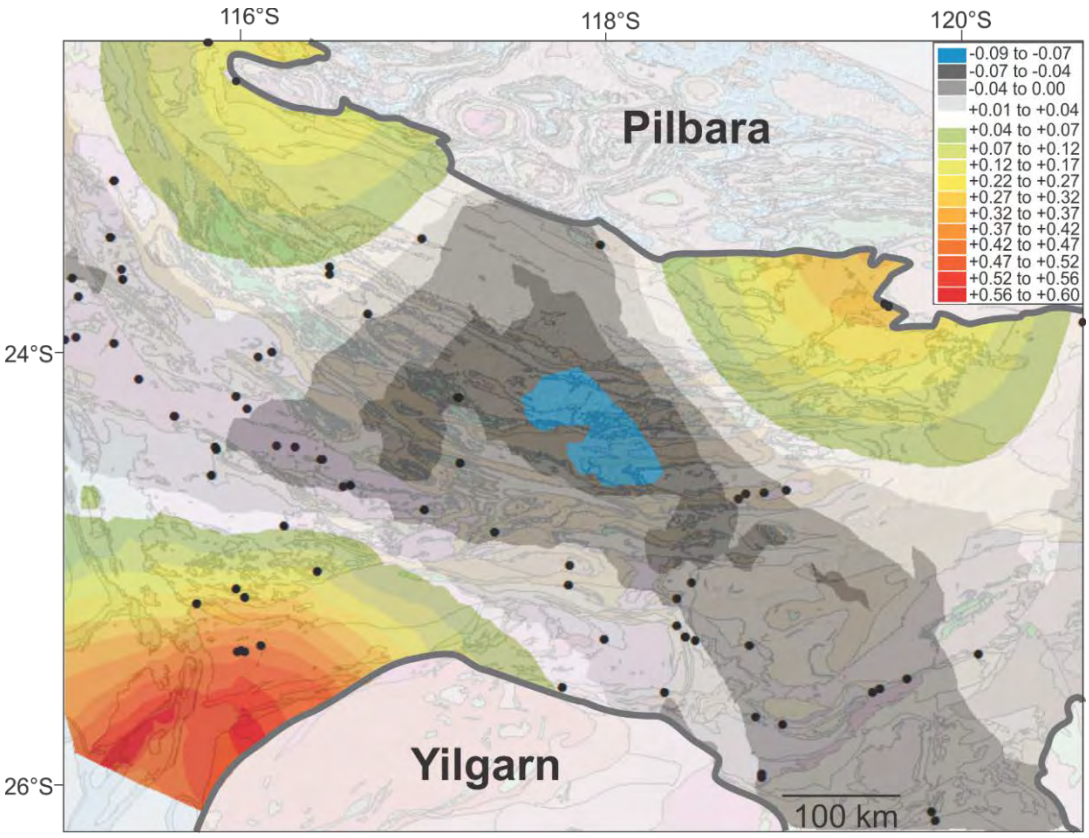

Figure 3.9. MIF-S model of the Capricorn Orogen. Samples with largest Δ33S values are located proximal to Archean cratons. Black dot indicate sample location and include granitoids, sediments and hydrothermal mineralisation. Modified after LaFlamme et al. (in review a).

Recycling of Archean MIF-S to juvenile Proterozoic granitoids and associated orogenic gold deposits has an important bearing on our understanding of the supercontinent cycle and indicates that craton amalgamation began with a significant incorporation of sedimentary rocks to the mantle. Therefore, we demonstrate how multiple sulfur isotopes can track sediment pathways (Figure 3.10; something that is blind to conventional radiogenic isotope tracers) during the supercontinent cycle and how this knowledge can aid in understanding the secular evolution of crust formation mechanisms through time.

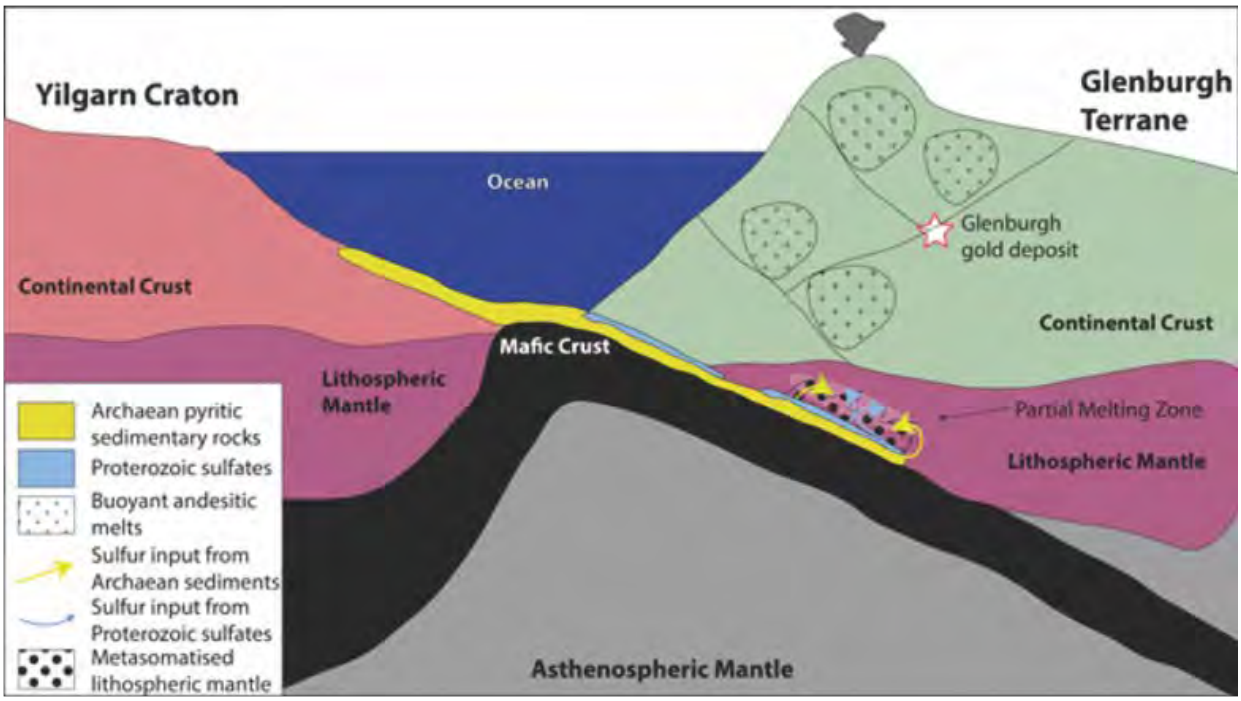

Figure 3.10. Model invoked to explain recycling of MIF-S to Glenburgh deposit and surrounding geology. Modified from Selvaraja et al. (2017a).

- **Multiple sulfur isotope studies of various Paleoproterozoic mineral occurrences**

Mineral occurrences that are known in the Capricorn Orogen are diverse and reflect a number of evolving tectonic environments during the formation of the orogenic belt (Pirajno, 2004). The investigation of the sulfur isotope record of many of these deposits provides critical information at the deposit-scale for exploration targeting but also a holistic understanding of sulfur cycling at craton margins. Preliminary multiple sulfur isotope analyses were collected by fluorination coupled with gas chromatography IRMS on many of the mineral occurrences in the Capricorn Orogen which is presented in Appendix H. We focus here on detailed efforts in four locations.

Paulsens gold deposit

Selvaraja, V, Fiorentini, ML, Jeon, H, Savard, DD, LaFlamme, C, Guagliardo, P, Caruso, S and Bui, TH 2017c, Evidence of local sourcing of sulfur and gold in an Archaean sediment hosted gold deposit: Ore Geology Reviews, v. 89, p. 909-930.

The Archaean sediment hosted ~1 Moz Paulsens gold deposit in the Pilbara Craton of Western Australia exhibits many of the characteristics of modern shale hosted gold deposits (e.g. Huijiabao Trend, Northern Carlin Trend and Sukhoi Log), in that 1) gold is hosted in pyrite as both free gold and dissolved gold in the lattice of the pyrite, and 2) multiple generations of pyrite have formed due to a variety of geological processes. Multiple sulfur isotope results collected in situ indicate that the diagenetic and nodule pyrite generations display similar and anomalous $\Delta^{33}S$ signatures (up to +0.4‰) to the mineralised hydrothermal pyrite, supporting the hypothesis that hydrothermal sulfur that carried gold derived from the Archaean black shales of the Hardey Formation, the host rocks of the deposit. Sulfur isotope data was collected in bulk and by in situ methods. The bulk data is presented in Appendix H and the in situ SIMS and is presented in Appendix I.

Chemical composition of early, syn-diagenesis pyrite by Nano Secondary Ion Mass Spectrometry (NanoSIMS), EPMA and LA-ICPMS show high concentrations of many trace elements (As, Ni, Co, Cu, Ag, Se, Te, Bi), including up to 1.5 ppm Au. LA-ICPMS data is presented in Appendix J. These elevated metal contents are also abundant in the multiple generations of mineralised hydrothermal pyrite and form clear patterns of growth associated with couple dissolution reprecipitation reactions. These findings clearly indicate that the fluid that transported the Au must have also been enriched in the base and precious metals that are contained in the early, syn-diagenesis pyrite. Data from this study clearly support the hypothesis that in some sediment hosted gold systems, all the sulfur and gold required to form the deposit are sourced from the local sedimentary package. By using the presence of anomalous mass independent sulfur isotope signatures as chemically conservative and indelible tracers, it is possible to fingerprint the source of sulfur in a wide range of mineral systems, thus enhancing predictive exploration strategies and the regional to camp scales.

Prairie Downs Zn-Ag-Pb deposit

Multiple sulfur isotope analysis was completed in bulk and by in situ methods to target pyrite, chalcopyrite, pyrrhotite, sphalerite and galena from mineralised occurrences along the Prairie Downs Fault (Prairie Downs and Wolf). Mineralised sections from drill holes 111, 205, and 206 (Prairie Downs) and Wolf (410) were investigated. Results reveal a mixing line in $\delta^{34}S$-$\Delta^{33}S$ space which may indicate sourcing of sulfur from a mixed source of Archean sedimentary sulfur and Paleoproterozoic seawater sulfate (Figure 3.11). The nearby Fortescue Basalt did not yield a MIF-S anomaly. In order to utilise the sulfur isotope data, better constraints on the geology of the deposit, timing of mineralisation events are required. However, it appears that the Prairie Downs and Wolf deposits, located 1 km from each other along the Prairie Downs Fault, source the same sulfur reservoirs. The full dataset which includes bulk analysis methods by both fluorination gas chromatography and continuous flow IRMS and in situ methods by SIMS is presented in Appendix K.

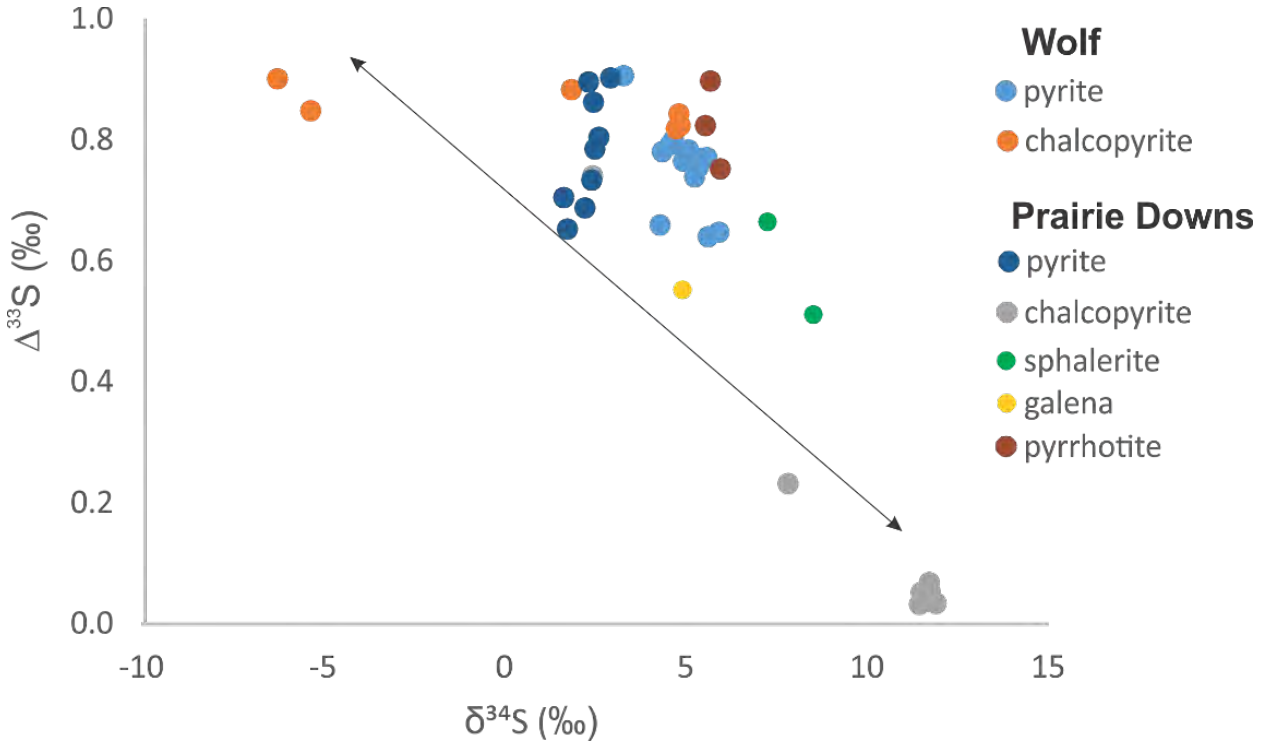

Figure 3.11. Data from the Prairie Downs deposit in δ34S-Δ33S space. The data may indicate mixing between a MIF-S bearing and a non-MIF-S bearing sulfur reservoir. Furthermore, it demonstrates that the sulfur reservoirs for Wolf and Prairie occurrences are similar.

Degrussa Cu-Au VMS deposit and the Bryah Basin

Bell, JM 2016, In situ multiple sulphur isotope analysis of the Degrussa VHMS deposit: implications for exploration and mineralisation. University of Western Australia, Honours unpublished thesis. 57 p.

Agangi, A, Reddy, S, Plavsa, D, Vieru, C, Selvaraja, V, LaFlamme, C, Jeon, H, Martin, L, Nozaki, T, Takaya, Y and Suzuki, K 2018, Subsurface deposition not Cu-rich massive sulphide underneath a Palaeoproterozoic seafloor hydrothermal system - The Red Bore prospect, Western Australia. Mineralium Deposita. In press.

Multiple sulfur isotopes by SIMS targeted the massive sulfides, including pyrite, pyrrhotite, and chalcopyrite following the procedures outlined above. Pyrite is the dominant ore mineral, occurring as small globulars intergrown with pyrrhotite and chalcopyrite. Detailed petrography indicate that euhedral pyrite overprints the main assemblage. All three sulfide phases (excluding the overprinting euhedral pyrite) within Conductors 1, 4, and 5, yield a normal distribution of $\delta^{34}S$ between –1‰ and +7‰. These values are comparable to the values of hydrothermal chalcopyrite ($\delta^{34}S$ = –2‰ to +5‰) from the sediment-hosted Guaymas Basin mid-ocean ridge spreading centers (McDermott et al. 2015). Pyrite within Conductors 1, 4, and 5 yield a mean $\delta^{34}S$ of +1.6‰ but distal to the ore deposits yield a mean of +3.5‰. The vectoring is best exemplified by sampling outside of Conductor 1 as displayed in Figure 3.12 in which primary $\delta^{34}S$ pyrite increases systematically distal to the ore lens.

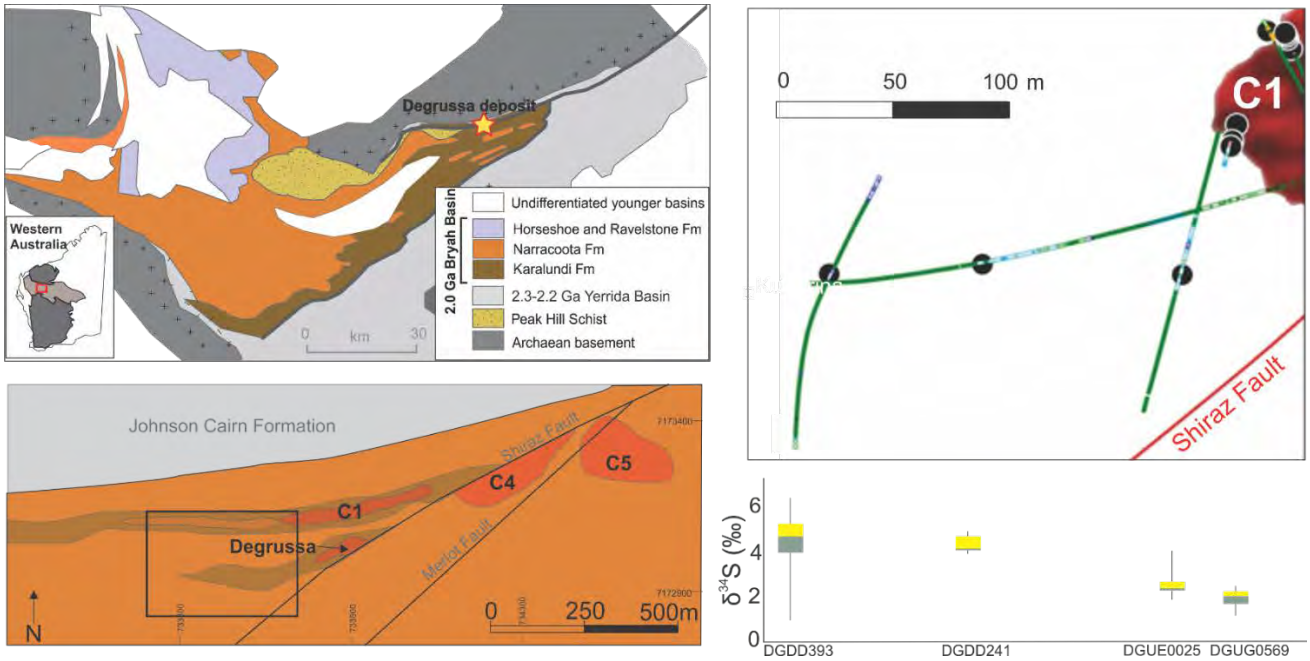

Figure 3.12. Box plot of multiple sulfur isotope data at and distal to Conductor 1 ore lens at the 2.0 Ga Degrussa VMS deposit. Degrussa deposit located within Narracoota Formation of the Bryah Basin, Capricorn Orogen, Western Australia.

Understanding of sulfur isotope vectoring in seafloor hydrothermal systems has been investigated in LaFlamme et al. in review b. As VMS deposits represent ancient analogues to seafloor hydrothermal systems, a comprehensive understanding of the sulfur isotope architecture of seafloor hydrothermal systems in three dimensions could lead to better metal vectoring (LaFlamme et al. in review b). Preliminary results indicate that the three studied ore lenses yield similar $\delta^{34}S$ values for co-genetic pyrite, pyrrhotite and chalcopyrite. However, $\delta^{34}S$ values away from the ore lenses into the adjacent sediments yield slightly heavier $\delta^{34}S$ values. Whereas, sulfur systematics of the NBC hydrothermal system of the Iheya North continental backarc are likely related to SO_2 disproportionation, the increase of $\delta^{34}S$ may be related a different mechanism in the sedimented mid ocean ridge environment. This may be attributed to the infiltration and mixing with seawater or thermochemical reduction of sulfate in the near surface as described by McDermott et al. (2015). This further emphasises the hypothesis that hydrothermal fluid and sediment interaction is minimal. Alternatively, sediments may control the heat required for phase separation reactions that are critical to metal precipitation.

Other sulfur isotope data was collected within the Narracoota and Karalundi Formations of the Bryah Basin. Agangi et al. (2018) demonstrate using sulfur isotope data that the nearby Red Bore prospect represents the subsurface root systems to the Degrussa deposit. Data from pyrite and chalcopyrite indicate a narrow range of $\delta^{34}S$ (-0.2 to +4.6‰) which is in agreement with data collected in this study. This genetic association of Red Bore mineralisation with the Degrussa deposit suggests a direct connection between magmatism and mineralising fluids responsible for VMS deposition at surface. Further, sulfur isotope data from pyrite-rich black shales of the Neptune prospect yield chalcopyrite and pyrite values with negative $\delta^{34}S$ values (-8.9 to -16.2‰). This likely indicates that sulfides were formed by bacterial reduction of seawater sulfate in this area. Data for this study is presented in Appendix L.

Abra Zn-Pb deposit and the Edmund Basin

Multiple sulfur isotopes were taken from drill holes proximal to the Abra deposit and within the Edmund Basin to sample all Supersequences that form the Edmund Basin. Overall, proximal to the Abra deposit, δ34S of pyrite and chalcopyrite are much heavier (+40‰) than the sediments outside the hydrothermally altered area (+5 to +21‰). Data for this study is reported in Appendix M.

Padbury Basin orogenic gold deposits

We present a representative sub-dataset of a regional-scale compilation of in situ sulfur isotopes from the Padbury Basin orogenic gold deposits within Capricorn orogenic belt in Western Australia. To better understand the processes promoting the remobilisation of anomalous $\delta^{34}S$ and (Archean) MIF sulfur to Proterozoic mineral deposits, sulfur isotope data of Au-associated hydrothermal pyrite are collected by SIMS are coupled with quantitative crystal lattice orientation measurements (EBSD) trace elemental maps (WDS-EPMA). Internal variations and zoning inherent to analysed grains from Fortnum and Nathan's mine are integral in deciphering: the primary source(s) of sulfur the mechanisms resulting in sulfur-liberating episodes. Here we find a nickel-rich rim in hydrothermal pyrite grains that is associated with elevated $\Delta^{33}S$ values (Figure 3.13). Data are presented in Appendix N.

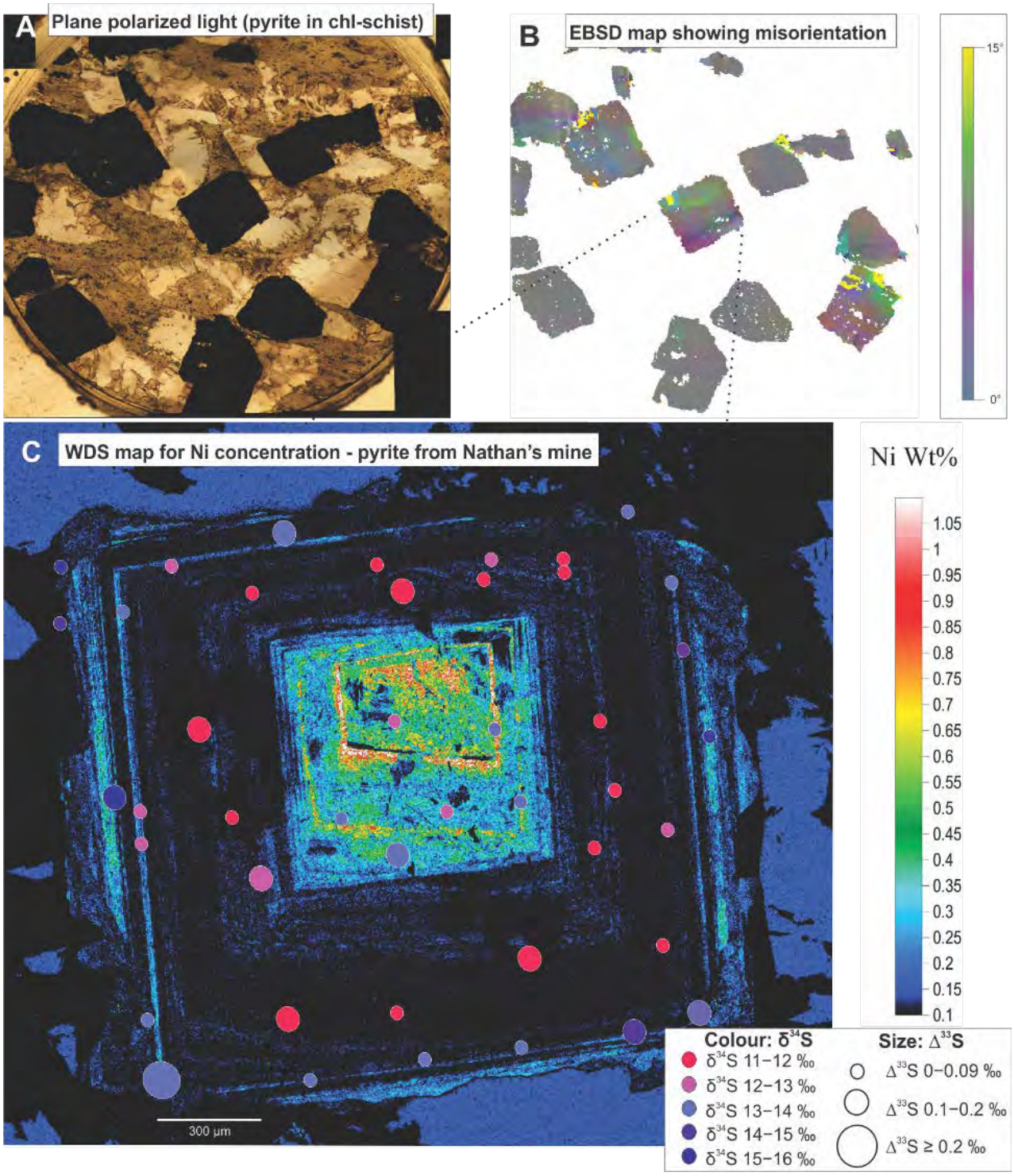

Figure 3.13. In situ multiple sulfur isotopes across multiple growth phases of gold-associated pyrite in the Padbury Basin. A) Plane polarized light of pyrite in chlorite schist from Nathan's mine in the Padbury basin, B) EBSD showing misorientation along the penetrative fabric. C) In situ multiple sulfur isotope analyses overlain on Ni concentration map (WDS). Sulfur $\delta^{34}S$ and $\Delta^{33}S$ variation related to growth zoning.

3.6 Conclusions

In conclusion, we have determined that the MIF-S isotope tracer is very useful in its application to geological problems. Firstly, we have compiled over 5500 analyses of multiple sulfur isotopes from sediments through time. This provides a background of the MIF-S signal from the Early Earth to recent times. We then have mapped the primary and recycled multiple sulfur isotope architecture of the metal endowed Yilgarn Craton. The work focussed on magmatic and hydrothermal systems, showing that the original signatures that were imprinted on mineral systems at the time of formation can be modified following late-magmatic and metamorphic processes (e.g., Caruso et al., 2017; Caruso et al., submitted; Caruso et al. In prep). Establishing the extent of the variability of the background multiple sulfur isotope signature in different Archean systems if pivotal in understanding how the Archean sulfur budget as a whole can be recycled into Proterozoic orogenic belts, potentially playing a key role on subsequent ore forming processes. We therefore fingerprinted the sulfur isotope signature of the Archean sulfur budget, delineating a sort of recognisable "sulfur DNA" that could be followed through successive orogenic cycles.

This MIF-S isotope signature is then traced in space and time through this lithosphere. In doing so, we demonstrate that at the craton-scale, the first major 'bloom' of orogenic gold deposits recycles a MIF-S-bearing sulfur reservoir from depth. Therefore, we have traced a reservoir from the surface of the Earth through the lithosphere during the amalgamation of the early ca. 2.7–2.5 Ga supercontinent Kenorland and the formation of orogenic gold deposits (LaFlamme et al. 2018b). From there, we move to the craton margin to the Yilgarn Craton – the Capricorn Orogen. Here, we demonstrate that Archean sedimentary rocks provide sulfur to gold deposits and the granitoid rock record within ca. 2.0 Ga continental arcs that formed after the Great Oxygenation Event, during the assembly of Archean cratons into the ca. 1.8 Ga supercontinent Nuna/Columbia (Selvaraja et al. 2017b; LaFlamme et al. in review a). These findings are amassing to demonstrate that during time periods coincident with crustal growth and/or reworking, significant amounts of surface-derived MIF-S-bearing sedimentary rocks have been recycled through the lithosphere.

In this project, the use of isotope tracers is applied across many scales. At the camp-scale, (Thébaud et al. in press; Sugiono, 2016) demonstrate that the Agnew District is formed over two mineralising events separated by over 30 million years and only recycles MIF-S in the later event. At the deposit-scale, (LaFlamme et al. 2018a) demonstrates that while MIF-S is present in Archean orogenic gold deposits of the Yilgarn Craton, it is often not being recycled from the surrounding host rocks. Rather a ubiquitous MIF-S ($\Delta^{33}S$ = 0 to +0.6‰) signal across many deposits indicates that a MIF-S reservoir exists at depth, indicating the devolatilisation of sediments plays a crucial role in providing sulfur to auriferous hydrothermal fluids (LaFlamme et al. 2018b; Selvaraja et al. 2017a). Further, in demonstrating that the source reservoir for sulfur remains constant, changes in $\delta^{34}S$ throughout the paragenetic sequence can be specifically linked to changes in the thermochemistry of the auriferous fluid, causing gold to precipitate (LaFlamme et al. 2018a).

In younger Proterozoic mineral occurrences, preliminary multiple sulfur isotope investigations demonstrate that near the boundary with the Pilbara Craton, sediment-hosted gold (Paulsens) and base metal deposits (Prairie Downs) do source sulfur from the surrounding geology (Selvaraja et al. 2017c; this study). Further, preliminary investigation into the base metal deposits of the Edmund Basin (Abra) and the Bryah Basin (Degrussa) with respect to the surrounding geology indicates that ore vectoring is possible by sulfur isotopes utilising samples that are well constrained in space and time (Bell 2016; this study).

3.7 Recommendations for Future Work

- Further investigate whether magmatic processes such as degassing from komatiites could impact on the evolving sulfur isotope signature of the Archean hydrosphere and atmosphere.
- Detailed investigation into how sulfur is recycled to the Yilgarn Archean granitoid crust as compared to the observations made in the Capricorn Proterozoic crust. This work is ongoing with a collaboration with Prof. Ueno at the Tokyo Institute of Technology.
- Investigation into how mafic intrusions recycle sulfur from endowed Archean cratons at their margins.
    - Honours thesis completed by Curtis Bersan at Double Magic prospect west of the Kimberley Craton in 2017.
    - MSc thesis by Kathleen Bathgate at the Nova deposit commenced in 2018
- Detailed investigation into orogenic gold deposits in which host rocks are variable. This approach will further our understanding of precipitation mechanics of gold from hydrothermal fluids:
    - Dennis Sugiono commenced Northern Star Resources sponsored project at Kanowna Belle in July 2017
    - Gascoyne Resources supported honours and masters' theses at Dalgaranga orogenic gold deposit of the Yilgarn Craton's Murchison Terrane were completed by Sam Busetti and Luke Blais in 2017. Manuscript in preparation.

3.8 References

Agangi, A., Hofmann, A., Eickmann, B., Marin-Carbonne, J.M. and Reddy, S., 2016, An atmospheric source of S in Mesoarchean structurally-controlled gold mineralisation of the Barberton Greenstone Belt: Precambrian Research, v. 285, p. 10-20.

Agangi, A., Reddy, S., Plavsa, D., Vieru, C., Selvaraja, V., LaFlamme, C., Jeon, H., Martin, L., Nozaki, T., Takaya, Y. and Suzuki, K., 2018, Subsurface deposition of Cu-rich massive sulphide underneath a Palaeoproterozoic seafloor hydrothermal system - The Red Bore prospect, Western Australia: Mineralium Deposita. https://doi.org/10.1007/s00126-017-0790-0

Armstrong, T.J., 1988, Quantitative analysis of silicates and oxide minerals: comparison of Monte-Carlo, ZAF, and Phi-Rho-Z procedures: Microbeam Analytical, v. 1, p. 239-246.

Australia Academy of Sciences 2012, Searching the Deep Earth, 43 pp.

Au Yang, D., Landais, G., Assayag, N., Widory, D., Cartigny, P., 2016, Improved analysis of micro- and nanomole-scale sulfur multi-isotope compositions by gas source isotope ratio mass spectrometry. Rapid Communications in Mass Spectrometry, v. 30, p. 897-907.

Barnes, S.J., 2004, Introduction to nickel sulfide orebodies and komatiites of the Black Swan area, Yilgarn Craton, Western Australia. Mineralium Deposita, v. 39, p. 679–683.

Baublys, K.A., Golding, S.D., Young, E. and Kamber, B.S., 2004, Simultaneous determination of δ33SV-CDT and δ34SV-CDT using masses 48, 49 and 50 on a continuous flow isotope ratio mass spectrometer: Rapid Communications in Mass Spectrometry, v. 18, p. 2765-2769.

Bekker, A., Barley, M.E., Fiorentini, M., Rouxel, O.J., Rumble, D. and Beresford, S.W., 2009, Atmospheric sulfur in Archean komatiite-hosted nickel deposits: Science, v. 326, p. 1086−1089.

Bell, J.M., 2016, In situ multiple sulphur isotope analysis of the Degrussa VHMS deposit: implications for exploration and mineralisation. University of Western Australia, Honours unpublished thesis. 57 p.

Bland, G., Elliot, L. and Bryant, R., 2014, JORC Technical Report for Resource and Reserves Estimation of the Paulsens Gold Deposit, Western Australia. Northern Star Resources.

Bühn, B., Santos, R.V., Dardenne, M.A. and de Oliveira, .CG., 2012, Mass-dependent and mass-independent sulfur isotope fractionation δ34S and δ33S, from Brazilian Archean and Proterozoic sulfide deposits by laser ablation multi-collector ICP-MS: Chemical Geology, v. 312, p. 163-176.

Caruso, S., Fiorentini, M.L., Moroni, M. and Martin, .LA.J., 2017, Evidence of magmatic degassing in Archean komatiites: insights from the Wannaway nickel-sulfide deposit, Western Australia. Earth and Planetary Science Letters, v. 479, p. 252-262.

Caruso, S., Fiorentini, M.L., Hollis, .S.P., LaFlamme, C., Baumgartner, R.J., Steadman, J.A. and Savard, D., The fluid evolution of the Nimbus Ag-Zn-(Au) deposit: an interplay between mantle plume and microbial activity. Precambrian Research (submitted).

Cassidy, K.F. and Bennett, J.M., 1993, Gold mineralisation at the Lady Bountiful Mine, Western Australia: an example of a granitoid-hosted Archaean lode gold deposit: Mineralium Deposita, v. 28, p. 388-408.

Cassidy, K.F., et al. 2006, A revised geological framework for the Yilgarn Craton, Western Australia. Geological Survey of Western Australia Record 2006/8, 8 p.

Cawood, P. and Tyler, I.M., 2004, Assembling and reactivating the Proterozoic Capricorn Orogen: lithotectonic elements, orogenies, and significant: Precambrian Research, v. 128, p. 201-208.

Chang, Z., Large, R. and Maslennikov, V., 2008, Sulfur isotopes in sediment-hosted orogenic gold deposits: evidence for an early timing and a seawater sulfur source. Geology, v. 36, p. 971-974.

Chen, M., Campbell, I.H., Xue, Y., Tian, W., Ireland, T.R., Holden, P., Cas, R.A.F., Hayman, P.C. and Das, R., 2015. Multiple sulfur isotope analyses support a magmatic model for the volcanogenic massive sulfide deposits of the Teutonic Bore Volcanic Complex, Yilgarn Craton, Western Australia: Economic Geology, v. 110, p. 1411-1423.

Davaadorj, E., 2015, Zinc mineralisation at the Prairie Downs deposit, Capricorn Orogen, Western Australia. University of Western Australia unpublished MSc Thesis.

DeLaeter, J.R., Bohlke, J.K., De Bievre, P., Hidaka, H., Peiser, H.S., Rosman, K.J.R. and Taylor, P.D.P., 2003, Atomic weights of the elements: Review 2000: Pure and Applied Chemistry, v. 75, p. 683-800.

Ding, T., Valkiers, S., Kipphardt, H., De Bievre, P., Taylor, P., Gonfiantini, R. and Krouse, R., 2001, Calibrated sulfur isotope abundance ratios of three IAEA sulfur isotope reference materials and V-CDT with a reassessment of the atomic weight of sulfur: Geochimica et Cosmochimica Acta, v. 65, p. 2433-2437.

Donovan, J.J., Snyder, D.A. and Rivers, M.L., 1993, An improved interference correction for trace element analysis: Microbeam Analytical, v. 2, p. 23-28.

Donovan, J.J. and Tingle T.N., 1996, An improved mean atomic number correction for quantitative microanalysis: Journal of Microscopy, v. 2, p. 1-7.

Duuring, P., Bleeker, W., Beresford, S.W., Fiorentini, M.L., and Rosengren, N.M., 2012, Structural evolution of the Agnew-Wiluna greenstone belt, Eastern Goldfields, Yilgarn Craton and implications for komatiite-hosted Ni sulphide exploration: Australian Journal of Earth Sciences, v. 59, p. 765-791.

Evans, D.A.D., et al. 2003, Revised geochronology of magmatism in the western Capricorn Orogen at 1805–1785 Ma: Diachroneity of the Pilbara–Yilgarn collision: Australian Journal of Earth Sciences, v. 50, p. 853-864.

Evans, D.A.D. and Mitchell, R.N., 2011, Assembly and breakup of the core of Paleoproterozoic-Mesoproterozoic supercontinent Nuna: Geology, v. 39, p. 443-446.

Evans, K.A., Tomkins, A.G., Cliff, J. and Fiorentini, M.L., 2014, Insights into subduction zone sulfur recycling from isotopic analysis of eclogite-hosted sulfides: Chemical Geology, v. 365, p. 1-19.

Farquhar, J., Bao, H. and Thiemens, M.H., 2000, Atmospheric influence of Earth's earliest sulfur cycle: Science, v. 28, p. 756-758.

Farquhar, J. and Wing, B.A., 2003, Multiple sulfur isotopes and evolution of the atmosphere: Earth and Planetary Science Letters, v. 213, p. 1-13.

Farquhar, J., Cliff, J., Zerkle, A.L., Kamyshny, A., Poulton, S.W., Claire, M., Adams, D. and Harms, B., 2013, Pathways for Neoarchean pyrite formation constrained by mass-independent sulfur isotopes: Proceedings to the National Academy of Science USA, v. 110, p. 17638-17643.

Fielding, I., Johnson, S.P., Zi, J.W., Rasmussen, B.R., Muhling, J.R., Dunkley, D.J., Sheppard, S., Meffre, S., Wingate, M.T.D. and Rogers, J.R., 2017, Dating orogenic gold mineralisation at the Paulsens deposit, Western Australia: Economic Geology, v. 112, p. 1205-1230.

Fiorentini, M.L, Beresford, S., Barley, M., Duuring, P., Bekker, A., Rosengren, N., Cas, R. and Hronsky, J., 2012, District to camp controls on the genesis of komatiite-hosted nickel sulfide deposits, Agnew-Wiluna greenstone belt, Western Australia: Insights from the multiple sulfur isotopes: Economic Geology, v. 107, p. 781-796.

Giacometti, F., Evans, K., Rebay, G., Cliff, J., Tomkins, A.G., Rosetti, P., Vaggelli, G. and Adams, D.T., 2014, Sulfur isotope evolution in sulfide ores from Western Alps: Assessing the influence of subduction-related metamorphism: Geochemistry, Geophysics, Geosystems, v. 15, p. 1-22.

Grey, K., et al. 2005, Lithostratigraphic nomenclature of the Officer Basin and correlative parts of the Paterson Orogen Western Australia: Geological Survey of Western Australia Report 93, 95 p.

Godefroy-Rodriguez, M., Hagemann, S., LaFlamme, C. and Fiorentini, M., 2017, Mass Dependent Fractionation in pyrite-from the Golden Mile: Evidence for a mantle connection during gold mineralization: Society of Economic Geology Annual Conference, Beijing, China.

Goldfarb, R. and Groves, D., 2015, Orogenic gold: Common or evolving fluid and metal sources through time: Lithos, v. 233, p. 2-26.

Hawke, M., Meffre, S., Stein, H., Hilliard, .P, Large, R. and Gemmell, J.B., 2015, Geochronology of the DeGrussa volcanic-hosted massive sulfide deposit and associated mineralisation of the Yerrida, Bryah and Padbury Basin: Precambrian Research, v. 267, p. 250-284.

Hodkiewicz, P.E., Groves, D.I., Davidson, G.J., Weinberg, R.F. and Hagemann, S.G., 2009, Influence of structural setting on sulphur isotopes in Archean orogenic gold deposits, Eastern Goldfields Province, Yilgarn Western Australia: Mineralium Deposita, v. 44, p. 129.

Hollis, S.P., Mole, D.R., Gillespie, P., Barnes, S.J., Tessalina, S., Cas, R.A.F., Hildrew, C., Pumphrey, A., Goodz, M.D., Caruso, S., Yeats, C.J., Verbeeten, A., Belford, S.M., Wyche, S. and Martin, L.A.J., 2017, 2.7 Ga plume associated VHMS mineralization in the Eastern Goldfields Superterrane, Yilgarn Craton: Insights from the low temperature and shallow water, Ag-Zn-(Au) Nimbus deposit. Precambrian Research, v. 291, p. 119–142.

Hronsky, J., Groves, D., Loucks, R. and Begg G., 2012, A unified model for gold mineralisation in accretionary orogens and implications for regional-scale exploration targeting methods: Mineralium Deposita, v. 47, p. 339-358.

Hulston, J.R. and Thode, H.G., 1965, Variations in the S33, S34, and S36 contents of meteorites and their relation to chemical and nuclear effects: Journal of Geophysical Research, v. 70, p. 3475-3484.

Jamieson, J.W., Wing, B.A., Hannington, M.D. and Farquhar, J., 2006, Evaluating isotopic equilibrium among sulfide mineral pairs in Archean ore deposits: case study from the Kidd Creek VMS deposit, Ontario, Canada: Economic Geology, v. 101, p. 1055-1061.

Johnson, S.P., Sheppard, S., Wingate, M.T.D., Kirkland, C.L. and Belousova, E.A., 2011, Temporal and hafnium isotopic evolution of the Glenburgh Terrane basement: an exotic crustal fragment in the Capricorn Orogen: Geological Survey of Western Australia Report 110.

Johnson, S.P., et al. 2013, Crustal architecture of the Capricorn Orogen, Western Australia and associated metallogeny, Australian Journal of Earth Sciences, v. 60, p. 681-705.

Johnston, D.T., Farquhar, J. and Canfield, D.E., 2007, Sulfur isotope insights into microbial sulfate reduction: when microbes meet models. Geochimica et Cosmochimica Acta, v. 71, p. 3929–3947.

Kaufman, A.J., Johnston, D.T., Farquhar, J., Masterson, A.L., Lyons, T.W., Bates, S., Anbar, A.D., Arnold, G.L., Garvin, J. and Buick, R., 2007, Late Archean biospheric oxygenation and atmospheric evolution. Science, v. 317, p. 1900-1903.

Kump, L.R., 2012, Sulfur isotopes and the stepwise oxygenation of the biosphere. Elements. DOI 10.2113/gselements.8.6.410

Labidi, J., Cartigny, P. and Moreira, M., 2013, Non-chondritic sulphur isotope composition of the terrestrial mantle: Nature, v. 501, p. 208–211.

LaFlamme, C., Martin, L., Jeon, H., Reddy, S., Selvaraja, V., Caruso, S., Bui, T.H., Roberts, M., Littman, S., Voute, F., Hagemann, S., Wacey, D., Wing, B., Fiorentini, M.L. and Kilburn, M., 2016, In situ multiple sulfur isotope analysis by SIMS of pyrrhotite, pentlandite and chalcopyrite to refine magmatic ore genetic models: Chemical Geology, v. 444, p. 1-15.

LaFlamme, C., Sugiono, D., Thebaud, N., Caruso, S., Fiorentini, M.L., Selvaraja, V., Jeon, H., Voute, F. and Martin, L., 2018a, Multiple sulfur isotopes monitor fluid evolution in MIF-S-bearing orogenic gold deposit. Geochimica et Cosmochimica Acta, v. 222, p. 436-446.

LaFlamme C., Jamieson J., Fiorentini M., Thebaud N., Caruso S., Selvaraja V., 2018b,Tracing volatile pathways through the lithosphere using mass independent fractionation of sulfur. Gondwana Research, v. 58, p. 27-38.

LaFlamme, C., Fiorentini, M.L., Lindsay, M., Bui, T.H., The fate of Archean surficial sulfur through a Proterozoic supercontinent cycle. In review a, Geochemical Perspective Letters

LaFlamme C., Hollis S., Jamieson J.W., Fiorentini M., Three dimensional spatially-constrained sulfur isotopes highlight processes controlling sulfur cycling in the near surface of the Iheya North hydrothermal system, Okinawa Trough, In review b, Geochemistry, Geophysics, Geosystems

Lampinen, H.M., Laukamp, C., Occhipinti, S.A., Metelka, V., and Spinks, S.C., 2017, Delineating alteration footprints from field and ASTER SWIR spectra, geochemistry and gamma-ray spectrometry above regolith-covered metal deposits – an example from Abra, Western Australia, Economic Geology, v. 112, p. 1977-2003.

Large, R.R., Bull, S.W. and Maslennikov, VV., 2011, A carbonaceous sedimentary source-rock model for carlin-type and orogenic gold deposits. Economic Geology v. 106, p.331-358.

Loucks, R.R. and Mavrogenes, J.A., 1999, Gold solubility in supercritical hydrothermal brines measured in synthetic fluid inclusions. Science, v. 284, p. 2159-2163.

Martin, D.M. and Thorne, A.M., 2004, Tectonic setting and basin evolution of the Bangemall Supergroup in the northwestern Capricorn Orogen: Precambrian Research, v. 128, p. 385-409.

Martin, D.M. and Morris, P.A., 2010, Tectonic setting and regional implications of ca 2.2 Ga mafic magmatism in the southern Hamersley Province, Western Australia. Australian Journal of Earth Sciences, v. 57, p. 911-931.

McCuaig T.C., Beresford S., Hronsky J., 2010, Translating the mineral systems approach into an effective exploration targeting system. Ore Geology Reviews v. 38, p. 128-138.

McDermott, J.M., Ono, S., Tivey, M.K., Seewald, J.S., Shanks, W.C. and Solow, A.R., 2015, Identification of sulfur sources and isotopic equilibria in submarine hot-springs using multiple sulfur isotopes: Geochimica et Cosmochimica Acta, v. 160, p. 169-187

Mole, D.R., et al. 2014, Archean komatiite volcanism controlled by the evolution of early continents: Proceedings to the National Academy of Science USA, v. 111, p. 10083-10088.

Moroni, M., Caruso, S., Barnes, S.J. and Fiorentini, M.L., 2017, Primary stratigraphic controls on ore mineral assemblages in the Wannaway komatiite-hosted nickel-sulfide deposit, Kambalda camp, Western Australia. Ore Geology Reviews, v. 90, p. 634–666.

Mueller, A.G., Hall, G.C., Nemchin, A.A., Stein, H.J., Creaser, R.A. and Mason, D.R., 2008, Archean high-Mg monzodiorite-syenite, epidote skarn, and biotite-sericite gold lodes in the Granny Smith-Wallaby district, Australia: U-Pb and Re-Os chronometry of two intrusion-related hydrothermal systems: Mineralium Deposita v. 43, p. 337-362.

Occhipinti, S.A., Sheppard, S., Passchier, C., Tyler, I.M. and Nelson, D.R., 2004, Palaeoproterozoic crustal accretion and collision in the southern Capricorn Orogen: the Glenburgh Orogeny: Precambrian Research, v. 128, p. 237-255.

Ono, S., Wing, B., Johnston, D., Farquhar, J. and Rumble, D., 2006, Mass-dependent fractionation of quadruple stable sulfur isotope system as a new tracer of sulfur biogeochemical cycles: Geochimica et Cosmochimica Acta, v. 70, p. 2238-2252.

Palin, J.M. and Xu, Y., 2000, Guilt by Association? Origins of Pyritic Gold Ores in the Victory Mesothermal Gold Deposit, Western Australia: Economic Geology v. 95, p. 1627-1634.

Paton C., Hellstrom J., Paul B., Woodhead J. and Hergt J., 2011, Iolite: freeware for the visulaisation and processing of mass spectrometry data: Journal of Analytical Atomic Spectrometry, v. 26, p. 2508-2518.

Penninston-Dorland, S.C., Wing, B.A., Nex, P.A.M., Kinnaird, J.A., Farquhar, J., Brown, M. and Sharman, E.R., 2008, Multiple sulfur isotopes reveal a magmatic origin for the Platreef platinum group element deposit, Bushveld Complex, South Africa: Geology, v. 36, p. 979–982.

Phillips G.N. and Groves D.I., 1983, The nature of Archaean gold-bearing fluids as deduced from gold deposits of Western Australia, Journal of the Geological Society of Australia, v. 30, p. 25-39.

Phillips G.N. and Powell R., 2010, Formation of fold deposits: a metamorphic devolatilisation model, Journal of Metamorphic Geology, v. 28, p. 689-718.

Pirajno, F. and Occhipinti, S.A., 2001, Three Palaeoproterozoic basins – Yerrida, Bryah and Padbury – Capricorn Orogen, Western Australia: Australian Journal of Earth Sciences, v. 47, p. 675-688.

Pirajno, F., 2004, Metallogeny in the Capricorn Orogen, Western Australia, the result of multiple ore-forming processes: Precambrian Research, v. 128, p. 411-439.

Pirajno, F., Chen, Y., Li, N., Li, C. and Zho, L., 2016, Besshi-type mineral systems in the Palaeoproterozoic Bryah rift basin, Capricorn Orogen, Western Australia: implications for tectonic setting and geodynamic evolution: Geoscience Frontiers, v. 7, p. 345-357.

Pirajno, F., Mernagh, T.P., Huston, D., Creaser, R.A. and Seltmann, R., 2016, The Mesoproterozoic Abra polymetallic sedimentary rock-hosted mineral deposit, Edmund Basin, Western Australia, Ore Geology Reviews, v. 76, p. 442-462.

Pokrovski, G.S. and Dubessy, J., 2015, Stability and abundance of the trisulfur radical ion S3- in hydrothermal fluids: Earth and Planetary Science Letters, v. 411, p. 298-309.

Reynolds, N. and Wilson, N., 2012, Exploration and resource potential of the Prairie Downs Project. Project evaluation report. Perth: CSA Global, pp.1, 4-12.

Ripley, E.M. and Li, C., 2017, A review of the application of multiple S isotopes to magmatic Ni-Cu-PGE deposits and the significance of spatially variable Δ33S values: Economic Geology, v. 112, p. 983-991.

Roche, L.K., 2014, Unravelling the upper amphibolite to granulite facies hosted Glenburgh Au deposit-metamorphosed gold? Glenburgh Terrane, Gascoyne Province, Western Australia. (University of Western Australia, MSc Thesis.

Schuhmacher, M., Fernandes, F. and De Chambost, E., 2003, Achieving high reproducibility isotope ratios with the Cameca IMS 1270 in the multicollection mode. Applied Surficial Science, v. 231-232, p. 878-882.

Selvaraja, V., Fiorentini, M.L., LaFlamme, C., Wing, B.A. and Bui, T.H., 2017a, Anomalous isotope signatures trace sulfur pathways in magmatic arcs: Geology, v. 45, p. 419-422.

Selvaraja, V., Caruso, S., Fiorentini, M.L., LaFlamme, C. and Bui, T.H., 2017b, Atmospheric sulfur in the orogenic gold deposits of the Archaean Yilgarn Craton: Geology, v. 45, p. 691-694.

Selvaraja, V., Fiorentini, M.L., Jeon, H., Savard, D.D., LaFlamme, C., Guagliardo, P., Caruso, S. and Bui, T.H., 2017c, Evidence of local sourcing of sulfur and gold in an Archaean sediment hosted gold deposit: Ore Geology Reviews, v. 89, p. 909-930.

Sharman, E.R., Penniston-Dorland, S.C., Kinnaird, J.A., Nex, P.A.M., Brown, M., Wing, B.A., 2013, Primary origin of marginal Ni-Cu-PGE, mineralization in layered intrusions: Δ33S evidence from The Platreef, Bushveld, South Africa: Economic Geology, v. 108, p. 365-377.

Sheppard, S., Occhipinti, S.A. and Tyler, I.M., 2004, A 2005–1970 Ma Andean-type batholith in the southern Gascoyne Complex, Western Australia: Precambrian Research, v. 128, p. 257-277.

Sheppard, S., Occhipinti, S.A. and Nelson, D.R., 2005, Intracontinental reworking in the Capricorn Orogen, Western Australia: the 1680–1620 Ma Mangaroon Orogeny: Australian Journal of Earth Sciences, v. 52, p. 443-460.

Sheppard, S., Bodorkos, S., Johnson, S.P., Wingate, M.T.D. and Kirkland C.L., 2010, The Paleoproterozoic Capricorn Orogeny: intracontinental reworking not continent–continent collision: Geological Survey of Western Australia Report 108, 33 p.

Sugiono, D., 2016, Sulfur isotope analysis at Archean gold deposits in Agnew Camp, Yilgarn Craton. University of Western Australia, MSc unpublished thesis. 66 p.

Thébaud, N., Sugiono, D., LaFlamme, C., Miller, J., Fisher, L., Voute, F., Tessalina, S., Sonntag, I., Fiorentini, M., 2018, The protracted and polyphased formation of the Agnew Gold Camp (Yilgarn Craton, Western Australia). Precambrian Research, v. 310, p. 291-304.

Thorne, A.M. and Trendall, A.F., 2001, Geology of the Fortescue Group, Pilbara Craton, Western Australia (No. 144). Geological Survey of Western Australia.

Tomkins, A.G., 2010, Windows of metamorphic sulfur liberation in the crust: implications for gold deposit genesis. Geochimica et Cosmochimica Acta, v. 74, p. 3246-3259.

Van Kronendonk, M.J., Smithies, R.H., Hickman, A.H. and Champion, D.C., 2007, Review: secular tectonic evolution of Archean continental crust: interplay between horizontal and vertical processes in the formation of the Pilbara Craton, Australia: Terra Nova, v. 19, p. 1-38.

Whitehouse, M., 2013, Multiple sulfur isotope determination by SIMS: Evaluation of reference sulfides for Δ33S with observations and a case study on the determination of Δ36S. Geostandards and Geoanalytical Research, v. 37, p. 19-33.

Wing, B. and Farquhar, J., 2015, Sulfur isotope homogeneity of lunar mare basalts: Geochimica et Cosmochimica Acta, v. 170, p. 266-280.

Xue, Y., Campbell, I.H., Ireland, T.R., Holden, P. and Armstrong, R., 2013, No mass-independent sulfur isotope fractionation in auriferous fluids supports a magmatic origin for Archean gold deposits. Geology, v. 41, p. 791-794.

Theme 6: 3D Digital Model Using Virtual Environments for Data Integration and Visualization

Theme 6A: Data Integration and Visual Analytics

P. Golodoniuc, N. Reid, A. Davis, A. Brown, A. Cornelius, V. Fazio, J. Klump, C. Soerensen, V. Metelka, A. Sobotkova, and B. Ballsun-Stanton

Theme 6B: Imaging 3D structure of the Paleoproterozoic Yerrida Basin with integrated structural interpretation and modelling

Mark Lindsay, Sandra Occhipinti, Lara Ramos, Crystal LaFlamme, Alan Aitken

4 Theme 6A: Data Integration and Visual Analytics

P. Golodoniuc, N. Reid, A. Davis, A. Brown, A. Cornelius, V. Fazio, J. Klump, C. Soerensen, V. Metelka, A. Sobotkova, and B. Ballsun-Stanton

4.1 Introduction

The Data Integration Theme enabled building the original SIEF project to a Program from crust to surface, with critical data integration. The data sets collected in Themes 1 to 5 are large and multi-scale. It was critical to enable integration and visualisation of these data sets and to develop tools for virtual interrogation of the data and production of 3D models that can be used in exploration targeting. This Theme developed a dedicated data management process and runs alongside the project to capture the data and enable data integration between software packages. Integration with the International GeoSample Number (IGSN) system played important role in cataloguing of samples and enabling data discovery via national and international IGSN registries.

This program also provided capability to the geophysics theme (Theme 2, Program 2.1 – Regional Cover Characterisation using Airborne Electromagnetic Data) to explore high performance data intensive data processing and visualisation of Airborne Electromagnetic (AEM) data sets. This provided insights how industry can benefit from new generation processing power and data integration for planning and targeting in exploration campaigns, model development and simulation of mineral system processes as well as to output the data through a common platform.

4.2 Data management

A data model and a respective spatial database have been developed to accommodate storage of heterogeneous specimen data along with laboratory measurements and metadata associated with sampling methods. The data model is compatible with the Open Geospatial Consortium (OGC) standards and ISO Observations and Measurements (O&M) conceptual model that ensures seamless integration between information systems via the use of open standards. The database was progressively populated with the project data and at the time of publication of this report consists of sample data for:

- 4,287 water samples
- 495 rockchip samples
- 367 regolith samples

including over 320K of observations and measurements taken on these samples.

Data infrastructure includes a spatial database management system managed by CSIRO, data management web-based application for data upload and classification of the data (Figure 4.1), and web services to enable discovery and access interface to the data.

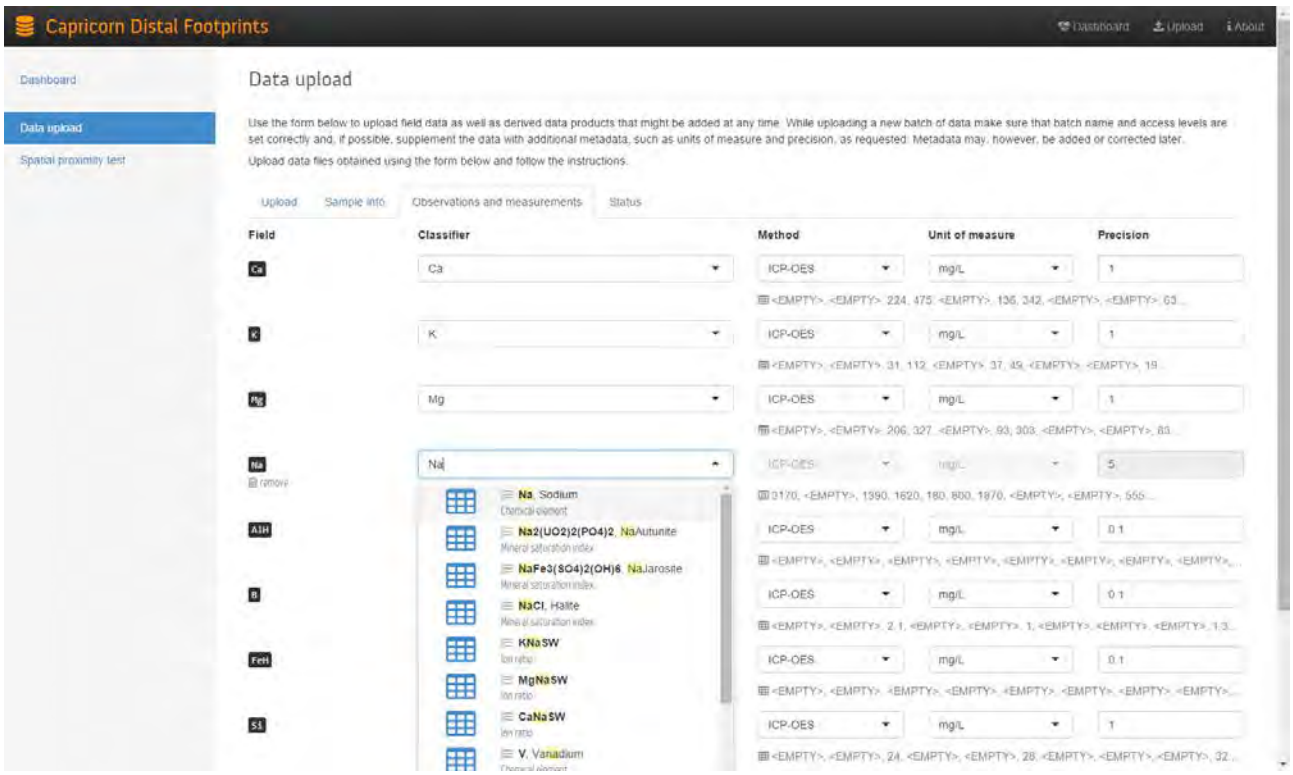

Figure 4.1. Web-based data management tool. Upload and data classification interface.

Data access is provided via Open Geospatial Consortium (OGC) Web Feature and Web Mapping Services (WFS/WMS) as well as stand-alone ArcGIS data products. The latter capture sample geospatial information, IGSN numbers, and metadata, whereas detailed laboratory measurements data is provided via secure Web Feature Service (Figure 4.2–4.3).

4.2.1 International GeoSample Number (IGSN)

Earth sciences are largely observational and rely on natural samples, types of which vary significantly between science disciplines. Sharing and referencing of samples in scientific literature and across the Web requires the use of globally unique identifiers essential for disambiguation. This practice is very common in other fields, e.g. ISBN in publishing, doi in scientific literature, etc. In Earth sciences however, this is still often done in an ad-hoc manner without the use of unique identifiers. The International Geo Sample Number (IGSN) system provides a persistent, globally unique label for identifying environmental samples.

The International Geo Sample Number (IGSN) provides an identifier system that is a persistent, globally unique label for environmental samples that are taken out of the natural environment or described in-situ. IGSN is governed by an international implementation organisation (IGSN e.V). CSIRO, along with Geoscience Australia and Curtin University, has recently become an allocating agent for IGSN. CSIRO developed an IGSN registration service and a descriptive metadata schema (Devaraju, 2015) to coordinate the IGSN registrations by different groups within the organisation. The Capricorn Distal Footprints project was one of the first projects to integrate the IGSN in its samples curation system. The adoption of IGSN will provide a common platform for referencing physical samples, their derived products and linking to datasets. The project aims at implementing a system that will provide a unified catalogue of samples, linking samples to data collected by researchers and historical data obtained through partner organisations.

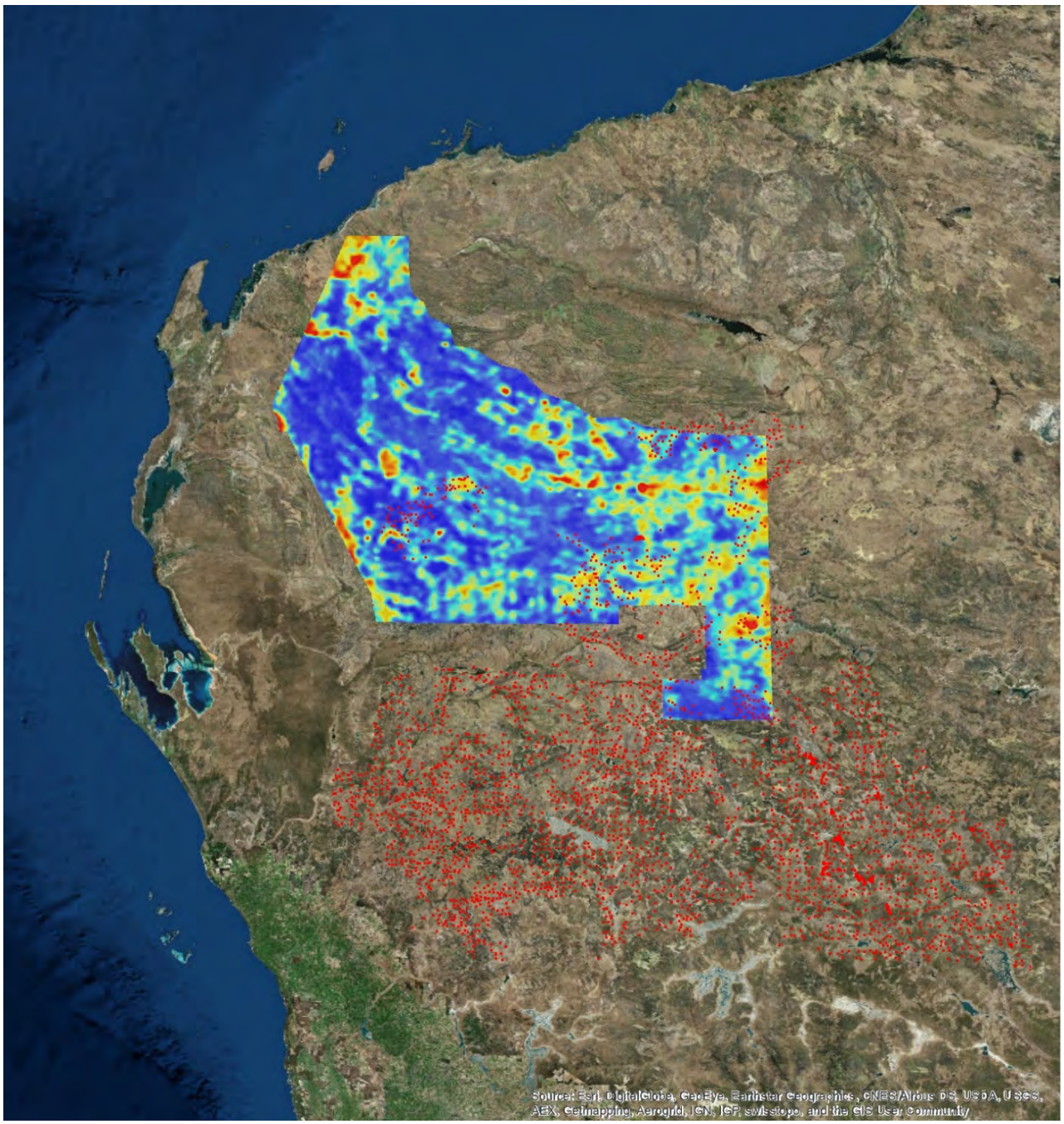

Figure 4.2. Sample database access via OGC Web Feature Service (WFS).

IGSN provides a mechanism for identification of new and legacy samples, as well as derived sub-samples. It ensures transparency and reproducibility in various geochemical sampling campaigns that involve a diversity of sampling methods. Hence, diverse geochemical and isotopic results are linked back to the parent sample, particularly where multiple children of that sample have also been analysed. This study has demonstrated the effectiveness of the proposed approach, while maintaining the flexibility to adapt to various media types, which is critical in the context of a multi-disciplinary project. The unambiguous identification of samples ultimately adds to the goal of enabling synoptic integration of heterogeneous geochemical datasets for regional-scale exploration.

- **Integration**

The data management system has been fully integrated with the International GeoSample Number (IGSN) system – unique IGSN numbers issued to 4,212 samples and registered in both Australian National IGSN Repository and the International IGSN Registry (Figure 4.3).

CSIRO hosts landing pages for the universally resolvable IGSN numbers and provides information about samples as per specified access policies.

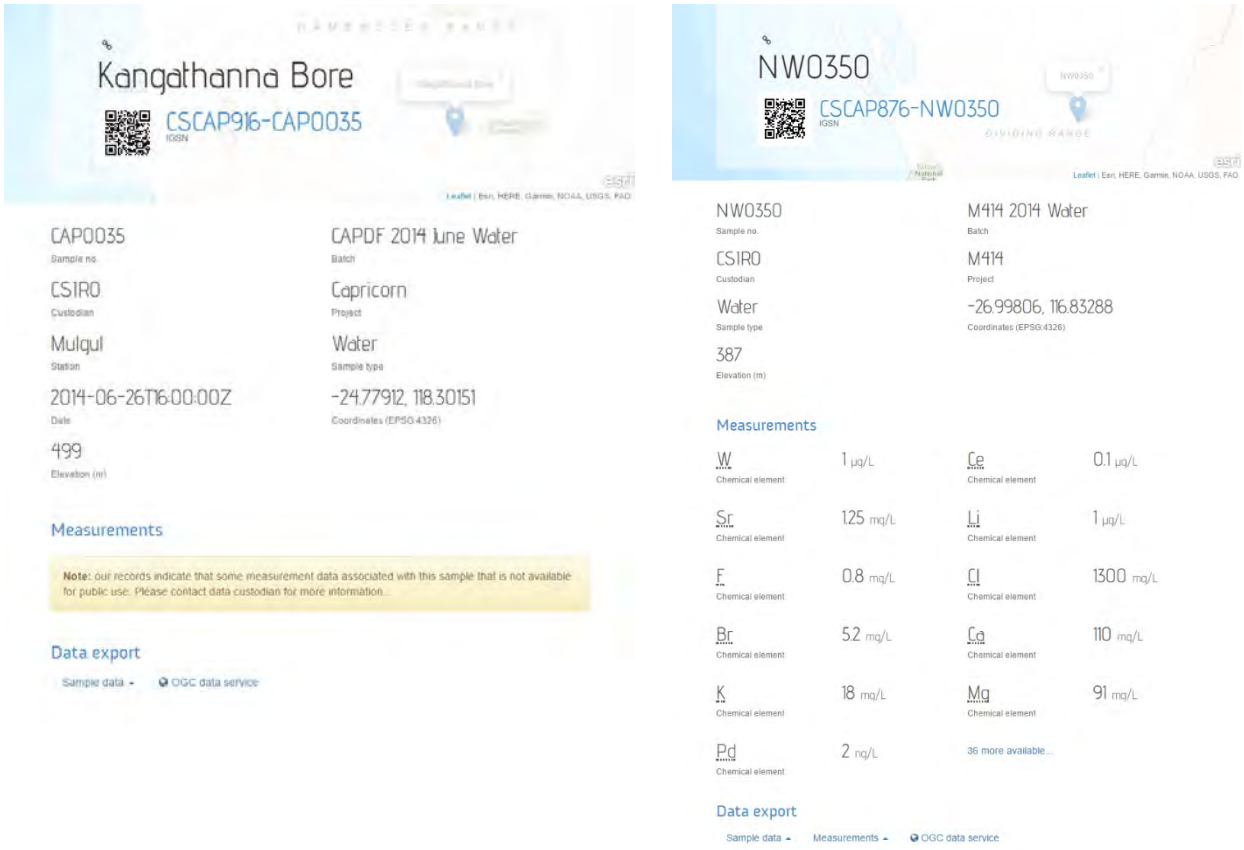

Figure 4.3. International GeoSample Numbers (IGSN) allocated to collected water samples along with associated laboratory measurement data.

- **Long-term data preservation**

Data Management Plan (DMP) plan has been developed that includes provisioning for mandatory IGSN allocation for sample data and post-project data infrastructure sustainability plan. The sample database and the database management application are now switched to read-only mode as the data has been archived in CSIRO Data Access Portal as per corporate data management policies.

4.3 FAIMS Field Data Acquisition application

4.3.1 Introduction

Capricorn Distal Footprints projects relies on large regional datasets obtained from previous hydrogeochemical, regolith, and resistate mineral studies around known deposits, as well as new data obtained from the recent field sampling campaigns around areas of interest. With thousands of water, vegetation, rock and soil samples collected over the past years, it has prompted us to look at ways to standardise field sampling procedures and review the data acquisition process. This process has evolved over the years (Golodoniuc et al., 2015; Klump et al., 2015) and has now reached the phase where fast and reliable collection of scientific data in remote areas is possible. The approach is backed by a unified discipline-agnostic platform – the Field Acquired Information Management System (FAIMS).

FAIMS is an open source framework for building mobile applications, developed at the University of New South Wales for archaeological field data collection. The FAIMS framework can easily be adapted to a diverse range of scenarios, different kinds of samples, each with its own peculiarities, integration with GPS, and the ability to associate photographs taken with the device embedded camera with captured data. Various modules have been developed so far (Figure 4.4), dedicated to geochemical water, soil, plant and rock sampling. All modules feature automatic date and position recording and reproduce the established data recording workflows. The rock sampling module also features an interactive GIS component allowing to enter field observations as annotations to a map. The open communication protocols and file formats used by FAIMS modules allow easy integration with existing spatial data infrastructures and third-party applications, such as ArcGIS.

All modules were trialled in the field on various occasions throughout the course of the project and feedback contributed to further improvement of the mobile application. The background for the sampling protocols for each sample type has come from CSIRO sampling protocols. Hydrogeochemistry field data book developed within the DET CRC formed the basis for the sampling procedure. This book was turned into the original ‘alpha’ test for the mobile application, which was trialled at Prairie Downs field sampling campaign with moderate success. This, in turn, has led to a more streamlined hydrogeochemical sampling protocol (providing input into Theme 4) as well as to the development of sampling protocols for other material types (e.g., plants, soils, etc.).

The remoteness of the focus areas in the Capricorn region required reliable mechanisms for data replication and an added level of redundancy. This was achieved with the FAIMS Server without adding a tightly coupled dependency on it – the mobile devices could continue to work independently in the case the server fails. To support collaborative fieldwork, “FAIMS on a Truck” offers networked collaboration within a field team using mobile applications as asynchronous rich clients. The framework runs on compatible Android devices (e.g., tablets, smart phones) with the network infrastructure supported by a FAIMS Server. The server component is installed in a field vehicle to provide data synchronisation between multiple mobile devices, backup and data transfer. The data entry process was streamlined and followed the workflow that field crews were accustomed to with added data validation capabilities.

The use of a common platform allowed us to adopt the framework within multiple disciplines, improve data acquisition times, and reduce human-introduced errors. We continue to work with other research groups and continue to explore the possibilities to adopt the technology in other applications, e.g., agriculture.

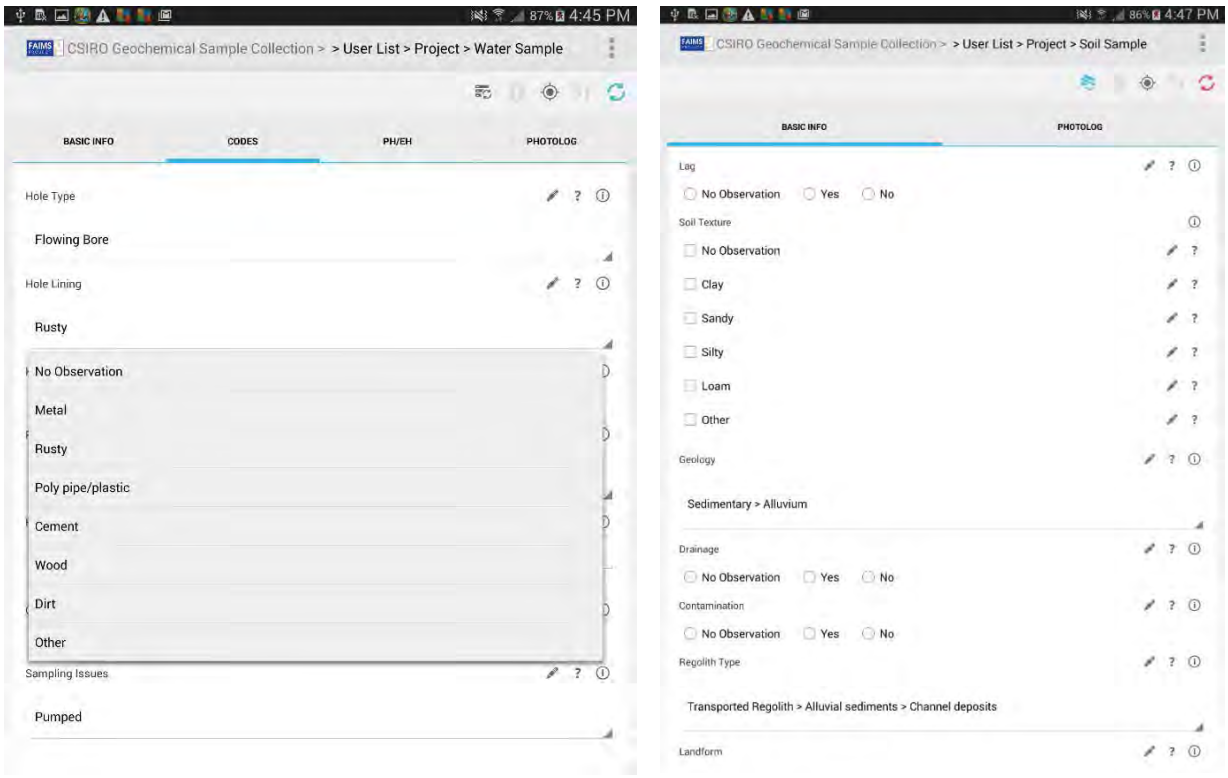

Figure 4.4. Water sample information with dropdown options (left) and soil sample sheet (right).

4.3.2 Capabilities

The capabilities of the mobile app include:

- using in-built or Bluetooth GPS to locate sample points (Figure 4.5);
- incorporates standard and incremental sampling names which are fed into the International GeoSample Number (IGSN) registry;
- allows for photo taking and tagging with the sample, sketches, user tagging per sample, dropdown menus for predetermined fields specific for each sample type;
- records viewer;
- basic mapping functionality showing the sampled points overlying maps (as GeoTIFF) that can be pre-loaded, it shows your current location, and allows for drawing of points and simple polygons to be later exported as shape files.

The field data acquisition system was commissioned as a vehicle-mounted portable server for complete autonomy where data connectivity is not available. This server box is constantly syncing with the tablets in the field via portable Wi-Fi access point (up to 100 m). It has a UPS that can run for up to 45 minutes when the vehicle is turned off, and a 1TB hard drive for storage of all data and photographs. The server can be logged into via any of the field tablets or laptop to download all the data collected to date or to just view it on the server.

The app has also been tested in the field (Figure 4.6) for soils and rock sampling. The outcomes of this trial led into developing the workflows for predicting and detecting the footprints of mineralisation in covered terrains.

The FAIMS framework along with custom-made data logging modules is released under open-source licence and is readily available for the industry uptake. Commercial organisations also manufacture FAIMS Server autonomous boxes.

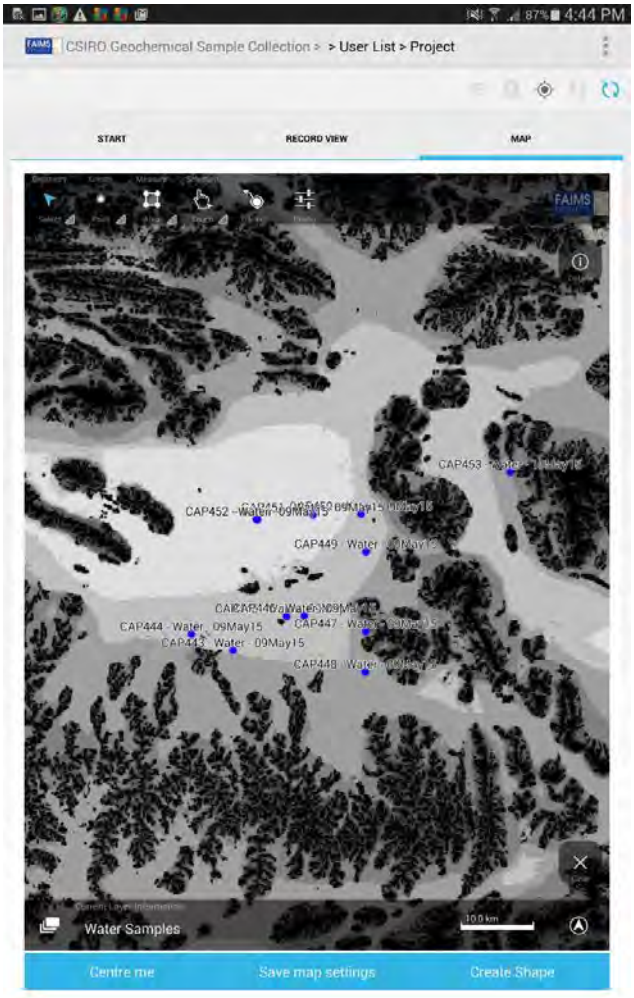

Figure 4.5. Mapping: water samples overlying the MrVBF imagery.

Figure 4.6. Field app and server being used in the field.

4.4 Airborne Electromagnetic (AEM) survey data processing

4.4.1 Introduction

Electromagnetic exploration techniques are extensively used for remote detection and measurement of subsurface electrical conductivity structures for a variety of geophysical applications such as mineral exploration and groundwater detection. Airborne electromagnetic (AEM) data is routinely used for the development of new exploration methods and feeds directly into Themes 1–2. It is often originally acquired for green- or brown-fields exploration for minerals but can be re-used for groundwater resource detection in the near-surface. This makes AEM data potentially useful beyond their initial purpose for decades into the future. Increasingly, AEM data are also used as a primary mapping tool for groundwater resources.

With surveys ranging from under 1000 km to tens of thousands of kilometres in total length, AEM data are spatially and temporally dense. Sounding stations are often sampled every 0.2 seconds, with about 30-50 measurements taken at each site, resulting in spacing of measurements along the flight lines of approximately 20-50 metres. This means that the size of a typical AEM surveys is in the order of millions of individual stations, with tens of millions of measurements.

Due to intrinsic noise of measurement equipment and noise induced by ground structures (e.g., powerlines, railways, sheds, etc.), AEM data needs to be examined for data quality before it can be inverted into conductivity-depth information. Data, which is gathered in survey transects or lines, is examined both along the line, in a plan view and for the transient decay of the electromagnetic signal of individual stations before noise artefacts can be removed. Certain noise artefacts can be efficiently detected and removed using numerical methods. Geospatial methods, e.g., proximity to ground structures, can also be employed in conjunction with auxiliary GIS data sets.

The complexity of the data, its size and dimensionality require efficient tools that support interactive visual data analysis and allow easy navigation through the dataset. A suite of numerical algorithms for data quality assurance facilitates this process through efficient visualisations and data quality metrics. The extensible architecture of the AEM Processing Toolkit (AEMVL) allows application of custom algorithms on-demand through a web-based user interface that seamlessly connects data processing workflow to geophysical inversion codes. Web-based platform for software delivery is chosen consciously to increase accessibility from the widest possible range of devices and operating systems. The toolkit architecture has a small client-side footprint and runs on a standard workstation, delegating all computationally-intensive tasks to the accompanying cloud-based processing unit.

4.4.2 Scope

To facilitate development of new exploration methods CSIRO required an operational platform that would provide elaborate interactive visualisation of large AEM surveys and flexibility to experiment with numerical codes without specialist knowledge in software application development. Interactive visualisations are at the core of data pre-processing phase — offering a suite of tools to inspect and remove noisy or inferior data before it can be further processed. Our approach to visualisation of the AEM survey data included development of a dashboard that incorporates (a) the survey plan (i.e. a map view) with topography, infrastructure, and satellite imagery along (b) the decay profile, so that the decays of the transients from individual soundings are seen versus time scale, and (c) individual soundings of decay-value versus time for single stations. These data views are linked together so that information in all three views can be updated and co-located. The user needs to be able to mask data out of the workflow and change the noise characteristics of the data in the survey. This immensely helps in the quality control of AEM data and forms

a baseline data snapshot before it can be inverted using a variety of methods and the results brought back for further visual analysis.

To improve human-computer interaction a range of techniques was applied including interactivity, data scaling, data-focusing and linking (Buja A. *et al.*, 1991; Buja A. *et al.*, 1996). Observation of user behaviour and analysis of visual data perception has contributed to design of visualisation components.

Additional attention is given to provenance tracking. It is important that the whole process is tracked so that future users can understand the steps taken to produce certain results. This is particularly important since most AEM data exists in the public domain and to improve the life cycle of the AEM data, we need to be able to maintain the digital value chain.

Although computer programs with such functionality exist, the workflow for accessing the existing codes is overly complex, slow and non-transparent, whereas numerical codes are often embedded and integration with new experimental codes is nearly impossible. Our solution streamlined the processing environment that is capable of efficiently handling spatially and temporally dense data sets on the order of several gigabytes.

4.4.3 AEM Processing Toolkit

Representing multi-dimensional data sensibly in static visualisations is notoriously difficult exercise. Multi-view representation offers a variety of perspectives on the same information depending on the current context and user actions. Interactivity encourages engagement with the data and empowers users to explore and analyse large data sets from a range of scales and perspectives. In our implementation we followed the Visual Information-Seeking Mantra, outlined by Ben Shneiderman (1996): overview first, zoom and filter, then details-on-demand.

Figure 4.7 demonstrates the AEM survey visualisation dashboard that consists of (a) plan view with a sidebar outlining survey structure and offering access to additional functionality (e.g., base maps, overlays, heatmaps, etc.), (b) decay profile showing decays of the transients from individual soundings versus time scale, and (c) individual soundings of decay-value versus time for single stations. The dashboard provides an inter-connected display of the AEM survey where actions in one view are reflected in all other views live. We employed modern rendering techniques, e.g., Scalable Vector Graphics (SVG) and Web Graphics Library (WebGL) along with high-performance data manipulation JavaScript libraries to achieve low latency rendering. Plan view also implements a combination of Douglas-Peucker (Douglas and Peucker, 1973) and Radial Distance algorithms for polyline simplification that significantly reduces the number of points being rendered on the canvas with no visual effect on polyline quality (i.e. shape).

The dashboard provides functionality to switch base maps and overlay AEM survey data with auxiliary GIS data or compute-generated visualisations, e.g., heatmaps to show generalised representation and variability of geophysical properties.

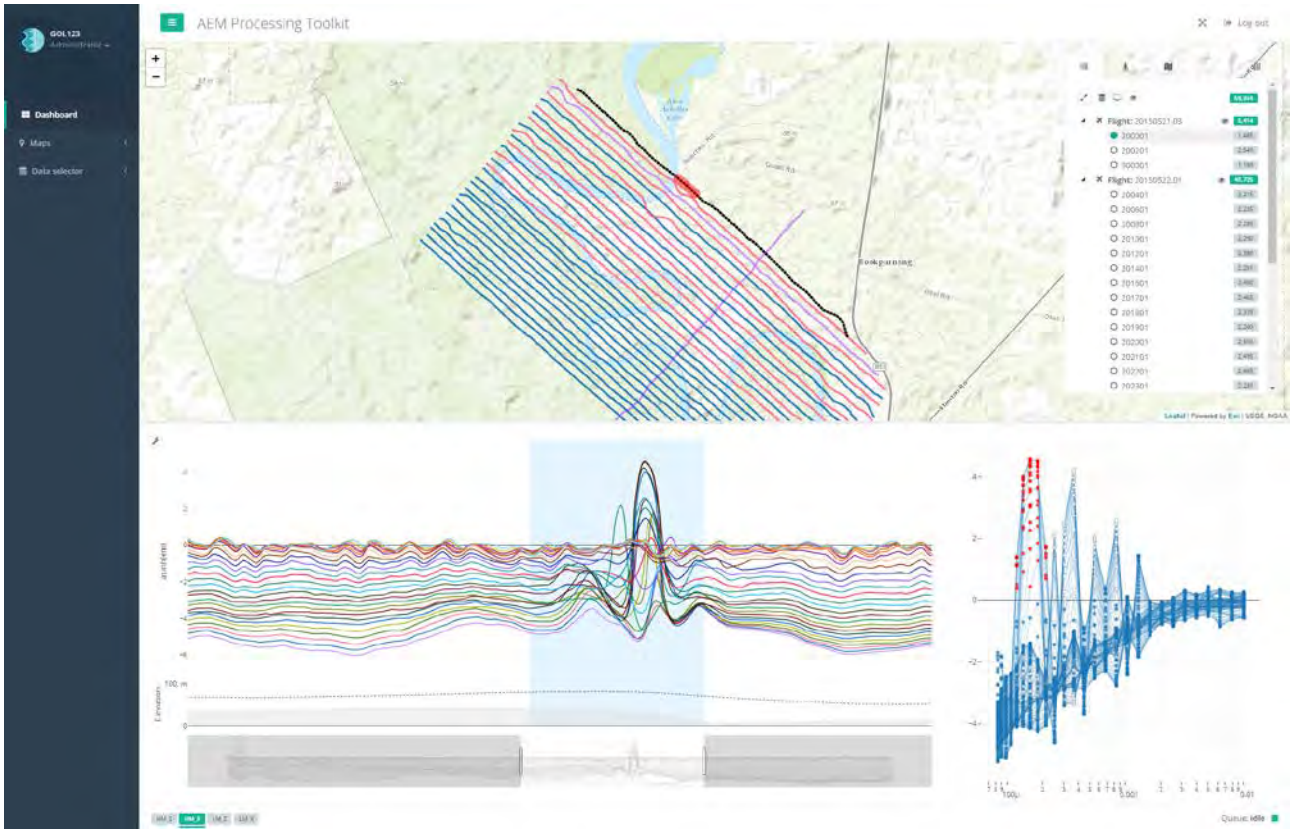

Figure 4.7. Interactive multi-view dashboard to provide inter-connected multi-dimensional visualisation of the AEM survey data: (top) survey plan as a map view with a sidebar outlining survey structure and additional functionality (base maps, overlays, heatmaps, etc.); (bottom left) decay profile view with zoom, focus and live cursor tracking; (bottom right) individual soundings of decay-value versus time for single stations.

- **Data-focusing and cursor tracking**

Dynamic and interactive visualisations encourage even greater engagement with the data when combined with clever user-guided animated transitions. This naturally establishes cognitive links between inspected sections of the data and allows deeper understanding of how data is connected or varies.

Decay profile view offers live cursor tracking functionality for all channels of a selected flight line in various modes: (a) live cursor tracking for an individual sounding of decay-value, (b) selection of a section of soundings along the flight line, and (c) 'frozen' view of an individual sounding or a section of soundings (Figure 4.8). Selection is automatically reflected in the adjacent view (right) for soundings of decay-value versus time.

4.4.4 Complete scientific workflow

AEM Processing Toolkit is a medium designed to connect users, visualisation tools, numerical algorithms, and computing infrastructure. Its architecture offers a range of extensibility interfaces – custom visualisation dashboards, data overlay widgets, numerical algorithms, as well as flexibility in the choice of cloud compute and storage infrastructures.

We implemented various visualisation widgets to provide a generalised view of AEM survey geophysical properties via interactive heatmaps (Figure 4.9). Near real-time performance is achieved with a range of techniques, e.g., dimensionality reduction, use of pre-computed data, caching, etc.

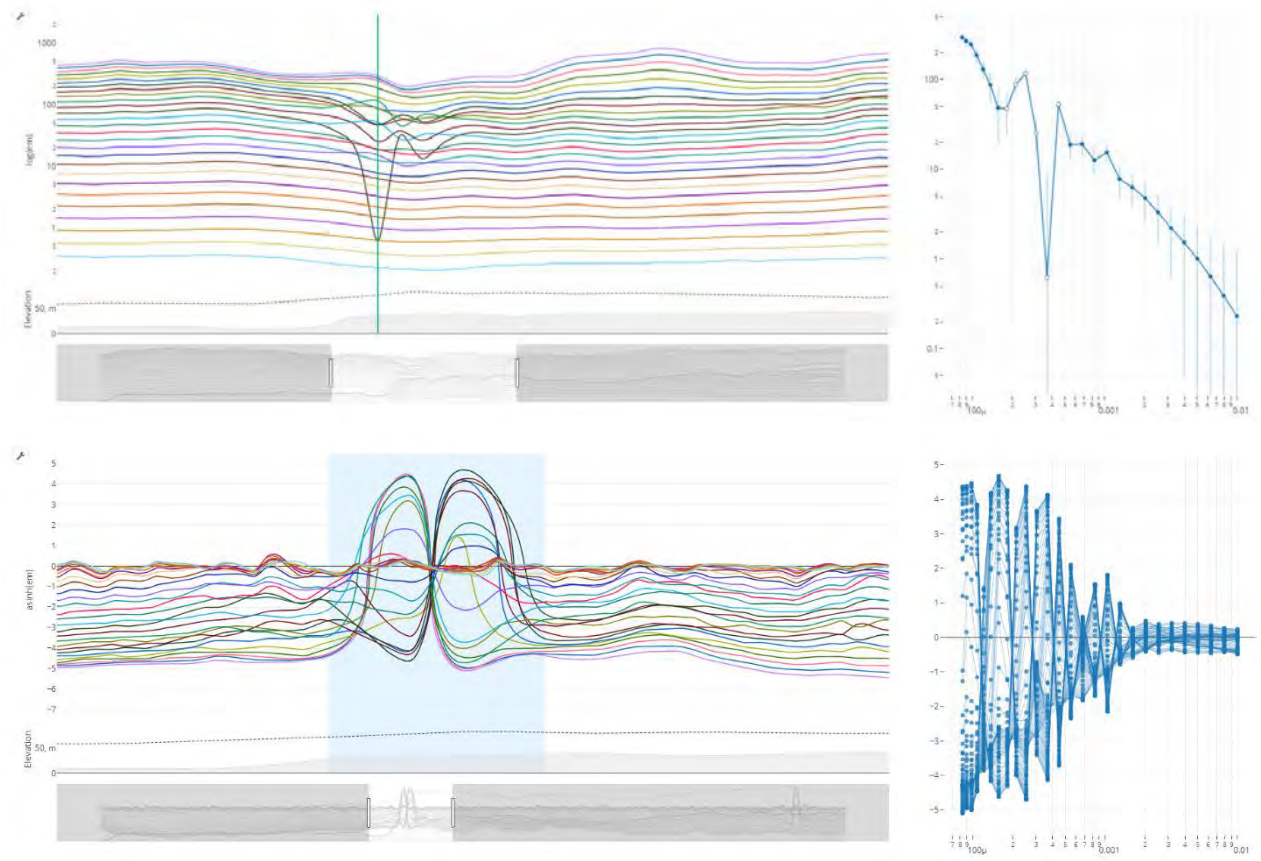

Figure 4.8. Live cursor tracking over decay profile modes: (top) live cursor tracking for an individual sounding of decay-value – right view implements animated transitions according to cursor position, (bottom) a section of sounding (bottom left) and editable decay-value versus time view (bottom right).

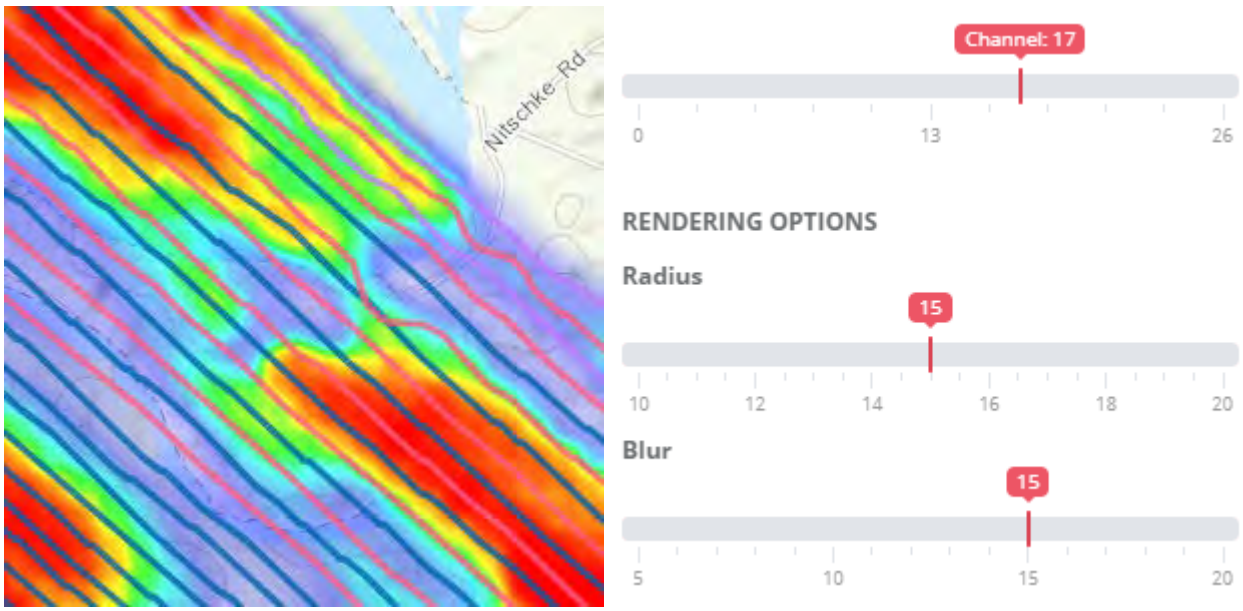

Figure 4.9. Interactive heatmap displaying generalised AEM survey geophysical properties.

A suite of assistive technology algorithms was designed to simplify and guide the user through data quality control procedure, including automatic noise detection and removal using mathematical, statistical and geospatial algorithms. AEMVL architecture and cloud deployment strategy allows users to introduce experimental codes without compromising the intellectual property sharing constraints as it is designed to run in an isolated virtual machine environment.

A similar approach is used to allow integration with existing third-party and proprietary experimental inversion codes. This encourages re-use of code, enables transparency, and reproducibility of the research. The toolkit is designed to be integrated with the CSIRO Earth Analytics Industry Innovation Hub (EAIIH) that implements a Science-as-a-Service approach to science delivery for Industry. This inherently provides:

- Data – data discovery and integration are simplified;
- Choice – your data, your algorithm, your parameterisation;
- Scalability – via cloud computing and automation you can explore the whole innovation landscape, to the limits of your time and expense budget;
- Science-as-a-Service – connecting new algorithms into broader business process;
- Lower upfront cost – subscribing to access and 'pay for what you use' to prove out a new market opportunity.

4.4.5 Impact and future research direction

This project directly impacts all aspects of airborne electromagnetic processing for minerals, groundwater, environmental and geo-technical applications. It could also be expanded to the use of ground-based electromagnetic applications, which is another important field. Intuitive workflow offers extensibility interfaces for future development that improves the efficiency of routine tasks of a geophysical data analyst and interpreter.

Interactive visualisations are at the core of the visual analytics approach to data science and this extends to other data-intensive science domains, including geosciences. AEM Processing Toolkit implements this approach, which has proven to add value as compared to static data visualisations. Focus, zoom/filter, and drill down methodology empowers and encourages users to explore data on their own, detect patterns and anomalies in the data and draw informed conclusions. Well-crafted visualisation is a great medium for exploratory data analysis, science communication and mechanism to engage audience. Although, publication of dynamic visualisations and capture of a specific state and context is still a challenge. This, however, is a topic for a separate discussion.

In our future research we will explore 3D visualisation techniques and immersive technologies, e.g., virtual reality (VR) and augmented reality (AR). In conjunction with this, we will conduct a broader study on the human perception of the information presented in these immersive environments.

4.5 References

Buja A., McDonald J.A., Michalak J. and Stuetzle W., 1991. Interactive data visualization using focusing and linking, Visualization. Visualization '91, Proceedings., IEEE Conference on, San Diego, CA, pp. 156-163, 419. doi: 10.1109/VISUAL.1991.175794.

Buja A., Cook D. and Swayne D.F., 1996. Interactive high-dimensional data visualization, Journal of Computational and Graphical Statistics Vol. 5, Iss. 1. doi: 10.1080/10618600.1996.10474696.

Devaraju A., Klump J., Cox S.J.D., and Golodoniuc P., 2015, The Internet of Samples: Representing and publishing physical sample descriptions: Computers & Geosciences Journal, doi:10.1016/j.cageo.2016.07.018.

Douglas D.H. and Peucker T.K., 1973. Algorithms for the reduction of the number of points required to represent a digitized line or its caricature. Cartographica: The International Journal for Geographic Information and Geovisualization, 10(2), pp.112-122. doi: 10.3138/FM57-6770-U75U-7727.

Golodoniuc P., Klump J., Reid N., and Gray D., 2015, Mobile data acquisition technology evolution in hydrogeochemical applications: Extended abstract, 21st International Congress on Modelling and Simulation (MODSIM), Broadbeach, Australia.

Shneiderman B., 1996. The Eyes Have It: A task by data type taxonomy for information visualizations. In Proceedings of the IEEE Symposium on Visual Languages, Washington. IEEE Computer Society Press, pp. 336-343.

5 Theme 6B: Imaging 3D Structure of the Paleoproterozoic Yerrida Basin with Integrated Structural Interpretation and Modelling

Mark Lindsay, Sandra Occhipinti, Lara Ramos, Crystal LaFlamme, Alan Aitken

5.1 Introduction

The Paleoproterozoic Yerrida Basin is located on the northern margin of the Archean Yilgarn craton, within the southern part of the Capricorn Orogen (Figure 5.1) and extends approximately 150 km from north to south, and 180 km from east to west. Other Paleoproterozoic basins are located at the margins to the Yerrida: and Bryah-Padbury Basin (north and west) and Earaheedy Basin (east). Archean rocks also bound the basin with the northern extent of the Wiluna Greenstone belt to the southeast, and granites to the east. The Archean Goodin Inlier sits within the Yerrida Basin, and the Marymia Inlier is located to the north, in part separated from the Yerrida Basin by part of the Bryah Basin.

The development of the Yerrida Basin began with deposition of the c. 2200 Ma Windplain Group, followed by the 2180 to 1996 Ma Mooloogool and Bryah Groups (Occhipinti et al., 2017; Pirajno and Occhipinti, 2000). The rocks of the Windplain Group are representative of a shallow coastal and possible epicontinental setting (Occhipinti et al., 2017), while the rocks of the Bryah and Mooloogool Group were deposited in relatively higher-energy, possibly rift environments (Occhipinti et al; 2017; Pirajno and Adamides, 2000). Periods of magmatism are recorded primarily by the basaltic volcanics and intrusives of the Killara and Narracoota Formations (Mooloogool and Bryah Groups, respectively), though other mafic intrusive and extrusive rocks are observed in other formations (eg. Juderina and Karalundi Formations, Occhipinti et al., 2017) and as dykes (Mueller, 2011). The geodynamic evolution of the Yerrida Basin is interpreted as a pull-apart opening consistent with a trailing-edge marginal sag-basin (Pirajno and Occhipinti, 2000), progressing to a rift in its north (Bryah Sub-basin) (Occhipinti et al., 2017; Olierook et al., 2018). Continued extension resulted in the intrusion and extrusion of the Killara Formation tholeiitic basalts (Occhipinti et al., 1997). Basin development ceased with deposition of the Maraloou Formation (Mooloogool Group) shales and siltstones in a lacustrine environment (Occhipinti et al., 2017; Pirajno and Adamides, 2000; Pirajno and Occhipinti, 2000).

The Yerrida Basin presents an opportunity to examine geological architecture with a range of geophysical techniques. This opportunity exists because multiple geophysical data are required to delineate anomalies that can be interpreted to be structure, as no one physical field adequately reflects all the elements required to construct a meaningful model. The scenario just described is not unique, and typically any geological investigation using geophysics requires at least two physical fields to reveal architectural elements to the interpreter (Aitken and Betts, 2009; Blewett et al., 2010; Dufréchou et al., 2014; Lindsay et al., 2017; Perrouty et al., 2012). There may be cases where increased confidence is provided through interpreting anomalies present in multiple datasets as co-located anomalies in gravity and magnetic data. For example, if an anomaly is present in multiple datasets, it suggests it can be interpreted as structure: (i) the anomaly has not been introduced as an artefact during data processing and (ii) it is significant enough that it influences each of the represented physical fields to produce a detectable anomaly. An alternative viewpoint is to not only use multiple datasets as a validation mechanism to provide confidence, but to detect anomalies, and thus structure, when they cannot be detected when considering datasets individually. An example pertinent to this study is using electrical data to detect conductive anomalies and delineate different rock units in the near surface, while the potential field data does not provide the petrophysical contrast or resolution to achieve the same aim.

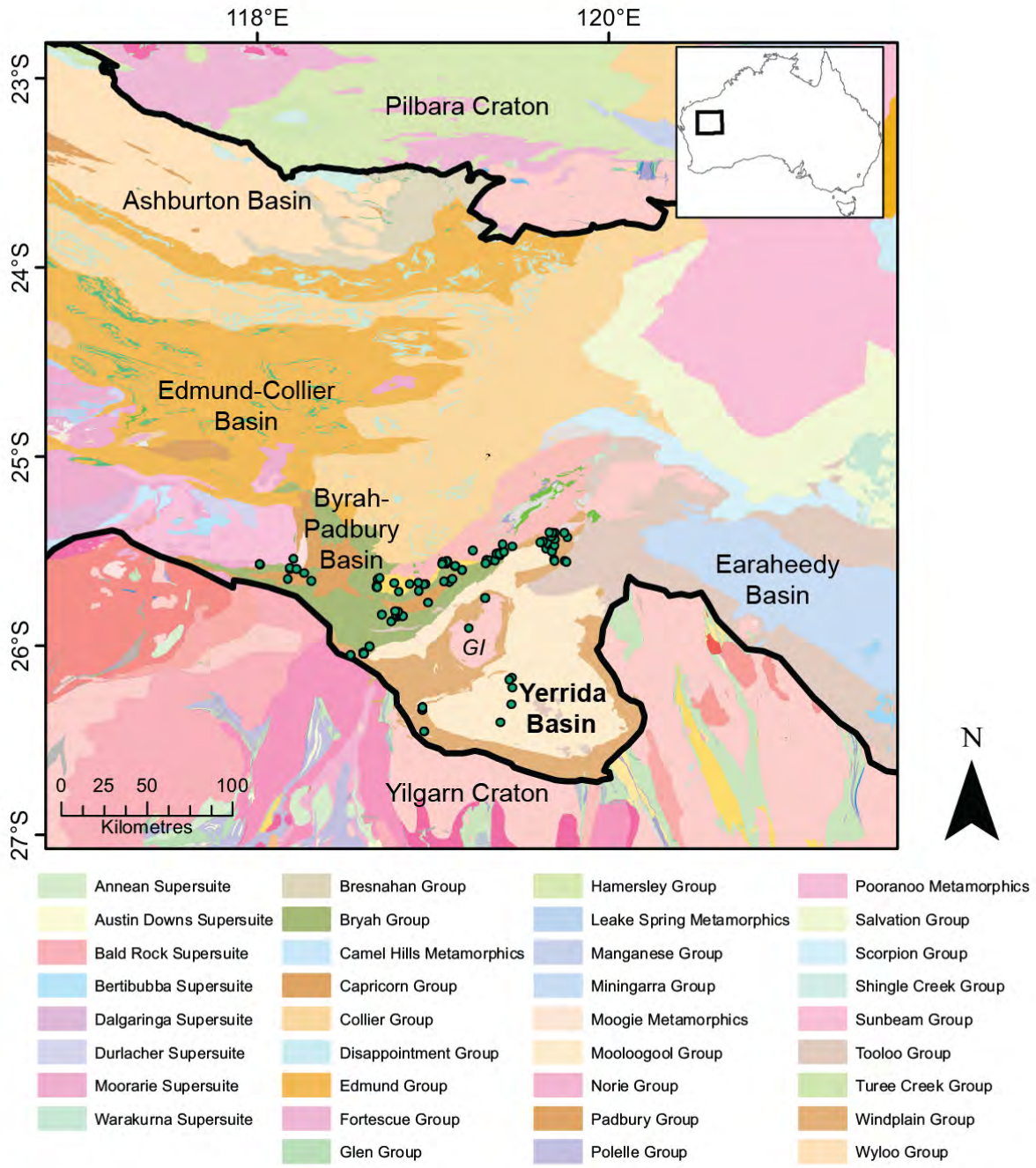

Figure 5.1. Location with deposits, site locations.

Electromagnetic (EM) data represents the electrical structure of the crust and is extensively used in exploration. EM data has been used to determine regolith profiles (González-Álvarez et al., 2016) and detect anomalies that may represent structure (Roach et al., 2014), ore bodies (Eberle et al., 2017; Peters and Buck, 2000) and rock bodies (Burschil et al., 2012; Schamper et al., 2014). The ability of EM data to detect conductive and resistive rock types is particularly useful in the Yerrida Basin as the degree of conductivity contrast allows discrimination of near-surface lithologies. In comparison, the magnetic susceptibility of the basin lithologies shows very little magnetic susceptibility contrast, and thus rendered the magnetic data to be less useful. Gravity data was found to be useful at larger scales, and identified high density anomalies, which were interpreted to be covered mafic units. The relatively low resolution of the gravity data precluded near-surface, detailed structural interpretation.

This paper describes how these different data sets were used to identify various parts of basin architecture through structural interpretation and geophysical forward modelling. Structure was interpreted through a combination of magnetic, EM and remotely-sensed data and integrated with petrophysical measurement and geological field observations. Geophysical modelling was used to further expand understanding of architecture into 3D. Geochemistry was used to determine whether the interpreted mafic bodies were likely to be the Killara Formation basalts, or different bodies that may be associated with the Juderina Formation, and thus suggesting a stratigraphic revision. The results were then considered to determine whether and where the Yerrida Basin may be prospective for VMS mineralisation.

This contribution presents a structurally- and petrophysically-constrained 3D model for the southern part of the Yerrida Basin, including the Mooloogool Sub-basin. The northern part of the Yerrida Basin (Bryah Sub-basin) was not included in the model because the basal units of the Windplain Group could not be delineated around it – in part due to the sub-basin being a deeper part of the Yerrida Basin, and also because of subsequent deformation during the Glenburgh and Capricorn Orogenies (Occhipinti et al., 2017; 2004).

5.2 Yerrida Basin geology

5.2.1 Definitions of bedrock, basement and cover

The Yerrida Basin is located in the southern part of the Paleoproterozoic Capricorn Orogen between the Archean Pilbara and Yilgarn cratons. Periods of rifting and convergence caused the development of a series of basins over the Glenburgh Terrane, and the margins of the Pilbara and Yilgarn cratons (Occhipinti et al., 2004; Occhipinti et al., 1998; Sheppard et al., 2004). The Yerrida Basin formed as a result of rifting of the Yilgarn Craton at c. 2200 to 1990 Ma, and its development may have been arrested in response to collision of the Yilgarn Craton with the combined Pilbara Craton and Glenburgh Terrane during the 2002-1947 Ma Glenburgh Orogeny (Martin et al., 2016; Occhipinti et al., 2004; Occhipinti et al., 2017).

The southern Yerrida Basin provides a snapshot of its basal architecture. The main components of the southern Yerrida Basin under investigation can be classified as either bedrock, basement or cover. The Archean Goodin Inlier, situated in the centre on the basin is considered to be part of the basement, being part of the underlying Yilgarn Craton, and outcrops to form a significant geological and geophysical presence. Bedrock geology is considered to be the rocks attributed to the Windplain and Mooloogool Groups. Basement is considered to be Archean Yilgarn granites and greenstones. Cover rocks are considered to be transported and in-situ regolith rocks and sediments.

The stratigraphy of the Yerrida Basin (summarised in Table 5.1 and by (Occhipinti et al., 2017)) starts with the underlying basement rocks, and is comprised of granite-greenstone rock association typical of the Yilgarn Craton. The Wiluna Greenstone Belt is located at the southeastern edge of and unconformably overlain by the Yerrida Basin, the Merri Greenstone Belt is located at the eastern edge of the Basin and is unconformably overlain by both Yerrida and Earaheedy Basin rocks. Aside from greenstone rocks, Archean granites form the basement to the Yerrida Basin. The Goodin Inlier is a 30 x 45 km fragment of Archean granitic basement and is unconformably overlain by the basal units of the Yerrida Basin. Goodin Inlier rocks are heavily weathered, dominantly monzogranite and mostly undeformed, except at its southwestern margin. East-southeasterly trending mafic dykes intrude the Goodin Inlier and are marked by sericitised feldspars produced by contact metamorphism (ref). Sedimentation patterns were likely influenced by the Goodin Inlier and uplift early in basin development.

The southern Yerrida Basin rocks contain the Windplain and Mooloogool sub-groups (Table 5.1). At the base of the Windplain Group is the Juderina Formation, which comprises siliciclastic, carbonate, chert, chert breccia, volcaniclastic and (locally) mafic volcanic rocks. The Juderina Formation outcrops in the southern,

northwestern and northeastern parts of the Basins. Thickness varies from 300-400 m except in the north where it is at least 750 m thick. The basal Finlayson Member in the Juderina Formation is a quartz sandstone up to a few hundred metres thick (Occhipinti et al., 1997). The stromatolitic carbonate Bubble Well Member overlies the Finlayson Member and includes evaporitic beds (Occhipinti et al., 1997). Overlying the Juderina Formation are the shales, siltstones and dolostones of the Johnson Cairn Formation.

The Mooloogool Subgroup overlies the Windplain Subgroup and consists of the Thaduna, Doolgunna Killara and Maraloou Formations (Table 5.1). The age of the Mooloogool Subgroup is derived from the underlying Windplain Group and overlying Tooloo Group to be 2180 Ma to 1996 Ma. The Thaduna and Doolgunna formations consist of intercalated siltstones and sandstones. The tholeiitic basalts of the Killara Formation intrude, interdigitate and overlie the Thaduna and Doolgunna Formations, and also interdigitate with the shales at the base of the overlying carbonaceous and argillaceous Maraloou Formation (Pirajno and Adamides, 2000). These relationships suggest magmatism was coeval with sedimentation of Mooloogool rocks. (Pirajno and Adamides, 2000) observed basaltic sills interpreted to be part of the Killara Formation intruding the Juderina Formation in the east of the Yerrida Basin.

The Mooloogool Group is unconformably overlain by the Yelma Formation (Tooloo Group), which forms the base of the Earaheedy Basin. The Yelma Formation includes sandstone, siltstone, minor conglomerate, and locally, stromatolitic carbonate and chert breccia, and is overlain by the Sweetwaters Dolomite (Occhipinti et al., 2017).

Table 5.1. Stratigraphy of the Yerrida Basin and surrounding geology (modified from (Occhipinti et al., 2017)). Maximum thickness of sedimentary rock units is shown in the right-hand column, providing valuable constraints to 3D basin modelling. The Bubble Well and Finlayson Member thickness are part of the overall maximum thickness of the Juderina Formation.

Earaheedy Basin	Tooloo Group	*Yelma Formation*		2700m
Yerrida Basin	Mooloogool Sub-group	*Maraloou Formation*		1000m
		Killara Formation		1000m
		Doolgunna Formation		2000m
		Thaduna Formation		5000m
	Windplain Sub-group	*Johnson Cairn Formation*		1250m
			Bubble Well Member	(100m)
		Juderina Formation		1000m
			Finlayson Member	(160m)
Yilgarn Craton		*Basement*	Goodin Inlier	

5.2.2 Mineralisation

The Yerrida Basin and margins are host to volcanogenic massive sulphide (VMS; DeGrussa, Horseshoe Lights and Red Bore), epithermal copper (Thaduna) and Mississippi Valley-Type (MVT: Magellan) deposits (Hawke et al., 2015; Pirajno and Adamides, 2000; Pirajno et al., 2010) (Figure 5.1).

- **Volcanogenic massive sulphide mineralisation**

The DeGrussa Cu-Au-Ag VMS deposit is located on the northern margin of the Yerrida Basin and is hosted in a sequence of interfingered shales and siltstones of the Karalundi and mafic rocks of the Narracoota Formation within the Bryah Group of the Bryah Sub-basin (Hawke et al., 2015). These rocks are also host to the Horseshoe Lights and Red Bore VMS deposits. Formation of these VMS deposits has been attributed to an extensional and basin-forming tectonic setting during the Glenburgh Orogeny (Hawke et al., 2015).

- **Mississippi Valley-Type mineralisation**

The Magellan Pb deposit is located in the southeast of the Yerrida Basin, about 30 km from the town of Wiluna. The deposit is hosted in the Yelma Formation and is on, or close to an unconformity between the underlying Maraloou Formation. The Magellan deposit is described as being the result of weathering and oxidation of pre-existing MVT stratabound sulphides (Pirajno et al., 2010). The result of weathering is that the sulphides no longer exist which makes this unique in the MVT-style group.

5.3 Methods and datasets

5.3.1 Rock properties

Rock properties measured from samples collected from the study area provide an important constraint for any structural interpretation or modelling of geophysical data. Magnetic susceptibility and density properties help to guide reasonable discrimination of rock types from magnetic and gravity datasets during interpretation. The rock properties are also used to constrain geophysical ambiguity during forward and inverse modelling in an attempt to ensure that some representation of the target geology is maintained. The rock property data collected from the study area guided the classification of geological units in the structural interpretation and provided the basis of the susceptibility and density values used in forward modelling.

5.3.2 Potential Field Data

Magnetic data (Figure 5.2a) was obtained from the Geological Survey of Western Australia in grid form with an 80 m cell size that had been differentially reduced to the pole (dRTP) (Brett, 2013). The resulting dRTP grid is a mosaic of government-funded aeromagnetic surveys with line-spacings between 200 m and 400 m. Various transforms and filters were applied to the dRTP grid to subdue or enhance particular features and included tilt, vertical and horizontal derivatives, analytic signal, upward continuation and dynamic range compression (DRC - see Kovesi et al., 2012 for details).

Bouguer gravity data (Figure 5.2b) were obtained from the Australian National Database maintained by Geoscience Australia and have been corrected for terrain and spherical-cap effects. Older data from the eastern part of the Capricorn Orogen preserve topographic effects as only the most recently acquired surveys are terrain-corrected. Most gravity data have a station spacing of between two and four km, however in areas of more sparse coverage spacing can be up to 11 km. Gravity grids were produced with a cell size of one km to provide the necessary detail and coverage.

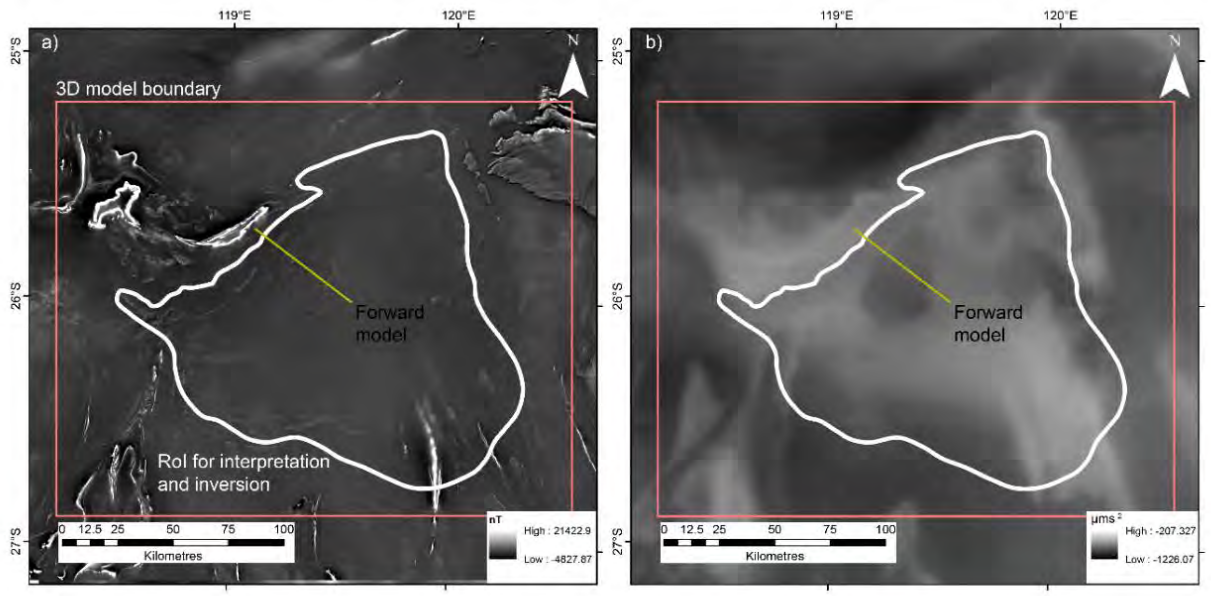

Figure 5.2. Geophysical grids and forward model location.

5.3.3 Structural Interpretation

Aeromagnetic data was used to interpret the upper crust to determine the smaller-scale structural architecture (e.g. (Aitken and Betts, 2008; Betts et al., 2007; Gunn et al., 1995; Lindsay et al., 2016b)). Significant time was devoted to processing to produce images deemed useful enough to perform an interpretation with confidence. Aspects of the magnetic data that confounded efforts to image the crust can be grouped into three categories: (1) the basin sedimentary rocks do not display enough magnetic susceptibility contrast to allow discrimination of structure; (2) the basin architecture is mostly flat-lying, thus most rock units boundaries (and thus potential locations of high petrophysical contrast) were parallel to the plane of view used during interpretation and: (3) highly susceptible regolith and stream sediments obscured the view of underlying structure.

Low-pass and upward continuation processing was used to remove the shorter wavelengths in the magnetic signal in order to lessen the obscuring effect associated with these magnetic cover units (Figure 5.3). Upward continuation also removed shorter wavelengths that may have been associated with the bedrock geology, making detailed near-surface structural interpretation more difficult.

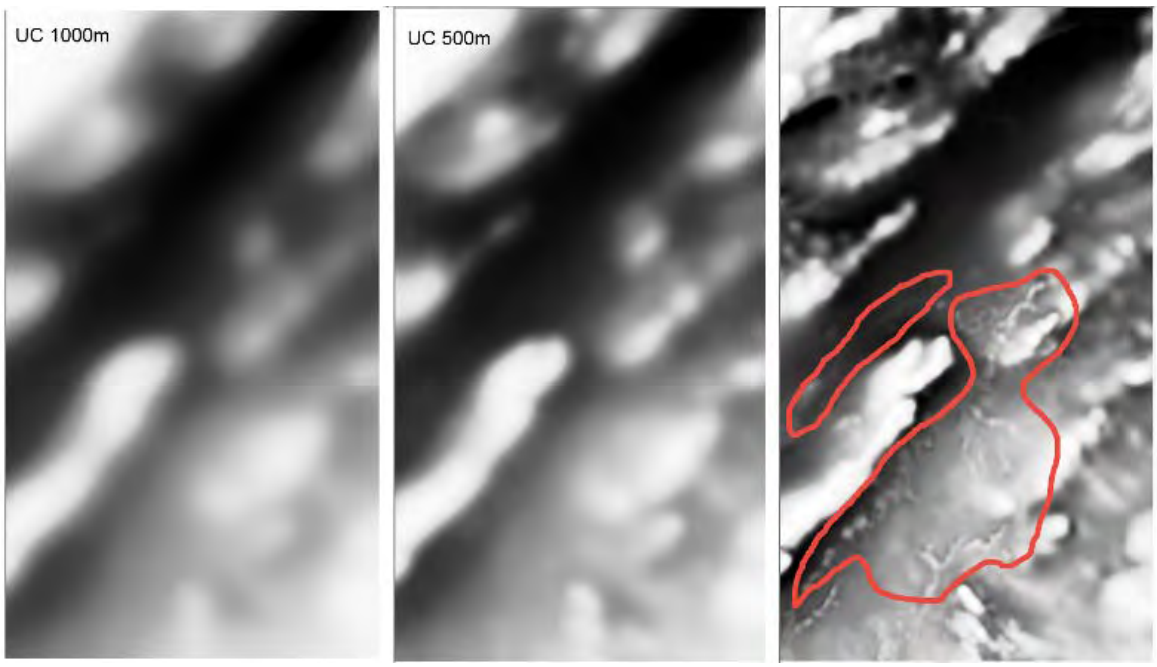

Figure 5.3 Results from upward continuation of magnetic data at 1000m and 500m. The right-hand image shows near-surface anomalies circled in red interpreted to be near-surface stream or channel sediments containing magnetic minerals. While spectacular and interesting for the geomorphologist, this was considered noisy when attempting to interpret the underlying basin rocks, and needed to be filtered.

The following filters proved the most useful for magnetic data in different areas on the Basin: first vertical derivative (1VD); auto-gain control (AGC); tilt-derivative (TDR) and dynamic range compression (DRC). 'Blending' grids facilitated better resolution of structure, where two grids are overlain, and one is made semi-transparent. This practice was particularly useful with the magnetic data. Bouguer gravity data and its 1VD was used to identify larger structures, and to provide additional insight to regions where magnetic susceptibility contrast was low (Almalki et al., 2015; Fairhead, 1976; Hildenbrand et al., 2000).

Field-based geological information was obtained from "WAROX" (the GSWA rock observation database) and used to locate some structures, but was principally employed to understand geometry and orientation of interpreted structures. WAROX data was invaluable for generating a 3D understanding.

5.3.4 Joint Magnetic and Gravity Forward Modelling

The map interpretation was supported by forward modelling along a section crossing the northwestern part of the Yerrida Basin (Figure 5.2a and b) to provide an understanding of the basin architecture at depth. The section transects the northwestern edge of the Yerrida Basin, the Goodin Inlier and part of the central part of the Basin. The structure and geology of the surface and upper crust was constrained predominantly by geological observations taken from WAROX and GSWA (Geological Survey of Western Australia) 1:100 000 and 1:250 000 scale maps (Appendix 1). The petrophysical model generated by forward modelling was supported and constrained with density and magnetic susceptibility data, as was the subsequent geological interpretation.

5.3.5 Airborne Electromagnetic data

The Capricorn 2013 AEM TEMPEST® (fixed-wing time-domain airborne electromagnetic) survey is one of the largest in Australia at 146,300 km^2 (Costello, 2014). Line-spacing is at 5km. Electromagnetic data (EM) measures the resistivity of rocks, and can image depths up to several hundred metres below the surface. Depth penetration depends primarily on the conductivity of the near surface, with highly conductive rocks or groundwater attenuating the EM signal measured by the sensor. If there is a conductive overburden for example, which is quite common in the Yerrida Basin, then the depth penetration can be relatively shallow, sometimes less than 30 m. Nonetheless, the TEMPEST data was useful in the Yerrida Basin at delineating lithological boundaries that were undetectable by magnetic data (due to lack of susceptibility contrast), gravity data (due to data resolution) or remote-sensing (due to widespread cover).

5.3.6 3D modelling and geophysical inversion

3D modelling was performed using Intrepid Geophysics Geomodeller© (Calcagno et al., 2008). The purpose of producing a model was two-fold: to better understand the 3D architecture of the basin; and to test the modelled architecture against observed regional geophysical response. Geophysical modelling techniques were both 3D forward modelling (Talwani and Heirtzler, 1964; Talwani et al., 1959) and geophysical inversion (Guillen et al., 2008). The Geomodeller software allows the stratigraphy to be defined, and interpreted structure to be assigned to each stratigraphic unit. As with all 3D modelling packages, some upscaling of data needs to be performed, so only the larger and more significant structures were included. This is because of limitations to these packages in producing detailed and mathematically complex geometries typically encountered in the natural world (Jessell et al., 2014). Stratigraphy was treated similarly, and the modelled units were limited to formations (i.e. the Finlayson and Bubble Well members were not modelled individually, but included in the Juderina Formation). The stratigraphic input data are summarised in Figure 5.4.

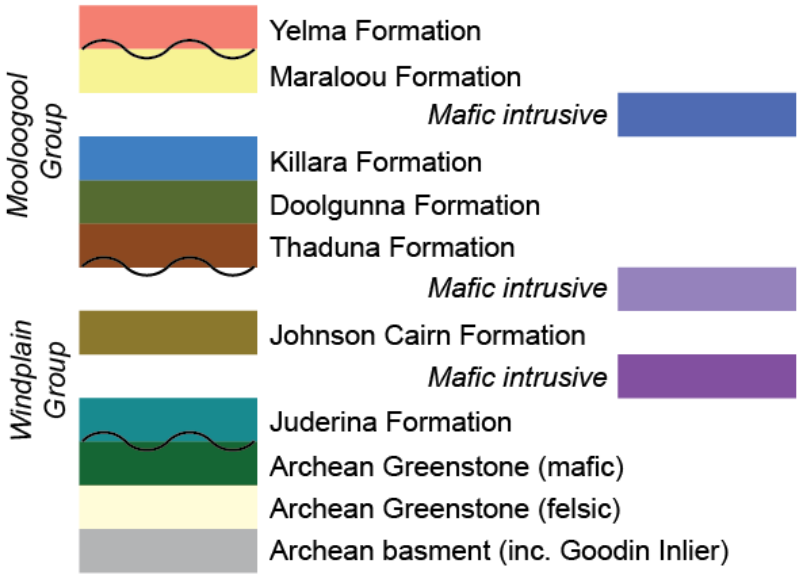

Figure 5.4. Stratigraphic input for Yerrida Basin 3D model.

5.4 Results

5.4.1 Petrophysics

Table 5.2 shows the measured values of both magnetic susceptibility (in SI×10^{-3} units) and density (gms/cm^3) from rocks representative of the Yerrida Basin stratigraphy and input for forward and inverse geophysical modelling. Figure 5.5 displays these values with error bars for magnetic susceptibility and Figure 5.6 shows the same but for density. The magnetic susceptibility values show very little variation between rock units. This, combined with the magnitude of error which envelops the range of susceptibility values across the measured rock unit, means that accurately differentiating geological bodies with magnetic data is highly unlikely. Density petrophysics do show greater variability between rock units with less error. This means that gravity data may be more useful than magnetic data to differentiate geological bodies during forward modelling, even at a lower resolution when compared to the magnetics data.

Table 5.2. Petrophysical statistics calculated from rock sample measurements.

Magnetic Susceptibility			
Formation / Rock type	*Sample size*	*Mean (SI×10^{-3})*	*SD (SI×$10^{-3)}$*
Dyke	30	0.006	0.004
Goodin Inlier	33	0.010	0.002
Juderina	164	0.005	0.004
Karalundi	44	0.005	0.003
Killara	56	0.006	0.006
Maraloou	85	0.005	0.004
Narracoota	127	0.003	0.003
Yilgarn Craton granitoid	22	0.006	0.004
Thaduna	32	0.007	0.005
Density			
		Mean (gm/cm^3)	*Standard deviation (gm/cm^3)*
Goodin Inlier	1	2.68	NA
Juderina	13	2.82	0.055
Killara	3	2.89	0.111
Marymia Inlier	4	2.73	0.086
Yilgarn Craton granitoid	2	2.68	0.029
Thaduna	1	2.40	NA

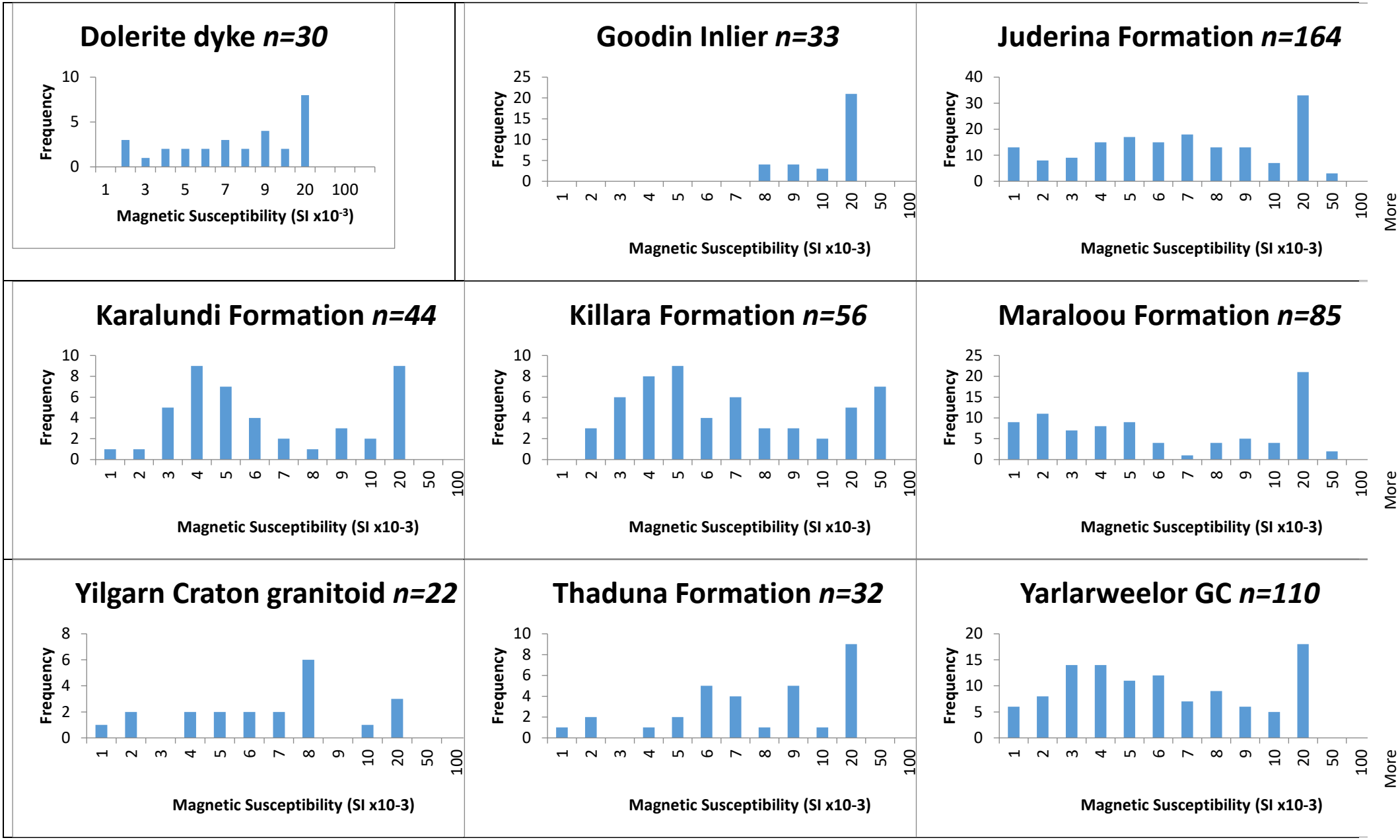

Figure 5.5. Magnetic susceptibility of the measured rocks in the Yerrida Basin. The points indicate the geometric mean of susceptibility in SI×10-3, with error bars indicating one standard deviation.

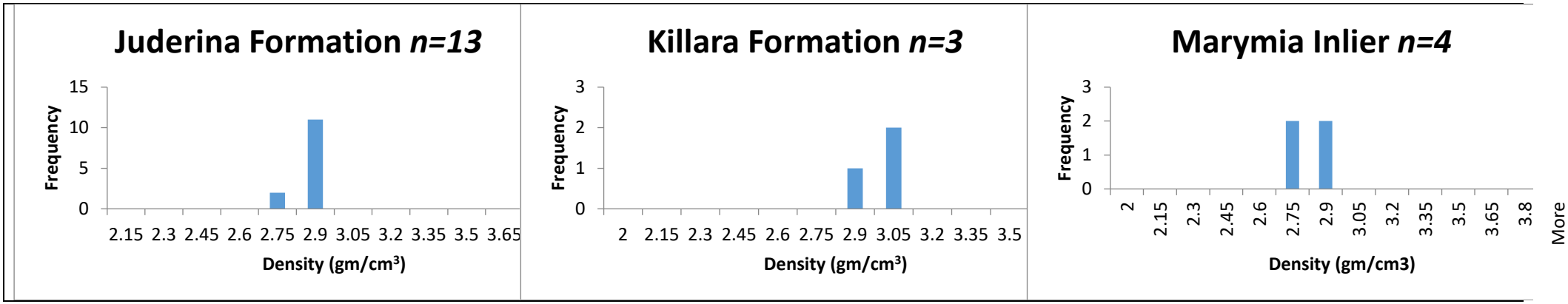

Figure 5.6. Density of the measured rocks in the Yerrida Basin. The points indicate the geometric mean of density in gm/cm3, with error bars indicating one standard deviation.

5.4.2 Structural Interpretation

Initial structural interpretation began from gravity data at the basin scale. The most useful combination of images at this stage was a blend of the Bouguer anomaly in colour and the 1VD of the RTP magnetics (Figure 5.7). Some obvious features are the greenstone belts (Wiluna in the south, and Merri in the east) characterised by a high magnitude gravity anomaly, and north-northwest trending strong and linear magnetic gradients, as shown in the 1VD of the RTP. The Goodin Inlier is particularly obvious due to its low gravity signature in contrast to moderate signature surrounding it. The higher magnitude, moderate gravity signature also appears to be quite extensive, and is observed all the way to the basin extents. This suggests the moderate magnitude anomaly is in response to Yerrida Basin rocks, rather than the lower magnitude response basement, as exemplified by the Goodin Inlier. The Wiluna Greenstone belt is interpreted to extend under the southern edge of the Yerrida Basin (indicated by the yellow line in Figure 5.7) as its characteristic signature extends almost as far north as 26' latitude, and dominates the gravity response of the southeastern corner of the basin.

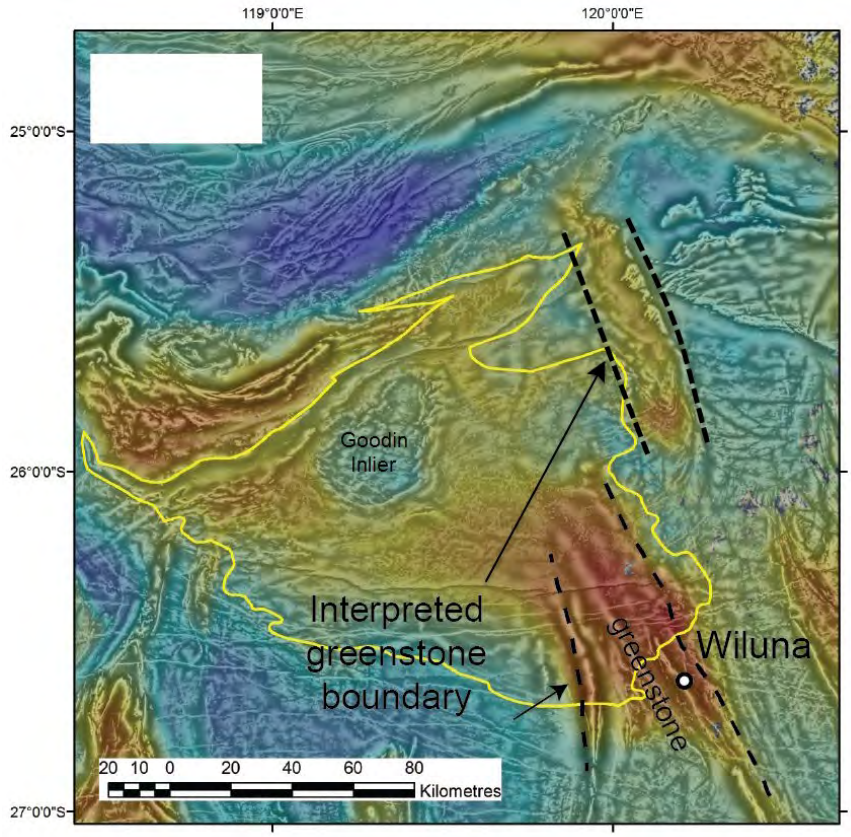

Figure 5.7. Basin-scale interpretation of gravity and magnetic data. Magnetic data is shown in greyscale and as a first vertical-derivative to highlight magnetic contrast. Bouguer gravity is shown in colour (blue = low; yellow = moderate; red = high). Surface extent of the Yerrida Basin and 3D model boundary is indicated by the yellow line.

More detailed structural interpretation at 1:100 000 scale relied upon existing GSWA geological maps, the WAROX (GSWA field observation database), magnetic data, orthophotos, digital elevation models, Landsat 8 and ASTER data provided as CSIRO Geoscience products. Gravity data was used where resolution allowed structure to be interpreted. Two stages of interpretation were conducted. First, linear and planar geologic structure such as faults, fractures, dykes and folding was interpreted by using a combination of the available data, then lithology was interpreted (Figure 5.8a). The two stages were not conducted in isolation, as each stage needed to be consistent with the other to maintain geological feasibility.

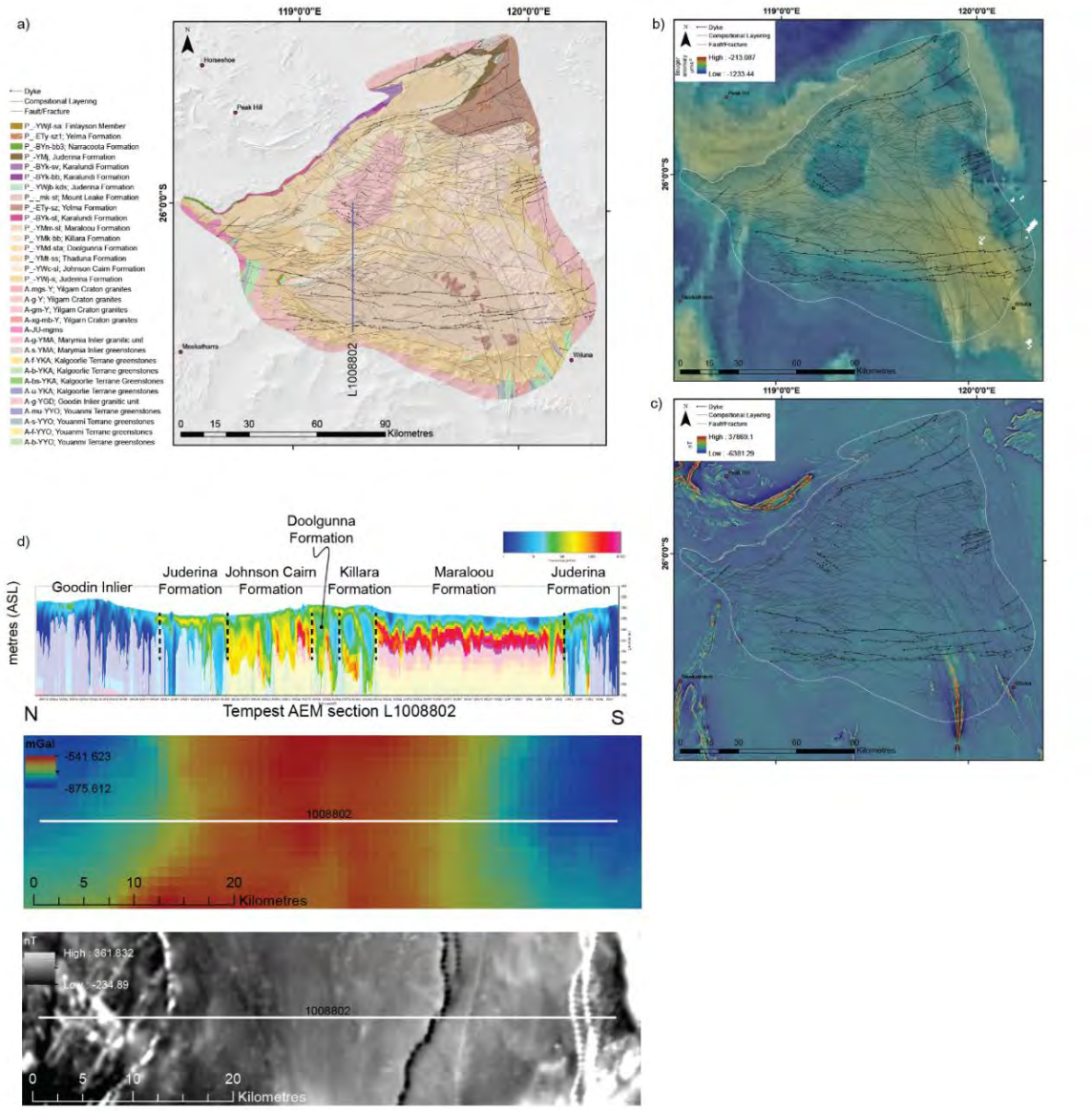

Figure 5.8. Structural geophysical interpretation of the Yerrida Basin. (a) Interpreted structure and rock units; (b) interpreted structure shown with gravity data (Bouguer anomaly shown with greyscale 1VD of the Bouguer anomaly); (c) interpreted structure shown with magnetic data (RTP shown in colour with 1VD of the RTP shown in greyscale); (d) AEM line 1008802 (high conductivity shown in warm colours and vice versa) and interpreted location of contacts. Also shown are the near-line gravity (colour) and magnetic response (greyscale) emphasising the increased geophysical fidelity from AEM at the near-surface.

In both parts of the interpretation, magnetic data proved to be less useful here than other data. The magnetic grids show very little contrast in the Yerrida Basin rocks (Figure 5.8c), and this is supported by the magnetic susceptibility results shown in Figure 5.5. Some of the interpreted faults are supported by field mapping, the geological maps, and our own field validation (Figure 5.1 – note site locations). Some faults were interpreted from anomalies using a combination of magnetic data processed using dynamic range compression (Kovesi, 2012), auto gain control and the 1VD. Nonetheless, in many cases suspect faults needed to be supported with remotely sensed data, with the DEM being particularly useful. As such, deeper faults may not have been captured in this interpretation, aside from those reflected in the gravity data.

Lithological interpretation relied even more heavily on datasets other than potential fields. Typically, lithologies can be discriminated successfully by observing textural differences in magnetic data, with variations in amplitude, frequency and orientation given particular lithologies as characteristic signature (Aitken and Betts, 2009; Betts et al., 2004; Lindsay et al., 2016a; Perrouty et al., 2012). The RTP data shows near-surface anomalies interpreted to be surface processes such as stream and channel sediments and magnetic regolith (for example Fe and/or Mg-rich lag) (Figure 5.3 – circled in red). Upward continuation was used to filter out these effects by attenuating the shortest wavelengths in the data.

Remotely-sensed data was more useful, but used with caution as regolith in the Yerrida Basin is widespread and covered any basin rocks that could be interpreted from satellite data. The widespread extent of regolith was confirmed by our own field observations. Airborne electromagnetic (AEM) data was helpful here.

The surveyed data was processed and inverted to produce images, displayed as geo-located sections, allowing a view to variations in conductivity and support lithological interpretation (Ley-Cooper et al., 2017). Figure 5.8a shows Line 1008802 starts in the north and within the Goodin Inlier, extending southward to finish near the southern margin of the Basin. Figure 5.8d shows the recovered conductivity from inversion, with the northern end of the section at left, and southern end at right (i.e. viewing towards the east). Differences in conductivity character can be seen, and were validated using geological maps to assign the corresponding rock units. The conductivity associated with the near-surface of the Goodin Inlier is moderate and relatively shallow. Further along the line, the Juderina is more conductive and appears to have a deeper conductivity extent. The Johnson Cairn Formation is highly conductive, while the Doolgunna and Killara formations are less so. The Maraloou Formation is quite distinctive, shown as highly conductive near the surface, so much so the AEM data beneath this cannot be resolved. Finally the Juderina Formation again appears, showing a similar response as is observed further north. Line 1008802 and others, provided a very useful tool to discriminate along-line resistivity variation to support the lithological and structural interpretation.

The interpretation (Figure 5.8a) shows an overall E-W, or WNW-ESE orientation of structure in the west and centre of the basin. The eastern part and the structures in particular show a different orientation of mainly NNW-SSE trending structures, similar to the underlying greenstone belt. The lithological interpretation differs little from GSWA maps, and shows that the Juderina Formation forms the base to much of, if not all, the Basin. The Johnson Cairn Formation is less extensive at the surface and is restricted to the western parts of the Basin. Some outcrop in the east suggests the Johnson Cairn may extend under the overlying Mooloogool Group rocks from west to east. A lack of outcrop and interpreted Johnson Cairn Formation in the south suggests it does not extend far to the south, if at all.

Mooloogool Group rocks are interpreted to be located in the central, west, east and northern parts of the Basin, with the youngest rocks of the Maraloou Formation being the southern-most. The tholeiitic basalts of the Killara Formation are most extensive in the east, with some outcrop in the central, northern and western parts. This was unexpected, as the initial interpretation of the gravity data showed a moderate magnitude anomaly to be extensive everywhere in the basin, and was loosely interpreted to be Killara Formation, due to the higher density of the mafic rocks relative to the basin sedimentary rocks. Thus our initial hypothesis is that the Killara Formation mafic rocks are more extensive undercover, and the initial interpretation shown in Figure 5.8a does not adequately represent the extent of the Killara Formation, nor properly accounts for the geophysical response of the region. The next sections describe forward modelling and inversion that attempt to falsify this hypothesis.

5.4.3 Forward modelling

Petrophysically constrained forward modelling of geophysical data was conducted to test the hypothesis that the Killara Formation is more extensive undercover than was shown through interpretation. Three stages of forward modelling were conducted: (1) a 3D conceptual study to validate our primary assumptions; (2) 2D section modelling of geophysical data with geological constraints and; (3) forward modelling a 3D geological model.

- **Conceptual modelling: Noddy**

'Noddy' is primarily a kinematic modelling package that allows input geological events and stratigraphy to generate a 3D understanding of the resulting architecture (Jessell, 1981; Jessell and Valenta, 1996). A useful part of Noddy is being able to generate the potential field forward response of the model. By assigning petrophysical values to each stratigraphic layer in the model, a representative grid can be generated (the 'calculated response') and compared to that provided by the geophysical survey (the 'observed response'). Figure 5.9c shows the basement configuration of the conceptual model with the assigned petrophysical attributes. Yerrida Basin units (not shown in Figure 5.9c) are thus assumed to have Archean basement, with the exposed Goodin Inlier forming a dome.

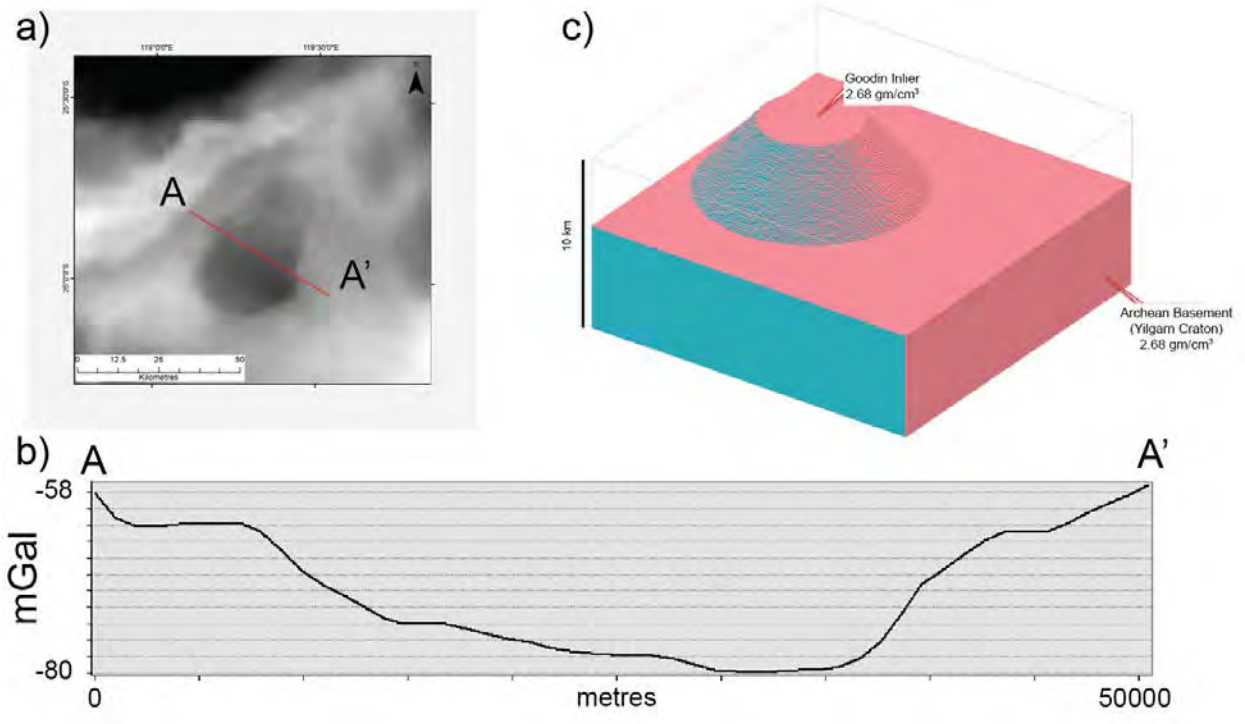

Figure 5.9. Initial conceptual model using 'Noddy': a) the observed gravity response from the Yerrida Basin, showing the location of the profile in part b); b) curve representing the gravity response of the Goodin Inlier calculated from the observed gravity; c) initial 3D model of the Goodin Inlier – the Yerrida Basin sedimentary rocks are not shown.

Three geological scenarios were explored (Figure 5.10). The first simulates that no Killara Formation is present to explore what the geophysical response would be if there was very little, or no high density material in the Basin (Figure 5.10a). The second simulates a 500 m thick layer of high density material simulating the Killara Formation in stratigraphic position (Table 5.1) between the Maraloou and Doolgunna formations (Figure 5.10b). The third simulates 2000 m of high density material (Killara Formation) in stratigraphic position (Figure 5.10c). The resulting gravity grids are shown in greyscale with the corresponding model, and profiles (A – A') sampled from the gravity grids.

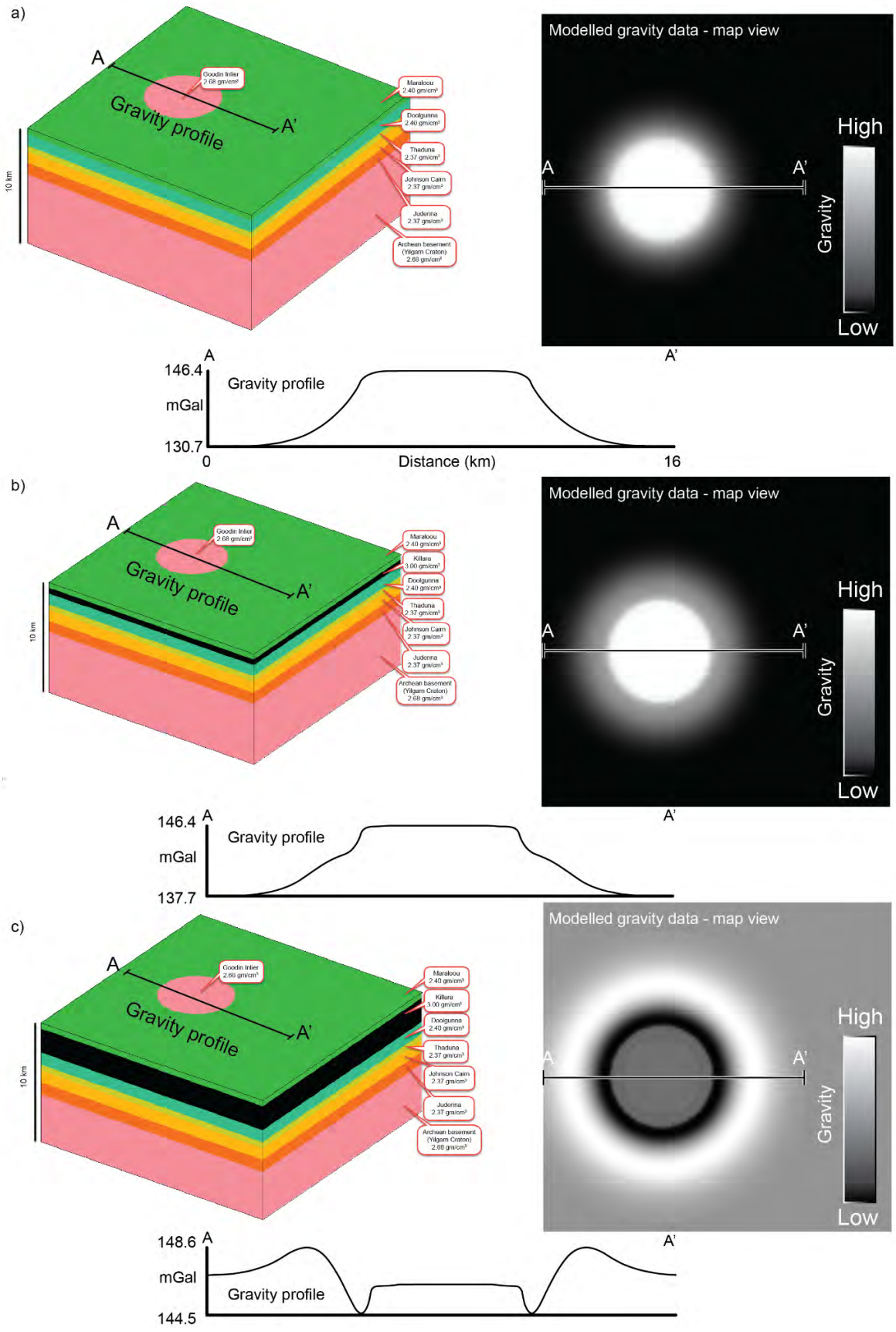

Figure 5.10. Conceptual forward modelling results obtained from Noddy. (a) No Killara formation; (b) 500 m of Killara Formation and (c) 2000 m of Killara Formation.

Having no dense material in the basin (Figure 5.10a) clearly does not recreate the desired gravity response with the Goodin Inlier producing a gravity high, rather than the low as shown in the observed response. Adding 500 m of dense material (Figure 5.10b) produces a marginally closer fit to the observed response, but the Goodin Inlier still produces a gravity high, though at a lower difference (8.7 mGal) than in the previous example (15.7 mGal). Adding 2000 m of dense material does produce a response which shows the Goodin Inlier to produce a gravity low, and somewhat similar to the observed response. However, this calls for the Killara Formation to be consistently 2000 m thick, which is twice as much as the 1000 m estimated from previous work (Pirajno and Adamides, 2000).

The results from conceptual modelling with Noddy support the hypothesis that a significant amount of dense material in the basin can produce the gravity response seen in the observed data. However, the reality is almost certainly more complex than a single, horizontal and lithologically homogenous layer. The dense material is likely to be a combination of widespread Killara Formation and sills or intrusions produced through related magmatism.

- **Testing intrusive scenarios: GM-SYS**

GM-SYS is a forward modelling platform (Talwani and Heirtzler, 1964; Talwani et al., 1959) that allows easy exploration of geologically complex scenarios. A profile was selected that extended from the northern edge of the basin to the southeast, across the Goodin Fault, the Goodin Inlier and into the centre of the basin (Figure 5.2) and in similar location to the profiles produced in Noddy (Figure 5.9a-c). The same hypothesis is being tested: whether the dense material, possibly the Killara Formation and its intrusive components, can account for the gravitational response in this region. However this form of forward modelling allows for more complex geometries to be tested. Figure 5.11a and b show both the magnetic and gravity (respectively) observed response (dots) and the calculated response (line). The calculated response is produced from the geological section (c), where petrophysical values are assigned according to values measured from the field. The geological section was constructed using geological observations taken from GSWA maps and WAROX (Appendix 1), and integrated into the model so that existing structural relationships are maintained, and general geological reasoning is not violated.

The model fits well to both the magnetic and gravity data. The Killara Formation has been successfully modelled as a set of faulted sills. This supports the idea that the Killara Formation may be the source of the moderately high gravity anomaly throughout the Yerrida Basin, though the model must now be modified to include the intrusive part of the formation.

At the northwestern end of the section (left hand side of Figure 5.11), the boundary between the Yerrida Basin rocks (Doolgunna and Juderina formations) and the Bryah Basin rocks (Karalundi Formation) has a distinctive signature, especially in the magnetic data (a). The geological model shows a very steep dip to the northwest (or left-hand side of the section) and a possible downward throw as indicated by the footwall Yilgarn Craton modelled on the Yerrida Basin side of the boundary. The Goodin Fault has been suggested to be at this location, and this model shows it to be a normal, northwest dipping fault, in contrast to the northwest dipping thrust structure reported by (Pirajno and Adamides, 2000). The analysis presented here is certainly not conclusive however, and the presence of the Goodin Fault is still under question, as are its characteristics. From here modelling was expanded to include the entire basin in 3D.

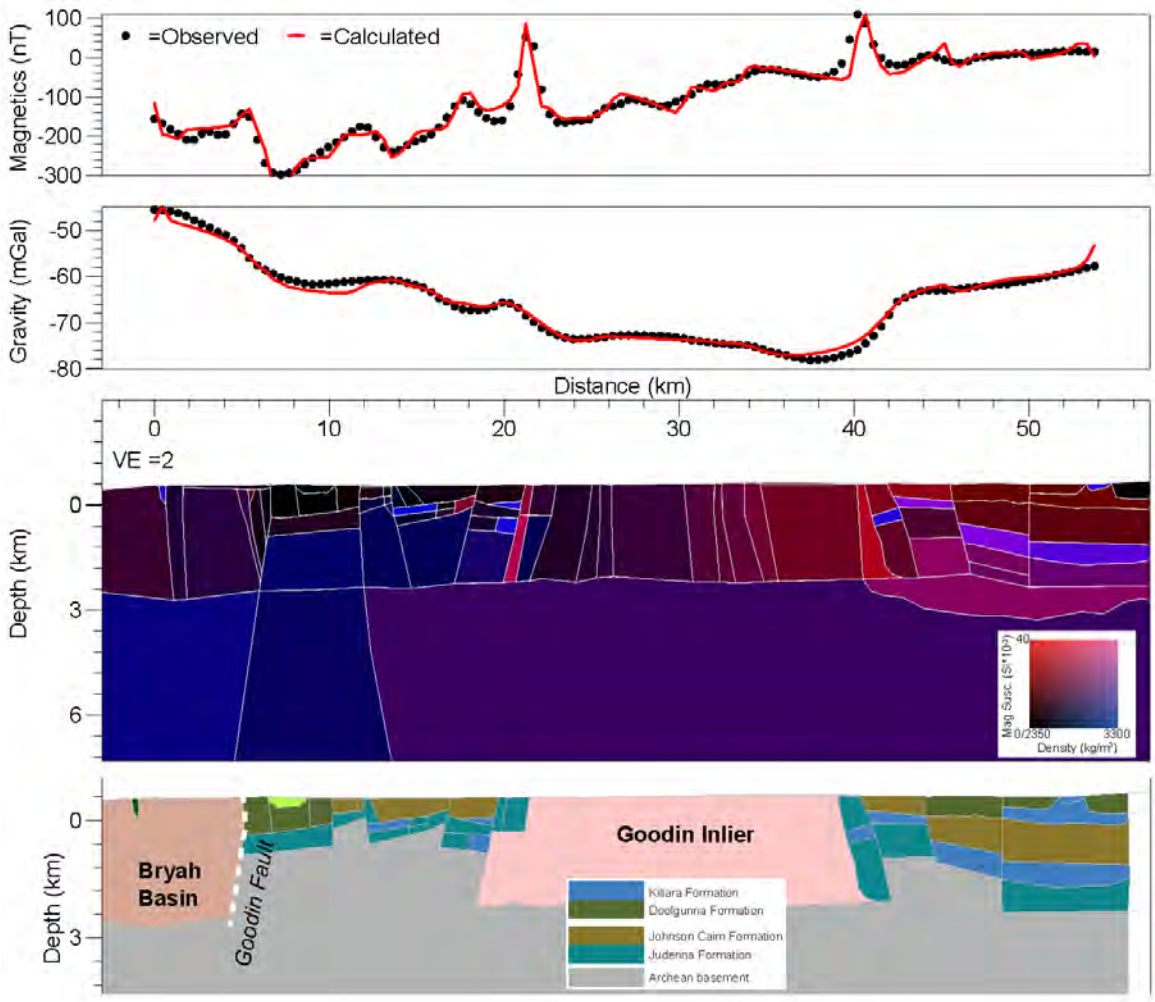

Figure 5.11. Section-based forward modelling of the Yerrida Basin and Goodin Inlier – location of profile shown in Figure 5.2. The top two panels show the fit between the observed (points) and calculated (line) geophysical response magnetic and gravity data. The middle panel shows the petrophysical model that was used to model the calculated geophysical response. The bottom panel shows the geological interpretation made from the petrophysical model.

- **3D model**

A 3D model was constructed using GeoModeller, an implicit modelling platform that allows models to be constrained by known stratigraphy, fault relationships and geological observations (Calcagno et al., 2008). GeoModeller also offers geophysical modelling tools, including forward modelling and inversion, which operate directly on the 3D geological model.

Data input to the model was gathered from the stratigraphy (Figure 5.4) and structural interpretation (Figure 5.7, Figure 5.8). However, only the larger faults were retained for 3D modelling, as the smaller, more insignificant faults degrade performance of the modelling engine, without providing a commensurate increase in geological understanding to this study. Each geological unit constructed in the 3D model has petrophysical values (Figure 5.5, Figure 5.6) assigned to allow a forward response to be calculated.

The 3D model contains what were considered to be important components to produce a representative geophysical response: the Goodin Inlier; Archean basement; Yerrida Basin sedimentary rocks; the Wiluna and Merri greenstone belts and various faults, including the north-northwestward extension of the Ida Fault (Figure 5.12). It is important to note the northwestern corner of the model, where the Bryah-Padbury basin would be, but is not included in the modelling.

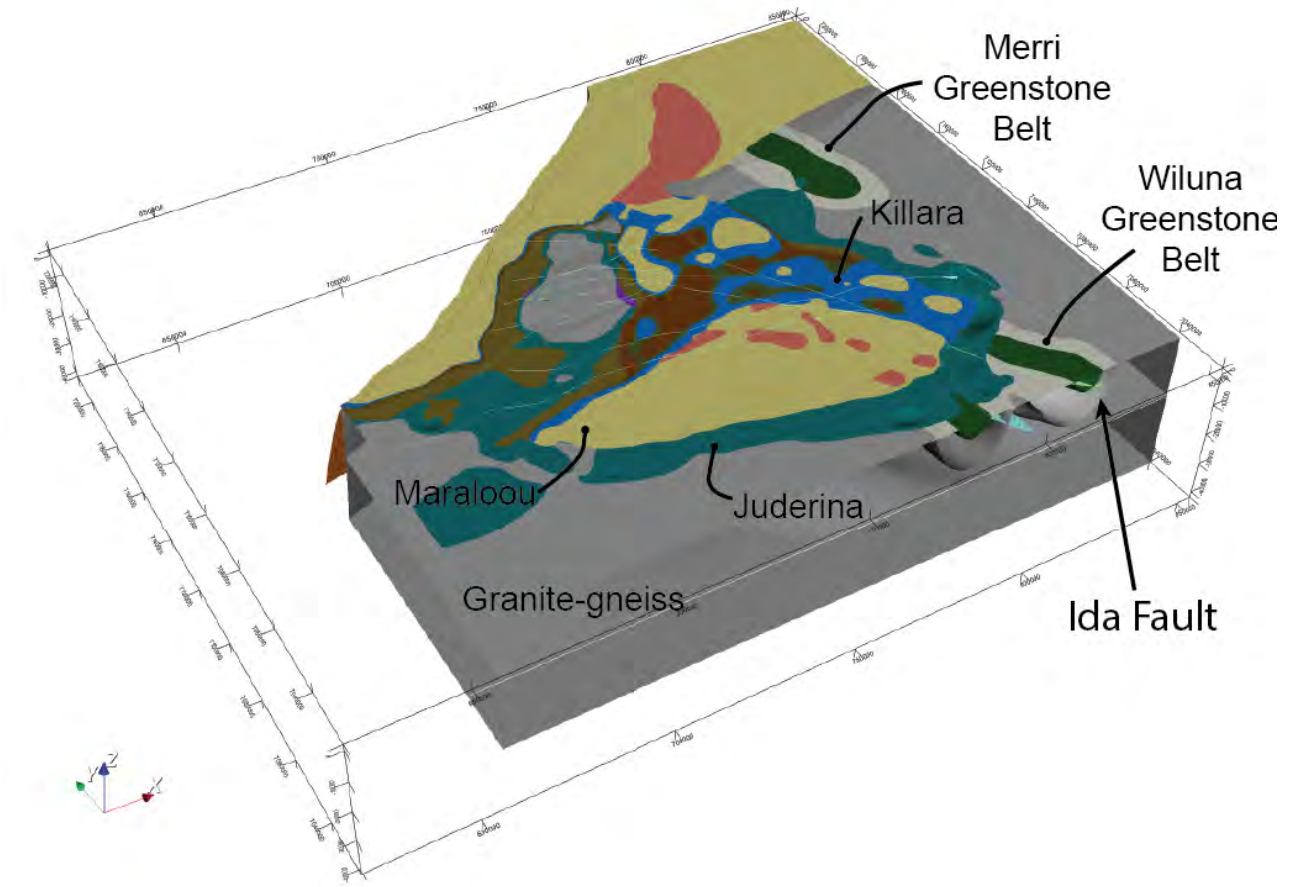

Figure 5.12. 3D model constructed to constrain geophysical inversion. Oblique view from SW - check marks on the X axis are at 50 km intervals; Y axis at 20 km intervals; Z axis 10 km.

5.4.4 3D forward modelling and inversion.

3D forward modelling was performed to investigate the density structure of the Yerrida Basin. Initial attempts at modelling the gravity produced similar results to those shown in the conceptual stage (Figure 5.9a and b). The difference in the initial 3D case was that the Killara Formation was included as a thin unit, and thus had almost no effect in producing a gravitational anomaly. This result was anticipated as subsequent modelling steps (Figure 5.10; Figure 5.11) had found a more significant intrusive component to the Killara Formation was required than just a stratabound layer of volcanic material.

The next stage was to include these intrusive bodies to the model and then test whether their presence was sufficient to produce the required response. The intrusive bodies were quite thick (=>1000m) and extensive but were still not sufficient to replicate the observed signal.

- **Juderina Formation and a possibly substantial mafic component.**

Drill core logging from a range of holes (THD1, DGDD347, DGDD020, DGDD278, DGDD279, DGDD281, DGDD319, DGDD320, DGDD404, DGDD406 and THDD 226) reveals that the Juderina Formation contains mafic sills, either as finer grained basaltic rocks, or doleritic rocks. This observation is particular to the Juderina Formation, and not the overlying Johnson Cairn, Thaduna, Doolgunna and Maraloou formations. Reasoning suggests that the mafic component to Juderina Formation was intruded during or soon after deposition of the clastic and carbonate component of the formation, and was thus restricted to just this formation. Another option is that the mafic component to the Juderina Formation is related to the intrusive parts of the Killara, Karalundi or Narracoota formations, however if this was true, the other overlying Johnson

Cairn, Thaduna and Doolgunna formations should also contain some proportion of mafic intrusive rocks, which (to our knowledge) they don't.

Geophysical inversion provides a means to test the hypothesis that higher density rocks can explain the anomalous density signature. Inversion has been used to falsify our hypothesis, rather than validate it. The following scenarios have been tested:

1. No additional high density intrusions are modelled – only the Killara Formation rocks are high density (>3.0 gm/cm^3).
2. A moderate increase in the volume of high density intrusions in locations suggested by the section-based forward model (Figure 5.11).
3. A large increase in the volume of high density intrusions, as guided by the location of high density anomalies in the observed gravity data.

Each inversion was executed to allow the contacts to the Juderina Formation, intrusive bodies and the Archean greenstone units to move if required by the inversion. All other units were left fixed. These constraints reflect the question as to whether the density structure can be explained by known higher density units.

All scenarios were successfully inverted and produced a root-mean-square (RMS) misfit of approximately 4 mGal from an initial misfit of over 20 mGal. While the reduction of RMS misfit is satisfactory (an 80% reduction), this value is inadequate as a measure of geological feasibility of the inversion results. Deeper geological analysis of the resulting model is needed. Results are shown in Figure 5.13. The upper panel of part (a) shows the geological model, the middle panel shows the observed gravity data that was input and the lower panel shows the prior model extents of the Wiluna and Merri greenstone belts ('W' and 'M' respectively). Part (b), (c) and (d) top panels show the geological prior model used for input (scenarios 1, 2 and 3 respectively) but only the included mafic intrusions displayed. The middle panels of (b), (c) and (d) show the gravity field calculated from the inverted model. The lower panel shows the distribution of locations determined by the inversion to be > 2.9 gm/cm^3. The threshold of 2.9 gms/cm^3 was chosen as dolomitised rocks (as possible source of higher densities) are unlikely to have a density higher than this value, and these locations are more likely to be those occupied by mafic rocks.

The middle panels of Figure 5.12 highlight two regions that are investigated in more detail: '1' – in the west; and '2', in the centre of the Yerrida Basin.

Region 1: The observed gravity data shows a high magnitude anomaly in Region 1. The lower panels in Figure 5.13 show that the inversion requires dense material >2.9 gm/cm^3 to be placed here to account for the anomaly in the observed data (Figure 5.13a middle panel), regardless of the geological prior model used for input. Scenarios 1 and 2 do not have mafic bodies modelled in this location (see upper panels), so rocks within the Juderina Formation exhibit densities at >2.9 gm/cm^3 in these inversion results from these scenarios. Scenario 3 includes a mafic body in this location (Figure 5.13d – top panel) and the inversion includes higher density material in this location as well, but more laterally extensive than in scenarios 1 and 2.

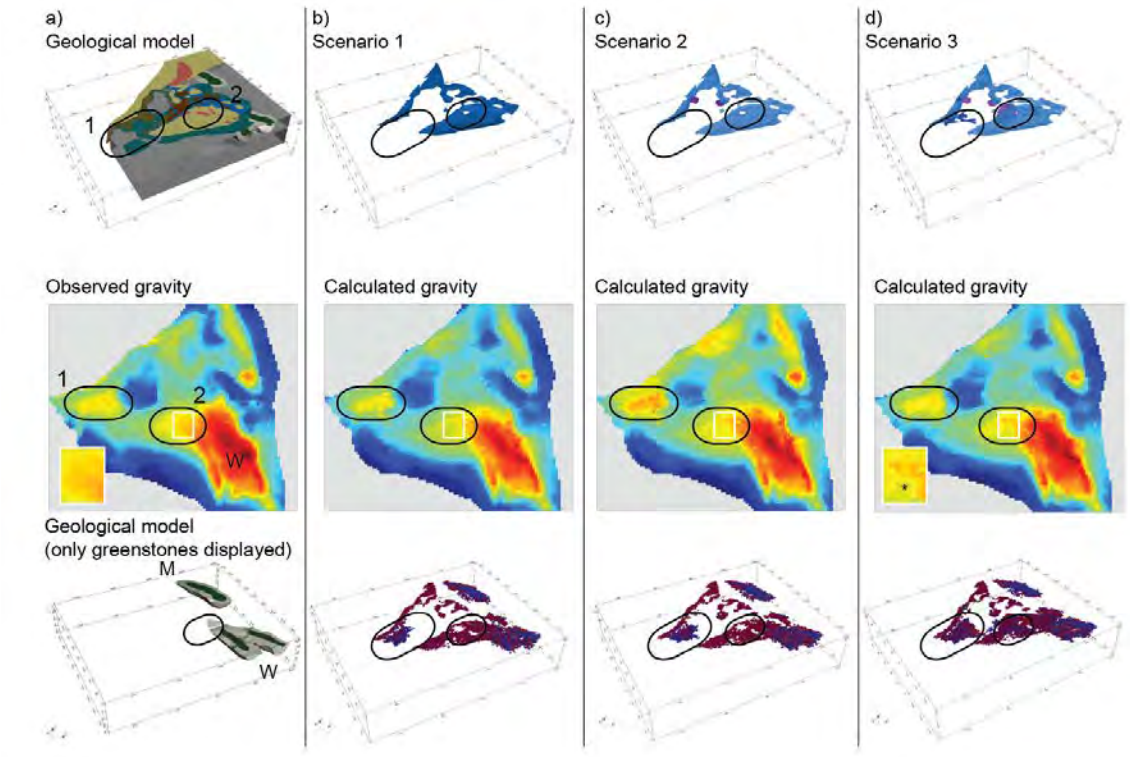

Figure 5.13. Geological models and mafic intrusive scenarios subjected to inversion modelling. a) Top panel: 3D geological model; middle panel – observed gravity response; bottom panel - location of greenstone belts. b-d) Results from scenarios 1-3 respectively: top – position of mafic intrusions; middle - calculated gravity response; bottom – distribution of locations determined by the inversion to be >2.9 gms/cm3. Colours in the gravity response indicate blue = low; yellow = moderate; red = high.

Region 2: The observed gravity data shows a higher amplitude gravity anomaly in this location (Figure 5.13a – middle panel). To the east, the deeper presence of the northern extension of the mafic component of the Wiluna Greenstone Belt (WGB) is interpreted to be the causative body of the higher magnitude gravity values (Figure 5.13a bottom – 'W'). The western edge of the high amplitude region also displays a high amplitude anomaly, though of lesser magnitude than the WGB (Figure 5.13a-d - white box). Scenarios 1 and 2 show that this part of the model is not adequately resolved through inversion, while Scenario 3 shows some improvement, though not enough to explain the southerly portion of the anomaly. A zoomed comparison is shown in the middle panel inset of Figure 5.13a (observed field) and Figure 5.13d (inverted model): the asterisk indicates where additional higher density material would need to be for a better fit to the observed field.

An extensive mafic body: A grid representing the misfit between the observed and calculated fields for Scenario 3 identifies a location in the south and central part of the model that has excess mass. This location is underneath the modelled surface extent of the Maraloou Formation and toward its contact with the Juderina Formation (Figure 5.14a and b). This region, marked by shades of blue in the misfit grid (Figure 5.14b) measures 45 by 15 km. If the basin was modelled to be thinner in this location then this misfit could be remedied. Removing high density mafic material from the model was considered, however no high density material was modelled in this location, and further modelling of reduced mafic material did not resolve the excess mass. This suggests that the position of misfit indicates where the basin thins substantially to the south.

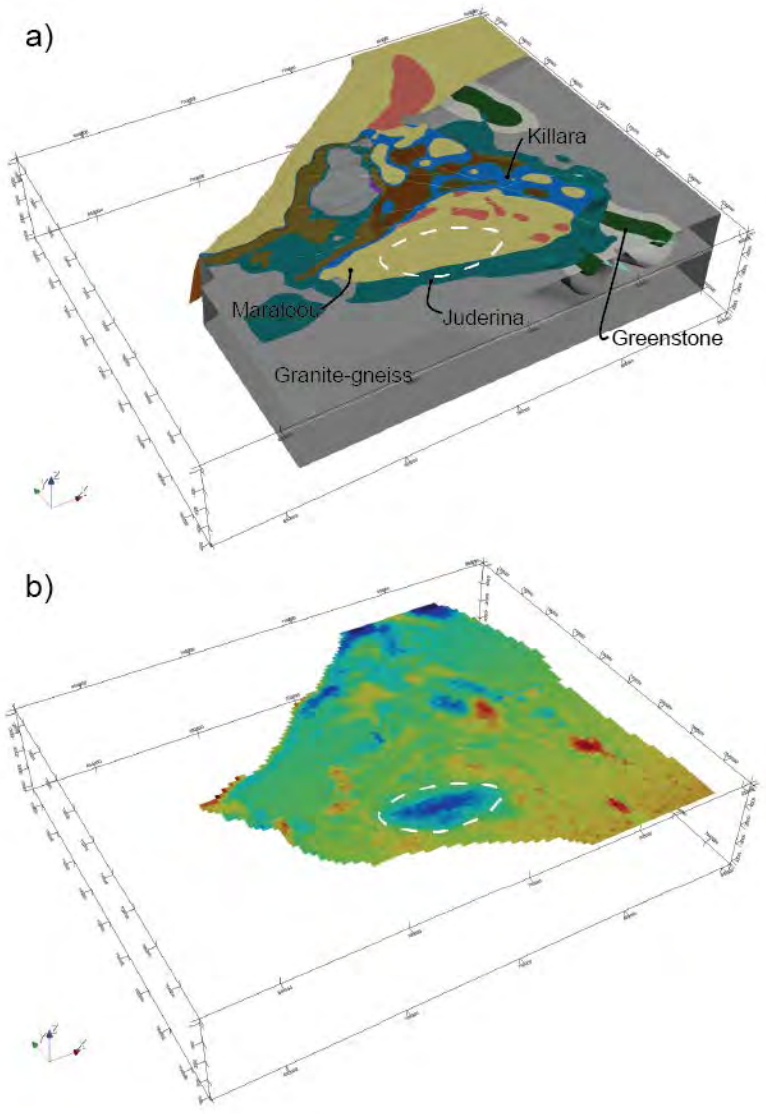

Figure 5.14. Position of large misfit region determined by Scenario 3. The white dashed line indicates the position where a portion of material needs to be removed to result in reduced misfit. The cause of this misfit is considered to be due to the modelled basin rocks being too thick.

5.5 Discussion

The process of collating, interpreting and modelling geoscientific data can be of great benefit, leading to a greater understanding of the capabilities of the available data, expanding existing knowledge of the target region, and identifying gaps in data, and thus, knowledge. The latter point is what then guides decisions for future data collection, interpretation and modelling. There is great benefit in these exercises to the geoscientist, who gains the knowledge and understanding: the critical point is whether these are effectively communicated so that a similar level of understanding is also disseminated. The discussion that follows attempts to do this by first presenting a range of outcomes that were considered useful. Some of these outcomes are not 'successful' in the traditional sense, but nonetheless are worthwhile reporting, in particular which datasets were useful for different purposes, and what aspects of the range of modelling procedures provided useful insight. The second part of the discussion synthesizes what was learned about the structure of the Yerrida Basin and potential for mineralisation.

- **Potential field and AEM data**

The magnetic data proved to be useful in limited cases. While it was still used during structural interpretation, it provided little confidence in imaging the geology. A variety of geophysical processing techniques were used to emphasise particular features that were interpreted as faults or contacts. Upward continuation of the data removed the more obvious short wavelength features attributed to magnetic stream and channel sediments, likely sourced from the Robinson Range banded iron formations to the north. Dynamic range compression (Kovesi, 2012), auto gain control and the 1VD filtering on the upward continued data then enhanced certain discontinuities in the magnetic data that were interpreted as faults.

It is not surprising that the magnetic data was not as useful as it can be. Firstly, the petrophysics reveals very little variation in susceptibility for the bulk of the geological units, including the Killara Formation (Figure 5.5 and Table 5.2). Small to imperceptible variations mean little petrophysical contrast, which results in a fairly bland and homogenous magnetic grid. This is not true of the entire region – the east-west trending dykes were easily discriminated, and structure within and at the extents of the Goodin Inlier was also relatively well defined (Figure 5.8c). Another reason why the magnetic data was less useful is flat-lying basin structure, so any magnetic contrast would not have been detectable unless they had been tilted to be closer to vertical, such as is more typical in orogenic belts. This is also shown in the gravity data, which did provide more contrast, but the flat-lying geometry didn't reveal the entire 3D nature of the anomalous density, and what depth they may be emplaced, necessitating the forward and 3D modelling.

Support for these interpretations was provided by the AEM data, which was effective at distinguishing lateral changes in geology through interpretation of the conductivity characteristics (Figure 5.8d). Caution was taken to ensure that near-surface conductivity related to regolith was not misinterpreted to be bedrock geology, and that interpretation below these highly conductive horizons was restricted (see Figure 5.8d – Johnson, Cairn and Maraloou formations). Nonetheless, the AEM data still distinguishes different lithologies more effectively than the potential field data: magnetics for reasons already stated and gravity due to orders of magnitude increase in resolution (metres versus kilometres). While the units interpreted from the AEM have a substantial regolith profile that affects their conductivity, the regolith and its conductivity displays overall distinctive signatures that are representative of the entire bedrock-regolith package, and thus can be used to discriminate between them.

5.5.1 Alternative for higher density material

The structural and lithological interpretation, augmented by existing GSWA mapping (WAROX) and field validation provided input to the 3D model. The central aim was to determine if the characteristic density signature of the Yerrida Basin was due to more extensive mafic rocks at depth, or some other geological reason. An alternative briefly introduced considered that later diagenetic or near-surface alteration caused this increase in density. Dolomitisation of carbonate rocks forms dolostone when calcite ions are replaced by magnesium ions. Calcite (mean density = 2.71 gm/cm^3) is less dense than dolomite (mean density = 2.84 gm/cm^3), thus dolomitisation is expected to increase the density of a rock. The magnitude of density increase depends on the carbonate proportion of the original rock (with lower proportions resulting in less carbonate to dolomitise, and thus a smaller density increase) and the degree that dolomitisation has occurred.

3D geophysical inversion was employed to explore both these scenarios, and the recovered density distribution leads us to which is more feasible. Region 1 required a significant increase in density when compared to the prior geological model to account for the density anomalies seen in the observed gravity data (Figure 5.13b-d – middle panels). The Juderina Formation forms a significant unit in this area, both in outcrop and at depth and is likely to contain dolomitic rocks. The carbonate portion of the Juderina Formation includes the relatively minor Bubble Well member, is not considered large enough to account for the gravity anomaly (Occhipinti et al., 2017). In addition, the magnitude of densities required to produce the required

anomaly (>2.9 gms/cm^3) is higher than is realistic for dolostone, even if the rock was made entirely of dolomite. Thus, an extensive mafic component in the subsurface is a more likely source of the gravity anomaly in this location. Modelling in region 2 (Figure 5.13b-d – middle panels; Figure 5.14a, b) also supports this reasoning, with a large high density (>2.9 gms/cm^3) body required to account for the observed gravity data. Here, the Juderina Formation is not as extensive as in region 1, and the position of the recovered density implies a closer spatial association with the Killara Formation.

5.5.2 Density distribution and geological implications

The distribution of mafic units in the Yerrida Basin was determined through geological modelling combined with petrophysically constrained gravity inversion. The distribution of these mafic units determined from modelling is shown in Figure 5.15, along with the extents of mapped and interpreted Killara Formation for comparison. Also shown are regions 1 and 2 from Figure 5.12, and region 3, which contains the area of misfit (Figure 5.14) and region 4, which will be discussed. The grey regions indicate our current knowledge of the extent of the Killara Formation as shown on GSWA maps and geophysical interpretation and can be assumed to only represent outcrop or near-surface (<50m) rocks. The coloured cells are outputs from the final inversion voxet, and represent the predicted extents of mafic material at the surface and at depth. The plan view shows a significant increase in the extent of mafic material from our current understanding. Region 4 is an extensive northeast-trending body of mafic material modelled as Killara Formation.

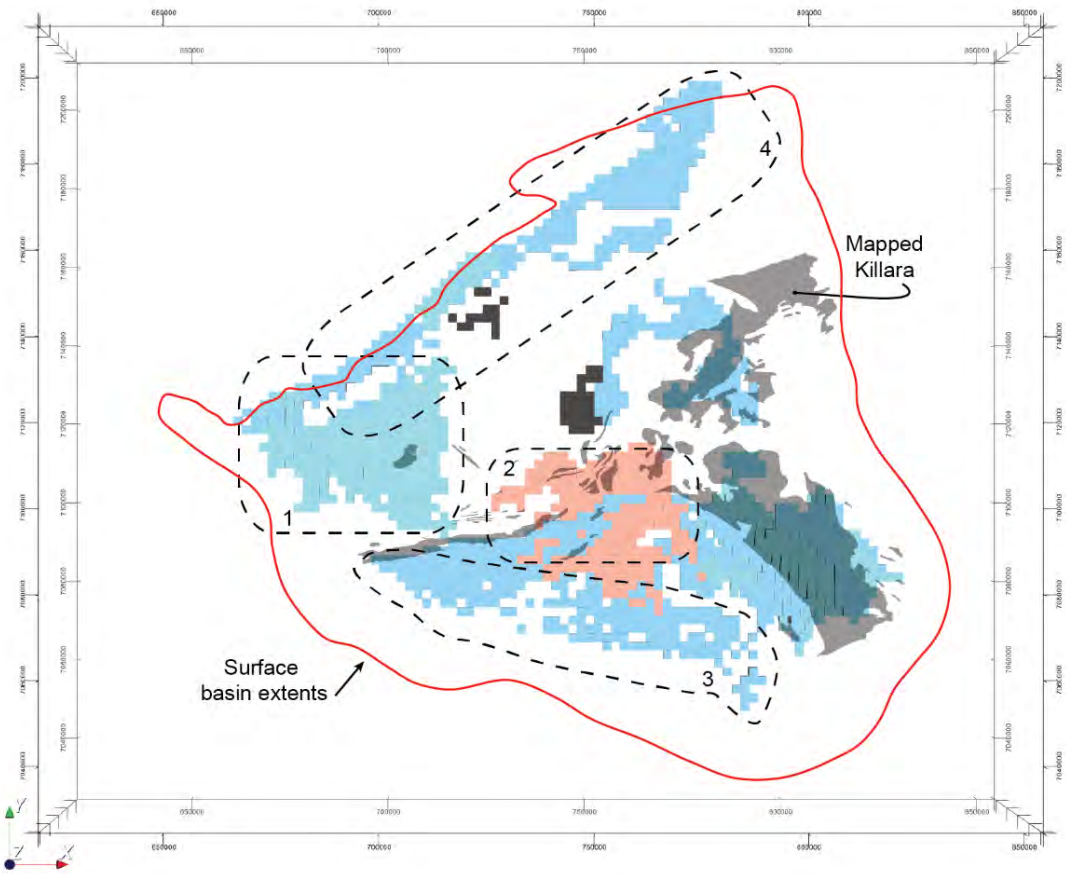

Figure 5.15. Comparison of mafic units at depth with mapped Killara Formation.

A series of 3D isometric views of the geological model determined through inversion are illustrated in Figure 5.16. These views, from the southwest, have an isometric view from above and below. These views show the depth extent of inverted geological units, in particular, the mafic units as depicted in the right-hand panels. The panels on the right show the distribution of mafic material, with the other units (sedimentary, granite-gneiss and greenstones) filtered out to allow a clearer view. The mafic bodies were modelled individually, and are colour-coded to differentiate each visually, but each body is not considered to be different stratigraphically or structurally.

Most of the higher density, mafic material is located close to the surface. The mafic material in region 4 is shown to extend deeper in the southwest part (Figure 5.16d), and could be part of the Killara Formation, or the mafic component to the Juderina Formation. Figure 5.16b – 'A' also shows the Juderina Formation is very thick (>10km, and up to 20km) towards the northeast. Twenty kilometres is almost certainly too thick, and is an artificial mis-estimation resulting from stochastic inversion. Nonetheless, it indicates that a thicker portion of the Yerrida Basin exists here.

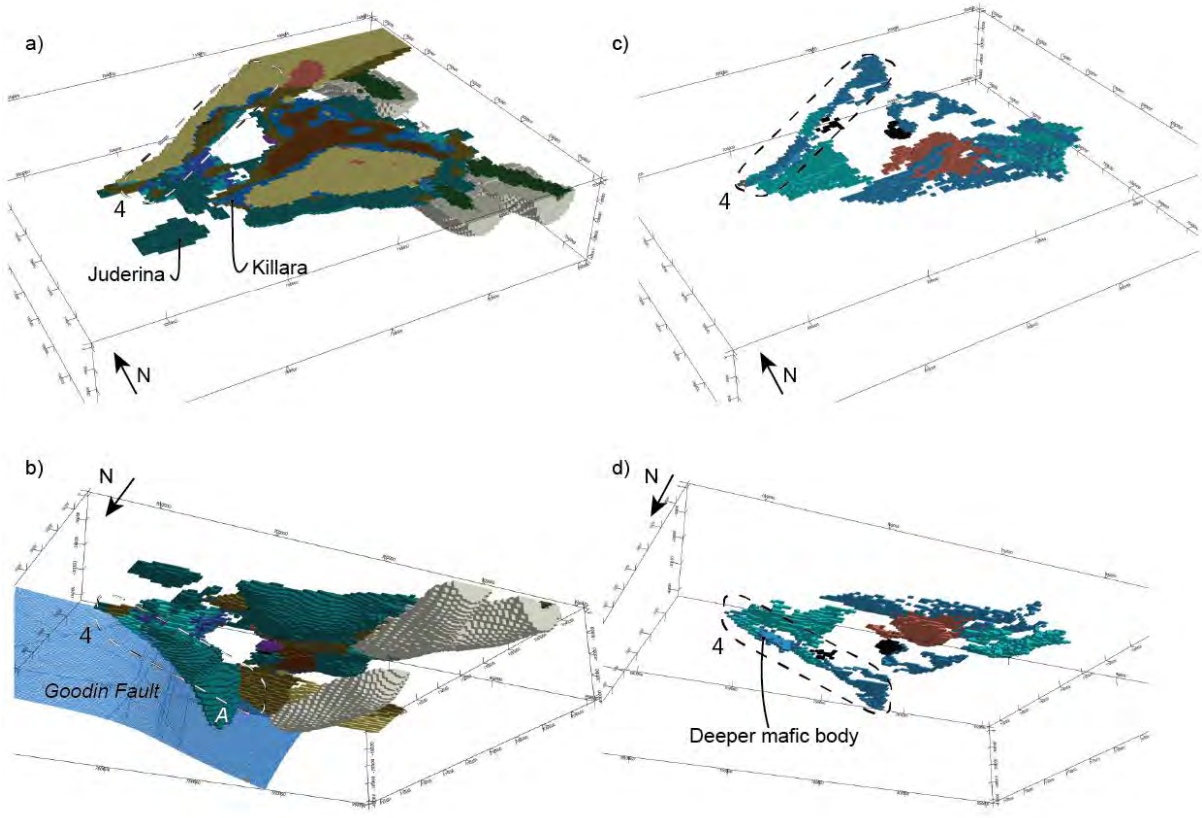

Figure 5.16. 3D model showing distribution of high density (>2.9 gms/cm3) material: a) – d) show different views of the model, with regions discussed in-text labelled accordingly.

5.5.3 Basin development

The location of this thicker mafic and sedimentary portion of the basin is juxtaposed against the Goodin Fault. The thicker part of the Yerrida Basin may then represent a deepening of the basin toward the northwest, which occurred during c. 2200 – c. 2000 Ma lithospheric extension and rifting (Occhipinti et al., 2017; Pirajno and Adamides, 2000; Pirajno and Occhipinti, 2000). The mafic component of rifting may have manifested in two forms. Extensive intrusion and extrusion contemporaneous with: (1) deposition of the Juderina Formation or (2) with the Killara Formation during development of the Mooloogool Sub-basin.

A period of extensive mafic volcanism at c. 2045 Ma saw the Narracoota Formation intrude and extruded onto the Karalundi Formation in the Bryah Sub-basin located to the north and northwest of our study area (Hawke et al., 2015). Occhipinti et al. (2017) suggest that the Killara and Narracoota formations are manifestations of magmatism during rifting in different basin depocentres that temporally overlap. This is supported by Pirajno and Adamides (2000) who interpret the Killara Formation as basalts extruded in a continental setting, with geochemical affinities to the hyloclastites of the Narracoota Formation. Gravity modelling performed and interpreted by Pirajno and Occhipinti (1998) found the Narracoota Formation thickens up to seven km depth toward the south and the Goodin Fault. If the high density material modelled here is part of the Killara Formation, then thickening of the mafic Narracoota Formation toward the south, and thickening of the Killara Formation towards the northwest supports the suggestion of (Occhipinti et al., 2017) that the current position of Goodin Fault may represent a rift axis and volcanic vent for this period of magmatism.

Regions 1, 2 and 3 identified from the modelled high density material are thick and suggest other sites that may represent vents and the source of mafic volcanism (Figure 5.12; Figure 5.16b and d). Region 1 is primarily hosted within Juderina Formation and may then represent the mafic component. Regions 2 and 3 are hosted within the Mooloogool Sub-basin rocks, may be more likely to be Killara Formation. The thickness of the basin around Region 2 is modelled to be thicker than elsewhere, and may represent another rift, smaller than the one centred on the Goodin Fault. Region 3 requires less mass, and indicates that the basin thins substantially at this location towards the south. The substantial high density material modelled here suggests Region 2 may indicate the locus of mafic magmatism and a vent, rather than simply a paleotopographic low, in which sedimentary and mafic material with provenance from elsewhere was deposited.

5.5.4 Mafic rock geochemistry

Geophysical inversion has been useful in revising the extent of mafic rocks in the Yerrida Basin. What geophysics cannot do with our current state of data is determine whether the interpreted mafic rocks all belong to the Killara Formation, or whether the mafic rocks have different compositions and thus reveal a more complex stratigraphy. Geochemistry has been obtained from drillcore (THD001, DGDD347 and the GSWA Geochemistry Database "WACHEM") and surface samples (UWA field work and WACHEM) to help us achieve this aim.

As DGDD347 is close to the northern boundary of the Yerrida Basin, we checked whether any of the mafic rocks sampled in the Juderina Formation are sills or dykes related to the Narracoota Formation. Figure 5.17a shows the geochemical distribution of mafic rocks sampled from the Yerrida and Bryah-Padbury basins on a basaltic Th/Yb vs Nb/Yb diagram (Pearce, 2014). This diagram is used to recognise magma types to provide insight into tectonic setting, with higher Th/Yb representing lavas modified by subduction-related processes, and those with higher Nb/Yb showing increasing levels of crustal contamination. While possible, we are not interpreting such settings from these results as more detailed stratigraphic and volcanologic work would be required as support. Nonetheless, the diagram proves useful to discriminate between different types of mafic rocks in the region that may have formed at different times and/or in different tectonic settings.

Samples from drillhole DDGD347 ("DG") and THD001 ("THD") are clustered toward the higher end of both ratios. Most of the DG and THD samples are close to, but not within, the MORB-OIB array. Importantly, the DG and THD samples are distinctive in their tight clustering and position with respect to the Narracoota and Killara Formation samples, meaning they are different geochemically, and were thus likely generated in a different setting. This interpretation is supported by Figure 5.17b, a similar diagram to Figure 5.17a, but uses a TiO_2/Yb ratio on the y-axis as a proxy for deep melting (Pearce, 2008). Here, the DG and THD samples are distinguishable from the Killara and Narracoota Formations based on both the TiO_2/Yb and Nb/Yb ratios. DG and THD can also be separated into their own classifications. The DG samples fall within the alkali classification, while the THD samples are mostly classified as tholeiitic basalts. The DG and THD samples have

a deep melting signature, whereas most of the Killara and Narracoota samples have a shallow melting signature.

The overall non-arc melting signature of Figure 5.17b is similar to the interpretation of (Olierook et al., 2018), where mafic magmatism in the southern Capricorn region was related to an intracontinental rift setting. Our results show that while the larger tectonic setting may not have changed, the magmatic history of the southern Capricorn is likely more protracted and complex than once thought (Occhipinti et al., 2017; Occhipinti et al., 1997; Pirajno and Occhipinti, 2000). We suggest a stratigraphic revision should be made, and that a mafic component to the Juderina Formation should be added.

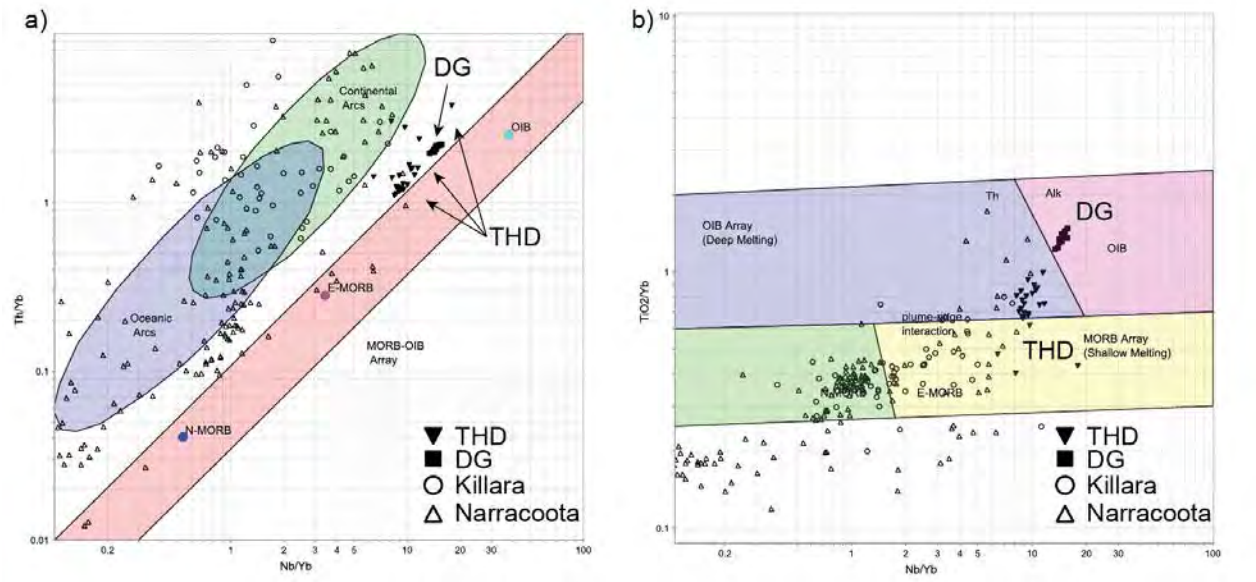

Figure 5.17. Discriminant basalt Th/Yb vs Nb/Yb diagram of mafic geochemistry from the Yerrida Basin.

REE patterns for both the DG and THD samples show these mafic units are un-prospective for VMS-style mineralisation. This was also reported by (Mueller, 2011) for THD001. Both spider diagrams for THD and DG show inclined HREE profiles whereas VMS-prospective rocks show flat HREE profiles and do not show significant negative Eu anomalies (Brown et al., 2002; Hollis et al., 2015; Lesher et al., 1986). An example of a flat HREE pattern from the Golden Grove VMS mine is shown in grey for reference (Hollis et al., 2015).

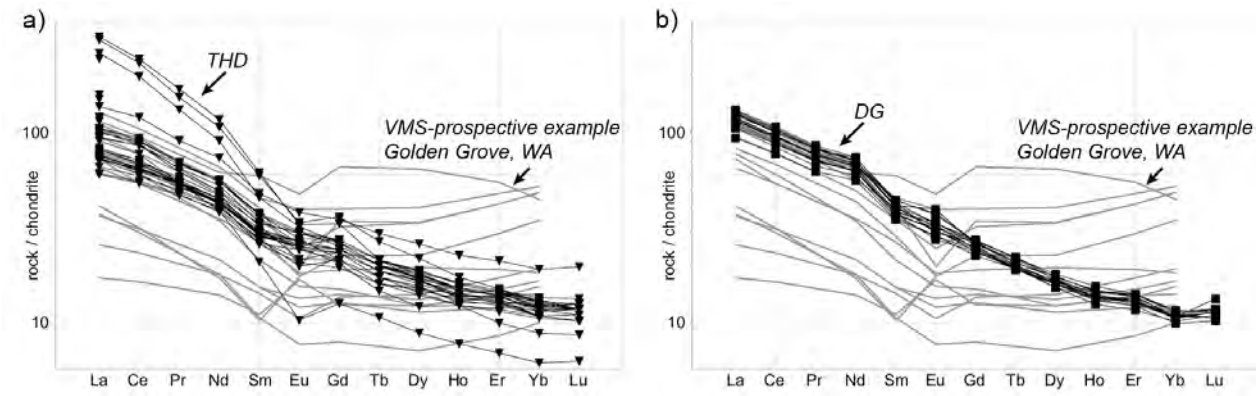

Figure 5.18. REE spider diagrams for mafic rocks sampled from a) THD001 and b) DDGD347. Note the inclined profiles for each indicated a non-prospective environment for VMS mineralisation.

5.6 Conclusions

A comprehensive structural and geophysical study of the Yerrida Basin, southern Capricorn Orogen has been completed. A variety of geophysical, geological and geochemical datasets have been used to achieve a better understanding of basin architecture and magmatic history. Structural interpretation with magnetic data was hindered by low- to no-contrast susceptibility and flat-lying geology, however the AEM data provided by the Capricorn TEMPEST Geophysical Survey gave critical support to lithological interpretation.

A widespread gravity anomaly associated with the sedimentary rocks was investigated and shown to suggest a considerably high density component that could not be explained with current exposure of high density rocks and stratigraphic understanding. The hypothesis that the higher density anomaly may be linked to mafic rock bodies was investigated using a set of forward modelling and inversion techniques. First, a conceptual 3D model around the Goodin Inlier was constructed in a kinematic modelling package to evaluate whether a higher density component was required to recreate the observed gravity response. 3D forward modelling showed that up to a 2000m thick layer of mafic material is required to produce a similar response to the observed response. These results were encouraging, but deemed too simple to adequately test the likely more complex architecture the gravity data represented.

2D section forward modelling was then used to investigate a transect across the Goodin Inlier to test whether intrusions associated with the Killara Formation (such as dykes and sills) were feasible candidates to produce the necessary gravity response. This was confirmed to be possible, so a larger scale 3D model was constructed in an implicit 3D modelling package to test the distribution of high density bodies. A number of gravity inversions were conducted in 3D that progressively added mafic bodies to obtain the most feasible results. Results show that the mafic composition of the Yerrida Basin is significantly larger than is shown on current maps and stratigraphy.

Geochemistry was used to analyse whether mafic units logged in the Juderina Formation from drillcore were the intrusive part of the Killara Formation. A different set of mafic bodies was revealed in both DDGD347 and THD001 cores, suggesting substantial mafic activity associated with the Juderina Formation. We recommend a revision to the stratigraphy of the Yerrida Basin based on these results to better represent the more complex early magmatic history of the southern Capricorn Orogen basins.

5.7 References

Aitken, A.R.A., and Betts, P.G., 2008, High-resolution aeromagnetic data over central Australia assist Grenville-era (1300 Ma-1100 Ma) Rodinia reconstructions: Geophys. Res. Lett., v. 35.

Aitken, A.R.A., and Betts, P.G., 2009, Multi-scale integrated structural and aeromagnetic analysis to guide tectonic models: An example from the eastern Musgrave Province, Central Australia: Tectonophysics, v. 476, no. 3-4, p. 418-435.

Betts, P., Williams, H., Stewart, J., and Ailleres, L., 2007, Kinematic analysis of aeromagnetic data: Looking at geophysical data in a structural context: Gondwana Research, v. 11, no. 4, p. 582-583.

Betts, P.G., Giles, D., and Lister, G.S., 2004, Aeromagnetic patterns of half-graben and basin inversion: implications for sediment-hosted massive sulfide Pb-Zn-Ag exploration: Journal of Structural Geology, v. 26, no. 6-7, p. 1137-1156.

Blewett, R.S., Czarnota, K., and Henson, P.A., 2010, Structural-event framework for the eastern Yilgarn Craton, Western Australia, and its implications for orogenic gold: Precambrian Research, v. 183, no. 2, p. 203-229.

Brown, S.J.A., Barley, M.E., Krapež, B., and Cas, R.A.F., 2002, The Late Archaean Melita Complex, Eastern Goldfields, Western Australia: shallow submarine bimodal volcanism in a rifted arc environment: Journal of Volcanology and Geothermal Research, v. 115, no. 3, p. 303-327.

Burschil, T., Scheer, W., Kirsch, R., and Wiederhold, H., 2012, Compiling geophysical and geological information into a 3-D model of the glacially-affected island of Föhr: Hydrol. Earth Syst. Sci., v. 16, no. 10, p. 3485-3498.

Calcagno, P., Chilès, J.P., Courrioux, G., and Guillen, A., 2008, Geological modelling from field data and geological knowledge: Part I. Modelling method coupling 3D potential-field interpolation and geological rules: Physics of the Earth and Planetary Interiors, v. 171, no. 1-4, p. 147-157.

Costello, M, 2014, The Capricorn 2013 AEM TEMPEST® survey. Managed by Geoscience Australia on behalf of the Geological Survey of Western Australia (GSWA). A contribution to the Distal Footprints of Giant Ore Systems: UNCOVER Australia. Geoscience Australia, Geocat Number: 81642, 3pp.

Dufréchou, G., Harris, L.B., and Corriveau, L., 2014, Tectonic reactivation of transverse basement structures in the Grenville orogen of SW Quebec, Canada: Insights from gravity and aeromagnetic data: Precambrian Research, v. 241, p. 61-84.

Eberle, D., Bastian, D., Ebel, N., and Schwarz, R., 2017, Locating hidden channels for placer gold exploration in the Cariboo District, British Columbia, Canada: A case study: Journal of Applied Geophysics, v. 136, p. 61-79.

González-Álvarez, I., Ley-Cooper, A.Y., and Salama, W., 2016, A geological assessment of airborne electromagnetics for mineral exploration through deeply weathered profiles in the southeast Yilgarn Cratonic margin, Western Australia: Ore Geology Reviews, v. 73, p. 522-539.

Guillen, A., Calcagno, P., Courrioux, G., Joly, A., and Ledru, P., 2008, Geological modelling from field data and geological knowledge: Part II. Modelling validation using gravity and magnetic data inversion: Physics of the Earth and Planetary Interiors, v. 171, no. 1-4, p. 158-169.

Gunn, P., Maidment, D., and Milligan, P., 1995, Interpreting aeromagnetic data in areas of limited outcrop: an example from the Arunta Block, Northern Territory: Exploration Geophysics, v. 26, no. 3, p. 227-232.

Hawke, M.L., Meffre, S., Stein, H., Hilliard, P., Large, R., and Gemmell, J.B., 2015, Geochronology of the DeGrussa volcanic-hosted massive sulphide deposit and associated mineralisation of the Yerrida, Bryah and Padbury Basins, Western Australia: Precambrian Research, v. 267, p. 250-284.

Hollis, S.P., Yeats, C.J., Wyche, S., Barnes, S.J., Ivanic, T.J., Belford, S.M., Davidson, G.J., Roache, A.J., and Wingate, M.T.D., 2015, A review of volcanic-hosted massive sulfide (VHMS) mineralization in the Archaean Yilgarn Craton, Western Australia: Tectonic, stratigraphic and geochemical associations: Precambrian Research, v. 260, p. 113-135.

Jessell, M., 1981, Noddy - an interactive map creation package [MSc: University of London, 52 p.

Jessell, M., Aillères, L., de Kemp, E., Lindsay, M., Wellmann, F., Hillier, M., Laurent, G., Carmichael, T., and Martin, R., 2014, Next generation three-dimensional geologic modeling and inversion: Society of Economic Geologists. Special Publications Series, v. 18, p. 261-272.

Jessell, M.W., and Valenta, R.K., 1996, Structural geophysics: Integrated structural and geophysical modelling, *in* Declan, G.D.P., ed., Computer Methods in the Geosciences, Pergamon, p. 303-324.

Kovesi, P., Phase Preserving Tone Mapping of Non-Photographic High Dynamic Range Images, *in* Proceedings 2012 International Conference on Digital Image Computing Techniques and Applications (DICTA)3-5 Dec. 2012 2012, p. 1-8.

Lesher, C.M., Goodwin, A.M., Campbell, I.H., and Gorton, M.P., 1986, Trace-element geochemistry of ore-associated and barren, felsic metavolcanic rocks in the Superior Province, Canada: Canadian Journal of Earth Sciences, v. 23, no. 2, p. 222-237.

Ley-Cooper, A.-Y., Munday, T., and Ibrahimi, T., 2017, Inversion of the Capricorn Orogeny regional Airborne Electromagnetic (AEM) survey, Western Australia. CSIRO Technical Report EP166290.

Lindsay, M., Aitken, A., Ford, A., Dentith, M., Hollis, J., and Tyler, I., 2016a, Reducing subjectivity in multi-commodity mineral prospectivity analyses: Modelling the west Kimberley, Australia: Ore Geology Reviews, v. 76, p. 395-413.

Lindsay, M.D., Occhipinti, S., Aitken, A.R.A., Metelka, V., Hollis, J. and Tyler, I., 2016b, Proterozoic accretionary tectonics in the east Kimberley region, Australia: Precambrian Research, v. 278, p. 265-282.

Lindsay, M.D., Spratt, J., Occhipinti, S.A., Aitken, A.R.A., Denith, M.C., Hollis, J.A., and Tyler, L.M., 2017, Identifying mineral prospectivity using 3D magnetotelluric, potential field, and geological data in the east Kimberley, Australia: Geological Society of London, v. Advances in characterisation of ore deposits.

Ltd, C. A. A. P., 2014, TEMPEST Geophysical Survey: Capricorn Regional Survey, Western Australia, Volume Project Number CGG Job 2446/GA Job 1265.

Martin, D.M., Hocking, R.M., Riganti, A., and Tyler, I.M., 2016, Geological map of Western Australia, 14th edition - Explanatory Notes: Geological Survey of Western Australia, Record 2015/14.

Mueller, D.H.A., 2011, Final report on drilling of THD001: a 1017.8 m vertical core hole on E52/1673: GSWA reference C144/2005: Sipa Exploration NL.

Occhipinti, S., Hocking, R., Lindsay, M., Aitken, A., Copp, I., Jones, J., Sheppard, S., Pirajno, F., and Metelka, V., 2017, Paleoproterozoic basin development on the northern Yilgarn Craton, Western Australia: Precambrian Research, v. 300, p. 121-140.

Occhipinti, S.A., Grey, K., Pirajno, F., Adamides, N.G., Bagas, L., Dawes, P., and Le Blanc-Smith, G., 1997, Stratigraphic revision of the Palaeoproterozoic rocks of the Yerrida, Bryah and Padbury Basins (formerly Glengarry Basin).

Occhipinti, S.A., Sheppard, S., Passchier, C., Tyler, I.M., and Nelson, D.R., 2004, Palaeoproterozoic crustal accretion and collision in the southern Capricorn Orogen: The Glenburgh Orogeny: Precambrian research, v. 128, no. 3-4, p. 237-255.

Occhipinti, S.A., Swager, C.P., and Pirajno, F., 1998, Structural-metamorphic evolution of the Palaeoproterozoic Bryah and Padbury Groups during the Capricorn orogeny, Western Australia: Precambrian Research, v. 90, no. 3-4, p. 141-158.

Olierook, H.K.H., Sheppard, S., Johnson, S.P., Occhipinti, S.A., Reddy, S.M., Clark, C., Fletcher, I.R., Rasmussen, B., Zi, J.-W., Pirajno, F., LaFlamme, C., Do, T., Ware, B., Blandthorn, E., Lindsay, M., Lu, Y.-J., Crossley, R.J., and Erickson, T.M., 2018, Extensional episodes in the Paleoproterozoic Capricorn Orogen, Western Australia, revealed by petrogenesis and geochronology of mafic–ultramafic rocks: Precambrian Research, v. 306, p. 22-40.

Pearce, J.A., 2008, Geochemical fingerprinting of oceanic basalts with applications to ophiolite classification and the search for Archean oceanic crust: Lithos, v. 100, no. 1, p. 14-48.

Pearce, J.A., 2014, Immobile Element Fingerprinting of Ophiolites: Elements, v. 10, no. 2, p. 101-108.

Perrouty, S., Aillères, L., Jessell, M.W., Baratoux, L., Bourassa, Y., and Crawford, B., 2012, Revised Eburnean geodynamic evolution of the gold-rich southern Ashanti Belt, Ghana, with new field and geophysical evidence of pre-Tarkwaian deformations: Precambrian Research, v. 204-205, p. 12-39.

Peters, B., and Buck, P., 2000, The Maggie Hays and Emily Ann nickel deposits, Western Australia: a geophysical case history: Exploration Geophysics, v. 31, no. 2, p. 210-221.

Pirajno, F., and Adamides, N.G., 2000, Geology and minerlization of the Palaeoproterozoic Yerrida Basin, Western Australia, Western Australia Geological Survey, Report 60, p. 43.

Pirajno, F., Burlow, R., and Huston, D., 2010, The Magellan Pb deposit, Western Australia; a new category within the class of supergene non-sulphide mineral systems: Ore Geology Reviews, v. 37, no. 2, p. 101-113.

Pirajno, F., and Occhipinti, S.A., 1998, Geology of the Bryah 1:100 00 sheet.: Geological Survey of Western Australia.

Pirajno, F., and Occhipinti, S.A., 2000, Three Palaeoproterozoic basins-Yerrida, Bryah and Padbury-Capricorn Orogen, Western Australia: Australian Journal of Earth Sciences, v. 47, no. 4, p. 675-688.

Roach, I.C., Jaireth, S., and Costelloe, M.T., 2014, Applying regional airborne electromagnetic (AEM) surveying to understand the architecture of sandstone-hosted uranium mineral systems in the Callabonna Sub-basin, Lake Frome region, South Australia: Australian Journal of Earth Sciences, v.61, no.5, p.659-688.

Schamper, C., Jørgensen, F., Auken, E., and Effersø, F., 2014, Assessment of near-surface mapping capabilities by airborne transient electromagnetic data — An extensive comparison to conventional borehole data: GEOPHYSICS, v. 79, no. 4, p. B187-B199.

Sheppard, S., Occhipinti, S.A., and Tyler, I.M., 2004, A 2005-1970 Ma Andean-type batholith in the southern Gascoyne Complex, Western Australia: Precambrian Research, v. 128, no. 3-4, p. 257-277.

Talwani, M., and Heirtzler, J.R., 1964, Computation of magnetic anomalies caused by two-dimensional bodies of arbitrary shape, *in* Parks, G.A., ed., Computers in the Mineral Industries: Stanford University, School of Earth Sciences, p. 464-480.

Talwani, M., Worzel, J.I., and Landisman, M., 1959, Rapid gravity computations for twodimensional bodies with application to the Mendicino submarine fracture zone: Journal of Geophysical Research, v. 64, p. 49-59.

Appendix 5.1 – Forward Model Constraints

The following data aided construction of the forward model shown in Figure 5.11.

Distance SOP m	Structure	Name	Rock W	Rock E
0	***SOP***			
550	Fault	Jenkin Fault	Narracoota	Karalundi
1600	Fault	Murchison Fault	Karalundi	Karalundi
6600	Fault	Goodin Fault	Karalundi	Doolgunna
8150	Contact		Doolgunna	Mt Leake
10350	Contact		Mt Leake	Doolgunna
11100	Contact		Doolgunna	Johnson Cairn
11750	Fault		Johnson Cairn	Johnson Cairn
13150	Fault		Johnson Cairn	Johnson Cairn
13250	Contact		Johnson Cairn	Juderina
13550	Contact		Juderina	Johnson Cairn
14150	Fault		Johnson Cairn	Johnson Cairn
18600	Fault		Johnson Cairn	Johnson Cairn
21900	Contact		Johnson Cairn	Juderina
23000	Contact		Juderina	Goodin Inlier
25000	Fault		Goodin Inlier	Goodin Inlier
25500	Fault		Goodin Inlier	Goodin Inlier
26150	Fault		Goodin Inlier	Goodin Inlier
32000	Fault		Goodin Inlier	Goodin Inlier
32250	Fault		Goodin Inlier	Goodin Inlier
33750	Fault		Goodin Inlier	Goodin Inlier
40550	Contact		Goodin Inlier	Juderina (mag)
41800	Contact		Juderina (mag)	Johnson Cairn
45500	Fault		Johnson Cairn	Johnson Cairn
45800	Contact		Johnson Cairn	Doolgunna
50000	Fault		Doolgunna	Doolgunna
53300	Contact		Doolgunna	Killara
53800	Contact		Killara	Doolgunna
55000	***EOP***			